

**Bangor University**

**DOCTOR OF PHILOSOPHY**

**Seabed Integrity Around Objects in a Complex Marine Environment**

Yiannoukos, Irinios

*Award date:*  
2022

*Awarding institution:*  
Bangor University

[Link to publication](#)

#### **General rights**

Copyright and moral rights for the publications made accessible in the public portal are retained by the authors and/or other copyright owners and it is a condition of accessing publications that users recognise and abide by the legal requirements associated with these rights.

- Users may download and print one copy of any publication from the public portal for the purpose of private study or research.
- You may not further distribute the material or use it for any profit-making activity or commercial gain
- You may freely distribute the URL identifying the publication in the public portal ?

#### **Take down policy**

If you believe that this document breaches copyright please contact us providing details, and we will remove access to the work immediately and investigate your claim.

Download date: 25. Apr. 2024

**Bangor University**

**DOCTOR OF PHILOSOPHY**

**Seabed Integrity Around Objects in a Complex Marine Environment**

Yiannoukos, Irinios

*Award date:*  
2022

[Link to publication](#)

#### **General rights**

Copyright and moral rights for the publications made accessible in the public portal are retained by the authors and/or other copyright owners and it is a condition of accessing publications that users recognise and abide by the legal requirements associated with these rights.

- Users may download and print one copy of any publication from the public portal for the purpose of private study or research.
- You may not further distribute the material or use it for any profit-making activity or commercial gain
- You may freely distribute the URL identifying the publication in the public portal ?

#### **Take down policy**

If you believe that this document breaches copyright please contact us providing details, and we will remove access to the work immediately and investigate your claim.

Download date: 13. Sep. 2022

# Seabed Integrity Around Objects in a Complex Marine Environment

Irinios Yiannoukos



PRIFYSGOL  
**BANGOR**  
UNIVERSITY

School of Ocean Sciences  
College of Environmental Sciences and Engineering

A thesis submitted in partial fulfilment of the requirements for the  
Degree of Doctor of Philosophy in Ocean Sciences.

Supervisors: Dr. Katrien J. J. Van Landeghem, Dr. Michael Roberts, Dr. Amelia Couldrey  
and Dr. Rory Quinn

6<sup>th</sup> July 2022





## Declaration and Consent

### Details of the Work

I hereby agree to deposit the following item in the digital repository maintained by Bangor University and/or in any other repository authorized for use by Bangor University.

**Author Name:** Irinios Yiannoukos

**Title:** Seabed Integrity Around Objects in a Complex Marine Environment

**Supervisor/Department:** Dr Katrien Van Landeghem, School of Ocean Sciences

**Funding Body:** Knowledge Economy Skills Scholarships (KESS 2)

**Qualification/Degree Obtained:** Doctor of Philosophy

This item is a product of my own research endeavours and is covered by the agreement below in which the item is referred to as “the Work”. It is identical in content to that deposited in the Library, subject to point 4 below.

### Non-exclusive Rights

Rights granted to the digital repository through this agreement are entirely non-exclusive. I am free to publish the Work in its present version or future versions elsewhere.

I agree that Bangor University may electronically store, copy or translate the Work to any approved medium or format for the purpose of future preservation and accessibility. Bangor University is not under any obligation to reproduce or display the Work in the same formats or resolutions in which it was originally deposited.

### Bangor University Digital Repository

I understand that work deposited in the digital repository will be accessible to a wide variety of people and institutions, including automated agents and search engines via the World Wide Web.

I understand that once the Work is deposited, the item and its metadata may be incorporated into public access catalogues or services, national databases of electronic theses and dissertations such as the British Library’s EThOS or any service provided by the National Library of Wales.

### **Statement 1**

This work has not previously been accepted in substance for any degree and is not being concurrently submitted in candidature for any degree unless as agreed by the University for approved dual awards.

Signed: (Irinios Yiannoukos)

Date: 06/07/2022

### **Statement 2**

This thesis is the result of my own investigations, except where otherwise stated. Where correction services have been used, the extent and nature of the correction is clearly marked in a footnote(s). All other sources are acknowledged by footnotes and/or a bibliography.

Signed: (Irinios Yiannoukos)

Date: 06/07/2022

### **Statement 3**

I hereby give consent for my thesis, if accepted, to be available for photocopying, for interlibrary loan and for electronic repositories, and for the title and summary to be made available to outside organisations.

Signed: (Irinios Yiannoukos)

Date: 06/07/2022

### **Statement 4**

I agree to deposit an electronic copy of my thesis (theWork) in the Bangor University (BU) Institutional Digital Repository, the British Library EThOS system, and/or in any other repository authorized for use by Bangor University and where necessary have gained the required permissions for the use of third-party material.

**In addition to the above, I also agree to the following:**

1. That I am the author or have the authority of the author(s) to make this agreement and do hereby give Bangor University the right to make available the Work in the way described above.
2. That the electronic copy of the Work deposited in the digital repository and covered by this agreement, is identical in content to the paper copy of the Work deposited in the Bangor University Library, subject to point 4 below.
3. That I have exercised reasonable care to ensure that the Work is original and, to the best of my knowledge, does not breach any laws – including those relating to defamation, libel and copyright.
4. That I have, in instances where the intellectual property of other authors or copyright holders is included in the Work, and where appropriate, gained explicit permission for the inclusion of that material in the Work, and in the electronic form of the Work as accessed through the open access digital repository, or that I have identified and removed that material for which adequate and appropriate permission has not been obtained and which will be inaccessible via the digital repository.
5. That Bangor University does not hold any obligation to take legal action on behalf of the Depositor, or other rights holders, in the event of a breach of intellectual property rights, or any other right, in the material deposited.
6. That I will indemnify and keep indemnified Bangor University and the National Library of Wales from and against any loss, liability, claim or damage, including without limitation any related legal fees and court costs (on a full indemnity bases), related to any breaches by myself of any term of this agreement.

Signed:

Date: 06/07/2022



## Acknowledgments

I would like to express my deepest gratitude to my supervisors, Katrien Van Landeghem, Amelia Couldrey, Rory Quinn and Michael Roberts for their guidance and support throughout my PhD. You all gave me great confidence to follow my intuition whilst helping to improve my skills. My PhD committee, Martin Austin and Jaco Baas, you have been very supportive throughout this process, thank you for your encouragement. I would also like to thank KESS2 for providing the studentship funding. I am also grateful to the company partner of this project, HR Wallingford and especially to Thomas Benson and Richard Whitehouse for supporting me throughout the project and for hosting me during a nine-month placement.

An acknowledgement of support and thanks are also extended, in no particular order, to: Connor McCarron for his great support and guidance throughout my PhD project; Ben Lincoln, Jonathan Malarkey, Brian Scannel for their support and guidance at different steps of this project; Steven Rowlands and Jim Bennel for processing the MBES data and providing guidance and support for the processing of backscatter data; Cathy Blakey for her time on storing and retrieving the MBES data; Timothy Witton, Tim D'Urban Jackson and Margot Saher for their support while collecting the grab samples around *SS Apapa*; the crew of *RV Prince Madog* for their support and patience during the offshore surveys; Sean Hoban, Jacob Morgan and Barney Clayton for their assistance in the flume lab; Ian Pritchard and Robert Evans for providing support to ensure the flume experiments ran smoothly; Dei Huws for his guidance and support and Intertek Energy and Water Consultancy Services for allowing me the time to finish and submit my thesis. To the office and lunchtime group at the School of Ocean Sciences, spending time with you was always great! Brad, Nia, Meg, Ed, Katie, Kate, Yueng, Gareth, Ben, Tom – thank you for everything! I would also like to thank Jonathan Beaudoin for his expertise advice and guidance on using the FMGT software.

To Maria, thank you for your support and patience throughout this journey. I can't imagine completing this journey without your motivation, company and support that always kept me going!

Finally, I would like to dedicate this thesis to parents, my family and in loving memory of my grandparents, who throughout my life, have provided me with support, love, guidance, and determination to set and achieve my goals.



## Abstract

The ever-increasing need for seabed infrastructure enabling offshore energy extraction and storage requires accurate prediction of erosion and deposition rates of the surrounding seafloor sediments. Seabed erosion and deposition (scour) can become catastrophic for the infrastructure itself but also for the surrounding habitats. Scour predictors largely assume that the bed is composed of unimodal sediments and objects have simple shapes. In mixed non-cohesive beds, however, complexity in the sediment transport process, including the hiding exposure (HE) effect, will likely impact the seabed erosion and deposition. Better understanding of scour dynamics in more complex settings can improve the ability to predict scour development around differently shaped objects sitting on mixed and coarse beds, which are ubiquitous in palaeo-glaciated environments, for instance.

In this work, the scour development around the 135 m long wreck of the ship *SS Apapa* was investigated through time-lapse analyses of multi-beam echosounder surveys over nine years (co-registered bathymetry and backscatter intensity), hydrodynamic measurements and sediment samples. Due to the interaction between the tidal flow and the wreck, flow velocities increased by about ~2.3 times downstream of the wreck, with the highest amplifications where an undisturbed flow first encounters the wreck. The extent of flow disturbance in the wake of the wreck measured between 0.76 and 2.3 times the length of the wreck, with the highest disturbance at slack tides. Vertical flow disturbance of up to 1.66 times the height of the wreck (17.5 m) was also identified directly over the wreck, with nearly a doubling of flow velocities. Laterally, a flow diversion of 90° was identified directly over the wreck. Two consistent ‘zones of bed mobility’ exist at either side of the wreck, at distances between 0.27 and 1 times the length of the wreck. The extent of these zones was identified by a drop in the bed mobility accompanied by a reduction of the flow speed between 30% and 35% when compared to the undisturbed background flow. The seafloor at the *SS Apapa* area was composed of mixed coarse sediment, with coarser material present in the deepest parts of the scour mark and finer material present at the depositional features. MBES datasets (bathymetric and backscatter) showed that the depositional feature remained fine over the years but was the most variable in bathymetry. Large variations in bed composition were also observed at the deepest points of the scour mark, where bathymetry varied less over time. A disintegration and shifting of *SS Apapa* between March 2018 and June 2019 changed the exposure of the wreck to the flow at the north-east and north-west sides of the wreck. This altered the hydrodynamics of the area and subsequently changed the erosional and depositional trends observed until 2018.

To investigate the role of the sediment mixture in scour dynamics in more detail, flume laboratory experiments were conducted with two flow speeds over a 9.4 cm long cylinder on a bed, using six sand and gravel mixtures, pure sand, and pure gravel. One lower flow speed mobilised just the sand fraction, whilst a higher flow speed mobilised both the sand and gravel fractions. The bed was acoustically scanned three times for each run and sediment cores were taken to analyse changes to bed composition laterally and with depth. For the lower flow, mobilising only the sand fraction, the scour mark was 66.4% longer, 12.1% deeper and 4.8% wider in a bed composed of 20% gravel and 80% sand, when compared to the pure sand bed. At the higher flow speed, mobilising both fractions,

the scour mark was 43.6% longer, 40.9% wider and 13% deeper in beds containing 12.5%, 5% and 20% gravel respectively, when compared to the pure sand bed. Two 'zones of bed mobility' emerged in the wake of the object. At the lower flow velocity, they sat at a mean distance of 2.6 and 9 times the object's length, with the first and second zones being longer for the bed consisting of 15% gravel (~4 times the object's length) and 12.5% gravel (10.7 times the object's length) respectively. At the higher flow velocity, the two zones sat at a mean distance of 2.2 and 8.6 times the length of the object with the first and second zones being longer for the bed consisting of 20% gravel (2.5 times the object's length) and 12.5% gravel (10.8 times the object's length) respectively.

To up-scale the application of all these offshore and laboratory findings, a model is needed where the parameters can be changed and scour in complex settings (in term of object shape and bed composition) can be predicted with better confidence. A coupled numerical hydrodynamic and sediment transport model (TELEMAC3D – GAIA) was therefore modified and used to replicate the SS *Apapa* site and the laboratory environment. An existing hiding-exposure correction was used in the sediment transport component of the model. The outputs of the model include hydrodynamic, bathymetric, bedload and suspended load information, and these were compared with the real-world analyses of flow modification and bed mobility, both offshore and in the laboratory. The modelled flow modifications around the wreck, deviated between 3% and 15% from the observations, while the modelled flow modifications around the cylinder in the lab experiments deviated less than 4% from the observations. The modelled scour extent for both the wreck and the cylinder measured withing 0-27% of the observations. The numerical model appeared to have difficulties in predicting the scour formation in the cases of the bed consisting of less than 10% gravel in the higher current speed but predicted well the scour mark formation for over 93% of the modelling work using different sediment mixtures. This gave confidence in the model to model the impact of changes to the object's exposure and the bed's composition. The numerical model has produced a 66% longer scour mark when increasing the object's exposure to the flow by 10% in the case of the laboratory work. The numerical model has also identified an increase in the produced turbulent kinetic energy of 33% when doubling the exposure of SS *Apapa* to the flow.

This knowledge and increased model capability should enable developers to find solutions where the impact on the bed is minimised. The results should also aid the design and extent for scour for scour protection, again minimising enhanced bed mobility and the associated costs from habitat loss and damage to the infrastructure.



# Contents

Declaration and Consent .....	i
Details of the Work .....	i
Non-exclusive Rights .....	i
Bangor University Digital Repository .....	i
Acknowledgments .....	v
Abstract .....	v
Contents .....	vii
List of Figures .....	xi
List of Tables .....	xx
Abbreviations .....	xxi
Notation .....	xxiii
Chapter 1 .....	1
1. Introduction .....	1
1.1 Overview and motivation .....	1
1.1.1 Seabed mobility effects on offshore development .....	2
1.1.2 Shipwrecks as relevant study objects .....	4
1.2 Flow around seabed objects, including shipwrecks .....	8
1.2.1 Amplification of flow .....	10
1.2.1.1 Shear stress .....	10
1.2.2 Complexities of flow around shipwrecks .....	11
1.3 Sediment transport and bedform migration on mixed beds .....	13
1.3.1 Sediment transport around seabed objects .....	16
1.3.2 Scour around shipwrecks .....	18
1.3.3 Complexity of scour in mixed sediments .....	21
1.4 Aims, Objectives and Outline .....	23
Chapter 2 .....	24
2. Materials and Methods .....	24
2.1 Methods used to address the aims of the project .....	24
2.2 High-resolution offshore data collection documenting processes around shipwrecks .....	24
2.2.1 Data collection platform and team .....	24
2.2.2 Seabed topography and backscatter strength – Multi Beam Echo Sounder (MBES) .....	25
2.2.3 Hydrodynamic monitoring - Acoustic Doppler Current Profiler (ADCP) .....	25
2.2.4 Seabed surface sediment sampling – Shipek grab sampler .....	26
2.2.5 Sediment Particle Size Analyses (PSA) of offshore grab samples .....	28
2.3 Flume Laboratory experiments of processes around a cylindrical object .....	29
2.3.1 Armfield recirculating flume experiments .....	29
2.3.2 Making different beds – sediment mixture preparation .....	29
2.3.3 High resolution bed topography – SeaTek Acoustic Bed Scanner .....	30
2.3.4 High resolution hydrodynamic monitoring - METFLOW Ultrasonic Doppler Velocity Profiler (UDVP) .....	31
2.3.5 Flume bed sediment “coring” .....	32

2.3.6 Sediment Particle Size Analyses (PSA).....	32
2.4 Numerical Modelling of flow and bed evolution around objects placed on mixed beds .....	33
2.4.1 Hydrodynamic model – TELEMAC-3D.....	33
2.4.2 Sediment transport model - GAIA .....	34
2.4.3 Coupled model (TELEMAC3D – GAIA) .....	35
Chapter 3 .....	37
3. How the shape of the wreck and the composition of the bed defines the scour around a wreck – A time lapse study over 8 years.....	37
3.1 Introduction .....	37
3.1.1 Aims and Objectives .....	41
3.1.2 SS <i>Apapa</i> and its environment .....	42
3.2 Methodology of identifying processes around SS <i>Apapa</i> .....	44
3.2.1 Monitoring flow amplifications .....	44
3.2.2 Time lapse analyses of the scour edge.....	50
3.2.3 Bed evolution changes within the scour marks .....	54
3.2.4 Time lapse analyses of bed composition using repeated MBES backscatter strength data .....	56
3.2.5 Sediment sample collection at the SS <i>Apapa</i> site using a seabed surface grab sampler (Shipek).....	60
3.2.6 Reconstructing the evolving wreck environment using a coupled Hydrodynamic and sediment transport model (TELEMAC3D – GAIA) .....	64
3.2.6.1 Reconstructing a pre-wreck artificial bed scenario.....	64
3.2.6.2 Reconstruction of the submerged object (wreck) in the model .....	66
3.2.6.3 Computational domain and mesh.....	66
3.2.6.4 Bedload transport formulation in GAIA .....	67
3.2.6.5 Hydrodynamic information used as input for the coupled model.....	68
3.3 Results.....	70
3.3.1 Observed flow velocities and flow amplification in the wake of the wreck .....	70
3.3.2 Observed evolution of scour mark geometry.....	75
3.3.2.1 Observed bathymetric changes within the scour mark .....	79
3.3.3 Observed evolution of bed composition in the scour mark .....	87
3.3.4 Modelled evolution of flow amplification, scour geometry and composition .....	100
3.4 Discussion .....	106
3.4.1 The role of bedforms near the SS <i>Apapa</i> site .....	106
3.4.2 Scour defined by bed composition.....	111
3.4.3 Disintegration of SS <i>Apapa</i> changing erosion and deposition .....	112
3.4.4. Numerical modelling of the SS <i>Apapa</i> site using a coupled TELEMAC 3D – GAIA model .....	114
3.5 Conclusions .....	115
Chapter 4 .....	117
4. How the effective transport of sedimentary beds composed from different sand/gravel mixtures defines the scour development around a cylindrical object – Laboratory experiments .....	117
4.1 Introduction .....	117
4.1.1 Aims and Objectives .....	119

4.2 Methodology of identifying processes around the object in the lab .....	120
4.2.1 The controlled laboratory environment.....	120
4.2.2 Experimental design .....	120
4.2.2.1 Flow velocities used in the laboratory experiments .....	124
4.2.2.2 Initiation and development of scour monitoring .....	125
4.2.3 Scour edge delineation and bed evolution .....	126
4.2.4 Monitoring flow amplification via bed mobility .....	127
4.2.5 Monitoring bed composition via down-core analyses of bed samples .....	129
4.2.6 Reconstructing the evolving flume bed environment using a coupled Hydrodynamic and Sediment transport model (TELEMAC3D – GAIA).....	130
4.3 Results.....	135
4.3.1 Observed flow amplification in the wake of the object.....	135
4.3.1.1 Flow amplification monitoring via bed mobility and bedform formation .....	136
4.3.1.2. Observed bathymetric changes downstream of the object ('zones of influence') ..	144
4.3.2 Observed evolution of scour mark geometry.....	145
4.3.3 Object's movement during the laboratory experiments .....	150
4.3.4 Observed evolution of bed composition (laterally and with depth) .....	151
4.3.5 Modelled evolution of flow amplification, scour geometry and bed composition .....	158
4.4 Discussion .....	166
4.4.1 Flume bed dynamic equilibrium .....	166
4.4.2 Impact of unintended object movement during experiments .....	168
4.4.3 Scour geometry changes with bed composition.....	170
4.4.4 The evolution of bed composition in amplified ripple development.....	172
4.5 Conclusions .....	174
Chapter 5 .....	176
5. Discussion.....	176
5.1 Highlights of the observations and aims of this discussion chapter.....	176
5.2 Impact of object's exposure, shape, and orientation on scour evolution .....	177
5.2.1 Impact of different exposure of the object to the evolution of scour.....	178
5.2.2 Impact of gradual changes in exposure of object to the evolution of scour .....	186
5.2.3 Impact of different orientation and shape of the object to the evolution of scour .....	188
5.3 Impact of mixed sediment composition on scour evolution around an object.....	190
5.3.1 Sediment composition around <i>SS Apapa</i> .....	190
5.3.1.1 Erosion and deposition around a wreck, guided by bed composition.....	191
5.3.2 Quantifying bed mobility of bimodal sediment fractions around the object .....	197
5.4 Implications for better predicting scour around complex objects in mixed beds .....	203
5.4.1 Anthropogenic infrastructure and scour .....	203
5.4.2 Object's shape and exposure to the flow influencing the scour mark formation .....	204
5.4.3 Implications for seabed stability and preservation.....	205
Chapter 6 .....	207
6 Summary and Synthesis.....	207
6.1 Brief summary of the rationale behind this research.....	207
6.2 Answer to the questions asked .....	207

Where is flow modification around the object strongest? .....	207
What is the lateral extent of flow amplification in relation to object size and background hydrodynamics? .....	209
How does a change in the object's shape impact flow modification (strength and extent) and how does that change impacts the evolution of scour? .....	210
How does the amplified flow downstream of the object impact the sediment movement of mixed coarse (sand and gravel) beds? .....	210
How does the mixed sediment composition impact scour evolution at different levels of grain entrainment? .....	211
For which bimodal non-cohesive sediment mixture will the scour be the greatest (in terms of depth and extent)? .....	211
Using more appropriate statistics of particle size distribution of mixed beds, which of those parameters will allow for the spatial extent of scour formation to be best predicted? .....	212
6.3 Summary of implications of this work .....	212
6.4 Recommendations for future research into flow and bed dynamics in complex seabeds....	213
7 References.....	216
8 Appendices .....	230
A. Multi-beam Echosounder (MBES) Specifications .....	230
B. Acoustic Doppler Current Profiler (ADCP) Specifications .....	234
C. Ultra-Short BaseLine (USBL) instrument specifications .....	236
D. Boud Minerals Technical Specification .....	239
E. Dean Tranter Technical Specification .....	241
F. IBM Implementation in TELEMAC.....	242
G. HE Implementation in TELEMAC .....	284

## List of Figures

Figure 1.1: Seabed sediment type around the UK from the British Geological Survey (BGS) through the Edina Digimap website ( <a href="https://digimap.edina.ac.uk/">https://digimap.edina.ac.uk/</a> ; DiGSBS250K, 2011).....	2
Figure 1.2: Scour depth (S) over Monopile diameter (D) as observed for five offshore marine renewable sites around the United Kingdom (Whitehouse et al., 2008).....	3
Figure 1.3: a) Distribution of ~14000 wrecks around the United Kingdom of Great Britain and Northern Ireland. The bathymetric data and Digital Terrain Model (DTM) data have been derived from the EMODned Bathymetry portal ( <a href="https://www.emodnet-bathymetry.eu/data-products">https://www.emodnet-bathymetry.eu/data-products</a> ). Wreck locations are sourced from the United Kingdom Hydrographic Office (UKHO) wrecks database ( <a href="https://datahub.admiralty.co.uk">https://datahub.admiralty.co.uk</a> ). b) Histogram showing the population of wrecks (number of wrecks) at each depth range. ....	5
Figure 1.4: Seabed sediment type at $n=11107$ shipwreck locations, with depths ranging between 0 and 200 m around the UK. The information about the seabed sediment type was taken from the British Geological Survey (BGS) through the Edina Digimap website ( <a href="https://digimap.edina.ac.uk/">https://digimap.edina.ac.uk/</a> ; DiGSBS250K, 2011). Wreck locations are sourced from the United Kingdom Hydrographic Office (UKHO) wrecks database ( <a href="https://datahub.admiralty.co.uk">https://datahub.admiralty.co.uk</a> ).....	6
Figure 1.5: Worldwide distribution of potentially polluting shipwrecks (DEEPP, 2007). ....	7
Figure 1.6: Explanation of vortex development and flow patterns around objects placed on the bed (Quinn, 2006 (bottom); Melville, 2008 (top)). ....	9
Figure 1.7: Schematic illustration of flow characteristics along the cross-sectional velocity profile (Van Rijn, 1993a). ....	10
Figure 1.8: Vessel at $60^\circ$ to the flow. a) 2-D flowlines, b) 3-D flowlines, c) flow velocity, d) pressure, e) wall shear stress (WSS) and f) turbulent kinetic energy (TKE) as derived from the CFD model (Quinn & Smyth, 2018). ....	12
Figure 1.9: The Shield's curve (Adapted from Sutherland & Soulsby (2011)) ....	14
Figure 1.10: Representation of global and local scour development around an offshore structure (Whitehouse, 1998). ....	18
Figure 1.11: Scour around shipwrecks because of different orientation to the flow and different type of flow (Quinn, 2006). ....	19
Figure 1.12: Erosional and depositional patterns around fully submerged shipwrecks as inferred from the output of Computational Fluid Dynamic models (Quinn & Smyth, 2018). ....	20
Figure 1.13: Schematic illustration of critical shear stress ( $\tau$ ) needed to mobilise fine and coarse material of a bimodal mixture (McCarron, 2019). ....	22
Figure 2.1: <i>RV Prince Madog</i> .....	25
Figure 2.2: Wildco 860-A10 grab sampler when retrieved with sediment. (source: <a href="http://attleborobio.blogspot.com/">http://attleborobio.blogspot.com/</a> ). ....	26
Figure 2.3: Schematic illustration of sample deviation for attaining the four sub-samples (a) and presence of seaweed in one of the samples (as an example) indicating undisturbed surface sediment (b). ....	27
Figure 2.4: Histogram of residuals produced from the USBL manufacturer's operating software for the estimation of the average error at the positioning of the grab samples. ....	27
Figure 2.5: Full half phi sieve stack from $-4.49 \Phi$ to $3.99 \Phi$ (a) and a schematic illustration of the two stacks used while mechanically shaking the sediment samples (b). ....	28
Figure 2.6: Endecott's Octagon 200 vibratory sieving machine used for PSA of sediment samples. ....	28
Figure 2.7: Schematic illustration of the experimental setup .....	29
Figure 2.8: Array of 24 transducers used for perpendicular to the flow scans (a) and array of 16 transducers used for parallel to the flow scans to record bedform development and migration rates during the laboratory experiments (b). ....	31
Figure 2.9: Syringe used for down-core sampling of the sediment bed in the flume.....	32
Figure 2.10: Schematic illustration of the stack of sieves used for PSA of the sediment samples collected during the laboratory experiments. ....	33
Figure 3.1: Welsh territorial waters strategic resource areas (Crown Estate, 2019). ....	37
Figure 3.2: Interaction of BS acoustic signal interacting by roughness (surface) or by volume (beneath surface) scattering (Wang et al., 2021). ....	39
Figure 3.3: SS <i>Apapa</i> (source: <a href="https://uboatproject.wales/wrecks/apapa/">https://uboatproject.wales/wrecks/apapa/</a> ).....	42
Figure 3.4: Seabed sediment type characterisation based on Folk (1957) (source: Edina Digimap (DiGSBS250K), 2011). ....	42

Figure 3.5: Tidal Ellipse produced when using the POLCOMS model via the Polpred software for a full year in 2014. ....	43
Figure 3.6: Dominant bedload transport directions in the Irish Sea (Van Landeghem et al., 2009). ....	44
Figure 3.7: The area around SS <i>Apapa</i> . An area of large bedforms present at the west of the wreck. ....	44
Figure 3.8: ADCP survey planning around the SS <i>Apapa</i> site to monitor changes in the hydrodynamics caused due to the presence of the wreck. The numbered points are the way points given to the crew of RV <i>Prince Madog</i> for accurate navigation. b) Tidal curve (tidal heights) from the Amlwch tide gauge during data collection and annotation of the ADCP transects during the survey, with a colour code also adapted in the map in Figure 3.8a. ....	45
Figure 3.9: Schematic illustration of a vessel-mounted ADCP (Ya-ping et al., 2000). ....	46
Figure 3.10: An example of the 4 ADCP beams (tidally corrected) over time (for one transect) to identify areas that all four beams were covering. ....	46
Figure 3.11: Flow velocity recorded from the ADCP instrument after the dataset was corrected for bottom tracking. Solid black line indicates a cut-off point, with anything below cleaned (erased) as not all four beams were projecting at the same point. ....	47
Figure 3.12: Surveyed transect from west to east (a) and comparison between the depth recorded from the ADCP and the depth at the same locations from the MBES (b). ....	47
Figure 3.13: Direct comparison via plotting the two sample populations against each other. The red line indicates the trendline of the comparison of the two sample populations. ....	48
Figure 3.14: Boxplots for comparison of depth of last bin of ADCP data after the correction and MBES data; For measurements at all depths (a), for depths deeper than -42.5 m (b) and for depths shallower than -42.5 m. The solid horizontal red line in the Box indicates the median for each sample and the boxes indicate the 25 <sup>th</sup> and 75 <sup>th</sup> percentiles. The whiskers (horizontal black solid lines) indicate the minimum and maximum values, where the red crosses indicate the extreme values of the measurements. ....	48
Figure 3.15: Tidal current as recorded from the ADCP instrument for one of the W-E transects. a) Presented in ArcGIS with the arrows indicating the depth averaged current velocity ( $\bar{U}$ ) and the orientation indicating the tidal current direction, b) short time average (STA) of the same transect (every 10 s), c) tidal current velocity plotted in MatLab, showing the variation both laterally and in depth. ....	50
Figure 3.16: Methods used in ArcMap aiming to identify the edge of the scour mark to test for lateral changes. a) contour, b) aspect and c) slope of the DEM. ....	51
Figure 3.17: Matlab interface (Image Analyst, 2021) used for image analysis for the identification of the scour edge. ....	52
Figure 3.18: 2-D profile positions (every 5 m) over the SS <i>Apapa</i> site that were later plotted for the identification of the scour edge. ....	53
Figure 3.19: Plot of one of the 2-D profiles over SS <i>Apapa</i> used for the identification of the scour edge (red arrows). ....	53
Figure 3.20: a) Profile following the depositional feature, b) bathymetric differences between consecutive datasets over the profile of (a) using the difference maps from the surveys mentioned in the legend and c) profiles used to identify drops in the bathymetric difference DEMs. ....	56
Figure 3.21: Explanation of the two modes of collecting the backscatter data (a; snippet and b; SSS-like) using the PDS2000 software window. c) the central unit of the MBES framework and the green line indicates the bottom profile ensonified by the MBES. The snippet and MBES data are logging at the same horizontal range (yellow line A), whereas the SSS-like data are logging including the whole central unit range, with the horizontal range including the distance from the transducer to the seabed (water column; red line D) and the range of acquisition (blue line B), along with null data (orange line C; Innangi et al., 2015). ....	57
Figure 3.22: Signal penetration <i>versus</i> mean grain size. Signal penetration calculated from empirical equations for acoustic attenuation in marine sediments. The Folk classes approximately assigned to the relative mean grain sizes: sG (sandy gravel), (g)mS (slightly gravelly muddy sand), mS (muddy sand), (g)M (slightly gravelly mud), sC (sandy clay) and C (clay) (Gaida et al., 2018). ....	58
Figure 3.23: BS angular response for a small patch of the seafloor. Gray line is the original observation where the solid black line is the BS angular response after application of all geometric corrections (with nadir at 80°). ....	59
Figure 3.24: Average BS curves for three types of sediment (Chotiros, 2006). ....	59
Figure 3.25: The working principle of BS measurements and interpretation. a) A swath pattern of incidence waves (marked with yellow on c, e), generated reflection (dark blue on e), scattered (light	

blue on e), backscattered (red on c-f) and transmitted (green on e) eaves. b) The backscatter echo intensity dependence on the incidence angle on the seafloor. A soft or flat seafloor (c) will generate a different angular dependence (d) than a rough or rocky interface (e, f) (Lamarche & Lurton, 2018).	60
Figure 3.26: Planned locations for grab samples collected around the area of SS <i>Apapa</i> .	61
Figure 3.27: Depth recorded from the USBL instrument (with drops showing sampling points) during grab sampling plotted against time.	62
Figure 3.28: Example of a bimodal sediment distribution (the two modes and the sample $d_{50}$ are indicated on the plot) showing that $d_{50}$ value is not representative of the bimodal sample.	63
Figure 3.29: Process of generating a pre-wreck situation DEM to use for the simulation of the initial scour development in the coupled numerical TELEMAC3D – GAIA model. a) the 2017 DEM, b) the 2019 DEM, c) the 2017 DEM without the extent of the 2019 DEM, d) the 2017 DEM merged with the 2019 DEM, e) the 2017 DEM with the 2019 state of the sandwave at the south and interpolated flat-bed over the scour mark, f) the flat bed without the wreck as it was in the 2012 DEM, g) the flat ‘pre-wreck’ bed with the state of the wreck in the 2012 DEM (g <sub>i</sub> ) and h) the flat ‘pre-wreck’ bed with the position of the wreck in the 2012 DEM elevated by 8m to sit on top of the surrounding bed (h <sub>i</sub> ).	65
Figure 3.30: 2-D mesh used for the modelling work – schematic explanation of node sizes within the computation domain	67
Figure 3.31: Explanation of IBM: nodes outlined by the blue triangles are the outer nodes, where the nodes outlined by the red triangles are the immersed boundary nodes.	67
Figure 3.32: Planned survey transects suggested from desk study (a) and final surveyed transects from RV <i>Prince Madog</i> (b).	70
Figure 3.33: Tidal and bottom tracked corrected flow velocity measurements from the ADCP instrument over the two full tidal cycles (25 hours) of surveying over the SS <i>Apapa</i> site.	70
Figure 3.34: Flow velocity measurements and a) the depth averaged ( $U$ ) flow velocity and b) maximum current velocity measurements over the SS <i>Apapa</i> site plotted over two full tidal cycles.	71
Figure 3.35: Depth averaged current velocity (left) and maximum current velocity values measured from the ADCP instrument. The * sign represents the mean value of the measurements. The solid red lines show the median standard deviation value of each population, and the boxes indicate the 25 <sup>th</sup> and 75 <sup>th</sup> percentiles. The whiskers indicate the minimum and maximum values.	71
Figure 3.36: Flow velocity amplification (when compared to the background flow) for one of the transects over the wreck and the scour marks, showing the influence of the wreck both laterally and in depth.	72
Figure 3.37: Current amplification (when compared with the background flow) at the stern and bow of the wreck recorded from the ADCP instrument during a N-S transect, b) zoomed-in version of the same transect for better visualisation of the flow amplification and direction around SS <i>Apapa</i> .	73
Figure 3.38: Downstream (influenced) and upstream (background) flow velocity comparison as a ratio and correlation with the state of the tide from the nearby Amlwch tidal gauge.	73
Figure 3.39: Observed maximum flow disturbance distances from the wreck plotted against tidal heights from Amlwch tide gauge.	74
Figure 3.40: Depth averaged flow velocity amplification and direction as measured from the ADCP instrument and a zoomed in version of the marked area (bottom) to visualise better the flow deviation around the wreck.	75
Figure 3.41: Surface coverage from the polygons delineating the scour edge for each survey.	76
Figure 3.42: Time lapse of the scour edge tracked using 2-D profiles for all the DEMs from the MBES surveys over SS <i>Apapa</i> and profiles used for distance calculations from the edge of the wreck (dashed black lines).	77
Figure 3.43: Distance between the wreck and the longest distance to the scour mark’s edge and the ratio of the length of the wreck/length of longest distance to the edge ratio for the multiple datasets.	78
Figure 3.44: Standard deviation map generated from the pixel-by-pixel calculation of $\sigma$ from the MBES data (a) and standard deviation map generated from the pixel-to-pixel calculation of the annualised depth difference between the consecutive surveys (b) using a linear classification.	79
Figure 3.45: Standard deviation ( $\sigma$ ) of depth (m) calculated using the DEM from the MBES surveys (left) and the standard deviation of depth (m) calculated using the annualised depth differences (right). The * sign represents the mean value of the measurements. The solid red lines show the median standard deviation value of each population, and the boxes indicate the 25 <sup>th</sup> and 75 <sup>th</sup> percentiles. The whiskers indicate the minimum and maximum values.	80

Figure 3.46: Average non-annualised depth difference (a) and average annualised depth difference (b) between consecutive datasets. The pronounced striping in the difference model is a survey/ de- iding artefact.....	81
Figure 3.47: Average depth difference calculated from the non-annualised depth difference maps (left) and average depth difference values calculated from the annualised depth difference maps (right). The * sign represents the mean value of the measurements. The solid red lines show the median standard deviation value of each population, and the boxes indicate the 25 <sup>th</sup> and 75 <sup>th</sup> percentiles. The whiskers indicate the minimum and maximum values.....	82
Figure 3.48: The minimum (shallowest; a), maximum (deepest; b) depths per pixel observed and the difference between the minimum and maximum values (c) showing the full range of the observed depth values.....	83
Figure 3.49: Boxplot of the maximum variation observed (calculated for each pixel) between the surveys. the * sign represents the mean value of the measurements. ....	84
Figure 3.50: The March 2018 DEM (a), the June 2019 DEM (b) and a difference map two surveys (c) indicating the larger observed disintegration of the wreck. The profiles at the right are the relative to the maps on the left 2-D profiles indicated at the map, showing depth along the profile from NW to SE. ....	85
Figure 3.51: Consistent 'zones of bed mobility' or 'zones of influence' generated by plotting 2-D profiles following features on the seabed at the SS <i>Apapa</i> site scour mark .....	86
Figure 3.52: Flow variation (reduction) at a) flooding and b) ebbing of the tidal current at the points where the 'zones of bed mobility' appear. ....	87
Figure 3.53: Standard deviation ( $\sigma$ ; a) and mean value ( $\bar{x}$ ; b) of BS values calculated using all the datasets around SS <i>Apapa</i> .....	88
Figure 3.54: Standard deviation values ( $\sigma$ ; left) and mean values ( $\bar{x}$ ) of BS strength calculated from all the surveys around the SS <i>Apapa</i> site. ....	89
Figure 3.55: Map showing the grabs attempted around SS <i>Apapa</i> . The green points denote the grabs that succeeded and the red points the grabs that failed to attain sediment. The dotted points are the grabs where the location was calculated using the vessel's location.....	89
Figure 3.56: Ternary diagram for coarse sediment (mud, sand, gravel) diagram used for sediment characterisation (Folk & Ward, 1957). ....	90
Figure 3.57: Sand, gravel and mud observed % from the PSA of the grab samples collected around the SS <i>Apapa</i> site.....	93
Figure 3.58: June 2019 BS mosaic (a), unsupervised classification (b) and supervised classification using only unimodal grab sediment samples. ....	94
Figure 3.59: Threshold of motion exceeded ( $\tau > \tau_{cr}$ ) for at least one mode in each grab sample (green), or threshold of motion not exceeded (red). Shear stresses calculated using each mode as grain size and the maximum bottom current observed from the ADCP survey.....	95
Figure 3.60: Sediment sample locations where threshold of motion is predicted to be exceeded ( $\tau > \tau_{cr}$ ) for only the fine (sand) mode (yellow), for at least one of the coarse (gravel) modes (green) or threshold of motion not exceeded ( $\tau < \tau_{cr}$ ) for any of the sample's modes (red) using Soulsby (1997) formulae plotted on the standard deviation of the bathymetry (a) and the depth difference map between the 2019 and the 2018 survey (b) where blue is deposition and red is erosion.....	96
Figure 3.61: a) Mean standard deviation ( $\sigma$ ) of depth (m) and b) depth difference between the 2019 and 2018 DEMs calculated at a 6.92 m buffer zone around each point for sediment material where threshold of motion is predicted to be exceeded ( $\tau > \tau_{cr}$ ) for only the fine (sand) mode (yellow), for at least one of the coarse (gravel) modes (green) or threshold of motion not predicted to be exceeded ( $\tau < \tau_{cr}$ ) for any of the sample's modes (red) using the Soulsby (1997) formulae. The 'x' sign represents the mean value of the measurements. The solid blue lines show the median value of each population, and the boxes indicate the 25 <sup>th</sup> and 75 <sup>th</sup> percentiles. The whiskers indicate the minimum and maximum values. ....	97
Figure 3.62: a) Standard deviation of depths observed at the location of the grab samples for different types of sediment mixtures. b) absolute depth difference (m) observed at the locations of different sediment mixtures between the 2019 and 2018 DEMs and c) the depth ranges where the different sediment mixtures were observed. The * sign represents the mean value of the measurements. The solid red lines show the median value of each population, and the boxes indicate the 25 <sup>th</sup> and 75 <sup>th</sup> percentiles. The whiskers indicate the minimum and maximum values, where the red + signs represent the extreme measurements. ....	98
Figure 3.63: Spatial locations where different sediment mixtures were observed during the sample processing.....	98



Figure 3.64: Comparison of differently sized sediment samples and their mobilisation over time for the maximum flow velocity as measured from the last bin of the ADCP instrument at the sampled location.....	99
Figure 3.65: BS values, showing bed composition compared with $\sigma$ of depth showing bed mobility over time. ....	99
Figure 3.66: Comparison of the modelled flow velocity values (from TELEMAC-3D) and the ADCP measured flow velocity values. ....	100
Figure 3.67: Comparison of the means between the measured flow velocity values using the ADCP instrument and the modelled flow velocity values from TELEMAC-3D.....	101
Figure 3.68: Prediction of scour formation from the coupled numerical model over the first 16 full tidal cycles (8 days). ....	102
Figure 3.69: a) Initial model conditions, b) seabed after one hour of computation with discharge at expected levels, c) depth difference between the result of the seabed formation after one hour of computation and the initial seabed imported in the model. ....	103
Figure 3.70: a) Maximum suspended load transport at plane 2 (1 <sup>st</sup> plane above the bed) and b) maximum bedload transport as modelled from the numerical coupled TELEMAC3D – GAIA model. ....	104
Figure 3.71: Maximum modelled turbulent kinetic energy values within the first 8 days of computation from a flat bed, using the coupled TELEMAC3D - GAIA model. ....	105
Figure 3.72: Schematic representation and definition of the sediment wave characteristics from Van Landeghem et al. (2012). 'a' and 'b' are two sediment waves. $h_{(cr)}$ is the water depth at the crest; $\Delta S$ is the sediment wave height; $L$ is the sediment wavelength (and Length components $L_1$ and $L_2$ ) derived from sediment wave trough spacing; $\lambda$ is the crest wavelength; $t_1$ is the time of the first bathymetric survey and $c_x$ is the displacement of the sediment wave crest over time interval $x$ . ..	106
Figure 3.73: 2-D profile over the large bedforms observed at the NW part of the SS <i>Apapa</i> scour mark; on the March 2018 DEM (a), on the June 2019 DEM (b) and c the 2-D profile plotted for the two surveys providing bathymetric information. ....	107
Figure 3.74: Bedforms used for the bedform characteristic calculation numbered on the 2018 and the 2019 DEMs. The arrows are showing the migration direction of the bedform (from the north). ....	108
Figure 3.75: Comparison between the bathymetry (a) and backscatter strength values (b) over the bedforms from the June 2019 data collection. The plotted 2-D profile shows the variation in BS strength values at the crests and troughs of the bedforms.....	109
Figure 3.76: Explanation of sediment movement and migration on mixed sedimentary beds (Allen, 1984).....	110
Figure 3.77: W-E transect showing the depth averaged flow amplification at the bedforms upstream of SS <i>Apapa</i> during flooding (eastwards tidal current), flow over the bedforms is amplified ~1.7 times in the present example when compared with the depth averaged background flow (at the far field, on the east of the wreck). ....	110
Figure 3.78: Standard deviation ( $\sigma$ ) calculated using the bathymetric surveys and the BS strength mosaics with the 2019 DEM not included in the calculations. The marked areas (with green) represent the areas where the two $\sigma$ values (BS strength and bathymetry) provide information about large mobilisation over the years as the sediment remained fine.....	111
Figure 3.79: (a) Standard Deviation map of bathymetry from 11 surveys (June 2019 survey not included), (b) $\sigma$ map of bathymetry from 12 surveys (June 2019 survey included) and (c) Difference map of $\sigma$ calculated including the June 2019 survey and not including the June 2019 survey. ....	112
Figure 3.80: Depth difference between the March 2018 and June 2019 DEMs and a zoom in to the variation at the wreck itself. ....	113
Figure 3.81: The 2018 BS strength mosaic (a) and its unsupervised classification ( $a_i$ ), 2019 BS strength mosaic (b) and its unsupervised classification ( $b_i$ ), the BS strength $\sigma$ calculated not using the 2018 BS strength mosaic (c) and the BS strength $\sigma$ calculated using the 2019 BS strength mosaic in the calculation (d). ....	114
Figure 4.1: Schematic illustration of the hiding-exposure effect (adapted from Wu et al., 2000). .	118
Figure 4.2: Grain size distributions (using 1/2 $\Phi$ sieve stack) of the sand-gravel mixtures used for the laboratory experiments. $f_g$ is the gravel content in each mixture. ....	122
Figure 4.3: PVC block used for sedimentary bed flattening when setting up the flume for the laboratory experiments. ....	123

Figure 4.4: Flow velocity as measured using the UDVP for two pump frequencies, at 1.5 m downstream of the 1st ramp and a schematic illustration of the UDVP transducer positioning in the Armfield recirculating flume. ....	124
Figure 4.5: Array of twenty-four SeaTek 5 MHz ultrasonic transducers, used for the bathymetric scans after the laboratory experiments. ....	125
Figure 4.6: 'Initial' flat bed, 'mature bed' and 'final' bed for the experiment with pure sand and flow speed of $31 \text{ cm}\cdot\text{s}^{-1}$ as recorded from the array of twenty-four SeaTek acoustic transducers and processed in ArcGIS. ....	126
Figure 4.7: A laboratory flume bed DEM produced from the SeaTek transducer measurements, and the 2-D profiles used for the delineation of the scour edge (green lines) in the flume environment. The plotted 2-D profile is one example of such 2-D profile, marked in red. ....	127
Figure 4.8: Visualisation of bedform analyses of parts of the bed upstream and downstream of the object, avoiding bedform distortions due to the ramp and the scour. The DEMs shown are from the experiment using 12.5% gravel in the mixture, at flow speed of $31 \text{ cm}\cdot\text{s}^{-1}$ . a) 'mature bed' Dem, b) 'final bed' DEM, c) 2-D bathymetric profile on the profile shown on (b), d) depth difference between the 'final bed' DEM and the 'mature bed' DEM. The vertical red lines denote the areas (and bedforms) used for the bedform characteristics analyses. ....	128
Figure 4.9: Array of sixteen SeaTek ultrasonic transducers, placed parallel to the flow, to monitor ripple migration rates upstream of the object at the full duration of the laboratory experiments. ...	128
Figure 4.10: The Armfield recirculating flume and a schematic illustration of the object's and SeaTek transducers positioning when recording the bed evolution and bedform formation during the laboratory experiments. ....	129
Figure 4.11: Syringe, sub-divided every 5 mm used for the laboratory sediment 'core' sampling. ....	129
Figure 4.12: Panoramic image of the dried bed after an experiment, showing the sediment sampling locations. ....	130
Figure 4.13: Explanation of sampled locations at bedform crests and troughs using a syringe. ...	130
Figure 4.14: Explanation of the generation of the model computation domain for the flume laboratory. ....	131
Figure 4.15: Process of generating the geometry file for the coupled numerical model. a) Generation of a polygon around the object, b) 'initial bed' without the object in place, c) 'initial bed' with an interpolation applied at the position of the object, d) 'initial bed' with the delineated final position of the object and the actual dimensions of the flume, e)'initial bed', interpolated for the actual dimensions of the flume and f) computation domain (and mesh) used as input for the model. ....	132
Figure 4.16: Schematic illustration of the rectangular polygon generated to delineate the object. ....	132
Figure 4.17: Depth averaged flow velocity measurements captured using the UDVP instrument at 7 locations in the flume. Two measurements were taken at each location for each pump frequency ( $30 \text{ Hz}$ and $45 \text{ Hz}$ ). Also shown, a schematic diagram of the locations where flow velocities were measured using the UDVP instrument. ....	135
Figure 4.18: a) Observed ripple migration rates upstream for different bed mixtures for the flow speed mobilising only the finer fraction ( $31 \text{ cm}\cdot\text{s}^{-1}$ ), b) Observed ripple migration rates upstream for different bed mixtures for the flow speed mobilising both fractions ( $45 \text{ cm}\cdot\text{s}^{-1}$ ). ....	136
Figure 4.19: Absolute ripple asymmetry upstream (left) and downstream (right) of the object, as calculated for the experiments conducted at the flow speed mobilising only the sand fraction ( $31 \text{ cm}\cdot\text{s}^{-1}$ ). The * sign represents the mean value of the measurements. ....	137
Figure 4.20: Absolute ripple asymmetry upstream (left) and downstream (right) of the object, as calculated for the experiments conducted at the flow speed mobilising only the sand fraction ( $45 \text{ cm}\cdot\text{s}^{-1}$ ). ....	138
Figure 4.21: Mean absolute ripple asymmetry, $A$ difference between the ripples measured downstream and upstream of the object, for the laboratory experiments conducted using the different mixtures and the flow speeds of $31 \text{ cm}\cdot\text{s}^{-1}$ (solid blue line) and $45 \text{ cm}\cdot\text{s}^{-1}$ (solid red line). ....	139
Figure 4.22: Ripple heights and lengths and a height/length comparison for ripples upstream of the object, for the experiments conducted at the flow speed of $31 \text{ cm}\cdot\text{s}^{-1}$ . ....	140
Figure 4.23: Ripple heights and lengths and a height/length comparison for ripples at the wake (downstream) of the object, for the experiments conducted at the flow speed of $31 \text{ cm}\cdot\text{s}^{-1}$ . ....	141
Figure 4.24: Ripple heights and lengths and a height/length comparison for ripples upstream of the object, for the flow speed of $45 \text{ cm}\cdot\text{s}^{-1}$ . ....	141
Figure 4.25: Ripple heights and lengths and a height/length comparison for ripples downstream of the object, for the experiments conducted at the flow speed of $45 \text{ cm}\cdot\text{s}^{-1}$ . ....	142

Figure 4.26: Zones of maximum bed mobility or 'zones of influence' as observed in the laboratory experiments conducted using the different sediment mixtures and the flow speeds of 31 cm·s <sup>-1</sup> and 45 cm·s <sup>-1</sup> . .....	144
Figure 4.27: Example of the DEMs produced using the SeaTek acoustic transducers, for the laboratory experiments using a bed with 7.5% gravel. a) 'Initial flat bed', b) 'mature' bed, c) bathymetric difference between the 'mature' DEM bed and the 'initial flat bed' DEM, d)'final bed' DEM, e) bathymetric difference between the 'final bed' DEM and the 'mature' bed DEM and f) difference map between the 'final bed' DEM and the 'initial flat bed' .....	146
Figure 4.28: 'North' side scour mark length a) for the flow speed mobilising only sand (31 cm·s <sup>-1</sup> ), b) for the flow speed mobilising both fractions sand (45 cm·s <sup>-1</sup> ) and scour length/ object length ratio for c) the flow speed mobilising only sand (31 cm·s <sup>-1</sup> ) and d) the flow speed mobilising both fractions (45 cm·s <sup>-1</sup> ). The * sign represents the mean value of the duplicated experiments. ....	147
Figure 4.29: 'North' side scour width as measured for laboratory experiments using different mixtures at flow speeds of a)31 cm·s <sup>-1</sup> , and b) 45 cm·s <sup>-1</sup> . c-d) scour length/scour width (L:W) ratio as measured for the laboratory experiments using different mixtures at flow speeds of 31 cm·s <sup>-1</sup> and 45 cm·s <sup>-1</sup> respectively. The * sign represents the mean value of the measurements from the two laboratory experiments using the same sediment mixtures and flow speed. ....	148
Figure 4.30: a) Mean flume bed depth observed from the laboratory experiments using different mixtures at the flow speeds of 31 cm·s <sup>-1</sup> (left) and 45 cm·s <sup>-1</sup> (right). b) Maximum flume bed depth observed from the laboratory experiments using different mixtures at the flow speeds of 31 cm·s <sup>-1</sup> (left) and 45 cm·s <sup>-1</sup> (right). The * sign represents the mean value of the measurements from the two laboratory experiments using the same sediment mixtures and flow speed. ....	149
Figure 4.31: Calculated scour sediment volume loss for the flow speeds of 31 cm·s <sup>-1</sup> (left) and 45 cm·s <sup>-1</sup> (right). The * sign represents the mean value of the measurements from the two laboratory experiments using the same sediment mixtures and flow speed .....	150
Figure 4.32: Object orientation to the flow as recorded using the 'final' DEMs, for flow speed mobilising only sand (left) and for the flow speed mobilising both the sand and the gravel fractions (right).....	151
Figure 4.33: Gravel % variation from the original mixtures as observed after conducting PSA on samples collected prior to the laboratory experiments to ensure the thorough mixing of the sediment. ....	151
Figure 4.34: Panoramic image over the object showing sediment composition around the object area and sampling points within the scour mark and depositional feature. The uni-directional flow in the laboratory experiment was from left to right. ....	152
Figure 4.35: Gravel % variation from the original mixture, as observed at the end of the laboratory experiments using the different mixtures at the flow speed mobilising only sand (31 cm·s <sup>-1</sup> ). The grey envelopes represent the standard deviation around the means (the dots) of "n" measurements at each depth from two duplicate experiments.....	153
Figure 4.36: Gravel % variation from the original mixture, as observed at the end of the laboratory experiments using the different mixtures at the flow speed mobilising both sand and gravel fractions (45 cm·s <sup>-1</sup> ). The grey envelopes represent the standard deviation around the means (the dots) of "n" measurements at each depth from two duplicate experiments. ....	154
Figure 4.37: Gravel % observed in down core samples and the maximum observed ripple height observed for each mixture for the experiments conducted at the flow speed mobilising only the sand fraction (31 cm·s <sup>-1</sup> ). The vertical lines indicate the highest sampled ripple crest point or depositional feature for each sediment mixture. ....	156
Figure 4.38: Gravel % observed in down core samples and the maximum observed ripple height observed for each mixture for the experiments conducted at the flow speed mobilising only the sand fraction (45 cm·s <sup>-1</sup> ). The vertical lines indicate the highest sampled ripple crest point or depositional feature for each sediment mixture. ....	157
Figure 4.39: Modelled and measured by the UDVP instrument depth averaged flow velocities upstream and downstream of the object in the laboratory experiments. ....	158
Figure 4.40: Numerical model outputs for bathymetry at the end of the runs replicating the laboratory experiments at initial flow speed of 31 cm·s <sup>-1</sup> . ....	160
Figure 4.41: Numerical model outputs for bathymetry at the end of the runs replicating the laboratory experiments at initial flow speed of 45 cm·s <sup>-1</sup> . ....	161
Figure 4.42: Numerical model outputs of maximum bedload for the runs replicating the laboratory experiments at initial flow speed of 31 cm·s <sup>-1</sup> . ....	162

Figure 4.43: Numerical model outputs for maximum suspended load for the laboratory experiments at initial flow speed of $31 \text{ cm}\cdot\text{s}^{-1}$ .....	163
Figure 4.44: Numerical model outputs for maximum bedload for the runs replicating the laboratory experiments at initial flow speeds of $45 \text{ cm}\cdot\text{s}^{-1}$ .....	164
Figure 4.45: Numerical model outputs for maximum suspended load for the laboratory experiments at initial flow speed of $45 \text{ cm}\cdot\text{s}^{-1}$ .....	165
Figure 4.46: Bedform heights and lengths development diagrams for experimental runs using 0.1087 mm quartz sand and flow speed of $0.37 \text{ m}\cdot\text{s}^{-1}$ (Baas, 1994). ....	166
Figure 4.47: Empirical relationships between the expected migration rates of equilibrium, current-generated ripples and their grain-related mobility parameter for the different sediment grain sizes. The equations show the best-fit power functions corresponding to the straight lines through the population points (Baas et al., 2000). ....	167
Figure 4.48: Positioning of the object at the beginning and at the end of the laboratory experiments, showing a $12^\circ$ deviation of the object's orientation to the flow. The flow direction is from east to west (right to left). ....	168
Figure 4.49: Object associated erosional and depositional patterns around shipwrecks placed at different orientations to the flow from the output of CFD models (Quinn & Smyth, 2018). ....	169
Figure 4.50: Comparison between the scour length/object length ratio as observed in the laboratory experiments with the Quinn & Smyth (2018) observations using a CFD model, for the experiments conducted at the flow speed a) mobilising only the sand fraction ( $31 \text{ cm}\cdot\text{s}^{-1}$ ) and b) mobilising both the sand and gravel fractions ( $45 \text{ cm}\cdot\text{s}^{-1}$ ). The object's angle to the flow was measured at the 'final bed' DEM. ....	169
Figure 4.51: Comparison of scour mark's length and width for the experiments conducted using the two flow speeds, mobilising either only sand or both sand and gravel, and a scour length / scour width ratio as a comparison. ....	171
Figure 4.52: Picture of the scour mark for the experiment conducted using a mixture containing 12.5% gravel at the flow speed mobilising only the sand fraction ( $31 \text{ cm}\cdot\text{s}^{-1}$ ). The blue line delineates the scour mark where the red line delineates the separation of sand and gravel within the scour mark. ....	172
Figure 4.53: Difference in the gravel % observed in the ripple crests upstream and downstream (a, c) and ripple troughs upstream and downstream (b, d) for the experiments conducted at the flow speed mobilising only sand (a, b) and the experiments conducted at the flow speed mobilising both fractions (c, d).....	173
Figure 5.1: Numerical model input - vertical positioning of the wreck to test the scour formation at different exposure of the wreck. a) Wreck positioned at the depth observed in 2012 (partially submerged into the artificial flat bed), b) wreck artificially lifted over the artificial flat bed (fully exposed to the incoming flow) and c) the depth difference between a and b. ....	180
Figure 5.2: Prediction of scour formation from the coupled numerical model over the first 16 full tidal cycles (8 days) a) with the wreck sitting at the depth as observed in the 2012 survey (partially submerged), b) with the wreck 'lifted' 8m to sit on top of the artificial bed and c) depth difference between b and a. ....	181
Figure 5.3: Prediction of turbulent kinetic energy (TKE) formation from the coupled model over the first 16 full tidal cycles (8 days) a) with the wreck sitting at the depth as observed in the 2012 survey, b) with the wreck 'lifted' 8m to sit on top of the artificial bed, c) TKE difference between a and b d) TKE as calculated by a CFD model with the wreck at $60^\circ$ to the flow and exposed 5m over the bed (Quinn & Smyth, 2018). ....	183
Figure 5.4: 2-dimensional flowlines (a) and 3-dimensional flow lines (b) as derived from a CFD model (Quinn & Smyth, 2018). ....	184
Figure 5.5: Numerical model outputs for depth averaged flow speeds with SS <i>Apapa</i> orientated at $58^\circ$ to the flow. a) Observed flow velocity and direction at the first plane above the bed (plane 2) and b) observed depth averaged velocity. ....	185
Figure 5.6: Numerical model prediction of the sedimentary bed after computation of 140 minutes for the laboratory experiment run with the sedimentary mixture consisting of 10% gravel and 90% sand. The object is exposed by: a) 85%, b) 80% and c) 75%. ....	187
Figure 5.7: a) Output from CFD model with the object embedded by 20% at a $90^\circ$ angle to the flow (Hatipoglu & Avci, 2003) and b) output of the coupled TELEMAC3D – GAIA numerical model developed for the present study with the object embedded by 20% at a $90^\circ$ angle to the flow. ....	188
Figure 5.8: a) Erosion and deposition prediction around shipwreck sitting at different orientations to the flow as predicted from a CFD model (Quinn & Smyth, 2018). b) Scour as observed offshore	

around the wreck of SS <i>Apapa</i> and c) scour around a cylinder as observed the laboratory experiments with the sedimentary bed consisting of pure sand. ....	189
Figure 5.9: Numerical model runs over the first 20 full tidal cycles (10 days) with the sediment composition around the SS <i>Apapa</i> site consisting of a) 78% gravel and 22% sand, b) 22% gravel and 22% sand and c) 100% sand. ....	193
Figure 5.10: Predicted (from the coupled numerical model) maximum bedload for the case of the bed around SS <i>Apapa</i> consisting of 78% gravel and 22% sand (offshore observations; top), the bed consisting of 78% sand and 22% gravel (test case; middle) and the bed consisting of 100% sand (HE sensitivity test; bottom). ....	195
Figure 5.11: Predicted (from the coupled numerical model) maximum suspended load transport for the case of the bed around SS <i>Apapa</i> consisting of 78% gravel and 22% sand (offshore observations; top) and the bed consisting of 78% sand and 22% gravel (test case; middle) and the bed consisting of 100% sand (HE sensitivity test; bottom). ....	196
Figure 5.12: Observed scour length, width and depth as observed from the laboratory experiments using the incoming flow speed mobilising only sand ( $31 \text{ cm}\cdot\text{s}^{-1}$ ) and both sand and gravel ( $45 \text{ cm}\cdot\text{s}^{-1}$ ). ....	198
Figure 5.13: Numerical model estimations of scour development around the object with only variable the bed composition (sand and gravel % in the mixtures). ....	199
Figure 5.14: a) Maximum bedload transport as predicted using the coupled model for a run at with the sedimentary bed consisting of 95% sand and 5% gravel, b) DEM produced from the final scan using the SeaTek transducers and c) 2-D profile showing the bed levels upstream and downstream of the object (red on c). ....	200
Figure 5.15: Maximum bedload as predicted from the coupled numerical model for test runs with only variable the bed composition (sand and gravel percentages in the mixtures). ....	201
Figure 5.16: Suspended load transport as predicted from the coupled numerical model for test runs with only variable the bed composition (sand and gravel content in the mixtures). ....	202
Figure 5.17: Explanation of a dynamic equilibrium of a wreck site over time. The site is initially at a dynamic equilibrium with the surrounding environment. After a localised event (disintegration), rapid changes are observed until the site reaches a new dynamic equilibrium. Adapted from Quinn & Boland (2010). ....	206
Figure 6.1: Digital elevation model (DEM) of the site around the wreck of SS <i>Cambank</i> with the depths (re ODN) as observed on November 11th, 2018. ....	214

## List of Tables

Table 1.1: Summary of morphological and dynamic characteristics of bedforms observed in sand and gravel mixtures (McCarron, 2020).....	16
Table 3.1: Comparison of seabed types and their relationship with backscatter (Monteys et al., 2013). .....	40
Table 3.2: Table of datasets collected around the SS <i>Apapa</i> site during 13 surveys. ....	61
Table 3.3: Distance between the farthest edge of the wreck and the farthest edge of the scour mark for all surveys and all four sides of the scour mark (The values in grey for the May 2012 survey were not used for the calculation of $\sigma$ and $x$ ). ....	78
Table 3.4: Sediment sample information, classification (according to Folk, 1957) and shear stresses calculated using Soulsby (1997) critical sediment transport formulae for the grab samples that ADCP data were available. The velocity used in the calculation was the maximum velocity observed from the last (bottom) bin of the ADCP instrument from the E-W transects of the ADCP (conducted during ebbing/flooding). ....	92
Table 3.5: Detailed sediment wave characteristics for the 7 Large sediment waves at the NW part of the SS <i>Apapa</i> scour mark, calculated using the Van Landeghem (2012) method. ....	108
Table 4.1: Sand-gravel mixtures used for laboratory experiments and their associated hydraulic properties. ....	121
Table 4.2: Porosity ( $n_p$ ) values calculated for the different mixtures .....	134
Table 4.3: Comparison between upstream and downstream mean measurements for ripple heights and lengths for experiments conducted using the two flow speeds. Positive values (green) mean that the downstream mean value was greater, where negative values (red) mean that the downstream mean value was smaller than the upstream. ....	143
Table 4.4: Measured mean distance between object and 'zones of influence' for the experiments using the two flow speeds. ....	145

## Abbreviations

(g)M	Slightly gravelly mud
(g)mS	Slightly gravelly muddy sand
(g)S	Slightly gravelly sand
AC	Alternating Current
ADCP	Acoustic Current Doppler Profiler
BBC	British Broadcasting Corporation
BGS	British Geological Society
BLS	Bedload sheets
BS	Backscatter
CFD	Computational Fluid Dynamics
CPU	Central Processing Unit
DEM	Digital Elevation Model
DGPS	Digital Geographical Positioning System
DTM	Digital Terrain Model
GPS	Geographical Positioning System
gS	Gravelly sand
GUI	Graphical User Interface
HE	Hiding-exposure
HPC	High Performance Computing
IBM	Immersed Boundary Method
IDW	Inversed Distance Weighted
LRBF	Low relief bedforms
MBES	Multi Beam Echo Sounder
MEC	Marine Energy Converter
mS	Muddy sand
MSL	Mean Sea Level
NERC	National Environment Research Council
N-S	Navier Stoke's
NW	Northwest
ODN	Ordnance Datum Newlyn
PSA	Particle Size Analysis
PVC	Polyvinyl chloride
RLBF	Rippled-like bedforms
RV	Research Vessel
sC	Sandy Clay
SCW	Super Computing Wales
SE	Southeast
sG	Sandy gravel

SS	Steamship
SSS	Side Scan Sonar
STA	Short-Term Average
TKE	Turbulent Kinetic Energy
UDVP	Ultrasonic Doppler Velocimetry Profiler
UK	United Kingdom
UKHO	United Kingdom Hydrographic Office
UNESCO	United Nations Educational, Scientific and Cultural Organization
USBL	Ultra-short Base Line
UTC	Universal Time Coordinated
WSS	Wall Shear Stress
WW	World War
WWI	1 <sup>st</sup> World War



## Notation

Symbol	Description	Units
$a$	Amplification factor	-
$C$	Chézy coefficient	-
$C_{eq}$	Equilibrium calculation	-
$C_f$	Dimensionless bed friction coefficient	-
$C_x$	Bedform crest displacement or migration rate	$\text{m}\cdot\text{s}^{-1}$
$d_{50}$	Median grain size	m
$d_i$	Grain size of the $i^{\text{th}}$ fraction	m
$e$	Euler's constant	-
$e_v$	Void ratio	-
$f_0$	Operating frequency	Hz
$f_g$	Gravel fraction	-
$f_s$	Doppler shift frequency	Hz
$g$	Acceleration due to gravity	$\text{m}\cdot\text{s}^{-2}$
$G_s$	Specific gravity of solids	-
$h$	Height above the bed	m
$h_{cr}$	Bedform crest depth	m
$k$	Von Kármán's constant	-
$k - \varepsilon$	Energy production and energy dissipation	-
$k_s$	Nikuradse roughness	m
$M_r$	Migration rate for bedforms	$\text{mm}\cdot\text{s}^{-1}$
$M_s$	Mass of solids	kg
$n$	The size of the population	-
$n_p$	Porosity	%
$P$	Rouse Number	-
$P_C$	Cycles per pulse	-
$P_L$	Pulse length	$\mu\text{S}$
$Q$	Discharge	$\text{m}^3\cdot\text{s}^{-1}$
$r$	Proportionality coefficient	-
$R^2$	Coefficient of determination	-
$R_d$	Relative difference	-
$Re^*$	Reynold's number	-
$s$	Specific density of sediment grains	-
$t$	Time	s
$\bar{t}$	Average time	s

$t_0$	Initial time for laboratory experiments scan	hours
$t_{final}$	Final time for laboratory experiments scan	hours
$T_R$	Period of acoustic wave	s
$TWT$	Two-way travel time of acoustic signal	s
$\bar{u}$	Depth averaged velocity	$m \cdot s^{-1}$
$u_*$	Current shear velocity	$m \cdot s^{-1}$
$u_f$	Maximum value of undisturbed velocity	$m \cdot s^{-1}$
$u_{*S}$	Skin friction velocity	$m \cdot s^{-1}$
$\nu$	Kinematic viscosity of fluid	$m^2 \cdot s^{-1}$
$V_S$	Volume of solids	$m^3$
$V_T$	Total volume	$m^3$
$w_s$	Settling velocity	$m \cdot s^{-1}$
$x$	Horizontal distance	m
$\bar{x}$	Average value	-
$x_i$	The $i^{th}$ value from a population	-
$x_{iO}$	Older survey	-
$x_{iR}$	Most recent survey	-
$y$	Flow depth	m
$z$	Water depth	m
$z'$	First $\sigma$ -layer height above the bed	m
$z_0$	Hypothetical vertical level with 0 velocity	m
$z_{av}$	Height equivalent to depth-averaged flow velocity	m
$z_b$	Distance to the bed	m
$z_{ref}$	Reference height	m
$\delta$	Layer thickness	m
$\Delta S$	Ripple height	m
$\delta_{xR}$	Horizontal resolution of the ultrasonic transducers	mm
$\delta_{zR}$	Vertical resolution of the ultrasonic transducers	mm
$\eta$	Eddy viscosity	$Pa \cdot s$
$\theta$	Shield's parameter	-
$\theta_{cr}$	Critical Shield's parameter	-

$\theta_{cr,i}$	Critical Shield's parameter for the $i^{th}$ fraction	-
$\theta_{cr}$	Critical Shield's parameter	-
$\theta_f$	Object's angle to the north	°
$\theta_i$	Shield's parameter for the $i^{th}$ fraction	-
$\kappa$	Von Kármán constant	-
$\lambda$	Wave length	m
$\mu$	The population mean	-
$\mu_v$	Absolute viscosity of the fluid	Pa·s
$\xi_i$	Hiding-exposure correction for the $i^{th}$ fraction	-
$\rho_c$	Cylinder's density	kg·m <sup>-3</sup>
$\rho_s$	Sediment density	kg·m <sup>-3</sup>
$\rho_w$	Water density	kg·m <sup>-3</sup>
$\sigma$	Standard deviation	-
$\tau$	Shear stress	N·m <sup>-2</sup>
$\tau''$	Drag originating bed shear stress	N·m <sup>-2</sup>
$\tau_0$	Current induced shear stress	N·m <sup>-2</sup>
$\tau_b$	Bed shear stress	N·m <sup>-2</sup>
$\tau'_b$	Skin related bed shear stress	N·m <sup>-2</sup>
$\tau_{cr}$	Critical shear stress	N·m <sup>-2</sup>
$\tau_{cr,i}$	Critical shear stress of the $i^{th}$ fraction	N·m <sup>-2</sup>
$\tau_t$	Shear stress due to turbulence	N·m <sup>-2</sup>
$\tau_v$	Shear stress due to viscosity	N·m <sup>-2</sup>
$\Phi_b$	Dimensionless current induced sediment transport rate	-
$\Phi_R$	Half-beam angle of ultrasonic transducers	°



# Chapter 1

## 1. Introduction

### 1.1 Overview and motivation

Oceans cover over 71% of the Earth's surface, however, only 35% of the seafloor has been surveyed and mapped using modern methods (NOAA, 2021) and only a fraction of that has been surveyed repeatedly, limiting the knowledge, and understanding of seabed mobility and sedimentary processes. Knowledge of the sediment composition around the seabed's surface is essential for marine planning (Wilson et al., 2018). Sediment composition impacts sediment mobility as mixed, non-unimodal beds can be more mobile than beds consisting of unimodal sediments (McCarron et al., 2019). The seabed composition surrounding the United Kingdom varies from fine sediment (clay) to hard, exposed bedrock, with over 25% of the seabed surface being mixed sediment. The fraction of mixed sediment within the Irish Sea is even higher, reaching percentages as high as 60% (Figure 1.1) due to glacial processes depositing different types of material over the millennia. **Sediment dynamics of this mixed sediment have not yet been fully understood and quantified** (Amoudry & Souza, 2011). Section 1.3 focusses on why this knowledge gap is a problem.

The effects of current deviation and its impact to the seabed have been investigated in the literature for vertically placed, unsubmerged piles, which are the most common structures placed in the oceans for energy extraction (i.e., monopiles for wind turbines), bridges, piers or even oil and gas extraction (e.g., Roulund et al. 2005, Ahmad et al., 2018; Min et al., 2018). However, there is a lack of studies focusing on differently shaped submerged objects, such as shipwrecks (Quinn, 2006; Smyth & Quinn, 2014; Quinn & Smyth 2018), horizontally placed current turbines (Chen & Lam, 2014), or even cylinders placed on the seabed, such as the Microsoft data centre (BBC News, 2018). Marine Renewable energy is likely to be extracted from various sources of energy in the future. There is, therefore, an ever-increasing need for installation of differently shaped and orientated infrastructure. This increases the need for a deeper understanding of the interactions between the objects and the often-complex seabeds (Figure 1.1), as these interactions can define the feasibility and sustainability of seabed development projects.

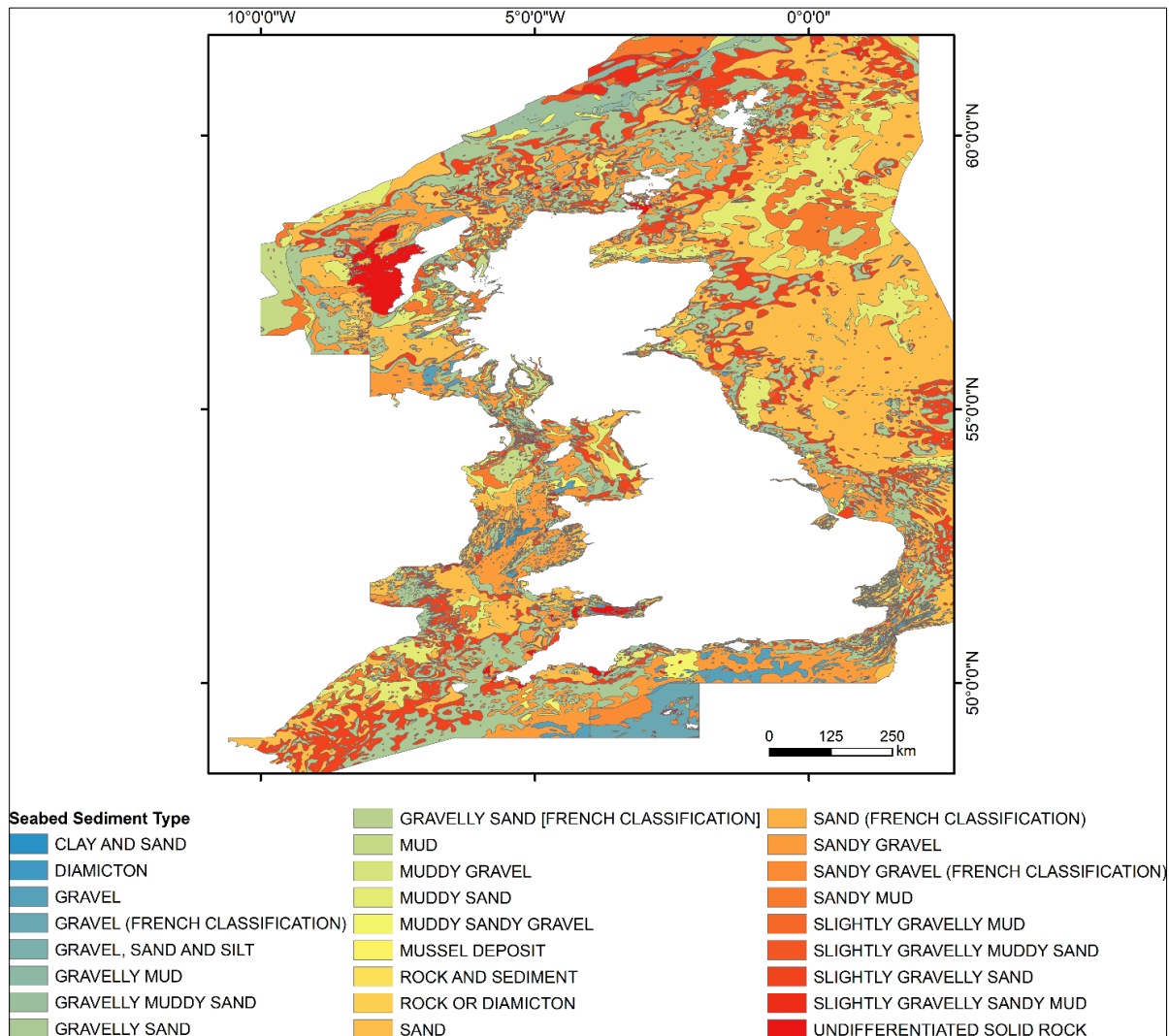


Figure 1.1: Seabed sediment type around the UK from the British Geological Survey (BGS) through the Edina Digimap website (<https://digimap.edina.ac.uk/>; DiGSBS250K, 2011).

### 1.1.1 Seabed mobility effects on offshore development

The introduction of an object to the seafloor, will alter the flow regimes around the object and its immediate environments, resulting in flow contraction, enhanced stress on the bed and scour as sediment is mobilised (Quinn, 2006; Smyth & Quinn, 2014; Quinn & Smyth, 2018; Fernández-Montblanc et al., 2018). Scour can be defined as the erosion of a submerged bed, caused by the existence of an obstacle (cable, pipe, wreck, infrastructure, or even a small rock) affecting the hydrodynamics of the area sufficiently to cause enhanced local shear stress and thus sediment transport that exceeds the ambient level (Soulsby, 1997; Hay & Speller, 2005; Quinn, 2006; Quinn et al., 2016; Fernández-Montblanc et al., 2018). The introduction of an object to the bed, can increase the local bed shear stress by up to a factor of four (Smyth & Quinn, 2014; Quinn et al., 2016; Quinn & Smyth, 2018).

Scour can be formed because of waves, currents or a combination of waves and currents (O'Neill, 2002; Soulsby, 1997; Whitehouse, 1998; Whitehouse et al., 2011). Tidal currents are the dominant parameter for scour in environments where sediment transport is not affected by sea surface waves. In the offshore environment tides typically cause bi-directional currents. Scour formation may cause

infrastructure to completely fail or collapse (Quinn, 2006) and can impact seabed habitats (McArthur et al., 2010). Scour dynamics will impact mine burial and detection and the preservation potential of shipwrecks. It is difficult to predict scour, however, the scour mark's morphology and size vary depending on the size and the angle/orientation of the obstacle to the incoming (to the site) flow (Whitehouse, 1998; Quinn et al., 2016). There is also a link between the scour mark's characteristics (length, width, depth, morphology) and the obstacle's width to height (W:H) ratio (Whitehouse, 1998; Saunders, 2005), with studies (e.g., Lambkin et al., 2006) showing that the object's orientation does not affect the scour mark's characteristics as much when the W:H ratio is over 10. An obstacle that is orientated parallel to the flow direction will cause a long, narrow scour mark, where an obstacle that is orientated in an angle to the flow, will cause short, wide scour patterns (Saunders, 2005; Smyth & Quinn, 2014; Quinn & Smyth, 2018). When an obstacle is introduced to the seabed on ideal hydrodynamic conditions, rapid scour will occur within the first few tidal cycles (Harris et al., 2010). The identification of scour developed around offshore infrastructures, used for example for renewable energy extraction has been scientifically investigated. There are also real-world examples, showing the damage that scour can cause, not only on the foundations themselves, by causing problems to the structural stability, but also on power cables transferring electricity from the platforms to transition stations or to the shore. Figure 1.2 shows real world measurements of scour developed around monopiles placed in the marine environment (Whitehouse et al., 2008). The authors suggest a dependence of the developed scour depth to the seabed sediment type and the thickness of the surficial sediment layer.

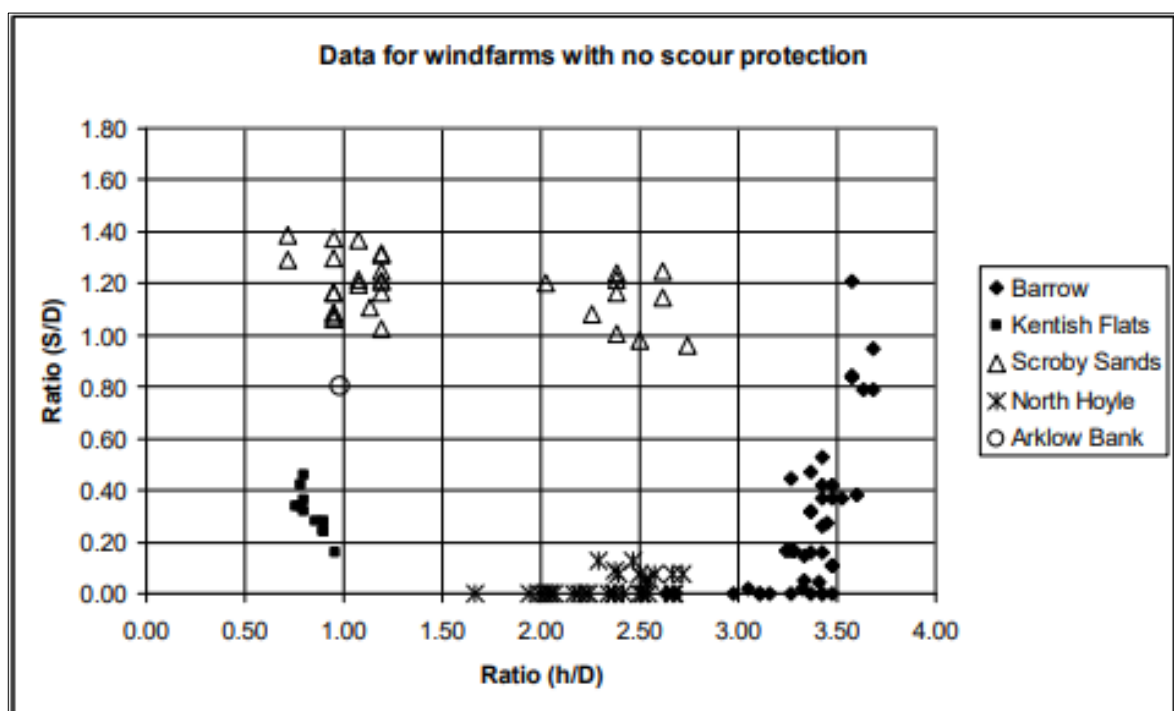


Figure 1.2: Scour depth (S) over Monopile diameter (D) as observed for five offshore marine renewable sites around the United Kingdom (Whitehouse et al., 2008).

It has been mentioned in the literature (Wardhana & Hadipriono, 2003) that flooding events and scour development were the main reason for the failure of ~53% of over 500 bridges failures reported in the United States between 1989 and 2000.

Scour predictive equations have been developed over the years focusing mainly on the prediction of the equilibrium scour depth around vertically placed structures like monopiles, bridges, or piers (i.e., Melville, 2008; Pandey et al., 2020; Rady, 2020). The prediction relies on steady flows, over uniform and non-cohesive beds, and depends on different parameters such as flow, fluid, pier geometry and sediment characteristics (Rady, 2020). Traditional predictors use the diameter of the object (width), water depth, depth averaged flow speed and the Froude number. More recent predictors use artificial intelligence-based modelling for the prediction of the equilibrium scour depth (Rady, 2020). The scour depth of circular piers is reported to be 10% smaller than rectangular piers and 20% smaller than sharp-nosed piers (Chang, 1988). The shape of the object has been incorporated to a degree in scour prediction using computational fluid dynamic (CFD) models (i.e., Smyth & Quinn, 2014; Quinn & Smyth, 2018, Majcher et al., 2022). Simple predictors based on shape may be difficult to apply for objects of variable shape (like shipwrecks), but if a site is monitored over time (i.e., the shape remains the same), scour evolution can be investigated in relation to the hydrodynamic forcing and the seabed composition.

### 1.1.2 Shipwrecks as relevant study objects

There are currently over 3 million shipwrecks in the ocean floor worldwide (UNESCO, 2014), with over 60000 of them sitting in the UK's territorial water, and only 1/3 of them (~20000) are named vessels (Cant, 2013). Many vessels sank in UK water during World Wars (WW) I and II, where about ten thousand of them sank during WWI (UNESCO, 2014). Figure 1.3a presents 14442 of the wrecks observed in UK Territorial waters, with information about the bathymetry relative to Mean Sea Level (MSL), showing some wrecks as deep as ~4 km below MSL and others exposed at low tides. However, over 95% (13763) of the wreck population sits between 0 and 200 m below MSL (Figure 1.3b) and over 86% (12530) of the wreck population is always submerged.

Shipwrecks can be used as a reference for the investigation and understanding of flow development around objects intentionally placed on the seabed in different environments. The ever-increasing need for seabed infrastructure enabling offshore renewable energy production (commercially), is currently focused to the use of energy produced by wind turbines (European Commission, 2020). Currently, offshore renewable energy structures are fixed to the seabed at depths from 0 to 50 m, with installation costs 1.9 times higher for foundations at depths of 40-50 m over those at depths of 10-20 m (Oh, et al., 2018). Nowadays, installation of foundations for wind energy extraction focuses on minimising disruptions to the seabed, concentrating on less expensive installations such as floating structures, requiring anchoring to the bed, installed at depths up to 200 m (European Commission, 2020).



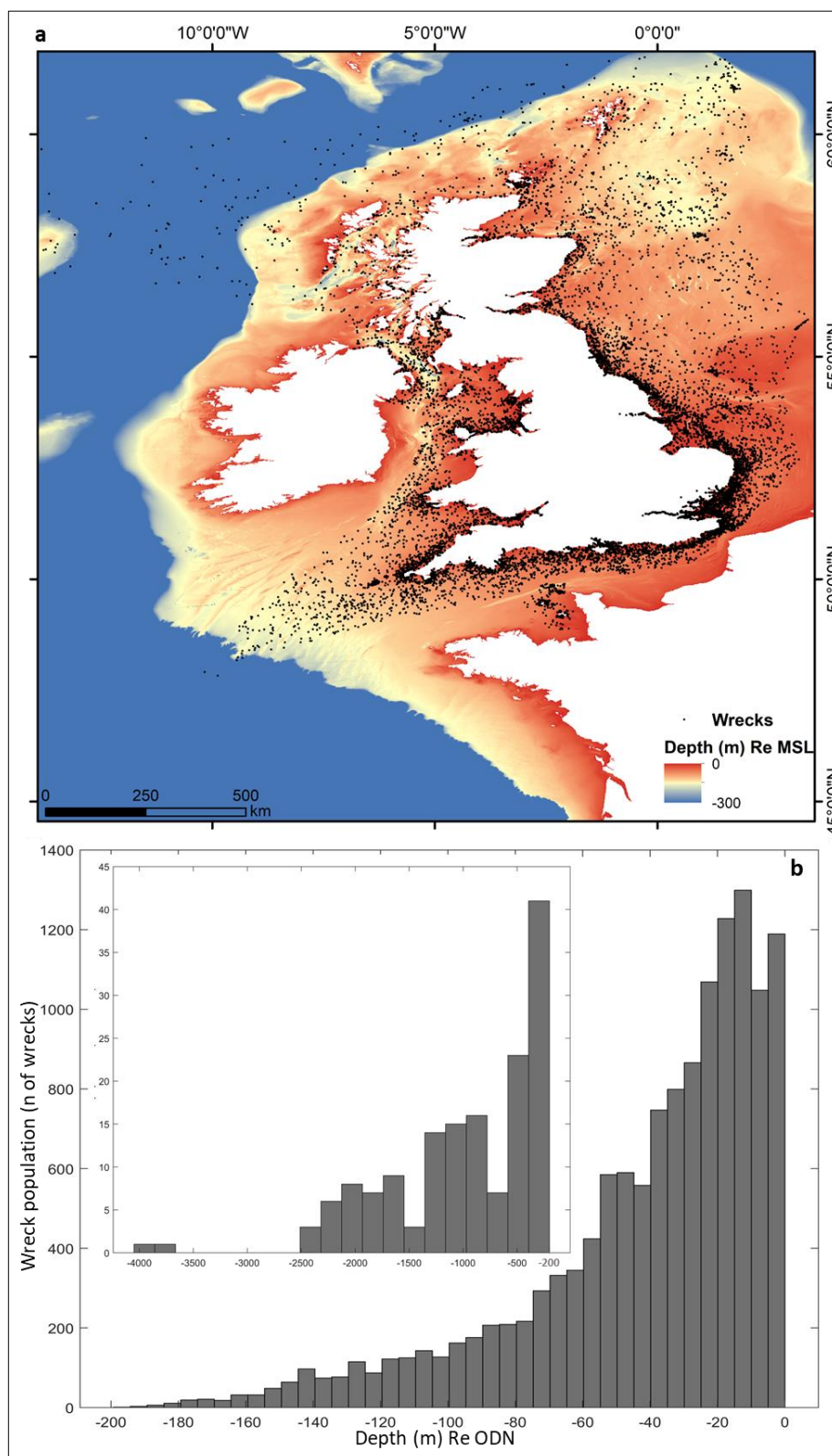


Figure 1.3: a) Distribution of ~14000 wrecks around the United Kingdom of Great Britain and Northern Ireland. The bathymetric data and Digital Terrain Model (DTM) data have been derived from the EMODned Bathymetry portal (<https://www.emodnet-bathymetry.eu/data-products>). Wreck locations are sourced from the United Kingdom Hydrographic Office (UKHO) wrecks database (<https://datahub.admiralty.co.uk>). b) Histogram showing the population of wrecks (number of wrecks) at each depth range.

As **Figure 1.3b** shows, there are over 9500 wrecks (~95%) sitting in depths between 0-50 m in UK's territorial waters. The wrecks have sunk at areas with different seabed surface sediment types and

different hydrodynamic conditions. Using the information gained from Figure 1.1, a histogram of the shipwrecks existing at different environments was made and is presented in Figure 1.4.

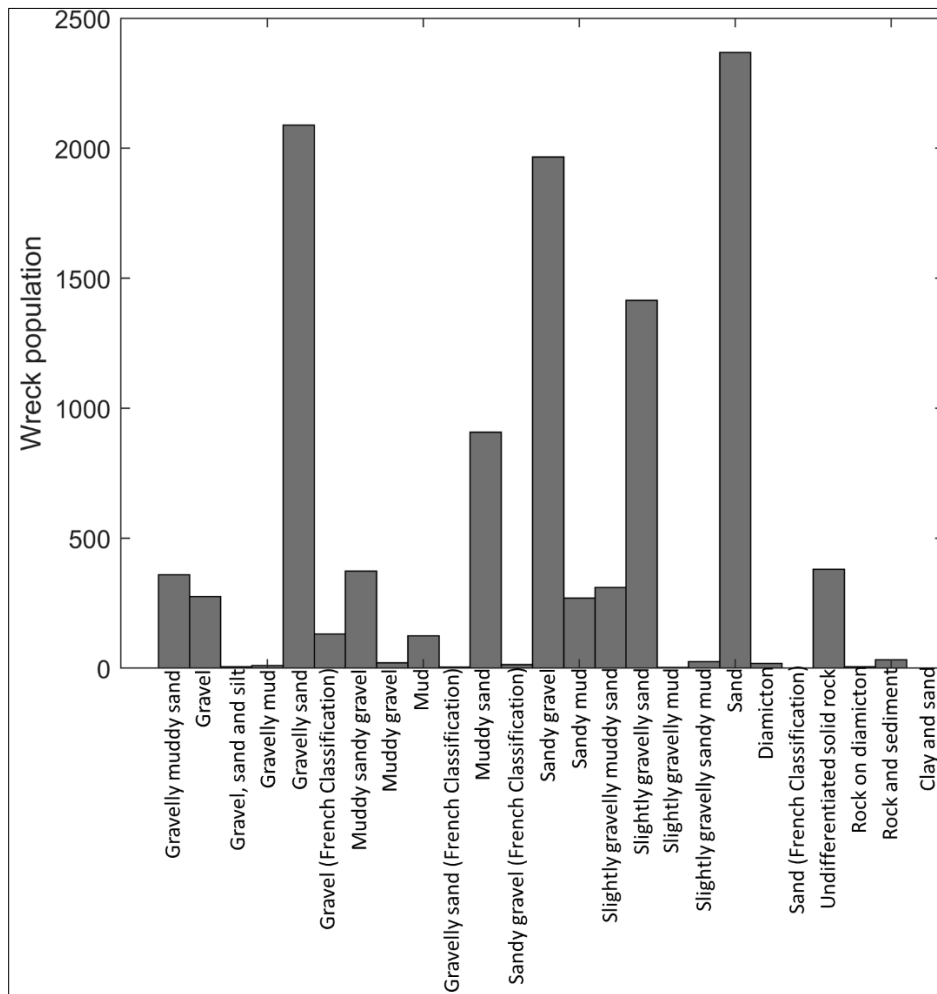


Figure 1.4: Seabed sediment type at  $n=11107$  shipwreck locations, with depths ranging between 0 and 200 m around the UK. The information about the seabed sediment type was taken from the British Geological Survey (BGS) through the Edina Digimap website (<https://digimap.edina.ac.uk/>; DiGSBS250K, 2011). Wreck locations are sourced from the United Kingdom Hydrographic Office (UKHO) wrecks database (<https://datahub.admiralty.co.uk>).

According to Figure 1.1 and the histogram presented in Figure 1.4, there are 11107 wrecks sitting on a known type of sediment, with 26.11% ( $n=2900$ ) of them located on unimodal sediment, while the remaining 73.89% ( $n=8207$ ) of them sits on mixed beds.

Shipwreck sites have been investigated in detail in the last decades, as site formation processes can be considered as a mechanism that can be understood and replicated to an extent (O'Shea, 2004; Church, 2014). Offshore anthropogenic infrastructures and shipwreck sites are open systems, allowing the exchange of material (sediment, water, nutrients) and energy (wave, tidal) across the system boundaries (Quinn, 2006; Quinn & Smyth, 2018). These systems can undergo modification over time due to external disturbance though: i) variations in inputs/outputs; ii) shifts in the internal system organisation and iii) development of energy or mass stores that can lead to lags between the disturbance and the system's response. The degree that a system can be characterised as open or

closed can impact the implementation of resource management techniques (Astley, 2016). Wreck sites can have an archaeological and scientific interest as their site formation is governed by a combination of chemical, physical, and biological processes. Whilst physical processes often dominate, corrosion or cover of the wreck by organisms can increase the roughness of the structure at many stages of the site's formation, for instance (MacLeod, 1993; Smyth & Quinn, 2014; Quinn & Smyth, 2018), which in turn affects the physical processes. The processes under investigation at wreck sites are also of a relevant time scale, as a significant number of wrecks sunk decades ago, which coincides with the projected life span of many anthropogenic infrastructures.

Shipwrecks have also been monitored as they can contain dangerous cargos, rating them a significant hazard for navigation around them (e.g., *SS Richard Montgomery*, BBC News, 2015). Additionally, a study by the European Commission development of European guidelines for potentially polluting shipwrecks project (DEEPP, 2007; Figure 1.5), has identified the importance of investing and understanding potentially polluting shipwrecks. These sites represent a serious hazard for the marine environment and the DEEPP (2007) report recommends the investigation and monitoring of the sediment dynamics at these sites over time, as scour processes contribute to wreck instability and disintegration.

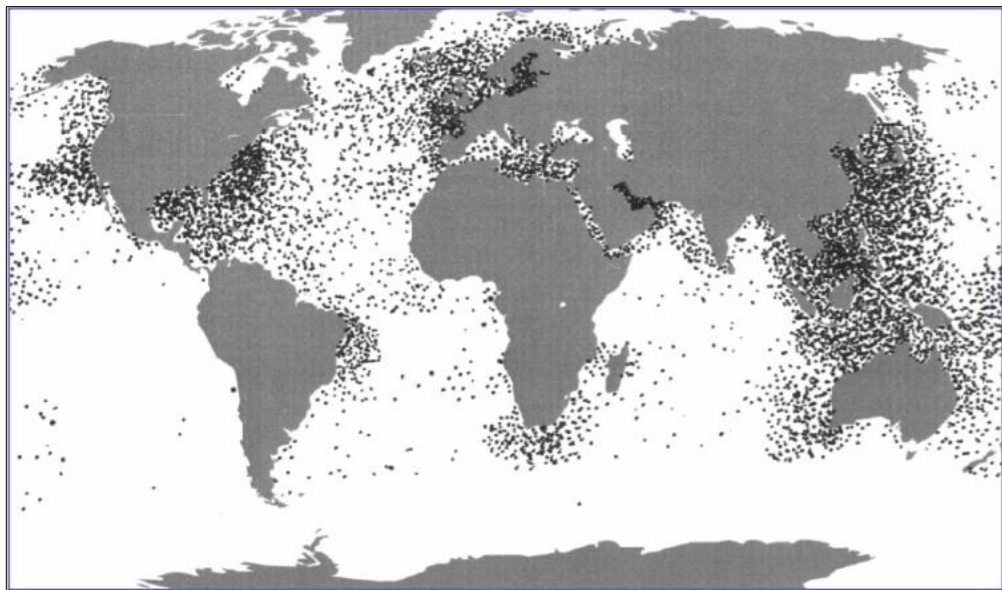


Figure 1.5: Worldwide distribution of potentially polluting shipwrecks (DEEPP, 2007).

## 1.2 Flow around seabed objects, including shipwrecks

The introduction of an object to the seafloor will change the flow pattern in the immediate environment and it is likely to result to the following phenomena (Sumer & Fredsøe, 2002):

- Flow contraction
- Formation of horseshoe vortex upstream of the structure
- Formation of lee wake vortices (with or without vortex shading) downstream of the structure
- Turbulence generation
- Reflection and diffraction of waves
- Wave breaking
- Change in the surrounding soil's pressure differentials that may produce liquefaction allowing material to be carried off by the incoming currents

Horseshoe vortices are formed upstream of the object, because of the incoming flow rotation. The boundary layer on the bed upstream of the object will undergo a 3-D separation due to the influence of the adverse pressure gradient caused by the existence of the object. The separated boundary layer will roll up to form a swirling vortex around the object and forms vortex trails downstream (Sumer et al., 1997). These horseshoe vortices can vary in morphology causing complex flow patterns (Whitehouse, 1998; Saunders, 2005; Smyth & Quinn, 2014; Quinn & Smyth, 2018). Lee wake vortices will form downstream of the structure because of the flow rotation in the boundary layer over the surface of the object, causing the emanation of the shear layers from the side edges of the object to roll up, to form these vortices (Sumer et al., 1997; Whitehouse, 1998; Melville, 2008). Therefore, turbulence forms because of the object's influence on the flow (Sumer et al., 1997; Whitehouse, 1998; Saunders 2005; Smyth & Quinn, 2014; Quinn & Smyth, 2018). Although the horseshoe vortices formed around objects in laminar steady flows have been significantly studied and understood (e.g., Baker 1979; Dargahi; 1982), the formation and the extent of lee wake vortices remains still to be fully quantified (Sumer et al., 1997). The existence of an object and its impact to the hydrodynamics will enhance the forces acting on the bed (i.e., bed shear stress and turbulence levels) by up to a factor of four with the increased forces existing many kilometres in the far field (Whitehouse, 1998; Sumer & Fredsøe, 2002; Smyth & Quinn, 2014; Quinn & Smyth, 2018), where amplification of up to a factor of 5-6 has also been reported (Hebsgaard et al., 1994; Majcher et al., 2022) depending on the lee wake vortices formation and extent, influenced by the shape of the obstacle and its orientation to the flow (Whitehouse, 1998; Saunders, 2005). **The present study aims to quantify the extent of the enhanced (influenced by the object) flow, by investigating changes in the sediment composition and bedform formation downstream of objects.** Figure 1.6 (top) explains schematically the flow contraction and vortex formation due to the interaction of the object and the incoming flow for a cylinder placed on the seabed and Figure 1.6 (bottom) for an object placed fully submerged in the water column.

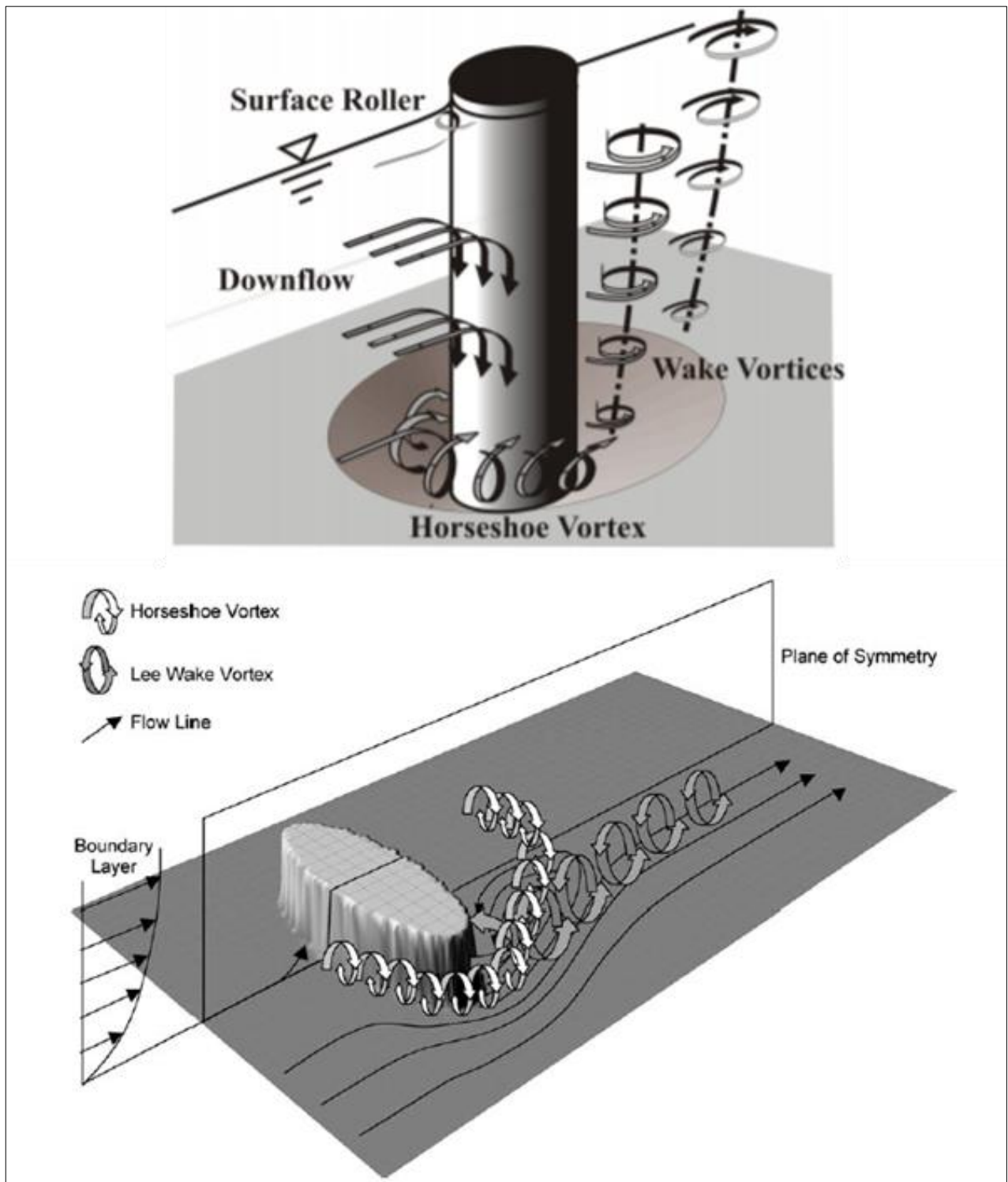


Figure 1.6: Explanation of vortex development and flow patterns around objects placed on the bed (Quinn, 2006 (bottom); Melville, 2008 (top)).



## 1.2.1 Amplification of flow

### 1.2.1.1 Shear stress

A current flowing over a bed has a decreasing velocity from the free stream velocity at the water (maximum velocity) to zero at or near the bed, with the assumption of no free surface extents (Figure 1.7; Van Rijn, 1993a).

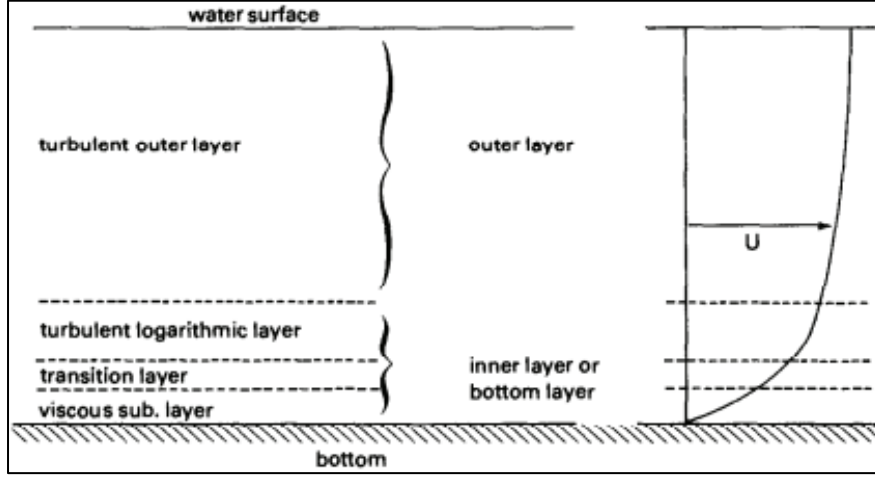


Figure 1.7: Schematic illustration of flow characteristics along the cross-sectional velocity profile (Van Rijn, 1993a).

Near the bed a no-slip condition is generated because of the frictional resistance exerted by the bed onto the flow. The difference in the vertical of the flow velocity ( $du/dz$ ) between the stream-wise layers of the water body generates shear in the form of shear stress ( $\tau_z$ ) that is resisted by the absolute viscosity of the fluid ( $\mu_v$ ). The shear stress due to viscosity in laminar flow can be calculated as (Equation 1.1):

$$\tau_v = \mu_v \frac{du}{dz}, \quad (1.1)$$

In turbulent flows, the shear stress due to turbulence is added to the equation, as shown in Equation 1.2:

$$\tau_t = \eta \frac{d\bar{u}}{dz}, \quad (1.2)$$

Where  $\eta$  is the eddy viscosity. Therefore, the total shear stress in turbulent flow is the sum of  $\tau_v + \tau_t$  that can be calculated using Equation 1.3 as:

$$\tau = \mu_v \frac{du}{dz} + \eta \frac{d\bar{u}}{dz}, \quad (1.3)$$

Shear stresses are generated in the region of the water body where  $\bar{u}$  is less than the free stream velocity ( $u_\infty$ ). The height of the boundary layer ( $\delta$ ) can be defined as the height where  $\bar{u}(z) = 0.99\bar{u}_\infty$ . Within the boundary layer, the flow's vertical cross section can be defined by different layers that depend on the dominance of viscous or turbulent shear. These layers are the viscous sub-layer where the viscous shear is dominant, the turbulent logarithmic and outer layer, where viscous stresses are absent or negligible and the transition layer, where both viscous and turbulent shears are important. In turbulent flow, the boundary layer appears random and chaotic, and it is controlled

by inertial forces. For the purposes of this thesis, although turbulent is present, the assumption of laminar flows will be made due to the fact that sediment sampled from the offshore environment presented in Section 3.3.3 has been identified to being sampled from locations where not significant amounts of turbulence were estimated from the numerical model (presented in Section 3.3.4). Also, evidence from the literature have shown that the ratio of TKE to shear stress is constant and can be defined by  $\tau_0 = C_1 TKE$ , with  $C_1$  being 0.20 (Soulsby, 1981) or 0.19 (Stapleton and Huntley, 1995; Thomson et al., 2003). Discussion of this will follow in Section 3.3.3. It is also noted that in the numerical modelling work presented in the current thesis, within the scour mark, TKE extracted at plane 2 (first layer above the bed; multiplied by 0.19 according to Pope et al., (2006)) was used for the calculation of the shear stress within the scour mark, where high values of turbulence were expected, following the method of Couldry et al. (2020). The flow of a liquid can be characterised as laminar, transitional, or turbulent, depending on the Reynolds number,  $Re^*$ , a dimensionless number used to describe the flow acting on grains in the boundary layer, using the friction velocity ( $u_*$ ), frictional forces (kinematic viscosity,  $\nu$ ) and the grain diameter ( $d$ ) calculated using Equation 1.4 as:

$$Re^* = \frac{u_* d_n}{\nu}, \quad (1.4)$$

The flow in the boundary layer can be categorised as laminar, for  $Re^* < 5$ , transitional for  $5 \leq Re^* \leq 65$ , or turbulent for  $Re^* > 65$  (Le Roux, 2004). The increase in the bed shear stress can be expressed in the terms of an amplification factor ( $\alpha$ ) defined by the bed shear stress ( $\tau$ ) and the bed shear stress for the undisturbed flow ( $\tau_\infty$ ), using Equation 1.5 (Sumer & Fredsøe, 1991):

$$\alpha = \frac{\tau}{\tau_\infty}, \quad (1.5)$$

### 1.2.2 Complexities of flow around shipwrecks

Shipwreck sites are open systems (Caston, 1979; Quinn, 2006; Majcher et al., 2020) and therefore their size, shape and orientation to the flow can cause different flow regimes (Quinn, 2006; Smyth & Quinn, 2014; Quinn et al., 2016; Quinn & Smyth, 2018). The flow around a fully submerged wreck is three-dimensional as it is for a horizontal cylinder (Testik et al., 2005), and can be characterised by the two basic flow structures of the horseshoe vortex and the lee-wake vortex (Quinn, 2006). Vortex shedding can also occur around shipwrecks, due to self-propelling and closed ring flow structures formed and transported by the flow (Testik et al., 2005; Quinn & Smyth, 2018).

The shape and orientation of the stern and bow of the shipwreck play a dominant role in the flow pattern and strongly influence the shape, structure, and extent of the vortices (Testik et al., 2005; Quinn, 2006). The lee-wake vortices formed from the surface of the vessel merge downstream of the wreck with the vortices generated at the stern and bow of the vessel, due to flow convergence (Smith et al., 2004; Testik et al., 2005; Quinn & Smyth, 2018). In addition, two counter-rotating vortices form another vortical region in the immediate wake, downstream of the wreck (Testik et al., 2005).

In the literature, computational fluid dynamic (CFD) models are often used to model and identify the flow patterns around shipwreck sites (Smyth & Quinn, 2014; Quinn & Smyth, 2018, Majcher et al., 2022) as they can successfully simulate and capture the flow regimes in wreck sites, like flow contraction, the generation of horseshoe vortices upstream of the object and the generation of lee wake vortices downstream of the wrecks, along with the increased wall shear stress and turbulence at the wake of the wrecks. CFD modelling investigates the interaction of fluids with surfaces defined by specific boundary conditions (Smyth & Quinn, 2014). Another important component of the flow investigation around submerged shipwrecks is the possibility of the wreck's disintegration, due to biological, physical, or chemical processes, altering the existing hydrodynamic conditions (Quinn, 2006; Macleod, 2006). A detailed study by Quinn & Smyth (2018) summarises the use of CFD model to predict the flow diversion and amplification around shipwreck sites, at different orientations to the flow. Figure 1.8 shows the outputs of a CFD model that run with the vessel placed at  $60^\circ$  to the flow with an incoming uni-directional depth averaged flow velocity of  $1.3 \text{ m}\cdot\text{s}^{-1}$  (Quinn & Smyth, 2018). Although the Quinn and Smyth (2018) study summarises the observations at various orientations of flow, the simulation conducted at  $60^\circ$  to flow is shown here as it is directly relevant to this study.

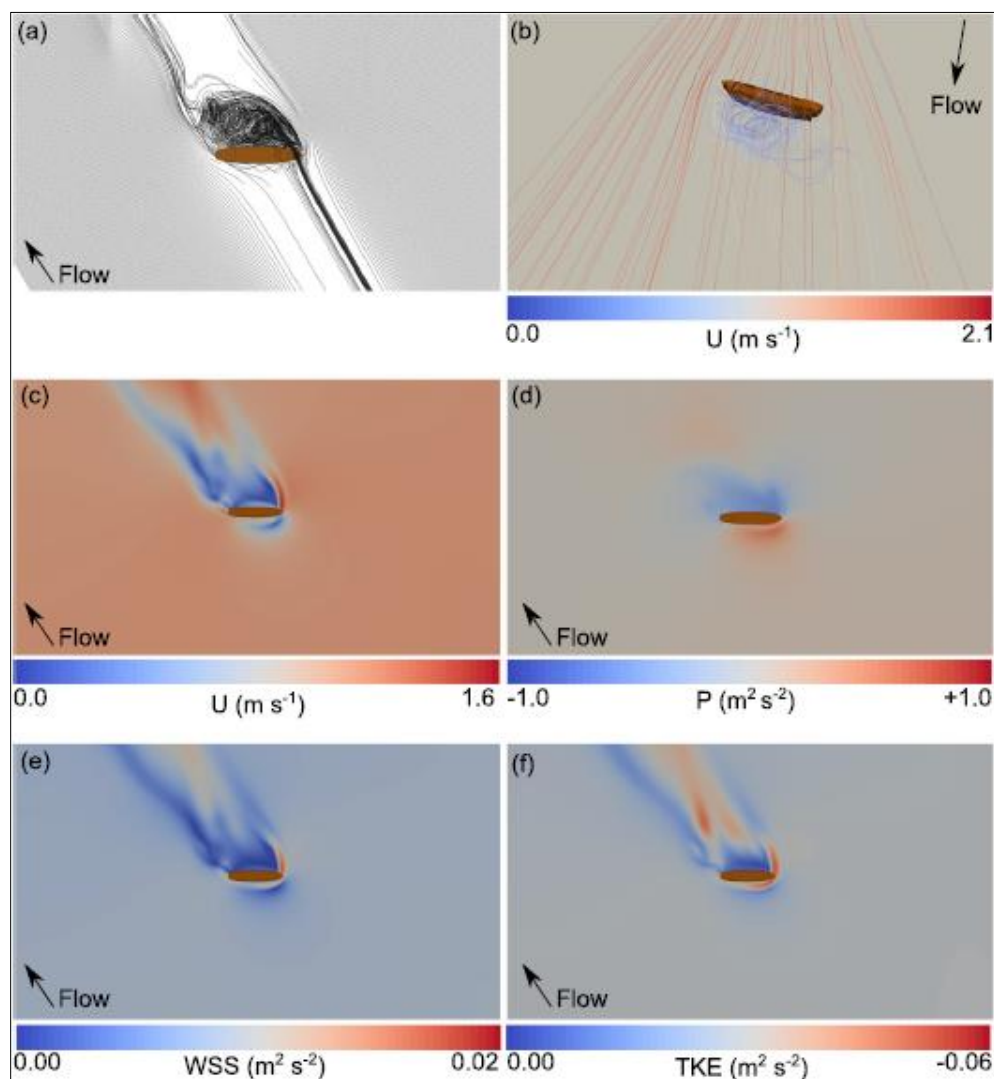


Figure 1.8: Vessel at  $60^\circ$  to the flow. a) 2-D flowlines, b) 3-D flowlines, c) flow velocity, d) pressure, e) wall shear stress (WSS) and f) turbulent kinetic energy (TKE) as derived from the CFD model (Quinn & Smyth, 2018).



### 1.3 Sediment transport and bedform migration on mixed beds

Amplified flow around objects is expected to cause enhanced sediment transport. Transport of depth-integrated sediment can be mobilised and moved in two different ways (Sutherland & Soulsby, 2011). Firstly, by bed load transport, which is the transport of sediment particles in a thin layer, with thickness  $\delta$  (order of 0.01 m), through rolling, sliding and saltating. Bed load transport normally occurs at areas with relatively weaker mean currents than the transport energy induced by waves. The second mechanism of sediment transport is suspended load transport, which takes place in the water column above the bed load transport layer. Suspended load can even occur at areas in the absence of currents, when concentrated suspended sediment exists in the thin turbulent near-bed wave boundary layer. The maximum suspended load sediment grain size for particles to enter in suspension is reported to be <0.2 mm, although the criterion for the limits of sediment grain sizes suspension can be calculated using Equation 1.6 (Soulsby, 1997).

$$u_{*s} = w_s \quad (1.6)$$

where:

$u_{*s}$ : Skin – friction velocity

$w_s$ : The mean grain size settling velocity

Sediment can enter and be transported in the suspended load when  $w_s < u_{*s}$ .

The sum of the net load and suspended load transport rates can be defined as total sediment transport. It is also important to mention that at sites with sloping beds, gravity can act to decelerate or accelerate sediment particle movement (Soulsby, 1997). While sediment transport is mainly driven by the hydrodynamic parameters of the flow, knowledge and understanding of sediment transport occurring under complex hydrodynamical forcing is still limited (Amoudry et al., 2009). The grain size and the grain distribution within sediment is another aspect of sediment movement, as the degree of a grain's exposure compared to the surrounding grains can affect the forces needed for the initiation of motion (the point where the grains will start mobilising), an effect known as the hiding exposure effect (Egiazarof, 1965; Soulsby, 1997; Janssen, 2010; McCarron et al., 2019). In steady flow conditions, initiation of motion occurs at the stage where the value of the bed shear stress is larger than a certain threshold value, called critical shear stress (Soulsby, 1997; Sutherland & Soulsby, 2011). Shear stress can be defined as the frictional force of the flow, just above a sedimentary bed, that acts on the sediment particles per unit area (Soulsby, 1997). The bed shear stress is the parameter that allows the sediment grains to remain at equilibrium, even in cases where the sediment is not set on a level surface (areas with slopes). The bed shear stress calculation requires knowledge of the depth-average current speed, the current direction, the sedimentary bed bathymetry, and the wave direction, period, and wavelength (Wilson et al., 2018).

The value of the critical shear stress ( $\tau_{cr}$ ) can be calculated using Equation 1.7 as:

$$\tau_{cr} = \theta_{cr} g (\rho_s - \rho_w) d_{50} \quad (1.7)$$

where:

$\theta_{cr}$ : The threshold of motion

$g$ : The acceleration of gravity

$\rho_s$ : The sediment density

$\rho_w$ : The water density

$d_{50}$ : The sediment median grain size

The initiation of motion of sediment in a fluid flow also depends on the local Shield's parameter (Quinn et al., 2016). The local Shield's parameter ( $\theta$ ) can be calculated using Equation 1.8 (Sumer, 2001) as:

$$\theta = \frac{U_f^2}{g(s-1)d_{50}} \quad (1.8)$$

where;

$s$ : The specific gravity of the sediment grains

$g$ : The acceleration due to gravity

$U_f$ : The maximum value of the undisturbed velocity

$d_{50}$ : The sediment median gain diameter

A combination of the Reynold's number and Shield's parameter can provide a first approximation of the point where the sediment particles of different sizes are expected to start mobilising (Sutherland & Soulsby, 2011).

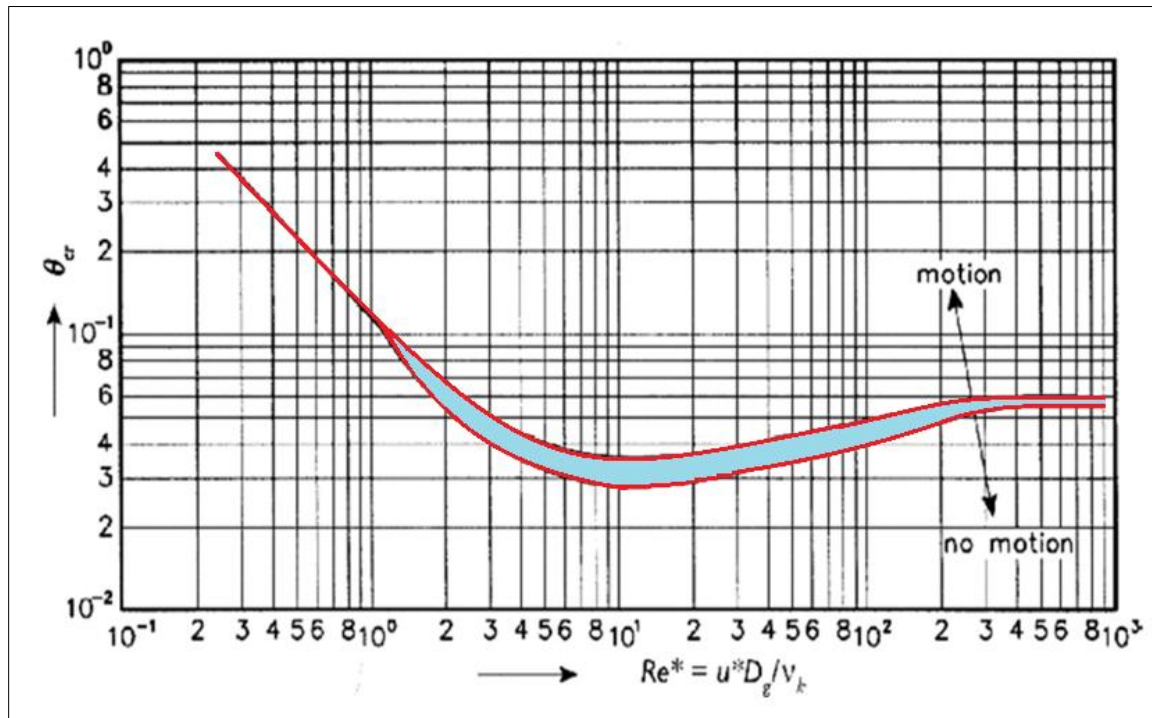


Figure 1.9: The Shield's curve (Adapted from Sutherland & Soulsby (2011))

Figure 1.9 shows the critical stage, where minor part of the bed surface will be mobilised along the bed. Sediment grains with  $\theta_{cr}$  and  $Re^*$  values above the top red line will be mobilised, where sediment grains with  $\theta_{cr}$  and  $Re^*$  below the bottom red line will remain on the seafloor. Sediment grains with their  $\theta_{cr}$  and  $Re^*$  values within the printed as light blue on Figure 1.9 are in an equilibrium state, just before they set in movement, or settle completely to the sedimentary bed (Sutherland & Soulsby, 2011).

The sediment particles are therefore set in movement, when the shear stress at the bed is higher than the frictional and gravitational forces that hold the grains to the bed (Callaway et al., 2009; Quinn & Smyth, 2018). The critical shear value is a function of the submerged density of the sediment and the mean sediment particle size (Callaway et al., 2009). Eventually, when the bed shear velocity or the bed shear stress is greater than the particle's settling velocity, the sediment grains will be mobilised by suspension (O'Neil, 2002). For mixed coarse sediments, the higher the sand concentration in a mixture, the lower the critical shear stress that is required to transport the gravel-sized fraction (Wilcock, 1998). Settling velocity is one of the parameters that controls the sediment's transport in suspension and is sometimes measured on *ex-situ* samples in the laboratory.

Settling velocity of non-cohesive sediment particles, can be measured using Stokes' law using Equation 1.9 (Teisson, 1991) as:

$$w_s = \frac{(\rho_s - \rho_w)gD^2}{18\nu} \quad (1.9)$$

where:

$w_s$ : Settling velocity ( $\text{m}\cdot\text{s}^{-1}$ )

$\rho_s$ : Sediment density ( $\text{Kg}\cdot\text{m}^{-3}$ )

$\rho_w$ : Water density ( $\text{Kg}\cdot\text{m}^{-3}$ )

$\nu$ : Kinematic viscosity of the fluid ( $\text{m}^2\cdot\text{s}^{-1}$ )

Nevertheless, Stokes' law makes some critical assumptions, such as spherical, smooth, and rigid sediment grains, a constant specific gravity, linear flow, and an infinite water body for sedimentation. These assumptions rarely occur in nature or under controlled laboratory conditions (Mantovanelli & Ridd, 2006).

Bedload transport processes have been investigated in the literature in the context of bedform studies, where their formation and transport rates depend on the interaction between current induced forces and underlying sediment. The migration rates of bedload features (such as ripples) can provide information about sediment bedload transport rates. Ripple development depends on the ability of the forcing current to mobilise the sediment that forms them. As previously outlined, sediment transport occurs when the bed shear stress ( $\tau_b$ ), expressed as dimensionless Shields ( $\theta$ ) parameter, and calculated using the water density ( $\rho_w$ ), depth averaged velocity ( $\bar{U}$ ) and a friction coefficient ( $C_f$ ) (Equation 1.10) exceeds the critical shear stress ( $\tau'_{cr}$ ):

$$\tau_b = \rho_w C_f \bar{U}^2, \quad (1.10)$$

The friction coefficient in Equation 1.11 is calculated as a relation of the Von Kármán constant ( $k$ ), the water depth ( $h$ ), the Nikuradse roughness ( $k_s$ ) and Euler's number ( $e$ ), as determined in Equation 1.11:

$$C_f = 2\kappa^2 \left( \log \left( \frac{30h}{k_s e} \right) \right)^{-2} \quad (1.11)$$

In the case of bedform formation, another roughness coefficient,  $k_s''$ , is introduced due to drag, which changes the bed shear stress ( $\tau_b$ ) through a combination of grain related bed shear stress ( $\tau'_b$ ) and bed shear stress originating from drag ( $\tau''$ ) (Soulsby, 1997; Amoudry & Souza, 2011).

Ripples are classified as bedforms with heights and wavelengths up to 0.6 m that can develop in sediment types with grain sizes up to 0.8 mm (Van Rijn, 1993a; Soulsby, 1997; Soulsby et al., 2012). Ripples can be generated by currents, waves or a combination of both. Although not the focus of the current thesis, current generated ripples formed on mixed coarse beds (sand and gravel mixtures) are sometimes investigated to help determine and monitor the result of the amplified flow and any potential changes caused in the ripple characteristics downstream of a submerged object. The formation of current-generated ripples is controlled by grain size and the bed shear stress (Van Rijn, 1993b; Baas, 1999; Soulsby et al., 2012). Ripple height ( $\Delta S$ ) and wavelength ( $\lambda$ ) can be used to calculate the time taken for these bedforms to reach an equilibrium point in their development (Lichtman et al., 2018). However, to date, much of the analyses of ripples has focused on their development in fine sediment (silt or sand) with the focus on the influence of biological cohesion in the ripple formation (Baas et al., 2011; Lichtman et al., 2018), and knowledge of their formation in non-cohesive sediment mixtures is limited (Chiew, 1991; Rauen et al., 2009). In sand and gravel mixtures, bedform formation is mainly driven by cyclical entrainment, transport and deposition of the different fractions within the sediment (Kuhnle et al., 2006). Bedforms in sand and gravel mixtures have been characterised with different names depending on their characteristics and formation parameters (e.g., Dietrich et al., 1989; Kleinhans et al., 2002; Kuhne et al., 2006). McCarron (2020) used the Kuhnle et al. (2006) study that classified bedforms reported in the literature on the basis of their dimensions and migration rates as: ripple-like bedforms (RLBF), bedload sheets (BLS) and low-relief bed forms (LRBF) (Table 1.1).

Table 1.1: Summary of morphological and dynamic characteristics of bedforms observed in sand and gravel mixtures (McCarron, 2020).

Bedform type	Bedform height, $\Delta_s$ (mm)	Bedform wavelength, $\lambda$ , (mm)	Migration rate (mm·s <sup>-1</sup> )
<b>RLBF</b>	3-5	30-802	4-34
<b>BLS</b>	4-13	71-1061	8-27
<b>LRBF</b>	8-17	2300-4489	9-25

### 1.3.1 Sediment transport around seabed objects

The ever-increasing need for seabed infrastructure, enabling for example marine renewable energy extraction and novel applications such as offshore centralised storage, requires the installation of objects on the seabed of many different shapes and sizes. Sediment transport around these seabed objects is expected to be amplified, due to the enhanced bed shear stress and turbulence levels (Sumer & Fredsøe, 2002; Quinn, 2006; Quinn & Smyth, 2018). Specifically, when the amplification

factor ( $\alpha$ ) from Equation 1.5 is greater than 1, the sediment transport capacity increases, and the bed erodes (scour). When  $\alpha=0$ , scour reaches a dynamic equilibrium point, as the obstacle has become part of the system (Whitehouse, 1998; Sumer & Fredsøe, 2002; Zhang et al., 2017). It is important to mention that scour does not only affect the immediate environment of the object, but enhanced forces also cause the formation of bedforms downstream, due to the persistent turbulent and enhanced forces in the far field (Bahaj, 2011). Scour has been categorised as live-bed scour, where there is sediment transport over the entire scour depth and clear water scour in areas where there is no sediment motion away from the structure (Sumer & Fredsøe, 2002; Saunders, 2005). Scour has also been classified as local, global/wake or seabed movement that can result in erosion of the underlying seabed (Whitehouse, 1998; Saunders, 2005). Finally, scour has been categorised as near-field which is the scour area directly attached to the object and far-field, which is the scour in the wake of the object (Quinn, 2006). Scour is widely recognised to cause engineering problems at anthropogenic infrastructure, requiring detailed design and scour mitigation, along with post-installation protection techniques in some cases (Whitehouse, 1998; Whitehouse et al., 2011).

Vertically placed piles are one of the most common anthropogenic infrastructures offshore, as they are commonly used for renewable energy extraction (wind, wave, currents) around the world (Ball et al., 1997; Amoudry et al., 2009; Yuan et al., 2017). The sediment composition in the areas of installation, bathymetric variation, and scour potential, must be considered prior to the design and installation of such structures (Whitehouse et al., 2011). It is widely accepted that scour is one of the main reasons of failure of piles in the marine environment (Whitehouse, 1998; Quinn, 2006). It is understood that for wind turbine piles, placed in areas with steady flows, the higher the flow depth and velocity, the higher the maximum predicted scour depth (Yuan et al., 2017). Similar observations are noted for bridge piers, with higher flow depths ( $y$ ) leading to deeper scour, up to a limit set by the flow depth ( $y$ ) / structure diameter ( $D$ ) ratio (Ettema, 1980; Chiew, 1984). When that limit ( $y/D$ ) is exceeded, flow depth influence on scouring ceases (Yuan et al., 2017). The flow depth parameter is also influenced by ratio of the structure's diameter ( $D$ ) to the grain size diameter ( $d_{50}$ ). When  $D/d_{50}$  values are high and values of  $y/D$  are close to 1, scour depth is almost independent of the flow depth (Yuan et al., 2017). In contrast, for low  $D/d_{50}$  values, scour depth is dependent on flow depth for values up to  $y/D=6$ . (Ettema, 1980; Melville, 2008).

Industry standards use predictive equation for monopiles with scour up to 1.3 times the diameter of the structure (Nielsen & Hansen, 2007), with the need for scour protection in some cases. Scour protection techniques, however, can affect both the hydrodynamics and sediment dynamics of the area (Whitehouse et al., 2011) and cause secondary scour around the installation (CEFAS, 2006). To reduce scour impacts, arrays of monopiles have been installed at some development sites. However, it has been observed that placing multiple monopiles on the seabed can result in scour marks comparable to those produced by larger structures (Ball et al., 1997). Arrays of monopiles can also cause large wakes downstream, impacting hydrodynamics and sediment dynamics in the far field. Figure 1.10 shows an example of scour formation around an offshore structure, where local



scour is shown around each pile of the structure and global scour is shown around the structure (Whitehouse, 1998).

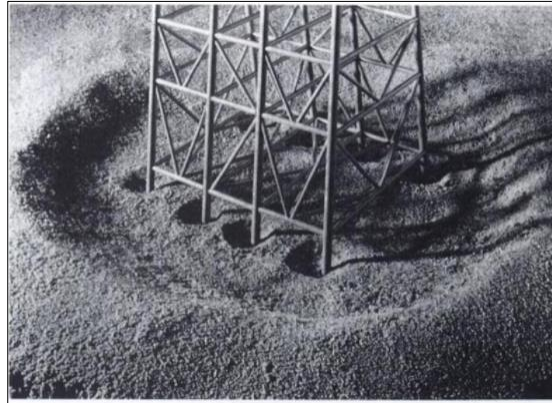


Figure 1.10: Representation of global and local scour development around an offshore structure (Whitehouse, 1998).

### 1.3.2 Scour around shipwrecks

Scour around shipwrecks can vary from short- to long-term, with short-term happening during localised events, and long-term scour mainly caused by parts of the wreck that are semi-buried. Wrecks can also become partially/fully buried and exposed again due to external forcing and bedform migration (Quinn, 2006).

Shipwrecks can be affected by aerobic bacteria that influence the exposed parts, and anaerobic bacteria, that influence the buried parts of the wreck. The effect of biological processes on the wreck can increase the corrosion rates, with the combination of these processes contributing even more on the wreck's site formation (Quinn et al., 2016). In wreck sites, scour is not only controlled by the sediment around the wreck, but also the wreck's orientation to the hydrodynamic regime (flow) and its category (i.e., linear, turbulent, oscillatory etc.), the bathymetry, the morphology and the size of the wreck and the geomorphology and geology of the site (Quinn, 2006). In shallow environments scour formation can be increased under the influence of waves (Fernández-Montblanc et al., 2016). Sub-surface geological structures can also affect the scour mark's formation and depth as the existence of an unerodable layer (i.e., bedrock) below the sedimentary bed will limit the depth but increase the lateral extent of the scour (Quinn, 2006; Majcher et al., 2021). Wrecks appear to be in dynamic equilibrium (not steady state) with their surrounding environment and sometimes are in negative disequilibrium, resulting to the wreck's disintegration (Quinn et al., 2016). Such events can be categorised as triggers and can alter the scour formation immediately, resulting in short term changes that settle once the site reaches a new dynamic equilibrium (Quinn & Boland, 2010). Figure 1.11 shows the expected scour formation around shipwrecks located at areas with different flow characteristics and positioned at different angles to the incoming flow (Quinn, 2006).

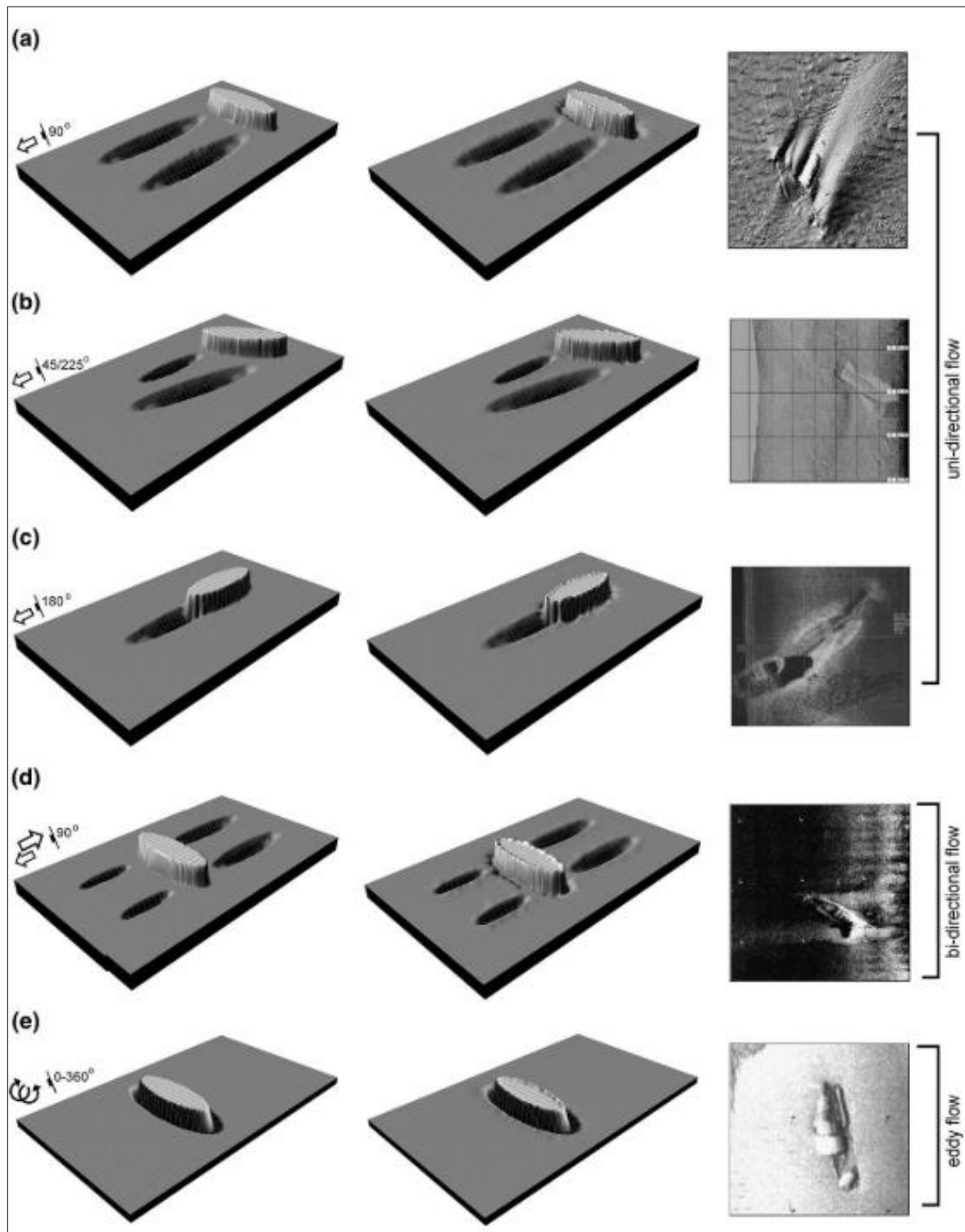


Figure 1.11: Scour around shipwrecks because of different orientation to the flow and different type of flow (Quinn, 2006).

Shipwreck sites have been used as open system scour investigation sites, as they allow for sedimentological, hydrodynamic, geotechnical, and biological controls (Caston, 1979; Quinn, 2006; Majcher et al., 2020). In the case of tidal environments, bi-directional scour marks are normally observed, with the longest signatures recorded in the direction of the dominant current and subsequent dominant sediment transport (Caston, 1979). Bedform formation can be considered part of the scour process (Whitehouse, 1998), and it is expected that the bedform crests will be orientated

perpendicular to the flow direction (Allen, 1984). As shipwreck sites have been observed to influence the normal sediment dynamics over tens of times the length of the wreck (Garlan et al., 2015), scour around shipwrecks is important to understand, not only for engineering, but also for archaeological or even transportation safety purposes, as the archaeological material carried in shipwrecks is likely to be kept within the scour pits, with some elements transported far away from the wreck (Astley, 2016).

Scour patterns around shipwreck sites have been identified from all around the globe. Some of these signatures extend great distances from the wrecks and are mostly parallel to the peak tidal flow (Sumer et al., 2005). The orientation of the wreck with respect to peak flow plays a major role to the site's formation. The expected erosion and deposition around wreck sites, as calculated using a computational fluid dynamic (CFD) model, is shown in Figure 1.12 (Quinn & Smyth, 2018).

**Seabed scour around irregular objects in unsteady three-dimensional flows is complicated and has not been studied significantly in the literature (Inman & Jenkins, 2005). The complexity of the flow diversion and amplification, along with the interaction of the bed in the wake of the object remains to be fully understood (Quinn & Smyth, 2018).**

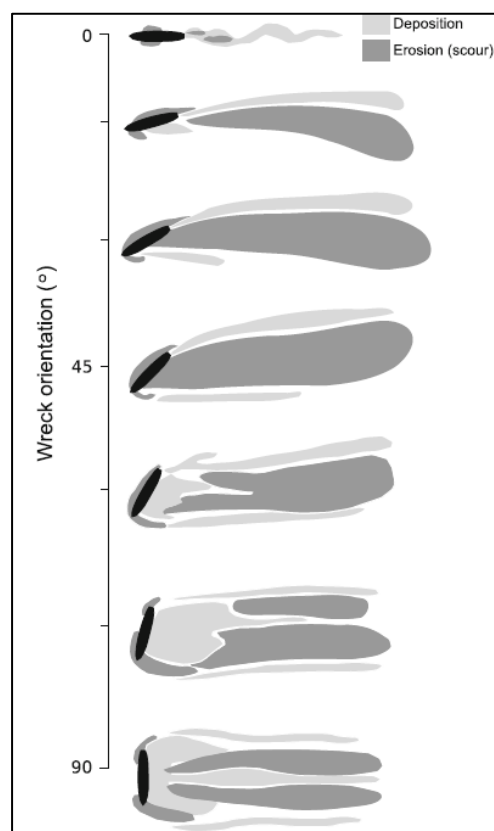


Figure 1.12: Erosional and depositional patterns around fully submerged shipwrecks as inferred from the output of Computational Fluid Dynamic models (Quinn & Smyth, 2018).

The complex flow patterns resulting in different patterns of scour formation around wreck sites is illustrated in the literature (Caston, 1979; Saunders, 2005; Quinn et al., 2016; Quinn & Smyth, 2018), with knowledge derived from field observations (Caston, 1979; Quinn, 2006), numerical modelling (Smyth & Quinn, 2014; Quinn & Smyth, 2018; Majcher et al., 2022) or laboratory-based experiments and models (Tastik et al., 2005; Saunders, 2005).



These knowledge sources, have their advantages and limitations, as detailed below:

- i) A single time step survey of a wreck site, although able to describe its environment at a certain time and it may not be representative of the long-term evolution of the site (Astley, 2016). Use of difference modelling of various bathymetric surveys over a period, can provide information about the site development over a period of time, but cannot be used to fully quantify changes of the site formation processes.
- ii) Use of physical modelling, through laboratory experiments can provide understanding of erosion and deposition processes, due to the ability of controlling parameters that influence scour (i.e., sediment type, flow, object shape and orientation to flow). However, laboratory experiments can be time consuming and cannot be used to replicate offshore sites due to scaling limitations, size of the flume environments and practical limitations related to reversing flow and wall effects.
- iii) CFD models can provide significant, precise information of flow patterns and processes around shipwrecks, and allow the use of multibeam echosounder data as model inputs (Smyth & Quinn, 2014). CFD models can use open source softwares (e.g., OpenFOAM) and are relatively inexpensive. They also allow the control of the modelling environment and scenario and hypothesis testing (Quinn & Smyth, 2014) and they can visualise the flow pathways at a certain time period or a fixed time point (Astley, 2016). A more recent study (Majcher et al., 2022) has also co-registered bathymetric difference modelling around shipwreck sites and CFD models to understand the evolution of tidally influenced wreck sites. To date, CFD model outputs have been compared against geomorphic changes but have not yet been compared to physical modelling (Majcher et al., 2022). CFD models can also evaluate the potential for sediment mobility by comparing two variables, the wall shear-stress exerted by the flow and the sediment type-specific critical shear stress (Majcher et al., 2022). These studies have however to date only investigated cases where the surrounding bed was uniform (Sumer, 2007; López et al., 2018; Majcher et al., 2022), assuming the use of the median grain size ( $d_{50}$ ) as a representative value of the sediment in sediment transport-predictive equations.

To date, the aforementioned methods have never all been combined. The complexity of the bed has not been fully assessed in the aforementioned studies and physical modelling has not been used in detail to identify the dominant processes in scour formation and evolution in the case of mixed beds. There is therefore **a gap in knowledge of how the characteristics of the flows developing downstream of the shipwrecks, alter the stresses on the bed in cases where the surrounding bed is more complex (i.e., consisting of mixed sediments).**

### 1.3.3 Complexity of scour in mixed sediments

In uniform sediments the local scour depths are not affected by sediment sizes, unless the sediment is relatively coarse, with studies showing that local scour is influenced by the sediment when the  $D/d_{50} < 50$  (Melville & Chiew, 1999). In non-cohesive uniform sediments on the other hand, as the grain size increases, the bed shear stress required to mobilise the bed increases, making larger grains more difficult to mobilise than finer grains. The high values of bed shear stress, produced by

the introduction of an object to the hydrodynamics for example, is likely to increase scour depths (Harris & Whitehouse, 2014). In the case of coarser surficial deposits, scour formation can expose underlying coarser material, extending the scour mark laterally rather than vertically (Caston, 1979). To date, the majority of studies have focused on scour around different shaped structures in fine and uniform beds (Whitehouse, 1998, Quinn, 2006; Smyth & Quinn, 2014; Quinn & Smyth, 2018). However, there is an **uncertainty of the bedload transport rates predictors that use single-class models, as a single fraction value (i.e.,  $d_{50}$ ) cannot be representative of mixed bimodal sediment (Wilson et al., 2018), prompting the question of the ideal approach to assessing sediment transport in non-unimodal sediment.** The main cause of this uncertainty is the influence of the hiding exposure (HE) effect. On the bed surface, the finer grains can be hidden from coarser grains, requiring more force to be mobilised. Larger grains in turn can be more exposed to the flow, requiring less shear stress for their mobilisation (Figure 1.13; McCarron et al., 2019).

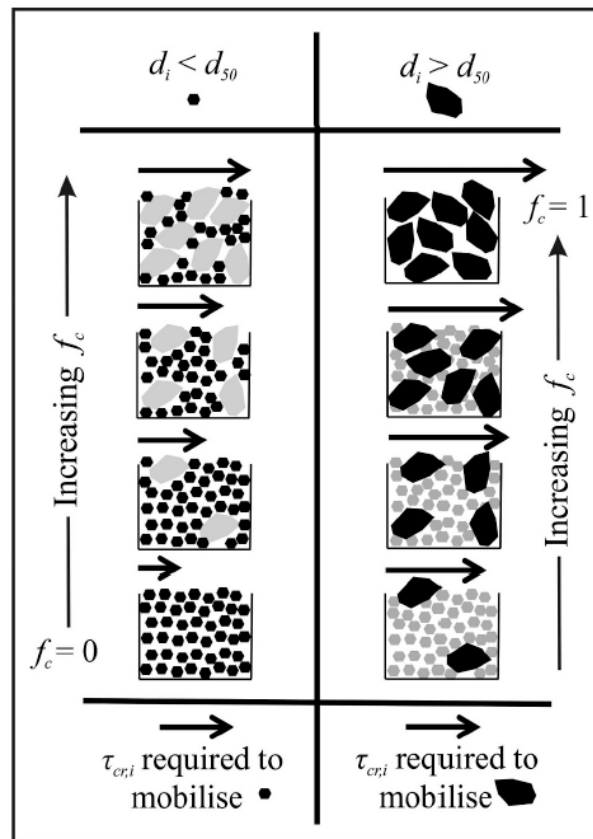


Figure 1.13: Schematic illustration of critical shear stress ( $\tau$ ) needed to mobilise fine and coarse material of a bimodal mixture (McCarron, 2019).

The formerly glaciated continental margin now represented by the North and Irish Seas that are characterised by a wide range of sediments of glacial origin, ranging from silts and clays, to sand, gravel, cobbles, and boulders (Clarke, 2005). To the author's knowledge, there is a **limited knowledge and information in the literature on scour formation around objects placed intentionally or unintentionally on mixed beds.**

## 1.4 Aims, Objectives and Outline

The overall aim of this thesis is to help better predict scour formation around objects placed on mixed beds, by a combination of all three of:

- i) Real-world site observation for scour development around a wreck;
- ii) physical modelling of bed mobility and
- iii) numerical modelling of flow modification and bed mobility using a coupled hydrodynamic and sediment transport model.

This aim is met through the following objectives and research questions:

**Objective 1:** Better understand and quantify the flow amplification and diversion around an object.

**Question 1.1:** Where is flow modification around the object strongest?

**Question 1.2:** What is the lateral extent of flow amplification in relation to object size and background hydrodynamics?

**Question 1.3:** How does a change in the object's shape impact flow amplification (strength and extent)?

**Objective 2:** Better understand and quantify the impact of the modified flow on the surrounding bed.

**Question 2.1:** How does the amplified flow downstream of the object impact the sediment movement of mixed coarse (sand and gravel) beds?

**Question 2.2:** How does the mixed sediment composition impact scour evolution at different levels of grain entrainment?

**Question 2.3:** For which bimodal non-cohesive sediment mixture will the scour be the greatest (in terms of depth and extent)?

**Question 2.4:** Using more appropriate statistics of particle size distribution of mixed beds, which of those parameters will allow for the spatial extent of scour formation to be best predicted?

**Question 2.5:** How does a change in the object's shape impact the evolution of the scour?

In this thesis, scour development around differently shaped objects sitting on mixed beds will be assessed. The influence of the shape of a wreck and its influence on the surrounding hydrodynamics and the subsequent scour development will be assessed and quantified. Chapter 2 contains the overall methodology used to address the objectives of this thesis along with the materials used. Site formation processes will be assessed through high-resolution bathymetric and hydrodynamic data and a coupled hydrodynamics and sediment transport model will be used for the prediction of scour development and flow deviation around the wreck of *SS Apapa* (Chapter 3). Physical modelling using a controlled laboratory environment was performed and will be presented, to identify the influence of bed composition and flow velocity on scour development downstream of a cylinder (Chapter 4). The input parameters and the results of the analyses from the physical model will be used in a numerical coupled hydrodynamics and sediment transport model for both input and validation. A discussion of the results presented in Chapters 3 and 4 will be presented in Chapter 5. Finally, answers to the questions asked in this section will be given, through a synthesis of the results of each chapter, in Chapter 6, along with an assessment of their wider implications and suggestions for further research.

## Chapter 2

### 2. Materials and Methods

In the present thesis both results chapters (Chapters 3 and 4) contain their own methodology section, written with sufficient detail to permit the reproducibility of the work conducted. To avoid repetition, this chapter contains only the specifications of the equipment and the materials used.

#### 2.1 Methods used to address the aims of the project

The overall aim of this study is to predict scour around objects placed on mixed beds. This chapter provides an overview of the strategy followed mapped onto the project's objectives as detailed below:

**Objective 1:** Better understand and quantify the flow amplification and diversion around an object. Offshore acoustic doppler current profiler (ADCP) data (Section 2.2.3) and flume-lab ultrasonic velocimetry doppler profiler (UDVP) data (Section 2.3.4) primes the hydrodynamic model (Section 2.4.1), which identify the strength and lateral extent of flow amplification, and how the shape of an object influences that.

**Objective 2:** Better understand and quantify the impact of the modified flow on the surrounding bed. Analysis of multibeam echosounder (MBES) bathymetry data from the wreck site of *SS Apapa* (Section 2.2.2) collected over 9 surveys from 2012 to 2019 identify amplified seabed mobility over time due to the impact of flow diversion and amplification around the wreck. Seabed mobility is then linked to seabed sediment composition from grab samples (Section 2.2.4) and analysed for particle size distribution (Section 2.2.5). Sediment composition is linked to MBES backscatter strength (BS), and changes over time in the BS signal related to the scour dynamics around the wreck.

In flume experiments, hydro- and sediment- dynamics around a cylindrical object are investigated as a function of bed composition (sand and gravel mixes) and flow strength. Flume bathymetry data (Section 2.3.3) identifies scour dynamics and the lateral extent of amplified bed mobility in relation to bed composition and grain entrainment. Finally, results from a coupled model (hydrodynamics coupled with sediment transport; Section 2.4.3) compared to data of amplified bed dynamics from the offshore and flume lab bathymetric data sets.

#### 2.2 High-resolution offshore data collection documenting processes around shipwrecks

##### 2.2.1 Data collection platform and team

Offshore data collection (presented in Chapter 3) was conducted by staff from the School of Ocean Sciences, Bangor University on several campaigns from 2012 until 2019. Data were collected from *RV Prince Madog* (Figure 2.1), a multi-purpose research vessel, owned and operated by P&O Maritime Ocean Sciences (POMOS), a joint venture between P&O Maritime Services UK and Bangor

University. *RV Prince Madog* has a length of 34.09 m, a draft of 3.7 m and a breadth mould of 8.5 m. She weighs 390 tonnes and can operate at maximum speeds of 10.5 knots. *RV Prince Madog* can provide a 24-hour, year around, operating capability and has an endurance of 10 days between ports.

For positioning the vessel uses a Simrad HPR-410P Hydroacoustic Positioning DGPS reference system.



Figure 2.1: *RV Prince Madog*

(source: <https://www.bangor.ac.uk/oceansciences/about/facilities/madog/index.php.en>)

### **2.2.2 Seabed topography and backscatter strength – Multi Beam Echo Sounder (MBES)**

MBES bathymetric and backscatter data were collected using a hull-mounted Reson SeaBat 7125 dual frequency (200 kHz and 400 kHz). The Reson 7125 can provide sample coverage from 0.5 to 500 m depth and has a maximum attainable vertical resolution of 6 mm. A pulse length of 300  $\mu$ s and a beam angle between 110° and 130° were used. Over the 9-year period, the data were collected by a team of 3 technicians working at Bangor University. The MBES datasets collected prior to 2016 were processed by Jim Bennell and the more recent datasets were processed by Steven Rowlands, at SeaCams, Bangor University. The processed gridded data provided for this project have a resolution of 0.2 m and 0.5 m. For the time-lapse investigation, data resolution was reduced to the coarser of the two (0.5 m). Tidal corrections and corrections for the pitch and roll movements of the vessel were applied while processing the datasets using the Teledyne PDS 2000 software. To remove noise from the datasets, spatial filters were applied and manual cleaning of points around (and directly on) the wreck was conducted. The MBES backscatter strength (BS) datasets were processed by the author of the present work using the Fledermaus Geocoder Toolbox (FMGT) software under the guidance of Jonathan Beaudoin, managing director at QPS. Full specifications of the MBES instrument can be found in [Appendix A](#).

### **2.2.3 Hydrodynamic monitoring - Acoustic Doppler Current Profiler (ADCP)**

In 2019, an ADCP survey was conducted over the *SS Apapa* wreck site using a four beam 300 kHz TELEDYNE RD Instruments (RDI) Workhorse monitor. The ADCP used a vertical bin range (vertical resolution) of 1 m and recorded measurements every 1.47 s. Assuming a vessel speed of 5 knots

( $2.57 \text{ m}\cdot\text{s}^{-1}$ ), a horizontal distance difference (horizontal resolution) of  $\sim 3.8 \text{ m}$  between two consecutive measurements can be calculated. The pole-mounted ADCP was downward facing, with a beam angle of  $20^\circ$  and was placed 4 m below the sea surface at the stern of *RV Prince Madog*. The ADCP used has a maximum range of up to 160 m and a maximum depth of 200 m. It can provide on board direct reading of the current speeds. The four-beam design improves the data quality, data accuracy and data reliability. Assuming a typical range of 83 m, a frequency of 300 kHz and a vertical bin range resolution of 1 m, the instrument has a standard deviation value ( $\sigma$ ) of  $12.8 \text{ cm}\cdot\text{s}^{-1}$ . Full specifications of the system can be found in [Appendix B](#).

#### 2.2.4 Seabed surface sediment sampling – Shipek grab sampler

*RV Prince Madog* is equipped with a Wildco 860-A10 Shipek grab sampler with a 20 x 20 cm sampling cylinder, providing a maximum attainable scoop volume of 3 L. The stainless-steel grab has a total weight of 61 kg and can be stable even at bed slopes of over  $20^\circ$ . The shipek grab sampler was attached to the 'A frame' of the vessel and released for a free fall led by gravity at predefined points. The position of the grabs was monitored by the surface position of the vessel and an Ultra-Short Base Line (USBL) system. The shipek grab sampler has a cylindrical shape and the sediment is captured at one side of the cylinder ([Figure 2.2](#)). Once the grab forced by gravity hits the seabed, a self-contained weight releases a spring mechanism that rotates the capturing part of the cylinder by  $180^\circ$ . Because of the fast release of the capturing part, the shear strength of the grab sampler is much greater than the sediment strength and it therefore cuts the surface sediment cleanly, especially when sampling soft material (sand and mud) but it also works well with pebbles as large as 2 to 5 cm. When the grab is closed, during retrieval, the sample is protected from washout due to the cylindrical design. This is because the bucket closes with the separation plane aligned horizontally rather than vertically, unlike most bottom samplers.



Figure 2.2: Wildco 860-A10 grab sampler when retrieved with sediment. (source: <http://attleborobio.blogspot.com/>).

Once the grab with the surface sediment was retrieved, the sediment sample was divided into four sub-samples. Two sub-samples were attained from the top  $\sim 5 \text{ cm}$  of the sample, to be used for the classification of the backscatter intensity data ([Section 2.2.2](#)). Two sub-samples were also collected from the sediment left at the bottom of the grab sampler to identify changes in bed composition and



mobilisation. As the samples appeared to be collected without much disturbance, this subsampling is regarded as a true representation of variations with depth in the top 10-20 cm. **Figure 2.3** shows how the sediment in the grabs was divided into 4 samples (**Figure 2.3a**) and how the sediment retrieved were undisturbed seabed surface sediment (**Figure 2.3b**).

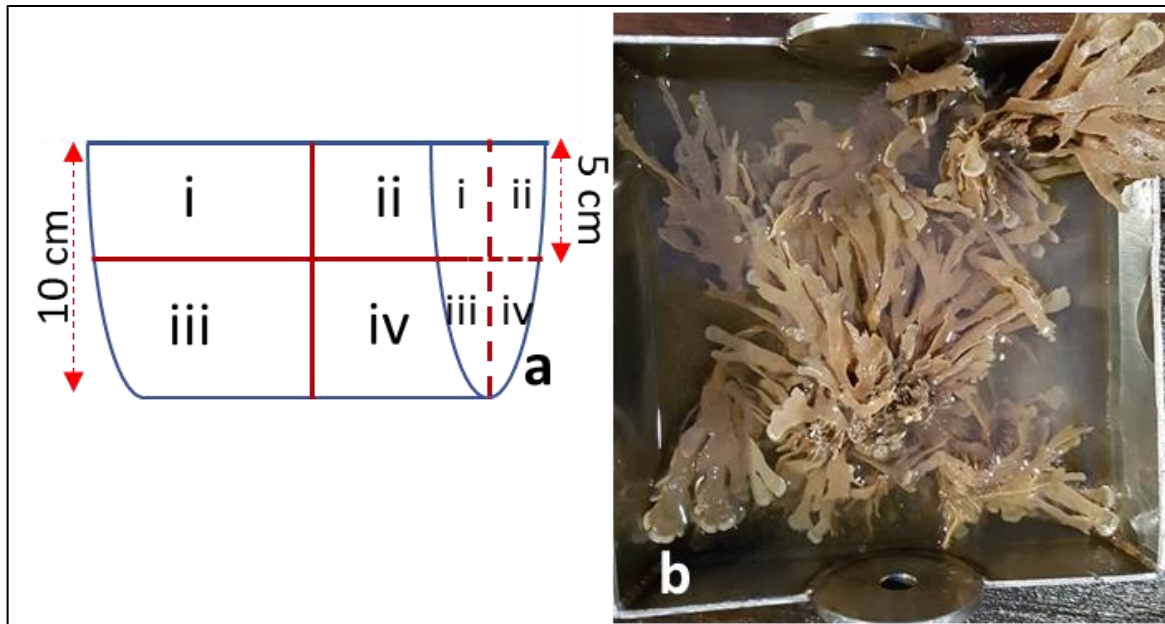


Figure 2.3: Schematic illustration of sample deviation for attaining the four sub-samples (a) and presence of seaweed in one of the samples (as an example) indicating undisturbed surface sediment (b).

For accurate positioning of the grab samples around SS *Apapa*, an Ultra-Short BaseLine instrument was attached to the Shipek grab sampler. The USBL used during the survey was the Easytrak Nexus Lite 2695 Series instrument manufactured by the Applied Acoustics Engineering (AAE) Underwater Technologies Group Company. Full instrument specifications can be found in **Appendix C**. The instrument specifications mention a maximum operating accuracy of 10 m, however, during the grab sample collection around SS *Apapa*, an accuracy of 6.92 m ( $\sigma$  of Observations) was calculated from the instrument's operating software (**Figure 2.4**).

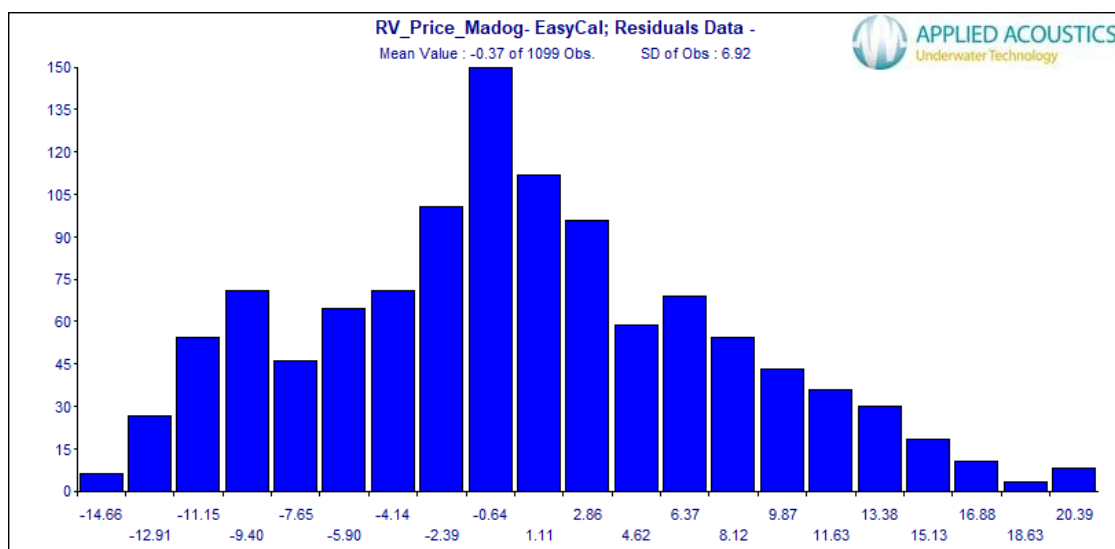


Figure 2.4: Histogram of residuals produced from the USBL manufacturer's operating software for the estimation of the average error at the positioning of the grab samples.

### 2.2.5 Sediment Particle Size Analyses (PSA) of offshore grab samples

The sediment samples collected from the SS *Apapa* site were sealed into zip lock bags and later processed in the sediment geotechnics laboratory, at the School of Ocean Sciences, Bangor University. The samples were washed through a 4  $\mu\text{m}$  filter in a Buchner funnel using distilled water to remove the salt content. The water left in the bottle below the filter was always clear. The washed sediment was then oven-dried at 80  $^{\circ}\text{C}$  for 24 hours, ready for dry sieving to perform particle size analysis (PSA) according to the British standard protocol (BS1377). A half phi (Figure 2.5) sieve stack (Folk and Ward, 1957) was used.

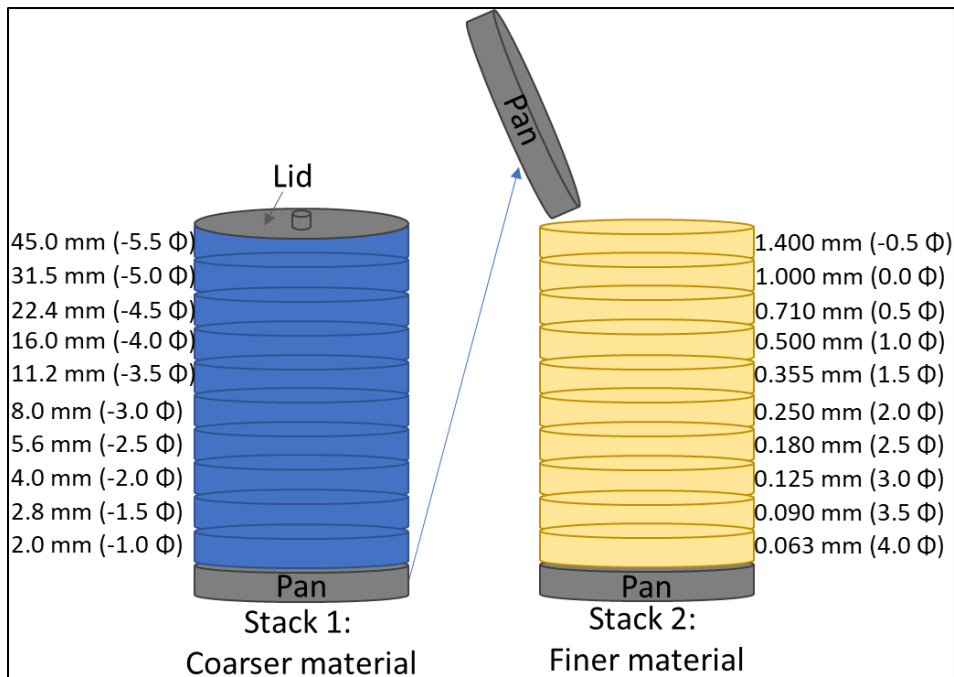


Figure 2.5: Full half phi sieve stack from -4.49  $\Phi$  to 3.99  $\Phi$  (a) and a schematic illustration of the two stacks used while mechanically shaking the sediment samples (b).

The samples were mechanically shaken for 15 minutes (using the Endecott's Octagon 200 shaker – Figure 2.6). The weight of the sediment retained for each sieve was measured with an accuracy of 0.04 g.



Figure 2.6: Endecott's Octagon 200 vibratory sieving machine used for PSA of sediment samples.



From each grab sample (Figure 2.3), one of the top 5 cm and one of the bottom sub-samples were sieved. The results from the dry sieving were input into GRADISTATv8 (Blott & Pye, 2001) for the calculation of the descriptive statistics for each of the samples along with the percentage losses/gains, but also the relevant multiple sample statistics for the sediment mixtures.

## 2.3 Flume Laboratory experiments of processes around a cylindrical object

The laboratory work described in Chapter 4 was conducted in the hydrodynamics laboratory at School of Ocean Sciences, Bangor University. The large Armfield recirculating flume was used for all the experimental work. Although the laboratory environment can never truly replicate the offshore environment, and scaling issues prevent direct comparisons, the flume experiments were conducted to understand and quantify the spatial extent of the amplified bed dynamics for the different flow speeds and bed compositions in a controlled environment.

### 2.3.1 Armfield recirculating flume experiments

The Armfield recirculating flume allow unidirectional linear currents to be created. The flume is: 10 m long, 0.3 m wide and 0.45 m deep. Equipped with a Hidrostral 7.5 kW AC screw-centrifugal pump, the flume is capable of recirculating solid material.

A smooth stainless steel, 9.4 cm long cylinder, with a diameter of 4.4 cm, weighing 1.17 kg and with a density ( $\rho_c$ ) of  $8.175 \text{ kg}\cdot\text{m}^{-3}$  was used to replicate SS *Apapa*. Experiments were completed with a test bed located in the middle section of the flume (between 3 and 7 m downstream). The cylinder was placed in the middle of the 4 m long sediment bed in order to allow ripples to form, both upstream and downstream of the object. Ripples were measured and sampled to provide information about how the enhanced forces on the bed manifested itself for different bed compositions. The sediment thickness was  $\sim 4 \text{ cm}$ , guided by the two 0.75 m long ramps before and after the sediment bed to keep the sediment in place and to provide a gradual slope of  $3.5^\circ$  (Figure 2.7).

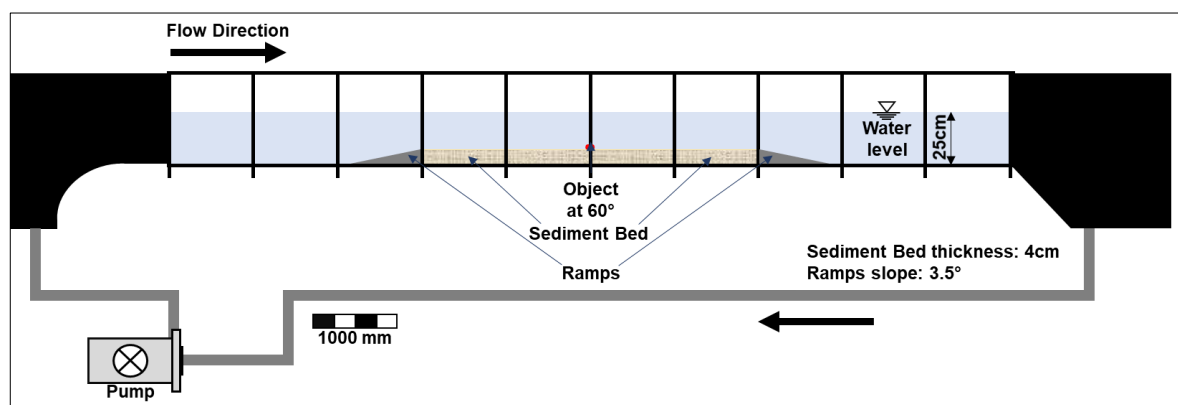


Figure 2.7: Schematic illustration of the experimental setup

### 2.3.2 Making different beds – sediment mixture preparation

The laboratory experiments were conducted using mixtures of well sorted quartz sand ( $0.1 - 0.3 \text{ mm}$ ,  $d_{50} = 0.25 \text{ mm}$ ) and fine gravel ( $2 - 3 \text{ mm}$ ,  $d_{50} = 46 \text{ mm}$ ). These sediments, provided by Boud

Minerals, were already cleaned from cohesive and biological materials. Specifications of the sediment ordered can be found in [Appendix D](#). Samples of the sediment were sieved to ensure the correct distribution of sediment particle sizes.

### 2.3.3 High resolution bed topography – SeaTek Acoustic Bed Scanner

An acoustic scanner system was used to collect bed elevation data. The bed scanner system was formed of an array of twenty-four 5 MHz SeaTek ultrasonic transducers in a PVC housing mounted on an automated carriage system. The carriage was developed by Connor McCarron and colleagues from the School of Computer Sciences and Electronic Engineering, Bangor University ([Griffiths et al., 2017](#)), while the housing was built at the school of Ocean Sciences mechanical workshop.

The ultrasonic transducers work on the principle of measuring the distance to the bed ( $z_b$ ; [Equation 2.1](#)), using the speed of sound in the water ( $c$ ) and the two-way travel time ( $TWT$ ) taken between the transmission and reception of an acoustic pulse where:

$$z_b = \frac{TWTc}{2}, \quad (2.1)$$

The carriage system, equipped with a two-stage stepper motor can move the array of transducers at a speed of  $3.9 \text{ mm} \cdot \text{s}^{-1}$ , providing a maximum potential step resolution of 0.2 mm. The acoustic transducers have a beam angle of  $1.8^\circ$  and a minimum theoretical pulse length of 0.2  $\mu\text{s}$ . The centre of each transducer was 1.6 cm away from that of the neighbouring transducer. The acoustic transducers have a maximum operating frequency of  $f_0 = 20 \text{ Hz}$ , which was used throughout the experiments.

The maximum attainable vertical ( $\delta z_R$ ) resolution of each transducer was 0.15 mm, using [Equation 2.2](#):

$$\delta z_R = \frac{cP_L}{2}, \quad (2.2)$$

where:  $c$  is the speed of sound in the water (assuming  $c = 1447 \text{ m} \cdot \text{s}^{-1}$  at  $10^\circ\text{C}$ ) and  $P_L$  is the pulse length of the ultrasonic transducers and can be calculated using [Equation 2.3](#):

$$P_L = P_C T_R = P_C \frac{1}{f}, \quad (2.3)$$

where  $P_C$  is the number of cycles per pulse and  $T_R$  is the period of the acoustic wave ( $T_R = 1/f$ ). Subsequently, the horizontal resolution ( $\delta x_R$ ) of each transducer was 6.3 mm, using [Equation 2.4](#):

$$\delta x_R = 2 z \tan\left(\frac{\Phi_R}{2}\right), \quad (2.4)$$

where  $\Phi_R$  is the beam angle and  $z$  is the water depth.

Bathymetric measurements were taken using all 24 transducers ([Figure 2.8a](#)) to capture the bed evolution before and at the end of the experiments (perpendicular scans along the full length of the bed). During the experiments an array of 16 transducers ([Figure 2.8b](#)) was placed horizontally (with the water flow) to capture the ripple migration rates. The text files with simultaneous depth

measurements per transducer were processed using Matlab vR2019a and plotted in ArcMap v10.7.1.



Figure 2.8: Array of 24 transducers used for perpendicular to the flow scans (a) and array of 16 transducers used for parallel to the flow scans to record bedform development and migration rates during the laboratory experiments (b).

### 2.3.4 High resolution hydrodynamic monitoring - METFLOW Ultrasonic Doppler Velocity Profiler (UDVP)

Current speeds in the flume laboratory were measured using a single METFLOW Ultrasonic Doppler Velocity Profiler (UDVP), with 5 mm diameter and operating frequency ( $f_0$ ) of 4.5 MHz. From flow velocity measurements during preliminary experiments, the appropriate flume pump frequency was defined for the desired flow speeds related to the critical grain entrainment of both sediment fractions used. The working principle of the UDVP instrument is that acoustic pulses transmitted from the transducers reflect from suspended particles in the water column. The time delay ( $t$ ) between transmission and reception can be used for the calculation of the horizontal distance ( $x$ ) of the reflecting particle from the transducer using Equation 2.5:

$$x = \frac{tc}{2}, \quad (2.5)$$

The doppler shift of the frequency ( $f_s$ ) can be used to the calculation of the velocity of the particle relative to the transducer using Equation 2.6:

$$v = c \frac{f_s}{2f_0}, \quad (2.6)$$

The above calculations are made with the assumption that the particles are relatively small, and their density allows them to remain in suspension when the current velocity is non-zero.

UDVP measurements were made in the middle of the flume in several locations along the length of the flume tank. The UDVP instrument recorded an average of 394 profiles in 90 seconds with a

blanking distance of approximately 10 mm for each of the 183 bins along the beam. The UDVP transducer had an on-axis velocity resolution of  $3.91 \text{ mm}\cdot\text{s}^{-1}$  and a bin size of 0.74 mm. The transducer was placed parallel to the flow, at an angle of  $90^\circ$  to the bed.

All calculations were conducted automatically using METFLOW's computer software UVO monitor v3.0. METFLOW recommends that the reflecting particles should have diameters larger than a quarter of the wavelength of the UDVP pulses ( $\lambda_0/4$ ) where  $\lambda_0 = c/f_0$ . Therefore, the recommended nominal diameter of the reflecting particles for the UDVP transducers is calculated to be  $93.5 \text{ }\mu\text{m}$  when using a velocity of sound in the water of  $1500 \text{ m}\cdot\text{s}^{-1}$ . Mica powder (potassium aluminium silicate) was used as seeding material, as it was available in graded particles with  $106 \text{ }\mu\text{m}$  diameter and bulk density of  $260 \text{ kg}\cdot\text{m}^{-3}$ . Mica powder is favoured as it does not float at the water surface and does not aggregate when mixed with water due to its anticaking properties. The mica powder used in the experiments was sourced from Dean Tranter and the associated data sheet is presented in [Appendix E](#).

### 2.3.5 Flume bed sediment “coring”

Sediment samples were collected at 10 locations over the bed at the end of each laboratory experiment, after the bed was left to dry overnight. The sediment samples were sub-sampled every 5 mm using sub-divisions on the syringe corer, with height of 7.5 cm and an inside diameter of 0.9 cm ([Figure 2.9](#)). A total of ~2800 samples were collected and assessed for this study.



Figure 2.9: Syringe used for down-core sampling of the sediment bed in the flume

### 2.3.6 Sediment Particle Size Analyses (PSA)

The same particle size analysis (PSA) procedure was followed as described in [Section 2.2.5](#), but with a custom-made set of sieves with mesh apertures designed to tailor the PSA to the bi-model mixture of the sand and gravel used in the experiments ([Figure 2.10](#)).

The sieve stack included sieves from 0.3 mm ( $1.74 \Phi$ ) to 0.106 mm ( $3.24 \Phi$ ) at half phi intervals for the sand fraction of the mixtures. To better separate the sand and gravel fractions, sieves with meshes of 1.7 mm ( $-0.77 \Phi$ ), 2.24 mm ( $-1.16 \Phi$ ) and 2.5 mm ( $-1.32 \Phi$ ) were purchased from UKGE Ltd. The coarser fraction of the mixtures was therefore passed through sieves with apertures of 2.8 mm ( $-1.49 \Phi$ ), 2.5 mm ( $-1.32 \Phi$ ), 2.24 mm ( $-1.16 \Phi$ ), and 2 mm ( $-1.00 \Phi$ ) ([Figure 2.10](#)). The mechanical shaking of the sediment samples was conducted for 2 minutes, due to the small sediment sample size and the large volume of samples (~2800). As a test, mechanical sieving of the same sample was conducted for 10, 5 and 2 minutes, with less than 2.3% differences in the measured dry sediment weights attained at each sieve.

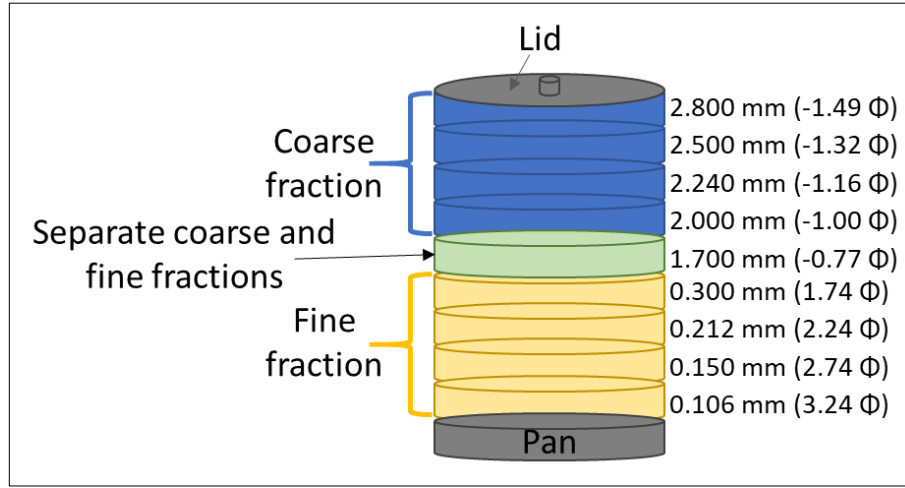


Figure 2.10: Schematic illustration of the stack of sieves used for PSA of the sediment samples collected during the laboratory experiments.

## 2.4 Numerical Modelling of flow and bed evolution around objects placed on mixed beds

A coupled numerical hydrodynamic and sediment transport model (TELEMAC3D – GAIA) model was used to provide a full numerical understanding of the enhanced diverted flows around submerged objects and the impact on several types of beds. The model was developed to replicate both the natural offshore environment of the SS *Apapa* site and the controlled flume laboratory environment.

### 2.4.1 Hydrodynamic model – TELEMAC-3D

The TELEMAC-3D *v8p1r1* model solves the Navier-Stokes equations using Boussinesq approximation for the momentum. TELEMAC-3D also calculates the depth-averaged velocities along with the bed shear stresses and are passed to any other module of TELEMAC (SISYPHE, GAIA, etc.). The bed shear stress,  $\tau_0$ , is calculated using the velocity of the first  $\sigma$ -layer above the bed using Equation 2.7 (Tassi and Villaret, 2019).

$$\tau_0 = \rho \left( \frac{1}{\kappa} \ln \frac{z'}{z_0} \right)^{-2} u(z')^2, \quad (2.7)$$

where  $\rho$  is the water density,  $\kappa$  is the unitless Von Kármán constant (0.41),  $z'$  is the first  $\sigma$ -layer height above the bed (m),  $z_0$  is a hypothetical level with 0 velocity (m) and  $u(z')$  is the velocity at the first  $\sigma$ -layer above the bed ( $\text{m} \cdot \text{s}^{-1}$ ).

In TELEMAC the quadratic friction coefficient related with the skin and bed friction combined (total friction) is calculated using Equation 2.8 as:

$$C_f = 2\kappa^2 \left( \log \left( \frac{30h}{k_{se}} \right) \right)^{-2}, \quad (2.8)$$

where  $h$  is the water depth. The total bed roughness,  $k_s$ , can either be specified by the user as a constant, to include the influence of bedforms, for ripples, or for ripples, dunes and megaripples respectively.

Friction was applied at the bed using the Nikuradse formula by applying a Chézy coefficient,  $C$  (Leroy, 2019) using Equation 2.9 as:

$$C = 7.83 \ln \left( \frac{12h}{k_s} \right), \quad (2.9)$$

where  $h$  is the water depth and  $k_s$  is the total bed roughness. The Nikuradse formula allows the prescription of friction based on a logarithmic velocity profile for a given roughness. The formula does not conduct any averaging of the velocity along the vertical and is therefore preferred over depth-averaged models for the simulation of non-quasi-horizontal flows (Leroy, 2019). TELEMAC also allows for the inclusion of turbulent flows in the calculations using several turbulent formulae. The  $k$ - $\varepsilon$  model was used to calculate the Turbulent Kinetic Energy (TKE) within the computation domain. The  $k$ - $\varepsilon$  model solves the balance equations of turbulence for  $k$  (energy production) and  $\varepsilon$  (energy dissipation) (Goll, 2016). The TKE- $k$  of the model is calculated using Equation 2.10:

$$\frac{\partial k}{\partial t} + u \cdot \nabla k = \nabla \left( \nu + \frac{\nu_t}{\sigma_k} \right) \nabla k + P - \varepsilon \quad (2.10)$$

and the accompanying equation of TKE- $\varepsilon$  (Equation 2.11):

$$\frac{\partial \varepsilon}{\partial t} + u \cdot \nabla \varepsilon = \nabla \left( \nu + \frac{\nu_t}{\sigma} \right) \nabla \varepsilon + C_{1\varepsilon} \frac{\varepsilon}{k} P - C_{2\varepsilon} \frac{\varepsilon^2}{k} \quad (2.11)$$

The TKE calculated from the  $k$ - $\varepsilon$  model was also used in the calculation of the bed shear stress within the coupled model, as the TKE is a dominant parameter of flow movement, especially in the wake of an object.

## 2.4.2 Sediment transport model - GAIA

GAIA is the new TELEMAC-MASCARET sediment transport and bed evolution module. After many upgrades from the old SISYPHE module, GAIA allows better simulation of the sedimentary processes at the water-(sea)bed interface. GAIA also makes it possible to incorporate and manage different sediment classes and sediment transport models, ideal for this study of mixed bed dynamics. In GAIA, the suspended sediment transport processes are dealt mainly by the TELEMAC hydrodynamic module, but the near-bed-bedload transport is modelled by GAIA (Audouin et al., 2019).

The bedload transport within the GAIA module of TELEMAC can be calculated using several transport formulae including Meyer-Peter and Müller (1948), Einstein and Brown (1950), Engelund and Hansen (1967), the modified Engelund-Handsen formulae of Cholley and Cunge (1979), and the Van Rijn (2007a, b) formulae. For this study, the Meyer-Peter and Müller (1948) formula was used, as it allows for the McCarron (2019) correction for the hiding exposure effect (HE) as a function of gravel percentage to be incorporated.



### 2.4.3 Coupled model (TELEMAC3D – GAIA)

The coupled model aimed to simulate and provide better understanding of the enhanced flows, forces on the bed, and resultant bed dynamics. Within the coupled model, shear stress and depth averaged velocities are calculated within the Hydrodynamics model (TELEMAC-3D) and are passed over to the sediment transport model (GAIA) for each node at each time step of the simulation. Use of the coupled model allows the suspended transport processes to be driven by TELEMAC-3D, while the near-bed, bedload and stratigraphic processes are led by GAIA (Audouin et al., 2019).

The van Rijn (1984) equation was selected for the suspended load transport within TELEMAC. This formula, uses the equilibrium calculation ( $C_{eq}$ ) to calculate the suspended load transport as Equation 2.12:

$$C_{eq} = 0.015d_{50} \left( \frac{\theta' / \theta_{cr} - 1}{z_{ref} D_*^{0.3}} \right)^{3/2}, \quad (2.12)$$

where  $\theta_{cr}$  is the critical Shields parameter and  $\theta' = \mu \cdot \theta$  the bed shear stress due to skin friction. The reference height  $z_{ref}$  is related to the total bed roughness,  $k_s$  with  $z_{ref} = 0.5 k_s$ .  $D_*$  is the dimensionless grain size.

The Van Rijn (1993a) formulae, that uses the dimensionless grain size ( $D_*$ ) for the calculation of the critical Shield's parameter ( $\theta_{cr,i}$ ) in the model (Equation 2.13) is:

$$\theta_{cr,i} = \begin{cases} 0.24D_*^{-1}, & D_* \leq 4 \\ 0.14D_*^{-0.64}, & 4 < D_* \leq 10 \\ 0.04D_*^{-0.10}, & 10 < D_* \leq 20 \\ 0.013D_*^{0.29}, & 20 < D_* \leq 150 \\ 0.045, & 150 \leq D_* \end{cases} \quad (2.13)$$

The Shields parameter ( $\theta_i$ ) and the critical Shields parameter ( $\theta_{cr,i}$ ) for each node of the computation domain ( $i$ ) at each time step are used to express the skin related bed shear stress  $\tau'_b$  and the critical bed shear stress  $\tau_{cr,i}$  respectively (Shields, 1936), using Equation 2.14 and Equation 2.15:

$$\theta_i = \frac{\tau'_b}{g(\rho_s - \rho)d_i}, \quad (2.14)$$

$$\theta_{cr,i} = \frac{\tau_{cr,i}}{g(\rho_s - \rho)d_i}, \quad (2.15)$$

As mentioned in Section 1.3, when bedforms are present, the magnitude of the bed shear stress,  $\tau_b$ , is defined of the grain related shear stress,  $\tau'_b$ , and the shear stress due to form drag,  $\tau''_b$ , that relates to the friction velocity as (Equation 2.16):

$$\tau_b = \tau'_b + \tau''_b = u_*^2, \quad (2.16)$$

For the applications of the present work, it is also important to mention that TELEMAC (and 2-D models in general) allows for the correction of the bed shear stress in cases where bedforms are considered using a skin friction parameter,  $\mu < 1$ , that is the ratio of the local skin friction,  $C'_f$ , to the total friction,  $C_f$ , according to Equation 2.17:

$$\mu = C'_f/C_f, \quad (2.17)$$

In case of bedforms the quadratic friction coefficient relating to the skin roughness,  $C'_f$ , is calculated using the grain, or skin related roughness,  $k'_s$ , instead of  $k_s$  in Equation 2.8 that relates to the median grain diameter,  $d_{50}$ , using the Nikuradse law with  $k'_s = 3d_{50}$  (Tassi & Villaret, 2019).

The modelling simulations were conducted using Supercomputing Wales (SCW) high performance computing facilities (<https://www.supercomputing.wales/>). For the simulations, a pre-compiled version of TELEMAC was used and several changes were made to the initial version, described in Chapters 3 and 4. For the laboratory simulations, 80 parallel cores on an Intel® Xeon® Gold 6148 CPU with a frequency of 2.40GHz were used. For the SS *Apapa* site simulations, 320 parallel cores were used.



## Chapter 3

### 3. How the shape of the wreck and the composition of the bed defines the scour around a wreck – A time lapse study over 8 years

#### 3.1 Introduction

There is an ever-increasing need for seabed infrastructure enabling offshore development for applications such as renewable energy extraction and conversion, centralised storage etc., requiring accurate predictions of erosion and deposition of the surrounding seafloor sediment. The Welsh territorial waters, depending on their seabed habitats and marine ecosystems, have been categorised into strategic resource areas to ensure a sustainable development (Figure 3.1; Crown estate, 2019).

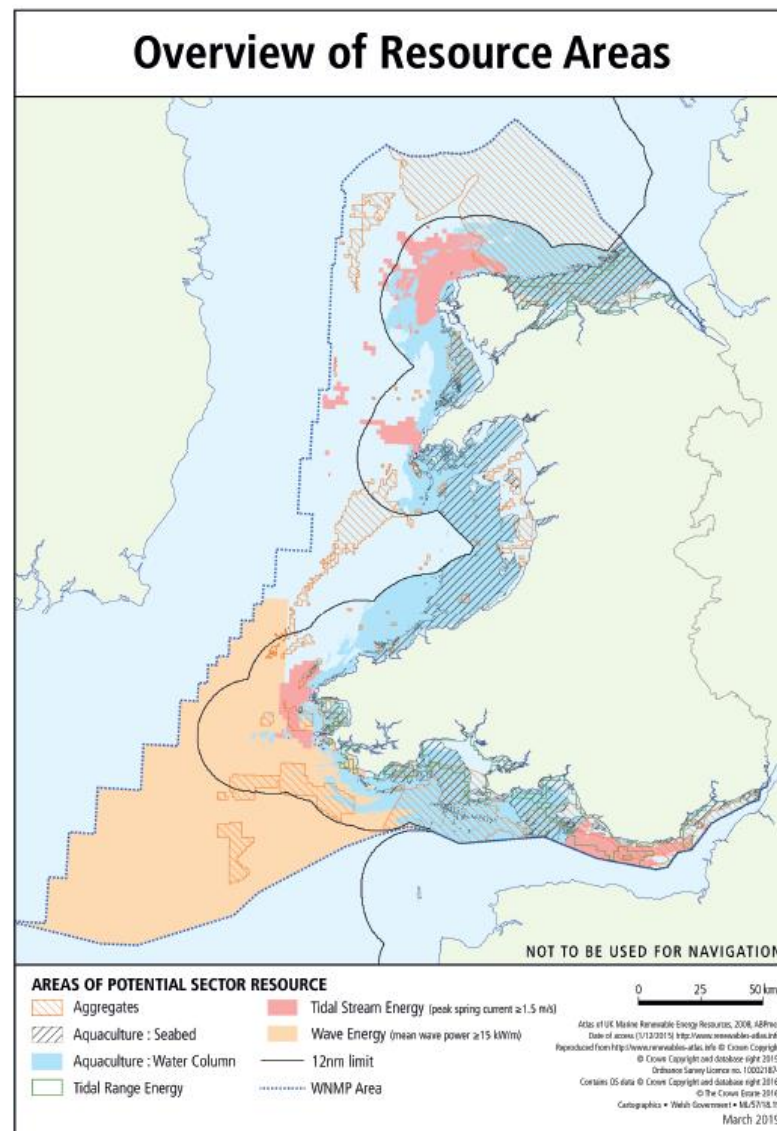


Figure 3.1: Welsh territorial waters strategic resource areas (Crown Estate, 2019).

The northern side of the Anglesey coast has recently become an area of interest for renewable energy infrastructures such as tidal turbines and offshore windfarms (Serhadlioglu et al., 2013;

Crown Estate 2019). Implementation of such anthropogenic infrastructure requires detailed planning to allow a maximum lifespan and efficiency of the installed devices and the development will require installation of arrays of differently shaped marine energy converters (MECs).

Flow around objects causes flow deviation and an amplification of the turbulent kinetic energy (TKE) and the wall shear stress (WSS) of up to a factor of four (Whitehouse, 1998; Quinn et al., 2016; Quinn & Smyth, 2018), with the shape of the object and its orientation to the flow being the controlling parameter of the flow/object interaction as differently shaped objects will cause flow amplification patterns at different locations and the subsequent scour development will also differ (Saunders, 2005; Quinn, 2006, Quinn et al., 2016). Flow amplification around seabed infrastructures can be monitored using acoustic instruments, such as acoustic doppler current profilers (ADCP) that use the doppler effect, projecting on particles that exist in the water column, to provide understanding of the current flow speeds. Computational fluid dynamic (CFD) models (Smyth & Quinn 2014; Quinn & Smyth, 2018) and other hydrodynamic models (such as TELEMAC; Yin et al., 2016) have also been widely used to monitor and understand the impact of an infrastructure to the flow.

The ever-increasing need for seabed infrastructures require accurate predictions of the enhanced diverted flow and its resulting erosion and deposition rates on the surrounding seabed. Although studies for differently shaped and orientated objects have been conducted for objects sitting on fine grained (silt or clay) uniform beds (Whitehouse et al., 2011) and on coarse grained (sand) uniform beds (Quinn et al., 2016, Quinn & Smyth, 2018), there are uncertainties on understanding the seabed mobility around objects sitting on complex sediment substrates (like sand and gravel mixtures). On mixed coarse beds (sand and gravel) the exposed larger grains will require less shear stress to mobilise, where hidden smaller grains will require more forcing (Janssen, 2010; McCarron et al., 2019). The aforementioned parameter, also known as hiding exposure effect of sediment grains on mixed coarse beds, is causing uncertainties on the prediction of sediment mobilisation (Wilson et al., 2018) and the subsequent erosion and deposition rates, as coarse sediment grains expected to be immobile (when on a uniform bed) can be mobilised and finer grains, expected to be mobile (when on a uniform bed) can become immobile. Anthropogenic applications on the seabed require deep understanding of the seabed characteristics to provide understanding and establish decisions and risks to seabed development, both for the infrastructure itself but also for the habitats, as erosion and deposition of seabed sediment can have implications for flora and fauna species on soft and hard substrata (McArthur et al., 2010). Exploration and characterisation of the seabed morphology often relies on the use of acoustic instruments for seafloor mapping (Bourillet et al., 1996; Brown et al., 2012; Lamarche & Lurton, 2018). Collection of sediment samples is impossible to be conducted for the full extent of the ocean floor as it is time consuming and expensive. Multi Beam Echo Sounders (MBES) data on bathymetry (i.e., depth) and backscatter strength (BS) can provide information about the morphology of a study area, the seabed composition, and the structure of targets at the seafloor (de Moustier, 1986). Repeat MBES surveys (time-lapse bathymetric surveys) can therefore provide information about erosion and deposition rates over time, by monitoring the bathymetric changes (using difference modelling) of an area and can provide information about

hydrological regimes, and sediment movement (Wheeler, 2002; Schmitt et al., 2008; Quinn & Boland, 2010). While bathymetry measurement from MBES instruments is fairly straightforward to process, using the echo intensity to gain information about the nature of the seabed is related to more complex physical processes (Lamarche & Lurton, 2018) and time-lapse studies of MBES backscatter strength are uncommon in the literature. The investigation of the seafloor using acoustic instruments relies on the transmission of the acoustic pulse from the instrument and the backscattering by the seafloor (Lurton, 2010). MBES backscatter strength datasets can provide information about the flora and fauna of an area (Brown et al., 2011; Lamarche & Lurton 2018) and although challenging, can also be used for habitat mapping of the ocean floor (Brown & Blondel 2009). Seafloor backscatter strength relates to the amount of the acoustic energy that is scattered back from the seabed to the MBES receivers after its interaction with the seabed (Figure 3.2; Wang et al., 2021).

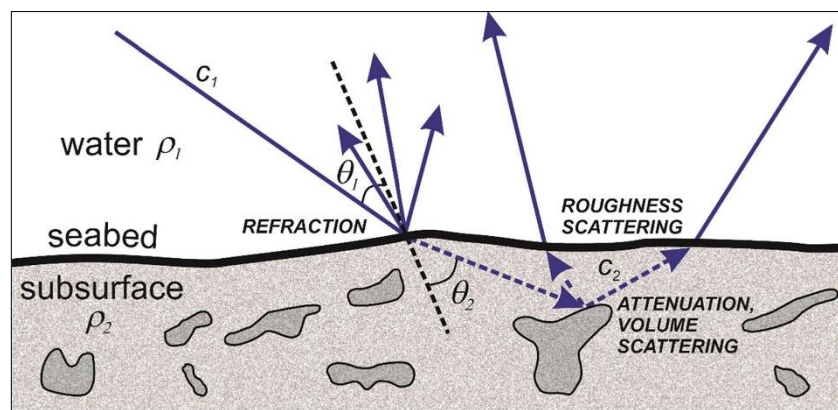


Figure 3.2: Interaction of BS acoustic signal interacting by roughness (surface) or by volume (beneath surface) scattering (Wang et al., 2021).

MBES backscatter strength relates to the sediment properties (Golf et al., 2004; Ferrini & Flood, 2006) and depends on the volume scattered due to sediment inhomogeneities and the interface scattering due to bottom roughness (Innangi et al., 2015). Stronger BS signal is a result of smooth surfaces, due to specular reflection. In contrast, rough surfaces cause scattering of the acoustic signal in different directions, resulting to lower values of BS recorded from the MBES transducer (Lurton and Lamarche, 2015). Mixed sediments are expected to have a large variability of BS values, due to the range of grain sizes simultaneously refracting the acoustic signal in different directions and at different strengths. The grain heterogeneity in mixed sediments leads to linear or dominant correlations between BS and grain sizes (Table 3.1; Monteys et al., 2013).

Table 3.1: Comparison of seabed types and their relationship with backscatter (Monteys et al., 2013).

Seabed Hardness	Sediment Type	Textural Categories (Folk's)	Acoustic Scattering	Backscatter Levels	Statistical Relationship backscatter / grain size
Soft	Unconsolidated, fine grained sediments	Mud to sand (unimodal to multimodal grain size distribution)	Interface and volume (subsurface penetration)	Low	Strong, linear correlation between backscatter and grain size parameters
	Unconsolidated, mixed sediments (fine dominated)	Gravelly-sand / gravelly-mud (bimodal grain size distribution)	Interface and volume (subsurface penetration)	Moderate	Strong, linear correlation between backscatter and grain size parameters
Hard	Unconsolidated, coarse dominated sediments	Sandy, muddy-gravel or gravel (unimodal to multimodal grain size distribution)	Interface (negligible subsurface penetration)	Moderate - High	Gravel fraction dominates backscatter. Weak correlation between sandy fraction and the backscatter
	Rock or hardgrounds	Bedrock, hardgrounds, carbonate crusts and other hard surfaces	Interface (no subsurface penetration)	High	No consistent relationship between rock type and backscatter parameters

The current lack in thorough understanding of the result of the enhanced diverted flow (and the amplified shear stress) around differently shaped and orientated objects sitting on mixed coarse beds is caused by uncertainties: in the flow diversion (and enhancing) caused by the object, the sediment mobilisation within the mixed coarse beds, the impact of the enhanced shear stress downstream of the object to the surrounding mixed coarse bed and the limited record of studies investigating seabed composition changes. These uncertainties are limiting seabed management around differently shaped and orientated objects placed on mixed coarse beds. This chapter focuses on the scour dynamics around a wreck (*SS Apapa*) that sunk over a century ago (World War I; WWI). The bed dynamics of the site have been monitored using repeat MBES surveys and the variations of the flow around the site were surveyed using an ADCP instrument. Sediment grab collection and MBES backscatter strength mosaics inform that the area surrounding the wreck consist of coarse bimodal sediment (mixture of sand and gravel), which makes the site ideal to investigate the impact of mixed beds on scour dynamics.

### 3.1.1 Aims and Objectives

There is currently a knowledge gap in the ability to predict the seabed dynamics, around differently shaped and orientated objects sitting on mixed coarse beds. The ultimate aim is to provide a significant tool (numerical model) that will be able to predict hydrodynamic and sediment transport processes around any submerged object sitting on mixed coarse, bimodal beds in the marine environment.

The current chapter aims to investigate and understand:

- i) The impact of an irregularly shaped object (wreck of *SS Apapa*) on the local flow;
- ii) The impact of sediment bimodality on seabed erosion and deposition rates and the identification of the most mobile sediment types, and
- iii) The impact of the enhanced diverted flow on the erosion and deposition rates of the surrounding bimodal bed.

The work presented in this chapter, aiming to answer the aforementioned questions was conducted in the following stages:

- Quantification of the influence of an object (wreck of *SS Apapa*) to the local flow (what is the amplification and diversion?).
- Identification of lateral and vertical changes of the scour mark. This assesses whether there is dynamic equilibrium and how erosion and deposition rates correlate with sediment composition.
- Correlate the two points above: How does the amplification and diversion of the flow correlate to changes in erosion and deposition rates and in bed composition?
- Use the parameterisation of the hydrodynamics, bed dynamics and bed composition around the wreck to build a coupled hydrodynamic and sediment transport numerical model (TELEMAC3D – GAIA) for the site and investigate if the model can predict scour dynamics around a wreck sitting on a bimodally distributed coarse bed.

The methodology for identifying the processes around the wreck is first described in [Section 3.2](#), followed by the results of the analyses in [Section 3.3](#). Discussion of the results is presented in [Section 3.4](#) and finally a summary of the main conclusions in [Section 3.5](#). An overall discussion chapter ([Chapter 5](#)) will place the results into wider context.



### 3.1.2 SS *Apapa* and its environment

SS *Apapa* (Figure 3.3) was built in 1914, had dimensions of 135 x 17.5 x 9.54 m ([www.wrecksite.eu](http://www.wrecksite.eu)) and had a gross tonnage of 7832 tons. On the 28<sup>th</sup> of November 1917, during WWI, SS *Apapa* was travelling from West Africa to Liverpool. Off Point Lynas, she was torpedoed by the Imperial German Navy submarine *U-96*. SS *Apapa* subsequently sank 2 km off the coast of North Anglesey, costing the lives of 77 people, whilst 174 passengers were saved by Lifeboats ([www.ubootproject.wales](http://www.ubootproject.wales)).

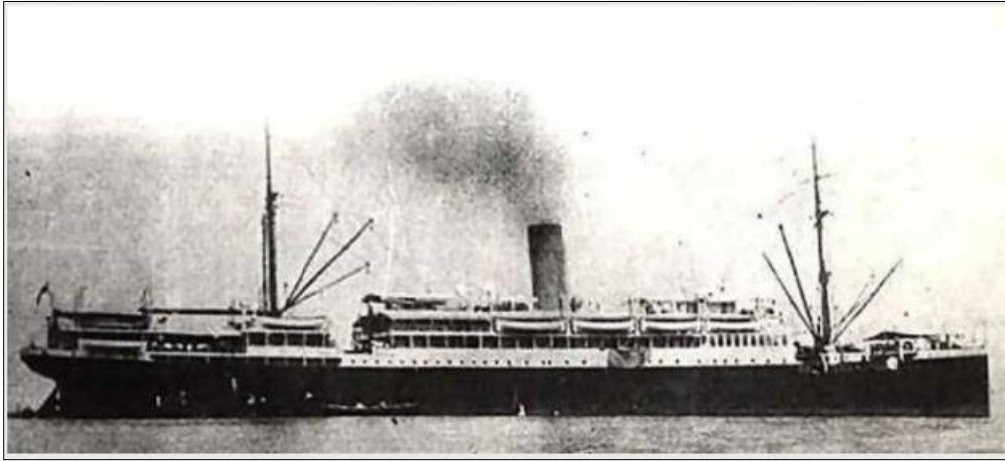


Figure 3.3: SS *Apapa* (source: <https://ubootproject.wales/wrecks/apapa/>)

The SS *Apapa* wreck site is on average -42 m deep, ranging between -56 m and -32 m. The wreck sits at a 150° - 330° angle to the north and it lays with the smokestack facing the northwest (NW). The area surrounding SS *Apapa* is characterised as sandy gravel (Figure 3.4; Edina Digimap (DiGSBS250K), 2011).

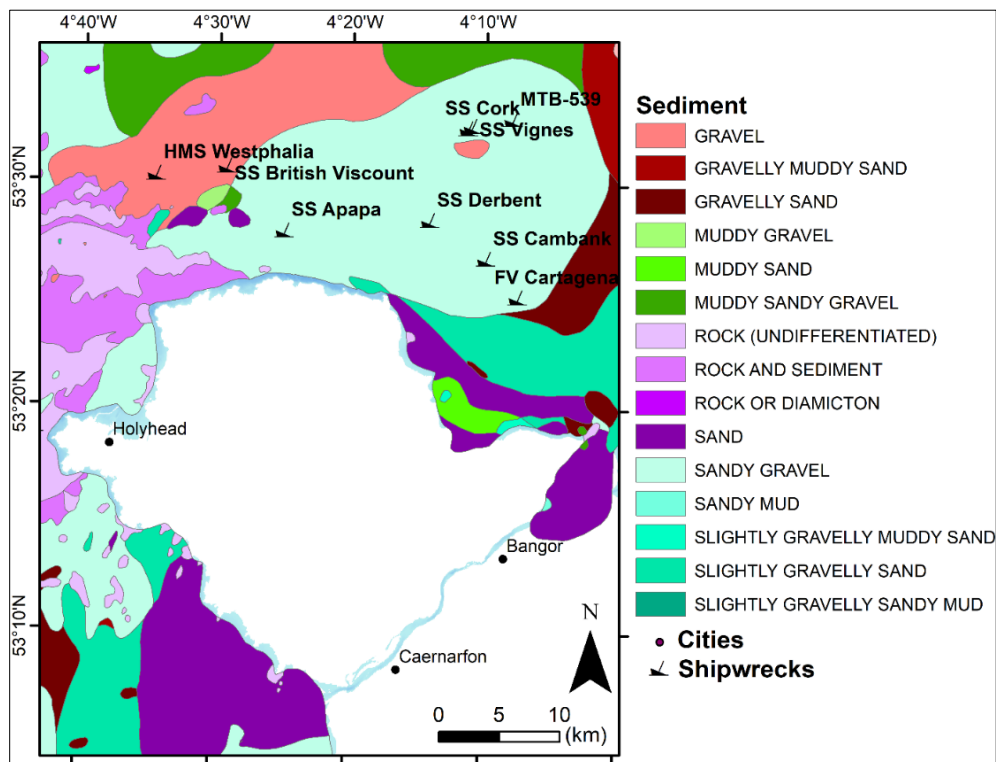


Figure 3.4: Seabed sediment type characterisation based on Folk (1957) (source: Edina Digimap (DiGSBS250K), 2011).

The Proudman Oceanographic Laboratory Coastal Ocean Modelling System (POLCOMS; Wakelin et al., 2009) model run for a full year in 2014 via the Polpred software, shows a maximum depth averaged current speed of  $\sim 1.3 \text{ m}\cdot\text{s}^{-1}$  at the SS Apapa site. The tidal current at the area has an east – west orientation ( $88^\circ - 268^\circ$ ; Figure 3.5), with the flood tide to the east. The dominant current is towards the west (ebb tide). The POLCOMS model is formulated on a B-grid, following Cartesian coordinates in the horizontal and solves the Boussinesq, hydrostatic equation of motion separated into depth independent and depth varying parts, to allow time splitting between baroclinic and barotropic components. The free surface elevation (water depth), horizontal velocity components, salinity and temperature fields are calculated at each node of the computational domain.

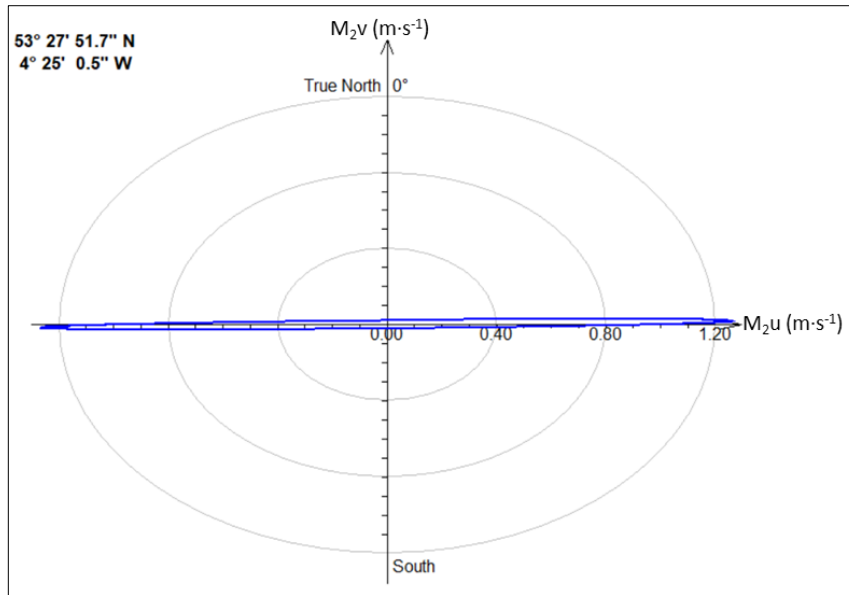


Figure 3.5: Tidal Ellipse produced when using the POLCOMS model via the Polpred software for a full year in 2014.

The dominant direction of the bedload transport around the Irish Sea (Figure 3.6) indicates an eastward direction of the dominant tidal current at the area surrounding the SS Apapa site (van Landeghem et al., 2009), and the expected (a)symmetry of the bedload transport along with the expected migration direction of the bedforms present at the area.

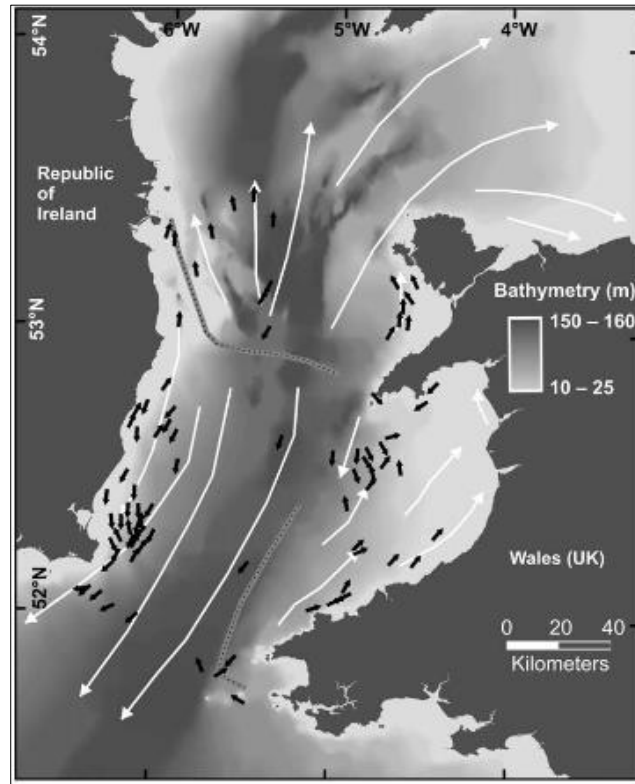


Figure 3.6: Dominant bedload transport directions in the Irish Sea (Van Landeghem et al., 2009).

Although British Geological Survey (BGS) and tidal model (POLCOMS) data provide background information about the area, this study required the collection of high-resolution flow and seabed dynamic data surrounding the SS *Apapa* site. Figure 3.7 presents a MBES produced digital elevation model (DEM) from the largest survey extent available around SS *Apapa*. To the west an area of large sediment waves is connected to the wreck site.

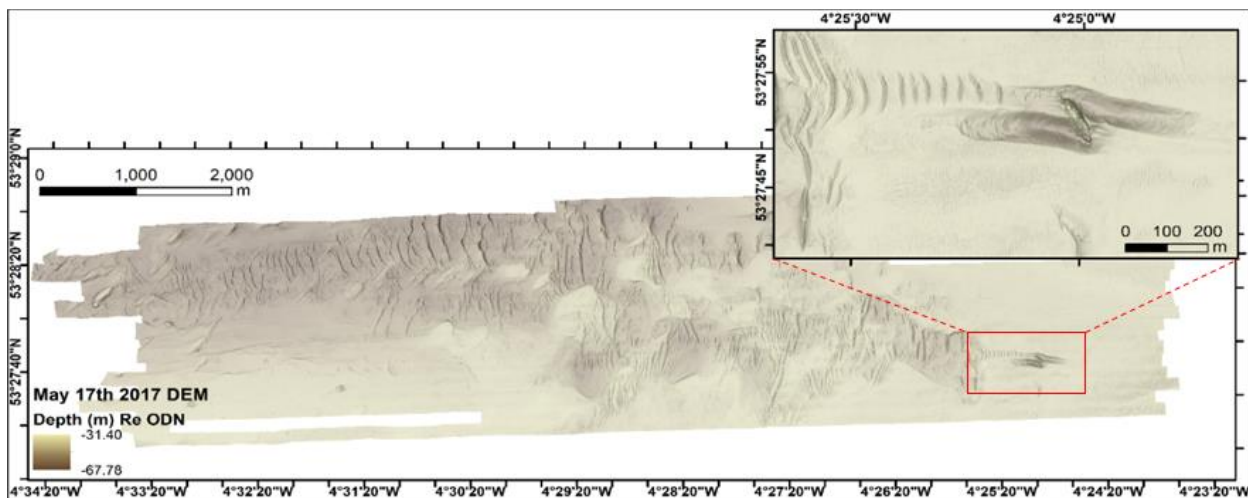


Figure 3.7: The area around SS *Apapa*. An area of large bedforms present at the west of the wreck.

## 3.2 Methodology of identifying processes around SS *Apapa*

### 3.2.1 Monitoring flow amplifications

The flow around the SS *Apapa* site was monitored through an ADCP survey, designed, and conducted over 2 full tidal cycles (25 hours) between 23:00 on the 14<sup>th</sup> of July 2019 and 00:00 (Universal Time Coordinated; UTC) on the 15<sup>th</sup> of July 2019. The survey was conducted using



transects of a 'figure 8' shape (Figure 3.8a) to capture the flow velocities near and at the far field of the wreck. The survey transects (blue lines) were designed to monitor the flow amplification formed over and downstream of the wreck and identify how far downstream (and at what depth) the flow is still influenced by the wreck. It was also designed to capture the flow deviation at the edges of the wreck and capture the likely undisturbed flow, away from the wreck. The red transects on Figure 3.8a (turning transects), were designed to monitor the likely undisturbed flow away from the wreck and outside of the direction of the tidal ellipse.

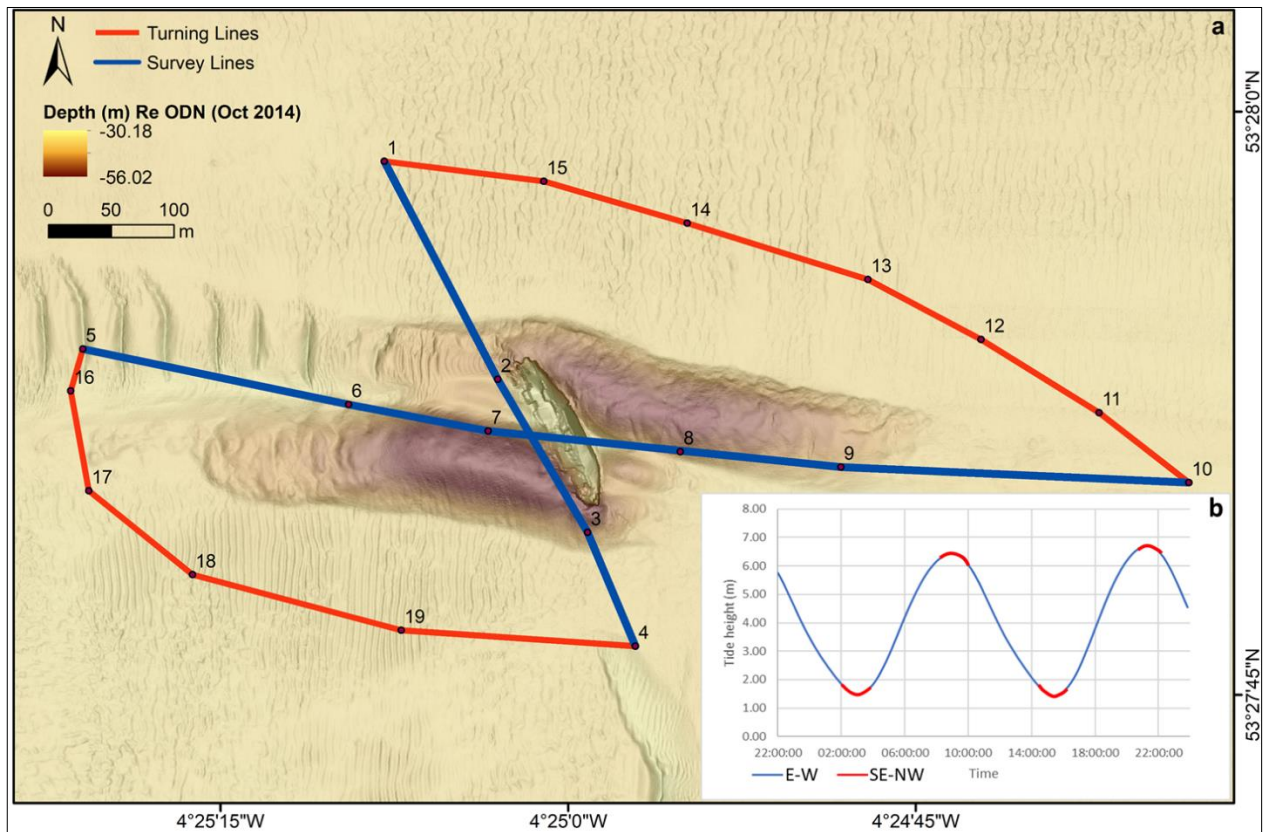


Figure 3.8: ADCP survey planning around the SS *Apapa* site to monitor changes in the hydrodynamics caused due to the presence of the wreck. The numbered points are the way points given to the crew of *RV Prince Madog* for accurate navigation. b) Tidal curve (tidal heights) from the Amlwch tide gauge during data collection and annotation of the ADCP transects during the survey, with a colour code also adapted in the map in Figure 3.8a.

For ease of navigation, the W-E transects were prioritised during tidal phases of maximum flow velocities where the SE-NW transects were prioritised during slack tides. Figure 3.8b presents the exact times that the transects were conducted.

Once collected, the ADCP data files, were visualized using the TELEDYNE WinADCP v 1.14 software. Raw data were displayed, and bottom tracking information was added to the data to identify the exact coordinates for each beam point and to correct the measured current velocities for vessel movement. The bottom tracked data were then processed further using MatLab R2019a software. The use of bottom tracked data also meant correction of the pitch and roll movements of the vessel. Tidal correction along with a depth correction for the ADCP placement in the water column were

applied to the data. Tidal data of the nearby Amlwch tide gauge (~7km to the SW) were used for the tidal height correction of the data to reference the heights to the mean sea level (MSL) values.

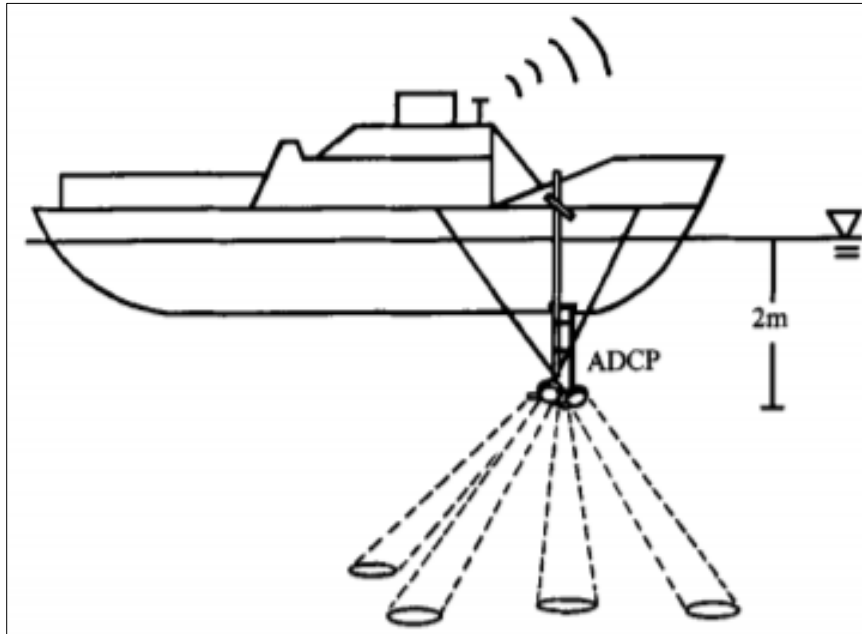


Figure 3.9: Schematic illustration of a vessel-mounted ADCP (Ya-ping et al., 2000).

Steep slopes near and further away from the wreck caused limitations while processing the ADCP data. The four beams of the ADCP project downwards with an angle of  $15^\circ$  which at a depth of 42 m means that the four beams project within a circular area of  $\sim 42 \text{ m}^2$  from the centre of the instrument (Figure 3.9). Therefore, with steep slopes at this site (of up to  $82^\circ$  in places), the four beams were not always pointing at the same depth at the same time. A method used by Simpson et al., 2011 was followed to identify the data that could be 'trusted'. The data covered by each of the four beams was plotted against time (Figure 3.10) and only the areas covered by all four beams (shallowest points) were kept identifying the ADCP data that could be 'trusted' and used for further analyses.

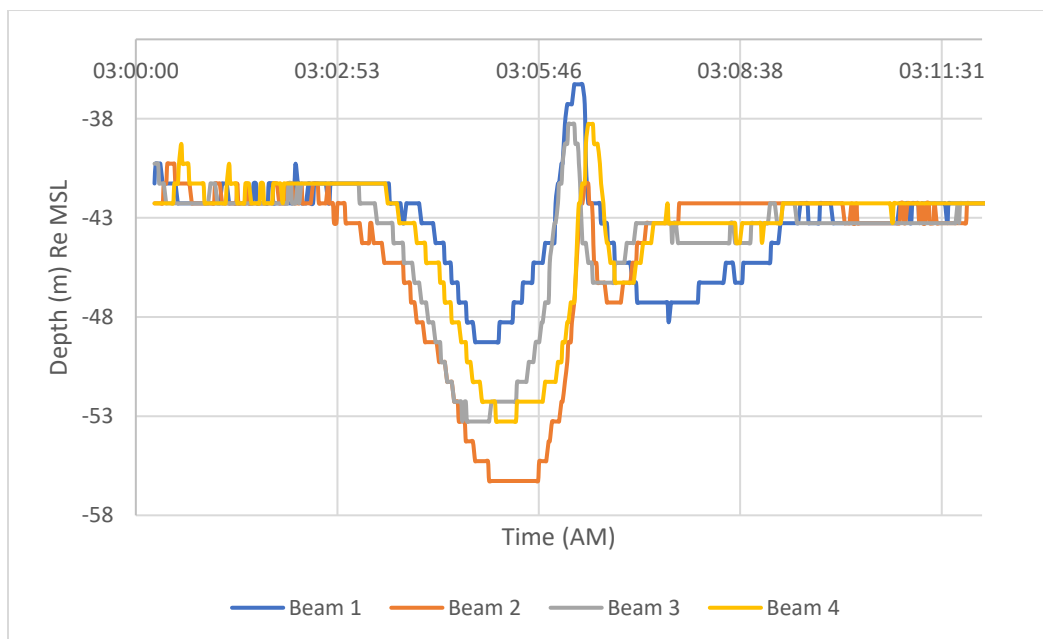


Figure 3.10: An example of the 4 ADCP beams (tidally corrected) over time (for one transect) to identify areas that all four beams were covering.

The cleaning method deleted 27.44% of the initial data volume especially within the scour mark but was essential to increase confidence levels. **Figure 3.11** visualises the data that were cleared from the dataset (any data below the black solid line).

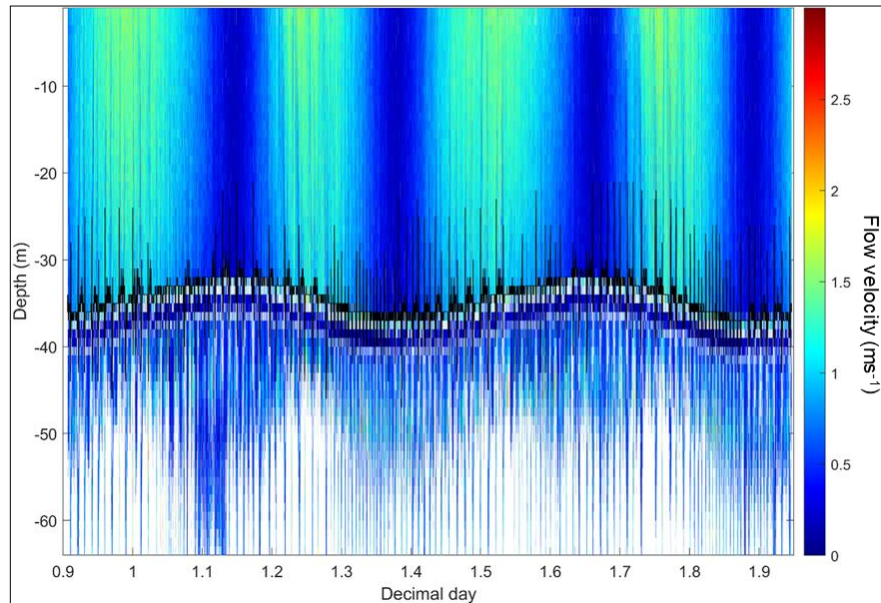


Figure 3.11: Flow velocity recorded from the ADCP instrument after the dataset was corrected for bottom tracking. Solid black line indicates a cut-off point, with anything below cleaned (erased) as not all four beams were projecting at the same point.

The fully processed and tidally corrected bottom tracked ADCP data were compared with the depth observed from the MBES surveys (**Figure 3.12**) to always increase the confidence level of the ADCP beam positions and to achieve an accurate investigation of the hydrodynamic changes along with a reliable direct comparison with the flow measurements predicted from a hydrodynamic model.

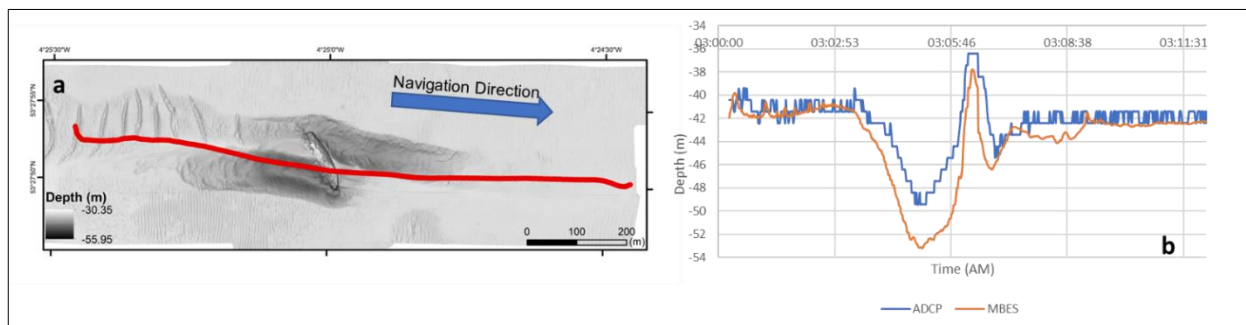


Figure 3.12: Surveyed transect from west to east (a) and comparison between the depth recorded from the ADCP and the depth at the same locations from the MBES (b).

When comparing the measured depth values of the two instruments directly for all the data (**Figure 3.13**) and applying a trendline (solid red line), the linear equation that provides the relation between the two datasets is  $y=0.8417x-7.9843$  (where  $x$  and  $y$  the ADCP depth and MBES depth data respectively) and the comparison provide a  $R^2$  value of  $\sim 0.47$ . Points with discrepancies larger than 5-15 m were observed around the wreck itself or at the depositional feature, as the four beams of

the ADCP were projecting at deeper areas. Both the bathymetric and ADCP dataset depths were referenced to the same vertical datum for this comparison.

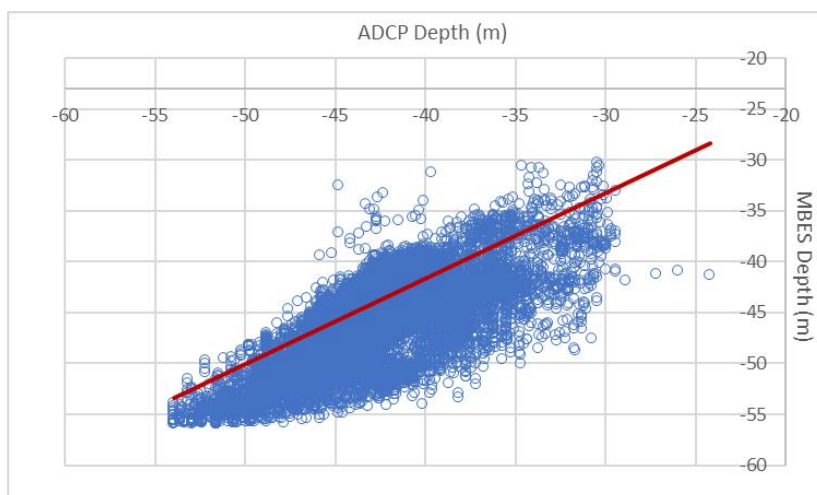


Figure 3.13: Direct comparison via plotting the two sample populations against each other. The red line indicates the trendline of the comparison of the two sample populations.

Boxplots with the depth data provided by the two instruments were also created to identify the ranges of depth values recorded from the two instruments (Figure 3.14).

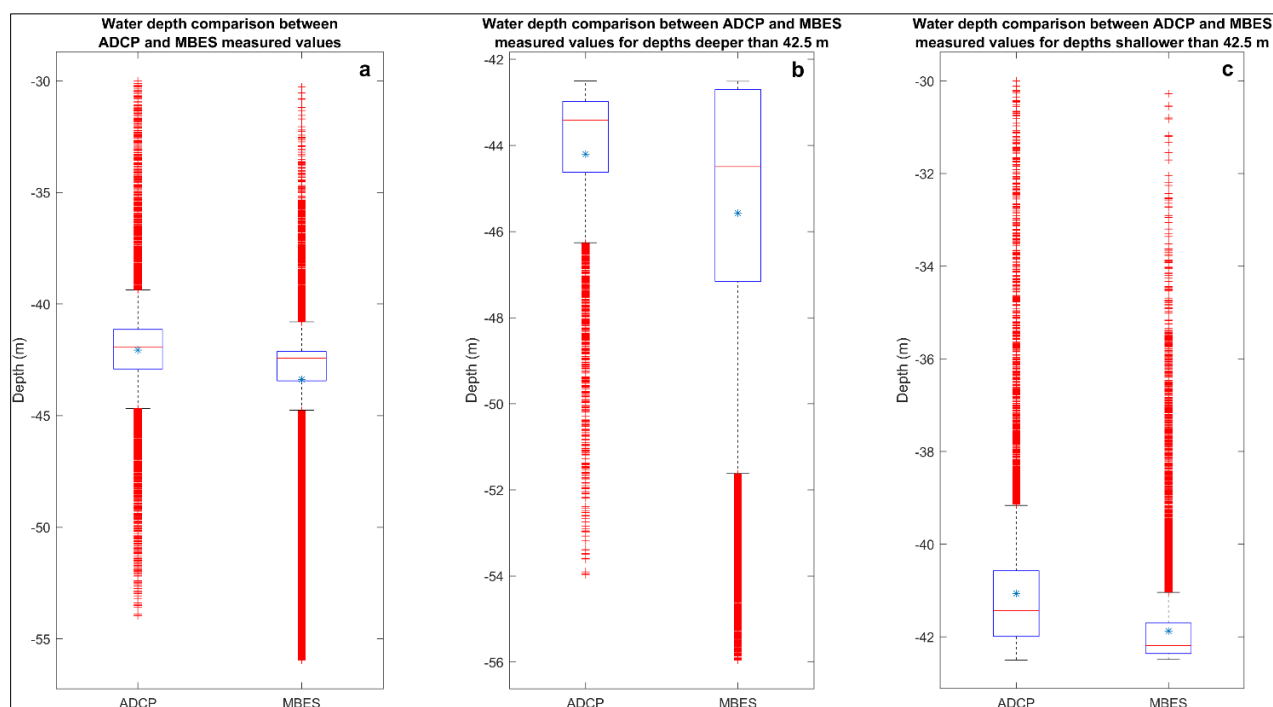


Figure 3.14: Boxplots for comparison of depth of last bin of ADCP data after the correction and MBES data; For measurements at all depths (a), for depths deeper than -42.5 m (b) and for depths shallower than -42.5 m. The solid horizontal red line in the Box indicates the median for each sample and the boxes indicate the 25<sup>th</sup> and 75<sup>th</sup> percentiles. The whiskers (horizontal black solid lines) indicate the minimum and maximum values, where the red crosses indicate the extreme values of the measurements.

The boxplots presented in Figure 3.14a show a median value of -41.94 m and -42.42 m (1.13% difference) and a mean value of -42.06 m and -43.37 m (3.02% difference) respectively for the depth of the last recorded bin of the ADCP and MBES measurements respectively. When plotting the data

for depth values that are smaller than -42.5 m (deeper), median values of -43.41 m and -44.49 m (2.43% difference) and mean values of -44.20 m and -45.57 m (3.01% difference) are calculated for the ADCP and MBES measurements respectively (Figure 3.14b). On the other hand, for depth values greater than -42.5 m (shallower), median depth values of -41.44 m and -42.19 m (1.78% difference) and mean values of -41.07 m and -41.88 m (1.93% difference) are calculated for the ADCP and MBES measurements respectively (Figure 3.14c). The separation point at the depth of -42.5 m was chosen as the 'flat' area surrounding the wreck has an average depth of  $\sim$ -42.5 m. The depth averaged flow speed and the maximum flow speed measured from the ADCP instrument were later plotted in ArcGIS and the upstream (background) and downstream (influenced from the wreck) velocities were compared. Figure 3.15a shows an example of one of the survey transects at a W-E direction, plotted in ArcGIS, with the colours of the arrows indicating the flow speed and the orientation of the arrows indicating the mean direction of the tidal current, where Figure 3.15b shows a short term average (STA), every 10s of the same transect, for better presentation of the flow diversion around the wreck. Figure 3.15c shows the same transect plotted in MatLab software, presenting the tidal current velocity variation both laterally and in-depth.

Similar plots were generated for all 126 survey transects to identify the amplification of the tidal current flow velocities at the wake, by choosing a representative value away from the wreck's influence and dividing all the measurements by that value. The mean variation between the tidal current upstream and downstream was investigated. Then the mean values of the observations upstream were compared with the mean values of the observations downstream of the wreck. Both the depth averaged and observed maximum tidal current velocities were compared using these two methods of presentation of the ADCP data shown in Figure 3.15.



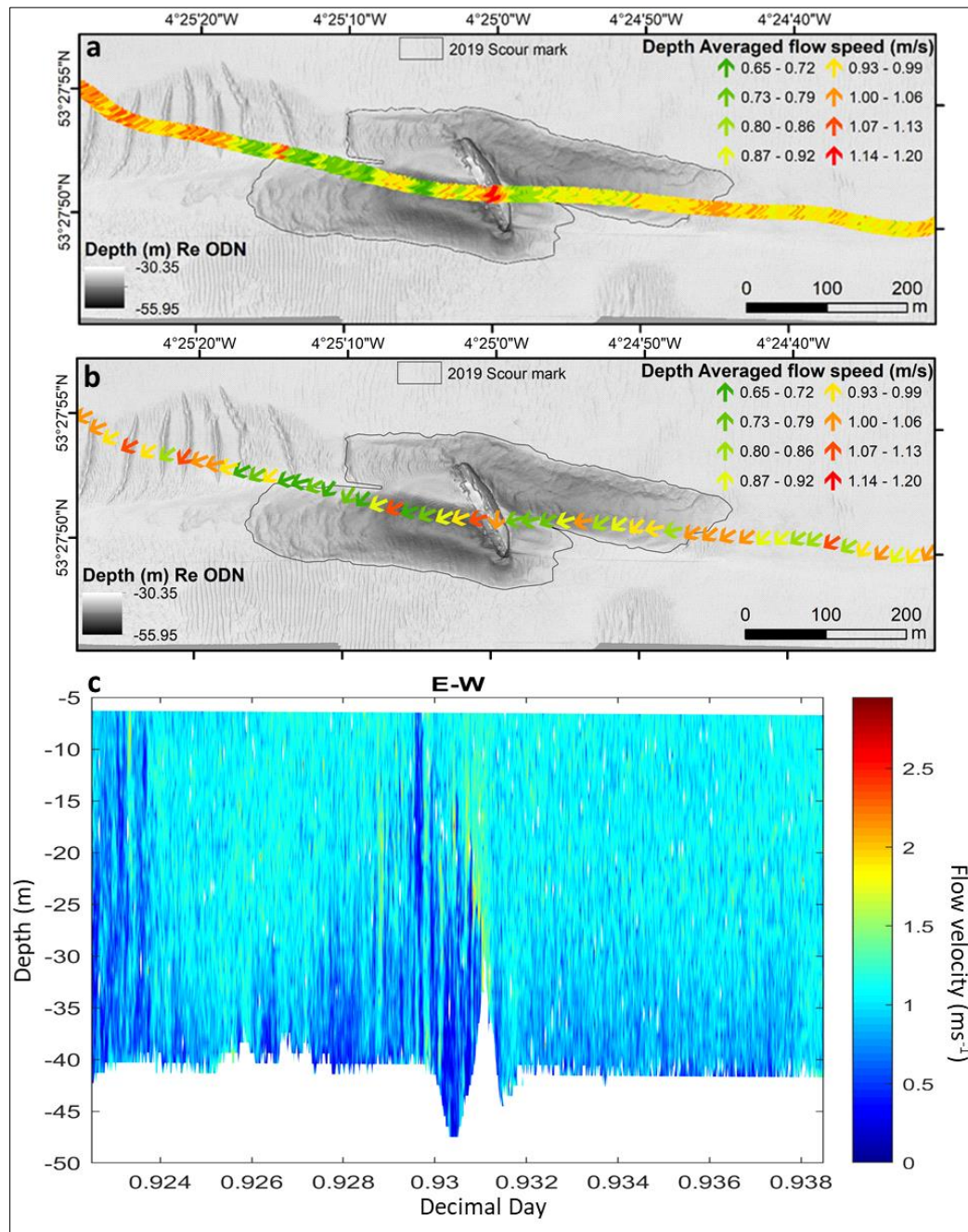


Figure 3.15: Tidal current as recorded from the ADCP instrument for one of the W-E transects. a) Presented in ArcGIS with the arrows indicating the depth averaged current velocity ( $\bar{U}$ ) and the orientation indicating the tidal current direction, b) short time average (STA) of the same transect (every 10 s), c) tidal current velocity plotted in MatLab, showing the variation both laterally and in depth.

### 3.2.2 Time lapse analyses of the scour edge

Time lapse analyses of the scour edge was conducted to identify the lateral changes in the scour mark's evolution during the last decade which required an accurate and precise method of tracking the scour edge for each MBES bathymetry dataset. The method had to be repeatable, so the same steps were followed for each survey's MBES dataset (DEM). During the process of creating an accurate method, different ways of identifying the scour edge were attempted and presented hereby. ArcMap was firstly used to identify if there was a quick and effective way of identifying the scour edge. Slope (gradient of steepness of each pixel), aspect (derivative of slope) and bathymetric

contour maps were calculated, combined, and analysed to identify if they were able to provide information about the end point of the scour mark (Figure 3.16).

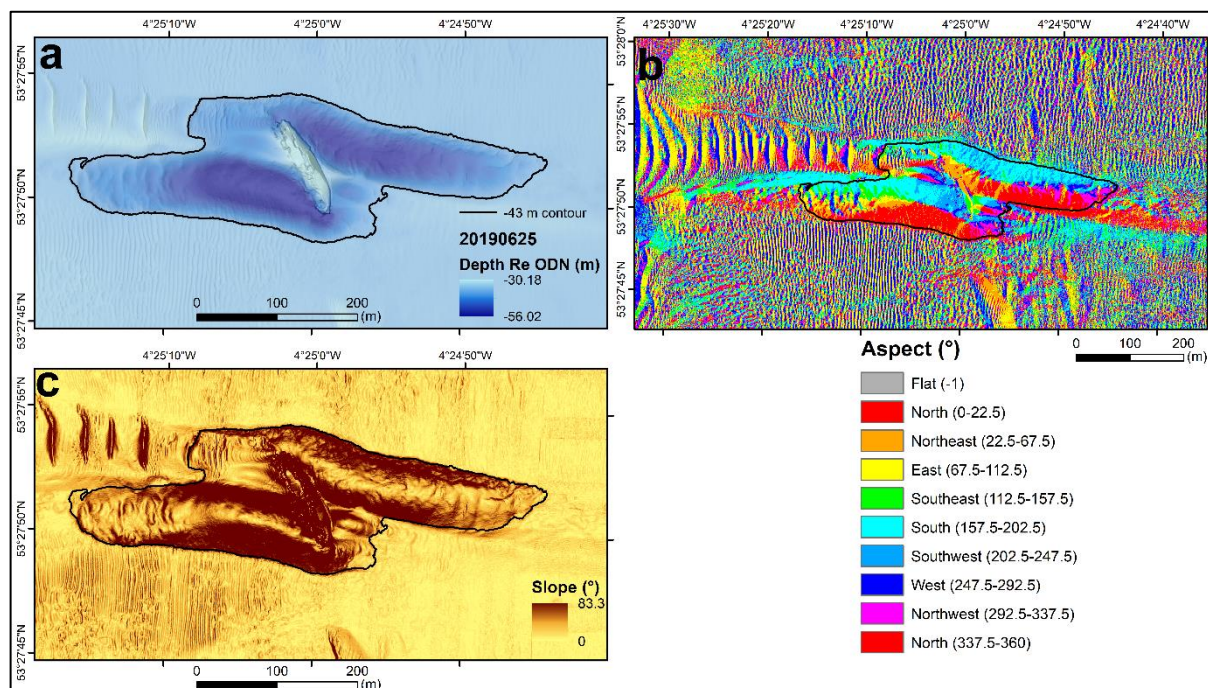


Figure 3.16: Methods used in ArcMap aiming to identify the edge of the scour mark to test for lateral changes. a) contour, b) aspect and c) slope of the DEM.

Although the slope and contours were able to provide a first direction towards delineating the scour edge, they could not be trusted as repeatable methods, due to the dynamics of the area, as differently sized bedforms are present at the surrounding area, changing the slope and bathymetry of the area between the different MBES datasets. This variability also prevents the use of aspect and contouring to delineate scour marks over time as choosing a specific contour for the delineation of the scour mark for one MBES dataset does not automatically mean that the same depth contour could be representative of the next dataset.

Secondly, an image analysis approach was tested using MatLab to detect scour edges in a consistent and automated way via differences in pixel intensity in an image generated from the Digital Elevation Models (DEM) presented at the same colourmaps and the slope map overlaying the DEM's layer at a certain transparency (80%). For the image analysis, the Graphical user interface (GUI) built by Image Analyst (2021) was used. The GUI allowed the user to identify the threshold value that would determine the cut-off point for the image analyses. The threshold value was basically masking out pixels with values (of a 256-bit grey scale image) less than the threshold value (with pixel intensity around 125), showing only the pixels with higher intensity. However, the visualisation of the imported image (DEMs overlayed with slope) was affecting the threshold value that the user had to provide, making the method ineffective, as MatLab only uses and analyses the image as 256 pixels subdivided grey scaled image (Figure 3.17), therefore the decision of the user as of the threshold value was crucial and not repeatable for every DEM.

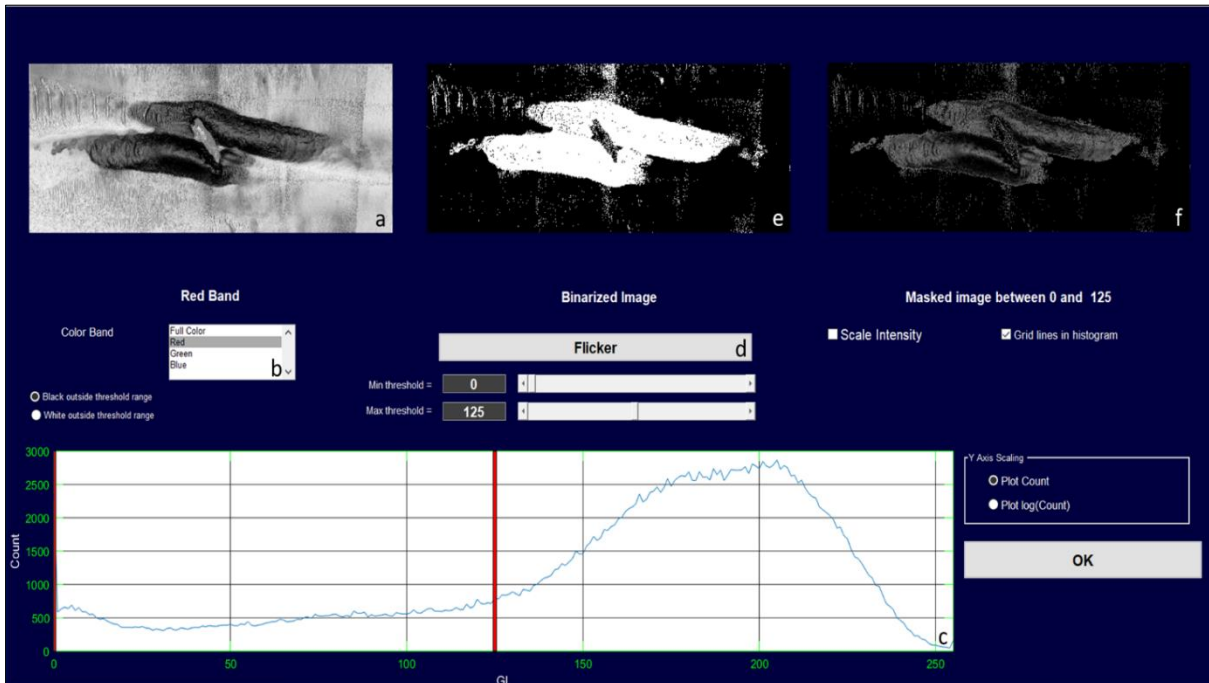


Figure 3.17: Matlab interface (Image Analyst, 2021) used for image analysis for the identification of the scour edge.

Due to the limitations to provide an automated, accurate and repeatable method of identifying the scour mark edge, the decision to manually generate many 2-D profiles was made. These profiles were generated every 5 m using the DEMs in ArcGIS. Point data, containing the coordinates and depth measurements were extracted every 50 cm (the same as the coarser grid resolution of the DEMs) using the densify tool in ArcMap. The 5 m distance between the profiles was chosen for time saving purposes. The profiles were created in a grid as perpendicular to the scour mark as possible (Figure 3.18). Similar techniques for time lapse analyses using 2-D profiles were used by Van Landeghem et al., 2009 for estimations of migration direction and migration rates of bedforms in the Irish Sea.



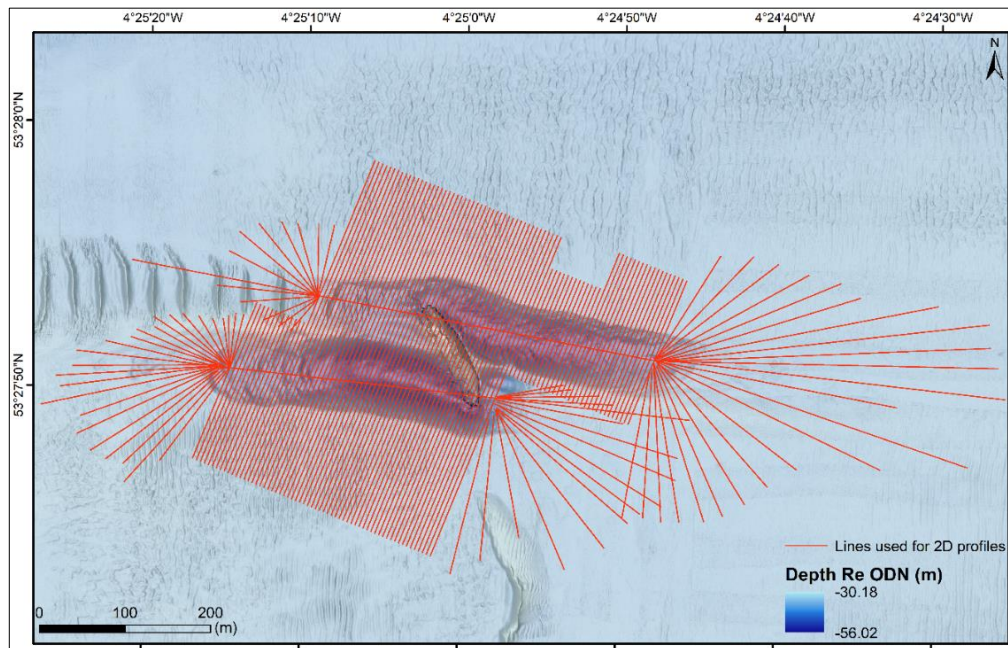


Figure 3.18: 2-D profile positions (every 5 m) over the SS *Apapa* site that were later plotted for the identification of the scour edge.

Distance of each point from the beginning of the line was calculated using its coordinates and the Pythagoras theorem. A script was produced in MatLab that allowed the production of interactive plots of distance along the profile against bathymetry, where the user was able to identify the edges of the scour mark (Figure 3.19). While the user identified the differences in bathymetry, the script was identifying the coordinate of each chosen point (representing the scour edge), producing a file with all the coordinates of the chosen points. The points were then connected with a polygon shapefile in ArcGIS and were used for presentation purposes and further analyses.

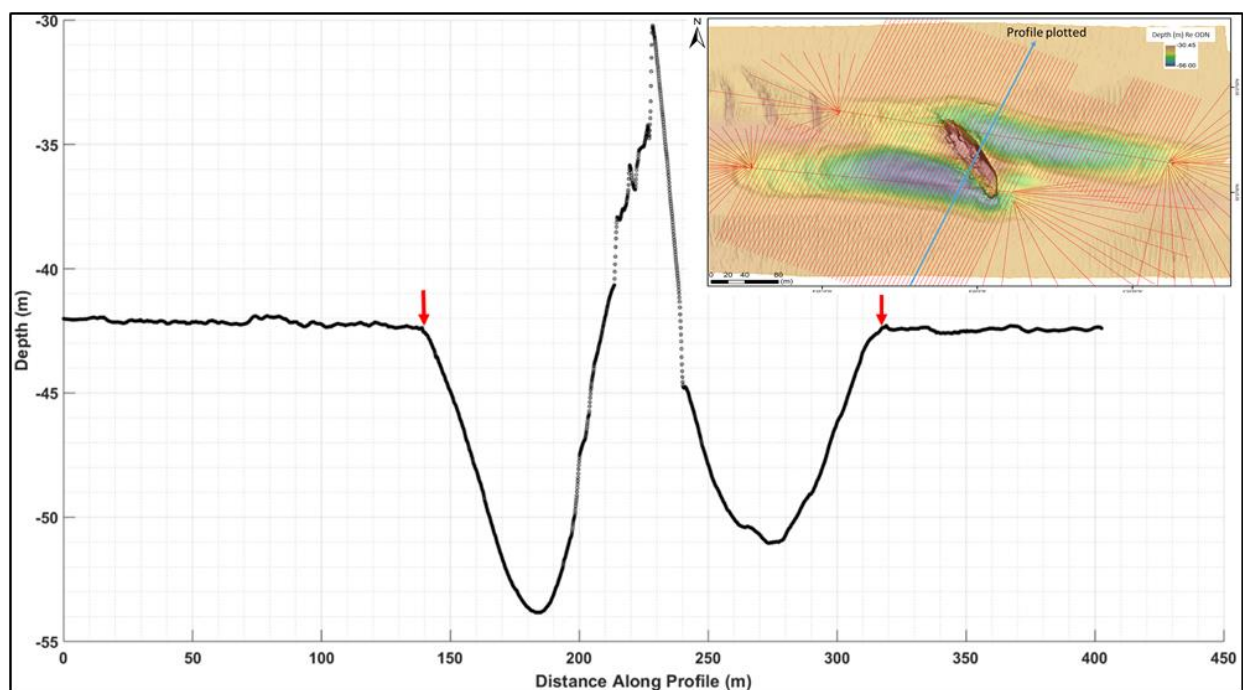


Figure 3.19: Plot of one of the 2-D profiles over SS *Apapa* used for the identification of the scour edge (red arrows).

### 3.2.3 Bed evolution changes within the scour marks

Bathymetric changes within the scour marks were monitored using difference modelling to identify the seabed changes during the last decade and to aid understanding of areas with larger variations. The process of investigating the lateral change of the scour marks was explained in the previous section. Along with the lateral changes, bathymetric changes within the scour mark and of the surrounding area were also investigated. The depth of the wider area (away from the scour mark), at areas with small bedforms (ripples) was compared between datasets to provide confidence of the survey data (minimise survey uncertainty). To investigate the bed evolution changes, difference maps were created in ArcGIS by subtracting the depth extracted from each pixel of one DEM, from the equivalent pixel of an older DEM. Positive values in a difference map thus represent deposition over time, negative values represent erosion. Maps with standard deviation ( $\sigma$ ) of bathymetry identify the difference over 8 years from the mean state of the area. The standard deviation was calculated using [Equation 3.1](#):

$$\sigma = \sqrt{\frac{\sum(x_i - \mu)^2}{n}}, \quad (3.1)$$

where:  $x_i$  is each value from the population,  $\mu$  is the population mean and  $n$  is the size of the population. The difference maps from survey to survey were also processed to identify the relative differences in bathymetry from the mean value of bathymetry from all the surveys. To calculate the relative differences ( $R_d$ ), the same point cloud as the one used for the calculation of the standard deviation ( $\sigma$ ) was used, however, this time the mean value from all the surveys was calculated and then the value from each survey was subtracted, following [Equation 3.2](#), for each of the points in the point cloud, using each point's location (coordinates):

$$R_d = \bar{x} - x_i, \quad (3.2)$$

The annualised depth variation was also calculated from the difference of the DEMs of consecutive surveys to identify the largest variations between the repeat surveys. Annualisation of the depth differences was conducted to normalise the effect of processes to compare their intensity over the same time period and was achieved by subtracting co-located depths, the more recent survey ( $x_{iR}$ ) subtracted from the older one, in groups of two ( $x_{iO}$ ), multiplying by the number of days in a year and dividing by the number of days that were in between the two surveys ( $N_{days}$ ), according to [Equation 3.3](#).

$$\text{Annualised depth difference} = ((x_{iR} - x_{iO}) * 365) / N_{days} \quad (3.3)$$

Using the result of the annualised depth difference between the surveys over the wreck, the annualised depth difference bathymetric standard deviation was also calculated, using [Equation 3.1](#) to identify if the changes in bathymetry over a couple of days (or months) can be representative of changes in bathymetries during longer time periods (years). Finally, the minimum and maximum of the depth variation of each point within the point cloud was calculated, along with the average of the difference maps from all the surveys to identify the areas with the maximum bathymetric changes over the years.

The bathymetric standard deviation maps generated using the DEMs can provide understanding of the bed mobility over time. However, these standard deviation maps cannot inform if sediment in an area is eroding or depositing over the years as it is comparing the measurement of each point in the point cloud with the mean of the measurements at each location. To investigate erosion and deposition rates over the years, 2-D profiles following seabed features (i.e, depositional features, deepest points of scour marks, areas with similar slopes etc.) were generated using the bathymetric difference maps between the consecutive datasets (difference modelling). An example of a seabed feature followed was the depositional feature at the west scour mark (Figure 3.20a), where Figure 3.20b presents the 2-D profiles plotted over distance (away from the wreck) and Figure 3.20c presents all the profiles used for the analyses. The profiles shown in Figure 3.20b were sampled using the bathymetric differences every 0.5 m and the distance from point to point was calculated using Pythagoras theorem.

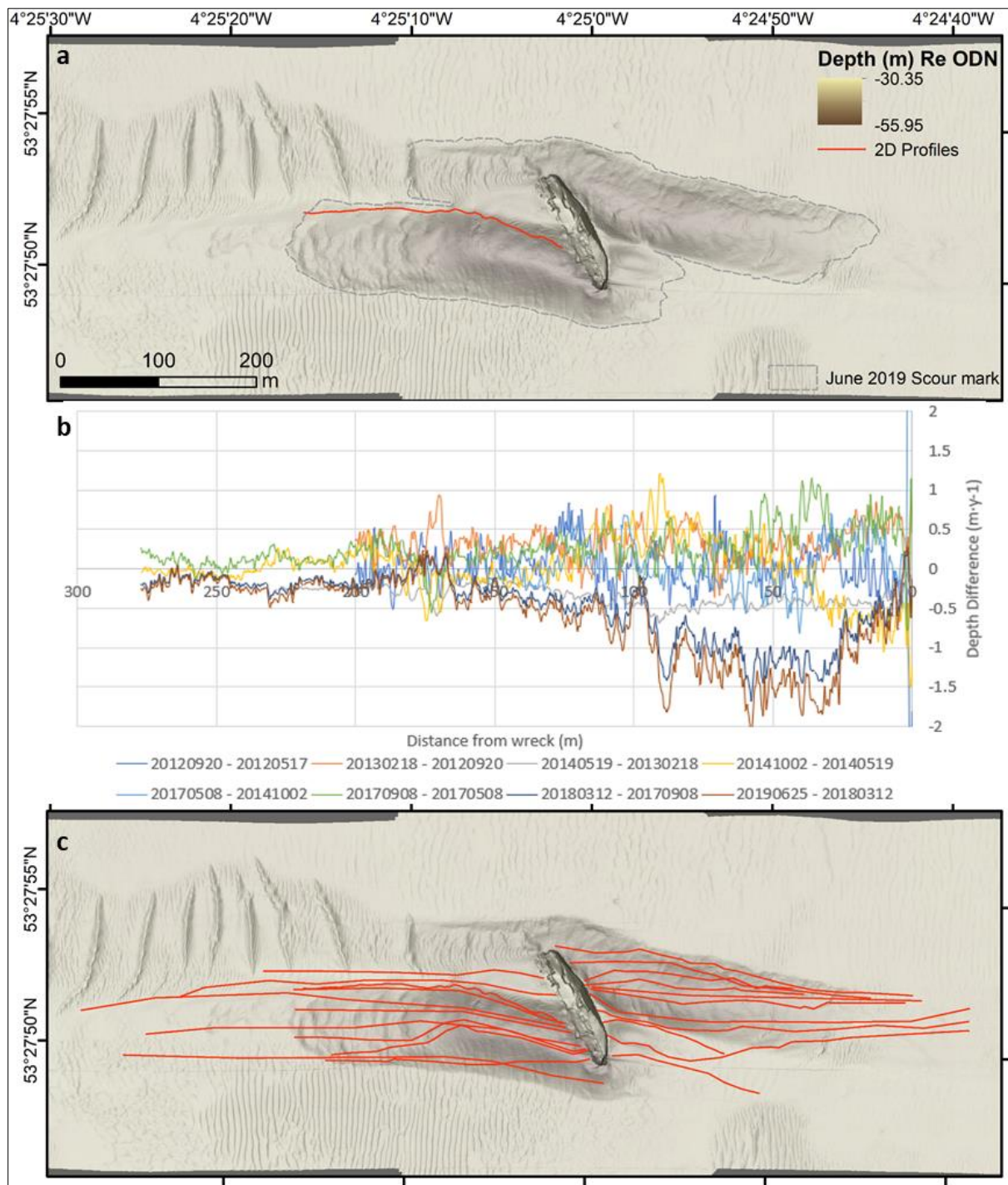


Figure 3.20: a) Profile following the depositional feature, b) bathymetric differences between consecutive datasets over the profile of (a) using the difference maps from the surveys mentioned in the legend and c) profiles used to identify drops in the bathymetric difference DEMs.

### 3.2.4 Time lapse analyses of bed composition using repeated MBES backscatter strength data

Time lapse analyses of bed composition was conducted to identify areas with similar sediment types that could potentially be linked with bed composition to help in understanding of the sediment types that are more mobile over time. For this study, backscatter strength (BS) data (secondary product of the MBES instrument) were assessed in order to identify changes in the bed composition. Bed composition data were used from repeat MBES BS data, as sediment samples were not collected



during every repeated survey. In contrast, backscatter data (in snippet mode) were collected instantaneously with the bathymetric data from the Reason 7125 MBES instrument and were available for all the surveys over the *SS Apapa* site. The MBES instrument can record the backscatter response in either snippet mode or side scan sonar (SSS) mode. Snippets are fragments of the full signal envelope that target on containing the seafloor backscatter from each beam. In contrast, the SSS-like mode, includes the full acquisition range of the MBES central unit, including the distance between the transducer and the bottom but also the chosen acquisition range. **Figure 3.21** shows graphically the difference between the projected beams using the two methods.

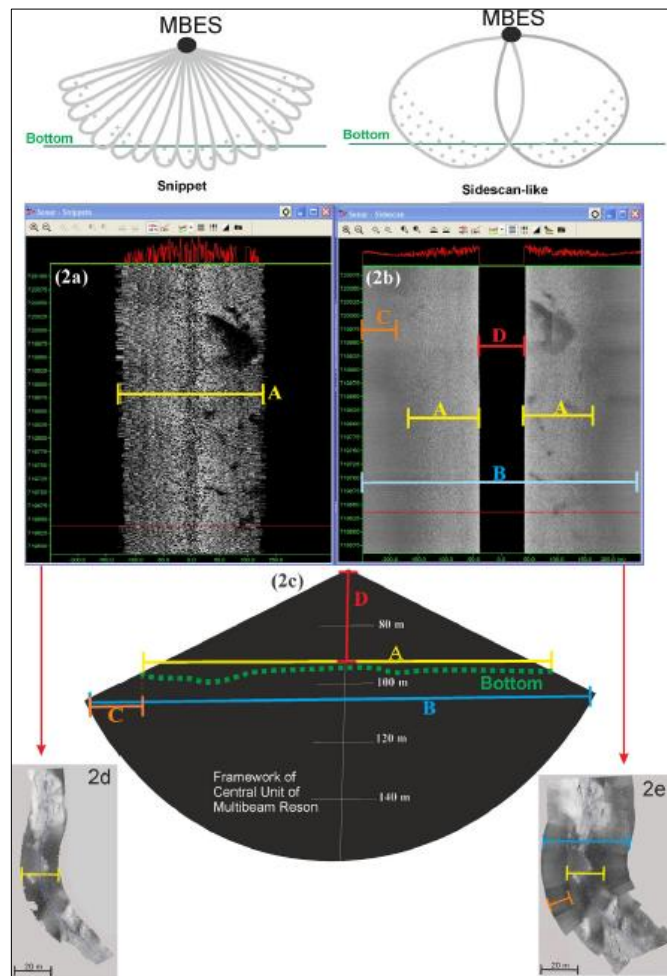


Figure 3.21: Explanation of the two modes of collecting the backscatter data (a; snippet and b; SSS-like) using the PDS2000 software window. c) the central unit of the MBES framework and the green line indicates the bottom profile ensonified by the MBES. The snippet and MBES data are logging at the same horizontal range (yellow line A), whereas the SSS-like data are logging including the whole central unit range, with the horizontal range including the distance from the transducer to the seabed (water column; red line D) and the range of acquisition (blue line B), along with null data (orange line C; [Innangi et al., 2015](#)).

The backscatter data were firstly opened in PDS2000 and converted to specific file formats (.s7k and .gsf) required for further processing using the Fledermaus Geocoder Toolbox (FMGT v. 7.8). The backscatter strength data are considered as secondary product of the MBES instrument, as the instrument was operating at a 400 kHz frequency to prioritise high-resolution bathymetry data. Surveys targeting seabed composition analyses, often use SSS instruments (insonifying the bed obliquely from just above the seabed) and are typically using frequencies of 100 kHz – 120 kHz

when seabed composition is the target for investigations. When the sound interacts with differently sized spheres (sediment grains), it is reflected (scattered) to different directions. Backscatter can be defined as the part of the scattered energy recorded by the receiver (Jackson & Richardson, 2007). However, high frequency acoustic surveys can also be used for the collection of high-resolution backscatter data, which at 100% coverage can become an effective seabed classification method, reducing survey costs (Preston, 2009). The frequency dependence of backscatter strength is driven by three factors (Gaida et al. 2018):

- i) The relationship between the acoustic wavelength and the seabed roughness;
- ii) the dominant scattering regime that depends on the particle size and the acoustic wavelength; and
- iii) the contribution of volume scattering, that is influenced by the signal penetration.

Several field and lab experiments showed that similar sediment types have varied acoustic response at different frequencies (Hefner et al., 2010). A study (Brown et al., 2017) showed that the frequency of 400kHz reflected only the surface sediments due to signal penetration. In contrast, survey of the same area using a MBES at 100 kHz has shown that depending on the thickness of fine surface sediment, resulted to backscatter from rough dredge spoils buried in the sub-surface beneath the fine sediment layer. In the case of coarse sediments, backscatter at different frequencies reflects mostly the surface sediments, with the depth of penetration of the acoustic signal shown in Figure 3.22 (Gaida et al., 2018).

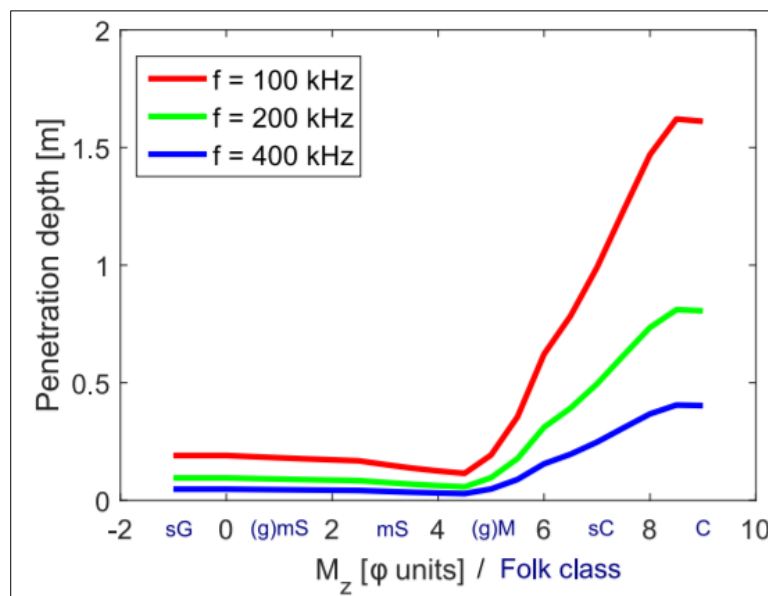


Figure 3.22: Signal penetration *versus* mean grain size. Signal penetration calculated from empirical equations for acoustic attenuation in marine sediments. The Folk classes approximately assigned to the relative mean grain sizes: sG (sandy gravel), (g)mS (slightly gravelly muddy sand), mS (muddy sand), (g)M (slightly gravelly mud), sC (sandy clay) and C (clay) (Gaida et al., 2018).

A combination of bathymetric and backscatter imagery together, can provide information about the seabed that may not have significant geomorphic signature, but have surface roughness (Lamarche et al., 2011). The backscatter strength data collected during the MBES surveys were corrected for angular response (a fundamental characteristic of the backscatter response; Clarke et al., 1997)

guided by Jonathan Beaudoin from QPS, who created the FMGT software for BS angular dependency corrections, using the geometry of the beams and the bed (Figure 3.23).

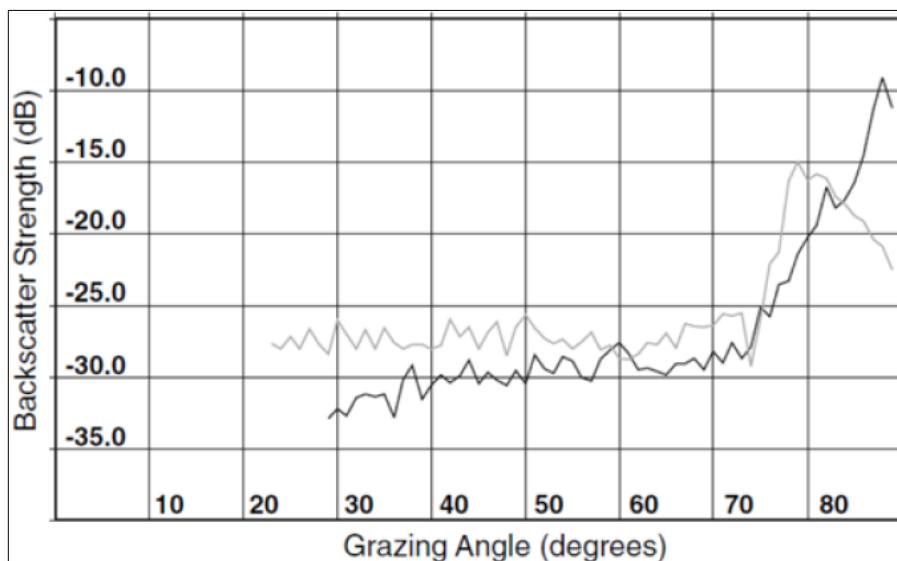


Figure 3.23: BS angular response for a small patch of the seafloor. Gray line is the original observation where the solid black line is the BS angular response after application of all geometric corrections (with nadir at 80°).

Hard, rough, rocky beds will provide an echo level that does not depend significantly on the incidence angle, as the echo intensity recorded over a full swath width appears to be stable whatever the angle. On the other hand, soft and flat seabed sediments generate an artificial, mirror-like response with very little scatter at the oblique angles, where most of the intensity is reflected at normal incidence (Figure 3.24).

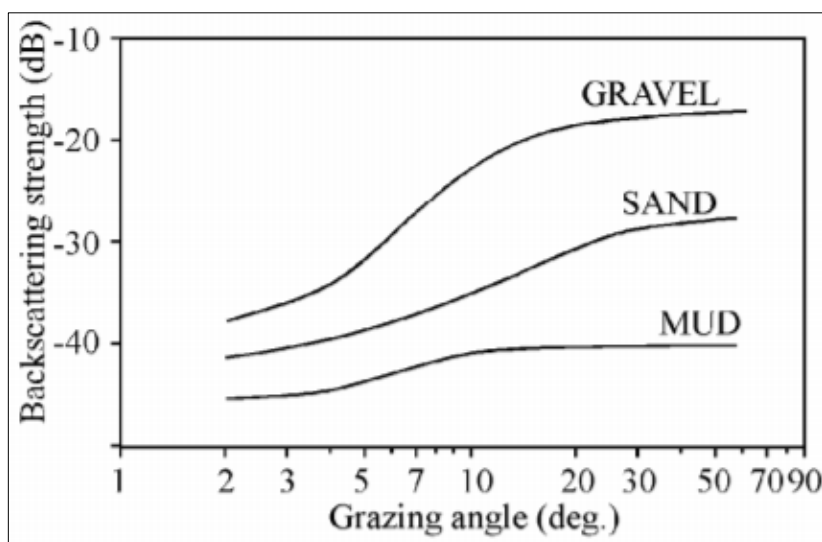


Figure 3.24: Average BS curves for three types of sediment (Chotiros, 2006).

The image produced by the sonar signal will therefore show an increased maximum at the nadir (centre of the image), accompanied with a fast decrease of the intensity on the sides (Figure 3.25; Lamarche & Lurton, 2018).

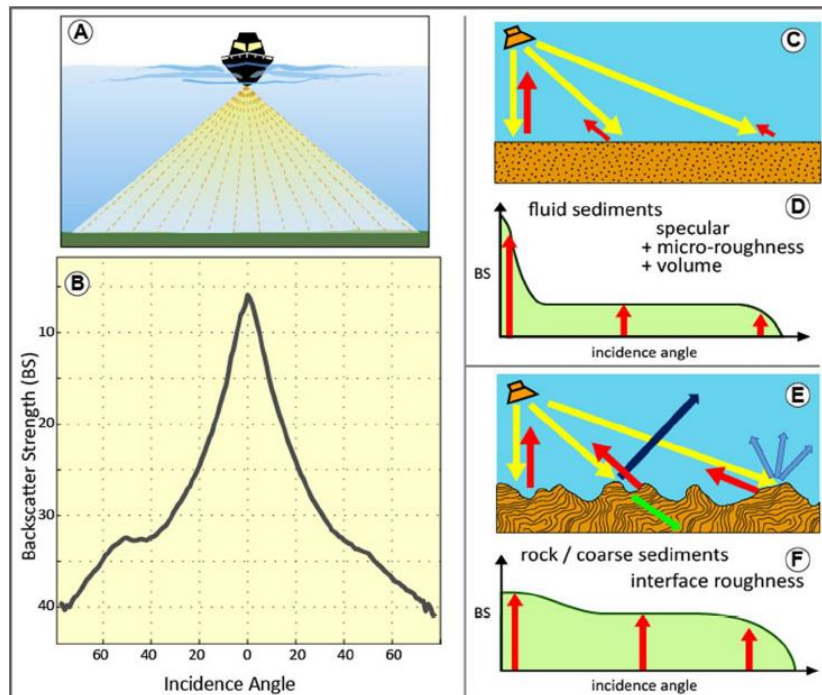


Figure 3.25: The working principle of BS measurements and interpretation. a) A swath pattern of incidence waves (marked with yellow on c, e), generated reflection (dark blue on e), scattered (light blue on e), backscattered (red on c-f) and transmitted (green on e) waves. b) The backscatter echo intensity dependence on the incidence angle on the seafloor. A soft or flat seafloor (c) will generate a different angular dependence (d) than a rough or rocky interface (e, f) (Lamarche & Lurton, 2018).

Processing of backscatter data becomes even more challenging when dealing with angles as high as  $82^\circ$ , which is the case of the present study. Steep angles are not only observed at the wreck itself but also around the scour mark. As an example, at the steepest point of the scour mark, the depth drops from  $\sim 42.5$  m to  $\sim 56$  m at a distance of  $\sim 30$  m with a seabed slope of  $30^\circ$ . The file containing the snippet information (.gsf) from the Reson 7125 acquisition software was used in the FMGT software along with the file containing information about sonar measurements in the form of angles/ranges for bathymetry and backscatter (.s7k). The FMGT software correlates the bathymetry information with the backscatter information and uses the two file types for the estimation of a 'normalised backscatter'. The data processing in FMGT involved the removal of the system's transmission loss, the calculation of angle of incidence, the correction of the beam pattern, the calculation of the angular backscatter response and the removal of the angular dependence. The final product of the FMGT was backscatter strength mosaics, with 100% blend between the survey transects and no nadir artefacts.

### 3.2.5 Sediment sample collection at the SS Apapa site using a seabed surface grab sampler (Shipek)

A sediment sample collection survey campaign was designed based on a desktop study. The decision of the grab sample locations involved analyses of bathymetric and backscatter data. The sediment sample collection was conducted to identify what sediment types exist at the area, use them to 'train' the BS mosaics and help understanding of the exact sediment types that appear to be



more mobile over time. The decision to sample 40 m away from the wreck to avoid hazards was taken after communication with the crew of *RV Prince Madog*. Forty grab sample locations were suggested (Figure 3.26), but due to excess time during the survey, sixty-three grab samples were collected by navigating to the suggested coordinates, dropping the grab and drifting with the tidal current. Positioning of the grab sample locations was monitored using the Easytrak Nexus Lite 2695 Series ultra-short baseline (USBL) system.

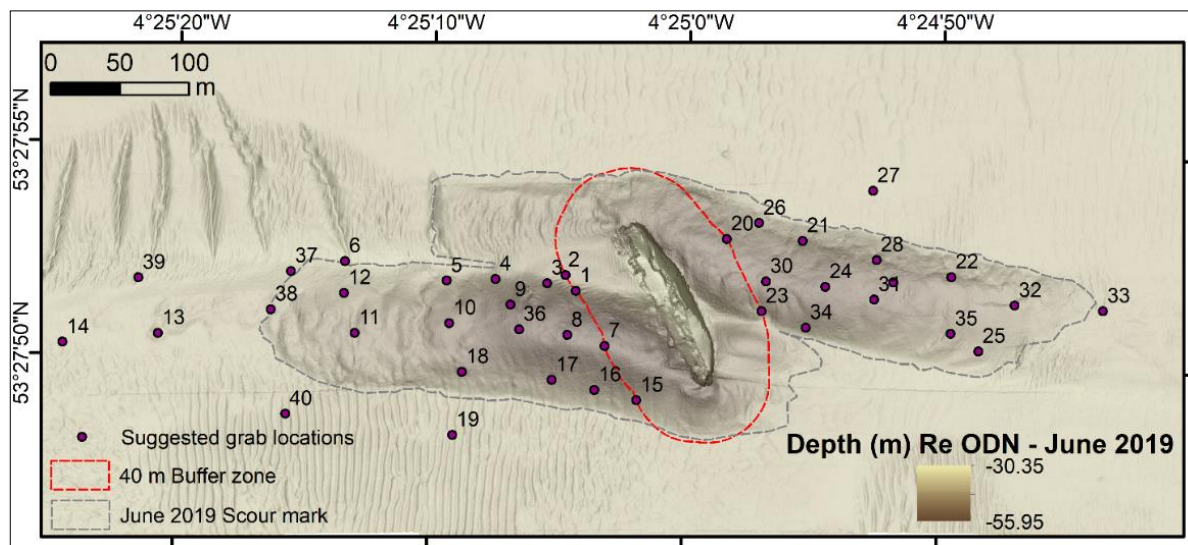


Figure 3.26: Planned locations for grab samples collected around the area of SS *Apapa*.

Table 3.2 describes the datasets collected during the 13 repeat surveys over the SS *Apapa* site and their inclusion or not while processing the datasets to identify different parameters.

Table 3.2: Table of datasets collected around the SS *Apapa* site during 13 surveys.

Survey date	Bathymetric Dataset (Y/N)	ADCP Dataset (Y/N)	Backscatter Strength Dataset (Y/N)	Used for scour edge delineation (Y/N)	Used for calculation of Bathymetric $\sigma$ (Y/N)	Used for calculation of BS $\sigma$ (Y/N)	Grab samples (Y/N)	Used for TELEMAC
17/05/2012	Y	N	Y	Y - Not the SW part due to limited coverage	Y	N	N	N
22/09/2012	Y	N	Y	N	Y	N	N	Y
18/03/2013	Y	N	Y	N	Y	N	Y (no USBL)	N
19/05/2014	Y	N	Y	Y	Y	Y	N	N
02/10/2014	Y	N	Y	Y	Y	Y	N	N
08/05/2017	Y	N	Y	N	Y	Y	N	N
12/05/2017	Y	N	Y	Y	Y	Y	N	N
17/05/2017	Y	N	Y	Y	Y	Y	N	Y
08/09/2017	Y	N	Y	Y	Y	Y	N	N
22/09/2017	Y	N	Y	Y	Y	Y	N	N
12/03/2018	Y	N	Y	Y	Y	Y	N	N
25/06/2019	Y	N	Y	Y	Y	Y	Y	Y
15/07/2019	N	Y	N	N	N	N	N	Y

The USBL software outputs a file with the instrument's location all the time, providing measurements of depth and coordinates every second. The time and coordinates from the output file were plotted against height/depth to identify times that the instrument and the grab were positioned at the seabed surface (Figure 3.27). These points (drops) were used, and their accompanied coordinates were attained to identify the sample locations.

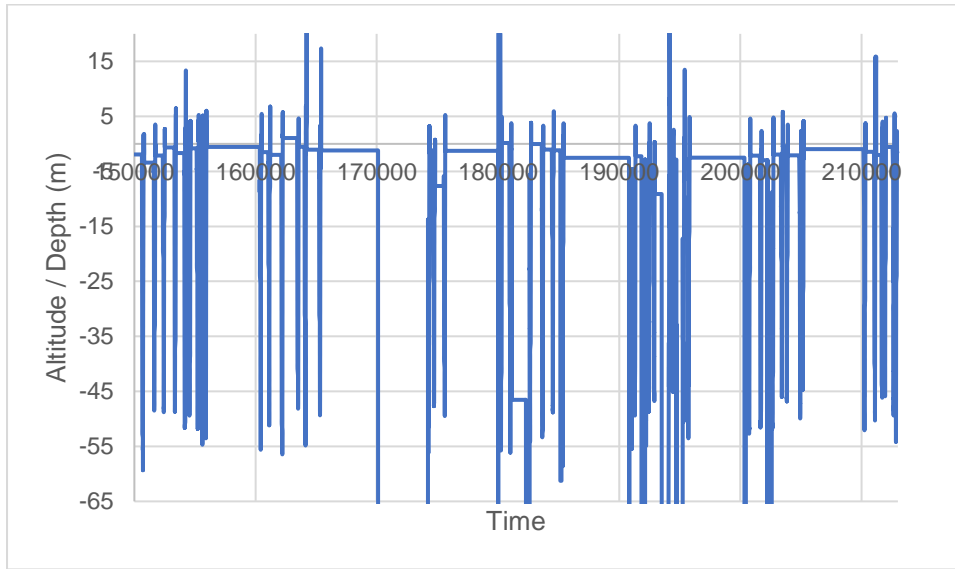


Figure 3.27: Depth recorded from the USBL instrument (with drops showing sampling points) during grab sampling plotted against time.

While grab sampling around SS *Apapa* the USBL instrument stopped working after the collection of the first 47 grabs due to a technical issue. As there was no accurate positioning for the last 16 grabs the position of the vessel was used. When the A-frame of the vessel is out the block, there is a distance of 28.7 m from the positioning of the ship's GPS head. This distance was combined with the heading of the ship's log data to calculate the layback, assuming that the grab dropped vertically. The observed current magnitude value ( $\text{m}\cdot\text{s}^{-1}$ ) was taken for all the time steps from the ADCP survey and was used for the calculation of the bed shear stress for each of the modes of the sediment samples that flow velocities was available. The calculation of the bed shear stress for each of the modes involved the generation of buffer zones at 6.92 m around each sample location ( $\sigma$  of USBL instrument) and the calculation of the maximum magnitude value for the last bin of the ADCP falling within that buffer.

Sediment mobility was estimated for each mode of the sediment samples using Soulsby's equations (Soulsby, 1997) for critical sediment transport, calculating the threshold Shield's parameter ( $\theta_{cr}$ ) as Equation 3.4:

$$\theta_{cr} = \frac{0.3}{1 + (1.2D^*)} + (0.055(1 - e^{-0.02D^*})), \quad (3.4)$$

The threshold Shield's parameter was used for the calculation of the threshold shear stress ( $\tau_{cr}$ ) as Equation 3.5:

$$\tau_{cr} = \theta_{cr} (d_{50})g(\rho_s - \rho_w), \quad (3.5)$$

with  $\theta_{cr}$  the critical Shield's parameter,  $g$  the acceleration due to gravity and  $\rho_s$  and  $\rho_w$  the density of solids and the water density respectively.

The critical current induced bed shear stress ( $\tau_0$ ) was calculated using Equation 3.6:

$$\tau_0 = \rho_w u_*^2 \quad (3.6)$$

with  $u_*$  the current shear velocity calculated using Equation 3.7:

$$u_* = \frac{\bar{U}}{7} \left( \frac{d_{50}}{z} \right)^{0.142857143} \quad (3.7)$$

with  $\bar{U}$  the depth averaged current velocity and  $z$  the water depth.

According to the values calculated from the Soulsby (1997) formulae, each mode of the sediment sample was estimated to be mobile when the current induces bed shear stress ( $\tau_0$ ) is greater than the threshold shear stress ( $\tau_{cr}$ ).

The corrected backscatter strength mosaics were later correlated with the grab samples collected from the area around SS Apapa to identify what each BS value means in terms of sediment composition. For the correlation the supervised and unsupervised classification tools in ArcMap were attempted. The differences between the two methods are that the supervised classification allows for the user to manually select areas of pixels with similar BS, that the image processing software will use as ‘training’ sites and the user is required to designate the number of classes that the BS image will be classified to. On the other hand, the unsupervised classification is solely based on automated analysis of the different classes from the image processing software, where the software uses techniques to identify pixels with similar BS and relate them into the different classes. However, the user can specify the different algorithms used and the number of the output classes. If the user choses a larger number than the number of classes that the software identifies as appropriate, the software uses the maximum number of classes that it accounts as appropriate. The supervised classification was trained using the unimodal sediment samples from the grabs collected around SS Apapa, as the  $d_{50}$  value is not representative of a bimodal sample (Figure 3.28).

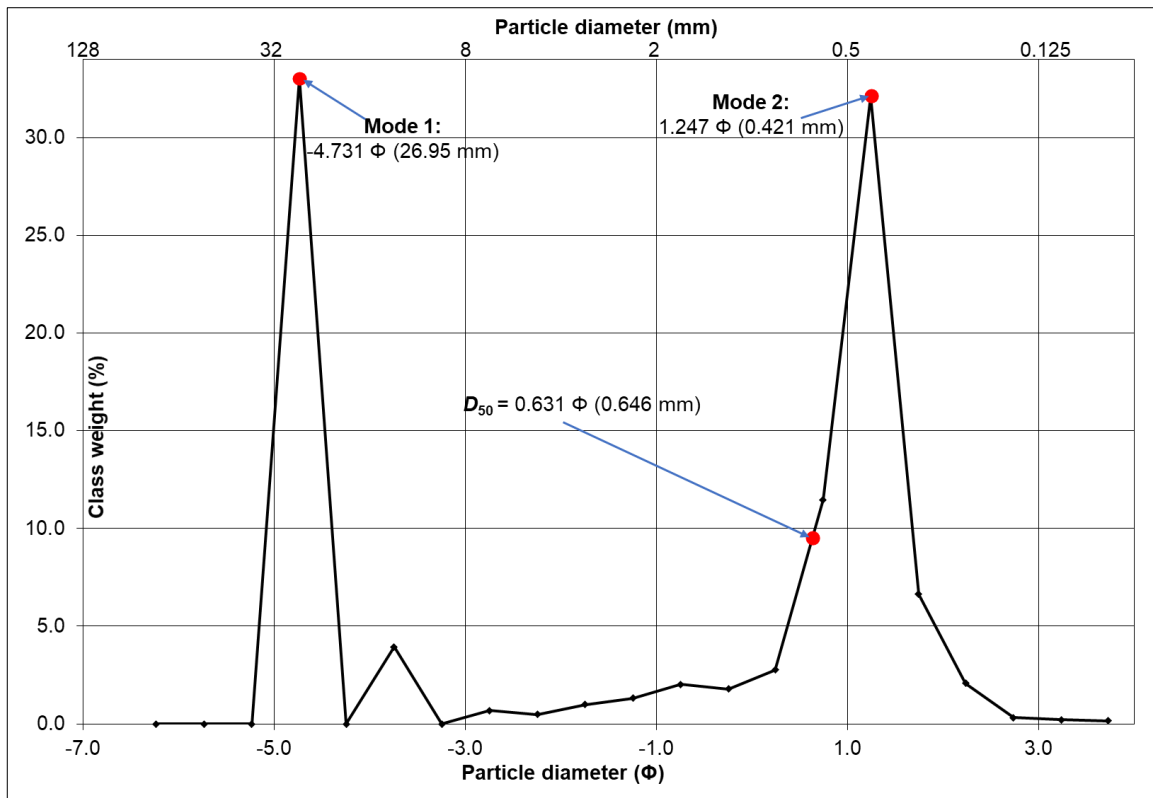


Figure 3.28: Example of a bimodal sediment distribution (the two modes and the sample  $d_{50}$  are indicated on the plot) showing that  $d_{50}$  value is not representative of the bimodal sample.

### 3.2.6 Reconstructing the evolving wreck environment using a coupled Hydrodynamic and sediment transport model (TELEMAC3D – GAIA)

#### 3.2.6.1 Reconstructing a pre-wreck artificial bed scenario

The purpose of the coupled TELEMAC3D–GAIA numerical modelling work was to use the information provided from the detailed research of the processes around SS *Apapa* as a case study to inform and validate a coupled hydrodynamic and sediment transport model that could potentially later be used for the prediction of processes around differently shaped submerged structures placed on mixed coarse beds.

Reconstructing the wreck environment appeared to be a challenging task due to the steep slopes around the wreck. A case study to represent the study site when the wreck sank was developed to test if the initial scour formation could be predicted from the model. To reconstruct the bathymetry of the area when the wreck sank, it was assumed that the surrounding area was flat. This assumption was because the surrounding area to the north and east is at present relatively flat and sits around -42.5 m, with slopes less than 4°. In contrast, the area to the west, has sediment waves with heights varying between ~2 – 5 m, where at the south there is only one sediment wave with a height that varied between ~3 – 4 m during the last decade. For the modelling work presented in this chapter, a new DEM was artificially created by combining the DEM from the survey conducted on the 17<sup>th</sup> of May 2017 (largest extent – [Figure 3.29a](#)), the DEM from the survey conducted on the 25<sup>th</sup> of June 2019 ([Figure 3.29b](#)) and the wreck positioned at the place that existed at the oldest DEM available (survey conducted on the 17<sup>th</sup> of May 2012). The process of generating the DEM involved the removal of the area that the 2019 DEM covered ([Figure 3.29c](#)) from the 2017 DEM ([Figure 3.29a](#)) and joining the two datasets together ([Figure 3.29d](#)). Once the two datasets were joined, the scour part of the wreck was removed ([Figure 3.29e](#)) and inversed distance weighted (IDW) interpolation was applied to the area. The IDW interpolation method assumes that the interpolating area is influenced mostly by the nearby points (12 at this case; default choice in ArcMap). The interpolated area is calculated to be the weighted average of the nearby scattered points and the weight that is assigned to each point is reducing as the distance between point – interpolated area increases. Once the process was at the stage of [Figure 3.29e](#), the area that the wreck was covering in the 2012 DEM was clipped out ([Figure 3.29f](#)) and the wreck from the 2012 DEM was applied to the raster ([Figure 3.29g](#)). However, due to the change of the bed because of scour, it appeared that the wreck in the 2012 survey was submerged within the bed ([Figure 29g](#)). Therefore, the decision to raise the wreck by ~8 m was taken to ‘force’ the wreck to sit on the ‘pre-wreck’ bed ([Figure 29h](#)). Consequently, the DEM used for the modelling work is the DEM shown in [Figure 3.29h](#).

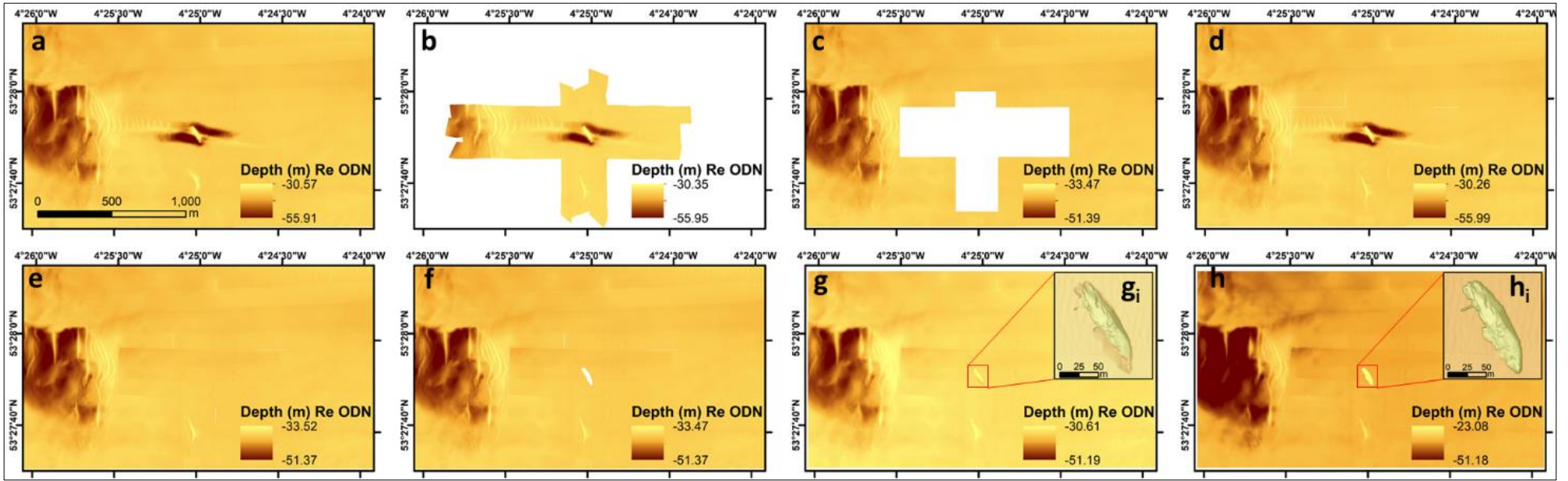


Figure 3.29: Process of generating a pre-wreck situation DEM to use for the simulation of the initial scour development in the coupled numerical TELEMAC3D – GAIA model. a) the 2017 DEM, b) the 2019 DEM, c) the 2017 DEM without the extent of the 2019 DEM, d) the 2017 DEM merged with the 2019 DEM, e) the 2017 DEM with the 2019 state of the sandwave at the south and interpolated flat-bed over the scour mark, f) the flat bed without the wreck as it was in the 2012 DEM, g) the flat 'pre-wreck' bed with the state of the wreck in the 2012 DEM (g<sub>i</sub>) and h) the flat 'pre-wreck' bed with the position of the wreck in the 2012 DEM elevated by 8m to sit on top of the surrounding bed (h<sub>i</sub>).

### 3.2.6.2 Reconstruction of the submerged object (wreck) in the model

Submerged objects appear to be difficult to implement in the model, as due to the steep slopes around them, instabilities are caused while modelling, making the model outcomes unreliable. For this study, the submerged wreck in the computation domain was defined using the immersed boundary method (IBM; Yin et al., 2016), by modifying the TELEMAC source codes. In the version of TELEMAC-3D used, triangular 2-D meshes are used to represent the computation domain. The vertical direction of the computation domain, however, undergoes a  $\sigma$ -mesh transformation that does not allow the flow around submerged objects or objects with steep slopes (or vertical walls) to be easily handled. The IBM applies direct forcing to some nodes of the mesh to impede the flow along the solid boundaries. The additional IB force, activated by the source terms in the Navier-Stokes (*N-S*) solved equations for the momentum, replaces the actual reaction force on the solid surface. The modified forcing step is then added in the pressure-continuity step of the *N-S* equations (last step of the momentum equations; Yin et al., 2016). Although the velocities on the immersed boundary (IB) nodes are set to zero, by applying the additional IB force, small velocity values can still be observed inside the object. Therefore, when dealing with submerged structures in the water, a zero-velocity condition is applied at each time step of the computation, at all the nodes inside the object (at all 3 cartesian dimensions – x, y and z).

### 3.2.6.3 Computational domain and mesh

The final product of the analysis in Section 3.2.6.1 (Figure 3.29) was used and a mesh with 10 m node size, changing to 2 m within the scour mark area and 0.5 m at the wreck was generated to achieve a good resolution without increasing the computation time enormously. Figure 3.30 shows the division of the computation domain into differently sized nodes. The mesh in the computation domain contains 117231 nodes in 2-D and 20 vertical layers (~2m for each layer), resulting to 2344620 nodes in total for the computation domain. The 20 vertical layers were chosen as increasing the number of layers increases the computation time linearly.



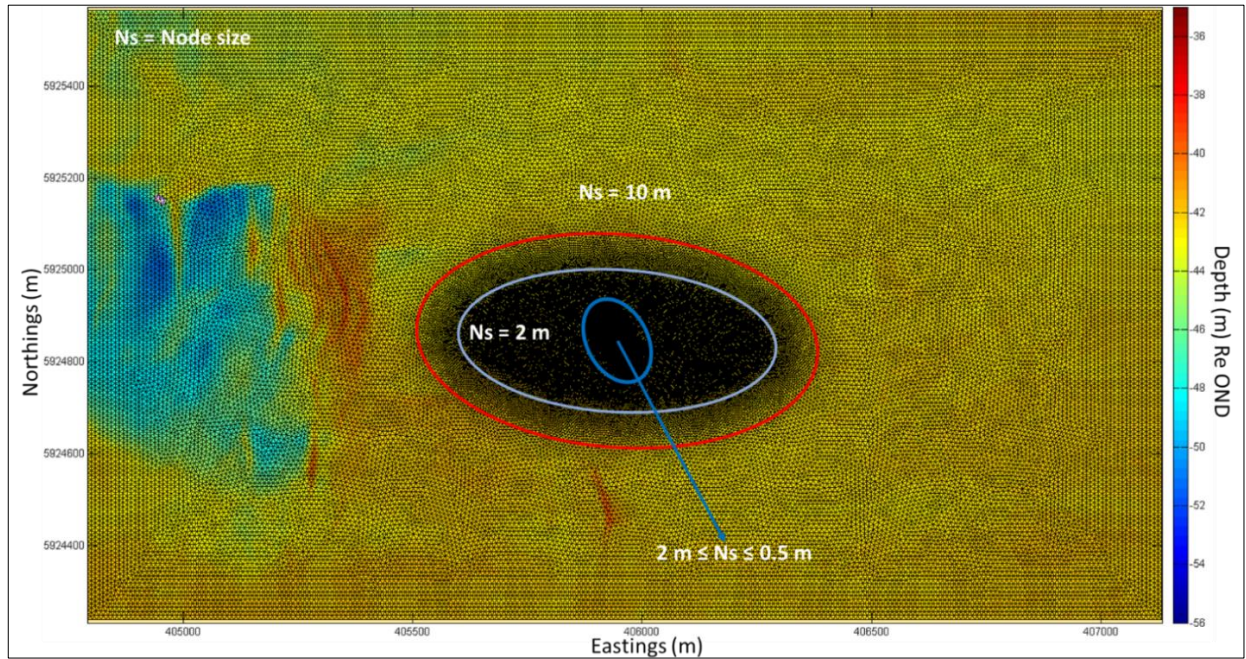


Figure 3.30: 2-D mesh used for the modelling work – schematic explanation of node sizes within the computation domain

For the application of the IBM, any nodes shallower than -42.5 m, at the area surrounding the wreck were treated as IB nodes. A representation of how the mesh looks like and an explanation of the IB nodes is shown in [Figure 3.31](#).

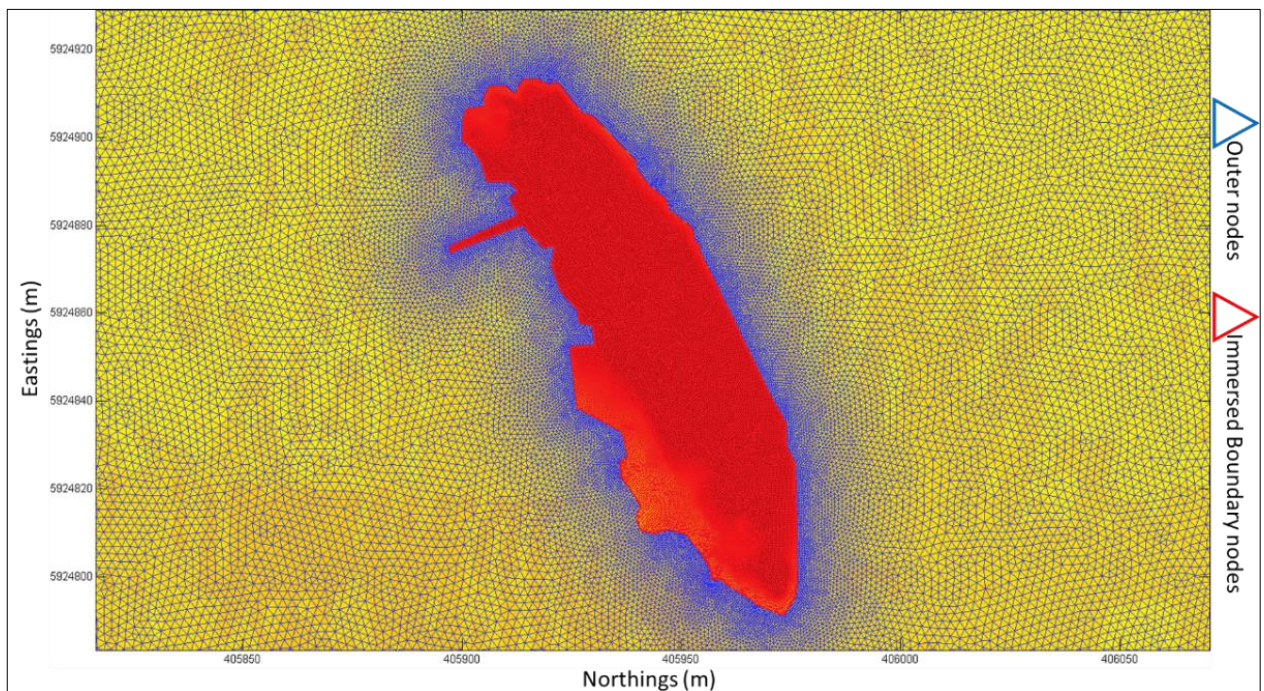


Figure 3.31: Explanation of IBM: nodes outlined by the blue triangles are the outer nodes, where the nodes outlined by the red triangles are the immersed boundary nodes.

### 3.2.6.4 Bedload transport formulation in GAIA

Bedload transport was calculated using the [Meyer-Peter and Müller \(1948\)](#) formula. The formula is based on the calculation of the bedload transport using directly the  $\theta_{cr,i}$  which has also been used for the hiding-exposure (HE) effect correction ([McCarron et al., 2019](#)) but also due to the fact that the

grain sizes used for this study ([0.6 & 15.4] mm) fall within the suggested sediment grain size when using the formulae ([0.4 – 29] mm). In the Meyer-Peter and Müller (1948) formula, the dimensionless current-induced sediment transport rate ( $\Phi_b$ ) is given by Equation 3.8:

$$\Phi_b = \begin{cases} 0 & \text{if } \theta < \theta_{cr}, \\ \alpha_{mpm}(\theta - \theta_{cr})^{\frac{3}{2}} & \text{otherwise} \end{cases} \quad (3.8)$$

where  $\alpha_{mpm}$  is a coefficient (default value in TELEMAC = 8). The volumetric bedload transport rate,  $q_{b,i}$  ( $\text{m}^3 \text{s}^{-1}$ ), is related to  $\Phi_b$  by Equation 3.9:

$$\Phi_b = \frac{q_{b,i}}{\sqrt{g(s-1)d_i^3}}, \quad (3.9)$$

The hiding-exposure effect correction (McCarron et al., 2019) was implemented in GAIA by modifying a version of the Egiazaroff (1965) subroutine (Appendix F) to amend the  $\theta_{cr,i}$  to utilise the HE corrections of Egiazaroff (1965) and Ashida and Michiue (1972). The McCarron et al. (2019) correction is implemented in the model using extracted gravel fraction ( $f_g$ ) from each node at the end of every model time step from the mass fraction of the  $i^{\text{th}}$  sediment classes in  $j^{\text{th}}$  layer ( $p$ ) and then use  $p$  to calculate the exponent  $\gamma$  in the McCarron et al. (2019) H-E equation. For each grid node, according to the  $d_i$ , the HE correction for the  $i^{\text{th}}$  fraction ( $\xi_i$ ) is calculated using  $\gamma$  and  $d_{50}$  and it is used to modify the critical Shield's parameter at each node ( $\theta_{cr,i}$ ; McCarron, 2020).

The turbulent kinetic energy (TKE) was used in the calculation of the bed shear stress around the submerged object (wreck). The modification applied in the TELEMAC source code to include the amended calculation of the bed shear stress by amending the Gaia\_prepare\_step.f subroutine (Yiannoukos et. al., 2020). The modification was an amended version of Benson et. al. (2014) taking the maximum of the friction velocity ( $u_*$ ) or the value of the TKE ( $k$ ) at the first  $\sigma$ -layer above the bed (plane 2) and including it in the calculation of the bed shear stress,  $\tau_0$ , in the form of Equation 3.10.

$$\tau_0 = \max(\rho u_*^2, \rho r k), \quad (3.10)$$

where  $r$  is a proportionality coefficient.

The sixty-three grab samples collected around the SS Apapa site were used to inform the coupled model about the bed composition of the surrounding area. The model was set to run for 22% sand sized 0.6 mm and 78% gravel sized 15.4 mm. The model was set to allow erosion and deposition to happen within the first 20 m of the sedimentary bed.

### 3.2.6.5 Hydrodynamic information used as input for the coupled model

The tidal currents at the SS Apapa site, have an E-W (and W-E) direction, therefore, for the model set-up, the two boundaries were treated as discharge and prescribed elevation. The discharge used as input for the simulation of the hydrodynamic forces at the area, was taken by running a larger scale hydrodynamics model and converting the depth-averaged velocity to discharge. A liquid file



with discharge and prescribed elevation information for every 15 minutes for a full month, starting on the 10<sup>th</sup> of July 2019 was created and was used for the modelling. The liquid file was set to ramp up the discharge within the first 3 hours of the computation, from 0 to the realistic value of the discharge while allowing for scour to happen during this transition period. The ramping of the discharge value was performed to reduce shocks and instabilities due to a large volume of fluid (water) entering the computation domain at a really short time (15 minutes), following a similar method from [Yiannoukos et al. \(2020\)](#). The ADCP survey explained in [Section 3.2.1](#) was used for the validation of the modelled velocities, both for the depth-averaged velocities and the velocities at each plane of the computation domain.

### 3.3 Results

In this section, the analysis of the hydrodynamics around SS *Apapa* is presented, followed by an analysis of the scour mark geometry (lateral and depth differences) evolution over the years and the bed composition change over the years. The modelled evolution of the aforementioned parameters is also presented.

#### 3.3.1 Observed flow velocities and flow amplification in the wake of the wreck

The ADCP transects were designed as explained in Section 3.2.1 to observe the impact of an irregular shaped object (wreck) to the hydrodynamics of the area (Aim 1). However, while collecting data offshore variations of 50-60 m on each side from the original survey plan were observed due to navigation difficulties. The survey transects followed by the vessel and the original survey plan can be found in Figure 3.32.

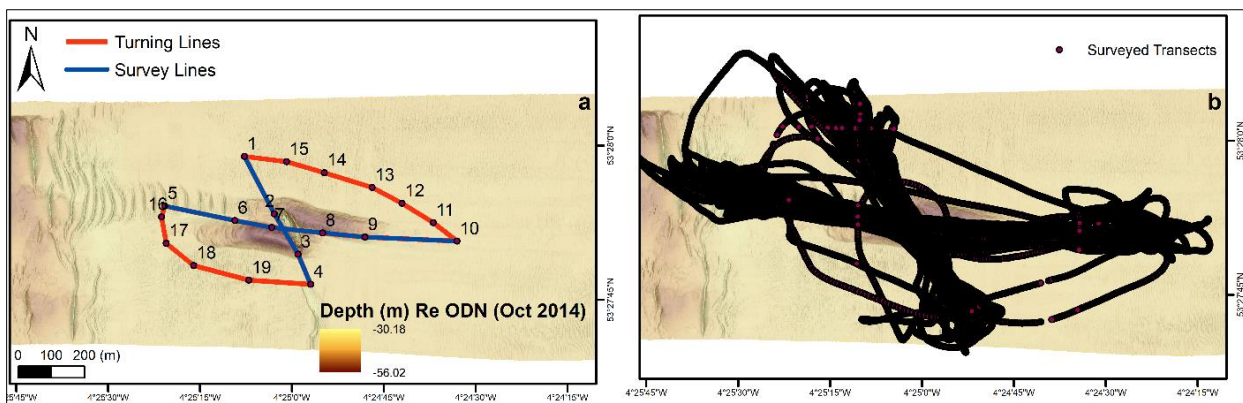


Figure 3.32: Planned survey transects suggested from desk study (a) and final surveyed transects from RV *Prince Madog* (b).

Figure 3.33 shows the bottom tracked and tidally corrected ADCP data over the two full tidal cycles (25 hours) of the survey over the SS *Apapa* site. The transects where the vessel navigated over the wreck and scour mark are obvious as there is a pick (shallower) or drop (deeper) respectively at the bathymetric extent of the ADCP velocity measurements.

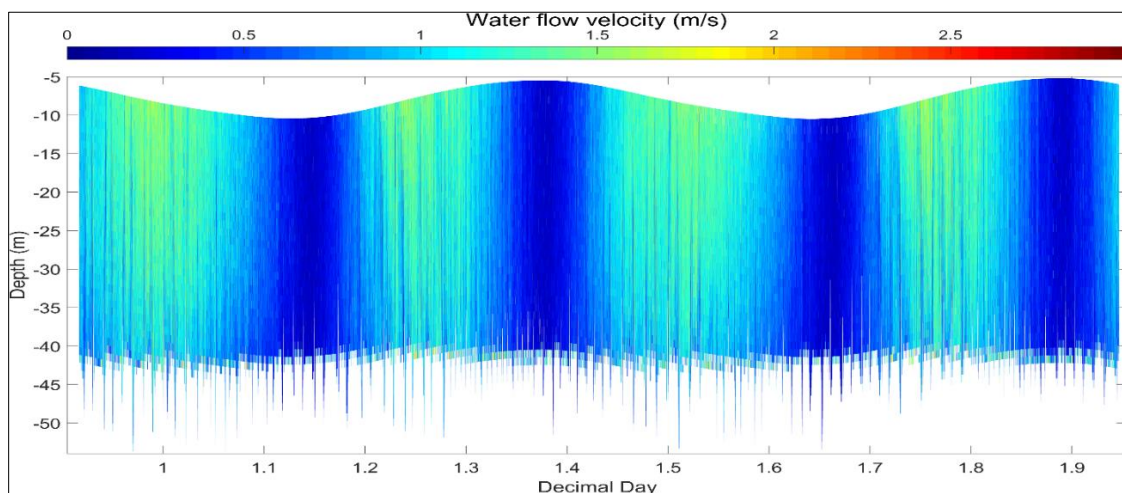


Figure 3.33: Tidal and bottom tracked corrected flow velocity measurements from the ADCP instrument over the two full tidal cycles (25 hours) of surveying over the SS *Apapa* site.

The maximum flow velocity measured from the ADCP instrument was  $\sim 3 \text{ ms}^{-1}$ , where the maximum depth averaged velocity ( $\bar{U}$ ) observed was  $1.94 \text{ ms}^{-1}$ . Both the depth averaged flow velocity ( $\bar{U}$ ), and the maximum observed flow velocity across the beams show variations of the current velocity within the scour mark and over the wreck (Figure 3.34; red point cloud for  $\bar{U}$  and Figure 3.34; black point cloud for the maximum current speed respectively).

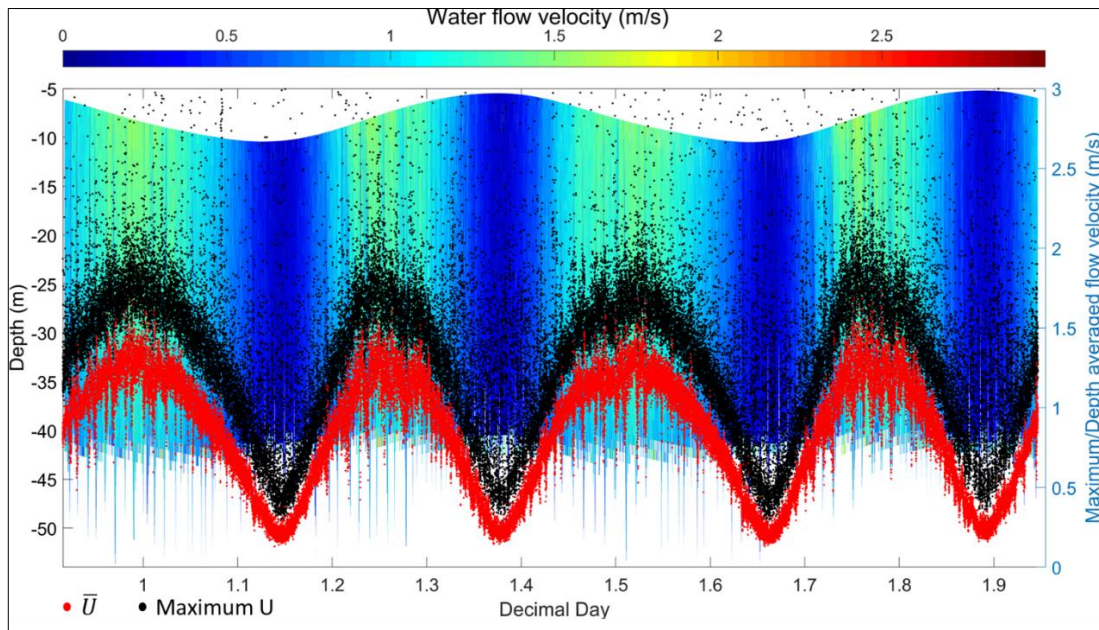


Figure 3.34: Flow velocity measurements and a) the depth averaged ( $\bar{U}$ ) flow velocity and b) maximum current velocity measurements over the SS *Apapa* site plotted over two full tidal cycles.

The boxplots shown in Figure 3.35 present the ADCP dataset values. The mean depth averaged ( $\bar{U}$ ) flow velocity observed at the area is  $0.84 \text{ ms}^{-1}$  where the average value of the maximum current speeds observed from the ADCP instrument is  $1.34 \text{ ms}^{-1}$ .

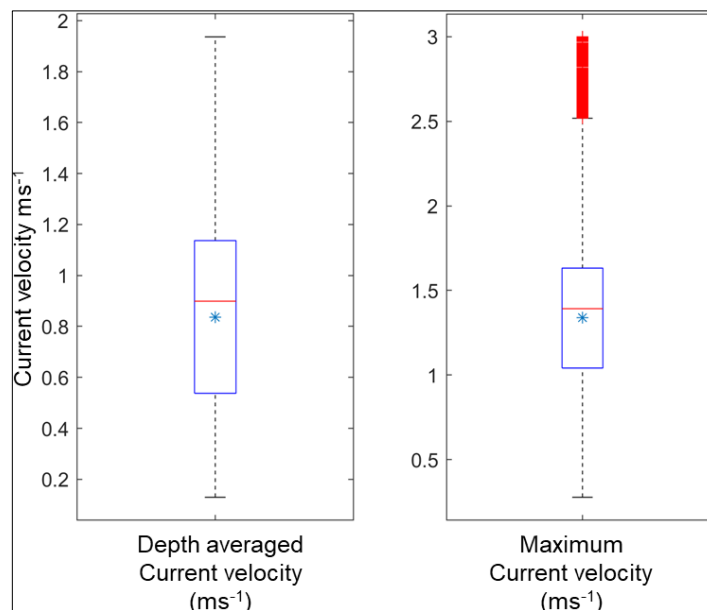


Figure 3.35: Depth averaged current velocity (left) and maximum current velocity values measured from the ADCP instrument. The \* sign represents the mean value of the measurements. The solid red lines show the median standard deviation value of each population, and the boxes indicate the 25<sup>th</sup> and 75<sup>th</sup> percentiles.

The whiskers indicate the minimum and maximum values.

The maximum current velocity during the E-W transects is observed at the wake of the wreck and at the deepest points of the scour mark, but also at the area directly over the wreck with variation present as shallow as -6 m depth where the wreck sits at -35 m depth below the sea surface at the time (Figure 3.36).

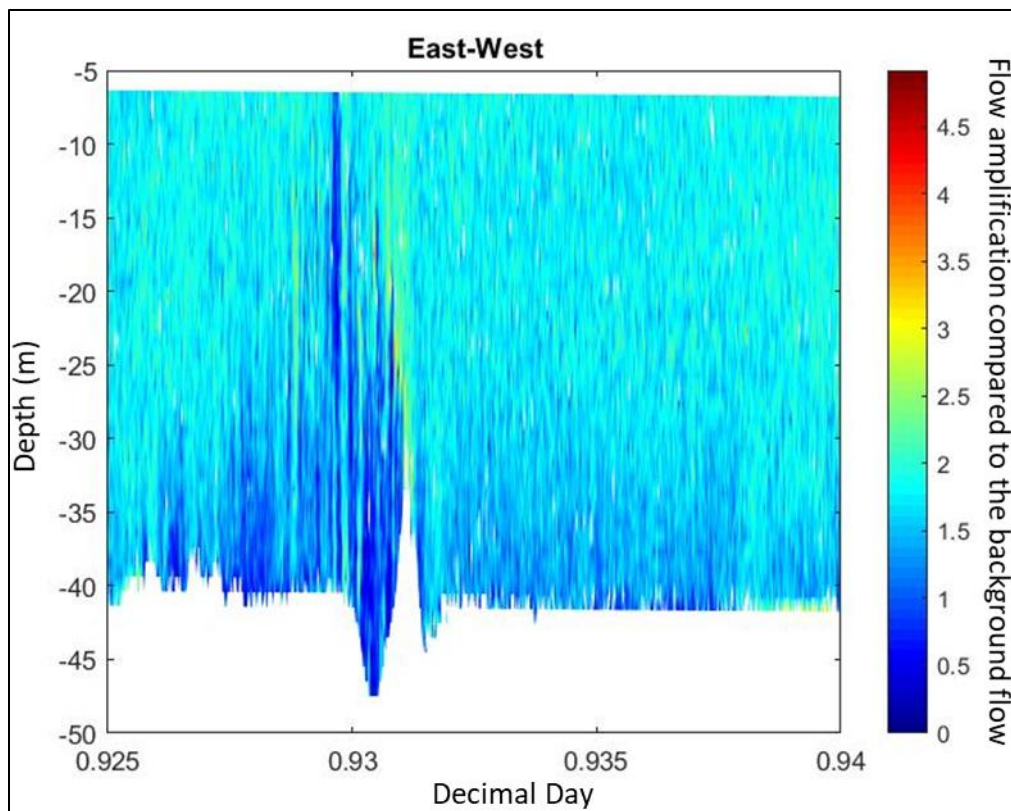


Figure 3.36: Flow velocity amplification (when compared to the background flow) for one of the transects over the wreck and the scour marks, showing the influence of the wreck both laterally and in depth.

On the other hand, when the S-N transects were followed (during slack tides) the maximum influence from the wreck is observed directly at the edges of the wreck, where there is also current deviation caused by the irregular shape of the wreck and the steep angles of the stern (NW) and bow (SE). The stern and bow of the wreck are the areas where the flow amplification is at its maximum during slack water and was not recorded during ebbing or flooding, as the vessel could not navigate easily across the tidal current. Figure 3.37a shows an example of one of the transects recorded at N-S direction with an amplification at the stern and bow of the wreck of ~2.3 times when comparing the maximum current speeds observed with the average of the maximum current speeds observed at the background flow (away from the wreck and the scour mark). Figure 3.37b is a zoomed-in version of Figure 3.37b for a better visualisation of the flow amplification and diversion around the wreck.



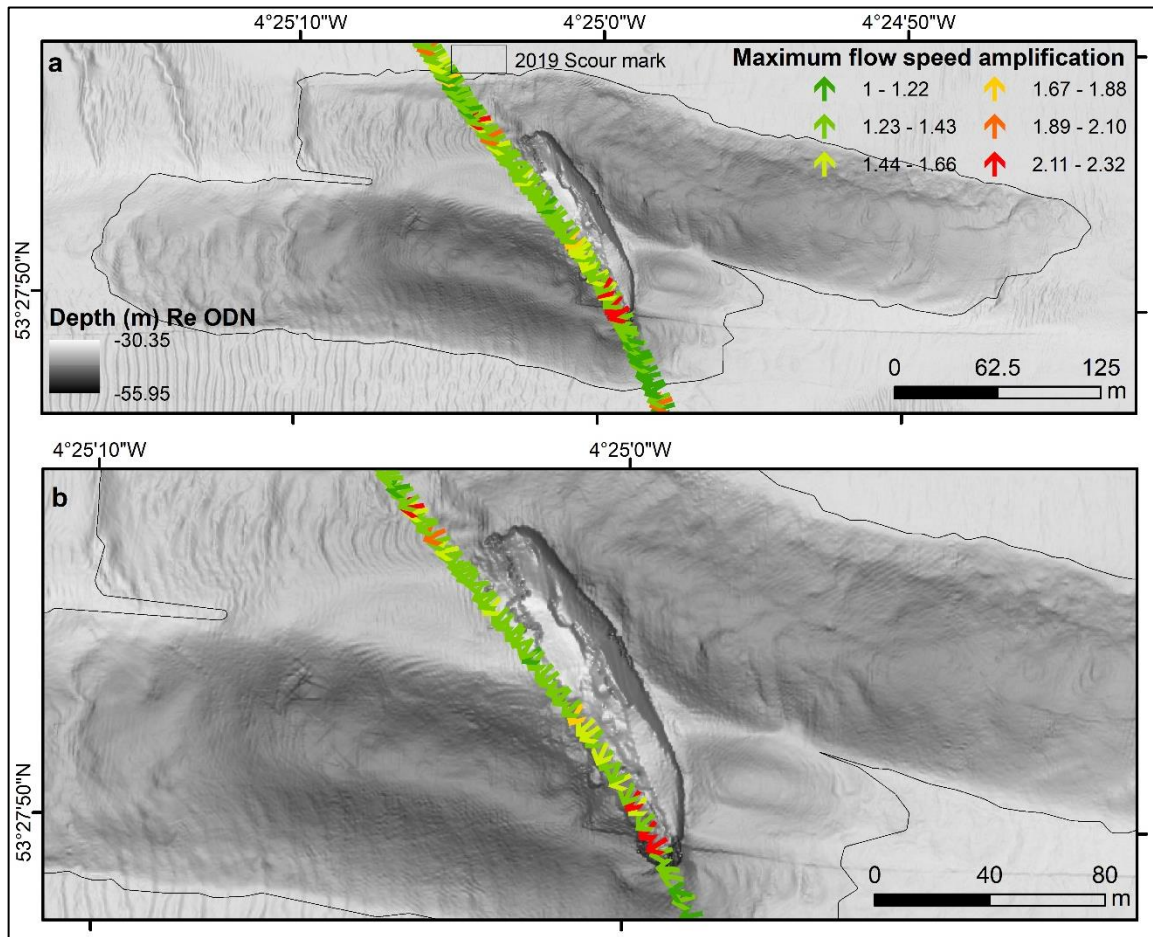


Figure 3.37: Current amplification (when compared with the background flow) at the stern and bow of the wreck recorded from the ADCP instrument during a N-S transect, b) zoomed-in version of the same transect for better visualisation of the flow amplification and direction around SS *Apapa*.

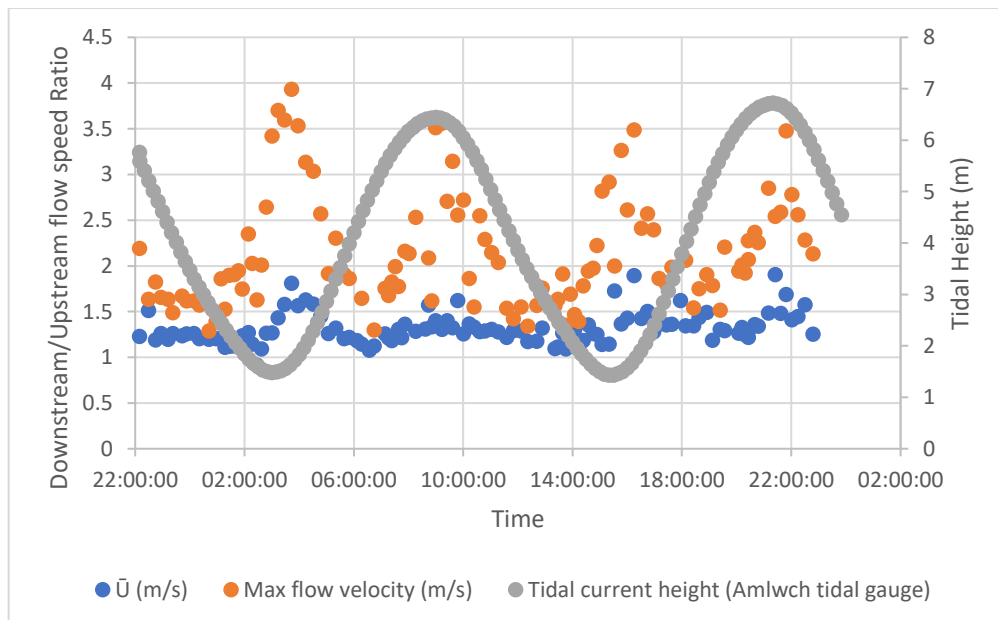


Figure 3.38: Downstream (influenced) and upstream (background) flow velocity comparison as a ratio and correlation with the state of the tide from the nearby Amlwch tidal gauge.

Figure 3.38 shows the comparison of the downstream of the wreck (influenced) and upstream, background (likely undisturbed) flow for both the mean depth averaged but also the mean maximum

observed current speeds. The largest amplification to the flow due to the existence of the object appears during slack tides, where the survey vessel navigated over the areas affected by the stern and bow of the vessel. The maximum flow disturbance distance recorded using the E-W transects (plotted in [Figure 3.39](#)) shows variations between 102 to 311 m away from the wreck (of length of 135 m) during ebbing and flooding with an increase to the disturbance distance at higher current speeds.

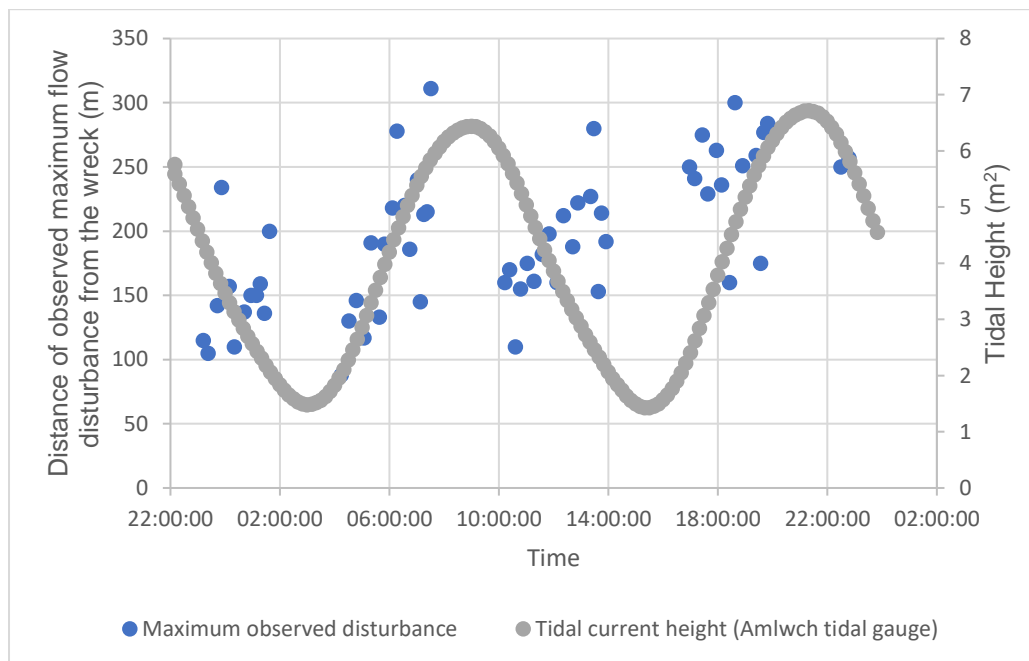


Figure 3.39: Observed maximum flow disturbance distances from the wreck plotted against tidal heights from Amlwch tide gauge.

The ADCP dataset was not aiming to the recording of turbulence in the water column, but the depth averaged current direction, shows a diversion of up to 90° from the direction of the upcoming background flow ([Figure 3.40](#)) over the wreck itself, but also within the scour mark.

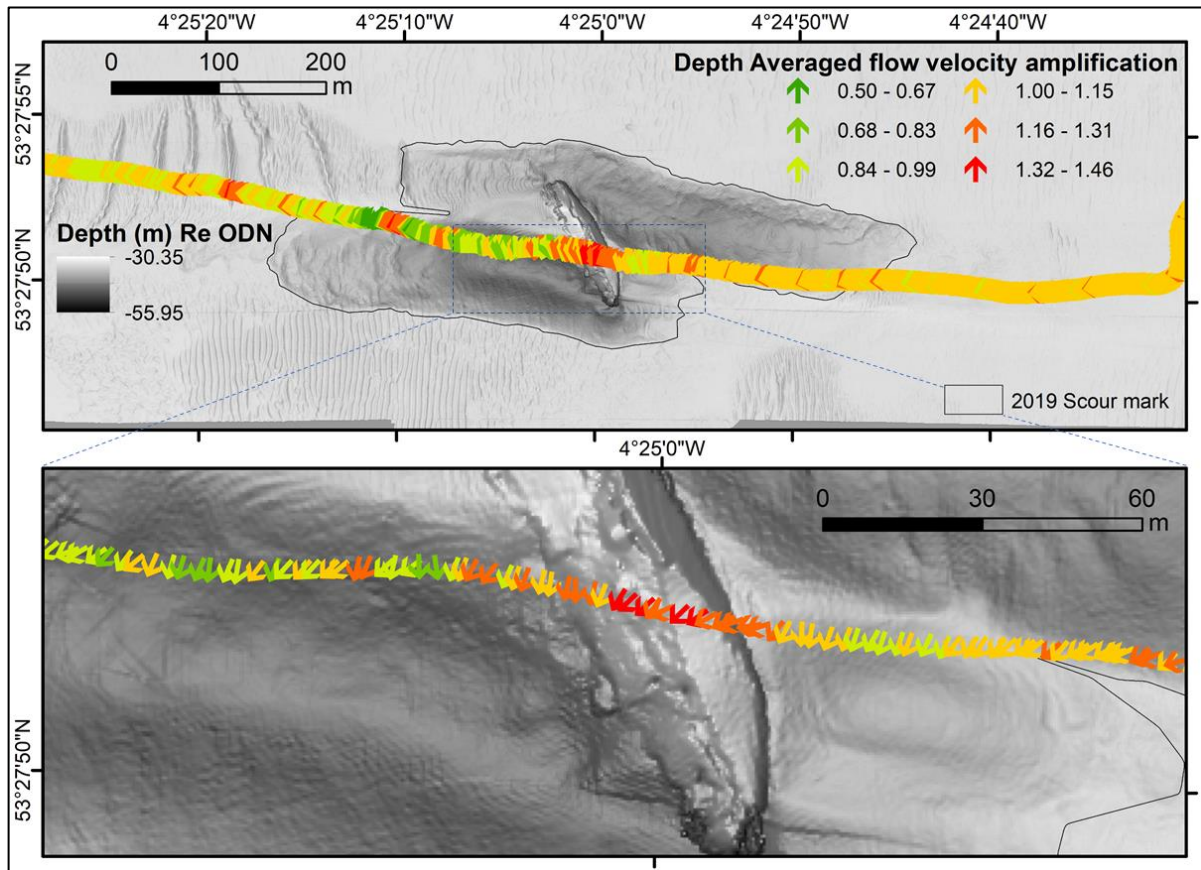


Figure 3.40: Depth averaged flow velocity amplification and direction as measured from the ADCP instrument and a zoomed in version of the marked area (bottom) to visualise better the flow deviation around the wreck.

### 3.3.2 Observed evolution of scour mark geometry

In this section the analyses of the scour mark geometry are sub-divided to the analysis of the lateral changes within the scour mark (as explained in the methods section) and the analysis of changes in bathymetry (erosion and deposition) over time, due to the bed dynamics within the scour mark. Analyses of repeat MBES bathymetry and MBES backscatter strength surveys over *SS Apapa* was conducted to identify the lateral changes of the scour mark, to observe the bed evolution changes within the scour mark by monitoring the erosion and deposition rates over the years, and to provide understanding of the sediment mobilisation of a mixed coarse bed (Aim 2). For the analyses, datasets spanning over 8 years, with time intervals ranging from 5 days to 2.5 years (948 days) were used.

The scour edge tracked for each DEM following the same method is presented in [Figure 3.42](#).

The results of the analyses show that the scour edge has an average annualised fluctuation in the order of 1-2 m from 2012 to 2019. The only observed consistent differences in the scour mark are found at the NW part where the confidence in scour edge delineation is affected by the mobile sediment waves. The extent of the May 2012 DEM did not cover the entire scour mark explaining the oddly shaped scour edge at the SW part of the scour mark.



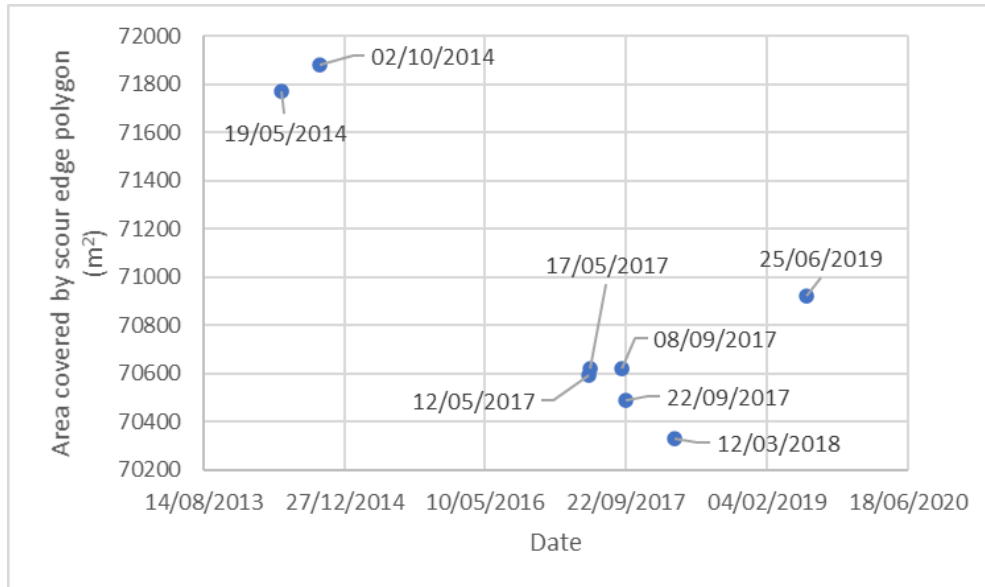


Figure 3.41: Surface coverage from the polygons delineating the scour edge for each survey.

While investigating the lateral changes of the evolution of the scour mark, the surface area covered by the polygons defining the edges of the scour mark was also calculated (Figure 3.41). The mean area covered by the polygons (2012 survey not included in the calculation) is 70902.59 m<sup>2</sup> where the standard deviation between the different surveys is 554.96 m<sup>2</sup> (8%). This variation shows the significance of 1-2 m fluctuation in the scour mark's lateral extent. The scoured area is largest in May and October 2014 with a mean coverage area of 71825.14 m<sup>2</sup>. The measured distance from the wreck to the scour edge's furthest edge (using the annotated profiles at Figure 3.42) was calculated to be 159, 335, 327 and 61 m for the NW, NE, SW (not including the May 2012 DEM) and SE sides of the scour mark respectively. Table 3.3 shows in detail the exact area covered by the scour outline for each survey (m<sup>2</sup>), the distances measured using the annotated profiles and the wreck (length) to distance from the edge (length of each profile) ratio as a comparison. In Table 3.3, the length to width (L:W) ratio of the scour marks at the 'North' and 'South' sides of the scour mark is also presented. The mean value of the 'north' side L:W ratio is 5.43 where the mean for the 'south' side L:W ratio is 4.26. Their accompanied standard deviations are 0.11 and 0.12 for the 'north' and the 'south' sides of the scour mark respectively. For the calculation of the 'south' side of the L:W ratio, the 2012 survey was not included as the dataset was not covering the full extent of the scour mark.

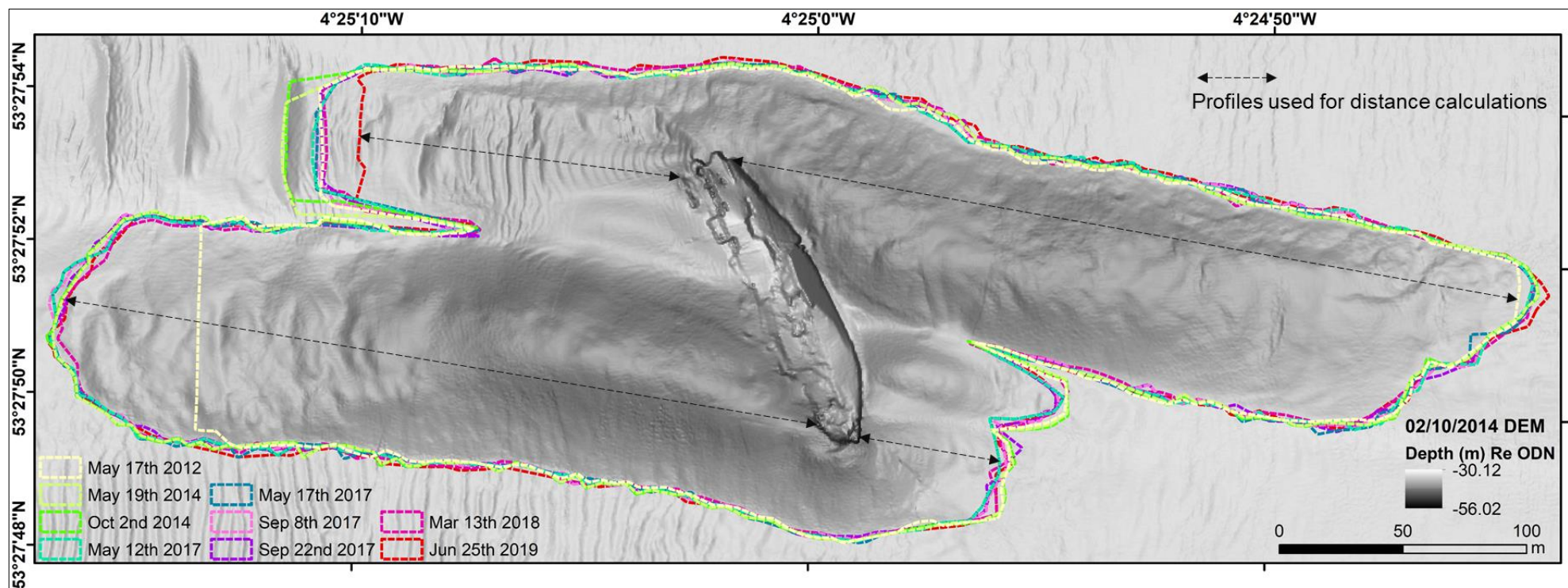


Figure 3.42: Time lapse of the scour edge tracked using 2-D profiles for all the DEMs from the MBES surveys over SS *Apapa* and profiles used for distance calculations from the edge of the wreck (dashed black lines).

Table 3.3: Distance between the farthest edge of the wreck and the farthest edge of the scour mark for all surveys and all four sides of the scour mark (The values in grey for the May 2012 survey were not used for the calculation of  $\sigma$  and  $\bar{x}$ ).

Survey date	Area (m²)	Distance from wreck to longest edge of scour mark (m)				Length of Wreck to Length of scour mark ratio (m)				L:W ratio	L:W ratio
		NW	NE	SW	SE	NW	NE	SW	SE	'North'	'South'
17/05/2012	66198.04	148.63	330.09	263.16	62.04	1.10	2.45	1.95	0.46	5.33	3.80
19/05/2014	71769.76	165.95	338.40	323.78	62.66	1.23	2.51	2.40	0.46	5.47	4.55
02/10/2014	71880.52	166.96	336.15	323.10	62.34	1.24	2.49	2.39	0.46	5.73	4.22
12/05/2017	70591.99	160.41	335.25	324.11	60.08	1.19	2.48	2.40	0.45	5.41	4.18
17/05/2017	70618.84	160.56	335.75	324.61	60.13	1.19	2.49	2.40	0.45	5.34	4.28
08/09/2017	70620.35	162.00	335.89	329.13	60.18	1.20	2.49	2.44	0.45	5.45	4.25
22/09/2017	70489.06	162.44	335.95	329.51	60.35	1.20	2.49	2.44	0.45	5.41	4.29
12/03/2018	70330.23	162.93	335.62	328.90	60.09	1.21	2.49	2.44	0.45	5.40	4.21
25/06/2019	70919.95	143.55	336.22	332.37	60.88	1.06	2.49	2.46	0.45	5.37	4.11
St. Dev. (σ)	554.96	7.44	2.08	3.22	1.01	0.06	0.02	0.02	0.01	0.11	0.12
Mean	70902.59	159.27	335.48	326.94	60.97	1.18	2.49	2.42	0.45	5.43	4.26

Figure 3.43 summarizes the observations from Table 3.3 into a plot for better visualisation of the outcomes.

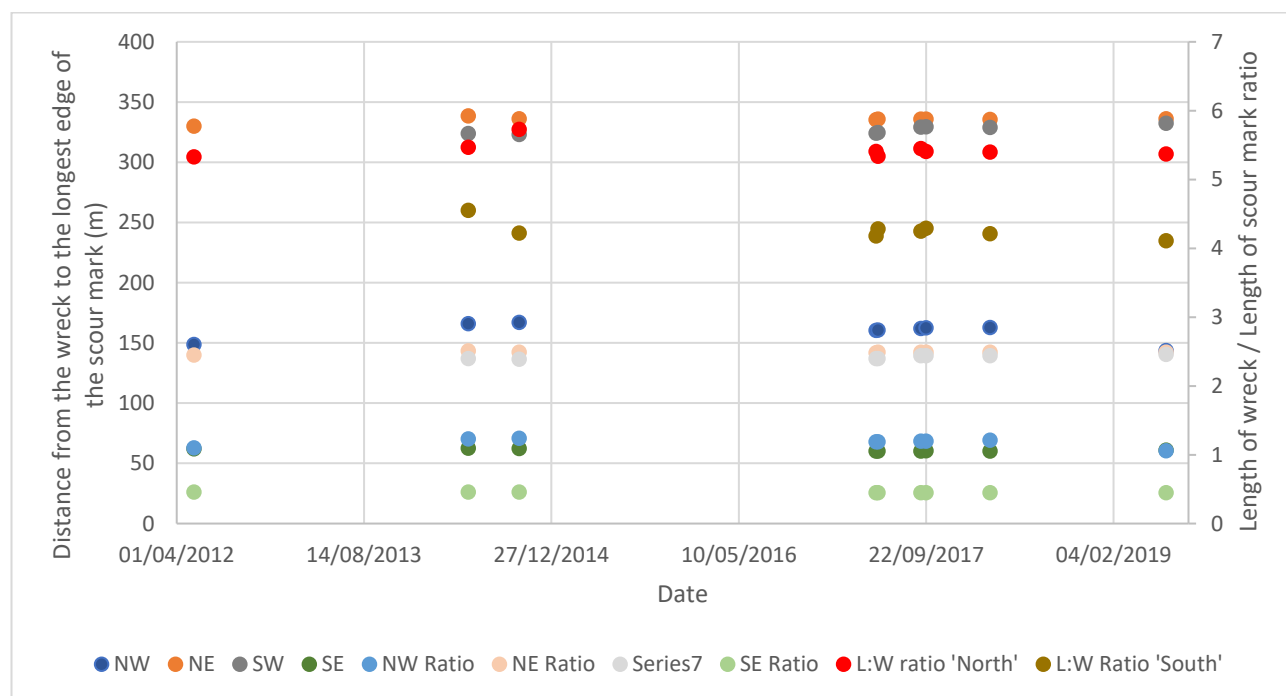


Figure 3.43: Distance between the wreck and the longest distance to the scour mark's edge and the ratio of the length of the wreck/length of longest distance to the edge ratio for the multiple datasets.



### 3.3.2.1 Observed bathymetric changes within the scour mark

The evolution of the lateral scour edge was described in Section 3.3.2. However, changes in bathymetry within the scour mark, but also changes of the depth and orientation/position of the wreck itself were also investigated, using 12 datasets (as explained in Table 3.2). The calculated standard deviation of depth values extracted for each point from the point cloud of the 12 datasets is presented in Figure 3.44a and the annualised depth difference standard deviation in Figure 3.44b.

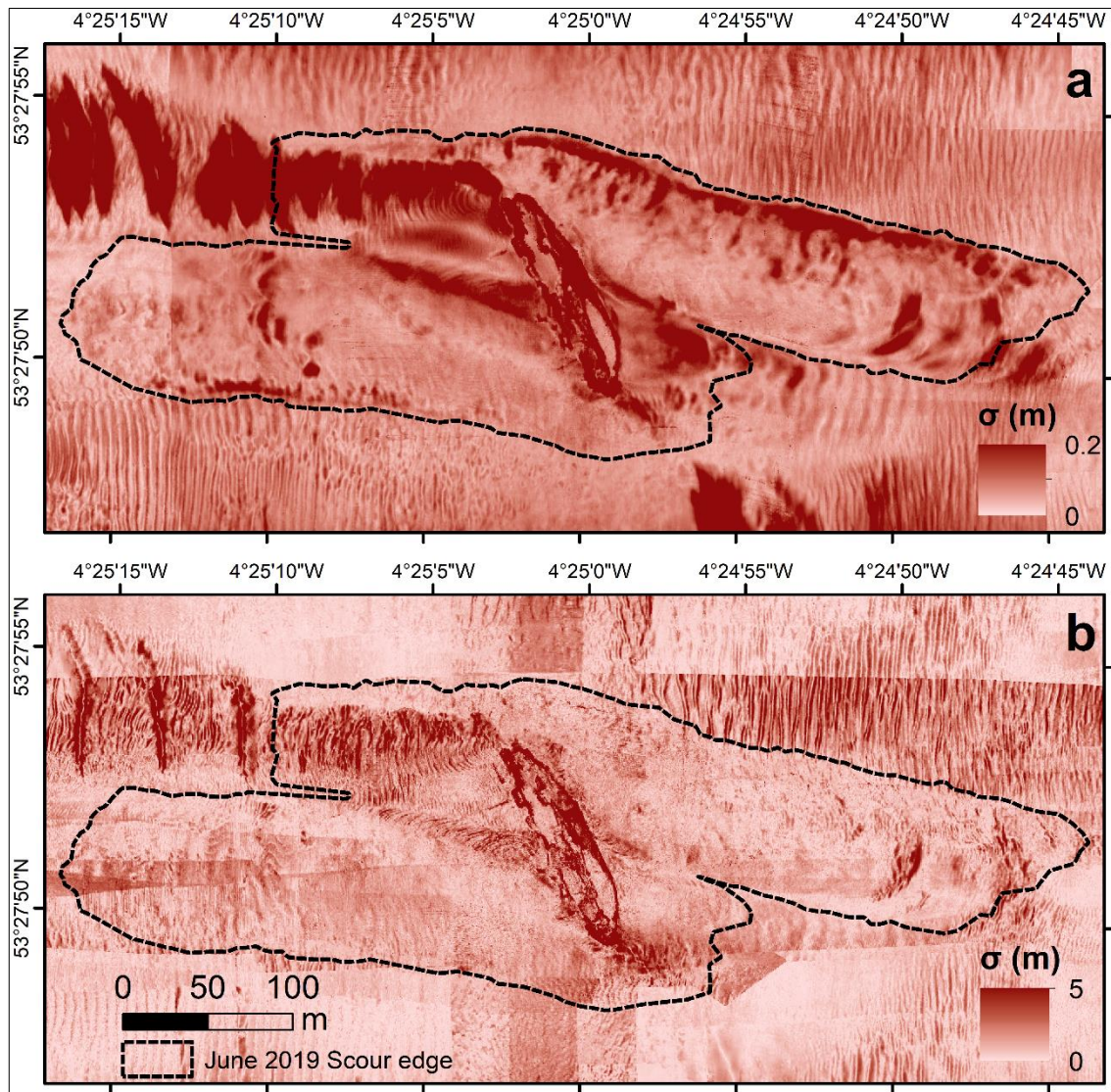


Figure 3.44: Standard deviation map generated from the pixel-by-pixel calculation of  $\sigma$  from the MBES data (a) and standard deviation map generated from the pixel-to-pixel calculation of the annualised depth difference between the consecutive surveys (b) using a linear classification.

The non-normalised data show a mean standard deviation of bathymetry value of 0.13 m and the median value of 0.08 m. In contrast, the normalised data (from the annualised depth difference DEMs) show a mean standard deviation value of 0.93 m and a median value of 0.62 m (Figure 3.45).

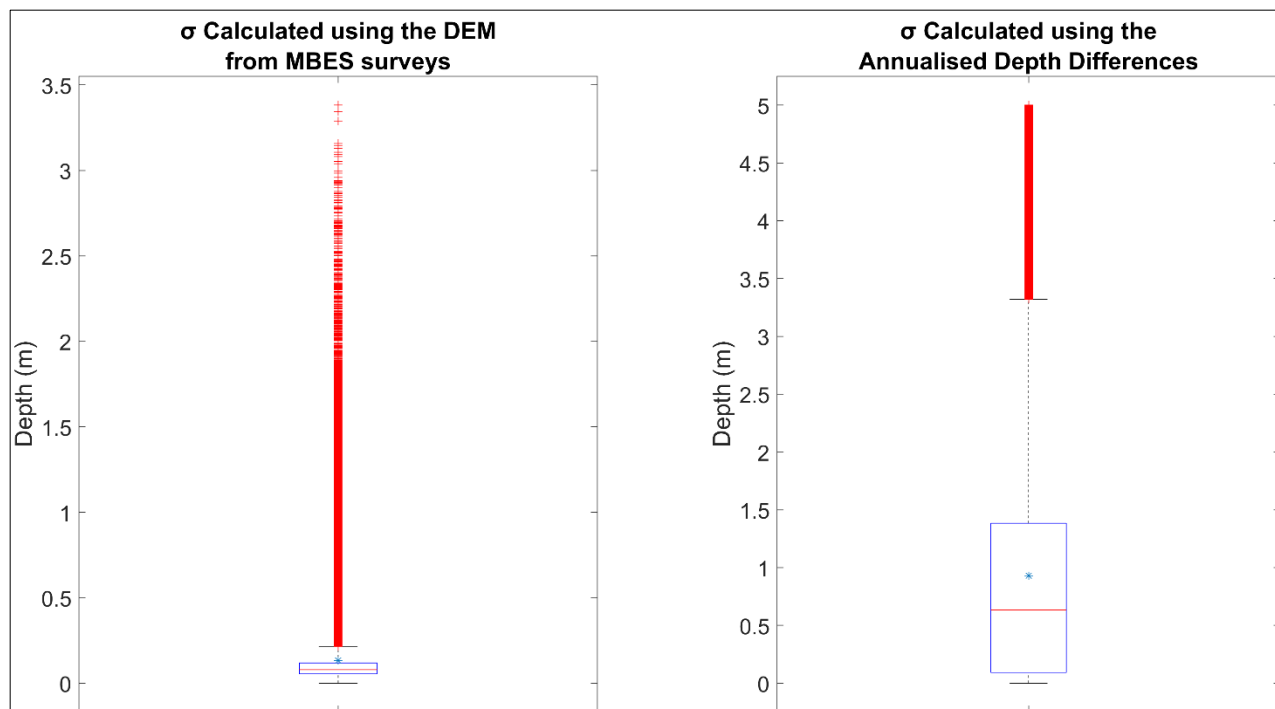


Figure 3.45: Standard deviation ( $\sigma$ ) of depth (m) calculated using the DEM from the MBES surveys (left) and the standard deviation of depth (m) calculated using the annualised depth differences (right). The \* sign represents the mean value of the measurements. The solid red lines show the median standard deviation value of each population, and the boxes indicate the 25<sup>th</sup> and 75<sup>th</sup> percentiles. The whiskers indicate the minimum and maximum values.

Figure 3.46a shows the mean non-annualised depth difference between consecutive datasets (using difference modelling), where Figure 3.46b shows the mean annualised depth difference between consecutive datasets. The mean non-annualised depth difference shows that the larger variations (erosion) are observed at the depositional feature on both sides of the wreck, where there is also an obvious erosional trend at the north and south sides of the scour mark. The largest variations are observed at the wreck itself and the bedforms at the NW. The wreck seems to be unstable, with the observed depth increasing at the east side and decreasing at the west. In contrast with the general erosional trend within the scour mark, deposition of sediment is observed at the NW part of the scour mark, directly attached with the stern of *SS Apapa*. On the other hand, the map produced from the annualised depth difference variations, (Figure 3.46b) shows different patterns than Figure 3.46a as it shows a larger variation of the site (one order of magnitude). Although still showing large variations at the bedforms observed at the NW, the DEM shows an altered trend of events on the wreck itself, while it also shows deposition at areas where the map produced from the non-annualised difference maps shows erosion. This data shown in this figure are important to understand that localised events, from time to time, and surveys conducted with days difference, cannot be representative of the whole site dynamics.



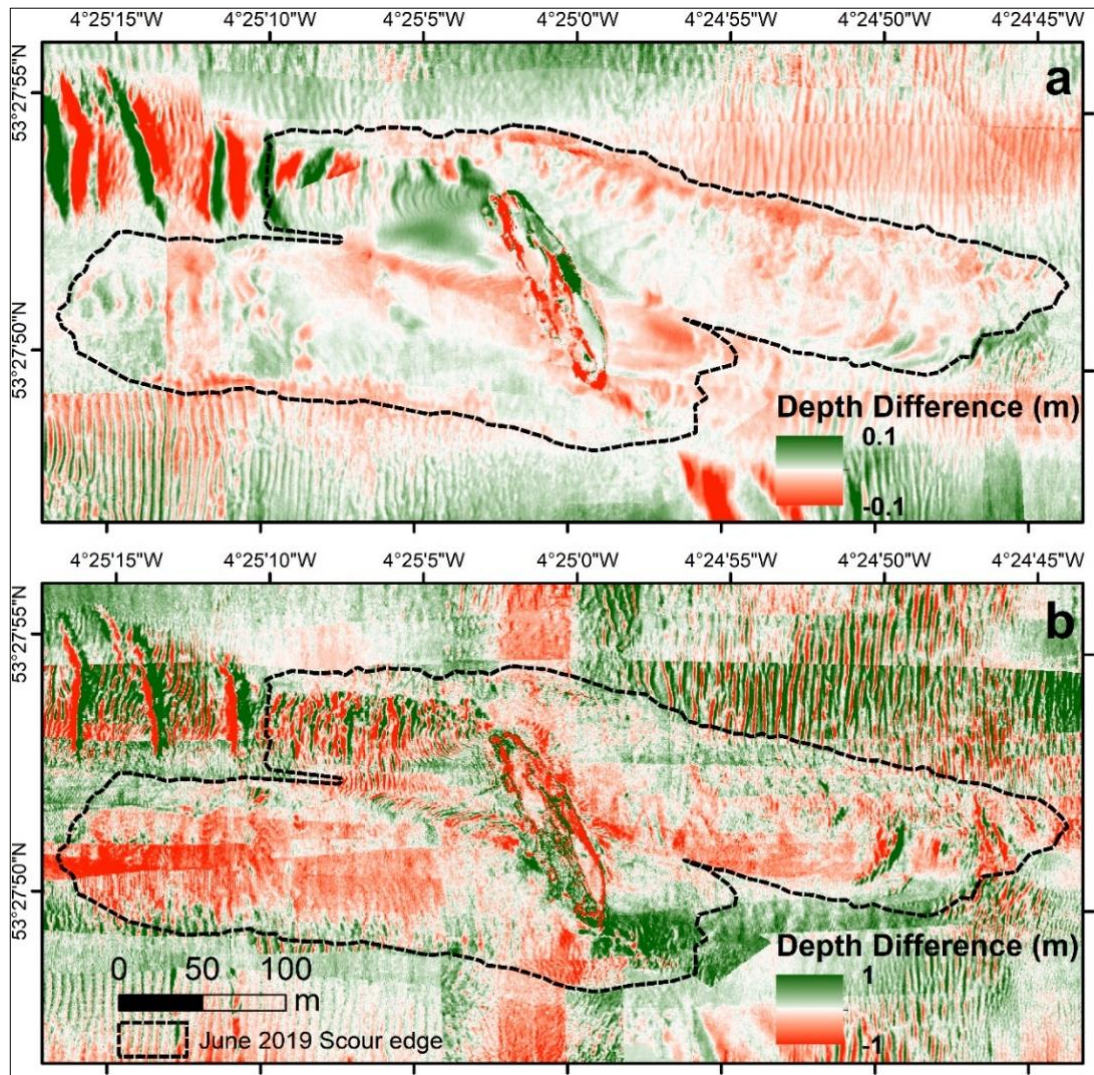


Figure 3.46: Average non-annualised depth difference (a) and average annualised depth difference (b) between consecutive datasets. The pronounced striping in the difference model is a survey/ de-iding artefact.

The boxplots generated from the point cloud used to generate the DEMs in Figure 3.46 are presented in Figure 3.47. A mean non-annualized depth difference value of 0.004 m and a median value of 0.003 m are calculated from the data. Also, a mean annualised depth difference of 0.06 m, with a median value of 0.05 m are observed. Although the mean and median values do not show much variation, it is important to understand that these values are also impacted by bathymetric differences in the surrounding of the wreck area, where no significant changes in bathymetry were observed over time.



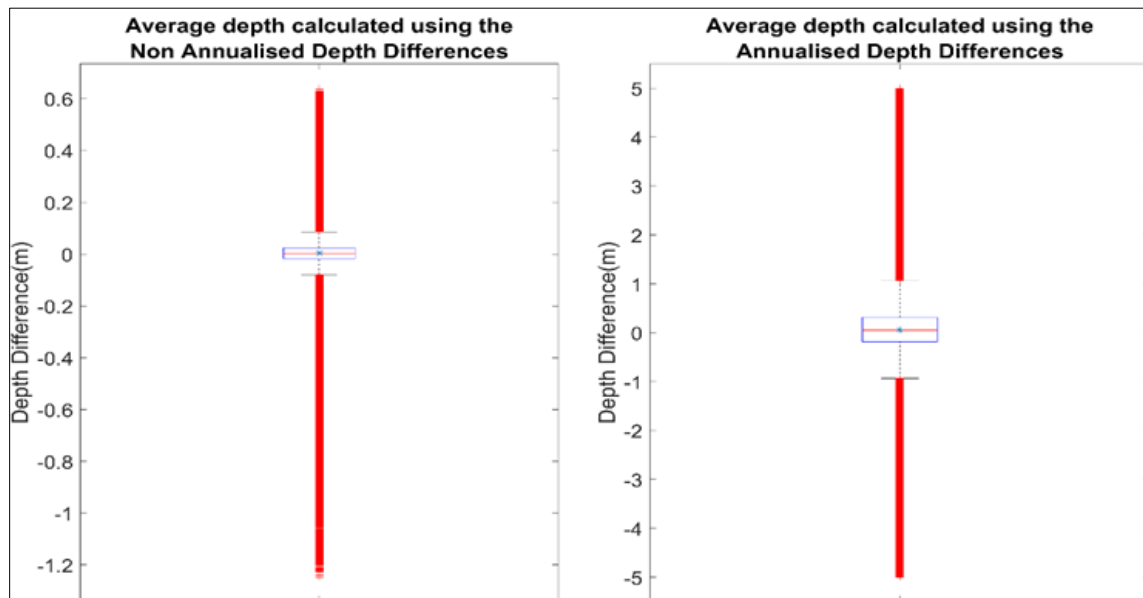


Figure 3.47: Average depth difference calculated from the non-annualised depth difference maps (left) and average depth difference values calculated from the annualised depth difference maps (right). The \* sign represents the mean value of the measurements. The solid red lines show the median standard deviation value of each population, and the boxes indicate the 25<sup>th</sup> and 75<sup>th</sup> percentiles. The whiskers indicate the minimum and maximum values.

The full range of depths per pixel, or the difference (Figure 3.48c) between the minimum (shallowest – Figure 3.48a) and maximum (deepest – Figure 3.48b) depth values range between 0 and 8.79 m, with an average of 0.33 m. The extreme values causing the range to extent to 8.79 m are mostly observed at the wreck itself and at the nearby large sediment waves, with variations also observed at the depositional features within the scour mark.

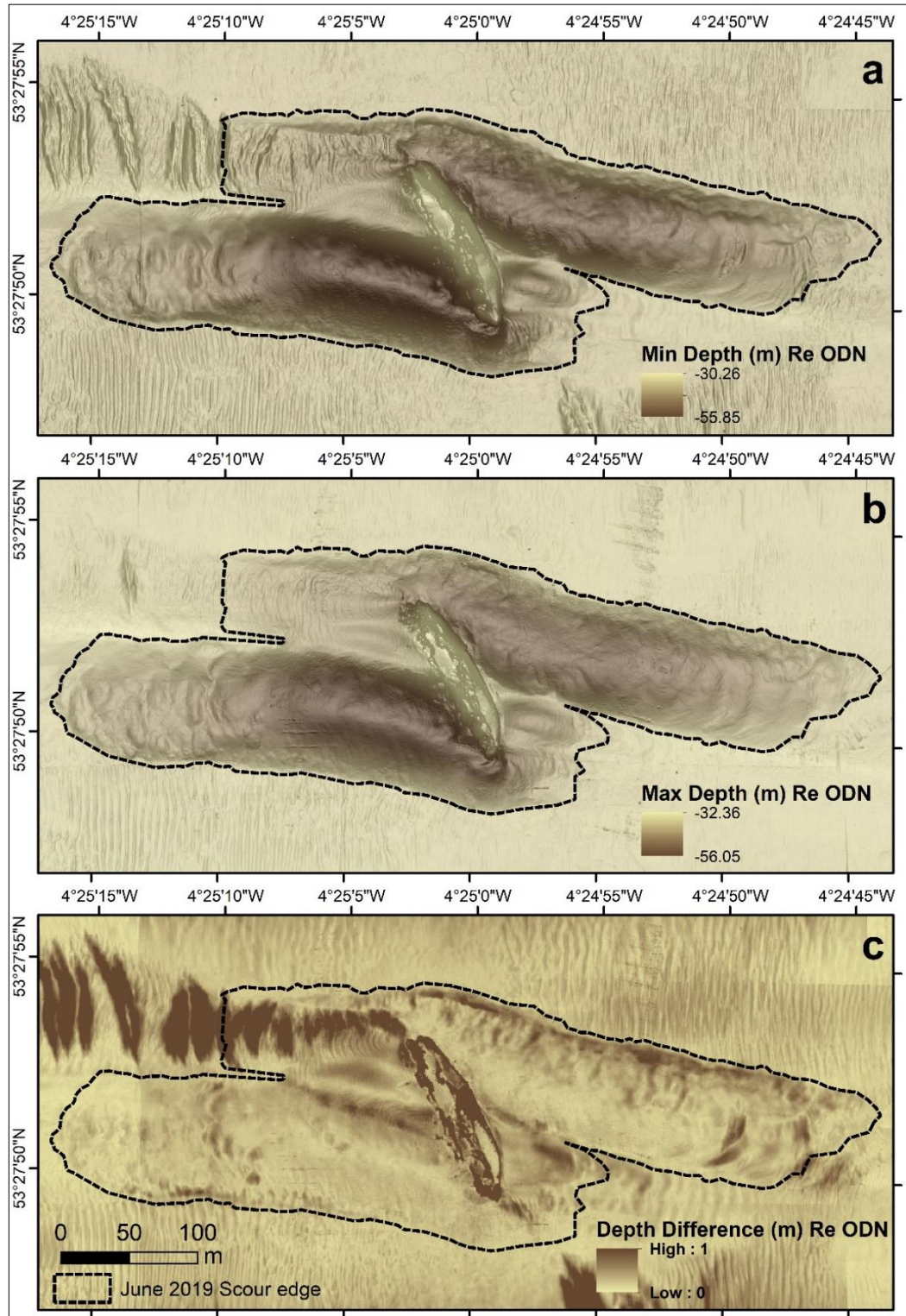


Figure 3.48: The minimum (shallowest; a), maximum (deepest; b) depths per pixel observed and the difference between the minimum and maximum values (c) showing the full range of the observed depth values.

Figure 3.49 Presents the boxplot of the point cloud used for the generation of the DEM presented in Figure 3.48c.

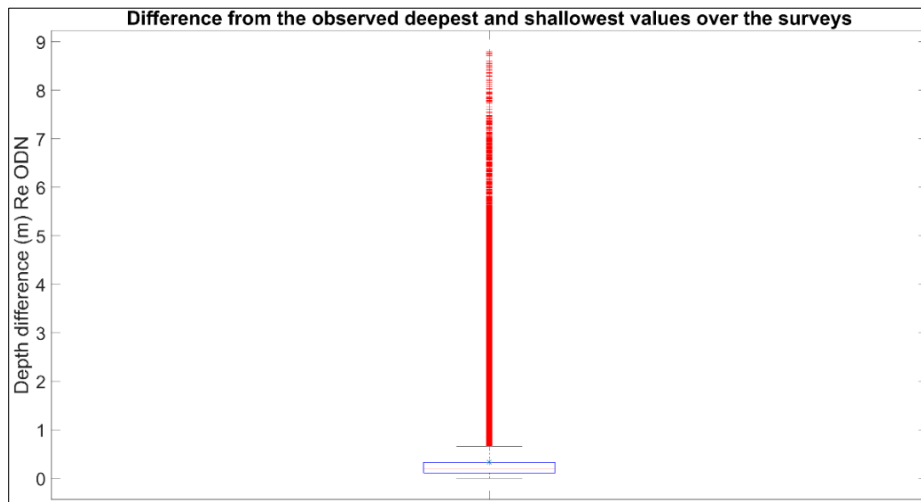


Figure 3.49: Boxplot of the maximum variation observed (calculated for each pixel) between the surveys. the \* sign represents the mean value of the measurements.

The largest variation (7 m) observed at the wreck itself, was recorded between the March 2018 and June 2019 datasets. This variation (disintegration/shifting of the wreck) has caused the largest change in the bed morphology within the scour mark observed during the datasets processed in the present study. A disintegration of the wreck was observed at the west side, where the east side of the wreck has moved shallower. The map in [Figure 3.50](#) presents the depth difference between the 2018 and 2019 surveys.

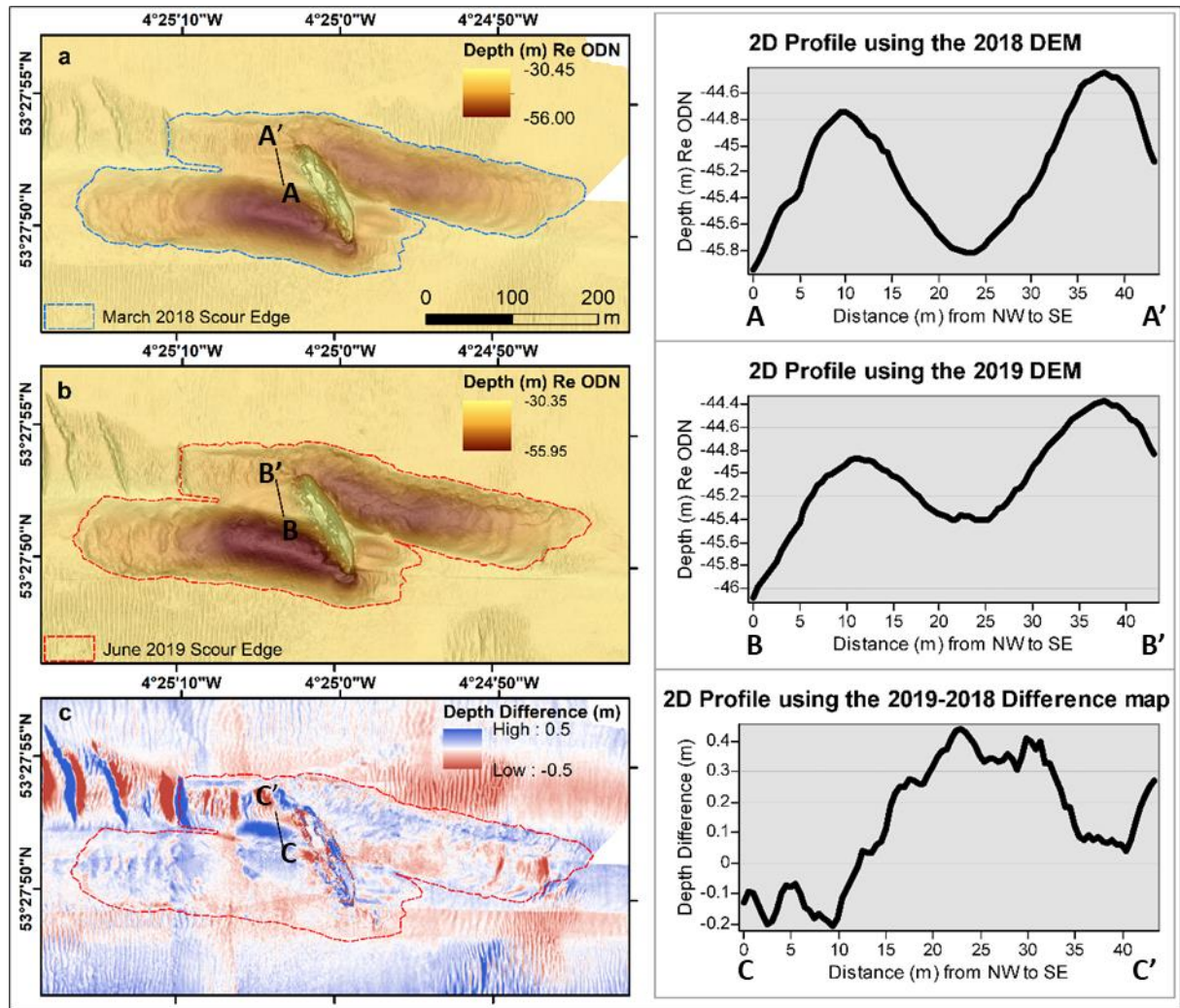


Figure 3.50: The March 2018 DEM (a), the June 2019 DEM (b) and a difference map two surveys (c) indicating the larger observed disintegration of the wreck. The profiles at the right are the relative to the maps on the left 2-D profiles indicated at the map, showing depth along the profile from NW to SE.

The variation caused by the disintegration to the erosion and deposition rates is significantly present at the June 2019 DEM. When focusing on the profiles of [Figure 3.50](#) and especially at [Figure 3.50c](#) and its accompanied 2-D profile (C-C'), a variation of  $\sim 0.45$  m is observed at the area that seems to have high depositional rates at the NW part of the scour mark (where the 2-D profile is shown). The volume of sediment needed to fill the aforementioned scour mark was calculated to be  $\sim 300$  m<sup>3</sup>. Smaller variations are also obvious at the mirroring area of the SE part of the scour mark, with significantly less deposition than the NW part.

The standard deviation maps of the observed depths provided information about the largest variations during a decade at the SS *Apapa* site. However, 2-D profiles following different seabed features and using the difference maps over time, can aid annotation of consistent 'zones of influence' from the wreck, showing the distance away from the wreck where maximum variations are observed over the years. [Figure 3.51](#) shows the observed consistent zones from the drops of variation at the 2-D profiles over the difference maps (difference modelling) between the datasets as explained in [Section 3.2.3](#).



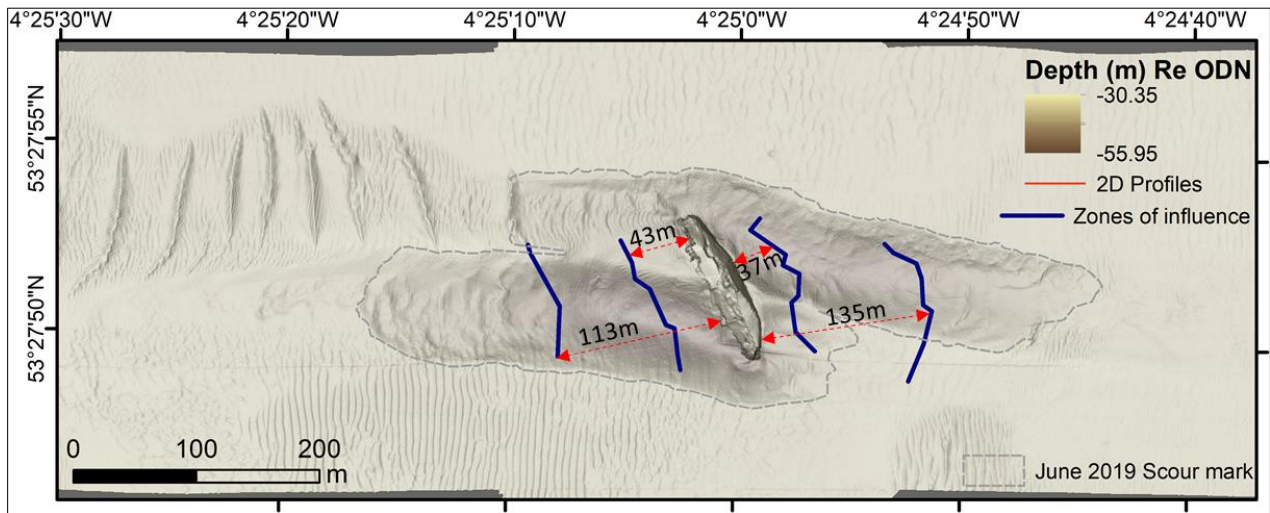


Figure 3.51: Consistent 'zones of bed mobility' or 'zones of influence' generated by plotting 2-D profiles following features on the seabed at the SS *Apapa* site scour mark

The average variation distance for the two 'zones of influence', measured parallel (from the wreck to the zone) appears to be 43 m and 113 m for the 1<sup>st</sup> and 2<sup>nd</sup> zones respectively for the west, and at 37 m and 135 m from the wreck for the 1<sup>st</sup> and 2<sup>nd</sup> zones respectively for the east sides of the scour mark.

The observed from the bathymetric changes between consecutive datasets 'zones of bed mobility', were compared with the ADCP dataset (depth averaged flow speed), showing a reduction of up to 30% when compared to the upcoming (outside the scour mark) flow at the western part of the scour mark. On the other hand, at the eastern part of the scour mark, the flow reduction at the 'zones of bed mobility' reaches the 35% when compared with the averaged upcoming (background) flow. **Figure 3.52** presents examples of flow variation (reduction) at the western (**Figure 3.52a**) and eastern (**Figure 3.52b**) parts of the scour marks at the points where the 'zones of maximum bed mobility' were observed within the scour mark when looking purely on erosion and deposition rates between consecutive datasets.

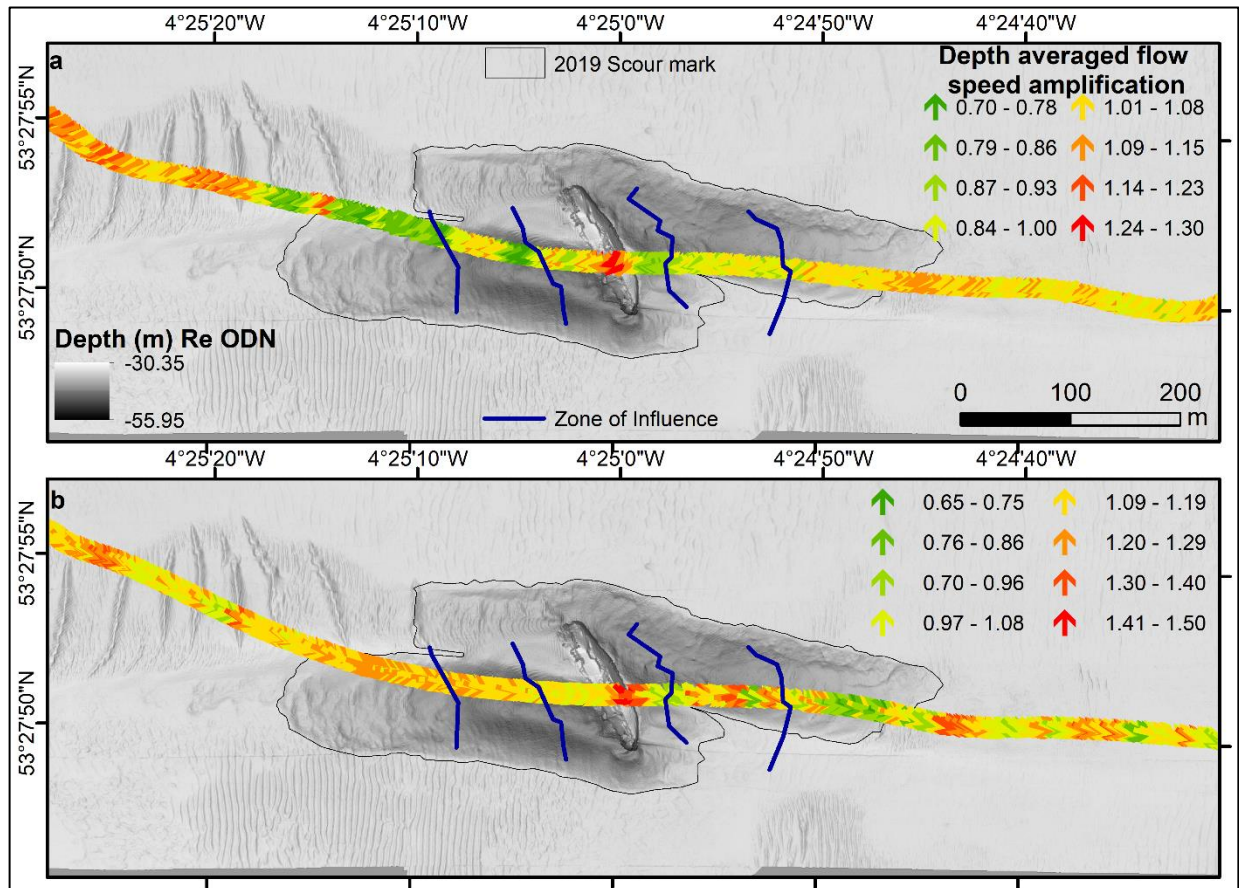


Figure 3.52: Flow variation (reduction) at a) flooding and b) ebbing of the tidal current at the points where the 'zones of bed mobility' appear.

### 3.3.3 Observed evolution of bed composition in the scour mark

Changes in the bed composition of the mixed coarse bed (sand and gravel mixture) surrounding SS *Apapa* were investigated, to provide understanding of the mobilisation of different sediment types over time (Aim 2). Monitoring and identification of changes was conducted using MBES backscatter strength data and sediment grab samples from the surrounding area. The bed composition is also investigated to identify relations with the erosion and deposition rates.

Backscatter strength data were processed and analysed to observe and identify seabed composition changes within the scour mark. The processed backscatter strength (BS) data from around the SS *Apapa* site are presented in this section, by generating standard deviation maps using the backscatter strength mosaics. Figure 3.53 shows  $\sigma$  of BS strength values as high as 34.07 dB with most of the data (box and whiskers from Figure 3.54) being within the 4-14 dB range. The mean standard deviation value between the surveys is calculated at 8.47 dB. The standard deviation map of the BS mosaics collected around the SS *Apapa* site is shown in Figure 3.53a along with the mean backscatter values from all the datasets in Figure 3.53b.



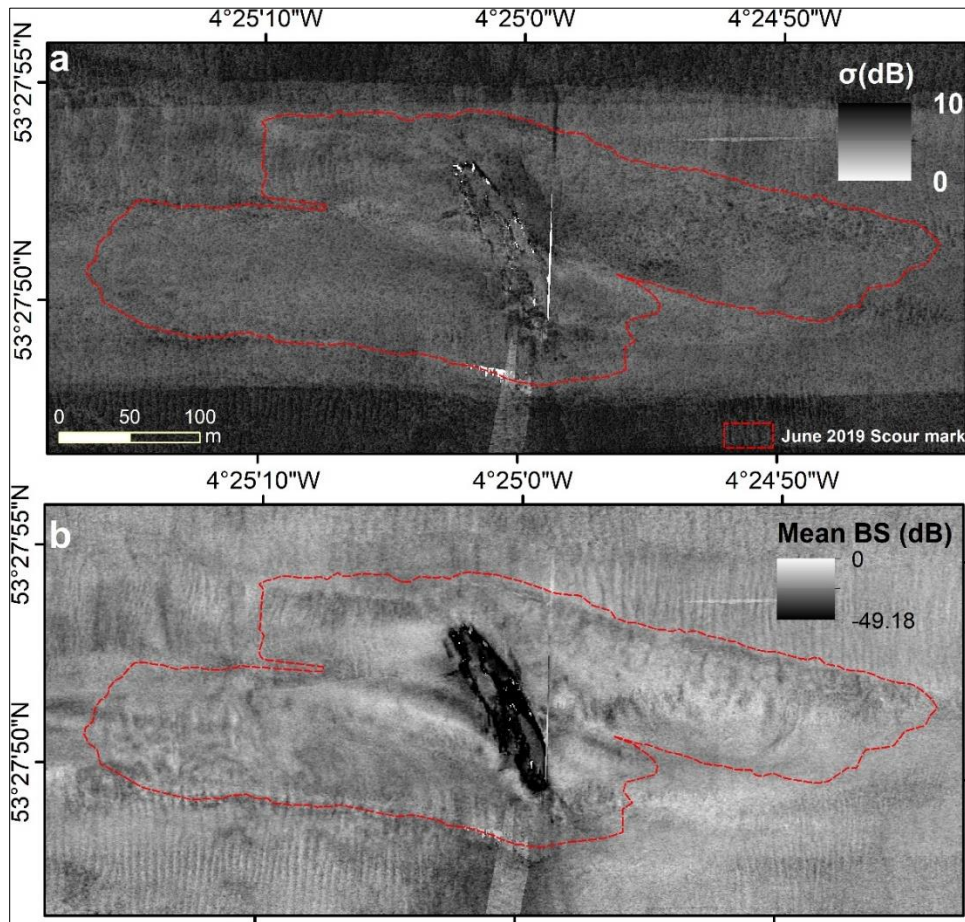


Figure 3.53: Standard deviation ( $\sigma$ ; a) and mean value ( $\bar{x}$ ; b) of BS values calculated using all the datasets around SS Apapa.

The maximum value of BS observed for all the surveys is -1.66 dB (0.87% of the initial signal) where the minimum is -70 dB (36.61% of the initial signal). The mosaic produced from the average BS observed over the years, indicates finer sediment at the depositional feature (low BS), followed by coarse material (high BS) on either side of it (Figure 3.53b). The average value of backscatter strength observed for the different datasets, shows a mean value of -29.06 dB, where the box indicating the 50% of the population sits between -30 dB to -28 dB (Figure 3.54). The whiskers of the boxplot show values between -34 dB to -25 dB.

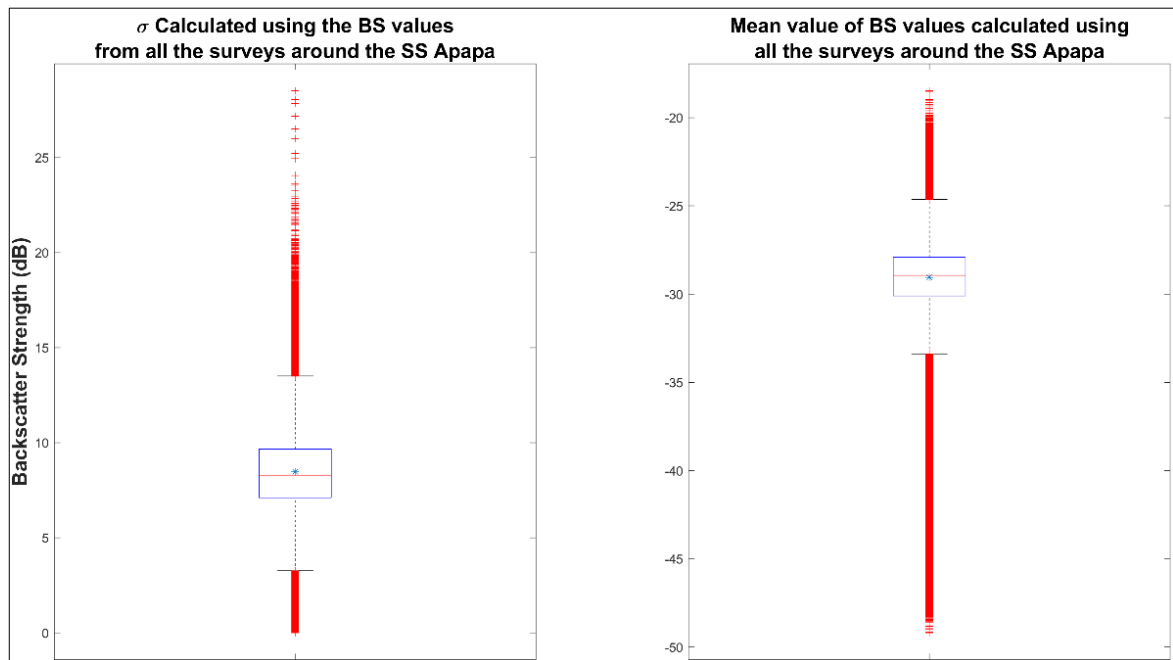


Figure 3.54: Standard deviation values ( $\sigma$ ; left) and mean values ( $\bar{x}$ ) of BS strength calculated from all the surveys around the SS *Apapa* site.

The survey around SS *Apapa* involved the collection of sixty-three grab samples around the wreck, using a Shipek grab, with fifty-three grabs attaining sediment (or sufficient amount) and ten grabs failing. The grabs that failed were mostly attempts to sample the deepest point of the SW part of the scour mark or sides with slopes over  $17.6^\circ$ . The success rate of the sampling is therefore calculated at 84.12%. The final positions of the grab samples as they were recorded from the USBL instrument, and the positioning processed from the vessel's location are presented in [Figure 3.55](#).

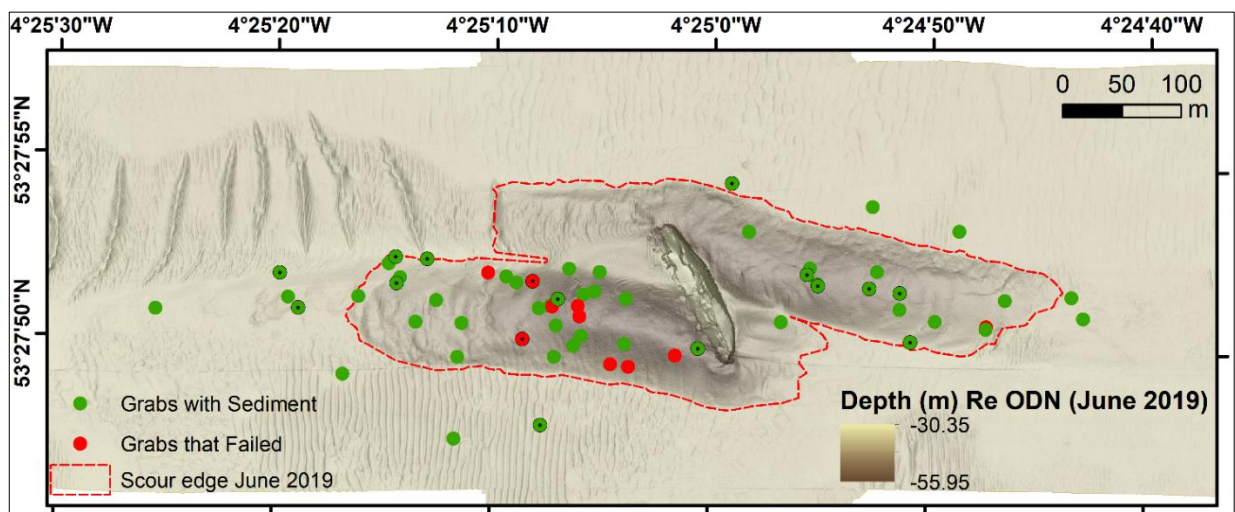


Figure 3.55: Map showing the grabs attempted around SS *Apapa*. The green points denote the grabs that succeeded and the red points the grabs that failed to attain sediment. The dotted points are the grabs where the location was calculated using the vessel's location.

The results of the PSA using the GRADITSTAT V.8 ([Blott & Pye, 2001](#)) show that all the samples are coarse, sitting on the gravel sand and mud diagram between slightly gravelly sand and Gravel (according to Folk classification; [Folk & Ward, 1957](#)).

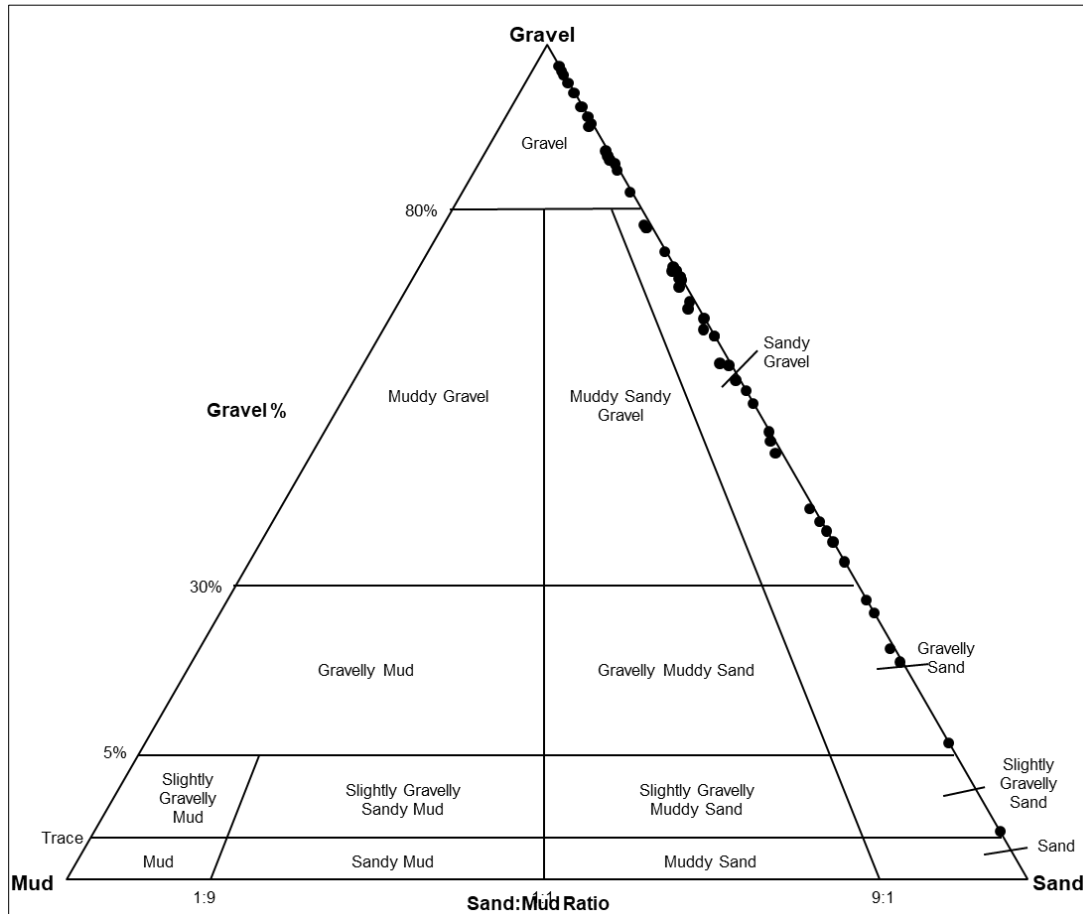


Figure 3.56: Ternary diagram for coarse sediment (mud, sand, gravel) diagram used for sediment characterisation (Folk & Ward, 1957).

According to the ternary diagram shown in **Figure 3.56** there is one sample that has less than 5% gravel (1.89% of total samples), five samples that have between 5% - 30% gravel (9.43% of total samples), thirty samples that have between 30% - 80% gravel in (56.60% of total samples) and seventeen samples that have over 80% gravel (32.08% of total samples). The maximum gravel % observed in a single sample is 99.5% and the maximum sand % observed in a sample is 98.7%. Mud is present at thirty samples (56.6%) but the maximum percentage of observed mud within a sample is 0.8%. The 26.42% of the samples were trimodal (fourteen grabs), 52.83% of the samples were bimodal (twenty-eight grabs) and only 20.75% of the grabs were unimodal (eleven grabs). Flow velocity observed at the last bin of the ADCP instrument (or max of all the values where more than one) was attained for all the sample locations that ADCP measured flow velocity was available and the critical movement was calculated for all the modes of the samples. **Table 3.4** presents the results of the analyses and shows information regarding the distance of the sample from the wreck, the depth, the excess stresses, the observed  $\sigma$  of the bathymetry and BS strength within the 6.92 buffer zones (from the measured  $\sigma$  in positioning accuracy), the maximum depth difference and the potential mobilisation or not of each mode of the samples. Grab sample 27 (green row) is a sample location where the information from the ADCP data was collected during slack water (at a turning transect) and therefore cannot be used for further analyses. However, it exists on the table as ADCP data were available at least for some period during the 25 hours of the ADCP survey. The maximum

TKE calculated from the numerical model (presented in Section 3.3.4) at plane 2 (1<sup>st</sup> plane above the bed) was also added in Table 3.4. This TKE was also used for the calculation of shear stress, using the equation proposed by Pope et al. (2006) described in Section 1.3. The results of the analyses showed that the shear stress calculated using the Soulsby (1997) formulae was greater than the shear stress calculated using the Pope et al. (2006) formula, for 60 out of 71 instances (84.5%) where shear stress was calculated. For 10 out of 11 cases where the Pope et al. (2006) formula was calculating higher values of shear stress than the Soulsby (1997) formulae, sediment mobilisation was already predicted by the Soulsby (1997) formulae. In the only case that the shear stress calculated by the Pope et al. (2006) method was higher than the Soulsby (1997) formulae and sediment mobilisation was not predicted using the Soulsby (1997) formulae (Mode 1 of grab 22), the excess shear stress needed to mobilise the sediment ( $\sim 20 \text{ N}\cdot\text{m}^{-2}$ ) was much higher than the difference between the shear stress calculated using the two methods ( $\sim 0.5 \text{ N}\cdot\text{m}^{-2}$ ).

Table 3.4: Sediment sample information, classification (according to [Folk, 1957](#)) and shear stresses calculated using [Soulsby \(1997\)](#) critical sediment transport formulae for the grab samples that ADCP data were available. The velocity used in the calculation was the maximum velocity observed from the last (bottom) bin of the ADCP instrument from the E-W transects of the ADCP (conducted during ebbing/flooding).

Successful Grab No	Maximum Mayntude at last beam (m·s <sup>-1</sup> )	Depth (m) Re ODN from 2019 DEM	Distance from the edge of the wreck (m)	Bathy $\sigma$ (m)	BS $\sigma$ (dB)	Max Depth Variation (m)	Inside (i) or Outside (o) the scour mark	Turbulent Kinetic Energy (TKE; J·kg <sup>-1</sup> )	$\tau_c$ ((C <sub>s</sub> T KE) <sub>p</sub> )	Mode 1 ( $\mu$ m)	$\tau_{cr}$ (N·m <sup>-2</sup> )	$\tau_{\theta}$ (N·m <sup>-2</sup> )	$\tau_{\theta} - \tau_{cr}$ (N·m <sup>-2</sup> )	Excess $\tau$ ( $\tau_{\theta} - \tau_{cr}$ )	Movement (1) or No Movement (0)	Mode 2 ( $\mu$ m)	$\tau_{cr}$ (N·m <sup>-2</sup> )	$\tau_{\theta}$ (N·m <sup>-2</sup> )	$\tau_{\theta} - \tau_{cr}$ (N·m <sup>-2</sup> )	Excess $\tau$ ( $\tau_{\theta} - \tau_{cr}$ )	Movement (1) or No Movement (0)	Mode 3 ( $\mu$ m)	$\tau_{cr}$ (N·m <sup>-2</sup> )	$\tau_{\theta}$ (N·m <sup>-2</sup> )	$\tau_{\theta} - \tau_{cr}$ (N·m <sup>-2</sup> )	Excess $\tau$ ( $\tau_{\theta} - \tau_{cr}$ )	Movement (1) or No Movement (0)	Sediment name (Folk, 1957)
3	2.3	-42.7	294.9	0.04	7.02	0.12	o	0.007	1.278	427.5	0.23	4.19	2.91	3.96	1	3400.0	2.49	7.57	6.29	5.07	1							Sandy Very Fine Gravel
4	1.9	-42.7	294.4	0.10	6.70	0.33	o	0.007	1.239	605.0	0.29	3.07	1.77	2.77	1	1700.0	0.96	4.12	2.82	3.16	1	13600.0	12.07	7.46	6.16	-4.60	0	Sandy Very Fine Gravel
5	1.8	-44.6	236.7	0.21	6.97	0.62	i	0.009	1.763	54000.0	47.50	10.45	8.69	-37.05	0	19200.0	17.00	7.78	6.01	-9.22	0	605.0	0.29	2.90	1.13	2.60	1	Sandy Very Coarse Gravel
6	2.0	-45.4	169.5	0.06	6.58	0.18	i	0.014	2.688	54000.0	47.50	12.03	9.35	-35.46	0	26950.0	23.79	9.87	7.18	-13.93	0							Very Coarse Gravel
8	2.0	-47.2	140.4	0.06	6.48	0.20	i	0.018	3.349	26950.0	23.79	10.12	6.77	-13.68	0	54000.0	47.50	12.34	8.99	-35.16	0							Coarse Gravel
9	1.4	-51.7	85.7	0.22	5.79	0.72	i	0.023	4.390	605.0	0.29	1.59	-2.80	1.30	1	1700.0	0.96	2.14	-2.25	1.18	1							Very Fine Gravelly Medium Sand
10	2.0	-45.3	38.0	0.22	5.79	0.72	i	0.013	2.395	2400.0	1.55	4.92	2.53	3.37	1	605.0	0.29	3.32	0.92	3.03	1							Sandy Very Fine Gravel
11	2.0	-45.3	40.2	0.13	6.25	0.44	i	0.013	2.395	26950.0	23.79	9.82	7.43	-13.97	0	605.0	0.29	3.32	0.92	3.03	1							Sandy Coarse Gravel
15	2.0	-45.3	73.8	0.08	6.68	0.32	i	0.016	3.014	2400.0	1.55	5.15	2.14	3.60	1													Sandy Very Fine Gravel
16	1.6	-45.1	129.5	0.06	7.01	0.24	i	0.016	3.109	19200.0	17.00	6.01	2.90	-10.99	0													Coarse Gravel
17	1.6	-51.7	118.0	0.09	7.16	0.38	i	0.014	2.733	26950.0	23.79	6.46	3.73	-17.34	0	6800.0	5.84	4.36	1.62	-1.49	0							Coarse Gravel
18	1.3	-51.8	75.1	0.11	6.12	0.40	i	0.021	3.935	54000.0	47.50	5.22	1.29	-42.27	0	26950.0	23.79	4.28	0.35	-19.51	0							Very Coarse Gravel
19	2.1	-46.0	46.1	0.14	7.11	0.54	i	0.016	2.960	1700.0	0.96	5.19	2.23	4.23	1													Very Fine Gravelly Very Coarse Sand
20	1.9	-51.1	65.6	0.07	6.59	0.24	i	0.021	4.043	2400.0	1.55	4.41	0.36	2.86	1	26950.0	23.79	8.80	4.75	-15.00	0							Sandy Very Fine Gravel
21	1.9	-52.0	118.4	0.16	7.28	0.60	i	0.010	1.813	605.0	0.29	2.97	1.15	2.67	1	4800.0	3.88	5.36	3.54	1.48	1	13600.0	12.07	7.21	5.40	-4.85	0	Sandy Very Fine Gravel
22	1.2	-51.1	51.4	0.10	9.57	0.30	i	0.022	4.219	26950.0	23.79	3.65	-0.57	-20.14	0	605.0	0.29	1.24	-2.98	0.94	1							Sandy Coarse Gravel
27	0.7	-42.1	232.3	0.07	6.44	0.27	o	0.009	1.624	605.0	0.29	0.48	-1.15	0.19	1	26950.0					0							Coarse Gravelly Coarse Sand
29	1.6	-52.3	96.4	0.08	6.59	0.28	i	0.009	1.784	13600.0	12.07	5.04	3.25	-7.03	0	427.5	0.23	1.88	0.09	1.85	1							Sandy Medium Gravel
31	1.3	-52.5	61.7	0.05	6.44	0.16	i	0.012	2.356	19200.0	17.00	3.64	1.29	-13.36	0	605.0	0.29	1.36	-1.00	1.06	1							Sandy Coarse Gravel
32	1.7	-43.3	273.5	0.08	6.85	0.28	i	0.009	1.718	54000.0	47.50	9.37	7.66	-38.12	0	26950.0	23.79	7.63	5.97	-16.11	0							Very Coarse Gravel
34	1.5	-45.4	209.8	0.05	6.74	0.14	i	0.009	1.633	19200.0	17.00	4.86	3.22	-12.15	0	6800.0	5.84	3.61	1.98	-2.23	0							Coarse Gravel
35	2.2	-41.5	229.3	0.11	6.37	0.40	i	0.009	1.798	38250.0	33.70	13.98	12.18	-19.72	0													Very Coarse Gravel
37	2.5	-43.5	140.7	0.03	6.57	0.09	i	0.016	2.965	26950.0	23.79	16.29	13.32	-7.51	0	13600.0	12.07	13.39	10.43	1.33	1	605.0	0.29	5.50	2.54	5.21	1	Sandy Coarse Gravel
38	2.5	-42.9	229.0	0.07	6.90	0.24	i	0.010	1.940	26950.0	23.79	15.46	13.52	-8.34	0													Coarse Gravel
39	1.4	-50.4	129.4	0.11	7.64	0.40	i	0.012	2.338	54000.0	47.50	5.59	3.25	-41.91	0	19200.0	17.00	4.16	1.82	-12.84	0	605.0	0.29	1.55	-0.79	1.25	1	Very Coarse Gravel
40	2.2	-52.0	12.8	0.08	7.07	0.30	i	0.016	3.099	26950.0	23.79	11.17	8.07	-12.63	0	605.0	0.29	3.77	0.67	3.48	1							Sandy Coarse Gravel
41	1.8	-41.1	198.3	0.06	7.15	0.19	o	0.012	2.235	54000.0	47.50	10.58	8.35	-36.91	0	26950.0	23.79	8.68	6.44	-15.12	0							Very Coarse Gravel
42	2.2	-41.0	221.2	0.04	6.56	0.12	i	0.010	1.947	19200.0	17.00	11.58	9.63	-5.42	0													Coarse Gravel
43	1.7	-43.7	232.8	0.05	7.60	0.13	i	0.010	1.866	605.0	0.29	2.36	0.49	2.06	1	19200.0	17.00	6.33	4.47	-10.67	0	6800.0	5.84	4.71	2.84	-1.14	0	Sandy Medium Gravel
45	2.2	-41.8	328.6	0.08	7.17	0.28	o	0.009	1.737	605.0	0.29	4.30	2.56	4.00	1													Slightly Very Fine Gravelly Coarse Sand
46	1.6	-51.6	109.7	0.07	6.57	0.22	i	0.018	3.411	26950.0	23.79	5.91	2.50	-17.88	0	13600.0	12.07	4.86	2.36	-7.20	0	605.0	0.29	2.00	-1.41	1.71	1	Sandy Coarse Gravel
48	2.2	-42.2	147.8	0.06	7.47	0.21	i	0.014	2.605	38250.0	33.70	13.16	10.55	-20.54	0													Very Coarse Gravel
49	2.3	-42.6	63.2	0.06	6.48	0.20	i	0.006	1.123	26950.0	23.79	13.31	12.19	-10.48	0	605.0	0.29	4.50	-7.69	4.21	1							Sandy Coarse Gravel
51	1.4	-51.7	83.5	0.07	6.71	0.21	i	0.023	4.405	38250.0	33.70	5.21	0.80	-28.49	0	605.0	0.29	1.59	0.79	1.30	1	1700.0	0.96	2.14	-2.27	1.18	1	Sandy Very Coarse Gravel
52	1.9	-48.9	148.2	0.07	6.95	0.23	i	0.017	3.159	38250.0	33.70	10.21	7.05	-23.49	0													Very Coarse Gravel
53	1.3	-50.2	125.5	0.06	7.74	0.17	i	0.019	3.612	38250.0	33.70	4.53	0.92	-29.17	0	605.0	0.29	1.39	0.47	1.09	1	1700.0	0.96	1.86	-1.75	0.90	1	Sandy Coarse Gravel



The analyses of the samples provided the information needed to generate a map with the sand and gravel % presence within the grab samples (Figure 3.57) that helps visualise spatially the sediment types.

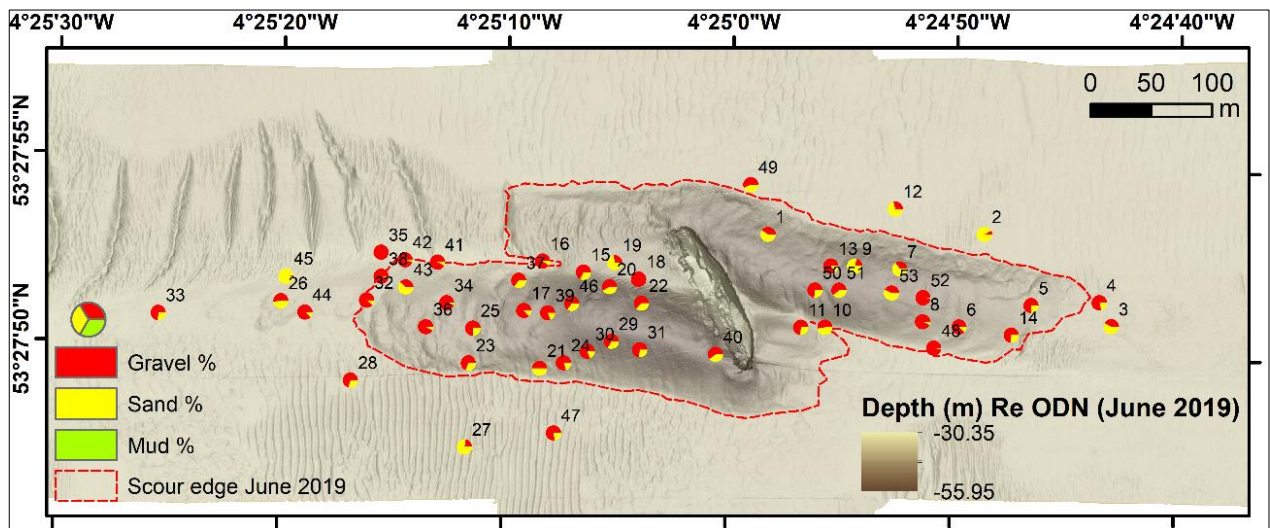


Figure 3.57: Sand, gravel and mud observed % from the PSA of the grab samples collected around the SS Apapa site.

The average grain diameter (coarser mode) observed from the coarse material is 15.353 mm ( $-3.94 \Phi$ ) where the average grain diameter (finer mode) observed for the fine material is 0.0605 mm ( $4.05 \Phi$ ). The June 2019 BS mosaic (Figure 3.58a) was classified to different classes, using unsupervised (Figure 3.58b) and supervised (Figure 3.58c) classification in ArcMap. The unimodal sediment samples were used for the supervised classification as  $d_{50}$  is not a representative value of bimodal sediment and only one value is allowed to be used while ‘training’ the image. The categorisation showed 3 classes (low, medium, high BS strength) when the unsupervised classification was used, where in the case of the supervised classifications 6 sedimentary classes are shown, based on the 6 classes observed from the unimodal sediment samples, varying from  $-5.325 \Phi$  to  $0.747 \Phi$  (0.596 – 37.661 mm).



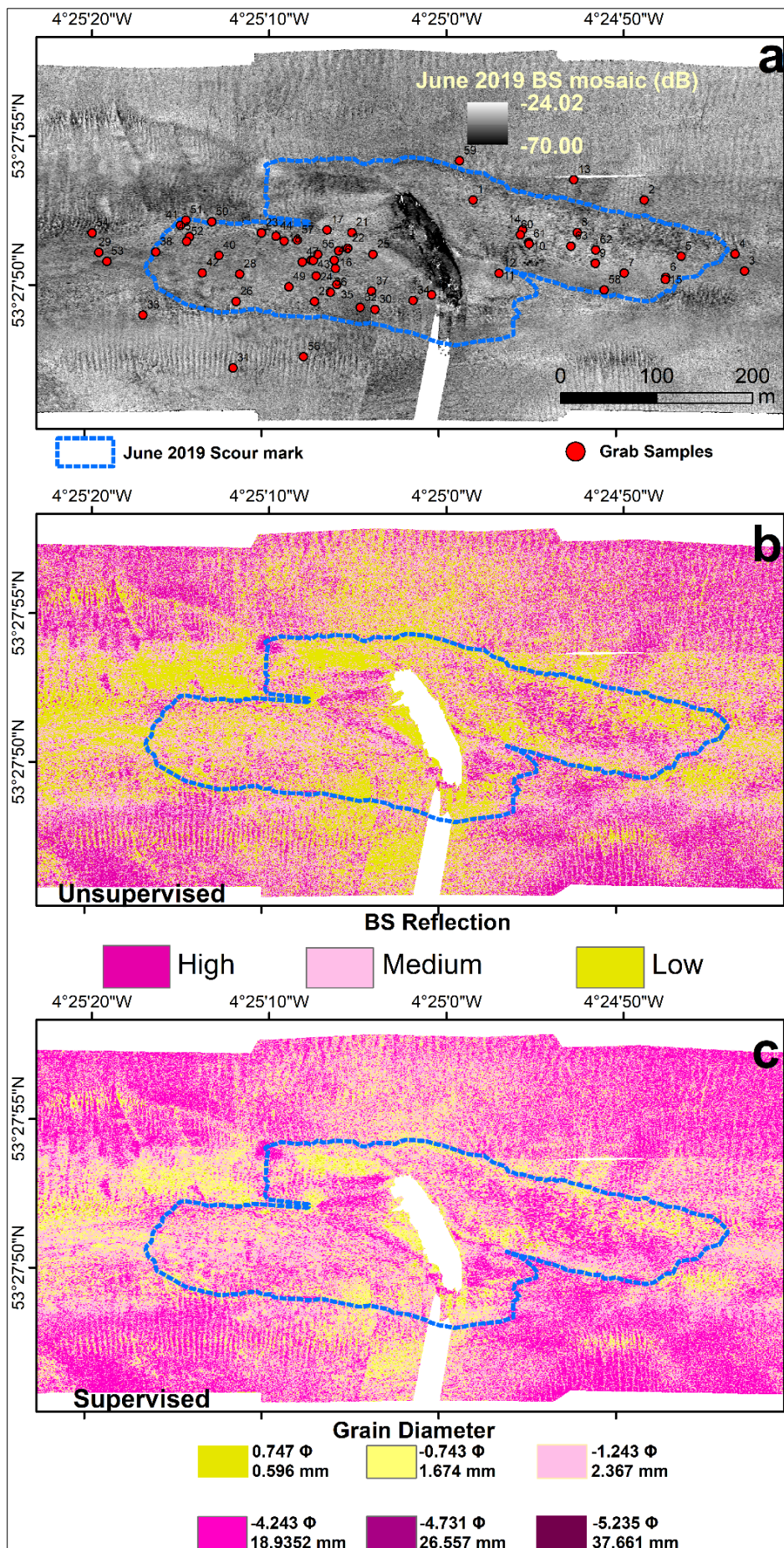


Figure 3.58: June 2019 BS mosaic (a), unsupervised classification (b) and supervised classification using only unimodal grab sediment samples.

The corresponding successful grab sample locations numbers used in Table 3.4 are shown in Figure 3.59. Also, the information gained from Table 3.4 was used to generate Figure 3.59, visualising the locations where the threshold of motion is exceeded ( $\tau > \tau_{cr}$ ) for at least one of the modes of the sediment mixture (green) or the threshold of motion is not exceeded ( $\tau < \tau_{cr}$ ) for any of the sample's modes (red).

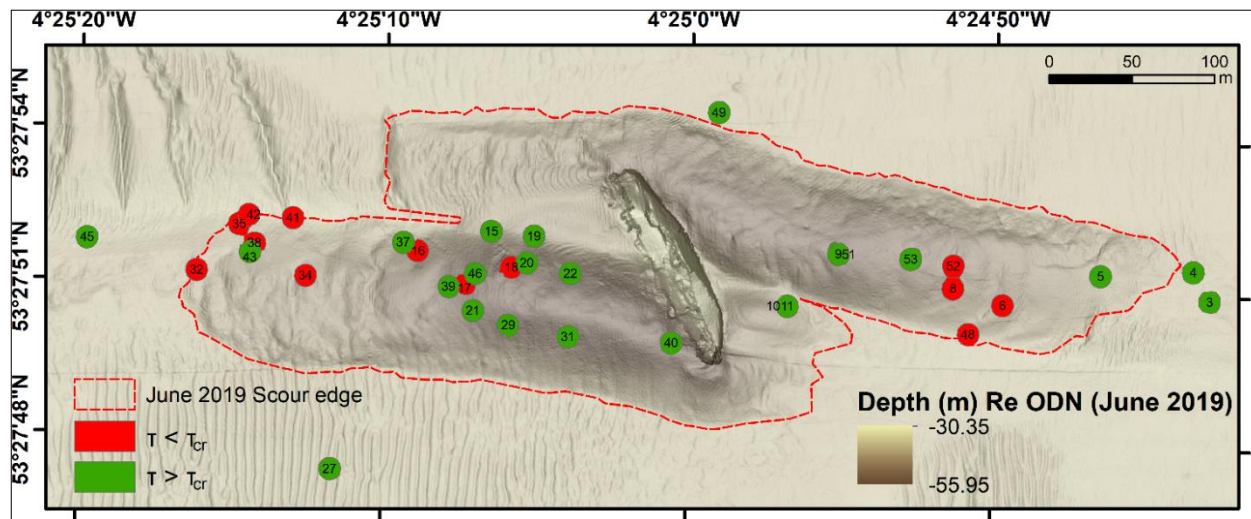


Figure 3.59: Threshold of motion exceeded ( $\tau > \tau_{cr}$ ) for at least one mode in each grab sample (green), or threshold of motion not exceeded (red). Shear stresses calculated using each mode as grain size and the maximum bottom current observed from the ADCP survey.

The mobilisation of bimodal sediment does not only depend on whether part of the sediment can be mobilised, but it also depends on how the sediment will act as a total (due to the hiding-exposure effect). The mean standard deviation value of the bathymetry and the mean depth difference between the 2019 and 2018 surveys, for each sample (at a buffer zone of 6.92 m) are presented in Figure 3.60, showing mobilisation of sediment samples shown as immobile (threshold of motion not exceeded) in Figure 3.59.



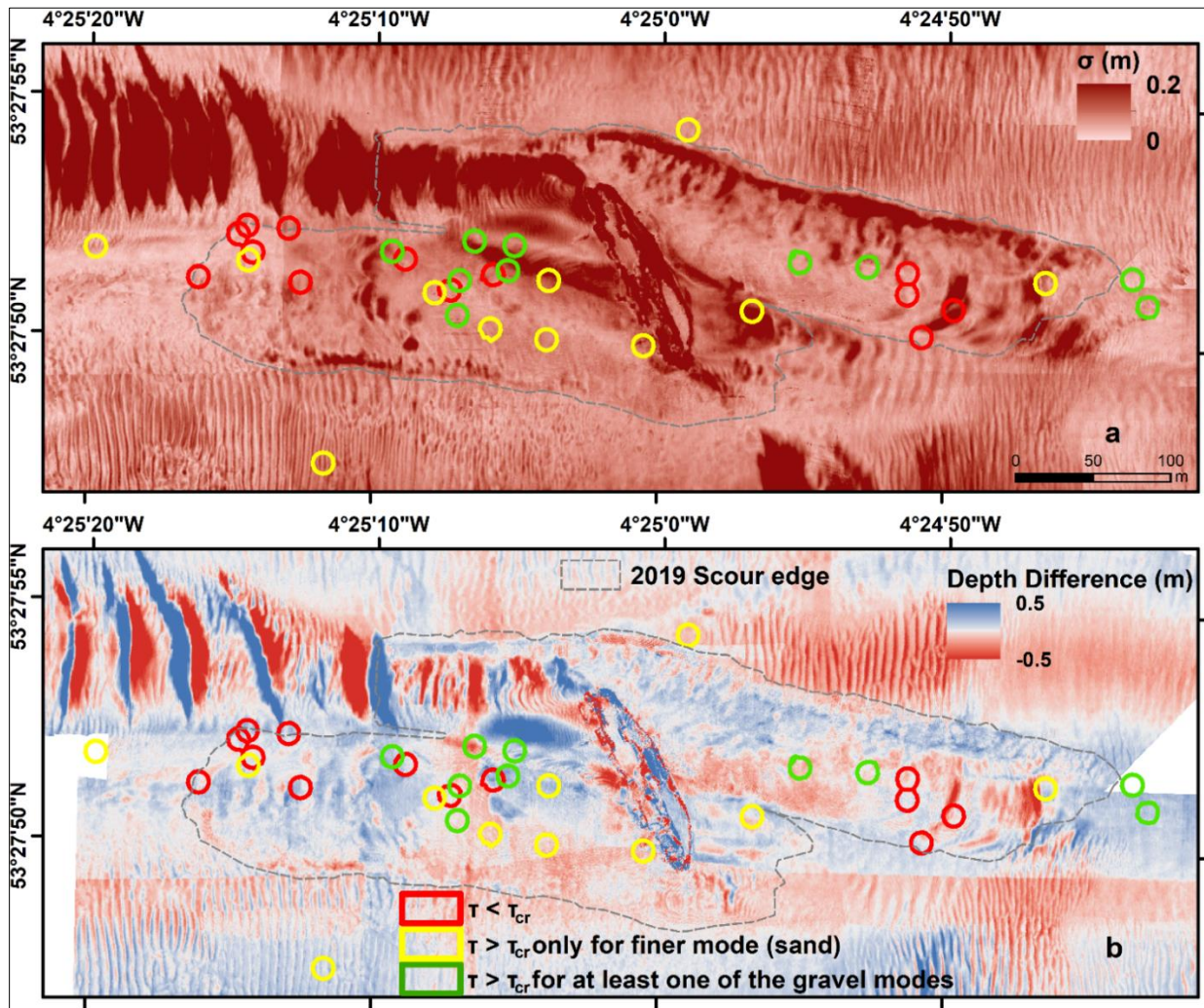


Figure 3.60: Sediment sample locations where threshold of motion is predicted to be exceeded ( $\tau > \tau_{cr}$ ) for only the fine (sand) mode (yellow), for at least one of the coarse (gravel) modes (green) or threshold of motion not exceeded ( $\tau < \tau_{cr}$ ) for any of the sample's modes (red) using Soulsby (1997) formulae plotted on the standard deviation of the bathymetry (a) and the depth difference map between the 2019 and the 2018 survey (b) where blue is deposition and red is erosion.

As Figure 3.59 and 3.60 show, although the calculations using Soulsby (1997) formulae for critical sediment movement did not predict any mobilisation for 37.14% of the samples presented in Figure 3.59, erosion and deposition still happened (in smaller or greater amount). More specifically, as the boxplots at Figure 3.61 show, there was an average absolute depth difference in the order of 0.08 m from 2018 to 2019 at the locations where the threshold of motion was exceeded only for the finer (sand) fraction of the samples, compared to 0.11 m at the locations where the threshold of motion was exceeded for at least one of the coarser (gravel) modes of the samples and 0.07 m at locations where the threshold of motion was not predicted to be exceeded for any of the sample's modes. Similarly, the average value of the bathymetric standard deviation was 0.10 at locations where  $\tau > \tau_{cr}$  only for the finer (sand) fraction, 0.10 at locations where  $\tau > \tau_{cr}$  for at least one of the coarser (gravel) modes and 0.08 at locations where  $\tau < \tau_{cr}$  for all the modes of the sample.

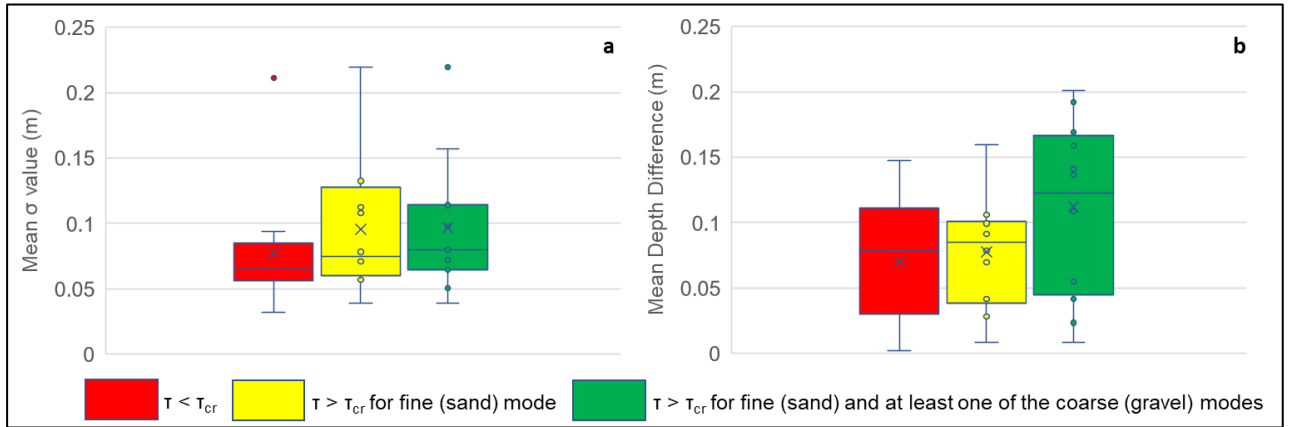


Figure 3.61: a) Mean standard deviation ( $\sigma$ ) of depth (m) and b) depth difference between the 2019 and 2018 DEMs calculated at a 6.92 m buffer zone around each point for sediment material where threshold of motion is predicted to be exceeded ( $\tau > \tau_{cr}$ ) for only the fine (sand) mode (yellow), for at least one of the coarse (gravel) modes (green) or threshold of motion not predicted to be exceeded ( $\tau < \tau_{cr}$ ) for any of the sample's modes (red) using the Soulsby (1997) formulae. The 'x' sign represents the mean value of the measurements. The solid blue lines show the median value of each population, and the boxes indicate the 25<sup>th</sup> and 75<sup>th</sup> percentiles. The whiskers indicate the minimum and maximum values.

The sediment type of the samples plotted on the standard deviation and difference maps between 2019 and 2018 can provide further understanding to what type of material is more mobile. Figure 3.62a shows that the mean value for standard deviation between the depths observed for the different mixtures categorises the sediment types from the more to the least mobile as: sG, gS, G and (g)S, with mean  $\sigma$  (of depth) values of 0.11 m, 0.10 m, 0.08 m, and 0.05 m respectively. Although the standard deviation showed that the locations with sediment characterised as sandy gravel was the most mobile, the absolute depth difference (Figure 3.62b) shows that the finer the material the higher the mobility, providing mean absolute depth difference values of 0.06 m, 0.08 m and 0.16 m for gravel, sandy gravel, and gravelly sand respectively. However, the difference map also confirms mobilisation of sediment not expected to be mobile. Finally, although Figure 3.62c does not provide any information about the sediment mobilisation and its relationship with depth, it was important to be presented as the slightly gravelly sand sample was not within the scour mark, but it appears at the west, at a depth of -41.7 m.

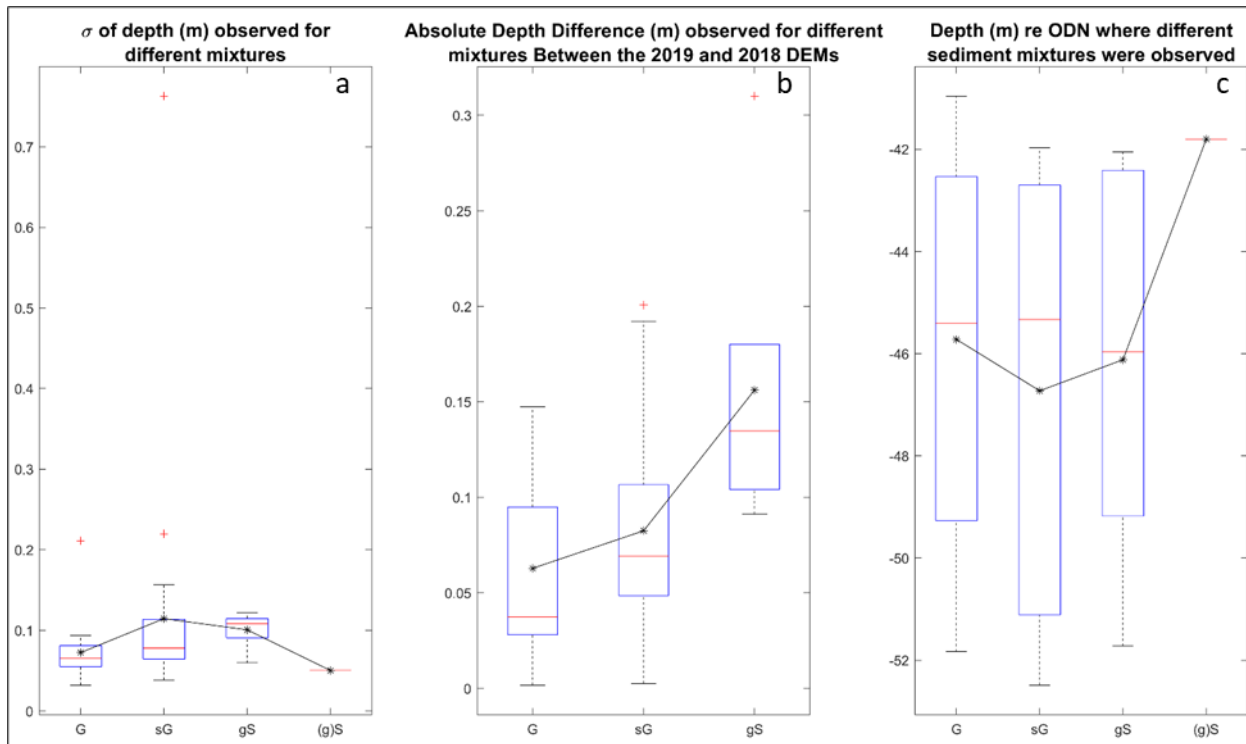


Figure 3.62: a) Standard deviation of depths observed at the location of the grab samples for different types of sediment mixtures. b) absolute depth difference (m) observed at the locations of different sediment mixtures between the 2019 and 2018 DEMs and c) the depth ranges where the different sediment mixtures were observed. The \* sign represents the mean value of the measurements. The solid red lines show the median value of each population, and the boxes indicate the 25<sup>th</sup> and 75<sup>th</sup> percentiles. The whiskers indicate the minimum and maximum values, where the red + signs represent the extreme measurements.

Presentation of the sample's sediment type (Figure 3.63) shows that within the scour mark, gravel and sandy gravel are present, where finer material (gravelly sand and slightly gravelly sand) is observed at the surrounding area of small bedforms (ripples) and at the depositional feature. Gravel is also present generally at the centre and at the edges of the scour mark.

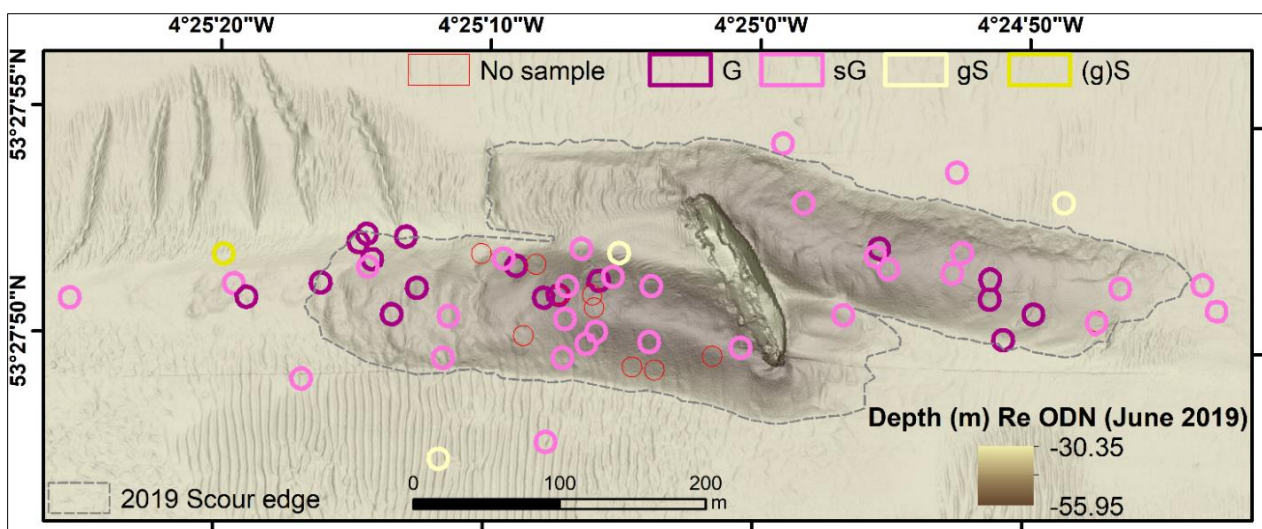


Figure 3.63: Spatial locations where different sediment mixtures were observed during the sample processing.

The maximum flow speeds measured at the last bin of the ADCP plotted against the  $\sigma$  maps of bathymetry (Figure 3.64), show that sediment described as gravel is more mobile at lower flow velocities where sandy gravel and gravelly sand are more mobile increasing the flow velocity. Also, it can be observed that gravel, is more mobile than sandy gravel and gravelly sand at lower flow velocities. The slightly gravelly sand sample appears to be less mobile than the gravel samples at a flow speed of  $2.25 \text{ m}\cdot\text{s}^{-1}$ , but as Figure 3.63 shows, the (g)S sample is located outside the scour mark, at an area where ripples with heights less than 0.3 m are formed.

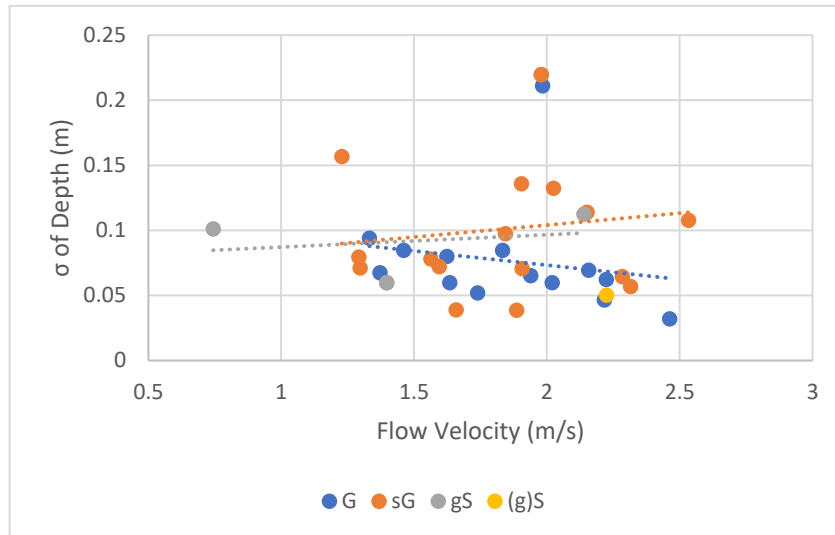


Figure 3.64: Comparison of differently sized sediment samples and their mobilisation over time for the maximum flow velocity as measured from the last bin of the ADCP instrument at the sampled location.

Comparison of the BS strength values of the known grab samples against the  $\sigma$  of bathymetry (Figure 3.65) can provide understanding of the quality and usage of the BS mosaics. In agreement with the outcomes of Figure 3.64, coarser material appears in cases to be more mobile than finer material. Also, according to Figure 3.65, when sediment categorised as gS appears at lower BS values (finer) is more mobile over time, where when sediment categorised as G and sG appears at higher BS values (coarser) is more mobile over time.

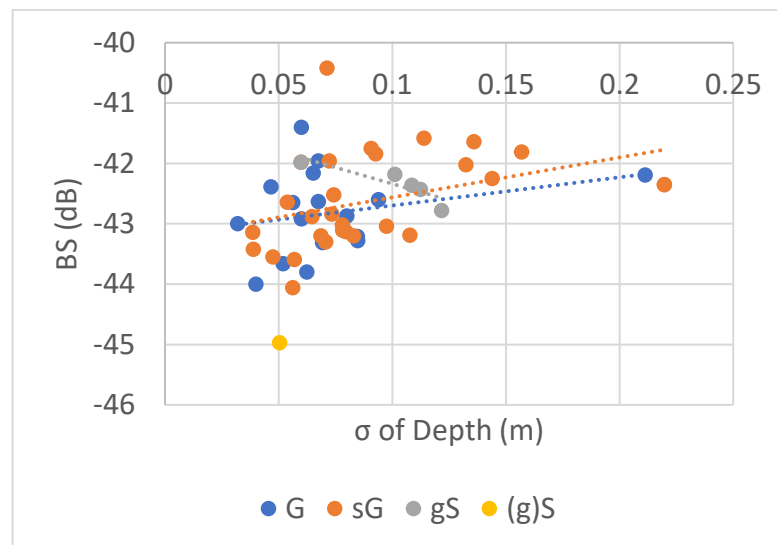


Figure 3.65: BS values, showing bed composition compared with  $\sigma$  of depth showing bed mobility over time.



### 3.3.4 Modelled evolution of flow amplification, scour geometry and composition

The knowledge gained from the analyses of the hydrodynamics, bed dynamics and bed composition parameters around the SS *Apapa* site were used to inform a coupled hydrodynamic and sediment transport numerical model (TELEMAC3D – GAIA) to investigate and predict the mobilisation of bimodal sediment from the enhanced fluid dynamics around the wreck (Aim 3). Bed composition and bathymetric data were used as input, but also for validation purposes, where ADCP data were used to validate the model predictions for flow around the wreck.

Comparison of ADCP data and hydrodynamic model (TELEMAC-3D) outputs, for 11 hours is presented in **Figure 3.66**. The numerical model was set to output information every 20 minutes (for storage purposes) where the ADCP provided information every 1.47 s. Therefore, the plot of **Figure 3.66** compares the model outputs at the times where ADCP and model information was available.

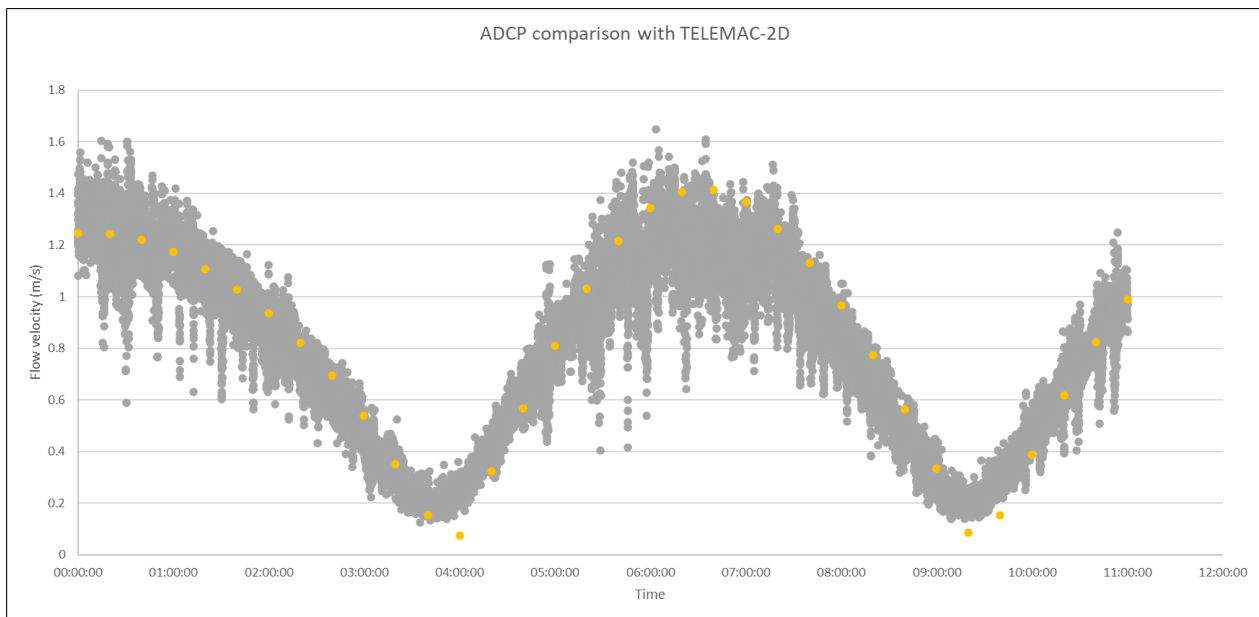


Figure 3.66: Comparison of the modelled flow velocity values (from TELEMAC-3D) and the ADCP measured flow velocity values.

The comparison of the means (**Figure 3.67**) shows a variation of the mean flow speeds between the modelled and measured values within the range of 3% - 50%, but there are two extreme values (during slack water). The variation between the ADCP and TELEMAC3D values is mainly within a 3% - 15% range. During slack water, the flow velocities are less than  $0.3 \text{ ms}^{-1}$  and therefore even the smallest variation in the flow speeds appears large when looking at the % difference.

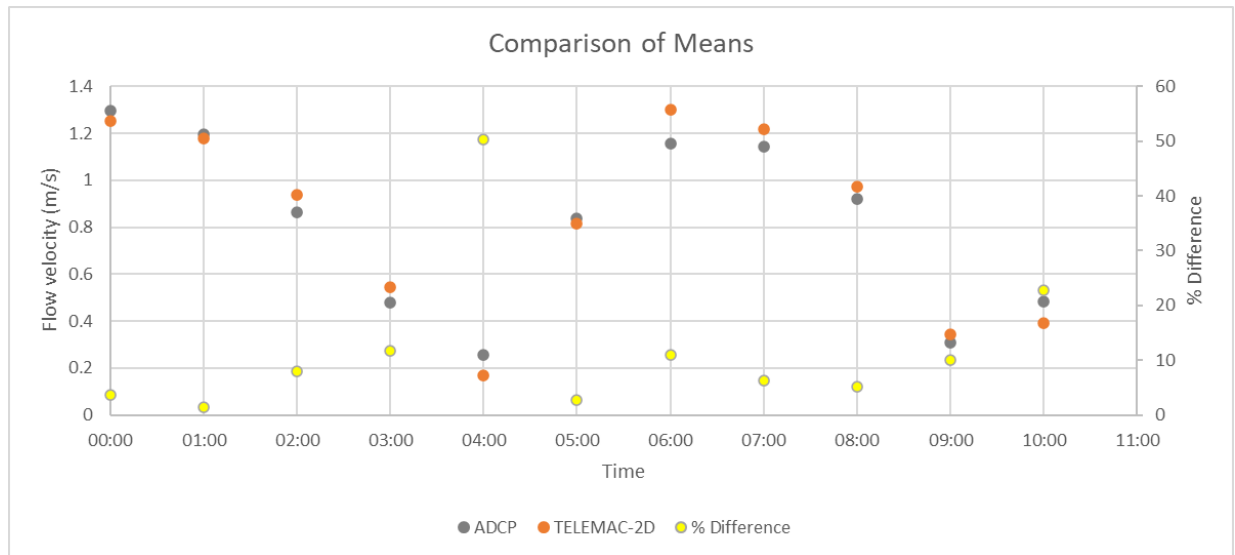


Figure 3.67: Comparison of the means between the measured flow velocity values using the ADCP instrument and the modelled flow velocity values from TELEMAC-3D.

The coupled hydrodynamic and sediment transport model was set to run for 8 days, from a flat bed, at a 1 s timestep, to understand the initiation of scour as scour is expected to form within the first few tidal cycles (Harris et al., 2010). The hydrodynamic component of the numerical model (TELEMAC) predicted amplification of the depth averaged flow speed of up to 0.8 times at the stern and bow of the wreck when compared to the background flow. The output of the sediment transport component of the model (GAIA) after this period, shows that the model does not predict the bedform formation. However, the purpose of this model was not to predict formation of bedforms, but to understand the scour formation on bimodal sediment due to the enhanced fluid dynamics around the wreck. The model predicts the shape of the scour well, as the length of the NE and SW parts of the scour mark are overestimated by only 0.6% and 1% respectively. The length to width ratio of the 'north' and 'south' scour marks is underestimated by 2.3% and overestimated by 2.6% respectively. The result of the model also shows an offset of the predicted 'north' scour mark to the north by an average of 30 m. Figure 3.68 shows the predicted scour mark formed around the wreck after the 8 days of computation time.

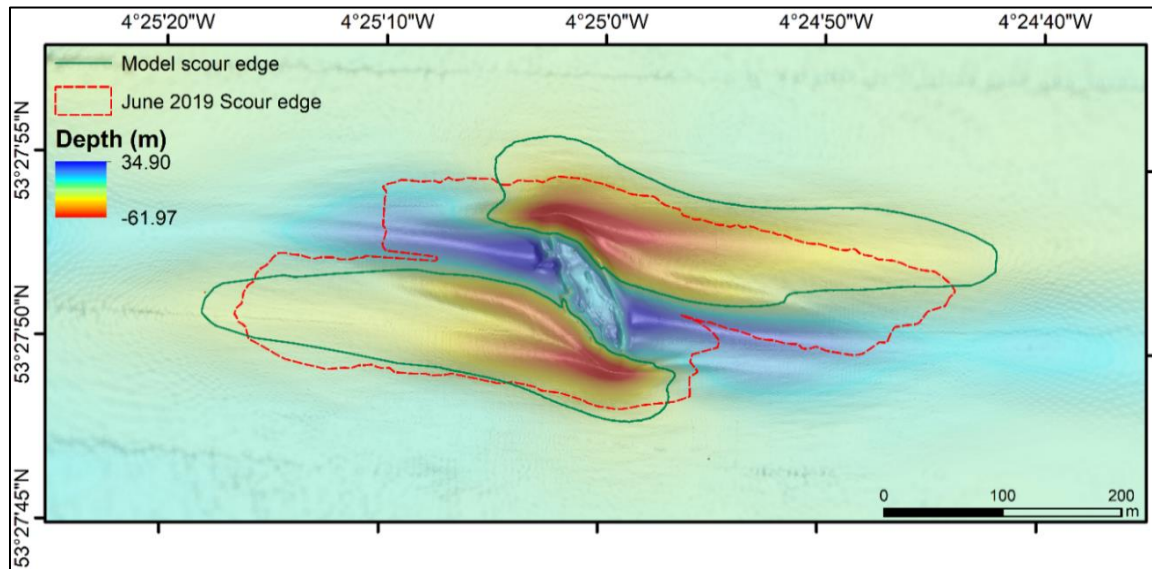


Figure 3.68: Prediction of scour formation from the coupled numerical model over the first 16 full tidal cycles (8 days).

The prediction of scour formation from the model also agrees to the fact that the initiation of scour started to happen at the point of the stern and bow of the wreck. The stern and bow of the wreck are the points where the ADCP data showed the largest variation between the enhanced (from the wreck) flow and the background flow. Initiation of scour formation started immediately when the computation started. Erosion and deposition of  $\sim 0.5$  m was recorded during the 1<sup>st</sup> hour after the discharge reached the expected (modelled from the largest scaled hydrodynamic model; 4 hours after the computation using the coupled model started) levels at the stern and bow of the wreck are presented in [Figure 3.69](#).

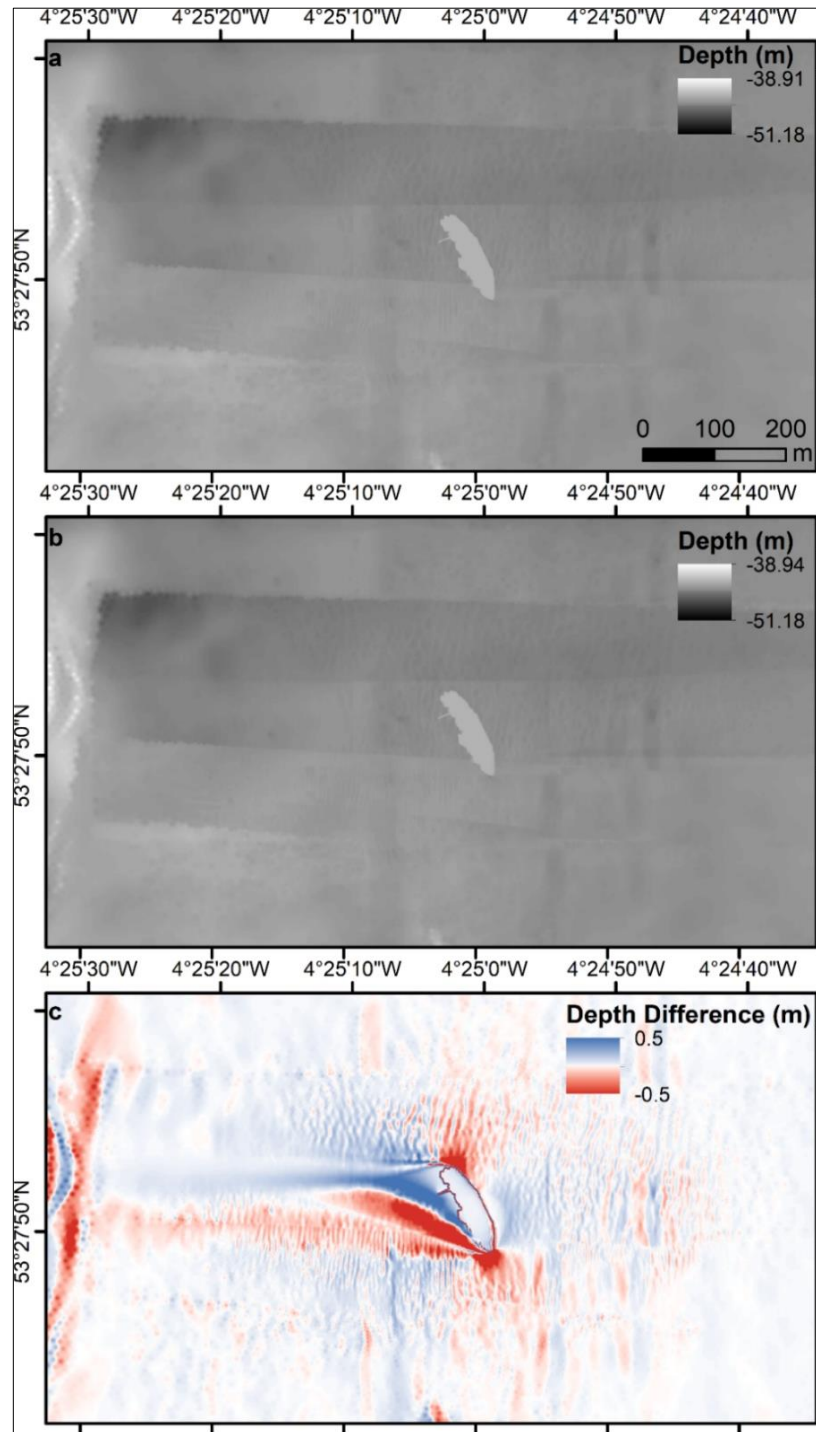


Figure 3.69: a) Initial model conditions, b) seabed after one hour of computation with discharge at expected levels, c) depth difference between the result of the seabed formation after one hour of computation and the initial seabed imported in the model.

The coupled numerical model can not only predict the scour formation, but it can also provide information about the amount of sediment that was mobilised at each node within the computation domain and the way that was transported. [Figure 3.70](#) shows the maximum suspended load transport at plane 2 (a) and bedload (b) transport within the first 8 days of the computation.

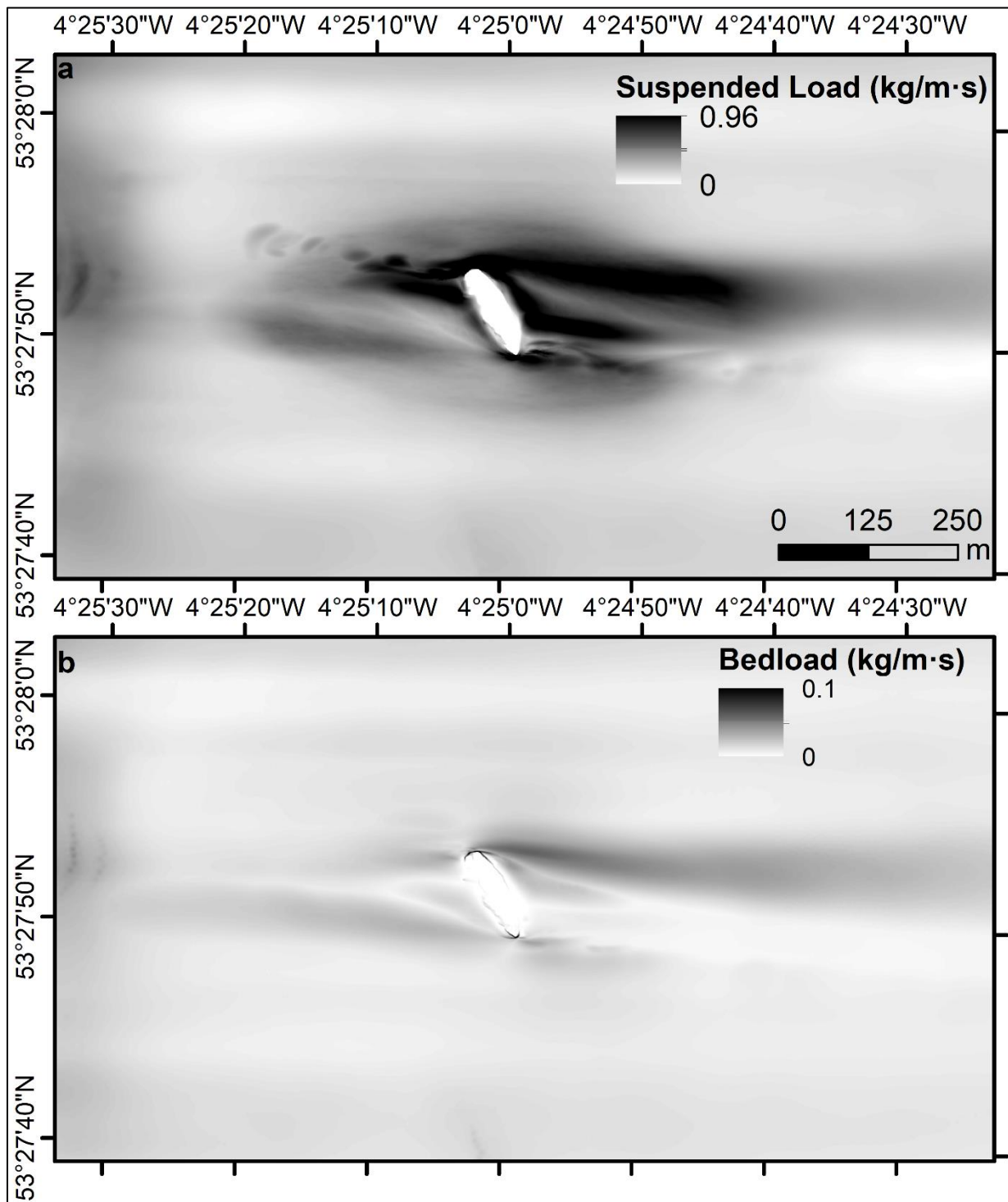


Figure 3.70: a) Maximum suspended load transport at plane 2 (1<sup>st</sup> plane above the bed) and b) maximum bedload transport as modelled from the numerical coupled TELEMAC3D – GAIA model.

The model results presented at [Figure 3.70a](#) show that the maximum suspended load transport is predicted to occur at the depositional features and the northeast and northwest sides of the scour mark whereas the maximum bedload transport (b) exists off the stern of the wreck, towards the east. The results of the BS strength analyses also showed that finer material deposited at the depositional feature, whereas within the scour mark the material is coarser. Suspended load was observed up to the 10<sup>th</sup> plane (~20 m over the seabed) of the computation domain, with maximum concentrations of less than  $1 \text{ kg} \cdot \text{m}^{-1} \cdot \text{s}^{-1}$ .



The computation started with the sand fraction being at 22% of the layer's thickness (10 m), but it has been observed that the first layer has completely eroded within the scour mark. The Soulsby (1997) formulae, as explained in Section 3.3.3 did not predict sediment mobilisation of the coarser fraction at the maximum observed flow velocities. However, the numerical model showed mobilisation of the coarser fraction, as erosion happened over the 2.2 m (22%) covered by the fine sediment, meaning that the hiding-exposure effect included using the McCarron et al., (2019) correction worked, and the exposed larger grains were mobilised.

As mentioned in Section 3.2.6, the turbulent kinetic energy (TKE), measured in Joules/Kg (J/kg) at plane 2 (1<sup>st</sup> plane above the bed) was used in the calculation of the bed shear stress. Figure 3.71 shows the maximum values of TKE observed at plane 2 during the first 8 days of the computation. As expected, the maximum values are present at the deepest points of the scour marks and at the stern and bow of the wreck and are as high as 0.067 J·kg<sup>-1</sup>. TKE values at the surrounding area were less than 0.005 J·kg<sup>-1</sup>. As expected, the adaption of the immersed boundary method did not allow TKE formation within the nodes covered by the wreck.

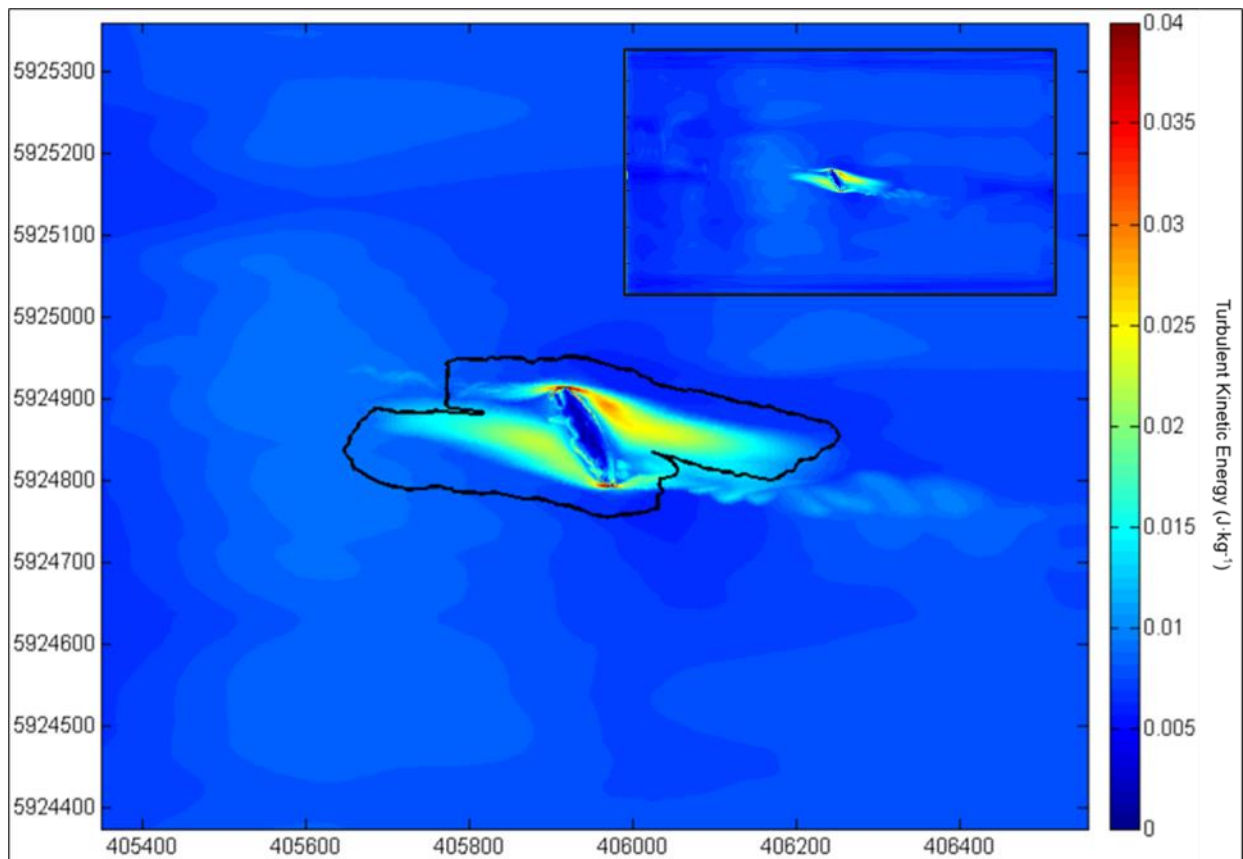


Figure 3.71: Maximum modelled turbulent kinetic energy values within the first 8 days of computation from a flat bed, using the coupled TELEMAC3D - GAIA model.

### 3.4 Discussion

#### 3.4.1 The role of bedforms near the SS Apapa site

Bedform formation can be categorised as part of the scour mark (Whitehouse, 1998; Quinn & Smyth 2018). Migrating with an average migration rate of  $7.2 \text{ m}\cdot\text{y}^{-1}$ , the bedforms at the NW of SS Apapa are responsible for the variations of the lateral changes of the scour mark geometry. The erosion and deposition of the surrounding area were the factors that caused uncertainties when trying to delineate the scour edge for each survey. However, the first large sandwave at the NW part of the scour mark was chosen to limit the scour edge's extent (Figure 3.42). Migration of the bedform meant variation on the lateral extent of the scour mark. Therefore, the surface area covered from the scour was highly impacted by that migration (Figure 3.41; Figure 3.42). During the 2014 surveys, the first large bedform (from the wreck) exists further west, increasing the surface covered by the delineated scour edge (Figure 3.42). On the other hand, during the disintegration of the wreck, the first bedform migrated eastwards, something surprising as it migrates at the reverse direction than the general migration direction observed over the 9 years of the repeat surveys over the SS Apapa site. In general, ripple sized bedforms (Carling, 1999; Kleinhans et al., 2002) were observed in the surrounding area, with the exemption of the large sediment waves at the NW and the one large at the south side of the wreck. The sand waves migrate perpendicular to their crests and in the direction faced by the steep lee side of the sand wave. Also, the sand wave migration rates are indicative for the sediment transport processes in the residual (dominant) tidal direction (Van Landeghem et al., 2012). Following the schematic of Van Landeghem et al. (2012); Figure 3.72, the wave characteristics of the 7 largest bedforms were attained from the March 2018 and June 2019 DEMs and are presented in Figure 3.74.

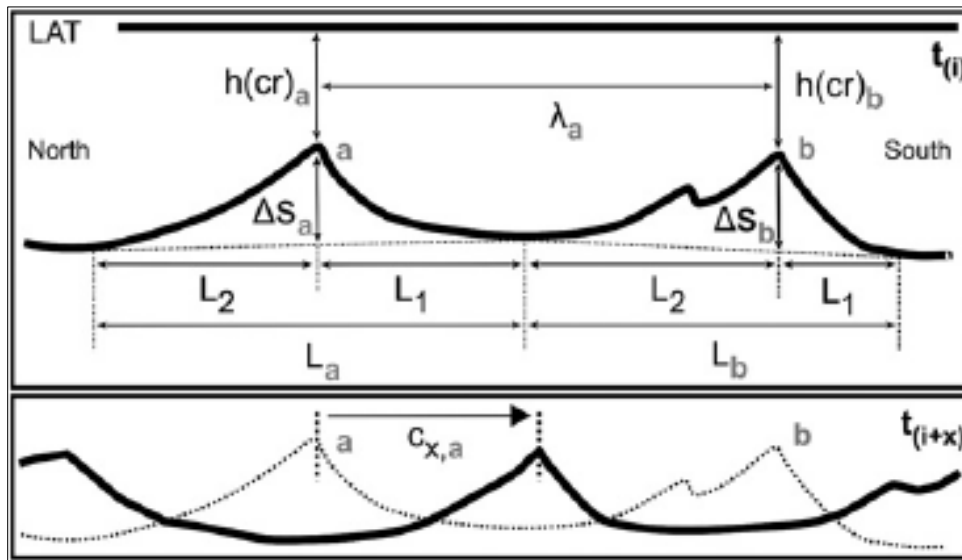


Figure 3.72: Schematic representation and definition of the sediment wave characteristics from Van Landeghem et al. (2012). 'a' and 'b' are two sediment waves.  $h_{(cr)}$  is the water depth at the crest;  $\Delta S$  is the sediment wave height;  $L$  is the sediment wavelength (and Length components  $L_1$  and  $L_2$ ) derived from sediment wave trough spacing;  $\lambda$  is the crest wavelength;  $t_i$  is the time of the first bathymetric survey and  $c_x$  is the displacement of the sediment wave crest over time interval  $x$ .

Figure 3.73 presents the 2-D profile drawn over the sediment waves to identify the bedform characteristics between the 2018 and 2019 surveys.

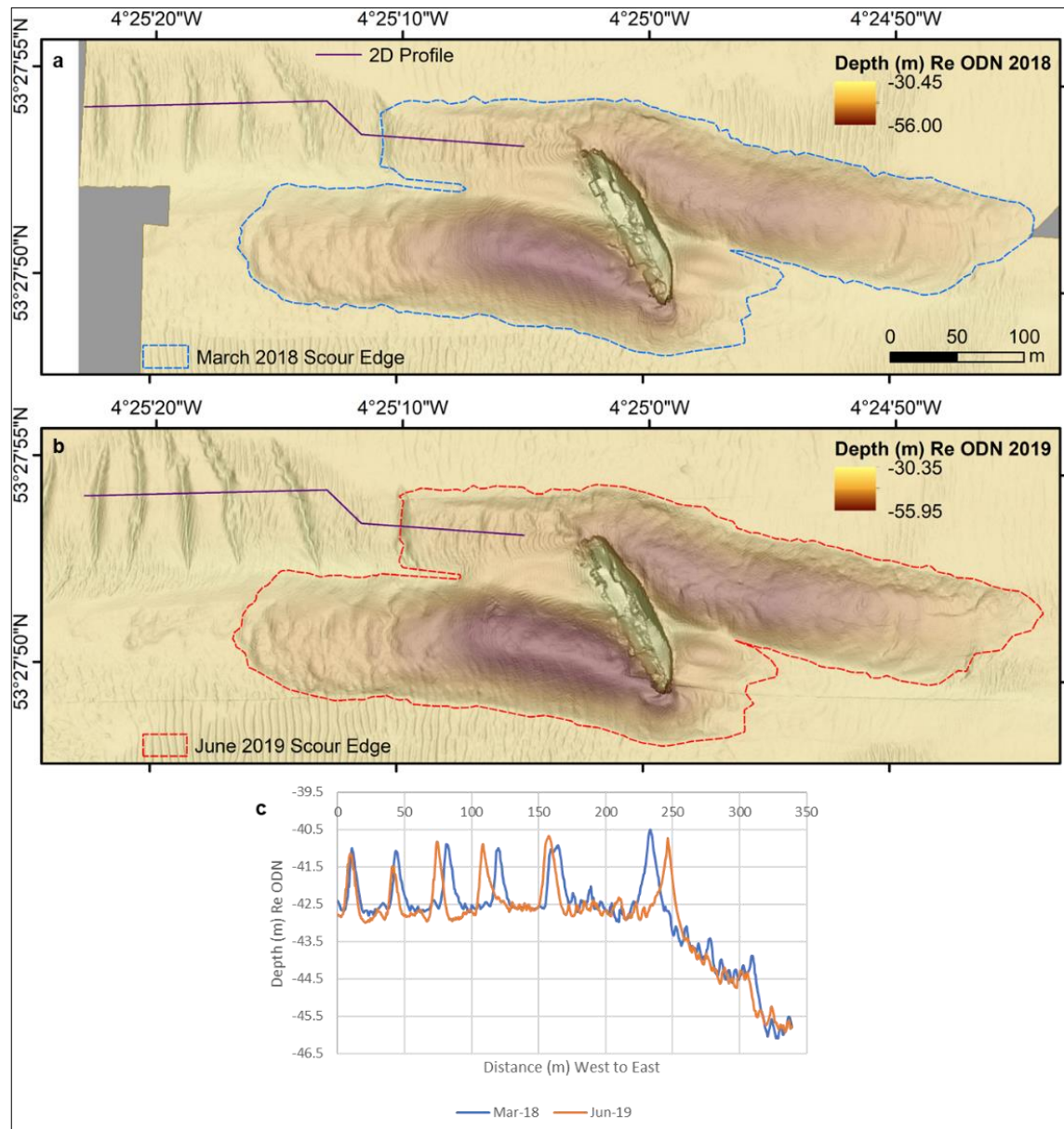


Figure 3.73: 2-D profile over the large bedforms observed at the NW part of the SS *Apapa* scour mark; on the March 2018 DEM (a), on the June 2019 DEM (b) and c the 2-D profile plotted for the two surveys providing bathymetric information.

Except for the 2018 to 2019 period, the migration direction of the sand waves observed from all the surveys around SS *Apapa* is westwards (Figure 3.46). In contrast, in the 2019 DEM, the bedform used for the delineation of the scour edge (bedform number 6 on Figure 3.74) migrated eastwards. Using the 2018 DEM, the asymmetry of the bedform is calculated at 0.067 where the bedform asymmetry using the 2019 DEM is calculated at 0.091. The bedform migrated 12.43 m to the east between 2018 and 2019, (migration rate of  $9.65 \text{ m} \cdot \text{y}^{-1}$ ). In Section 3.4.2 the filling of the NW part of the scour mark with sediment will be discussed and the reversed migration of the bedform could have possibly explained the observed deposition of sediment. However, the height of the bedform increased from 2.1 m in 2018 to 2.4 m in 2019, meaning that there was no sediment loss from the

bedform itself. **Figure 3.74** presents the sediment waves used for the analyses (only the 7 largest) and their migration direction.

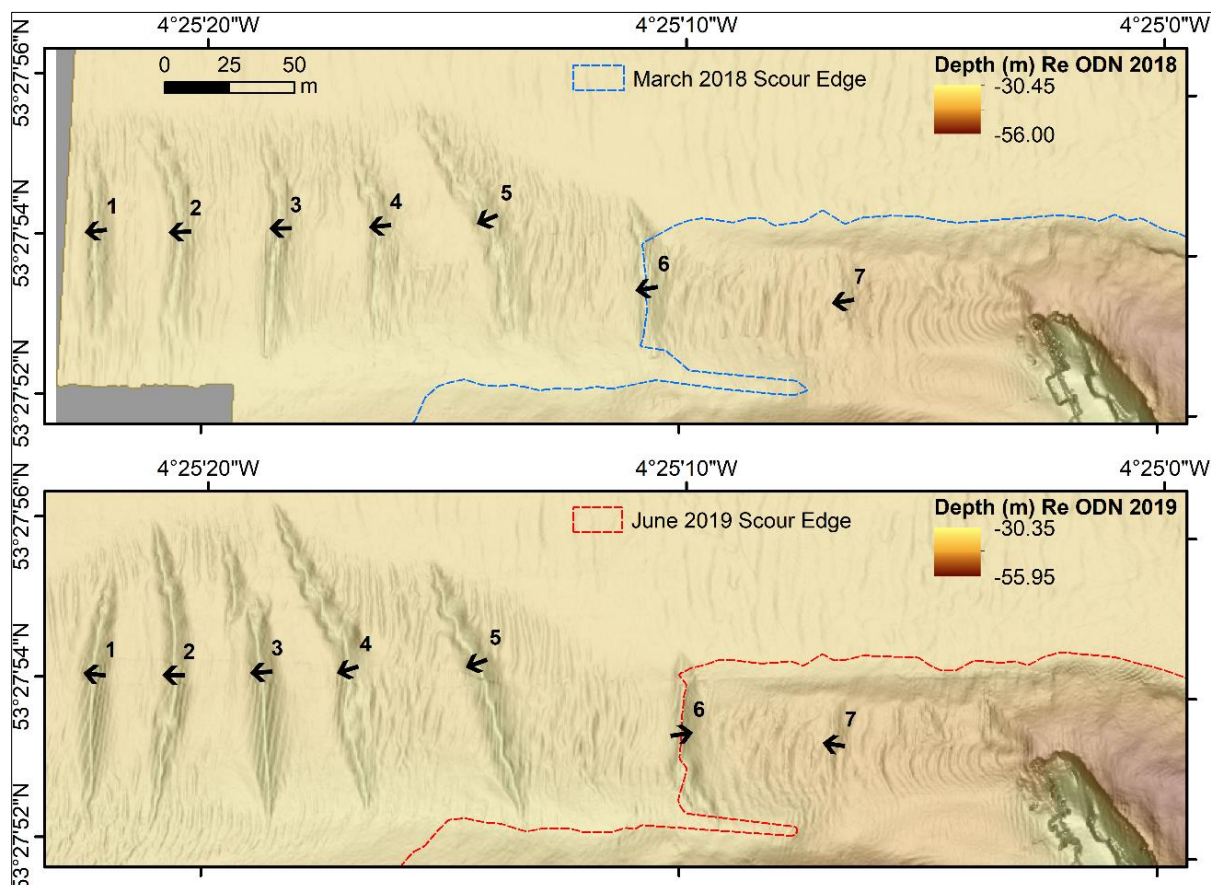


Figure 3.74: Bedforms used for the bedform characteristic calculation numbered on the 2018 and the 2019 DEMs. The arrows are showing the migration direction of the bedform (from the north).

The accompanied **Table 3.5** details the sediment wave characteristics, asymmetries, and migration rates of the large bedforms observed at the NW part of the SS *Apapa* scour mark.

Table 3.5: Detailed sediment wave characteristics for the 7 Large sediment waves at the NW part of the SS *Apapa* scour mark, calculated using the **Van Landeghem (2012)** method.

Bedform Number	Mar-18								Jun-19								2018 to 2019	
	Crest Depth (h) (m)	Crest position (m)	Crest Height (ΔS) (m)	Lee Slope Length (L1) (m)	Stoss Slope Length (L2) (m)	Trough length (L1+L2) (m)	Sand Wave Asymmetry (A=(L2-L1)/L) (m)	Migration Direction (°) from North	Crest Depth (h) (m)	Crest position (m)	Crest Height (ΔS) (m)	Lee Slope Length (L1) (m)	Stoss Slope Length (L2) (m)	Trough length (L1+L2) (m)	Sand Wave Asymmetry (A=(L2-L1)/L) (m)	Migration Direction (°) from North	Migration (m)	Migration (m/yr)
1	-41.04	14.93	1.70	6.47	8.46	14.93	0.13	263.69	-41.18	14.43	1.80	9.76	10.45	20.21	0.03	276.55	0.50	0.39
2	-41.02	47.77	1.65	5.97	10.45	16.42	0.27	267.37	-41.37	45.29	1.55	5.98	8.46	14.44	0.17	270.00	2.48	1.93
3	-41.04	86.09	1.60	5.97	8.96	14.93	0.20	269.30	-40.92	78.63	2.05	7.47	9.45	16.92	0.12	266.62	7.46	5.79
4	-41.22	123.35	1.50	5.95	10.75	16.70	0.29	264.09	-40.76	112.43	2.00	7.95	6.45	14.40	-0.10	252.66	10.92	8.48
5	-40.97	160.60	1.63	4.95	13.86	18.81	0.47	247.23	-40.66	159.12	2.09	9.91	12.87	22.78	0.13	249.66	1.48	1.15
6	-40.59	17.97	2.10	10.48	11.98	22.46	0.07	260.59	-40.66	30.40	2.40	11.44	13.74	25.18	0.09	81.42	-12.43	-9.65
7	-43.88	93.32	1.00	2.99	11.48	14.47	0.59	260.59	-44.33	89.83	0.55	1.50	4.99	6.49	0.54	278.16	3.49	2.71

**Van Landeghem et al. (2012)**, have also observed reversed sediment wave migration in the Irish Sea but the exact reason for their cause remains unknown. Nevertheless, migration rates and characteristics of bedforms in an open environment are expected to be different than the bedforms



discussed in the present study, caused by the enhanced forces acting on the bed due to the existence of an obstacle.

It is also important to mention that the bedforms starting from *SS Apapa* lead to a large field of sand waves to the west, but it is uncertain at this stage if the existence of *SS Apapa* is able to cause the driving forces for the generation of those large bedforms.

The difference in the observed BS strength values between the crests and troughs of the sand waves was also investigated using the 2019 BS strength mosaic (Figure 3.75). Even on a complex, mixed coarse bed environment with the presence of smaller bedforms it can be observed that the crests are finer (lower BS values) where the troughs consist of coarser sediment (higher BS values).

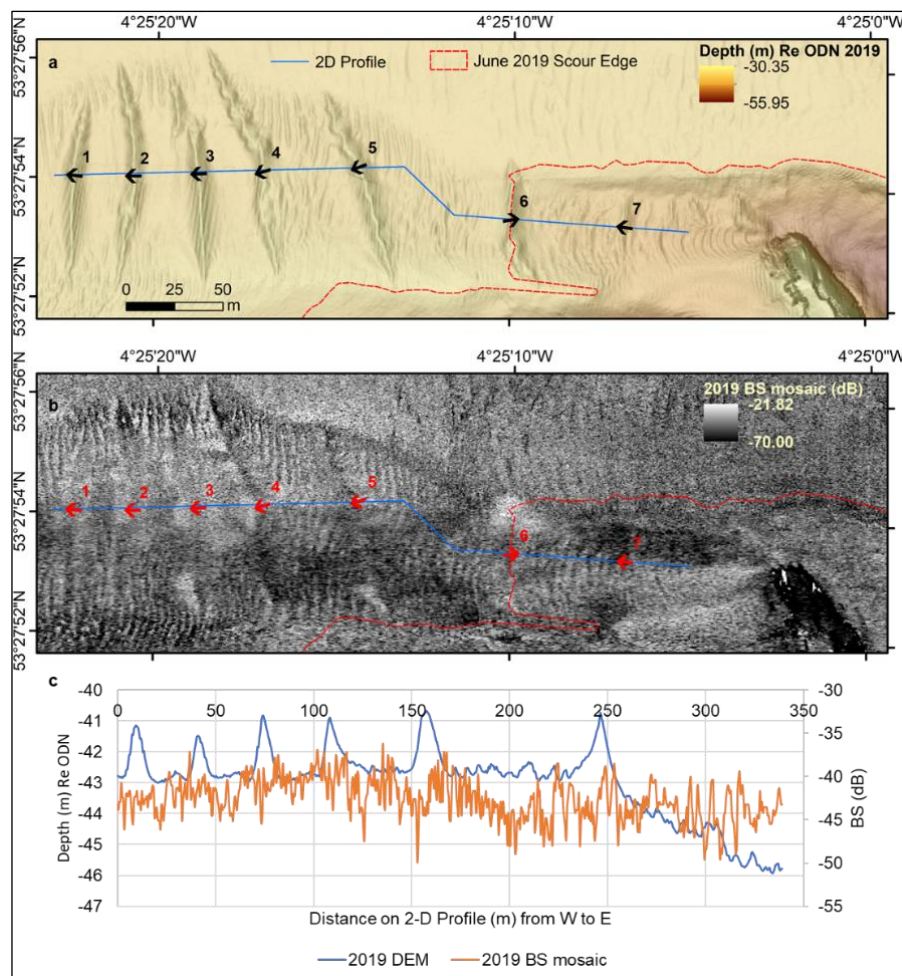


Figure 3.75: Comparison between the bathymetry (a) and backscatter strength values (b) over the bedforms from the June 2019 data collection. The plotted 2-D profile shows the variation in BS strength values at the crests and troughs of the bedforms.

The deviation between the sediment observed at the crests and troughs of the sediment waves was expected and was also explained by previous studies (Allen, 1984). As Figure 3.76 explains graphically (Allen, 1984), the coarser material deposits at the lower part of the lee slopes (troughs) where the finer material rolls (or suspends) and deposits on the stoss side of the following bedform.



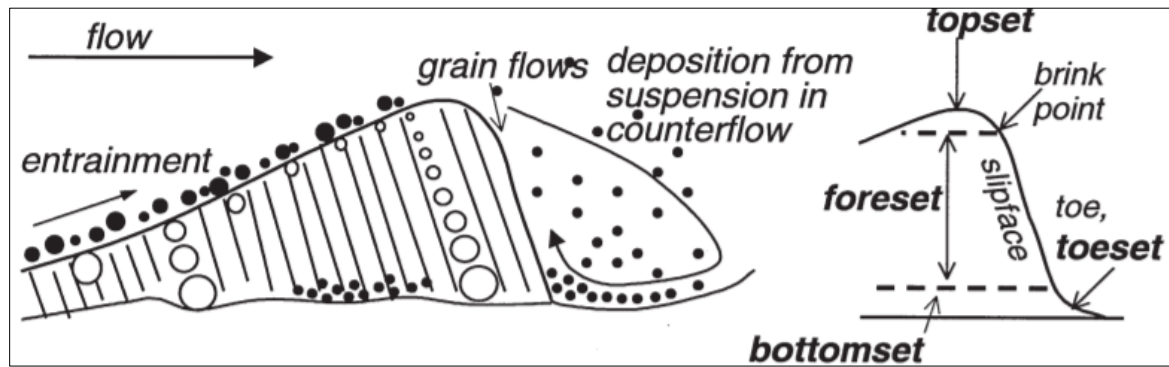


Figure 3.76: Explanation of sediment movement and migration on mixed sedimentary beds (Allen, 1984).

The migration direction of the large bedforms at the SS *Apapa* site, are reversed when compared with the dominant bedload transport in the Irish Sea, as investigated by Van Landeghem et al, 2009 (Figure 3.6), who have observed an eastwards migration direction, at an obviously much larger scale. The SS *Apapa* site is a localised, more complex area due to the existence of the wreck and the subsequent enhanced forces. The bedforms present around the SS *Apapa* site cause flow enhancement by up to a factor of  $\sim 1.7$  when comparing the mean depth averaged flow velocities observed at the bedforms and the mean background flow far downstream of the wreck (Figure 3.77).

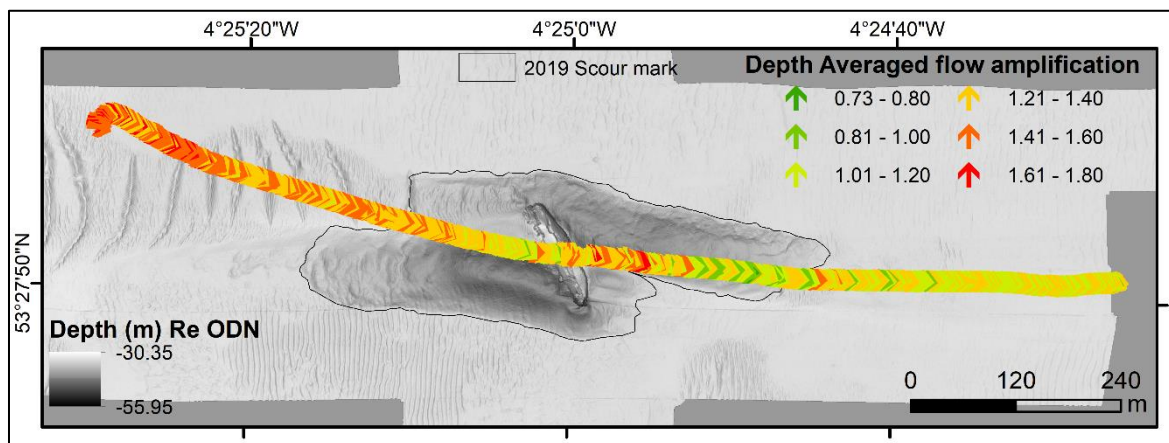


Figure 3.77: W-E transect showing the depth averaged flow amplification at the bedforms upstream of SS *Apapa* during flooding (eastwards tidal current), flow over the bedforms is amplified  $\sim 1.7$  times in the present example when compared with the depth averaged background flow (at the far field, on the east of the wreck).

Flow amplification around bedforms was expected (Holmes and García, 2008; Trembanis et al., 2011), with a reduction of bed velocity at the stoss side of the bedforms and an increased bed velocity at the lee side of the bedforms (Nelson et al., 1993). The enhanced flow entering the SS *Apapa* site can possibly be linked with the mean extent of the NE scour mark, that appears to be 10m or (3%) longer than the mirroring SW scour mark, as the enhanced flow from the bedforms enhances even more when reaching the wreck, possibly causing a longer scour mark. The observed 'zones of influence', generated from the analyses of 2-D profiles following features at the difference maps between the consecutive surveys, also showed a larger influence at the east part of the scour mark, with the second zone observed at 135 m at the east part, instead of 113 m at the west part of the scour mark.

### 3.4.2 Scour defined by bed composition

The bed composition and the bimodality of the sediment at the *SS Apapa* site is a dominant parameter influencing the scour geometry along with the hydrodynamics of the area. The hydrodynamic forces and the subsequent scour around *SS Apapa* influence the bed composition. Comparison of the standard deviation map of the bathymetry from the MBES datasets and the standard deviation map from the BS values observed between the surveys (Figure 3.78), show similar trends. For the comparison, the 2019 survey was not included in the calculations, as due to the disintegration/shifting of the wreck, the dynamics of the area changed, changing the trends observed until 2018.

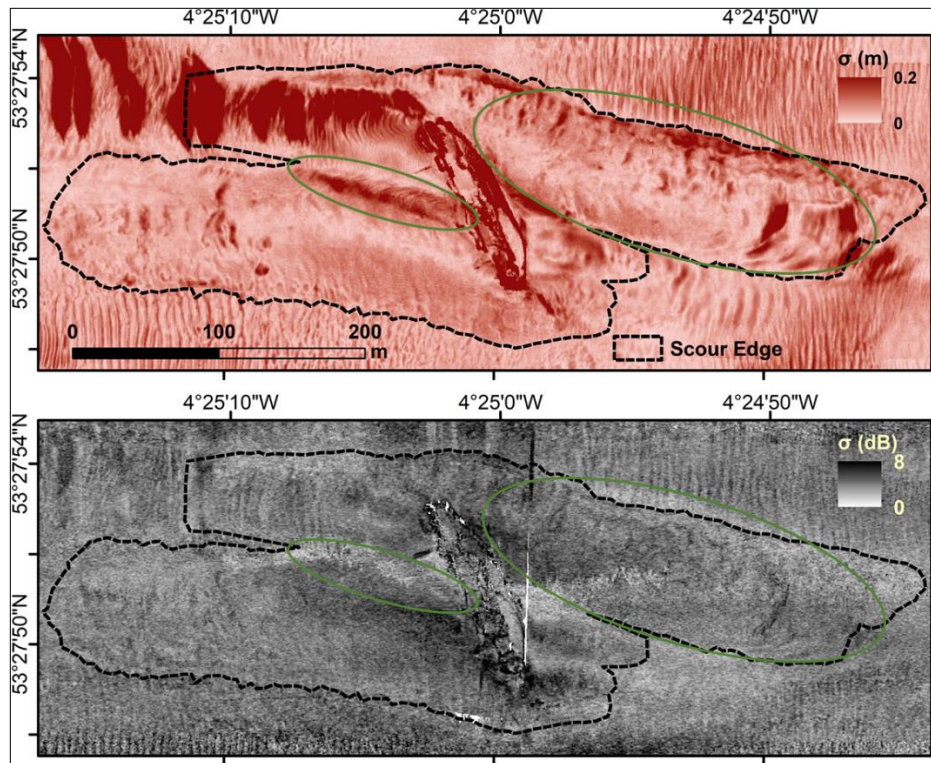


Figure 3.78: Standard deviation ( $\sigma$ ) calculated using the bathymetric surveys and the BS strength mosaics with the 2019 DEM not included in the calculations. The marked areas (with green) represent the areas where the two  $\sigma$  values (BS strength and bathymetry) provide information about large mobilisation over the years as the sediment remained fine.

Figure 3.78 shows the depositional features at both sides of the wreck appear to remain fine, but these features are the most variable in bathymetry during the years along with the bedforms (as expected due to their migration). BS  $\sigma$  also shows large variations in bed composition at the deepest points of the scour mark, where the  $\sigma$  of bathymetry shows less variation over time. The numerical model estimations for the maximum bedload and suspended load transport at the area also come to confirm these observations, as the maximum suspended load transport is present at the depositional feature where the maximum bedload transport happened within the scour marks (Figure 3.70). The analyses of the results, however, showed that the coarser sediment was also mobile, at flow speeds that according to Soulsby (1997) formulae it was expected to be immobile. The coarser fraction sediment mobilisation comes to confirm the fact that in mixed coarse beds, such as sand and gravel

mixtures, due to the hiding-exposure effect, the exposed larger grains will require less shear stress to mobilise (McCarron et al., 2019).

When investigating the BS strength mosaic from the 2019 survey but also the unsupervised and supervised classification, it can be observed that finer sediment is generally located at the scour mark edges (lower backscatter strength), where coarser sediment is present at the deepest points of the scour mark. Quinn et al. (2016), mention that when scour occurs, fine-grained sediment is moving away from the area in suspension (present at the depositional feature in this study), leaving the seafloor with not enough sediment for backfilling, where coarser material also deposits in the scoured areas.

### 3.4.3 Disintegration of SS *Apapa* changing erosion and deposition

The standard deviation map of bathymetry shows an obvious variation between the 2019 bathymetric DEM and the prior to 2019 bathymetric DEMs, confirming the large disintegration that happened between March 2018 and June 2019. When the 2019 DEM was included in the calculation of  $\sigma$  (Figure 3.79b), a variation of up to 0.2 m appeared within the NW part of the scour mark, that was not present in the seabed level  $\sigma$  (of bathymetry) DEM calculated without the inclusion of the 2019 bathymetric dataset (Figure 3.79a). The  $\sigma$  of bathymetry DEM difference, confirms that this depositional area was absent from any of the prior to 2019 bathymetric datasets (Figure 3.79c).

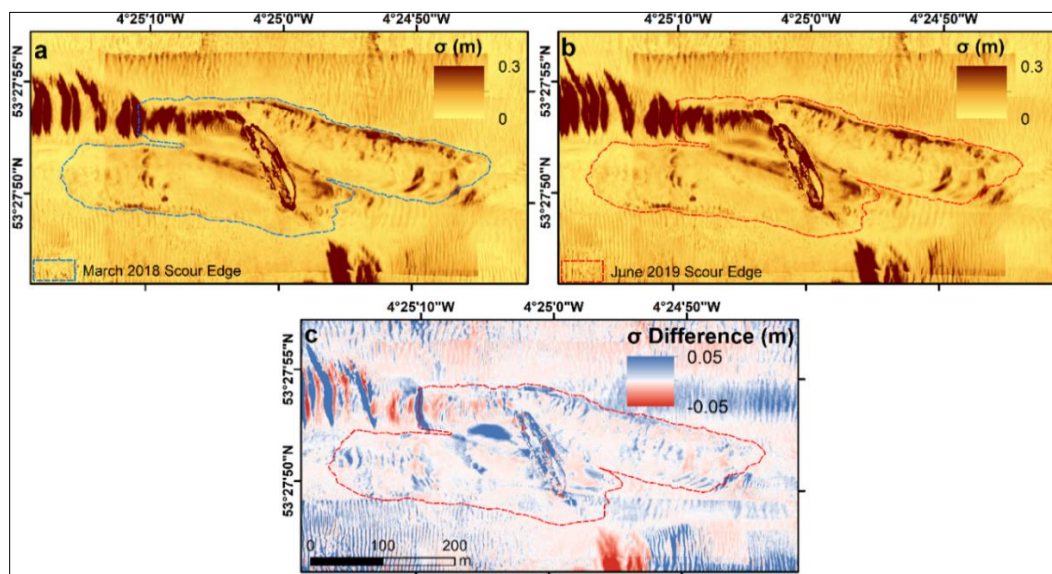


Figure 3.79: (a) Standard Deviation map of bathymetry from 11 surveys (June 2019 survey not included), (b)  $\sigma$  map of bathymetry from 12 surveys (June 2019 survey included) and (c) Difference map of  $\sigma$  calculated including the June 2019 survey and not including the June 2019 survey.

The difference map in Figure 3.80, shows that the wreck has either disintegrated, shifted, or both disintegrated and shifted. The wreck on the 2019 DEM appears 7.8 m deeper at the west side (-6.06 m annualised variation) and 7.39 m shallower on the east side (5.4 m annualised variation). Disintegration of wrecks at this age has been observed in the literature and especially at wooden wrecks due to physical, chemical, and biological processes (Muckelroy, 1978; Ward et al., 1998). Steel wrecks such as SS *Apapa* are expected to last longer to these conditions, where chemical



disintegration (corrosion) will be dominant and the disintegration would be as rapid as sulphate – reducing bacteria permit (MacLeod, 1993; Ward et al, 1998).

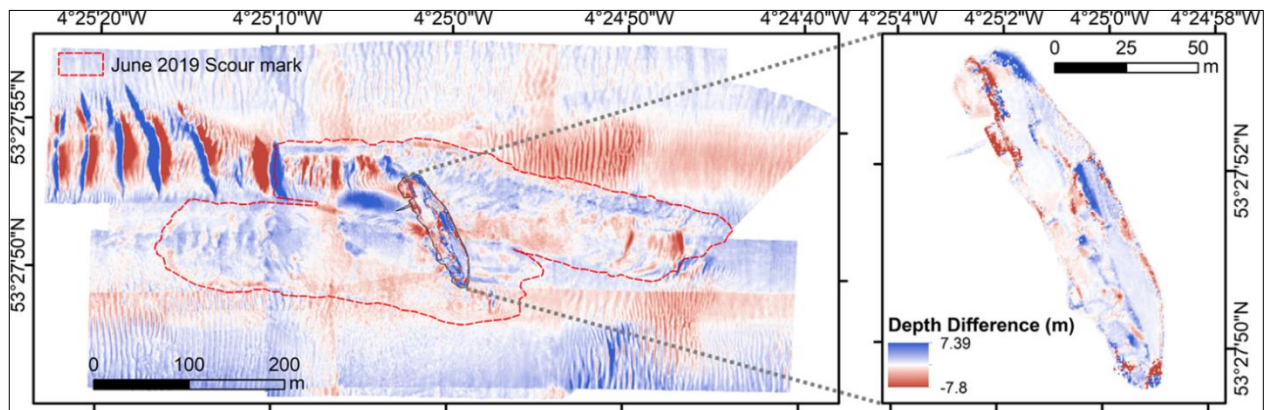


Figure 3.80: Depth difference between the March 2018 and June 2019 DEMs and a zoom in to the variation at the wreck itself.

However, although chemical disintegration is expected to be dominant, biological colonisation of steel wrecks has also significant contribution on their disintegration (MacLeod, 2016). The aforementioned studies focus on the significance of the disintegration from an archaeological perspective and especially at the protection and management of the cultural heritage (Heldberg et al., 2004). The disintegration or shifting of the wreck has changed in a small degree the orientation of the wreck to the flow. It has also increased the exposure of the wreck to the flow especially at the NE and E sides of the wreck, changing the exposed width to height (W:H) ratio of the wreck, a controlling parameter of the scour formation (Whitehouse, 1998; Saunders, 2005; Quinn, 2006; Lambkin et al., 2006). These changes on the wreck changed the hydrodynamics, the forces acting on the bed in the area and have subsequently changed the bed composition. The variation in the hydrodynamics of the area changed the prior to 2019 observed shear stress pattern acting on the bed, changing the observed erosion and deposition rates. The hydrodynamic and bed dynamic processes, at the area, are expected to continue evolving, until the area reaches a new dynamic equilibrium point, where the new placement of the wreck will already be once again part of the system (Whitehouse, 1998; Zhang et al., 2017).

The change in the forces acting on the bed between the two surveys, is also present at the BS strength mosaics of the two datasets, as they show a variation of the bed composition. The 2018 BS strength mosaic show low (fine sediment) BS strength at the depositional feature, the north and south edges of the scour mark and the wreck itself (Figure 3.81a). On the 2019 BS these features are not obvious (Figure 3.81b) and the bed surrounding the wreck appears to be all mixed and coarse. Also, the area where sediment was deposited, appears to have coarse sediment in the 2018 BS mosaic, where in the 2019 BS mosaic the same area appears to have medium strength (mixed sediment). As a comparison, the unsupervised classification of the two surveys presented in Figure 3.81a<sub>i</sub> and Figure 3.81b<sub>i</sub>. The  $\sigma$  (of BS strength) maps when the 2019 BS strength mosaic was and was not included on the calculation of the  $\sigma$  values are also presented in Figure 3.81c and 3.81d respectively.

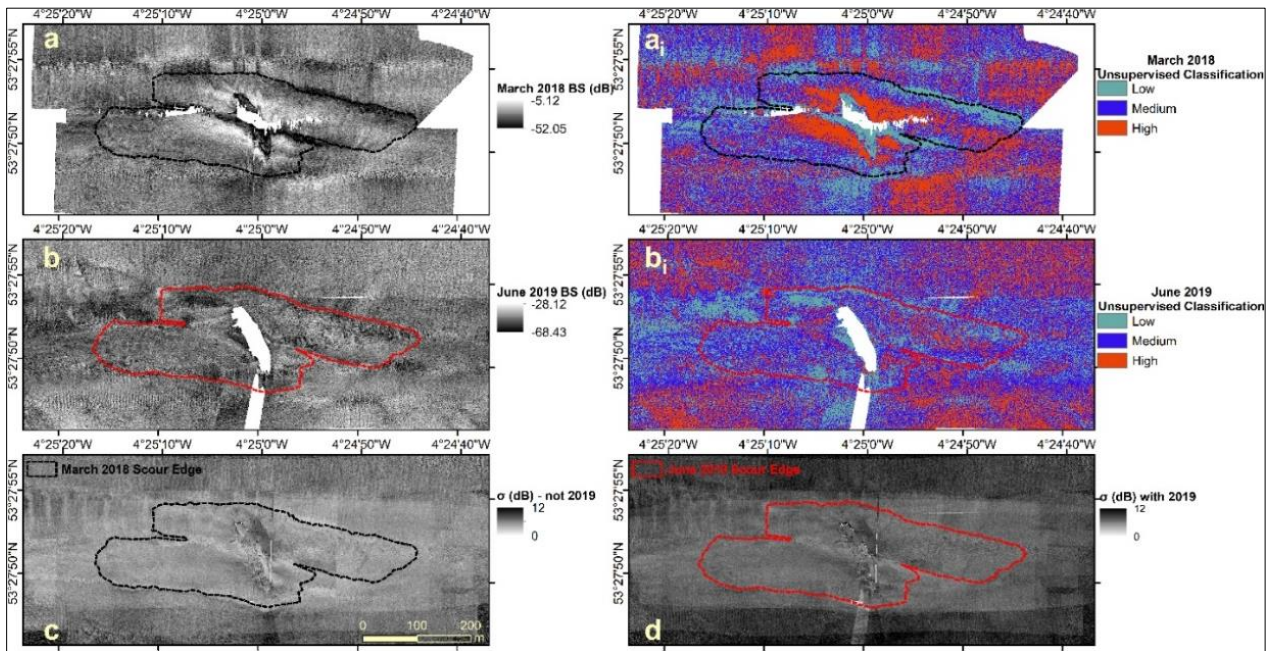


Figure 3.81: The 2018 BS strength mosaic (a) and its unsupervised classification (a<sub>i</sub>), 2019 BS strength mosaic (b) and its unsupervised classification (b<sub>i</sub>), the BS strength  $\sigma$  calculated not using the 2018 BS strength mosaic (c) and the BS strength  $\sigma$  calculated using the 2019 BS strength mosaic in the calculation (d).

The present study shows the importance of wreck's disintegration not only for archaeological purposes, but also for seabed management, as it can change the bed composition, erosion, and deposition of the area. A wreck sitting on the seabed for over a century disintegrates and it is to this stage unsure how the wreck, but also the surrounding environment will be in the future, but also how the scour mark around it will form and evolve responding to the wreck's changes.

#### 3.4.4. Numerical modelling of the SS *Apapa* site using a coupled TELEMAC 3D – GAIA model

The numerical model predicted well the flow velocities at the site for the first 11 hours of the computation with discrepancies between the modelled and measured (using the ADCP) instrument flow velocities being mainly within 3-15%. Variations up to 50% were also noted during slack tides, but this is because even the smallest variation at low values of flow velocity appeared to be significant. It can be therefore assumed that the input of flow velocity using discharge, (described in Section 3.2.6) was suitable for this modelled case. In addition, the way the wreck was treated in the computation domain (exposure, placement on flat bed etc.), but also the sediment grain sizes seemed to represent well the site (when the wreck sank) for the numerical modelling work. It can be argued that sediment sizes used in the numerical modelling work were not ideal and that sediment sizes should have been taken from the grabs at undisturbed (away from the scour mark) site. It is however believed that this top sediment layer was eroded within the first few tidal cycles, when scour occurred (Harris et al., 2010). In addition, the coupled numerical model predicted well the scour length, with underestimation of less than 2.6%. The predicted (from the coupled numerical model)



scour mark was of similar shape (with some discrepancies at the NW part) to the scour mark observed offshore, showing that all the parameters used, and the set-up of the model was appropriate for this study. The numerical modelling work was also used to test some hypothetical scenarios presented in Chapter 5 where this work is also further discussed.

### 3.5 Conclusions

In this chapter, the aims were to investigate and understand:

- i) The impact of an irregularly shaped object (wreck of SS *Apapa*) to the hydrodynamics of the area;
- ii) the impact of the sediment bimodality at the erosion and deposition rates and identification of the more mobile sediment and
- iii) the correlation between the enhanced diverted flow caused by the existence of the wreck to the surrounding mixed coarse bed

These aims were completed by investigating the hydrodynamics around the wreck of SS *Apapa*, using a flow velocity and direction dataset, from a vessel mounted ADCP instrument on a survey conducted over two full tidal cycles over the wreck. A depth averaged flow velocity increase of up to a factor of 2.3 than the background flow was observed downstream of the wreck. Flow deviation of up to 90° was also observed over (and downstream) of the wreck and within the scour mark. The maximum disturbance of the flow appeared at the stern and bow of the wreck. Hydrodynamic analyses of the area were conducted using a hydrodynamic numerical model (TELEMAC 2D/3D) and comparison was presented between the ADCP dataset and the hydrodynamic model. The comparison of the depth averaged flow velocities showed that there was a good correlation between the model outputs and the ADCP measurements, as for 80% of the data population the variation in the measured and computed flow velocities was less than 15%.

The bimodality of the sediment and its impact to the erosion and deposition was also investigated and it was observed that coarser material (characterised as gravel), although expected not to be mobile, using Soulsby (1997) formulae for critical sediment transport, was at cases more mobile than the finer material, at similar flow speeds, especially below  $1.75 \text{ m}\cdot\text{s}^{-1}$ . Finer sediment was observed at the depositional feature and at the bedform crests where the coarser material was observed at the deepest points of the scour mark and the bedform troughs. Analyses of bathymetric changes (between consecutive bathymetric datasets) using 2-D profiles identified two consistent 'zones of maximum bed mobility' at the west and east sides of the wreck.

The comparison of the enhanced diverted flow caused by the existence of the wreck to the surrounding mixed coarse bed showed that the drop in seabed change at the ends of the 'zones of maximum bed mobility' agreed with the observations of the reduction of the depth averaged flow speed recorded from the ADCP instrument. At the end of these zones, a reduction of up to 35% of the depth averaged flow speeds was observed when compared to the background flow. The coupled numerical hydrodynamic and sediment transport model (TELEMAC3D – GAIA) showed good

corelation of less than 1% at the estimation of the scour extent for the NE and SW parts of the scour marks. The inclusion of the HE formulae (McCarron et al., 2019) improved the ability of the coupled model to predict scour formation more accurately at mixed beds, as coarser sediment that was expected not to be mobile (when on a uniform bed), was mobilised once mixed with finer material. The shape of the object is no longer a limiting parameter, as with the adaption of the immersed boundary method (Yin et al., 2016), differently shaped objects can be used and the hydrodynamics and bed dynamics around them can be modelled.

## Chapter 4

### 4. How the effective transport of sedimentary beds composed from different sand/gravel mixtures defines the scour development around a cylindrical object – Laboratory experiments

#### 4.1 Introduction

In Chapter 3, seabed evolution around the SS Apapa site was assessed. The impact of the object on the hydrodynamics was quantified, and the impact of sediment bimodality on erosion and deposition rates investigated. Key observations include:

- i) Flow diversion occurs around the wreck, and flow amplification is observed at the bow and stern up to 2.3 higher than the undisturbed incoming flow.
- ii) Amplified flow is observed up to 311 m downstream of the wreck.
- iii) The lateral extent of the scour mark varied 1-2 m over the last decade, where the depth in the scour mark varied ~0.5 m, with sediment moving through the site.
- iv) Two 'zones of maximum bed mobility' were defined from difference-modelling, located 37 m (E) and 43 m (W) of the wreck and the second at 113 m (W) and 135 m (E) of the wreck. In the areas where a decrease in the erosion/deposition rate is observed, a corresponding drop in the depth averaged flow velocity (up to 35% when compared with the upcoming undisturbed flow) is noted.
- v) Interpretation of sediment and backscatter data suggest that coarse bimodal sediments not predicted to be mobile using the Soulsby (1997) formulae, are in fact mobile.
- vi) The disintegration and shifting of the wreck between 2018 and 2019 altered the hydrodynamics of the area, changing the subsequent forces acting on the bed and caused deposition of sediment in areas previously eroding.

Several limitations arose when attempting to model the wreck environment using the numerical model, due to uncertainties in bed conditions when the vessel sank and due to uncertainties in the actual seabed composition at the time of sinking.

In this chapter, the aim is to better understand the processes defining the formation and development of scour around an object using physical modelling, through laboratory experiments. In particular, the influence of bed composition on scour development will be assessed at flow speeds able to mobilise the bed partially or fully. This will address the observation that areas with bimodal sediment that were expected to remain immobile using the Soulsby (1997) formulae in the SS Apapa site, ended up being more mobile than areas with predicted mobility. Bedform formation and development play an important role in the bed dynamics around the object, and therefore feature in this chapter as well. Although not the focus of the overall thesis, current generated ripples formed on mixed

coarse beds (sand and gravel mixtures) are investigated here to help determine and monitor the impact of amplified flow around an object.

Tidal currents are the dominant parameter for scour in most environments (Quinn, 2006) and the morphology and size of the scour features vary depending on the size and the orientation of the obstacle to the flow (Saunders, 2005; Quinn, 2006; Quinn et al, 2016; Quinn & Smyth, 2018). It is also known that rapid scour occurs in the first few tidal cycles (Harris et al., 2010), or in the case of the laboratory experiments, within the first minutes of the introduction of an obstacle to the flow.

Scour formation has been investigated and identified/modelled for objects placed on sandy beds (e.g., Saunders, 2005; Melling, 2014; Smyth & Quinn, 2014; Quinn & Smyth, 2018) or beds that consist of finer material like mud (Sumer et al., 2007). Seabed dynamics around objects sitting on mixed and coarse beds (sand and gravel mixtures) are difficult to understand and model, both due to uncertainties in flow dynamics and sediment transport. In mixed coarse beds, sediment transport can depend on fractional transport, mixing and sorting through transport, winnowing, and armouring and hiding and exposure (Wilcock & McArdeell, 1993). The transport of mixed sediments leads to the generation of bed surface grain distribution that differs from the initial type of the seabed. Fractional transport is the transportation of a specific grain sized sediment due to the incoming forces, and the interaction of the seabed configuration and the sediment transport (Wilcock & Southard, 1989). In sedimentary beds consisting of sediments with similar sized grains, the sediment flux is controlled by the absolute grain size of bed composition. In contrast, in sediment beds consisting of mixed sediments, the different sediment fractions within the mixture act uniquely with the flow, resulting in a 'selective entrainment', causing issues when trying to estimate sediment transport (McCarron et al., 2019). The term 'selective entrainment' is widely referred to and known as the 'hiding-exposure effect', since the smaller grains are hidden behind the larger, exposed to the flow grains. In Figure 4.1 for example, particle  $d_j$  is completely exposed to the flow, as there are no other particles upstream, where particle  $d_i$  is 'protected' or hidden by particle  $d_j$  and it is less exposed to the flow. The finer sediment grains (grain  $d_f$ ) within the mixture are completely hidden within larger grains, needing more force to set into movement.

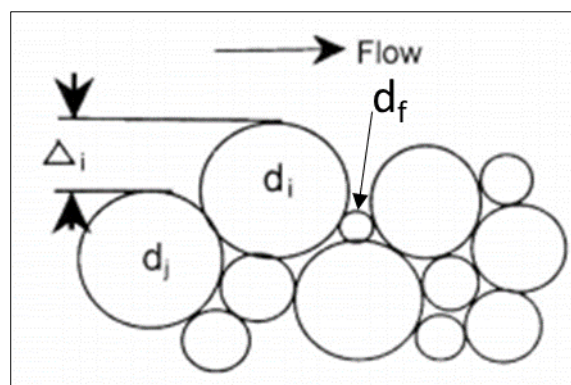


Figure 4.1: Schematic illustration of the hiding-exposure effect (adapted from Wu et al., 2000).

Traditional sediment transport models use a single representative statistical fraction of grain size (i.e.,  $d_{50}$ ) of the sediment composition for the estimation of sediment transport. Use of the  $d_{50}$  in the

case of sedimentary beds consisting of mixed coarse sediment cannot be ideal, as the  $d_{50}$  value assumes a homogenous grain size distribution and does not account for differences in mobility of differently sized grains. In the case of mixed beds, a hiding-exposure factor is usually added in the traditional equations of sediment transport (e.g., [Egiazaroff, 1965](#); [Wu et al., 2000](#); [Janssen, 2010](#); [McCarron, 2019](#)). It has been shown that in mixed coarse beds, the mobility of fine sediment decreased by up to 75% and the mobility of the coarser sediment increased by 64% in some cases, depending on the ratio of the coarse and fine modes in the sediment mixture ([McCarron et al., 2019](#)). Accurate prediction of the sediment movement of mixed coarse beds can aid resource management and spatial planning of anthropogenic offshore infrastructures ([Stephens & Diesing, 2015](#); [Ward et al., 2015](#)). However, to the author's knowledge, limited studies in the literature have focused on scour formation around objects sitting on mixed coarse beds (sand and gravel mixtures), especially in a controlled laboratory environment that can aid understanding of undermining processes.

#### 4.1.1 Aims and Objectives

There is currently a knowledge gap in the ability to understand bed dynamics around objects sitting on mixed coarse beds. This is mainly due to the so-called hiding-exposure (HE) effect ([Janssen, 2010](#); [McCarron, 2019](#)), that causes uncertainties on the sediment mobilisation of coarse bimodal sediment. These uncertainties are increased when dealing with sediment mobilisation around an obstacle, due to the complex hydrodynamical patterns generated around it and the increase of the bed shear stress by up to a factor of four ([Quinn, 2006](#)). The laboratory work presented in this chapter, does not aim to replicate the offshore, real-world environment of the *SS Apapa* site, but does aim to aid understanding of the processes underpinning seabed evolution around a cylinder placed on different sand and gravel mixtures.

The main aims of this chapter are to assess and quantify:

- i. The impact of the enhanced flow around a cylinder on bed mobility in the wake of the object;
- ii. the impact of the enhanced flow around a cylinder on the sediment composition in the wake of the object;
- iii. the impact of the sediment composition on bed mobility, and
- iv. to update a 3-D numerical model that can accurately predict scour around a cylinder placed on different sand/gravel mixtures.

The objectives to achieve the aims are:

- To monitor bed mobility upstream of the object using ripples generated;
- to quantify the influence of a cylindrical object to the local flow, assessed indirectly by ripple formation, ripple migration and erosion/deposition rates;
- to identify scour mark development in different sand/gravel mixtures;
- to identify changes to sediment composition in different sand/gravel mixtures as the uni-directional flow to the bed alters the bed downstream of the object, and



- to use the controlled laboratory environment data and analyses to inform a coupled hydrodynamic and sediment transport numerical model (TELEMAC3D – GAIA) for the case of the controlled laboratory environment, investigate if the numerical model can predict scour accurately in a much smaller scale, and to test the numerical model's performance on different sand/gravel mixtures.

The methodology of identifying the scour processes around a cylinder in the laboratory environment is described in Section 4.2, followed by the results of the analyses in Section 4.3. A brief discussion of the results is presented in Section 4.4 and a summary of the main conclusions in Section 4.5. An overall discussion in Chapter 5 compares the processes operating around the wreck of *SS Apapa* in the real-world to the processes simulated around a cylinder in the flume-tank experiments.

## 4.2 Methodology of identifying processes around the object in the lab

### 4.2.1 The controlled laboratory environment

The laboratory work described in this chapter was conducted in the flume laboratory, School of Ocean Sciences, Bangor University. The Armfield recirculating flume (Figure 2.7) was used for the experimental work and different sediment mixtures were assessed for comparison of the changes caused by a similar experimental set-up to differently formed sand and gravel beds at two different flow velocities.

The stainless-steel cylinder mentioned in Section 2.3.1 was placed at a 60° angle over the bed in the middle of a 4 m sedimentary bed to replicate the wreck of *SS Apapa* as observed in the offshore environment. The controlled laboratory allows for a precise, constant, linear uni-directional flow to be applied and allows repeatability of experimental runs with similar set-up. For the laboratory work, two flow speeds were used, mobilising only the sand fraction (31 cm·s<sup>-1</sup>) or both the sand and gravel fractions (45 cm·s<sup>-1</sup>) within the mixtures. The flume's pump allowed slow increase of the frequency to the desired, so that the flow becomes steady. The bed composition for each experiment was also changed and a total of 6 sediment (sand and gravel) mixtures were tested (containing 5%, 7.5%, 10%, 12.5%, 15% and 20% gravel). For each experiment, a repeat run was conducted. Experiments were also conducted using the pure sand and pure gravel as controlled beds. The length of the object in the laboratory experiments was less than 1/3 of the flume width and was placed in the middle of the flume to minimise interference from the flume's walls ('wall effect') with the scour formation and associated processes aiming to be monitored downstream of the object.

### 4.2.2 Experimental design

The main focus of this chapter is to monitor the scour development downstream of the object and especially the side of the scour mark in the flume environment that corresponds to the SW component of *SS Apapa* scour mark. The sediment mixtures (using the sediment described in Section 2.3.2) used in the laboratory experiments, were based on previous studies (Gribble, 2018;

Hocking, 2019), aiming to identify the influence of the hiding-exposure (HE) effect (Egiazaroff; 1965; Janssen, 2010; McCarron et al., 2019) to sediment mobilisation of coarse bimodal sediment. Previous studies (McCarron et al., 2019) showed that the maximum influence of the HE effect on sand and gravel mixtures is when the gravel fraction is ~10%. The sand and gravel mixtures used in the experimental work and their associated hydraulic properties are presented in Table 4.1.

Table 4.1: Sand-gravel mixtures used for laboratory experiments and their associated hydraulic properties.

<b>G %</b>	<b><math>d_{50}</math> (mm)</b>	<b><math>\tau'_b</math> (N m<sup>-2</sup>)</b> <b>0.31 m·s<sup>-1</sup></b>	<b><math>\tau'_b</math> (N m<sup>-2</sup>)</b> <b>0.45 m·s<sup>-1</sup></b>	<b><math>\theta'</math></b>	<b><math>Re^*</math></b>
<b>0</b>	0.255	0.220	0.477	0.054	2.853
<b>5</b>	0.264	0.222	0.481	0.053	2.967
<b>7.5</b>	0.267	0.223	0.482	0.052	3.003
<b>10</b>	0.270	0.223	0.484	0.052	3.042
<b>12.5</b>	0.273	0.224	0.485	0.051	3.083
<b>15</b>	0.277	0.224	0.486	0.051	3.127
<b>20</b>	0.284	0.226	0.490	0.050	3.222
<b>100</b>	2.462	0.414	0.897	0.011	37.795

The bed shear stress, Shield's parameter and Reynold's number in Table 4.1 were calculated using Equation 1.10, 2.14 and 1.4 respectively. The friction velocity ( $u_*$ ) used to calculate the Reynold's number was calculated using Equation 4.1.

$$u^* = \left( \frac{\tau_b}{\rho_w} \right)^{0.5} \quad (4.1)$$

The Reynold's number can characterise the condition of the flow in the boundary layer as laminar ( $Re^* < 5$ ), transitional ( $5 \leq Re^* \leq 65$ ) or turbulent ( $Re^* > 65$ ) (Le Roux, 2004). The calculated Reynold's numbers presented in Table 4.1 show that flow conditions within the boundary layer are laminar for all the sediment mixtures used in the laboratory experiments but not the pure gravel, where the flow in the boundary layer is characterised as transitional. It is appreciated that the flow conditions downstream of the object might not always be laminar, however, the same equations as the ones used in Chapter 3 are used hereby.

The grain size distribution curves for each mixture, using  $\frac{1}{2} \Phi$  distribution for each sand-gravel mixture are presented in Figure 4.2.

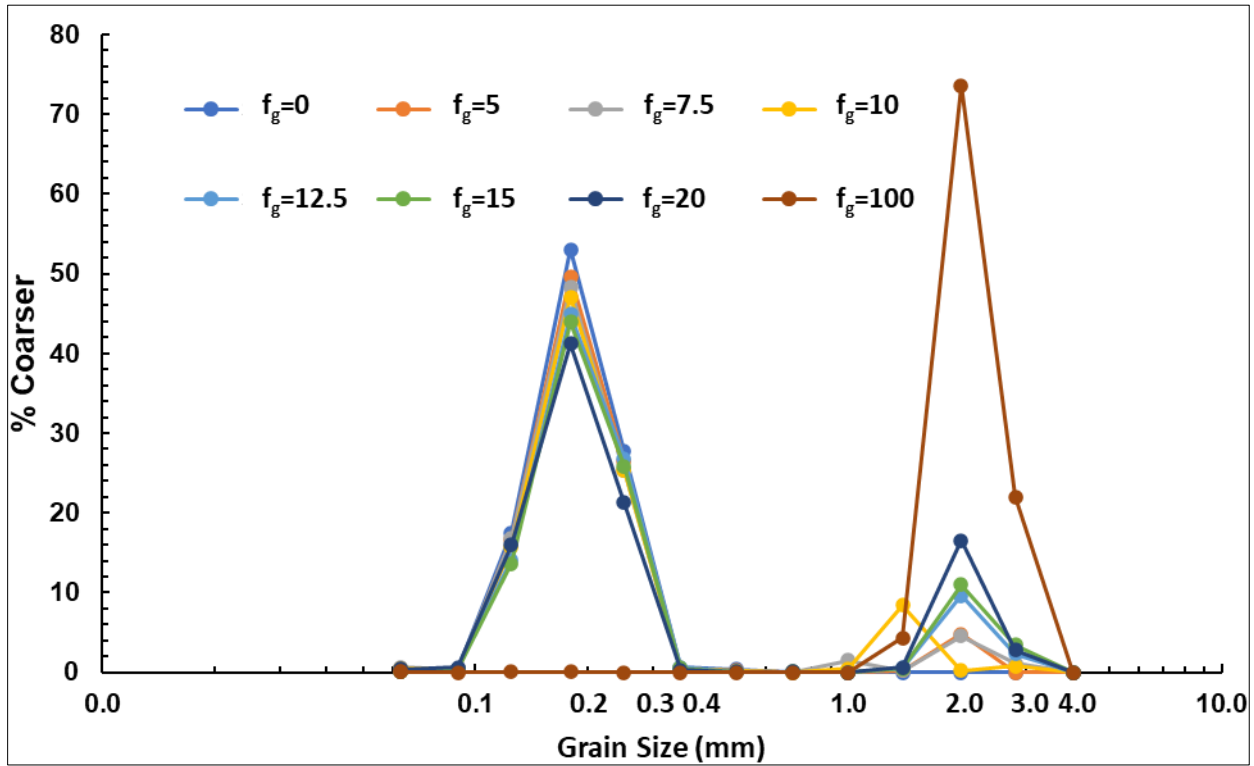


Figure 4.2: Grain size distributions (using 1/2  $\Phi$  sieve stack) of the sand-gravel mixtures used for the laboratory experiments.  $f_g$  is the gravel content in each mixture.

The sediment mixtures were mixed in 40 kg and 35 kg batches, due to the large volume of sediment required for a 4 m long bed of 4 cm thickness in the Armfield flume. Dry weight of each fraction was added in the mixture to achieve a total dry weight (of the mixture) of 75 kg. Freshwater was added to the sediment mixer together with the sediments (less than 20% of dry weight of mixture) to help with mixing. An Altrad Belle mini-mix 150 mixer was used to mix the sand and gravel fractions for 15 minutes for each batch of sediment.

Once mixed, sediment was transferred to the flume using buckets and the sedimentary bed was flattened using a PVC block, attached using poles (Figure 4.3) to a base running at the top of the flume, ensuring that it was gently touching the sedimentary bed to avoid compression of sediment and change in hydraulic parameters.



Figure 4.3: PVC block used for sedimentary bed flattening when setting up the flume for the laboratory experiments.

At the stage of flattening, the flume was filled with about 50% of the required water volume. Once the bed was flat, more water was added in the flume until the required (for the experiments) water level (25 cm relative to the base of the flume or 21 cm relative to the sedimentary bed).

A perpendicular bed scan was conducted using an array of twenty-four SeaTek 5 MHz ultrasonic transducers prior to the initiation of flow for the laboratory experiments when the sedimentary bed was 'flat'. During the experiment, ripple heights and wavelengths were measured using a ruler from the side of the flume and were assumed to be at a dynamic equilibrium when their heights and lengths were approaching an asymptotic straight line when plotted over time. When the developed bedforms upstream of the object were close to a dynamic equilibrium point or when scour development stopped, the pump (water discharge) was stopped to conduct another scan of the 'mature bed' using the array of SeaTek transducers. The flume experiments were continued for 20 minutes after the 'mature bed' scan and the pump was stopped again for a third, final scan using the SeaTek transducers. For the presentation of all the figures produced for the laboratory experiments (using the DEMs), the multidirectional hillshade functions for all the DEMs was set at 80% transparency to better visualise the bedforms and erosional and depositional areas within the flume.

During the experiments, when the pump was on, an array of sixteen SeaTek transducers was placed parallel to the flume at 1.5 m downstream of the 1<sup>st</sup> ramp used to hold sediment together to allow monitoring of the undisturbed (from the object and potentially from the ramp) sedimentary bed. The bedforms upstream and downstream of the object, were used to identify either the state of the bed (mature or not) but also the result of the amplified flow at the downstream of the object sedimentary bed.

#### 4.2.2.1 Flow velocities used in the laboratory experiments

Water flow velocities were calculated using the Soulsby (1997) formulae to mobilise either sand only, or both the sand and gravel in the mixtures, and this mobilisation was tested visually through laboratory observations. Pump frequencies of 30 Hz and 45 Hz generated desired flow velocities of  $31 \text{ cm}\cdot\text{s}^{-1}$ , and  $45 \text{ cm}\cdot\text{s}^{-1}$  (measured using the MetFlow Ultrasonic Doppler Velocity Profiler (UDVP) instrument – Figure 4.4) with 21 cm of water above the bed. The first ~20 mm of the measurements in the low current speed and the first ~40 mm on the high current speed are not accounted when measuring the flow velocity, as it is the blanking distance of the UDVP instrument.

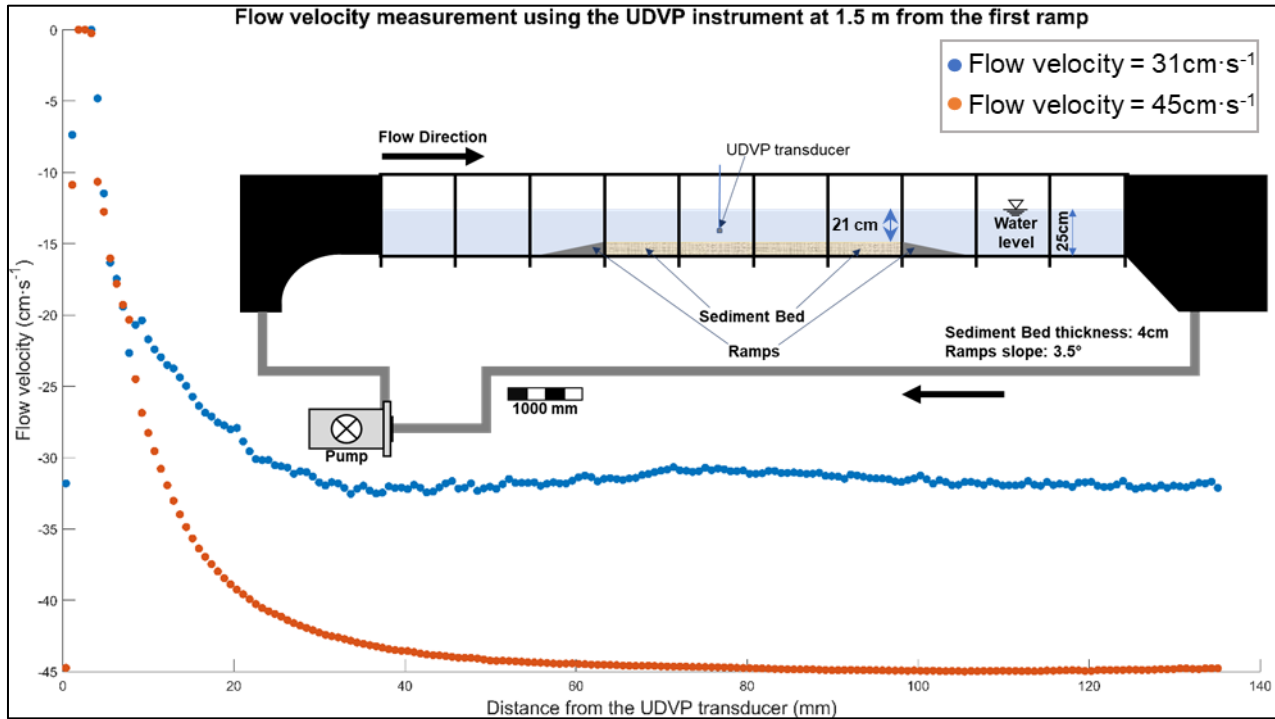


Figure 4.4: Flow velocity as measured using the UDVP for two pump frequencies, at 1.5 m downstream of the 1<sup>st</sup> ramp and a schematic illustration of the UDVP transducer positioning in the Armfield recirculating flume.

The height (above the bed) of the UDVP transducer ( $z_{av} = 7.7 \text{ cm}$ ) was chosen such, that the measured flow velocity was the equivalent to the elevation over the bed where the depth-averaged velocity ( $\bar{U}$ ) would be observed assuming a logarithmic velocity profile, using Equation 4.2 (Ma et al., 2019) as:



$$z_{av} = \frac{h}{e}, \quad (4.2)$$

where:  $h$  is the water depth above the bed, and  $e$ , is the Euler's number (2.7182...). The UDVP instrument recorded an average of 394 profiles in 90 s with a blanking distance of approximately 20 - 40 mm for each of the 183 bins along the beam. The UDVP transducer had an on-axis velocity resolution of  $3.91 \text{ mm}\cdot\text{s}^{-1}$  and a bin size of 0.74 mm. The transducer was placed directly parallel to the flow, at an angle of  $90^\circ$  to the bed.

#### 4.2.2.2 Initiation and development of scour monitoring

A time lapse camera set to record still images of the bed every 5 s was placed over the object area (2 m along the sedimentary bed), to monitor scour initiation and development. Scour marks were scanned by the SeaTek transducers after each flume experiment. No monitoring of scour development was possible using the SeaTek transducers during the laboratory experiments. Keeping the transducers in the water during the experiment was affecting the already disturbed (due to the existence of the object) flow. The entire bed and the scour was scanned using the array of twenty-four SeaTek transducers, mounted on a PVC housing (frame) with an offset to provide a better resolution (Figure 4.5) at three stages during the laboratory experiments (the “initial” bed before flow was generated, a “mature” bed after dynamic equilibrium was assumed to be reached or scour stopped, and the “after” bed that was the result of an extra 20 minutes of flow over the bed; see section above on experimental design).. The carriage system (presented in Section 2.3.3), driven by a two-stage stepper motor, has a maximum potential step resolution of 0.2 mm, traversing the flume at a speed of  $3.9 \text{ mm}\cdot\text{s}^{-1}$  (Griffiths et al., 2017; Hocking, 2019).

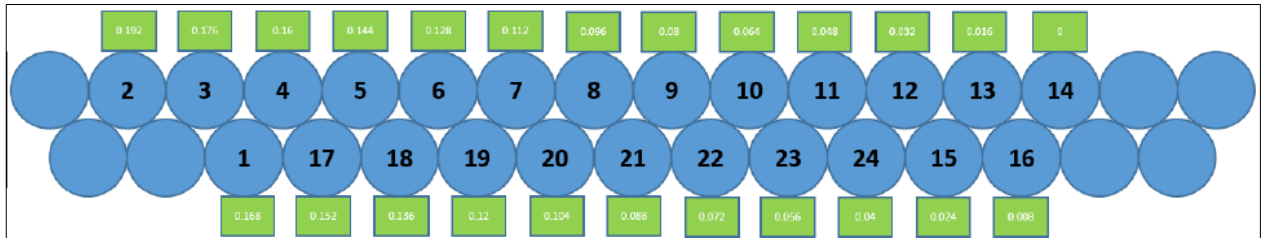


Figure 4.5: Array of twenty-four SeaTek 5 MHz ultrasonic transducers, used for the bathymetric scans after the laboratory experiments.

The output file of the acoustic transducers was a text file with bathymetric measurements as measured from each transducer at different time steps. Analyses of the coordinates of the transducers was conducted using Microsoft Excel. The y coordinate of the transducers was constant for all the measurements as the positioning of each transducer on the frame was consistent. The z of the transducer was the bathymetric measurement. For the x coordinate of the transducers, the time that the transducers were located at the 0 m position and at the 4 m position were taken from the output file of the SeaTek transducers and were also co-registered with the time recorded from the carriage system when positioned at the same locations as a confirmation. Once the total duration

of the scan was known, the travel speed of the carriage system was calculated, by subtracting the final time step from the first time step and dividing by the total travel distance (4 m), using Equation 4.3, where  $u$  is the travel velocity of the carriage system and the acoustic transducers and  $t_{final}$  and  $t_0$  the time at the last and first bathymetric measurement respectively.

$$u = \frac{4m}{\frac{t_{final}}{t_0}}, \quad (4.3)$$

Assuming a constant travel velocity of the carriage system, the distance between two measurements ( $x$  resolution) from the same transducer was calculated to be  $9.8 \times 10^{-4}$  m, using the time steps that the transducers were measuring and Equation 4.4.

$$x_2 = ((t_2 - t_1) * u) + x_1, \quad (4.4)$$

where  $u$  is the travel velocity of the carriage system,  $x_1$  and  $x_2$  the distance between two consecutive measurements and  $t_1$  and  $t_2$  the time between two consecutive measurements.

For the analyses, the initial position of the front row of the SeaTek transducers (Figure 4.5) was set at 0 m, where the initial location of the second row was set at -0.03 m. Once the  $x$  coordinates of the transducers were calculated as explained above, a .xyz file was generated for further analyses. The .xyz file generated using Microsoft Excel was opened in ArcMap and an Inversed Distance Weighted (IDW) method was applied to generate the DEMs of each bed scan. A total of 86 DEMs were therefore generated for all the laboratory experiments conducted for the purpose of the current study. An example of the three DEMs (initial 'flat' bed, 'mature bed' and 'final' bed) available for each laboratory experiment, attained from the perpendicular scans using the array with the twenty-four SeaTek transducers is presented in Figure 4.6.

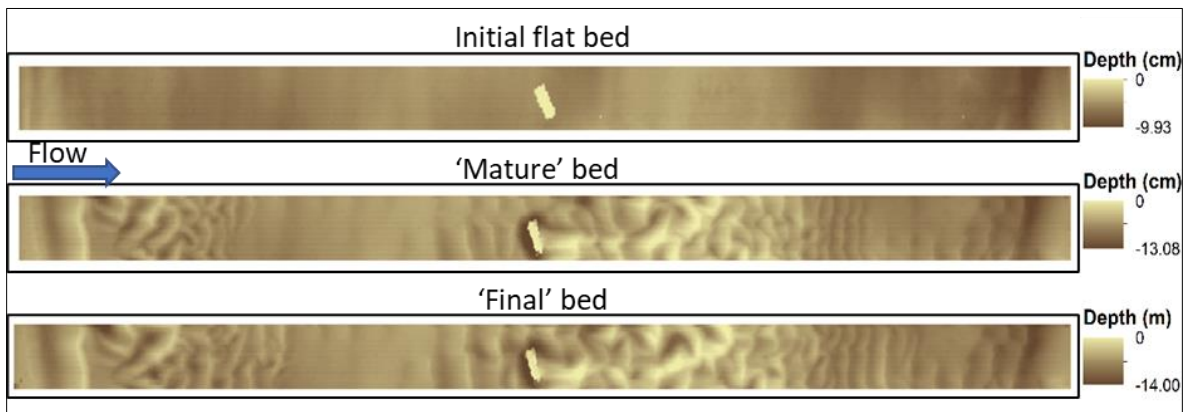


Figure 4.6: 'Initial' flat bed, 'mature bed' and 'final' bed for the experiment with pure sand and flow speed of  $31 \text{ cm} \cdot \text{s}^{-1}$  as recorded from the array of twenty-four SeaTek acoustic transducers and processed in ArcGIS.

#### 4.2.3 Scour edge delineation and bed evolution

Scour edge delineation was performed using a methodology like the one used for the MBES data around the SS *Apapa* wreck (Section 3.2.2), in this case with 2-D profiles generated every 5 mm perpendicular to the scour edge (Figure 4.7). The scour edge was delineated twice for every

laboratory experiment, using the DEM produced from the scan at the ‘mature bed’ point and from the ‘final bed’.

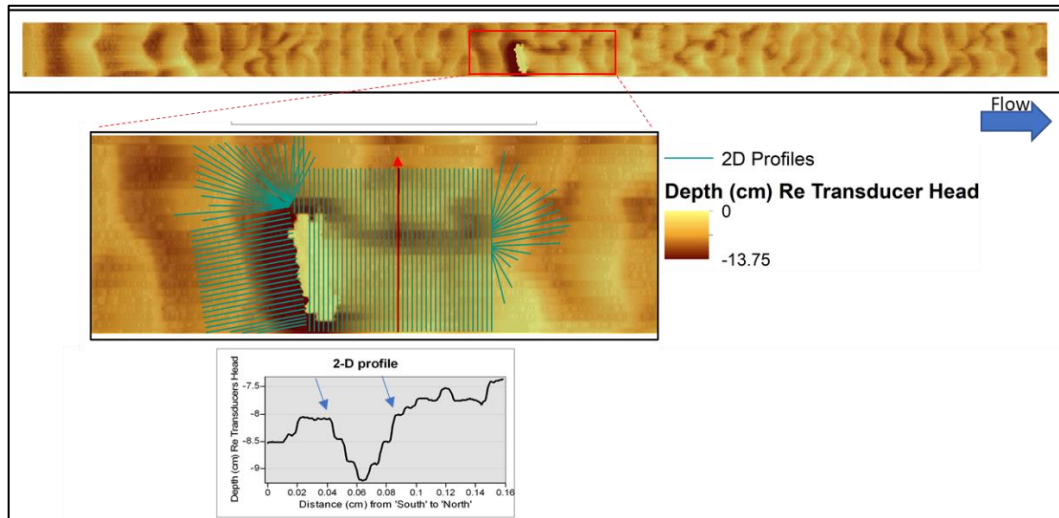


Figure 4.7: A laboratory flume bed DEM produced from the SeaTek transducer measurements, and the 2-D profiles used for the delineation of the scour edge (green lines) in the flume environment. The plotted 2-D profile is one example of such 2-D profile, marked in red.

Bed evolution within the scour mark was assessed to identify the experimental bed changes of the laboratory experiments using the three DEMs. Difference maps were created in ArcGIS by subtracting the depth extracted from each pixel of one DEM, from the equivalent pixel of an older DEM. Positive values in a difference map thus represent deposition over time, negative values represent erosion in the most recent DEM. In addition to measurements of length, width and depths, the volume of sediment loss in the scour mark was calculated using the ‘surface volume’ tool in ArcMap.

#### 4.2.4 Monitoring flow amplification via bed mobility

Ripple heights and wavelengths were measured upstream and downstream of the object, using a 2-D profile generated using the ‘final’ DEM of each laboratory run to identify the changes in bedform development caused due to the existence of the submerged object. Difference-modelling was performed on the DEMs from the bed scans before and after the last 20 minutes of each experiment (Figure 4.8). This allowed comparison of ripple characteristics upstream of the object (undisturbed bed, and thus baseline condition) and downstream of the object (assumed to have higher stresses due to far-reaching flow amplification in the wake of the object). The analysed area upstream of the

object avoided the effects of flow deviation above the ramp, and the analysed area downstream of the object avoided the effect of erosion and deposition immediately after the object.

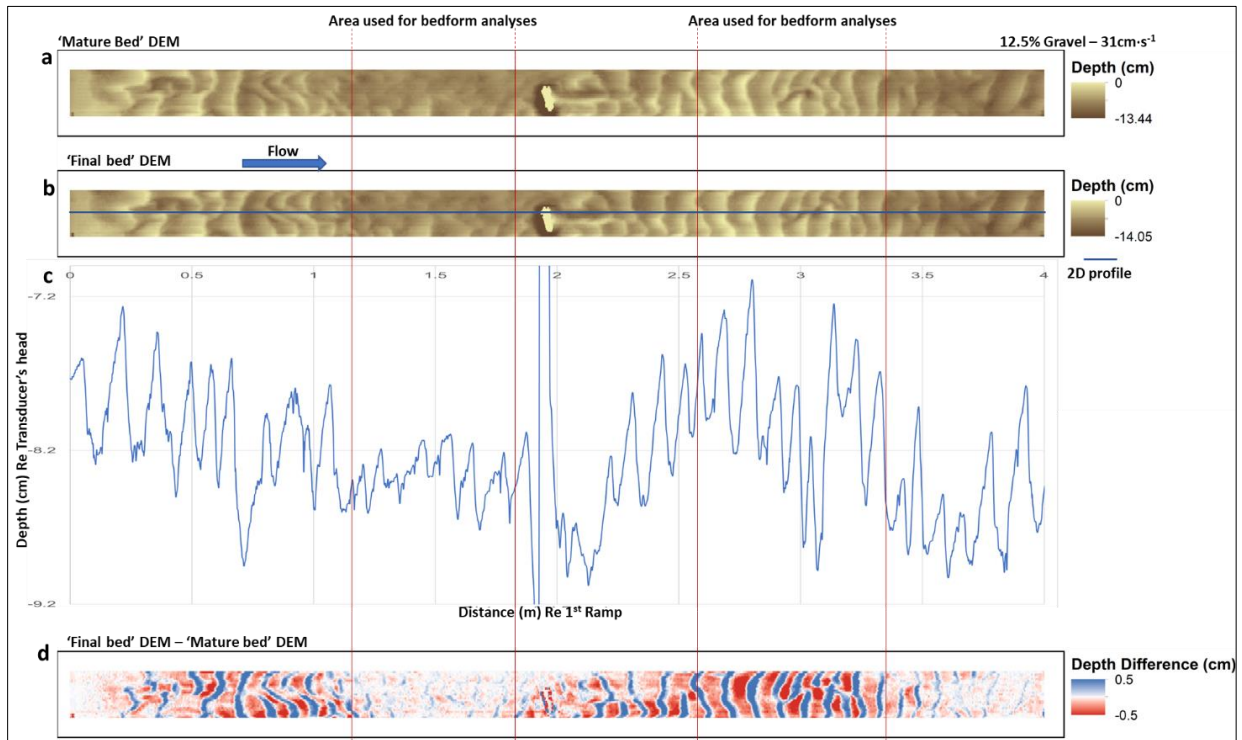


Figure 4.8: Visualisation of bedform analyses of parts of the bed upstream and downstream of the object, avoiding bedform distortions due to the ramp and the scour. The DEMs shown are from the experiment using 12.5% gravel in the mixture, at flow speed of  $31 \text{ cm}\cdot\text{s}^{-1}$ . a) 'mature bed' Dem, b) 'final bed' DEM, c) 2-D bathymetric profile on the profile shown on (b), d) depth difference between the 'final bed' DEM and the 'mature bed' DEM. The vertical red lines denote the areas (and bedforms) used for the bedform characteristics analyses.

Bedform migration rates upstream of the object (at 1.5 m from the first ramp) were measured during the experiments, using an array of sixteen SeaTek 5 MHz acoustic transducers placed parallel to the flow by completely removing the second array of transducers and repositioning transducers 1, 15 and 16 to fill the gaps of the first array (Figure 4.9). Monitoring of the upstream, undisturbed bedforms was conducted to identify if the bimodality of the sediment was influencing the bed mobility of the undisturbed (from the object) bed. The array of transducers was placed as high as possible in the water column (less than 2 cm submerged in the water) to prevent air layer formation between the water and the transducers (due to flow contraction) but also to minimise the flow disturbance downstream of the array. The disturbance to the flow was minimal and was not affecting the incoming at the area of the object flow. This was tested visually by dropping mica powder and investigating the movement of particles in the water column.

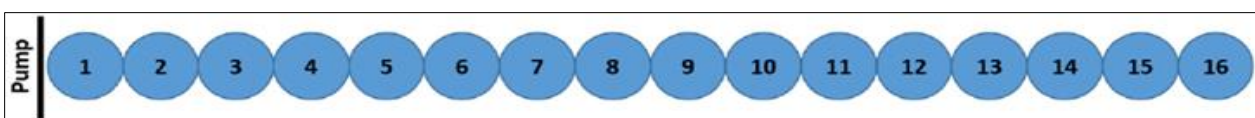


Figure 4.9: Array of sixteen SeaTek ultrasonic transducers, placed parallel to the flow, to monitor ripple migration rates upstream of the object at the full duration of the laboratory experiments.

For the purpose of monitoring bedform migration rates, the carriage system was set to be fixed at the aforementioned position ([Figure 4.10](#)).

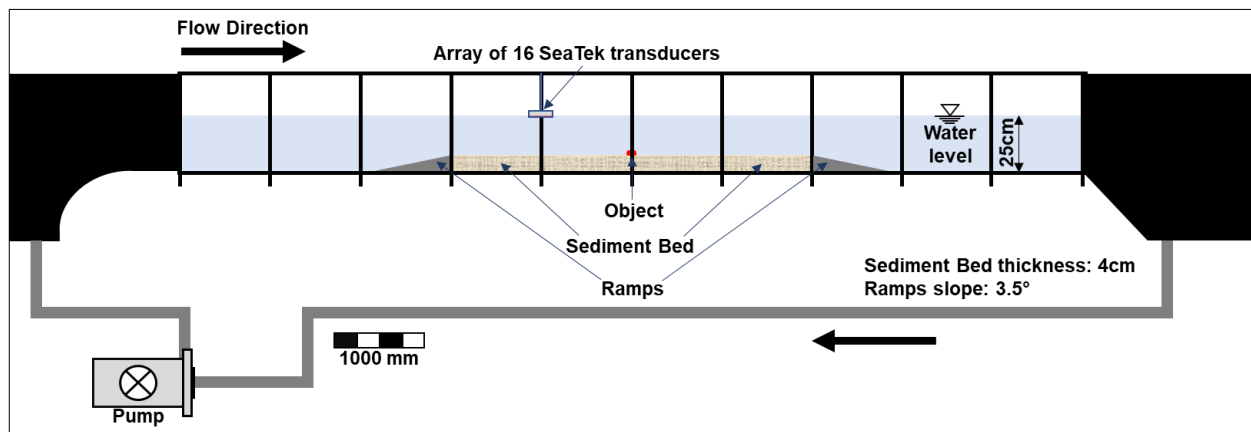


Figure 4.10: The Armfield recirculating flume and a schematic illustration of the object's and SeaTek transducers positioning when recording the bed evolution and bedform formation during the laboratory experiments.

The height of the sedimentary bed was recorded and plotted against time using MatLab. The ripple migration rates were calculated as the average time needed for a bedform crest to migrate from one transducer to its following (distance of 16 mm). Therefore, the migration rates ( $M_r$ ) were calculated by dividing the average distance that a bedform crest travelled ( $\bar{x}$ ) by the average time needed ( $\bar{t}$ ) for the migration from one transducer to its following as [Equation 4.5](#).

$$M_r = \frac{\bar{x}}{\bar{t}}, \quad (4.5)$$

The existence of 'zones of maximum bed mobility', as observed at the case study of SS *Apapa* presented in [Section 3.3.2](#) was also investigated for the laboratory experiments using the difference maps of the three DEMs from each experiment. 2-D profiles of bed changes were generated parallel to the flume every 0.5 cm and bathymetric measurements were extracted at every 1 mm along each profile (similar technique with the one used in [Section 3.2.3](#)).

#### 4.2.5 Monitoring bed composition via down-core analyses of bed samples

Down-core sampling of the bed with a syringe ([Figure 4.11](#)) was conducted at the end of the experiment for that mixture, after the water was drained from the flume and the sedimentary bed had dried overnight.



Figure 4.11: Syringe, sub-divided every 5 mm used for the laboratory sediment 'core' sampling.



The upstream samples were taken at an area that was not disturbed by the 1<sup>st</sup> ramp and the samples downstream were taken at an area influenced by the object, but not too close to the object. A minimum of 8 neighbouring ‘cores’ were taken along each sampling ‘site’ to provide a sufficient volume of sediment for particle size analyses (PSA) to be conducted. Panoramic images of the flume, taken using a mobile phone attached to a mobile base, were compared with the DEMs of the scans to identify which ripples were sampled.

Figure 4.12 show-cases the sampling strategy, with ripple crests and troughs sampled for 2 bedforms upstream and downstream of the object, and the scour mark sampled in both the erosional and depositional parts.



Figure 4.12: Panoramic image of the dried bed after an experiment, showing the sediment sampling locations.

The syringe used for the ‘cores’ was sub-divided every 5 mm (Figure 4.12). The sediment samples were transferred per 5 mm slice into pre-labelled sample holders. For each site, the neighbouring ‘core’ 5 mm slices with corresponding depth from the top of the bed were combined. The samples were transferred into the oven to dry for 24 hours at 80°C. Over 2800 sediment samples were assessed, requiring over 3 months in the sediment geotechnics laboratory for particle size analyses.

Figure 4.13 provides a schematic illustration of the sampled locations at bedforms crests and troughs.

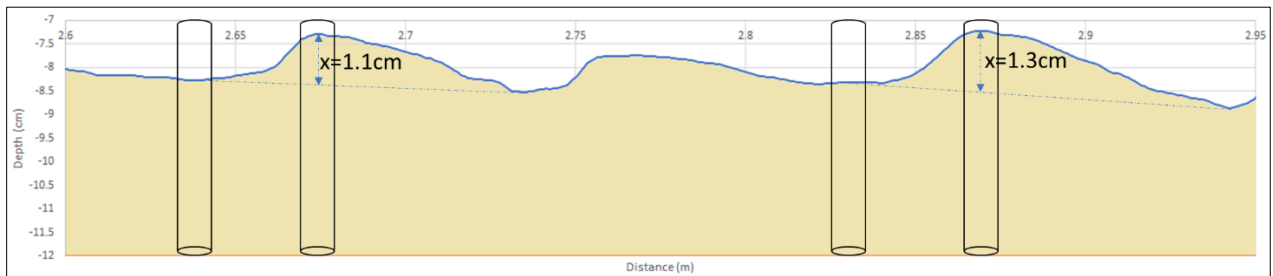


Figure 4.13: Explanation of sampled locations at bedform crests and troughs using a syringe.

Sediment sampling was conducted on the initial bed to test if the bed consists of the same intended mixture along the bed. For these control samples, the bed was sampled every 0.5 m with a minimum of 8 cores at each sampling location.

#### 4.2.6 Reconstructing the evolving flume bed environment using a coupled Hydrodynamic and Sediment transport model (TELEMAC3D – GAIA)

In Section 3.2.6, the process of modelling the area surrounding SS *Apapa* (using the coupled numerical model) was described and the results of the modelling work presented in Section 3.3.4.

The method of reconstructing the evolving flume environment using the coupled TELEMAC3D-GAIA process is similar for the laboratory environment (Yiannoukos et al., 2020).

The flume environment was reconstructed as a rectangle, with the 'north' and 'south' as solid walls, where a small friction was applied, using the 'FRICTION COEFFICIENT FOR LATTERAL BOUNDARIES' keyword in the TELEMAC-3D steering file and the 'west' (upstream) and 'east' (downstream) as discharge and prescribed elevation boundaries respectively (Figure 4.14).

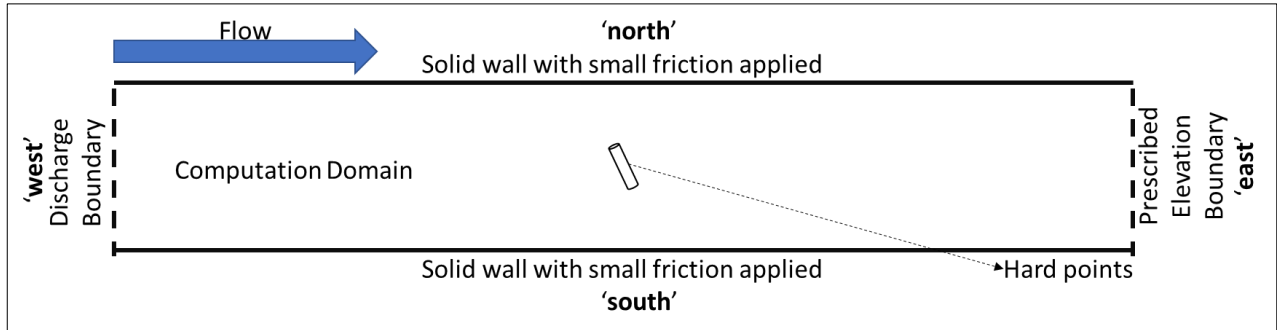


Figure 4.14: Explanation of the generation of the model computation domain for the flume laboratory.

The discharge ( $Q$ ) for the laboratory case, was calculated using the depth averaged flow velocity ( $\bar{U}$ ), the water height ( $h$ ) and the flume width ( $w_f$ ) using Equation 4.6.

$$Q = \bar{U} \times h \times w_f, \quad (4.6)$$

Using Equation 4.6, the calculated water discharge for the pump frequency of 30 Hz ( $\bar{U} = 31 \text{ cm s}^{-1}$ ) is  $Q = 0.023 \text{ m}^3 \text{ s}^{-1}$  where for the pump frequency of 45 Hz ( $\bar{U} = 45 \text{ cm s}^{-1}$ ) is  $Q = 0.034 \text{ m}^3 \text{ s}^{-1}$ . The discharge was prescribed using a liquid file and was set to increase linearly from 0 to the discharge values for each frequency within the first 5 minutes of the simulations to prevent instabilities, while still allowing for scour to happen.

An average thickness of the mobile bed at the location of the object was taken from all the laboratory measurements. The object was defined as a cylinder using the immersed boundary method (IBM, Yin et al., 2016). The way the IBM was implemented (full modification in Appendix G) allows the user to generate a cylindrical object and place it at a certain height in the computation domain. The IBM also allowed for the object to have 'overhanging nodes' over the sedimentary bed and to be treated as solid below the bed. The 'initial flat-bed' DEM and 'final' DEM were used for the reconstruction of the input geometry file for the model as the object unintentionally moved during the laboratory experiments. A polygon was created around the object (Figure 4.15a) and that area was then removed (Figure 4.15b). The point cloud was used for an interpolation of that area, resulting in an 'initial flat-bed' without the object in place (Figure 4.15c). Then, a polygon was generated around the object at the 'final' DEM, the centre point of the polygon was calculated (Figure 4.15d) and a mesh was generated. As the acoustic transducers only captured 19.2 cm out of the 30.0 cm flume, interpolation was applied to cover the remaining 10.8 cm of flume environment (Figure 4.15e; 4.15f) as otherwise the walls interfere with the numerical model data (the 'wall effect').

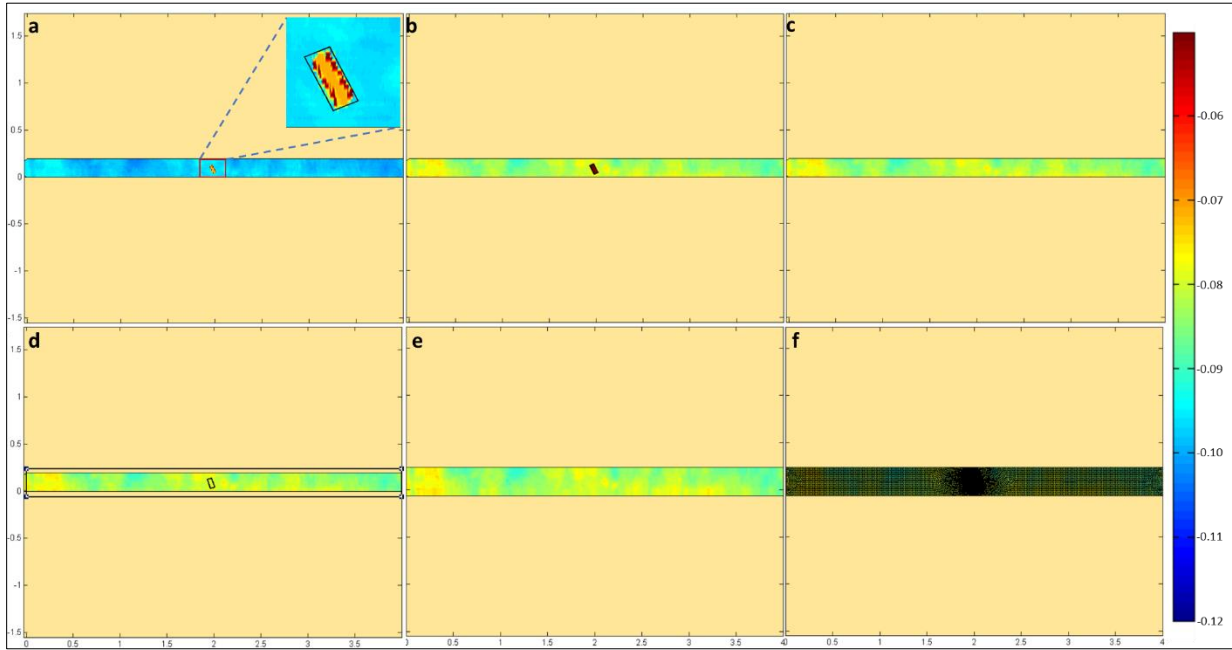


Figure 4.15: Process of generating the geometry file for the coupled numerical model. a) Generation of a polygon around the object, b) 'initial bed' without the object in place, c) 'initial bed' with an interpolation applied at the position of the object, d) 'initial bed' with the delineated final position of the object and the actual dimensions of the flume, e) 'initial bed', interpolated for the actual dimensions of the flume and f) computation domain (and mesh) used as input for the model.

Modification of the 'in\_cylinder' subroutine in the TELEMAC source code allowed for the generation of an artificial cylinder, with its centre at the location  $(x, y, z)$  of the polygon at the object's 'final' location (Figure 4.15d) and its height and orientation (from the north) the ones recorded using the 'final' DEM.

Figure 4.16 shows a schematic illustration of the rectangular polygon used to delineate the object for the mesh generation and the geometry file used in the model simulations.

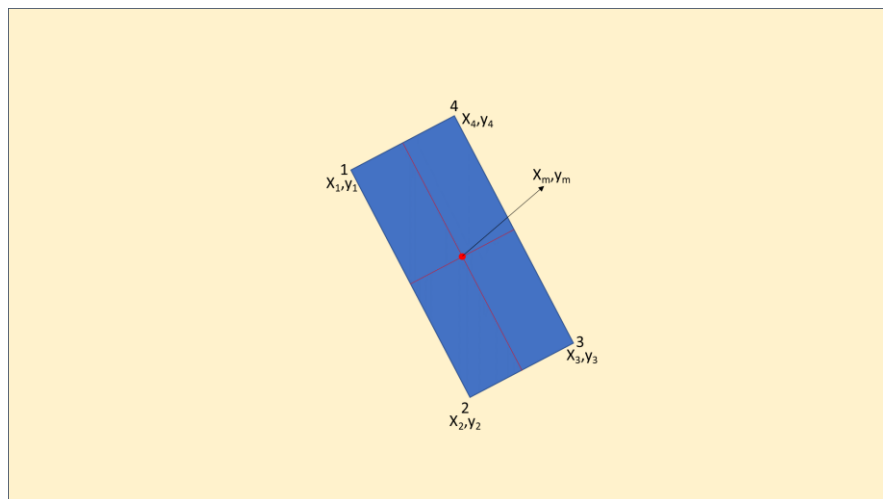


Figure 4.16: Schematic illustration of the rectangular polygon generated to delineate the object.

The  $x$  location of the middle point ( $x_m$ ) as shown in Figure 4.16 was calculated using Equation 4.7 as:

$$x_m = \overline{(x_1, x_4), (x_2, x_3)}, \quad (4.7)$$

where  $x_1, x_4$  the x location of the four corners of the rectangle as shown in [Figure 4.16](#).

The y location of the middle point ( $y_m$ ) as shown in [Figure 4.16](#) was calculated using [Equation 4.8](#) as:

$$y_m = \overline{(y_1, y_2), (y_3, y_4)}, \quad (4.8)$$

where  $y_1, y_4$  the y location of the four corners of the rectangle as shown in [Figure 4.16](#).

Finally, the final orientation of the object ( $\theta_f$ ) to the north was calculated as the slope of the line connecting corners 1 and 2 in [Figure 4.16](#) using [Equation 4.9](#) as:

$$\theta_f = \tan^{-1} \frac{x_2 - x_1}{y_2 - y_1} \quad (4.9)$$

The use of the IBM to generate the cylinder in TELEMAC was to overcome the problem caused due of the smoothness of the object at the DEMs. Owing to their resolution, the SeaTek transducers did not characterise the object as cylinder, but rather as an irregular-shaped object.

The numerical coupled model used a time step of 0.00625 s and the mesh separated the computation domain into two areas; the bed away from the object with a node size of 20.0 mm and the object area with a node size of 2.5 mm. Instability between the two numerical model areas was minimised by dropping from the coarser resolution to the finer at a step of 5% between the nodes. The total simulation time for each model run was kept the same as the laboratory experiment. The sedimentary classes used for the numerical modelling work presented in this section, were the  $d_{50}$  values of each fraction. For each mixture, the gravel percentage was set, and the bed was assumed to be uniformly mixed along the length and width of the bed. The computation was conducted in a sedimentary bed of 4 cm (height of ramps holding the sediment in place) allowing bed dynamic processes to happen at the full depth of the sedimentary bed.

The [Meyer-Peter \(1948\)](#) formula, as described in [Section 3.2.6](#), was used in both the offshore and laboratory numerical modelling cases for calculating bedload transport, with the HE correction.

Porosity ( $n_p$ ) calculations for the different mixtures were conducted by using the total volume of sediment ( $V_T$ ) used, calculated using [Equations 4.10 – 4.13](#).

$$V_T = \bar{h}_{sed} \times w_f \times l_f, \quad (4.10)$$

where  $\bar{h}_T$  the average height of the sedimentary bed as measured from the acoustic transducers,  $w_f$  the width of the flume (30 cm) and  $l_f$  the length of the sedimentary bed (4 m).

Once the total volume was known, the volume of solids ( $V_s$ ) was calculated using the mass of solids ( $M_s$ ), the specific gravity of the solids ( $G_s$ ) and the water's density ( $\rho_w$ ), using [Equation 4.11](#).

$$V_s = \frac{M_s}{G_s \rho_w}, \quad (4.11)$$

The accompanied void ratio ( $e_v$ ) was calculated using the total volume ( $V_T$ ) and the volume of solids ( $V_s$ ), using [Equation 4.12](#).

$$e_v = \frac{V_T - V_s}{V_s}, \quad (4.12)$$

Finally, porosity ( $n_p$ ) was calculated using Equation 4.13, as:

$$n_p = \frac{e_v}{1 + e_v}, \quad (4.13)$$

Using Equations 4.10 – 4.13 the porosity calculations for the different mixtures, provided the values listed in Table 4.2.

Table 4.2: Porosity ( $n_p$ ) values calculated for the different mixtures

Gravel % in the sediment mixture	Porosity ( $n_p$ ) value
0% (Pure Sand)	44%
5%	41%
7.5%	41%
10%	41%
12.5%	42%
15%	42%
20%	42%
100%	46%



## 4.3 Results

### 4.3.1 Observed flow amplification in the wake of the object

Depth averaged flow velocity measurements using the UDVP instruments were taken from 1 m downstream of the first ramp, and for every 0.5 m. No flow velocity measurements were taken directly over the object (2 m downstream of the first ramp). Velocities measured between  $30.3 \text{ cm}\cdot\text{s}^{-1}$  and  $31.7 \text{ cm}\cdot\text{s}^{-1}$  for the pump frequency of 30 Hz and between  $43.6 \text{ cm}\cdot\text{s}^{-1}$  and  $47.1 \text{ cm}\cdot\text{s}^{-1}$  for the pump frequency of 45 Hz. Flow velocity measurements were also taken at 3.75 m downstream the first ramp (0.25 m upstream of the 2<sup>nd</sup> ramp) rather than directly above the second ramp. Figure 4.17 shows the distance from the first ramp that flow velocity measurements were taken and their accompanied recorded depth averaged flow speeds. The flow speeds presented at Figure 4.17 are the two measurements taken at each location for each pump frequency used.

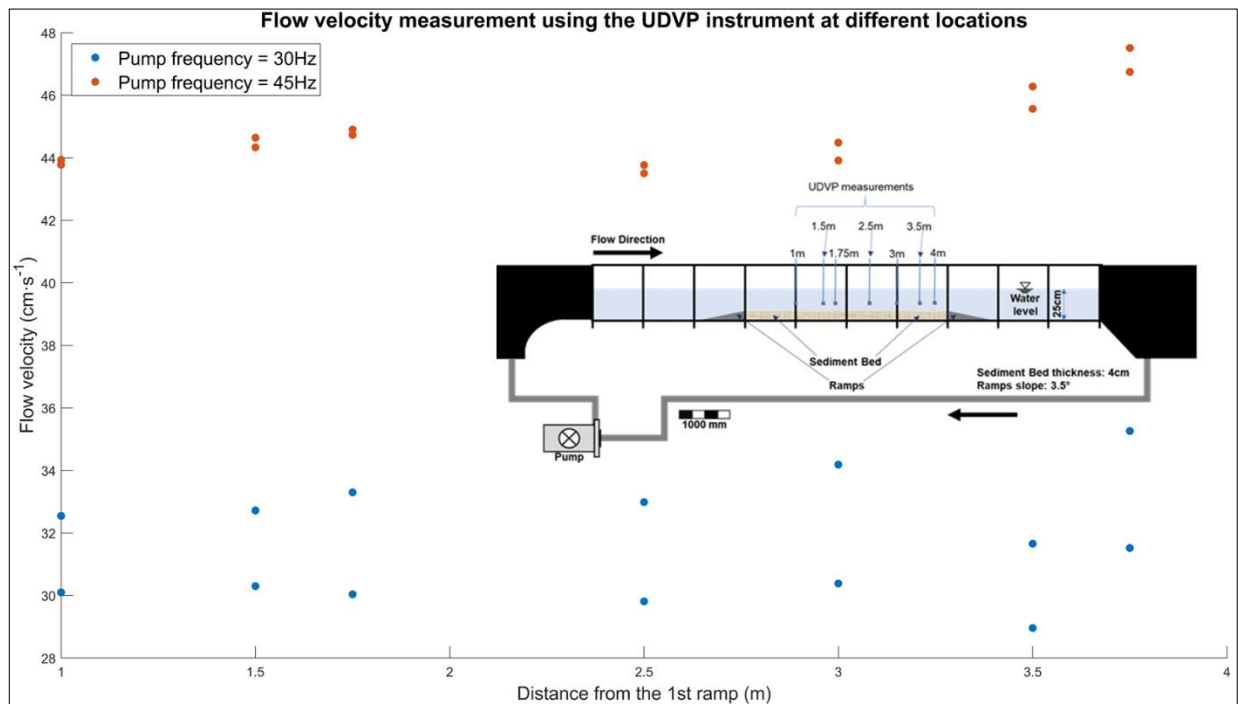


Figure 4.17: Depth averaged flow velocity measurements captured using the UDVP instrument at 7 locations in the flume. Two measurements were taken at each location for each pump frequency (30 Hz and 45 Hz).

Also shown, a schematic diagram of the locations where flow velocities were measured using the UDVP instrument.

For the experiments conducted at the experiments using the pump frequency of 30 Hz the depth averaged flow velocity measurements show a mean amplification of 1.1% downstream, with mean depth averaged flow velocities upstream and downstream of the object of  $31.5 \text{ cm}\cdot\text{s}^{-1}$  and  $31.8 \text{ cm}\cdot\text{s}^{-1}$  respectively. For the experiments conducted using the pump frequency of 45 Hz a difference of 1.9% was observed in the flow velocities upstream and downstream of the object, with mean measured depth averaged velocities of  $44.3 \text{ cm}\cdot\text{s}^{-1}$  and  $45.2 \text{ cm}\cdot\text{s}^{-1}$  respectively.

#### 4.3.1.1 Flow amplification monitoring via bed mobility and bedform formation

Ripple migration rates were measured upstream of the object, at 1.5 m from the first ramp using the array of the SeaTek transducers. **Figure 4.18** shows the recorded ripple migration rates for the experiments conducted using the flow velocity only mobilising the sand fraction ( $31 \text{ cm}\cdot\text{s}^{-1}$ ). The highest ripple migration rates were recorded at the experiments conducted using pure sand. For the sediment mixtures, ripple migration rates increased from the experiments conducted using the mixtures containing 5% gravel to 10% gravel, where higher migration rates were recorded. Then, ripple migration rates slowed upon increasing the gravel percentage in the mixture, for the experiments conducted using the 12.5% and 20% gravel mixes. It is also important to note that ripple migration rates were higher at the experiments conducted using the 12.5% gravel mixture than those using the 5% and 7.5% gravel mixes. Ripple formation was not observed at the experiment with the bed consisting of pure gravel.

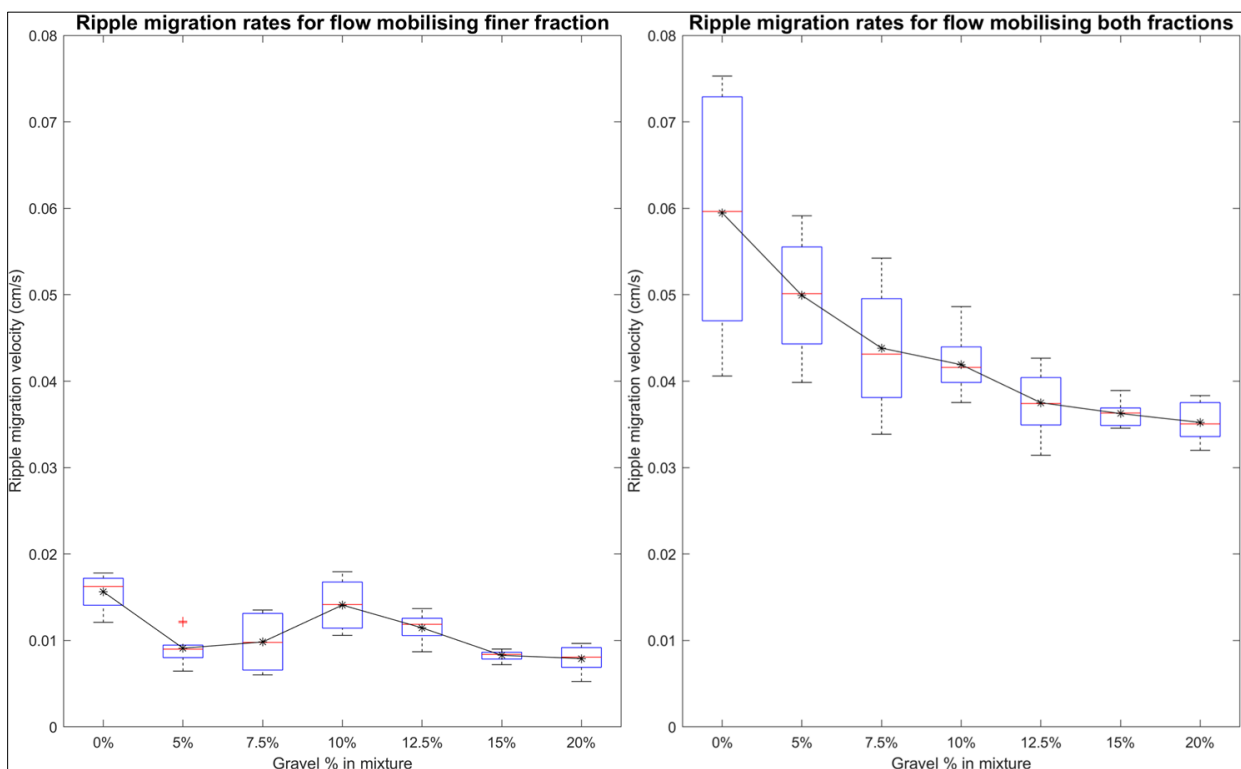


Figure 4.18: a) Observed ripple migration rates upstream for different bed mixtures for the flow speed mobilising only the finer fraction ( $31 \text{ cm}\cdot\text{s}^{-1}$ ), b) Observed ripple migration rates upstream for different bed mixtures for the flow speed mobilising both fractions ( $45 \text{ cm}\cdot\text{s}^{-1}$ ).

**Figure 4.18b** shows the bedform migration rates upstream of the object for the experiments conducted using the flow speed mobilising both fractions ( $45 \text{ cm}\cdot\text{s}^{-1}$ ). Ripple formation was once again not observed for the experiments conducted at the experiment with the bed consisting of pure gravel.

An exponential trendline was added on the graph (Figure 4.18b) of the mean migration rates (y-axis) plotted against the gravel percentage in the mixture (x-axis) for the experiments conducted at the flow speed mobilising both fractions ( $45 \text{ cm}\cdot\text{s}^{-1}$ ). The exponential trendline has an equation of  $y = 0.056e^{-0.028x}$  with a  $R^2$  value of 0.92, declaring that ripple migration rates decrease at a constantly increasing gravel % within the sediment mixtures. The  $R^2$  value shows that there is good fit between the data and the regression model. At higher concentrations of the coarser fraction, the hiding-exposure effect but also the content of the coarse gravel needed higher shear stress to mobilise, something that the flow speeds used was not sufficient to provide.

No ripple migration rates were recorded downstream, due to the limited number of SeaTek transducers used and because when the transducers were submerged in the water column, they interacted with the already disturbed flow downstream, possibly creating even more complex flows. These factors would lead to unreliable results, as it would have been impossible to know if the disturbance and the migration of bedforms was caused by the object or the interaction of the transducers with the disturbed downstream flow. Although ripple migration rates were not recorded downstream, the ripple characteristics were calculated using the DEM produced from the 'final' bed scan. The calculated absolute ripple asymmetry ( $|A|$ ) for the experiments conducted at the flow speeds mobilising only the sand fraction ( $31 \text{ cm}\cdot\text{s}^{-1}$ ) and both sand and gravel fractions ( $45 \text{ cm}\cdot\text{s}^{-1}$ ), are presented in Figure 4.19 and 4.20 respectively.

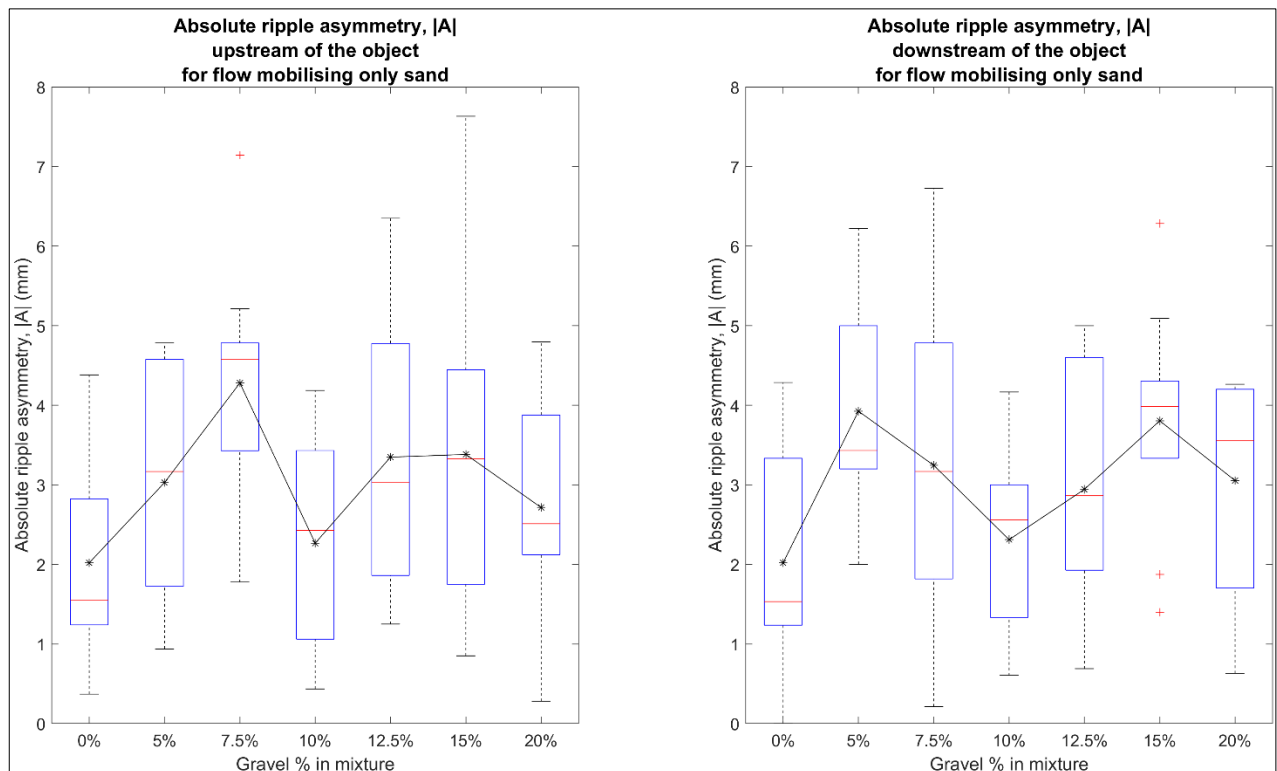


Figure 4.19: Absolute ripple asymmetry upstream (left) and downstream (right) of the object, as calculated for the experiments conducted at the flow speed mobilising only the sand fraction ( $31 \text{ cm}\cdot\text{s}^{-1}$ ). The \* sign represents the mean value of the measurements.

Figure 4.19 shows that the mean absolute ripple asymmetry ( $|\bar{A}|$ ) upstream of the object, appears to increase between the experiments conducted using sediment containing 0% to 7.5% gravel and drops at the experiments conducted using the sediment mixture containing 10% gravel. In contrast, for the ripples recorded downstream of the object, the mean absolute ripple asymmetry increases for the experiments conducted with sediment containing 0% and 5% gravel and drops at the experiments conducted using the sediment mixtures containing 7.5% and 10% gravel. In both the upstream and downstream ripples, lower values of  $|A|$  are recorded at the experiments conducted using the mixture containing 10% gravel. At the sediment mixtures containing 12.5% to 15% gravel, increase of the ripple  $|A|$  both upstream and downstream of the object is noted. The ripple  $|A|$  upstream of the object for the experiments conducted using the sediment mixture of 20% gravel seems to have lower values than  $|A|$  in the case of the experiments conducted using sediment mixtures of 12.5% and 15% gravel. In contrast,  $|A|$  downstream of the object for the case of the experiments conducted using the sediment mixture containing 20% gravel has higher values than  $|A|$  as measured for the experiments conducted using the sediment mixture containing 12.5% gravel.

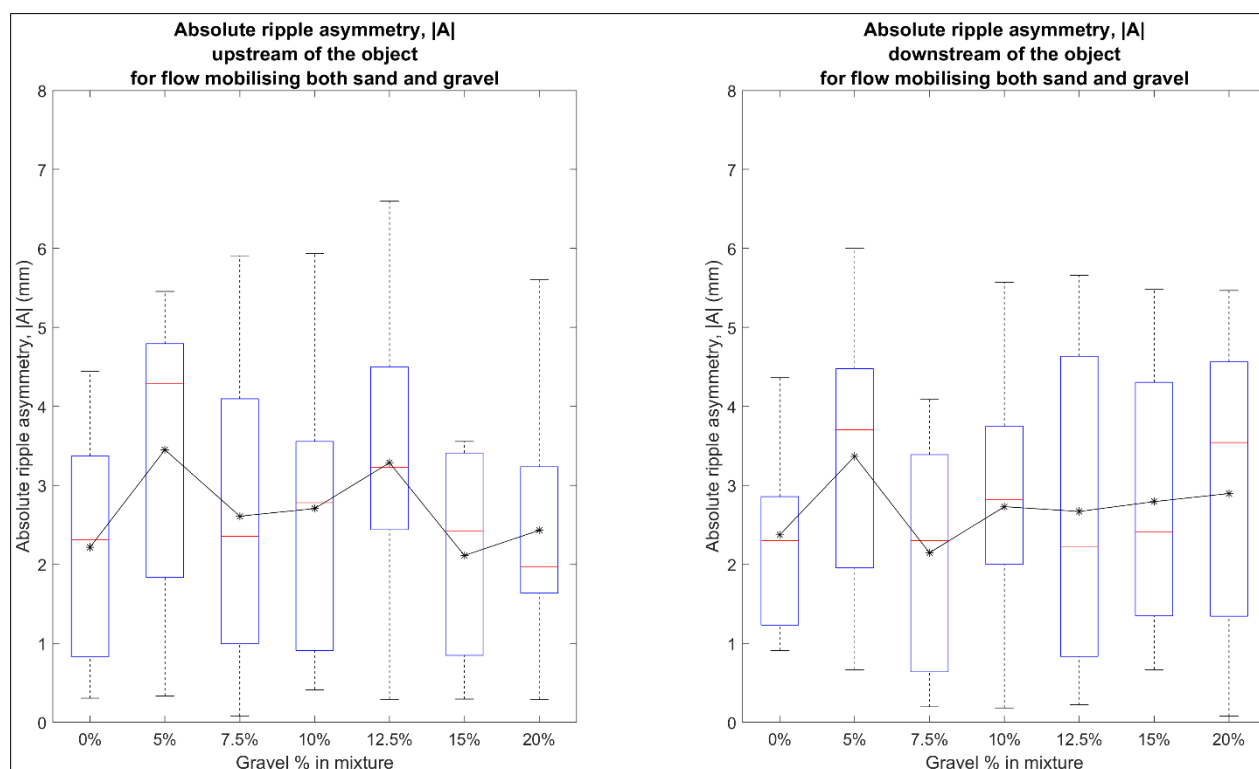


Figure 4.20: Absolute ripple asymmetry upstream (left) and downstream (right) of the object, as calculated for the experiments conducted at the flow speed mobilising only the sand fraction ( $45 \text{ cm}\cdot\text{s}^{-1}$ ).

Figure 4.20 shows that  $|A|$  has higher values both upstream and downstream of the object in the experiments conducted using the sediment mixture containing 5% gravel. Both upstream and downstream of the object, there is an increase in  $|A|$  between the experiments conducted at sediment mixtures containing 7.5% and 10% gravel. Upstream of the object, a decrease in  $|A|$  was recorded for the experiments conducted using the sediment mixture containing 12.5% gravel and 15% gravel, with an increase in  $|\bar{A}|$  for the experiments conducted using the sediment mixture

containing 20% gravel. In contrast, the  $|\bar{A}|$  as recorded downstream of the object, appears to be increasing when increasing the sediment gravel in the mixture, for the experiments conducted using the sediment mixtures containing 12.5% to 20% gravel.

Figure 4.21 shows the comparison between the mean absolute ripple asymmetry upstream and downstream, for the experiments conducted using the different sediment mixtures at the flow speed of  $31 \text{ cm}\cdot\text{s}^{-1}$  (Figure 4.21 solid blue line) and  $45 \text{ cm}\cdot\text{s}^{-1}$  (Figure 4.21 solid red line).

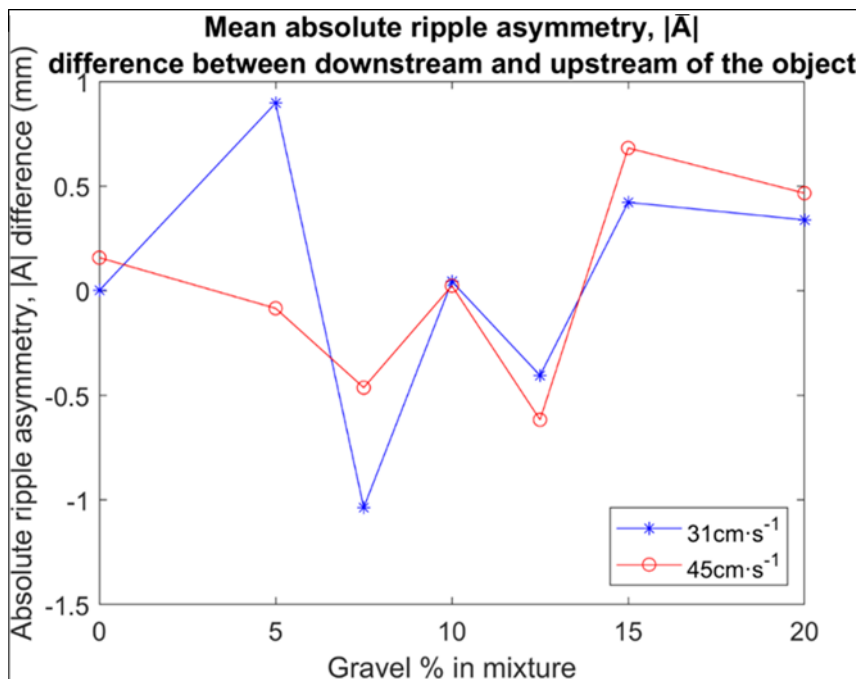


Figure 4.21: Mean absolute ripple asymmetry,  $|\bar{A}|$  difference between the ripples measured downstream and upstream of the object, for the laboratory experiments conducted using the different mixtures and the flow speeds of  $31 \text{ cm}\cdot\text{s}^{-1}$  (solid blue line) and  $45 \text{ cm}\cdot\text{s}^{-1}$  (solid red line).

Negative values in Figure 4.21 mean that the mean absolute asymmetry of the upstream ripples was higher than the mean absolute asymmetry of the downstream ripples. Therefore, for the experiments conducted using the mixtures containing 5%, 7.5% and 12.5%, the ripples downstream appear to have smaller mean absolute asymmetry value than the ripples upstream for both flow speeds, except for the experiments conducted at the flow speed of  $31 \text{ cm}\cdot\text{s}^{-1}$  and the sediment mixture containing 5% gravel. For these experiments, the ripples upstream had smaller mean absolute asymmetry than the ripples downstream of the object. For the experiments conducted at the sediment mixture containing 10% gravel, the ripples upstream were less asymmetric than the ripple downstream for the experiments conducted at speeds of  $31 \text{ cm}\cdot\text{s}^{-1}$  and  $45 \text{ cm}\cdot\text{s}^{-1}$ . Finally, for the control experiment using the pure sand (0% gravel) and the experiments conducted using 15% and 20% gravel the ripples downstream were more asymmetric than the ripples upstream. The exception was for the experiment conducted using the pure sand at the flow speed of  $31 \text{ cm}\cdot\text{s}^{-1}$ , where there is no variation observed between the asymmetry of the ripples formed downstream and upstream of the object.

The height and length of the bedforms also differs upstream and downstream of the object. Figure 4.22 and Figure 4.23 show the comparison of the observed bedform heights and lengths upstream



and the observed bedform heights and lengths downstream of the cylinder respectively for experiments conducted at the flow speed of  $31 \text{ cm}\cdot\text{s}^{-1}$ .

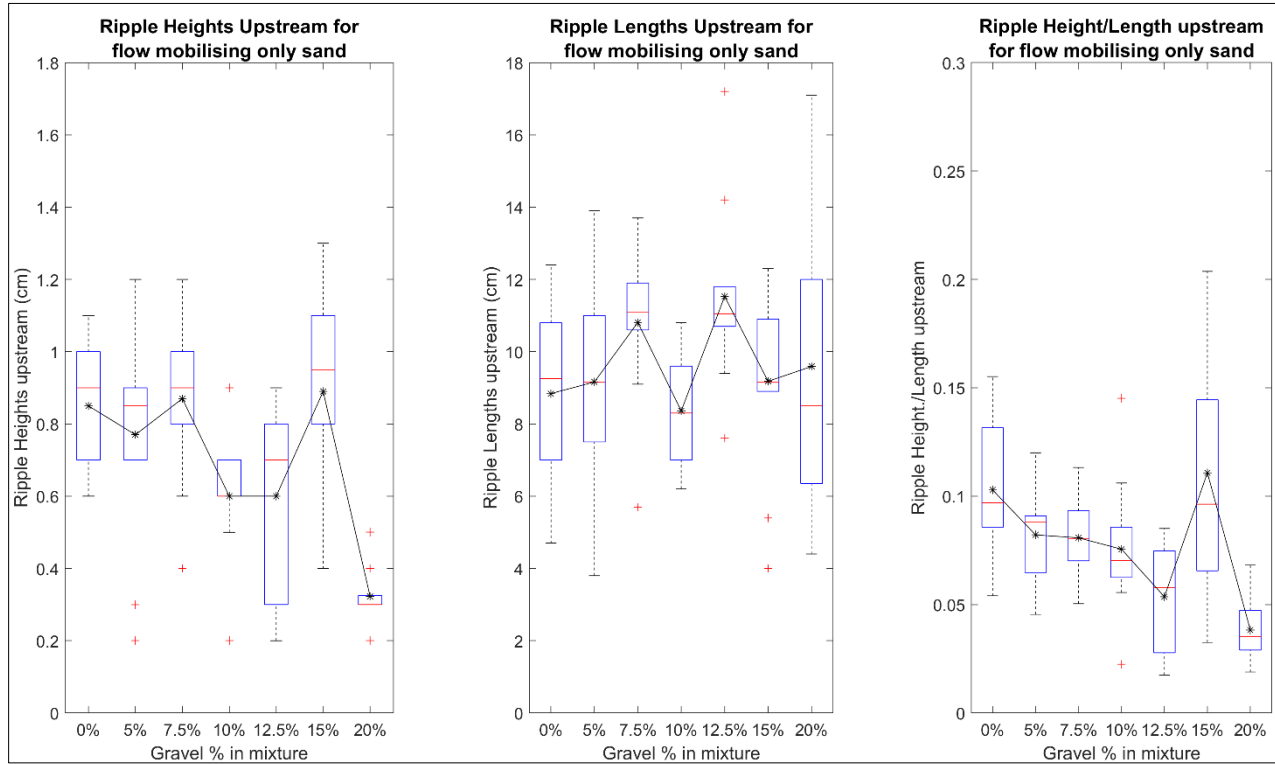


Figure 4.22: Ripple heights and lengths and a height/length comparison for ripples upstream of the object, for the experiments conducted at the flow speed of  $31 \text{ cm}\cdot\text{s}^{-1}$ .

The mean ripple heights upstream of the object (Figure 4.22) for the experiments conducted at the flow speed of  $31 \text{ cm}\cdot\text{s}^{-1}$  vary between 0.30 and 0.89 cm. The mean ripple lengths upstream vary between 8.36 and 11.53 cm, where the mean height/length ratio of the ripples formed upstream vary between 0.038 and 0.110. For the ripples formed downstream of the object (Figure 4.23), the mean ripple heights vary between 0.40 cm and 1.14 cm. The mean ripple lengths downstream vary between 8.01 and 10.23 cm and the mean height/length ratio varies between 0.045 and 0.122. Therefore, the ripples upstream of the object are observed to be less high but longer than the ripples downstream of the object. Upstream of the object, a drop in ripple heights and lengths is noted in the experiments conducted using the sediment mixture containing 10% gravel. This observation was also present at the length of the downstream ripples, but the drop in height was observed at the sediment mixture containing 12.5% gravel. The lowest ripples were observed in the experiments conducted using the sediment mixture containing 20% gravel. Although no clear trend is observed for any of the ripples upstream of the object, the ripples downstream seem to reduce in height with increasing gravel component. Exceptions were observed for the experiments where the sedimentary bed consisted of 7.5% and 15% gravel.

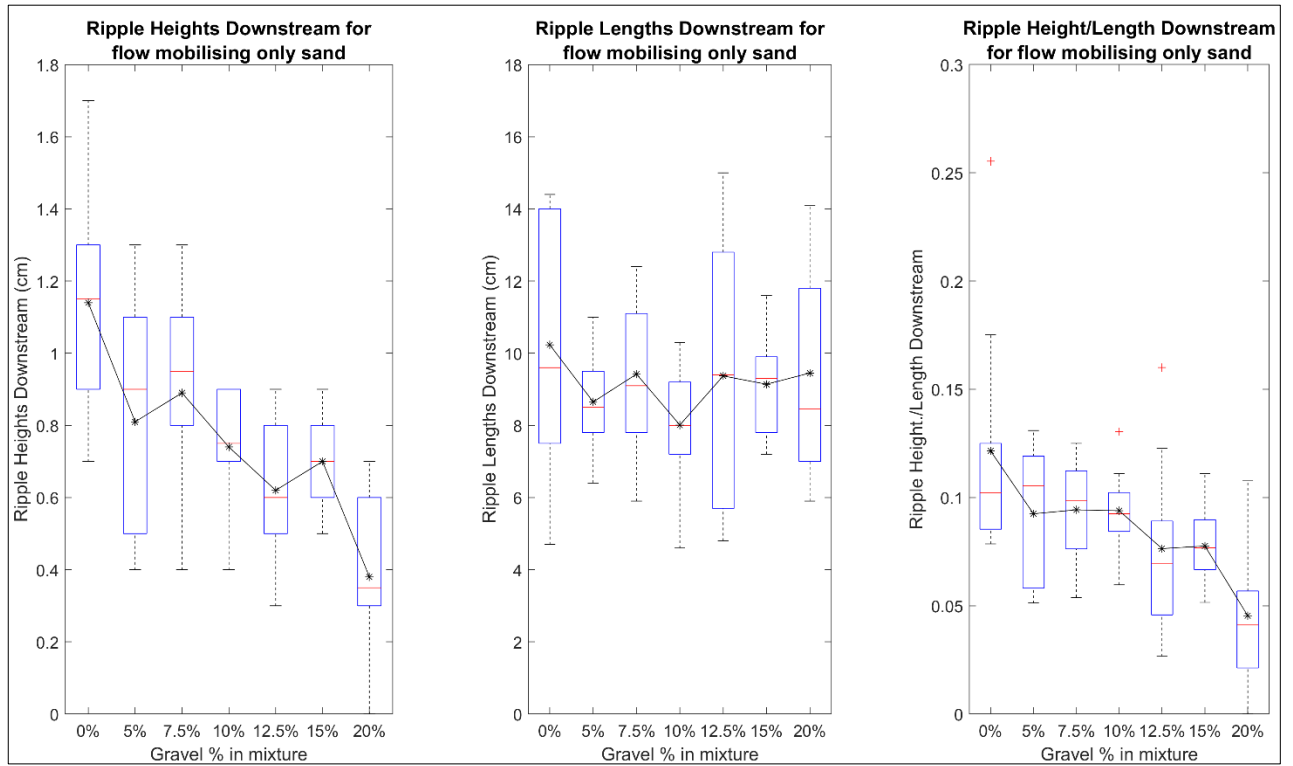


Figure 4.23: Ripple heights and lengths and a height/length comparison for ripples at the wake (downstream) of the object, for the experiments conducted at the flow speed of  $31 \text{ cm} \cdot \text{s}^{-1}$ .

Figures 4.24 and 4.25 show the comparison of the observed ripple heights and lengths upstream and downstream (at the wake) of the cylinder respectively for the experiments conducted at the flow speed of  $45 \text{ cm} \cdot \text{s}^{-1}$ .

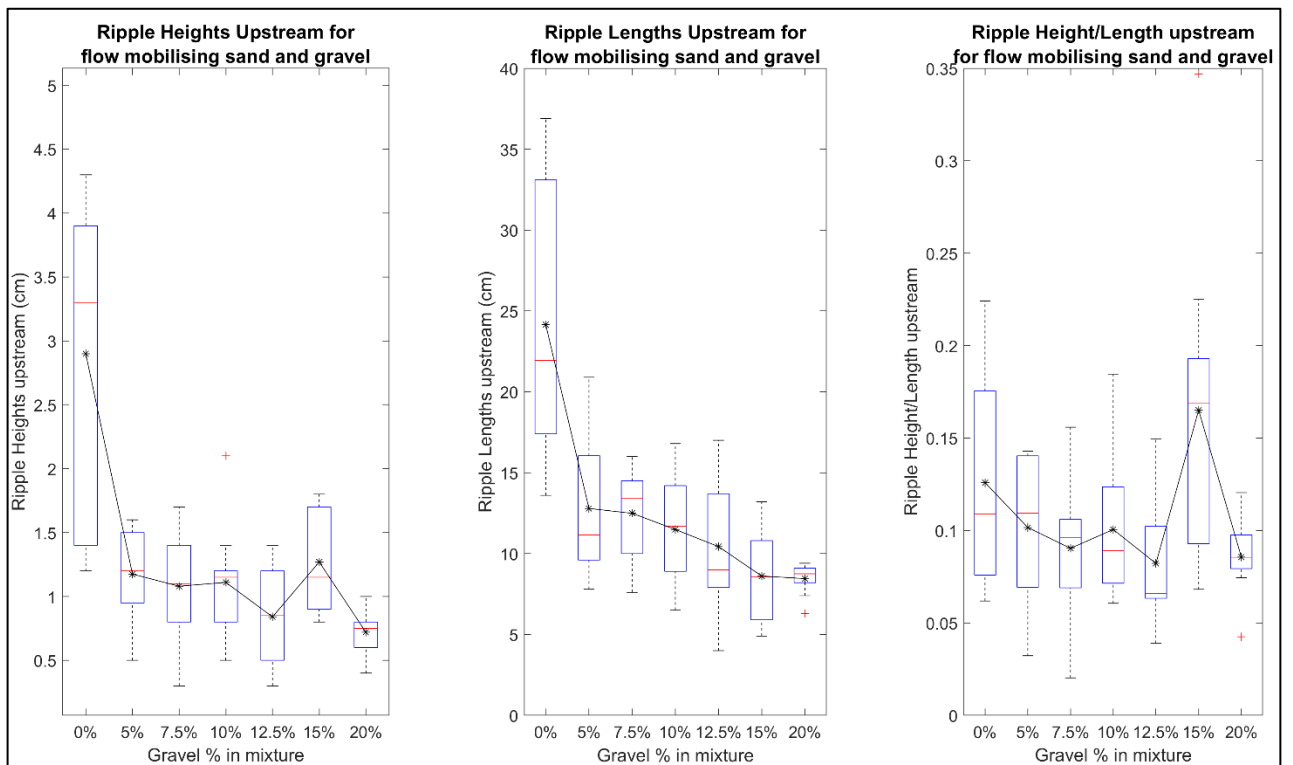


Figure 4.24: Ripple heights and lengths and a height/length comparison for ripples upstream of the object, for the flow speed of  $45 \text{ cm} \cdot \text{s}^{-1}$ .

The mean ripple heights upstream of the object ([Figure 4.24](#)) for the experiments conducted at the flow speed of  $45 \text{ cm}\cdot\text{s}^{-1}$  vary between 0.72 cm and 2.90 cm. The mean ripple lengths upstream vary between 8.45 and 24.15 cm, where the mean height/length ratio of the ripples formed upstream vary between 0.082 and 0.126. For the ripples formed downstream of the object ([Figure 4.25](#)), the mean ripple heights vary between 0.40 and 1.14 cm. The mean ripple lengths downstream vary between 8.24 and 20.97 cm and the mean height/length ratio varies between 0.073 and 0.121. Therefore, the ripples upstream of the object are observed to be longer and higher than the ripples downstream of the object. In the case of the ripples formed upstream of the object there seems to be a drop in the ripple height and length when increasing the gravel percentage in the sediment mixture. In the case of ripple heights, exceptions are noted in the experiments conducted using the sediment mixture consisting of 15% gravel. In contrast, the ripples formed downstream of the object have a general trend of reduced length when increasing the gravel percentage in the sediment mixture. The ripples downstream of the object have increased heights for the experiments conducted using the sediment mixtures containing 7.5% and 10% gravel, with the general trend of lower ripples with increasing the gravel component for the experiments conducted using the rest of the sediment mixtures.

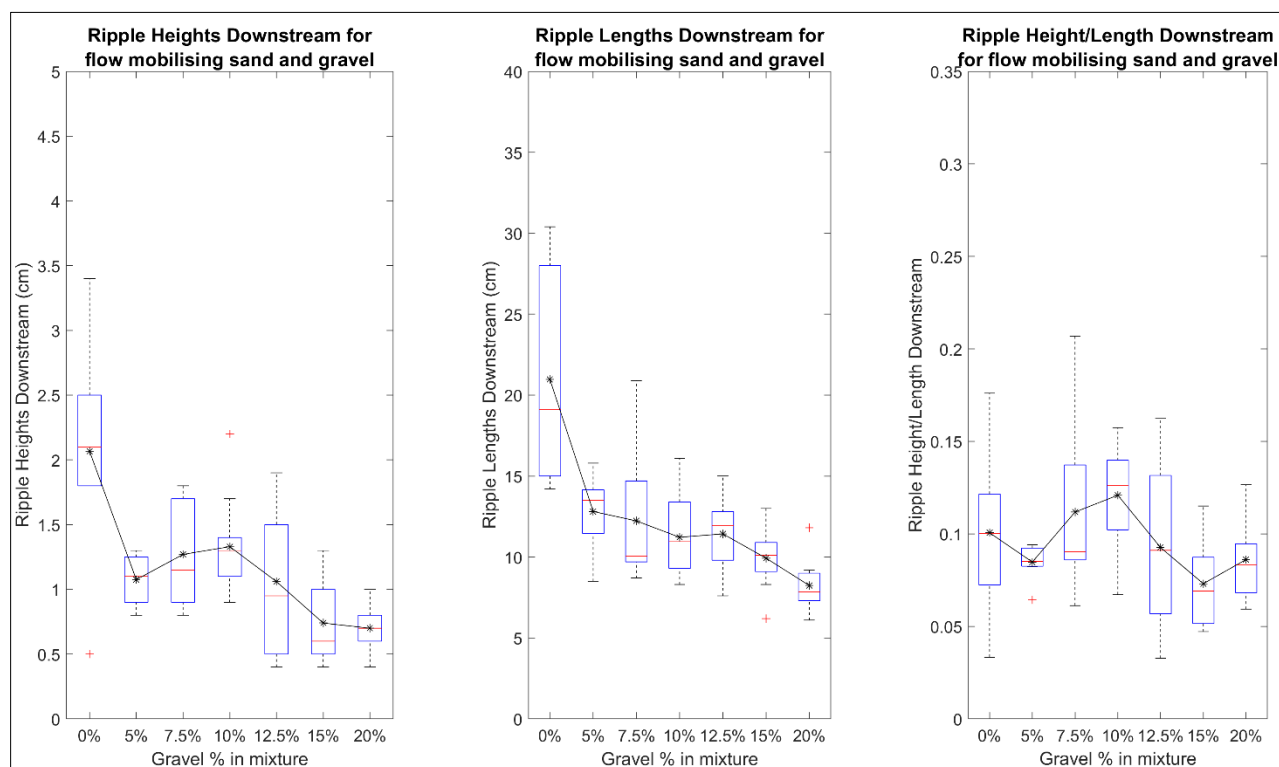


Figure 4.25: Ripple heights and lengths and a height/length comparison for ripples downstream of the object, for the experiments conducted at the flow speed of  $45 \text{ cm}\cdot\text{s}^{-1}$ .

[Table 4.3](#) shows the percentage difference between the upstream mean measurements of height and length and the downstream mean measurements of height and length for both flow speeds used in the laboratory experiments.

Table 4.3: Comparison between upstream and downstream mean measurements for ripple heights and lengths for experiments conducted using the two flow speeds. Positive values (green) mean that the downstream mean value was greater, where negative values (red) mean that the downstream mean value was smaller than the upstream.

	Flow speed mobilising only sand (31 cm·s <sup>-1</sup> )						
Gravel %	0 %	5 %	7.5 %	10 %	12.5 %	15 %	20 %
% Difference in ripple heights upstream and downstream	+25.4%	+4.9%	+2.3%	+18.9%	+3.2%	+27.1%	+15.2%
% Difference in ripple lengths upstream and downstream	+13.6%	-5.9%	-14.8%	-4.4%	-23.1%	-0.4%	-1.5%
% Difference in ripple height/length ratio upstream and downstream	+15.3%	+11.2%	+14.4%	+19.6%	+29.9%	-42.8%	+15.8%
	Flow speed both sand and gravel (45 cm·s <sup>-1</sup> )						
Gravel %	0 %	5 %	7.5 %	10 %	12.5 %	15 %	20 %
% Difference in ripple heights upstream and downstream	-40.3%	-9.3%	+15.0%	+16.5%	+20.8%	-71.6%	-2.9%
% Difference in ripple lengths upstream and downstream	-15.2%	+0.2%	-2.1%	-2.4%	+8.8%	+13.3%	-2.6%
% Difference in ripple height/length ratio upstream and downstream	-25.1%	-19.9%	+19.2%	+16.9%	+11.3%	-125.9%	+0.6%

The height and length of the ripples formed downstream of the object provided a first observation of the influence of the enhanced flow (due to the interaction with the object) on the bed. Although trends were not so clear, Table 4.3 shows that for the experiments conducted using the flow speed mobilising only the sand fraction, the mean ripple heights downstream were lower than the mean ripple heights upstream, for all the experiments conducted using sediment mixtures (but not the pure sand bed). In contrast, the mean ripple lengths upstream were longer than the mean ripple lengths downstream for the experiments conducted using the sediment mixtures. For the experiments conducted using the flow speed mobilising both fractions, the ripples downstream were higher for the experiments conducted using the sediment mixtures containing 7.5% to 12.5% gravel, but lower for the experiments conducted using the rest of the sediment mixtures. The only case where the ripples downstream were higher and longer than the ripples upstream of the object, was the case of the experiments conducted using the sediment mixture containing 12.5% gravel.

The height and length of the ripples formed downstream of the object provided a first indication of the influence of the enhanced flow (due to the interaction with the object) on the downstream bed.

#### 4.3.1.2. Observed bathymetric changes downstream of the object ('zones of influence')

Two consistent zones of maximum bed mobility (zones of influence) due to the enhanced flow downstream emerged from this analysis (Figure 4.26 top and Figure 4.26 bottom) for the experiments conducted at flow speeds of  $31 \text{ cm}\cdot\text{s}^{-1}$  and  $45 \text{ cm}\cdot\text{s}^{-1}$  respectively and can be used to quantify how far downstream from the object the bed behaves differently. These 'zones' were defined using the difference maps produced from the three different bed scans and generating 2-D profiles parallel to the flume wall and the bathymetry sampled every 0.5 cm. The generated profiles were plotted using a similar method to the one used for SS Apapa (Section 3.2.3) and points where trends were identified were marked and connected to create the 'zones'.

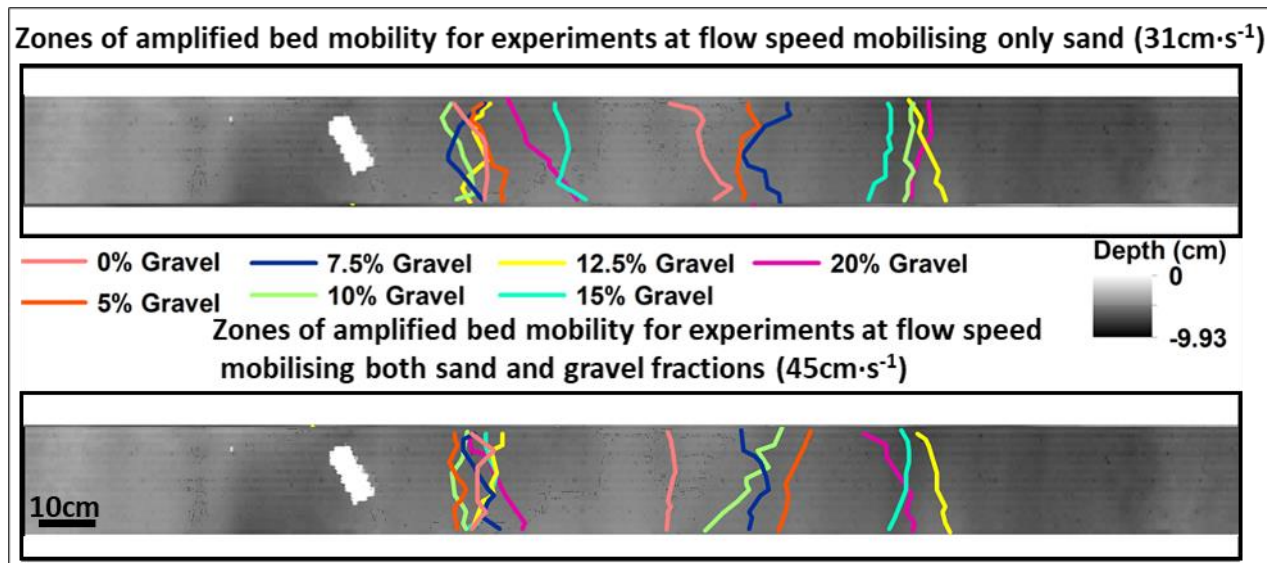


Figure 4.26: Zones of maximum bed mobility or 'zones of influence' as observed in the laboratory experiments conducted using the different sediment mixtures and the flow speeds of  $31 \text{ cm}\cdot\text{s}^{-1}$  and  $45 \text{ cm}\cdot\text{s}^{-1}$ .

The observed distances between the object and the 'zones of influence' for all bed mixtures and flow speeds are summarised in Table 4.4. Figure 4.26 and Table 4.4 show that for the experiments conducted at the flow speed mobilising only sand ( $31 \text{ cm}\cdot\text{s}^{-1}$ ) the second 'zone of influence' appeared to be closer to the object for the mixtures with  $f_g \leq 7.5\%$  where for the experiments conducted at the flow speed that mobilises both fractions ( $45 \text{ cm}\cdot\text{s}^{-1}$ ) the second 'zone of influence' appeared to be closer to the object for the mixtures with  $f_g \leq 10\%$ . For the experiments conducted at the flow speed mobilising only sand, the first 'zone of influence' appeared to be further away from the object for the experiments conducted using sediment mixtures with  $f_g \geq 15\%$ . For the experiments conducted at the flow speed mobilising both fractions, the first 'zone of influence' appeared to be at the same distance from the object for the experiments conducted using all the sediment mixtures.



Table 4.4: Measured mean distance between object and 'zones of influence' for the experiments using the two flow speeds.

Gravel % in the mixture	Flow speed mobilising only sand fraction (31cm·s <sup>-1</sup> )				Flow mobilising both sand and gravel fractions (45cm·s <sup>-1</sup> )			
	Zone1		Zone2		Zone 1		Zone 2	
	Distance (cm)	Mean Zone 1 Distance / Length	Distance (cm)	Mean Zone 1 Distance / Length	Distance (cm)	Mean Zone 1 Distance / Length	Distance (cm)	Mean Zone 2 Distance / Length
0	20.3	2.2	61.6	6.6	20.7	2.2	55.7	5.9
5	22.4	2.4	67.4	7.2	16.2	1.7	76.1	8.1
7.5	17.2	1.8	70.9	7.5	20.7	2.2	69.8	7.4
10	18.0	1.9	97.0	10.3	16.9	1.8	68.4	7.3
12.5	20.5	2.2	100.6	10.7	22.8	2.4	101.5	10.8
15	37.2	4.0	92.8	9.9	22.7	2.4	96.1	10.2
20	33.3	3.5	99.6	10.6	23.6	2.5	95.5	10.2

### 4.3.2 Observed evolution of scour mark geometry

To quantify how long the scour mark is in relation to the gravel percentage in the mixture and the potential of the flow to mobilise sand and/or gravel, the scour mark was tracked on the DEMs produced using the 'final' scan from the SeaTek 5 MHz acoustic transducers. Scour depth, width, length, and volume calculations were made from the analyses of the DEMs of the 'Initial flat bed', 'mature bed' and the 'final' scans for each laboratory experiment (see example in [Figure 4.27](#)).

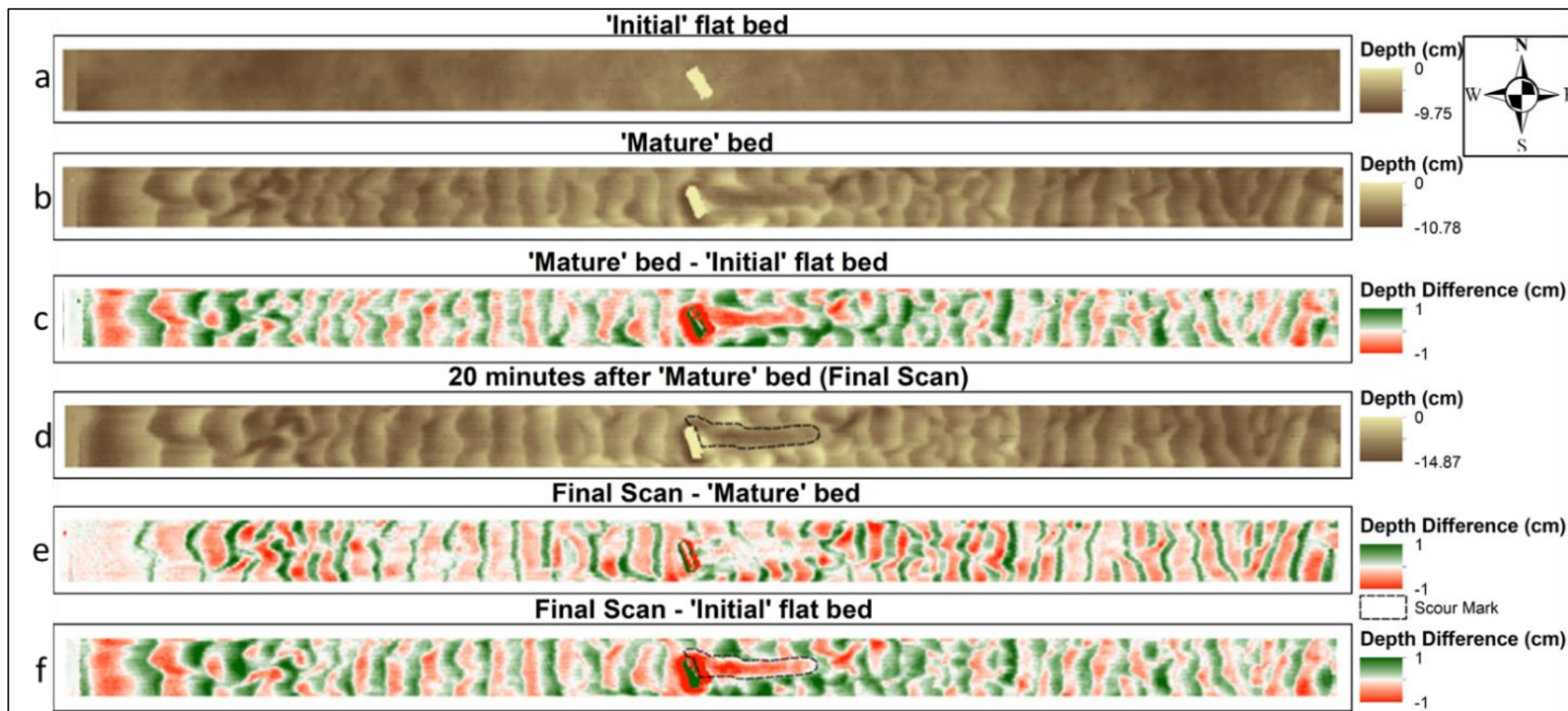


Figure 4.27: Example of the DEMs produced using the SeaTek acoustic transducers, for the laboratory experiments using a bed with 7.5% gravel. a) 'Initial flat bed', b) 'mature' bed, c) bathymetric difference between the 'mature' DEM bed and the 'initial flat bed' DEM, d)'final bed' DEM, e) bathymetric difference between the 'final bed' DEM and the 'mature' bed DEM and f) difference map between the 'final bed' DEM and the 'initial flat bed'

The scour mark's length measurements as recorded for the 'north' side of the scour mark (see Figure 4.27) for the experiments conducted at the flow speed mobilising only sand ( $31 \text{ cm}\cdot\text{s}^{-1}$ ) are presented in Figure 4.28a. No scour development was recorded in the case of the bed consisting of pure gravel. Results for the experiments conducted at the flow mobilising both fractions ( $45 \text{ cm}\cdot\text{s}^{-1}$ ) are presented in Figure 4.28b. Figures 4.28c and 4.28d present a scour length / object length ratio as a comparison, for the two flow speeds.

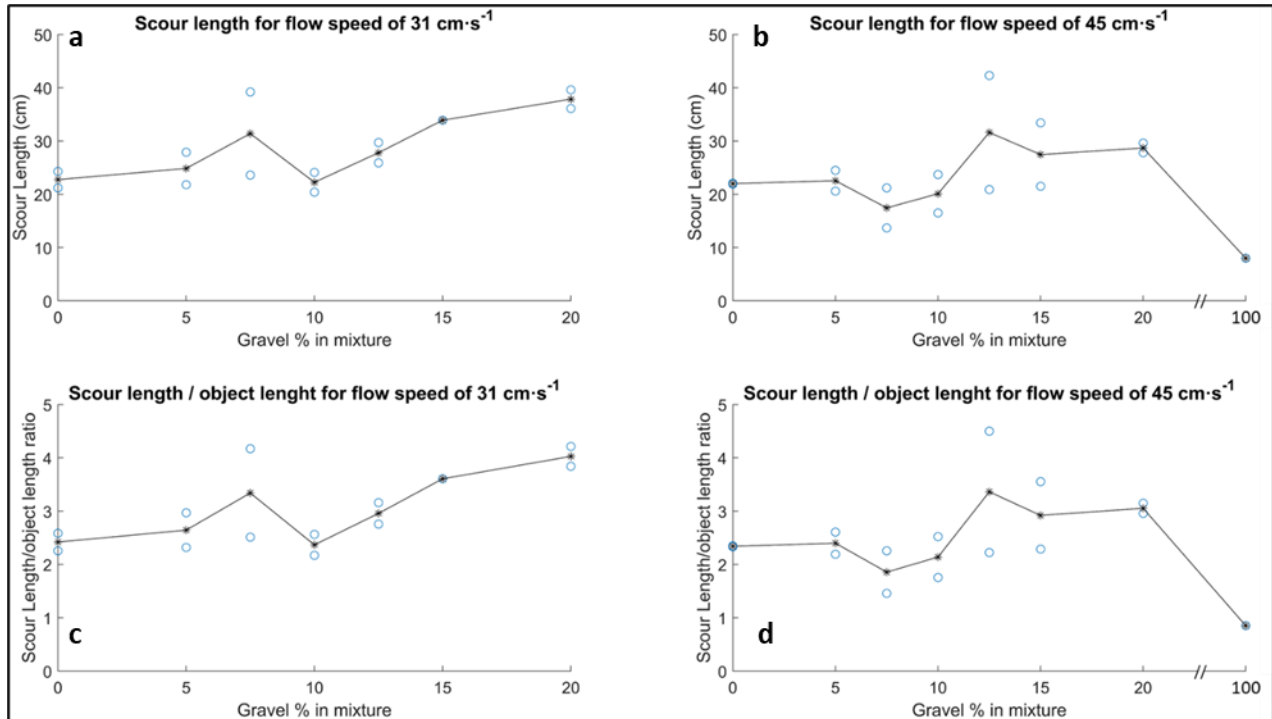


Figure 4.28: 'North' side scour mark length a) for the flow speed mobilising only sand ( $31 \text{ cm}\cdot\text{s}^{-1}$ ), b) for the flow speed mobilising both fractions sand ( $45 \text{ cm}\cdot\text{s}^{-1}$ ) and scour length/ object length ratio for c) the flow speed mobilising only sand ( $31 \text{ cm}\cdot\text{s}^{-1}$ ) and d) the flow speed mobilising both fractions ( $45 \text{ cm}\cdot\text{s}^{-1}$ ). The \* sign represents the mean value of the duplicated experiments.

The longest scour was observed at the bed with 20% gravel and at the flow speed mobilising only sand ( $31 \text{ cm}\cdot\text{s}^{-1}$ ), with a mean length of 37.8 cm, which is 4.03 times the length of the object and with variation around the mean of 1.9 cm. The second longest scour mark for this lower flow speed was observe in the bed with 15% gravel. For the experiments using the higher flow speed, the longest scour mark was observed in the mixture with 12.5% gravel, with a mean length of 31.6 cm, which is 3.37 times the length of the object and with variation around the mean of 7.6 cm. The second longest scour mark for this high flow speed was observed in the bed with 20% gravel.

When using the flow speed of  $31 \text{ cm}\cdot\text{s}^{-1}$ , the lowest mean scour width was measured at the mixture with 7.5% gravel and a general widening of the scour mark with higher gravel percentage in the bed mixture (Figure 4.29). When using the flow speed of  $45 \text{ cm}\cdot\text{s}^{-1}$ , the opposite was observed: the highest mean scour width was observed for the bed with 5% gravel, and a general reduction of the scour mark's width was noted with increasing the gravel percentage in the mixture. The scour L:W ratio however, shows a higher ratio at the experiments with 7.5% gravel and at the flow speed of 31

$\text{cm}\cdot\text{s}^{-1}$ , with a general increase of the gravel % in the mixture, with higher variations around 7.5% to 12.5% gravel. Finally, the L:W ratio for the experiments conducted at the flow speed of  $45 \text{ cm}\cdot\text{s}^{-1}$ , show highest values at the experiments with 12.5% gravel, where once again the largest variations to the general trend appear when the gravel is between 7.5% and 12.5.

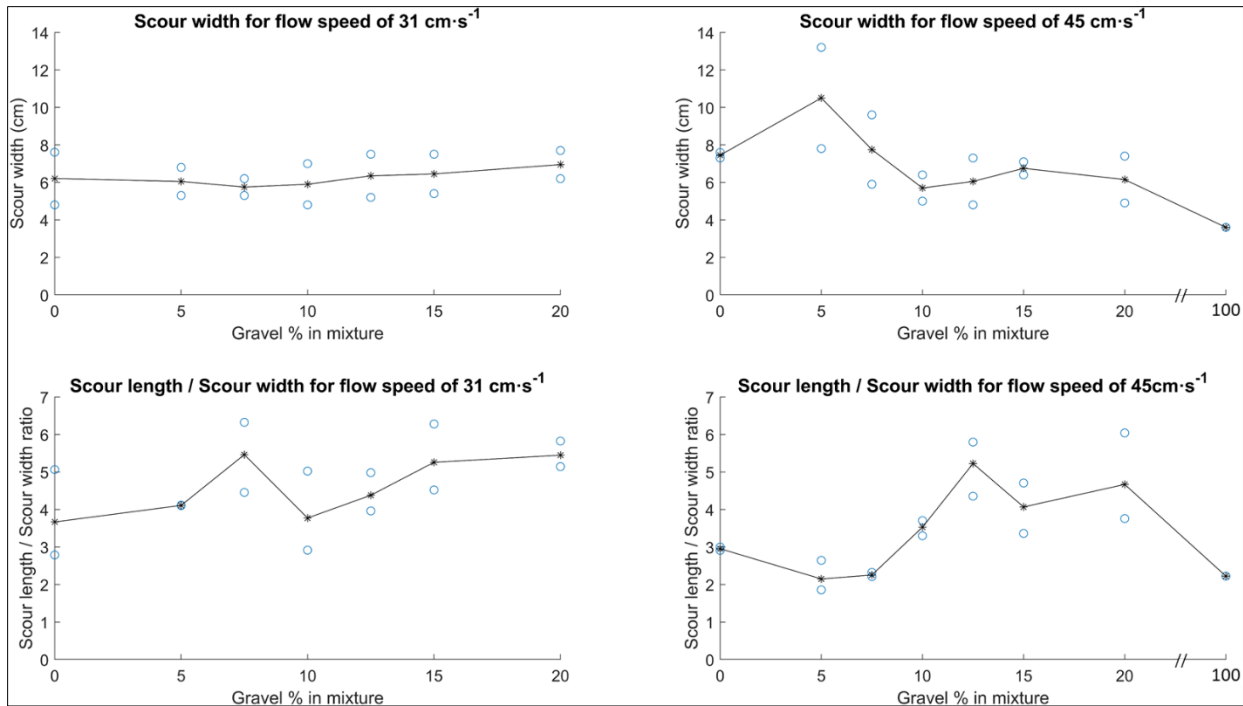


Figure 4.29: ‘North’ side scour width as measured for laboratory experiments using different mixtures at flow speeds of a)  $31 \text{ cm}\cdot\text{s}^{-1}$ , and b)  $45 \text{ cm}\cdot\text{s}^{-1}$ . c-d) scour length/scour width (L:W) ratio as measured for the laboratory experiments using different mixtures at flow speeds of  $31 \text{ cm}\cdot\text{s}^{-1}$  and  $45 \text{ cm}\cdot\text{s}^{-1}$  respectively. The \* sign represents the mean value of the measurements from the two laboratory experiments using the same sediment mixtures and flow speed.

The mean flume bed depth for all the experiments varies between -7.8 cm and -8.8 cm (Figure 4.30). For the lower flow speed, the largest mean scour depth occurs in a bed with 20% gravel, and the lowest mean scour depth in the bed with 10% gravel. For the higher flow speed, the largest mean scour depth occurs in a bed with 20% gravel and the lowest mean scour depth in a bed with 7.5% gravel (and the control, pure sand case). In the case of the lower flow speed, the mean scour depth decreases with increasing gravel percentage in the mixture up to the case of 10% gravel and becomes deeper in the cases of beds consisting of 12.5% to 20% gravel. For the case of the higher flow speed, the scour depth generally increases with increasing the gravel percentage in the mixture, with the exception of the experiments conducted using 5% gravel (and the cases of control beds).

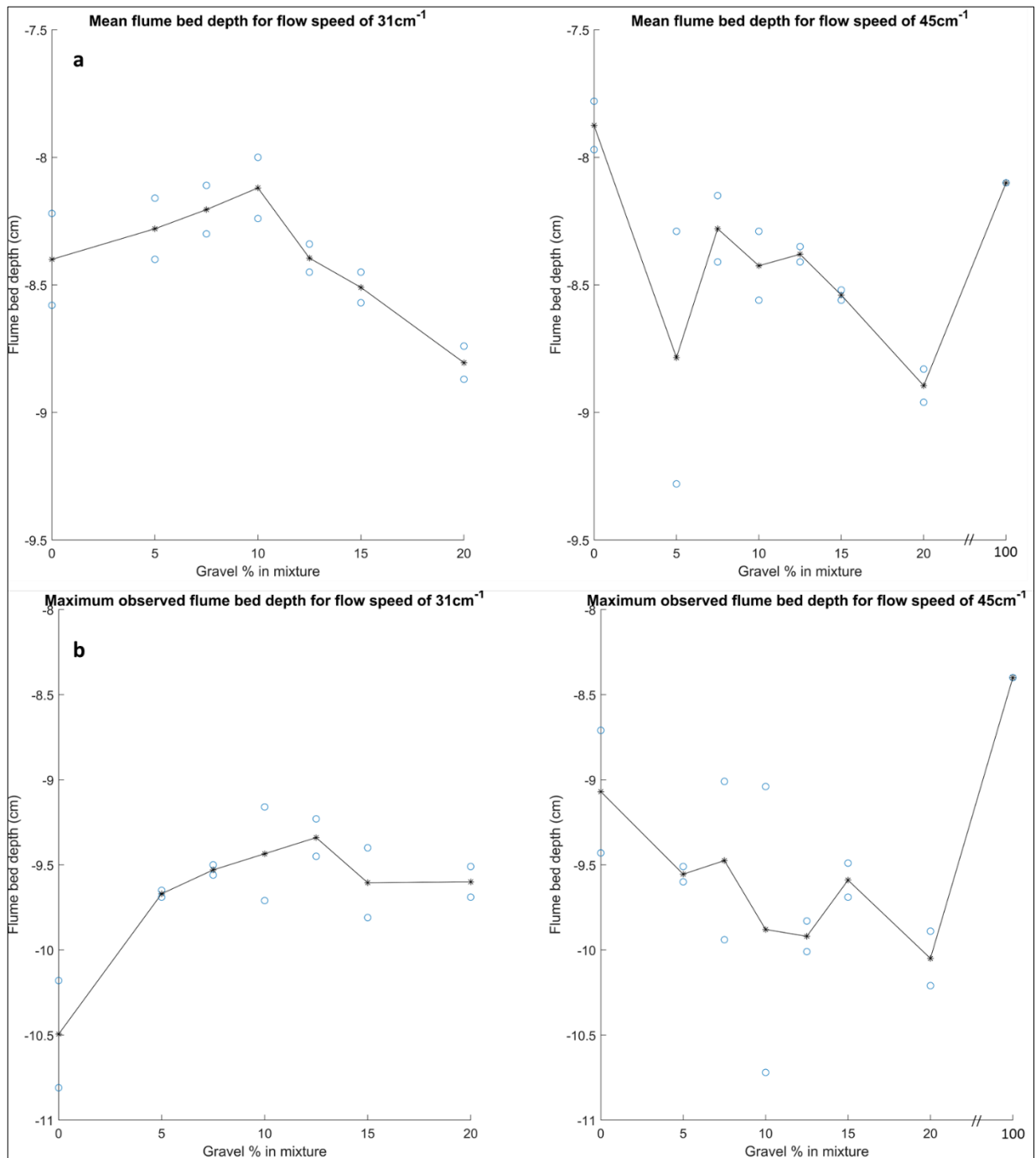


Figure 4.30: a) Mean flume bed depth observed from the laboratory experiments using different mixtures at the flow speeds of 31 cm·s<sup>-1</sup> (left) and 45 cm·s<sup>-1</sup> (right). b) Maximum flume bed depth observed from the laboratory experiments using different mixtures at the flow speeds of 31 cm·s<sup>-1</sup> (left) and 45 cm·s<sup>-1</sup> (right). The \* sign represents the mean value of the measurements from the two laboratory experiments using the same sediment mixtures and flow speed.

The maximum flume depth observed within the scour mark for the laboratory experiments using the different sediment mixtures and flow speeds is presented in [Figure 4.30b](#). The mean maximum bed depth value of the two duplicate laboratory experiments using the flow speed of 31 cm·s<sup>-1</sup>, varies between -9.34 cm and -10.50 cm. For this flow speed, the largest maximum scour depth occurs in a bed with pure sand and 5% gravel, and the lowest maximum scour depth occurs in a bed with 12.5%



gravel. The mean maximum bed depth value of the two duplicate laboratory experiments using the flow speed of  $45 \text{ cm}\cdot\text{s}^{-1}$ , varies between  $-8.30$  and  $-10.05 \text{ cm}$ . For this flow speed, the largest maximum scour depth is observed in a bed with pure sand and 20% gravel, and the lowest maximum scour depth in a bed with 7.5% gravel.

Figure 4.31 presents the sediment volume that was transported away within the area of the ‘northern’ side of the scour mark during the full duration of the laboratory experiments.

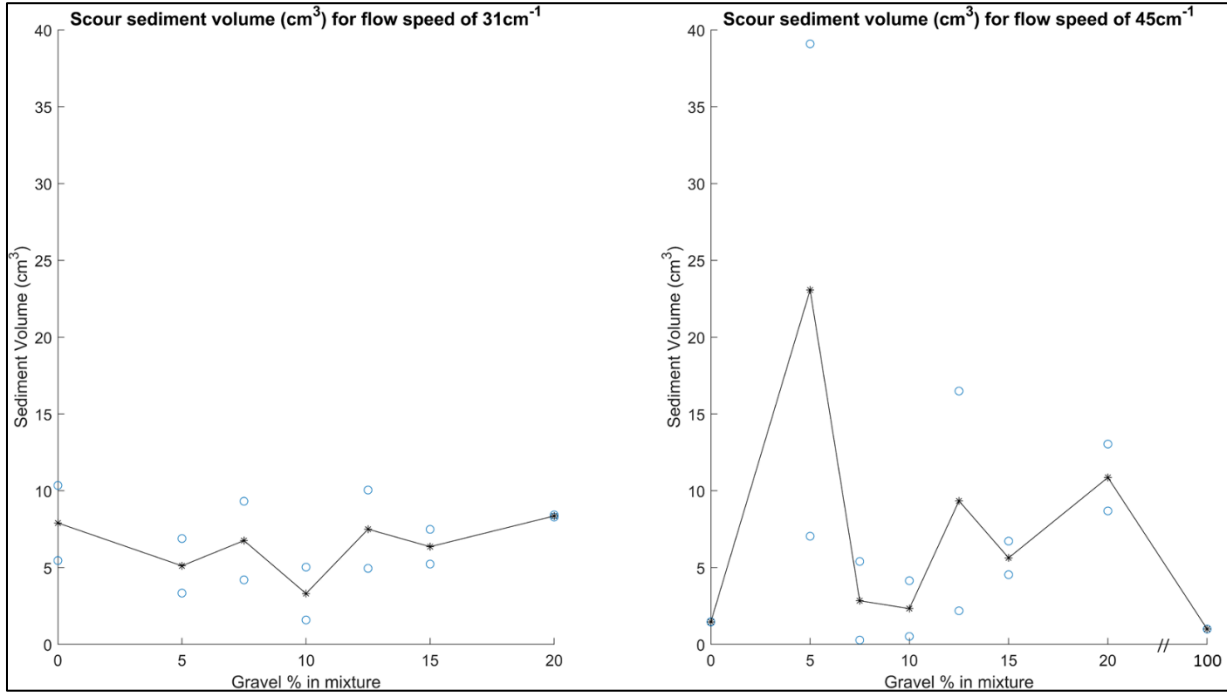


Figure 4.31: Calculated scour sediment volume loss for the flow speeds of  $31 \text{ cm}\cdot\text{s}^{-1}$  (left) and  $45 \text{ cm}\cdot\text{s}^{-1}$  (right). The \* sign represents the mean value of the measurements from the two laboratory experiments using the same sediment mixtures and flow speed

The calculated mean volumetric loss of the two duplicate laboratory experiments using the flow speed of  $31 \text{ cm}\cdot\text{s}^{-1}$ , varies between  $3.3$  and  $8.4 \text{ cm}^3$ . For this flow speed, the largest sediment loss occurs in a bed with 20% gravel and the lowest sediment loss in a bed with 10% gravel. The calculated mean volumetric loss of two duplicate laboratory experiments using the flow speed of  $45 \text{ cm}\cdot\text{s}^{-1}$ , varies between  $1.1$  and  $23.1 \text{ cm}^3$ . For this flow speed, the largest sediment loss occurs in a bed with 5% gravel and the lowest sediment loss in the bed with 10% gravel.

### 4.3.3 Object's movement during the laboratory experiments

The object was placed at  $60^\circ$  to the flow at the beginning of all laboratory experiments. However, during all laboratory experiments, apart from the cases of the bed consisting of pure gravel, the object moved unintendedly, changing the object's orientation to the flow to between  $67^\circ$  and  $89^\circ$ . This deviation was higher for the high flow speed ( $45 \text{ cm}\cdot\text{s}^{-1}$ ), with minimum and maximum angles of  $69^\circ$  and  $89^\circ$  respectively. Using the low current speed ( $31 \text{ cm}\cdot\text{s}^{-1}$ ) the changed angle of the object to the flow varied between  $67^\circ$  and  $76^\circ$  respectively. Figure 4.32 shows the observed object

orientation at the end of the laboratory experiments using the different sediment mixtures and flow speeds.

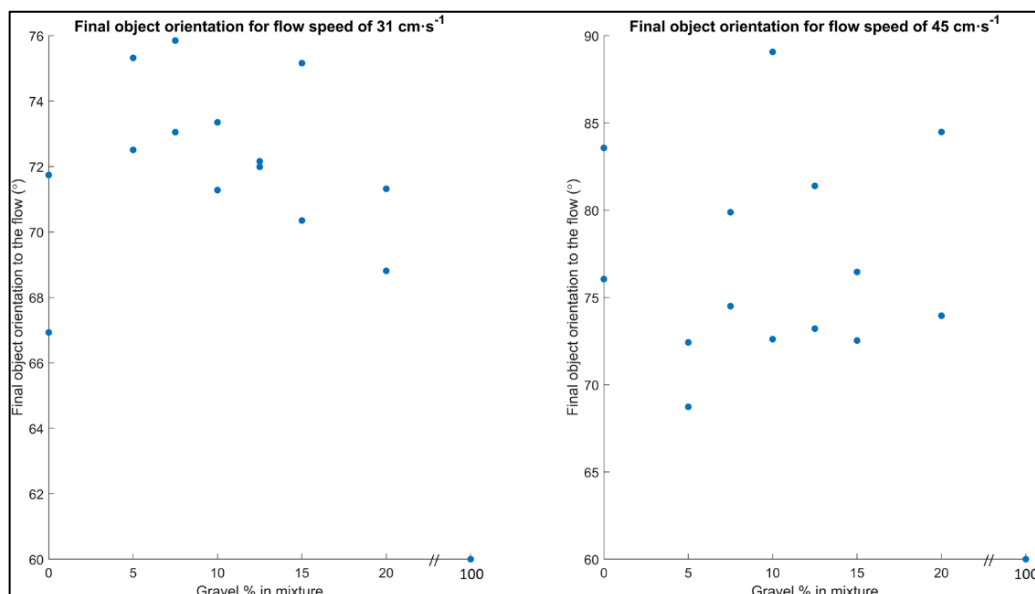


Figure 4.32: Object orientation to the flow as recorded using the 'final' DEMs, for flow speed mobilising only sand (left) and for the flow speed mobilising both the sand and the gravel fractions (right).

#### 4.3.4 Observed evolution of bed composition (laterally and with depth)

To investigate the impact of enhanced flow around a cylinder on the sediment composition in the wake of the object, bed composition was visually monitored during the laboratory experiments, but it was also monitored using the down core sediment samples. To observe if the sediment was mixed well both laterally and vertically, as the bed was prepared, some preliminary tests were done via down-core sediment analyses prior to the laboratory experiments. PSA from sediment sample taken with a syringe at different locations of the bed prior to the experiments, showed that the gravel percentage within the mixture varied between -0.5 to +1.74%. For 90.63% (29 out of 32) of the samples, the variation of the gravel % from the intended mixture was between -0.5 and +0.6% (Figure 4.33) meaning that the sediment mixture was thoroughly mixed using the method described in Section 4.2.2 and that the sampling method is unlikely to be largely disruptive.

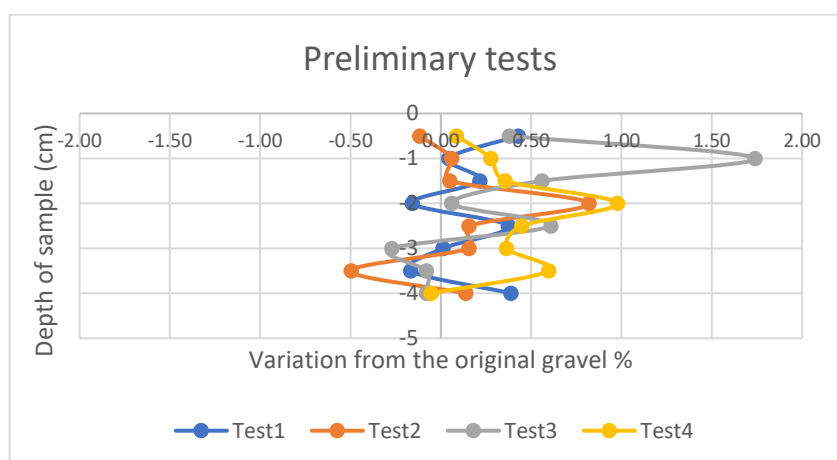


Figure 4.33: Gravel % variation from the original mixtures as observed after conducting PSA on samples collected prior to the laboratory experiments to ensure the thorough mixing of the sediment.

During the laboratory experiments, coarser sediments generally deposited in the bedform troughs and in the scour marks, whilst finer sediment was deposited at the bedform crests and the depositional feature. **Figure 4.34** shows a panoramic image of the flume (and sampling locations in scour mark and depositional feature), visualising the surface sediment composition across the flume.

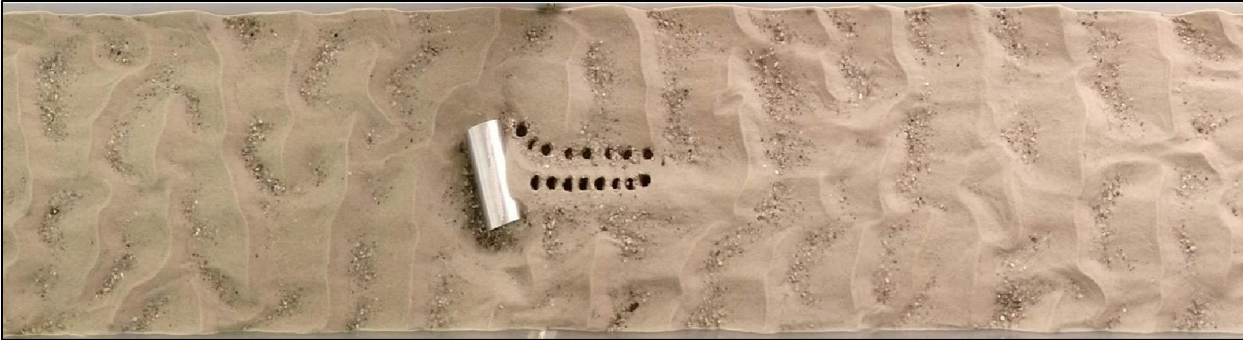


Figure 4.34: Panoramic image over the object showing sediment composition around the object area and sampling points within the scour mark and depositional feature. The uni-directional flow in the laboratory experiment was from left to right.

**Figure 4.35** and **Figure 4.36** present the analyses of the down-core sediment samples taken at the 10 sample locations described in Section 4.2.5.

For both flow speeds, increased gravel percentages were found in the scour mark and the bedform troughs both upstream and downstream of the object. Decreased gravel percentages were observed at the bedform crests and the depositional feature.

For the flow speed of  $31 \text{ cm}\cdot\text{s}^{-1}$  (**Figure 4.35**), the highest variations were observed at the samples collected from the top 0.5 cm of the sedimentary bed. More specifically, for the bedform crests and bedform troughs upstream, the mean variation from the original gravel percentage was between -4.17% and -9.01%, and +2.49% and +14.19% respectively. On the other hand, a mean variation between -3.71% and -11.00% was observed at the bedform crests downstream, and a mean variation between +6.99% and +16.91% at the bedform troughs downstream. The gravel % within the top 0.5 cm of the scour mark varied between +7.56% and +28.71% from the original percentage, where for the depositional feature it varied between -0.68% and -8.58%. For the flow speed of  $45 \text{ cm}\cdot\text{s}^{-1}$  (**Figure 4.36**), the gravel percentage in the first 0.5 cm of the sedimentary bed varied between -5.76% and +1.75% for the bedform crest upstream, and +6.17 % and +13.66% for the bedform troughs upstream. Similarly, for the bedform crests downstream the variation was between -4.29% and -11.76%, where for the bedform troughs downstream the variation was between +6.24% and 8.99%. Finally, for the scour mark, the observed variation from the original percentage was between 7.56 % and 15.12% where for the depositional feature the gravel % varied between -2.89% and -9.09% from the original mixture.

No obvious trends were observed for the rest of the down-core variation of the gravel percentage; however, it can be stated that for over 90% of the samples, the variation was within 5% of the original mixture. Higher variations were observed, in most cases at the bottom of the sediment core. No sediment samples were attained from the experiments using the pure gravel bed.

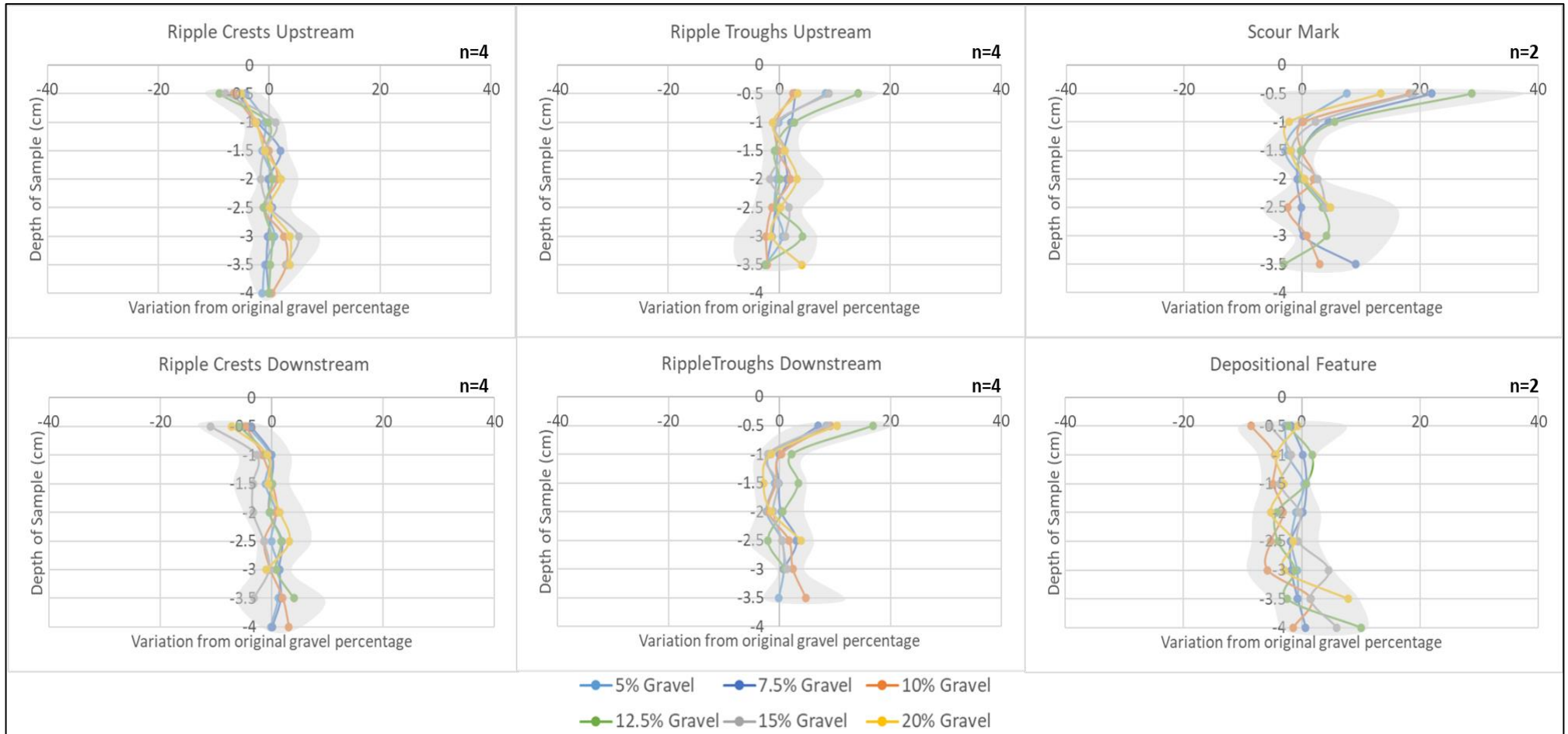


Figure 4.35: Gravel % variation from the original mixture, as observed at the end of the laboratory experiments using the different mixtures at the flow speed mobilising only sand ( $31 \text{ cm}\cdot\text{s}^{-1}$ ). The grey envelopes represent the standard deviation around the means (the dots) of “ $n$ ” measurements at each depth from two duplicate experiments.

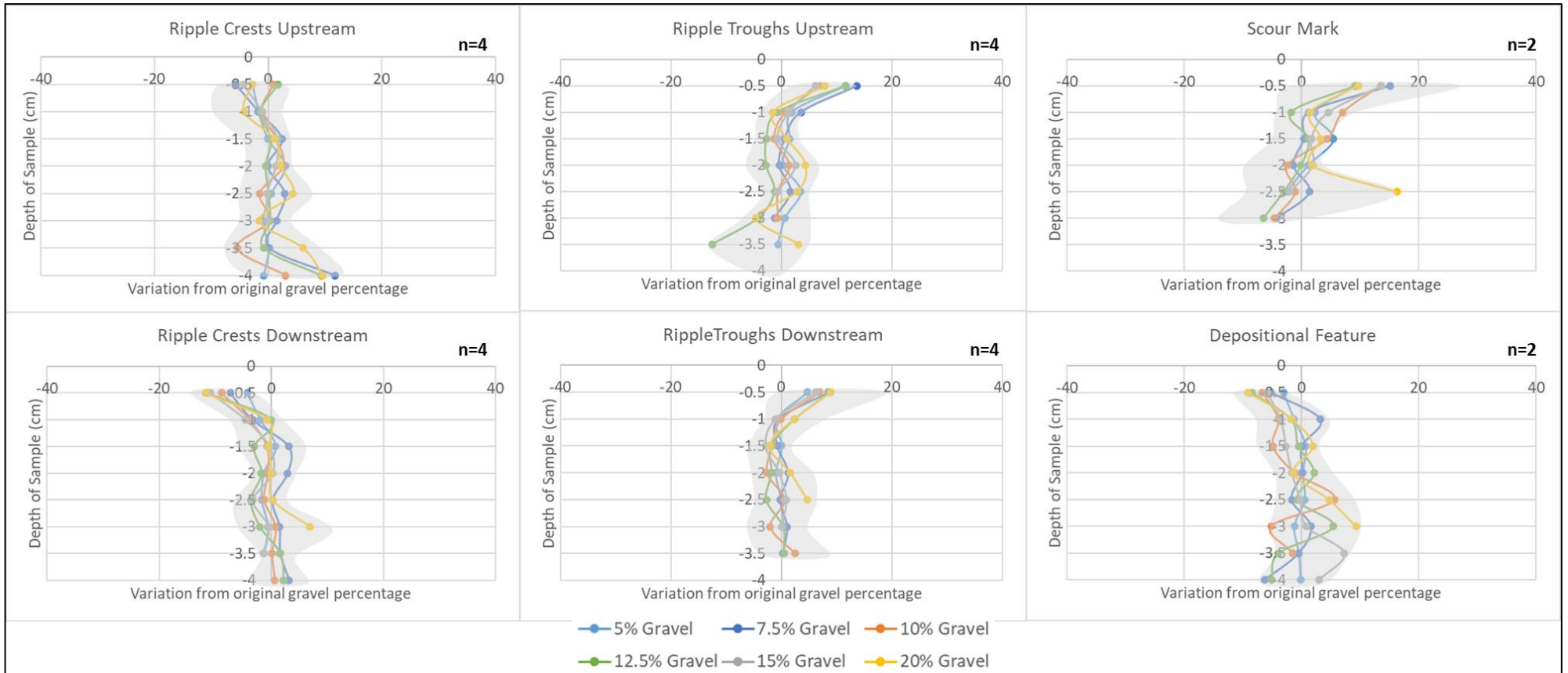


Figure 4.36: Gravel % variation from the original mixture, as observed at the end of the laboratory experiments using the different mixtures at the flow speed mobilising both sand and gravel fractions ( $45 \text{ cm} \cdot \text{s}^{-1}$ ). The grey envelopes represent the standard deviation around the means (the dots) of "n" measurements at each depth from two duplicate experiments.



Figures 4.37 and 4.38 are similar to Figures 4.35 and 4.36, but instead of the  $\sigma$  envelope, they contain information of the height of the bedform crests (straight lines) for the bedforms upstream and downstream and the scour marks and depositional features. This is done to investigate the correlation of the gravel percentage variation with the ripple formation processes, but also to understand the cause of the down-core gravel percentage variation.

Figure 4.37 and Figure 4.38 show that the first large variation in the gravel percentage down-core can be explained to an extent by the height of the ripple crests, for the experiments conducted at low flow velocities. In contrast, for the experiments conducted at high flow velocity, the variation of the gravel continues further down-core, with no obvious trends present, or direct correlation with the ripple crest or depositional feature heights.

Gravel % appears to vary throughout the sedimentary bed and at depths underneath the visibly mobilised sediments, suggesting that the definition of the sedimentary “active layer” extent ending at the level underneath the bedforms (deepest part of bedform troughs) may not be correct. Figures 4.35 – 4.38 suggest that mixed beds do not remain mixed at the same proportions after sediment mobilisation (scour or bedform formation processes). This interactive process between sediment mobilisation and bed composition (that constantly changes) causes more difficulties in thorough understanding of the relationship between the two using physical modelling (laboratory experiments).

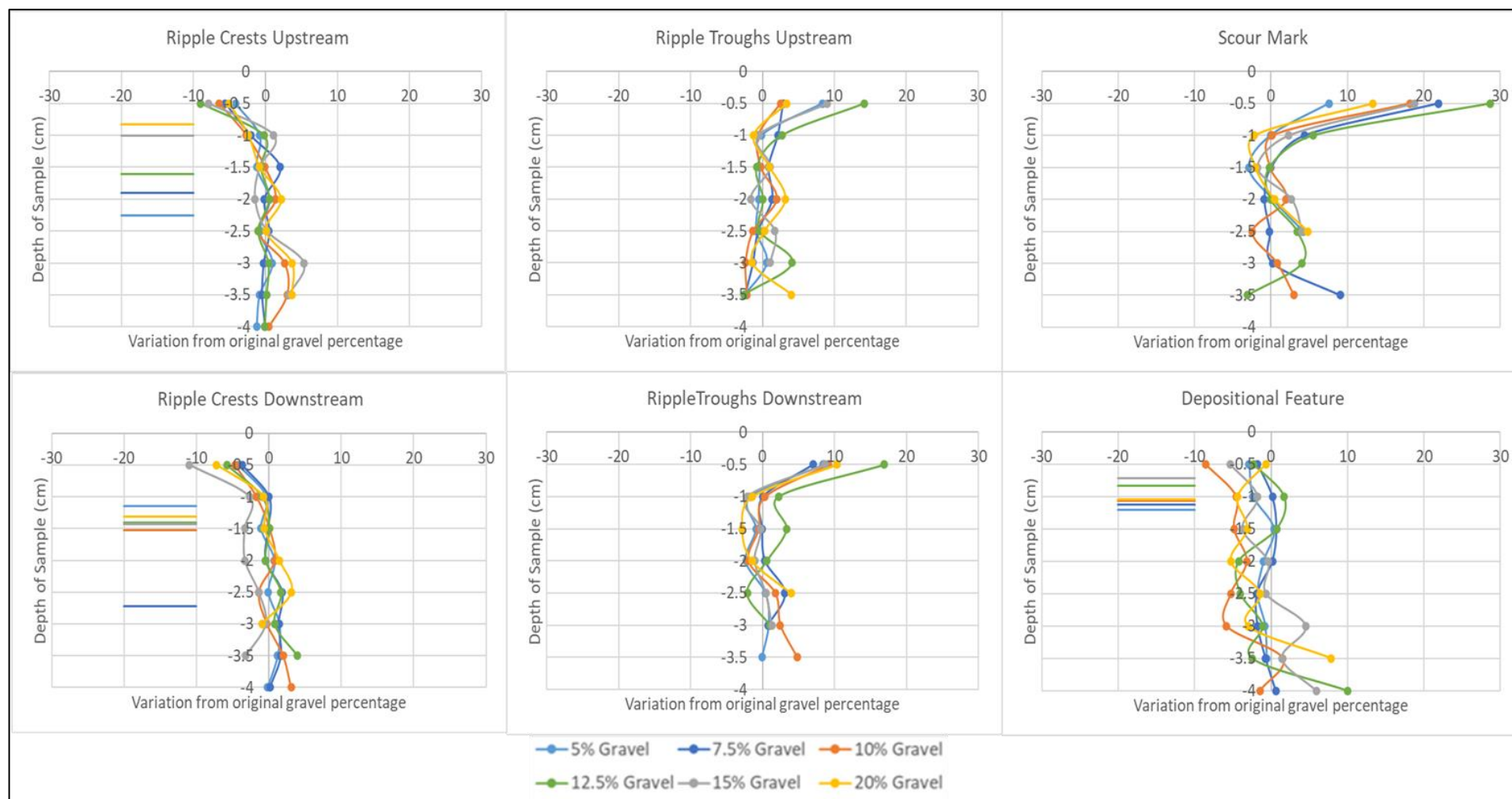


Figure 4.37: Gravel % observed in down core samples and the maximum observed ripple height observed for each mixture for the experiments conducted at the flow speed mobilising only the sand fraction ( $31 \text{ cm}\cdot\text{s}^{-1}$ ). The vertical lines indicate the highest sampled ripple crest point or depositional feature for each sediment mixture.

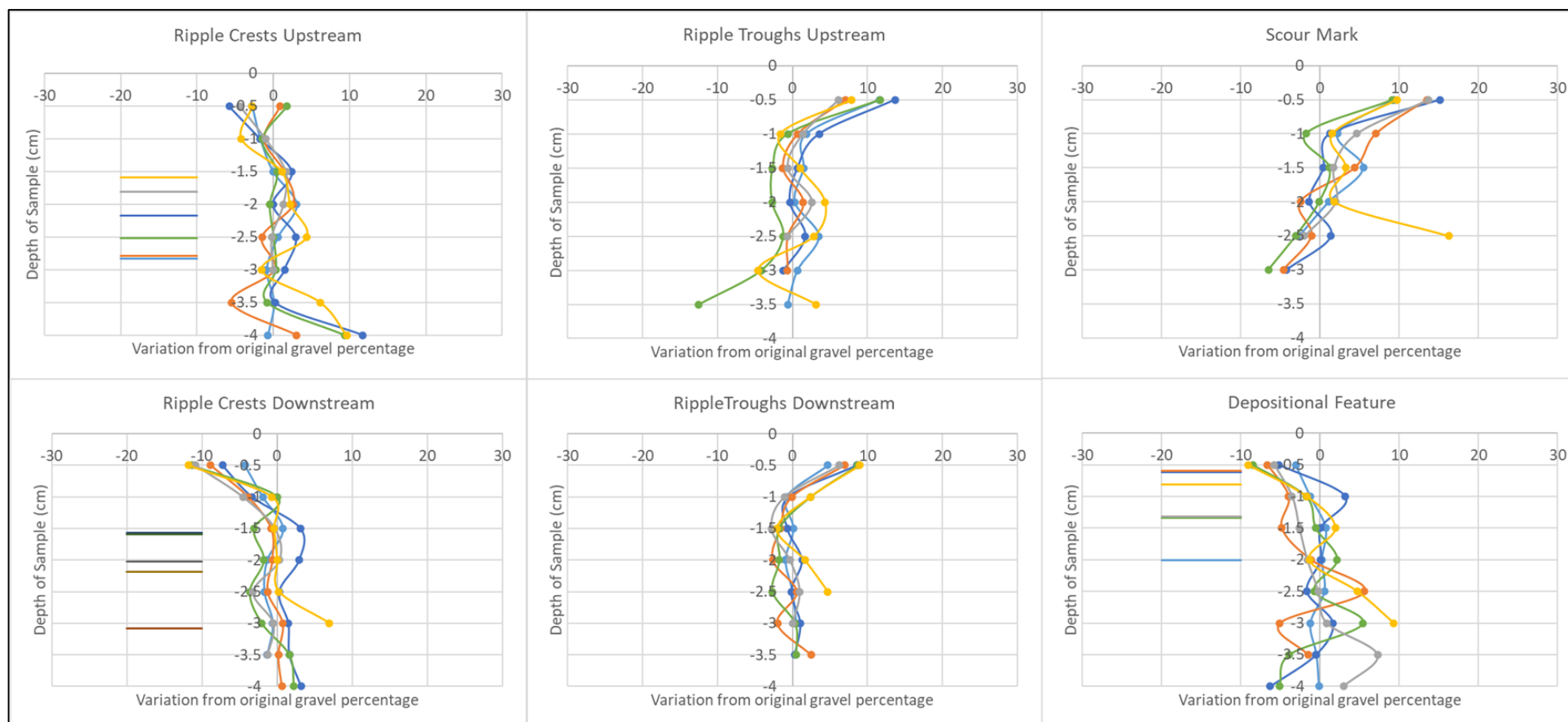


Figure 4.38: Gravel % observed in down core samples and the maximum observed ripple height observed for each mixture for the experiments conducted at the flow speed mobilising only the sand fraction ( $45 \text{ cm}\cdot\text{s}^{-1}$ ). The vertical lines indicate the highest sampled ripple crest point or depositional feature for each sediment mixture.

#### 4.3.5 Modelled evolution of flow amplification, scour geometry and bed composition

The input parameters of the laboratory experiments (physical modelling) were used to inform a coupled hydrodynamic and sediment transport model (TELEMAC3D – GAIA), to investigate the effect of the enhanced flow dynamics downstream of the object and the effect of the bed composition on scour formation downstream of the object. The bed composition (that was known in contrast with the *SS Apapa* site) and bathymetric data collected from the SeaTek transducers were used as input and as validation of the model's outputs. As a reminder, depth averaged flow velocities were measured using the MetFlow UDVP instrument upstream and downstream of the object. In contrast with the *SS Apapa* case, no detailed measurements of flow were taken within the scour mark and at the 'edges' of the cylinder, due to limitations of the UDVP instrument and time restrictions.

Comparison of the measured and modelled incoming and disturbed from the object depth averaged flow velocity is presented in [Figure 4.39](#).

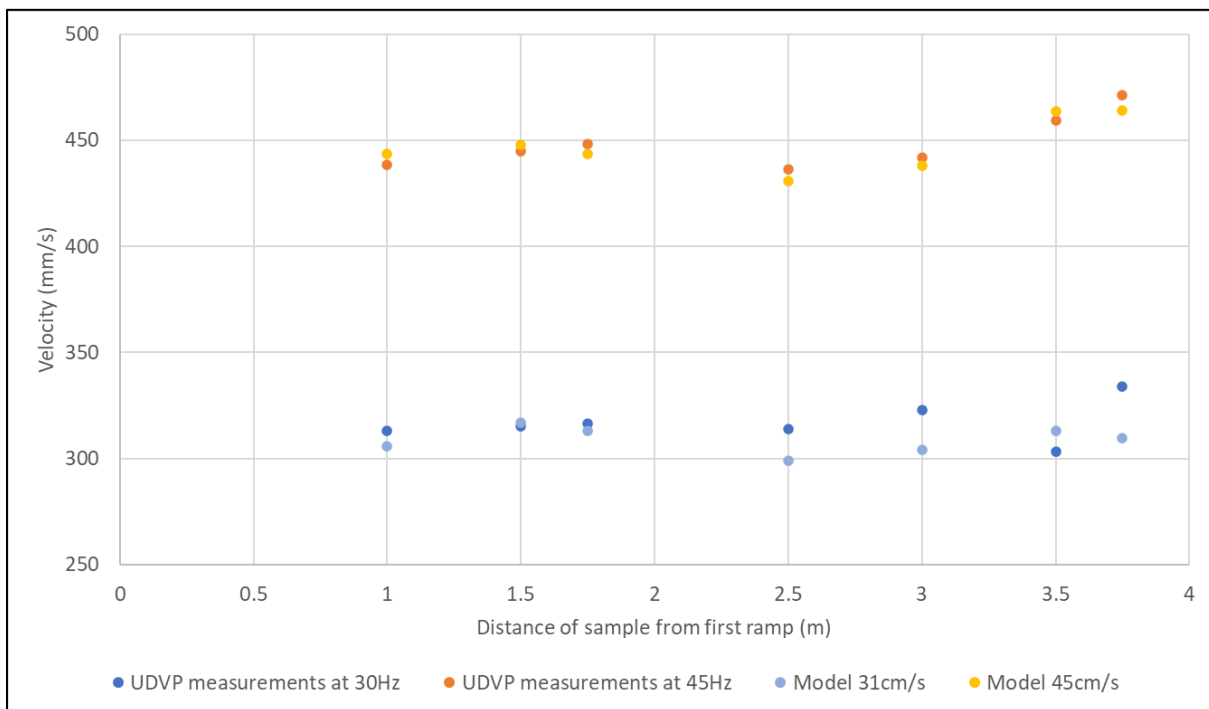


Figure 4.39: Modelled and measured by the UDVP instrument depth averaged flow velocities upstream and downstream of the object in the laboratory experiments.

The comparison of the flow velocities shows a good estimation of the depth averaged flow velocity, both upstream and downstream of the object by the hydrodynamic component (TELEMAC2D/3D) of the numerical model. More specifically, for the numerical modelling work of the laboratory experiments conducted at the flow speed of  $31 \text{ cm}\cdot\text{s}^{-1}$ , the comparison shows that the numerical model underestimates the flow speed upstream of the object by  $\sim 1\%$  and the depth averaged flow speed downstream of the object by  $\sim 4\%$ . For the numerical modelling work of the experiments conducted at the flow speed of  $45 \text{ cm}\cdot\text{s}^{-1}$ , the comparison shows that the numerical model overestimates the flow speed upstream of the object by  $\sim 0.3\%$  where it underestimates the depth averaged flow speed downstream of the object by  $\sim 0.7\%$ . The numerical model seems to have

variations in the order of 0.3% to 4% from the measured using the UDVP instrument depth averaged velocities. However, these variations are within the error margin of the UDVP instrument used for the experimental measurements (0.4 – 5%). Thus, as the numerical modelled flow speeds fall within the instrument's accuracy, the depth averaged flow velocities measured from the model can be trusted.

The coupled hydrodynamics and sediment transport numerical model was set to run for the exact same duration as the laboratory experiments using each sediment mixture. The coupled numerical model was set to run using the 'pre-run' (undisturbed) bed, with a timestep of 0.00625 s, and the object placed on the bed as explained in Section 4.2.6. Estimations of the depth averaged flow velocities using the hydrodynamic component of the coupled numerical model, shows a 10% increase in the depth averaged flow velocity downstream of the part of the cylinder that the flow hit first, for the numerical modelling work conducted using the flow speed of  $31 \text{ cm}\cdot\text{s}^{-1}$ . For the numerical modelling work conducted at the flow speed of  $45 \text{ cm}\cdot\text{s}^{-1}$ , the model predicts an increase of the depth averaged flow speed of up to 7% at the same location. The output of the bed dynamic component of the numerical model (GAIA) showed similarity with the SS *Apapa* case in the sense that the numerical model did not predict the bedform formation upstream and downstream of the object. The purpose of this numerical model, however, was not to predict the bedform formation, but to aid understanding of the processes co-existing for the scour formation on bimodal sediment, due to the fluid dynamics around the object.

The coupled numerical model predicts the shape of the scour downstream of the object well, for all the mixtures for the experiments conducted at the flow speed of  $31 \text{ cm}\cdot\text{s}^{-1}$ . The scour mark's length is within a 5% over- or under-estimation from the model. Although the scour mark's length is predicted well, the position of the scour is in most cases predicted further 'north' than the scour mark observed in the laboratory experiments (Figure 4.40). Where the numerical model was run with an initial bed of 15% gravel, it predicted scour mark formation at 3 places, with the 'middle' scour mark exactly at the location where scour mark was observed in the laboratory experiments.



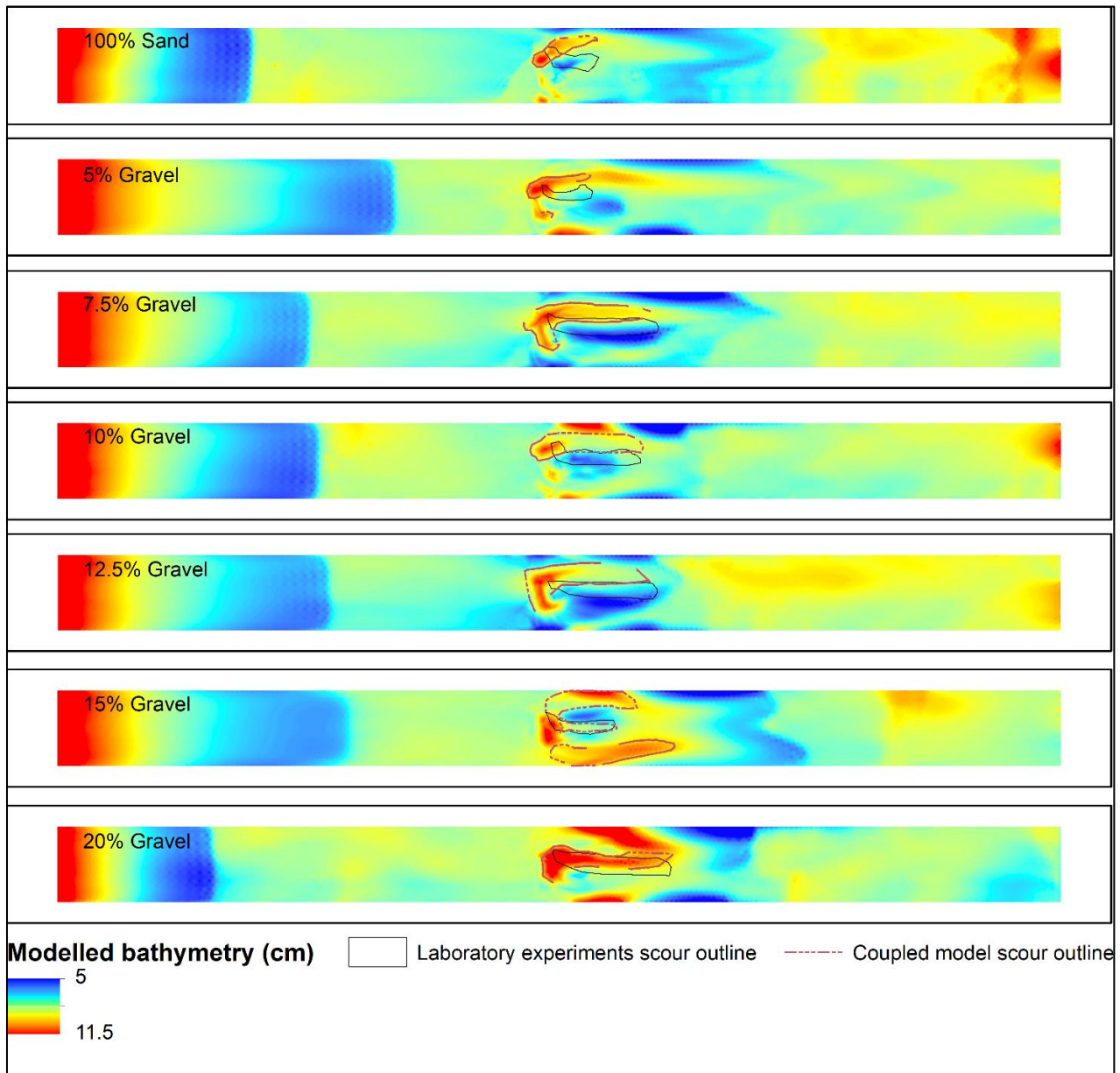


Figure 4.40: Numerical model outputs for bathymetry at the end of the runs replicating the laboratory experiments at initial flow speed of  $31 \text{ cm} \cdot \text{s}^{-1}$ .

For the laboratory experiments and numerical modelling work conducted using the flow speed of  $45 \text{ cm} \cdot \text{s}^{-1}$ , the numerical model overestimates the scour mark's extent for all the sediment mixtures. Overestimation of almost 93% in the scour mark's extent is observed at the pure sand mixture, where for the numerical modelling work conducted with the initial beds as mixed sediments, the overestimation of the scour mark's length is less than 27% (Figure 4.41). It is worth mentioning that in the case of the pure sand, 3-D bedforms were formed in the laboratory experiments (the model can't predict these) and scour edge delineation stopped where these bedforms started.

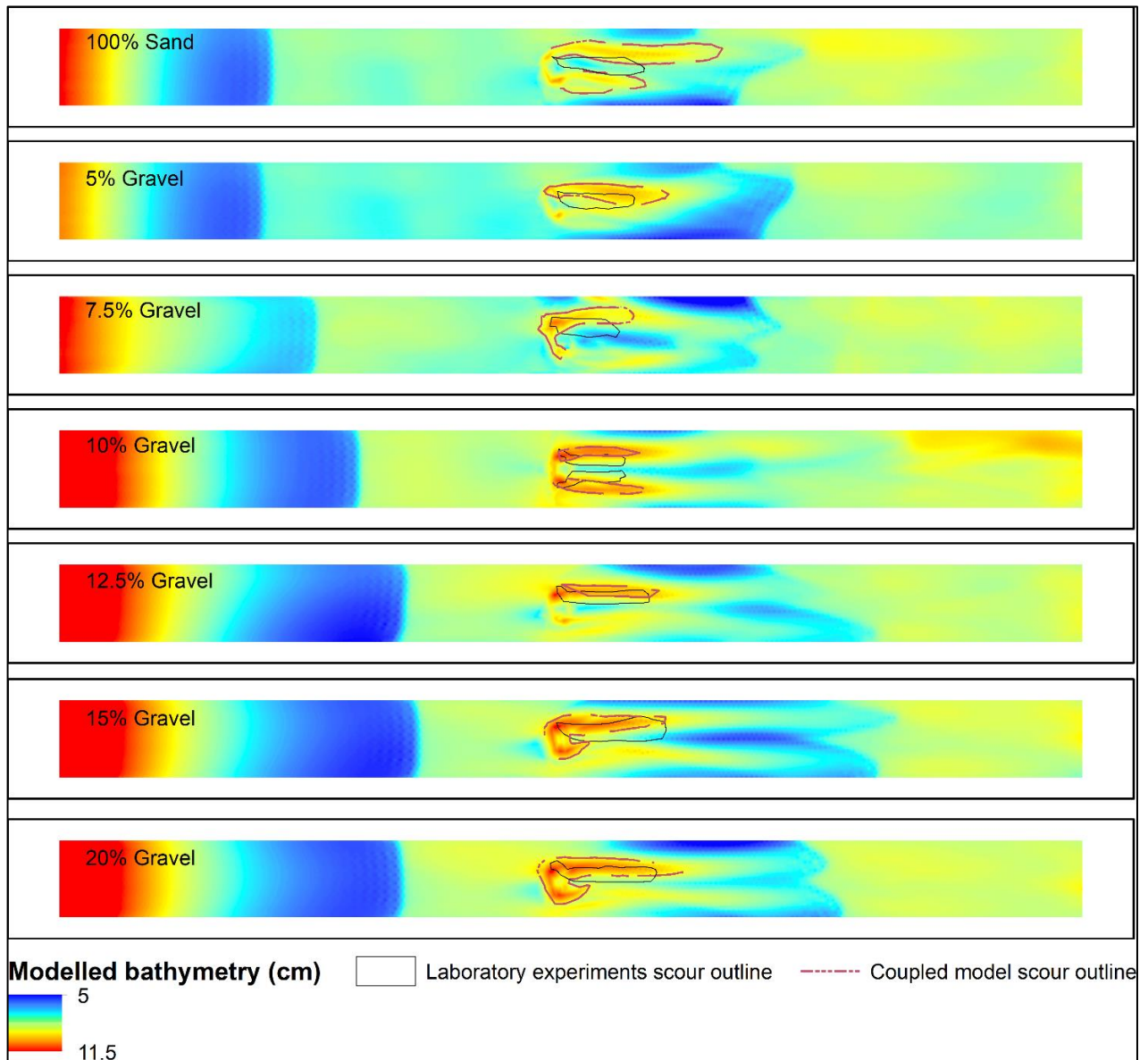


Figure 4.41: Numerical model outputs for bathymetry at the end of the runs replicating the laboratory experiments at initial flow speed of  $45 \text{ cm} \cdot \text{s}^{-1}$ .

The numerical model outputs as presented in [Figure 4.40](#) and [Figure 4.41](#) show that the numerical model predicts the scour mark best for the laboratory experiments conducted at the low current speed, for all the sediment mixtures. In contrast, for the high current speed, the numerical model predicts best the scour mark formation for the cases of the bed consisting of over 10% gravel, where it does not predict well the scour formation for the cases of the bed consisting of pure sand, 5% and 7.5% gravel.

The scour mark predicted from the numerical model, initiates at the sides of the cylinder with vertical edges. Scour formation started immediately when the computation using the numerical model started. The observed maximum bedload and suspended load transport rates as calculated from the coupled numerical model (maximum of all of the model's outputs) are presented in [Figure 4.42](#) and [Figure 4.43](#) for the numerical modelling work conducted using the income flow velocities of  $31 \text{ cm} \cdot \text{s}^{-1}$ .

1.

As Figure 4.42 shows, the higher values of bedload are present in the cases of sediment mixtures containing 5%, 7.5% and 10% gravel, with the longest extent being at the numerical model outputs of the run with the initial mixture consisting of 5% gravel. Longer extents of high values of bedload are present in the cases of the mixed beds, compared to the case of pure sand.

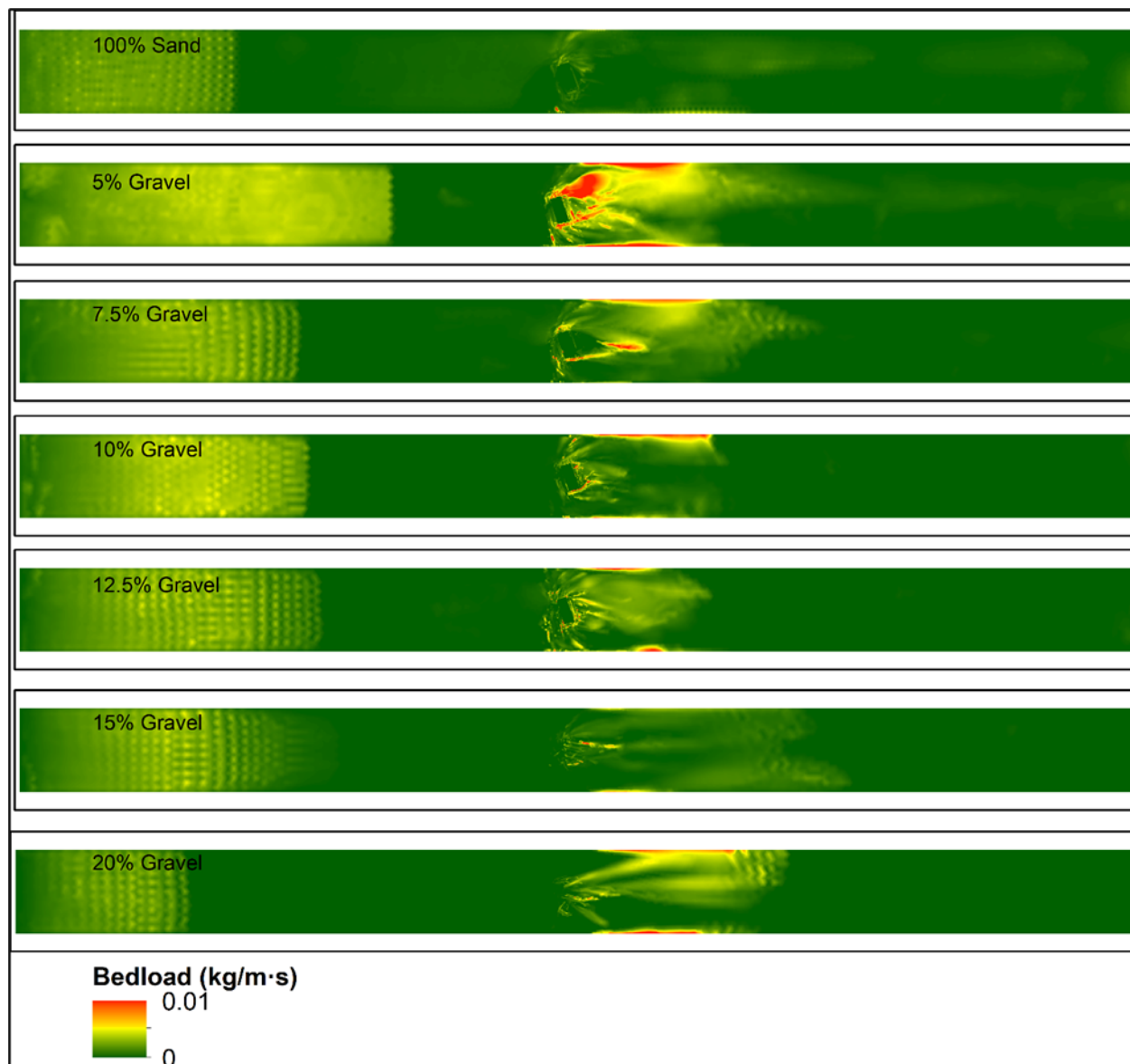


Figure 4.42: Numerical model outputs of maximum bedload for the runs replicating the laboratory experiments at initial flow speed of  $31 \text{ cm}\cdot\text{s}^{-1}$ .

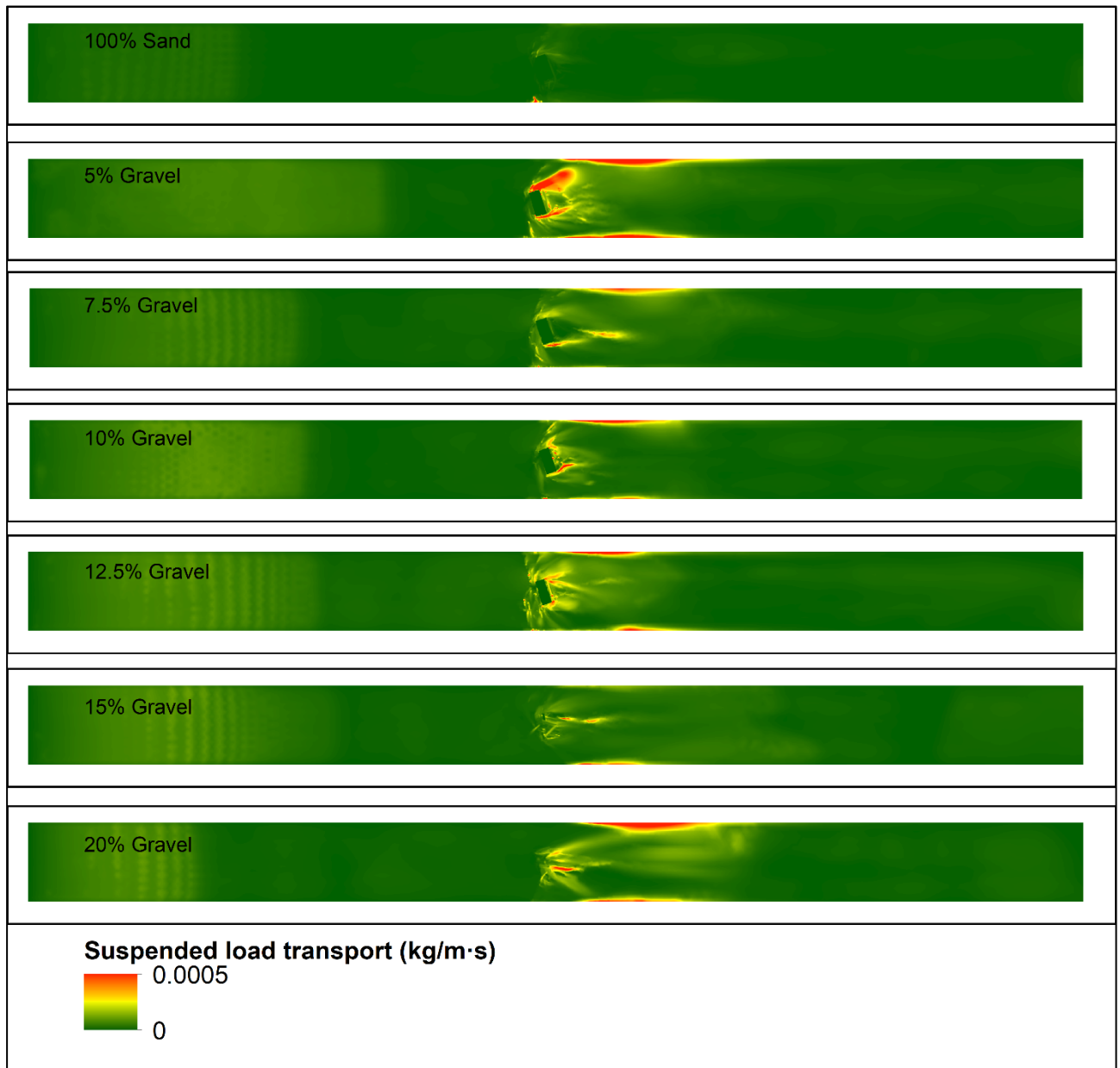


Figure 4.43: Numerical model outputs for maximum suspended load for the laboratory experiments at initial flow speed of  $31 \text{ cm}\cdot\text{s}^{-1}$ .

The numerical model predicts higher values of suspended load in the sediment mixtures containing 5%, 7.5%, 10% and 12.5% gravel, with the longest extent being at the numerical model outputs of the run with the initial mixture consisting of 5% gravel (Figure 4.43). Once again, longer extents of high bedload values are present in the cases of mixed beds, compared to the case of pure sand. In mixed beds, high values of bedload are observed at the edges of the flume downstream of the object. In the case of the numerical modelling work conducted with the initial flow at  $45 \text{ cm}\cdot\text{s}^{-1}$ , the modelled bedload (Figure 4.44) shows high values in all cases. As aforementioned this flow speed was monitored (visually and theoretically) to being able to mobilise both sediment fractions. The numerical model outputs show longer extent of bedload transport in the runs where the bed consisted of 15% and 20% gravel. Bedload transport initiates in all cases from the edges of the cylinder (sharp vertical edges), where the scour was also predicted to be the deepest.



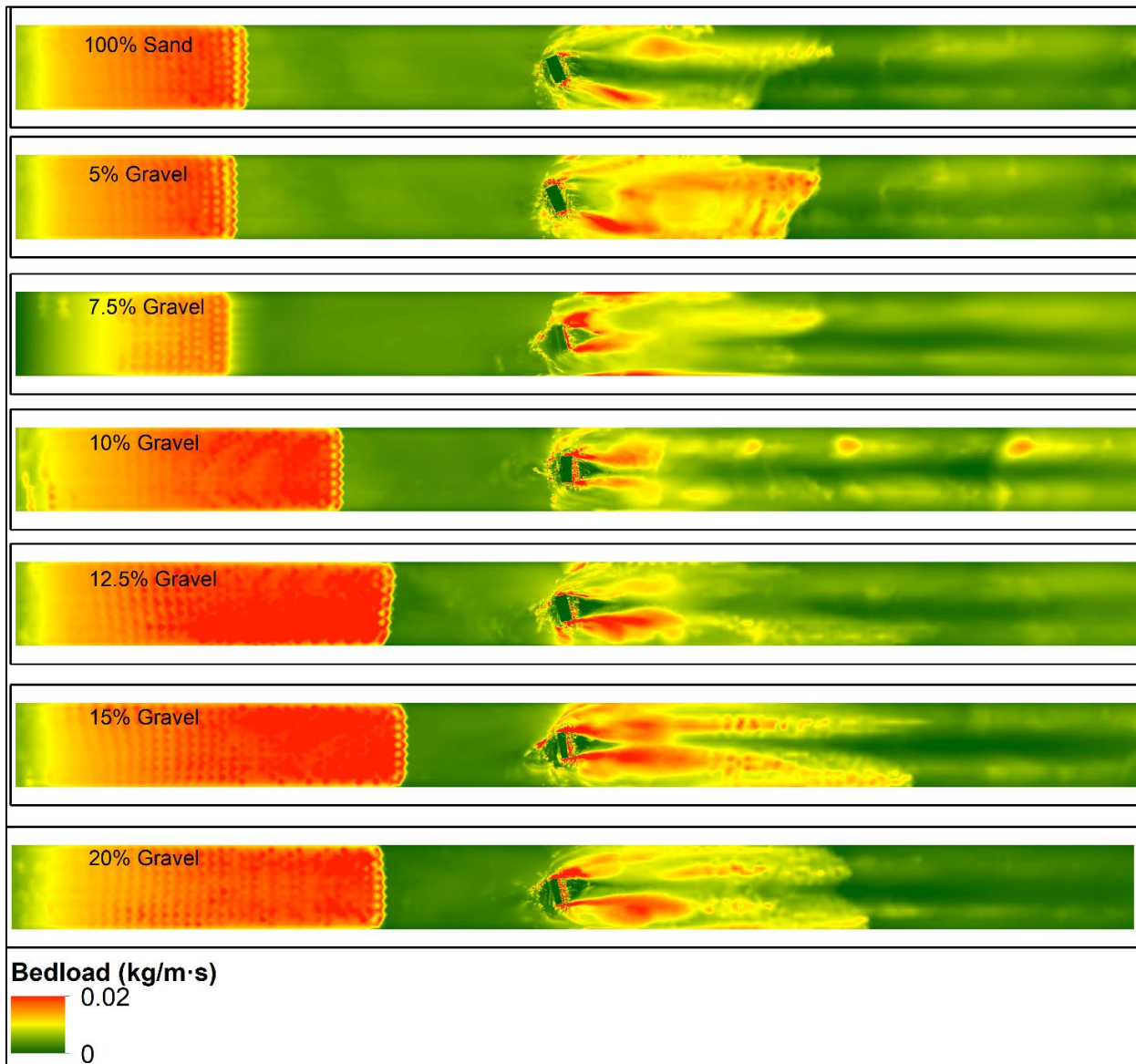


Figure 4.44: Numerical model outputs for maximum bedload for the runs replicating the laboratory experiments at initial flow speeds of  $45 \text{ cm}\cdot\text{s}^{-1}$ .

The modelled suspended load with flow speeds of  $45 \text{ cm}\cdot\text{s}^{-1}$  (Figure 4.45) also shows increased suspended load transport when the bed has 15% and 20% gravel. Once again initiation of the sediment transport is observed from the edges of the cylinder. The numerical model shows higher values of suspended load when the bed is mixed (mixture of sand and gravel) rather than the pure sand case. This is counter-intuitive, as the finer fraction is estimated to be in suspension at flow speeds of  $45 \text{ cm}\cdot\text{s}^{-1}$ , therefore increased suspension was expected for pure sand. The modelling work shows that in all cases, there is higher bedload and suspended load at the scour marks.



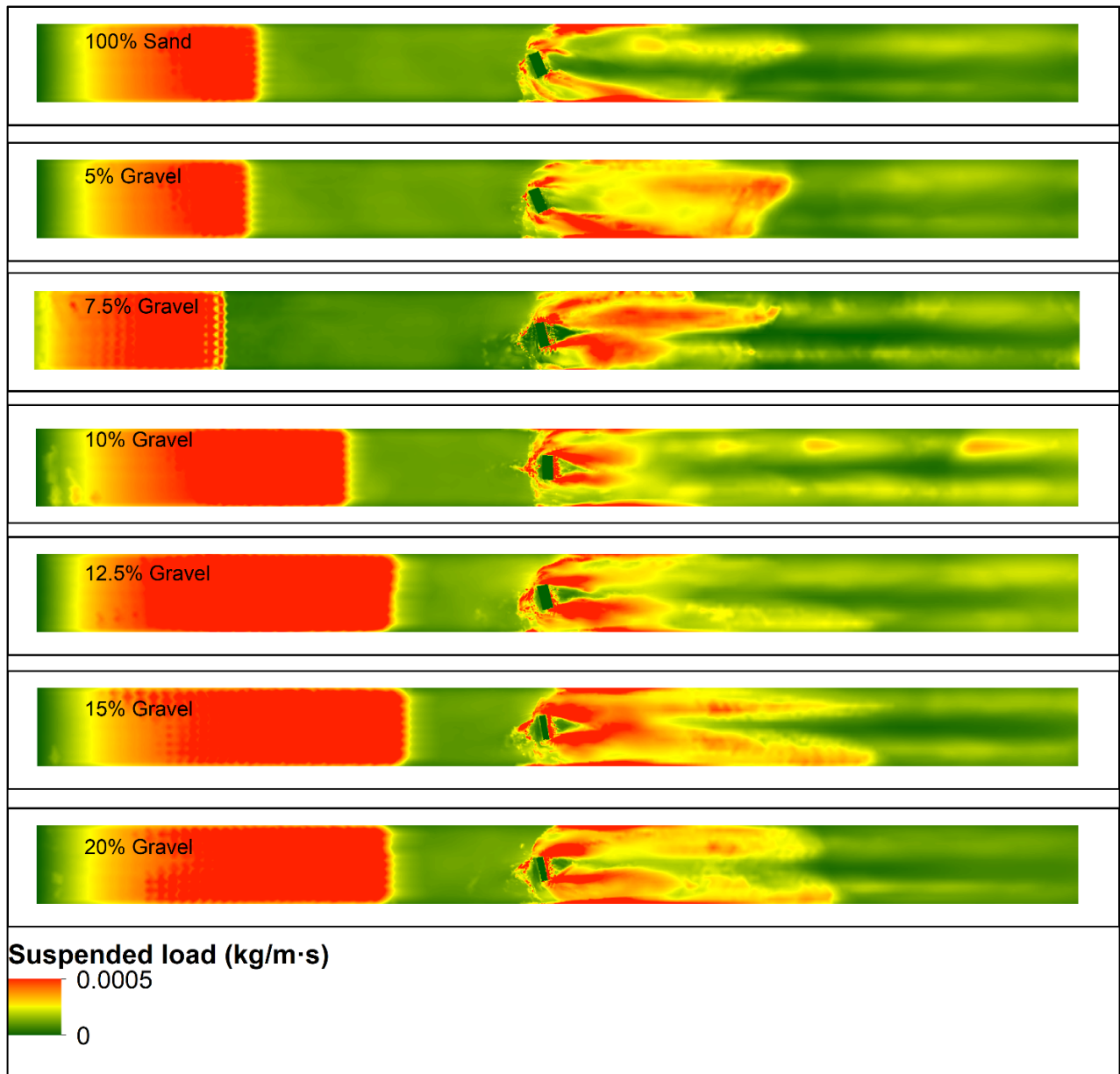


Figure 4.45: Numerical model outputs for maximum suspended load for the laboratory experiments at initial flow speed of  $45 \text{ cm} \cdot \text{s}^{-1}$ .

It is important to mention that erosion/deposition of sediment was predicted from the numerical model north and south of the object (due to 'wall effect'), and this erosion extended far downstream. Also, this sediment movement was also accompanied by higher values of bedload and suspended load transport. At these areas, in the laboratory experiments (physical modelling), bedform formation was observed.

## 4.4 Discussion

This discussion will detail some challenges in the methodology and the analyses, and how they may have impacted the results. The conclusions section will then aim to provide an answer to the questions asked in this chapter.

### 4.4.1 Flume bed dynamic equilibrium

The flume bed dynamic equilibrium was monitored visually by measuring the height and length of the ripples formed upstream of the object at a point that was not influenced by the 1<sup>st</sup> ramp. The bedforms were located between 1.2 and 1.8 m downstream of the first ramp, to avoid capturing the interference that the ramp (used to hold sediment together) had on the sedimentary bed. The bed dynamic equilibrium was monitored, as initially, the plan for the modelling work was to use a computational fluid dynamic model (CFD) called OpenFOAM, instead of the coupled TELEMAC3D – GAIA numerical model. The computation time of the CFD model was much larger than the computation time of the numerical modelled used, hence a smaller modelling period was needed. Therefore, the initial plan was to stop the flume at the ‘mature bed point’ and run for an extra 20 minutes, to use the DEM produced from the two scans using the SeaTek acoustic transducers, at the ‘mature bed point’ as the input file for the computation and the DEM produced from the ‘final scan to validate the results of the CFD model. However, during this project, the GAIA module of TELEMAC was released and the decision to use the novel coupled numerical model was taken. Although the CFD model was not used at the modelling work, the dynamic equilibrium point measurements were also used as a comparison of where the experiments were stopped. Studies (Baas, 1993; Baas, 1994; Baas, 1999) suggest that dynamic equilibrium is not easy to monitor, as the equilibrium line of the ripples height and length over time might appear to reach the equilibrium point early (straight asymptotic line in Figure 4.46) but the asymptotic line might change with time, especially within the first few hours of the experiments.

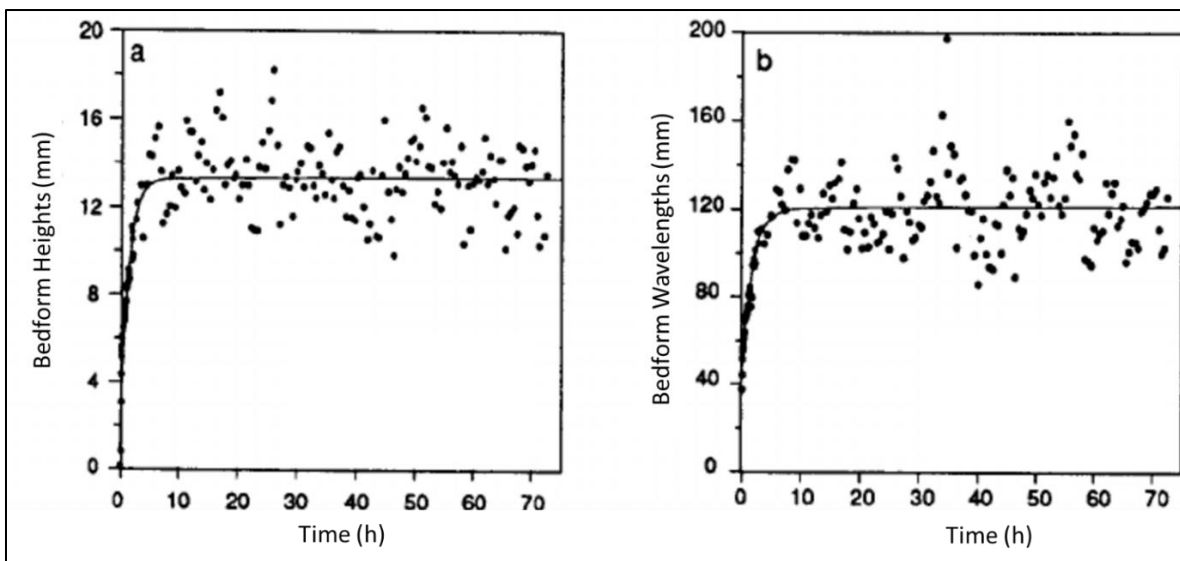


Figure 4.46: Bedform heights and lengths development diagrams for experimental runs using 0.1087 mm quartz sand and flow speed of  $0.37 \text{ m}\cdot\text{s}^{-1}$  (Baas, 1994).

Although previous studies have focused on the prediction of bedform formation in fine sand, or sand/mud mixtures (e.g., Baas, 1993; Baas, 1994; Soulsby & Whitehouse, 2005), no studies were found on predictors used for the prediction of bedform properties in mixed coarse beds (sand and gravel mixtures). As an example, in Figure 4.47, the migration rates recorded from Baas et al. (2000), for different finer sediment mixtures, show an inverse relationship with that shown in Figure 4.18b.

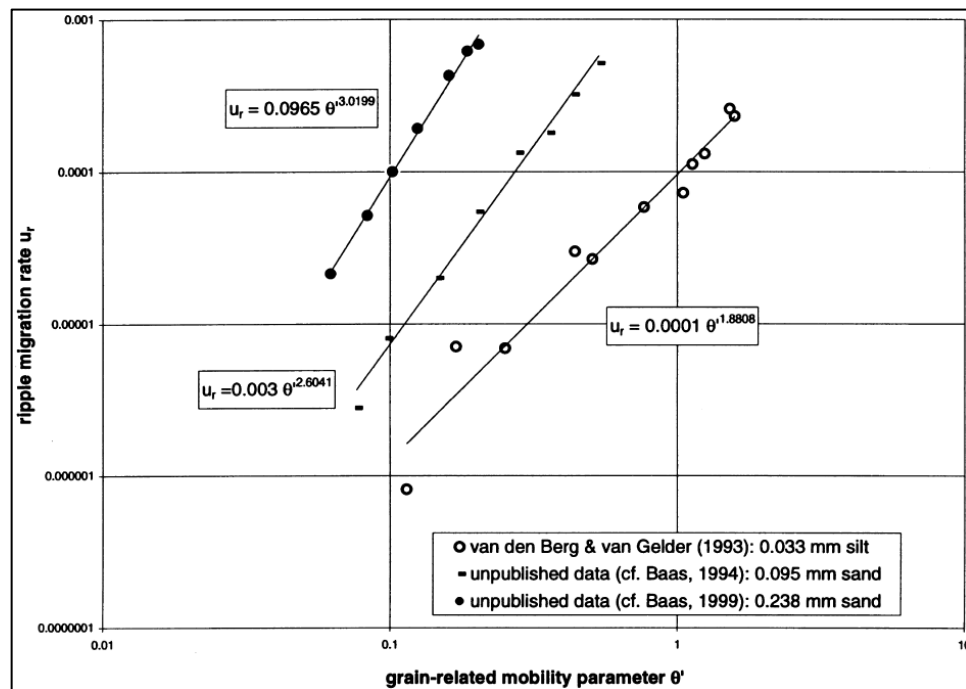


Figure 4.47: Empirical relationships between the expected migration rates of equilibrium, current-generated ripples and their grain-related mobility parameter for the different sediment grain sizes. The equations show the best-fit power functions corresponding to the straight lines through the population points (Baas et al., 2000).

The new results presented in this thesis show that the use of the formulae developed for the prediction of the dimensions and mobility of ripples in sand, or finer sediment mixtures, do not fully represent the ripple formation in sand-gravel mixtures. Using similar experiments (same sand/gravel grain ratio) with different grain sizes, McCarron (2020) also noted this concluding that published predictors for finer material do not account for the bed roughness present in coarser beds, such as sand and gravel mixtures. Also, published predictors fail to account for the hiding- exposure effect on bed mobility, which is responsible for the variability in bed mobility of the finer and coarser fractions in the mixed coarse beds, and the sediment mixture as a whole.

Finally, it is important to note, that the focus of the current work was not the ripple formation, and therefore once scour processes stabilised, the flow was stopped, even if the ripple formation was not at the dynamic equilibrium point. Moreover, the ripple formation is based mostly on the bedload transport, where the scour formation is based in the enhanced suspended load around the obstacle. Hence the DEM produced at the 'dynamic equilibrium' point of ripple formation is not referred to using this term in the thesis; instead, it is termed 'mature bed'.

#### 4.4.2 Impact of unintended object movement during experiments

The shape of the object in the modelling work was not a limiting parameter as with the adaption of the immersed boundary method (Yin et al., 2016), not only can the object be placed at any position (x, y, z) and orientation on the sedimentary bed, but it is also treated as solid below the bed. The orientation of the object, however, is worthy of further discussion. The object in the laboratory experiments was set at the beginning of the experiments to sit in the middle of the sedimentary bed, in the Armfield recirculating flume, at an orientation of  $60^\circ$  to the flow, intending to replicate the orientation of SS *Apapa* to the flow in the offshore real-world (during ebbing). The cylindrical object in the laboratory experiments was not attached to any other structure, and did not have a base, to avoid interfering with the results. Not anchoring the object and placing it on top of the bed meant that the object was free to move in all the laboratory experiments. Scour formed upstream (Figure 4.48b) causing a movement and fall of the object into the scour mark. As explained in Section 4.3.3, the object's orientation to the flow changed up to  $\sim 30^\circ$  during the laboratory experiments.

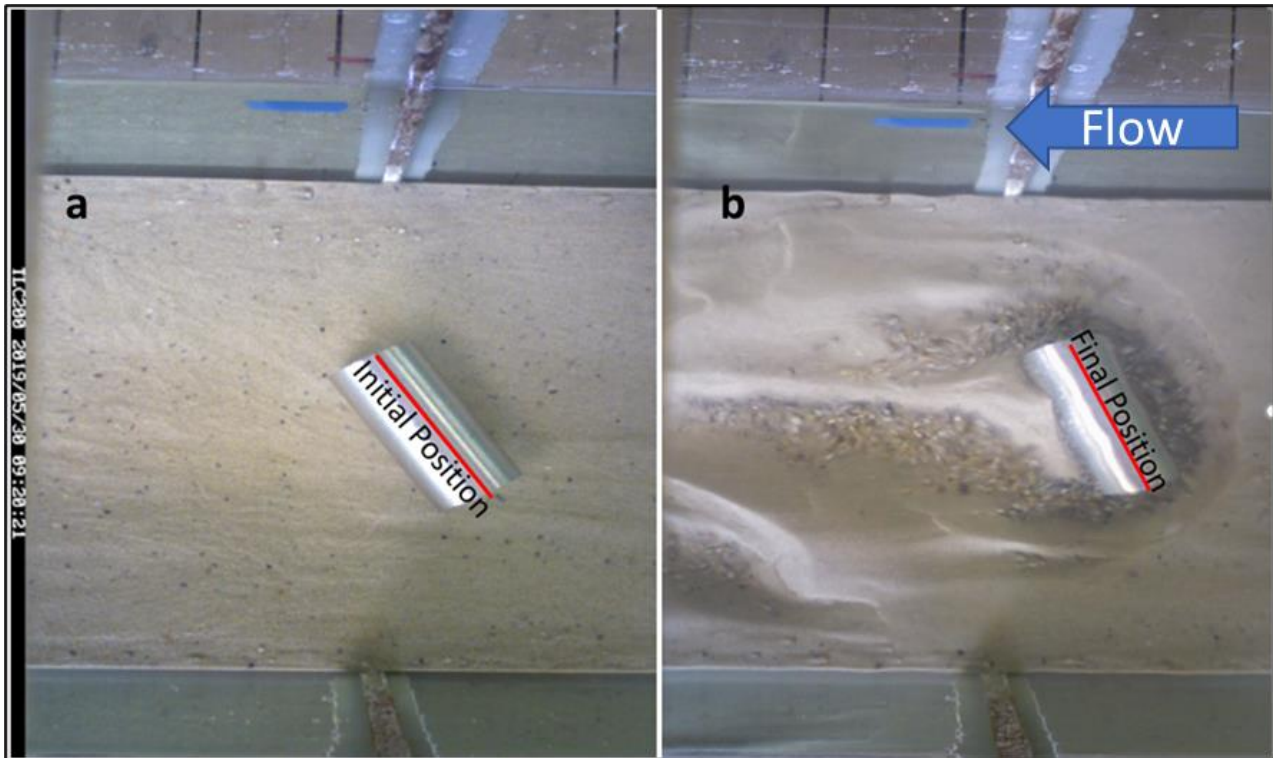


Figure 4.48: Positioning of the object at the beginning and at the end of the laboratory experiments, showing a  $12^\circ$  deviation of the object's orientation to the flow. The flow direction is from east to west (right to left).

Studies (Caston, 1997; Quinn, 2006; Quinn et al., 2016; Quinn & Smyth 2018) have shown the importance of the object's orientation to the flow in scour formation (Figure 4.49), and therefore changes in the object's orientation to the flow, means variability in the expected scour development

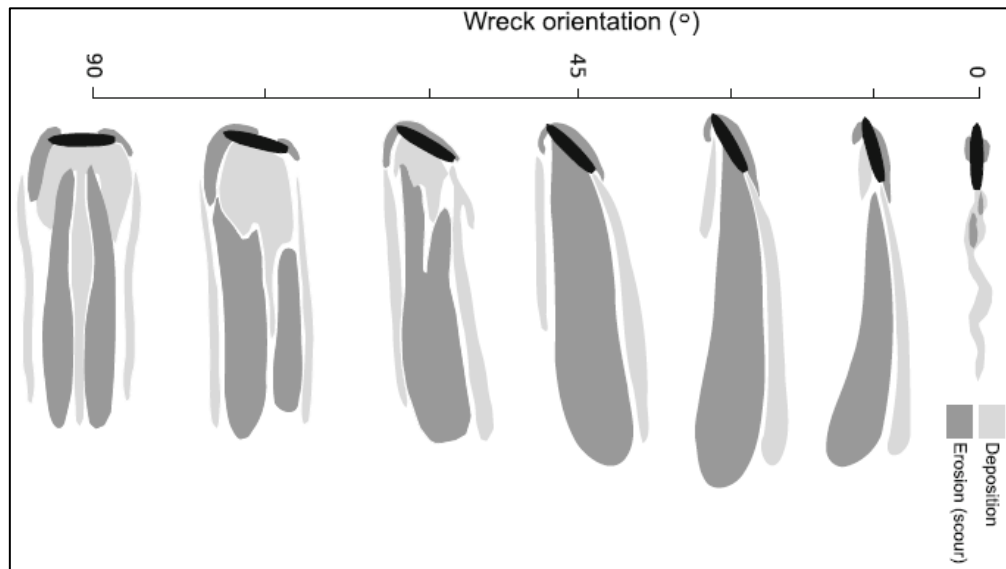


Figure 4.49: Object associated erosional and depositional patterns around shipwrecks placed at different orientations to the flow from the output of CFD models (Quinn & Smyth, 2018).

Figure 4.50 shows a comparison between the scour mark's length, as recorded for the different laboratory experiments, with the modelling work of Quinn & Smyth (2018).

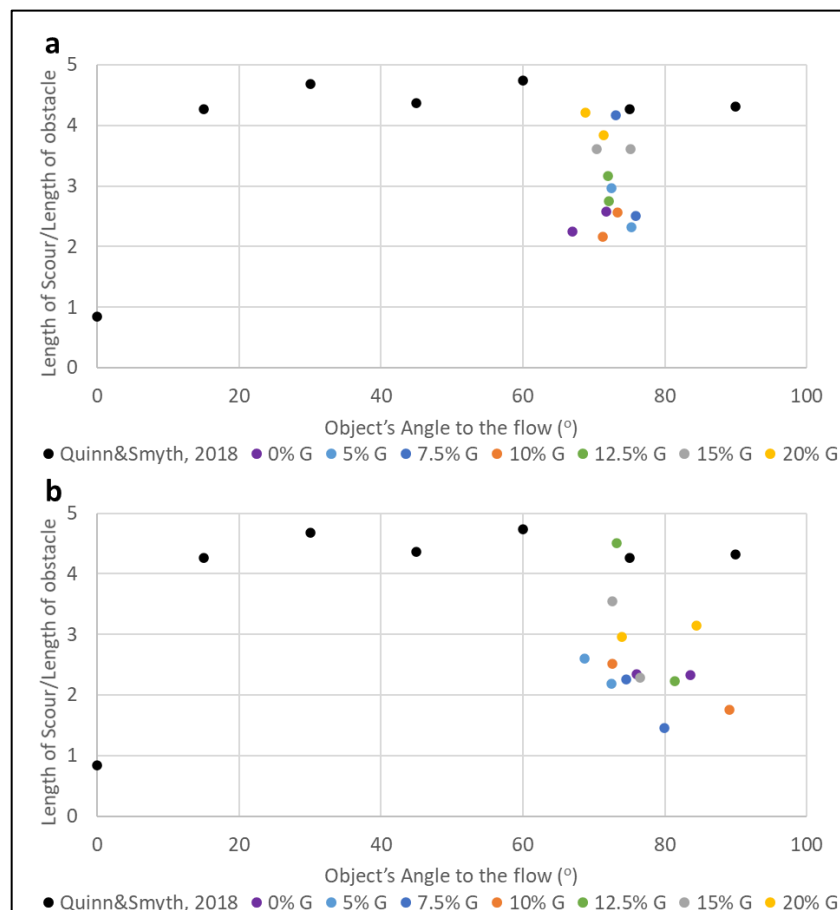


Figure 4.50: Comparison between the scour length/object length ratio as observed in the laboratory experiments with the Quinn & Smyth (2018) observations using a CFD model, for the experiments conducted at the flow speed a) mobilising only the sand fraction ( $31 \text{ cm} \cdot \text{s}^{-1}$ ) and b) mobilising both the sand and gravel fractions ( $45 \text{ cm} \cdot \text{s}^{-1}$ ). The object's angle to the flow was measured at the 'final bed' DEM.



Comparison with the Quinn & Smyth (2018) study shows that there is no significant relationship between their model outputs on the scour length/wreck length ratio and the laboratory work presented here, but the scour patterns observed broadly agree with the suggested erosional and depositional patterns from the CFD simulations. However, the variability of the scour development in the present study became even more complex due to the sediment mixtures used for the laboratory experiments and the fact that the object unintentionally moved during the laboratory experiments. The CFD simulations by Quinn & Smyth (2018), were conducted using the parameters (roughness, porosity etc.) of a fine sandy bed, and a differently shaped object.

The scour mark that formed upstream during the flume experiments caused the object to move unintentionally, changing its orientation and modifying the exposed W:H ratio (Whitehouse, 1998; Saunders 2005), as part of the structure was not as exposed to the flow after rotating into the upstream scour mark.

The modelling work conducted for the purposes of this thesis (and published at the Telemac Mascaret User Conference, 2020; Yiannoukos et al., 2020) shows the importance of the shape and burial of the object in the flume environment. More information about the observed (from the coupled TELEMAC3D - GAIA model) importance of the object's exposure to the flow, is discussed in Section 5.2.2.

#### **4.4.3 Scour geometry changes with bed composition**

Scour depth, width and length measures have been used in the literature to describe scour and compare scour marks produced because of the disturbance caused on the bed by differently shaped and orientated obstacles. Studies (e.g., Whitehouse; 1998; Saunders, 2005; Quinn, 2006; Smyth & Quinn, 2014; Quinn & Smyth 2018) have used the width and length of the scour, as the third dimension (depth) depends on the sediment availability that can be eroded. In the flume experiments presented here, the sediment depth available within the flume was enough, as the base of the flume was not exposed during scouring in any of the experiments. The results of this study suggest that there is an obvious dependence of the scour mark's width, depth, and length, with the sedimentary bed composition around the obstacle. As Figure 4.51 shows, there was an obvious drop in the scour mark's length for the experiments conducted using 10% gravel in the mixture and a flow speed of 31 cm·s<sup>-1</sup>, whereas for the experiments with higher gravel percentage in the mixture, the higher the gravel fraction, the longer the scour mark, with the exclusion of a spike in the scour's length in the experiments conducted using 7.5% gravel. Scour width appears to be increasing when increasing the gravel % in the mixture, with the exemption of the mixes containing 5%, 7.5% and 10% gravel, with the narrowest scour observed at the experiments conducted using 7.5% gravel (in contrast to the scour length, where a spike was observed). The scour length/width follows a similar trend as the scour length measurements. However, it worth noting that the scour mark's lengths were tracked to the 1<sup>st</sup> ripple downstream, as the separation between erosion and deposition was difficult to identify.

Other studies have included bedforms in the description of scour (e.g., [Whitehouse, 1998](#); [Quinn, 2006](#)), meaning that the limited formation of ripples at higher gravel% might have caused uncertainties in the scour mark's extent and delineation. On the other hand, for the laboratory experiments conducted at the flow speed of  $45 \text{ cm}\cdot\text{s}^{-1}$ , the longest scour mark is observed at the experiments conducted using 12.5% gravel in the mixture. The wider scour mark is observed at the experiments conducted using 5% gravel in the mixture. The general trend shows narrower, but longer scour marks when increasing the gravel percentage in the sediment mixtures. Similarly to the experiments conducted at low current speed, the scour length/width ratio follows similar trend as the scour length, with the exemption of the experiments conducted using 5% and 12.5% gravel in the mixtures.

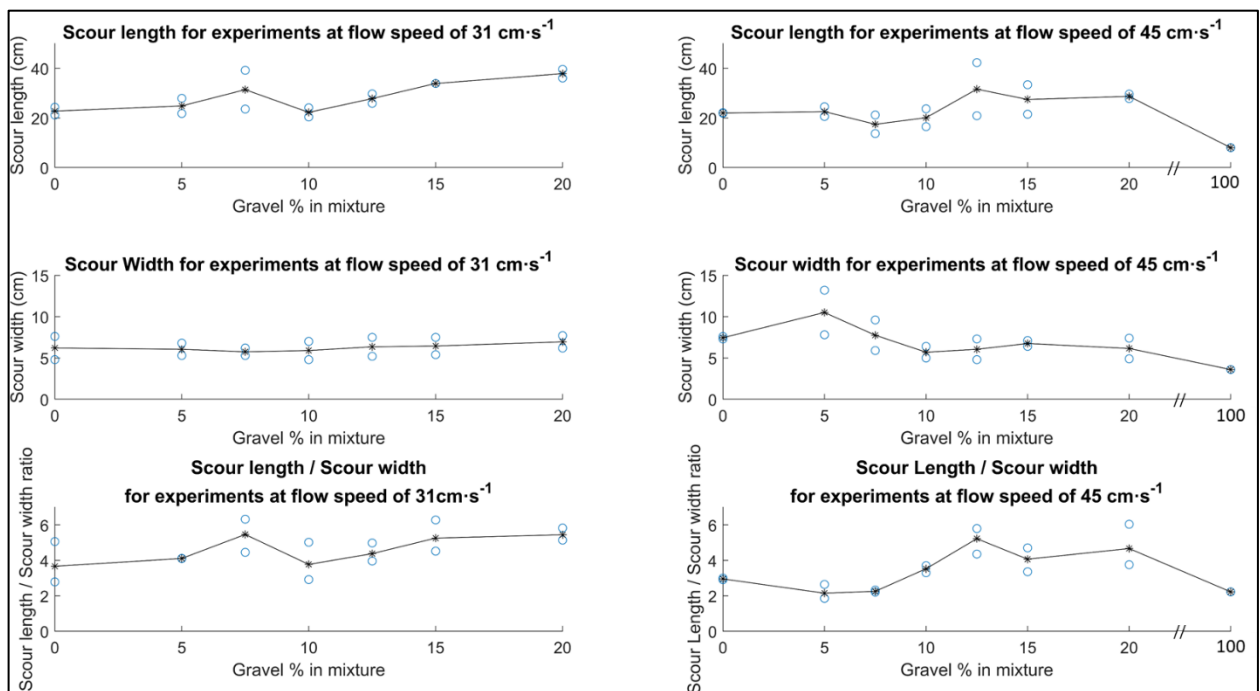


Figure 4.51: Comparison of scour mark's length and width for the experiments conducted using the two flow speeds, mobilising either only sand or both sand and gravel, and a scour length / scour width ratio as a comparison.

Previous studies ([Gribble, 2019](#); [McCarron, 2020](#)) have shown an increase of the coarser fraction's mobilisation at around 10% gravel concentration in the mixtures due to the hiding-exposure effect. ([Gribble 2019](#)) also detected variations at up to 20% gravel in the mixture, where at experiments conducted at higher gravel concentrations, the scour length and width reduced, as the sediment (as a whole) became less mobile. The coupled numerical model used for the current thesis, has shown good correlation with the observed (in the laboratory experiments) scour mark, however, further development and the inclusion of bedform formation, can provide more confidence in the results.

#### 4.4.4 The evolution of bed composition in amplified ripple development

The presence of the object and its influence on the hydrodynamics causes change in bed composition downstream. As Figure 4.52 shows, within the scour mark, there is an obvious separation of the sand and gravel. Due to the enhanced forces caused by the formation of turbulence and flow amplification directly downstream of the object, finer sediment goes into suspension and deposits at the depositional feature and at the edges of the scour mark (sites with high slopes), where the coarser sediment remains at the deepest points of the scour mark.

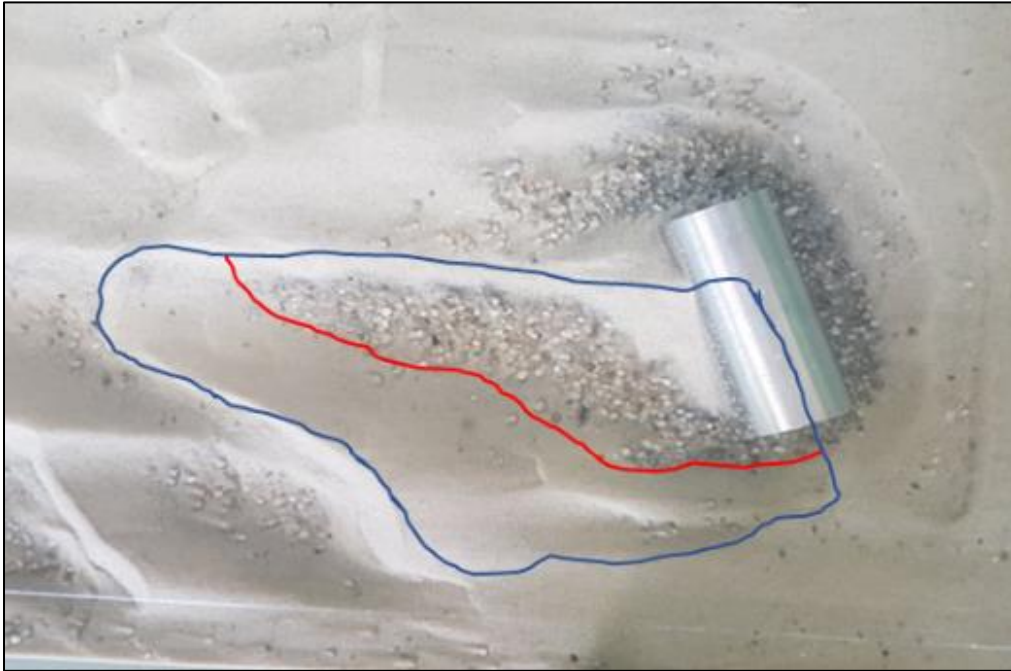


Figure 4.52: Picture of the scour mark for the experiment conducted using a mixture containing 12.5% gravel at the flow speed mobilising only the sand fraction ( $31 \text{ cm}\cdot\text{s}^{-1}$ ). The blue line delineates the scour mark where the red line delineates the separation of sand and gravel within the scour mark.

Figure 4.53 shows the differences between the gravel fraction's percentage from the original mixtures, from samples taken at the ripple crests and troughs upstream and downstream of the object. Negative values in the plots of the ripple crests and troughs mean that the ripples upstream had less gravel percentage than the ripples downstream of the object. For the experiments with mixes containing less than 15% gravel and conducted at a flow speed of  $31 \text{ cm}\cdot\text{s}^{-1}$ , ripple crests upstream appear to have less gravel than ripple crests downstream, confirming the mobilisation of coarser sediment due to higher forces downstream of the object. This potentially also indicates that the hiding-exposure effect in ripple dynamics is most effective for gravel percentages less than 15%. Similar observations were made in the ripple troughs downstream of the object, where the gravel percentage of the sediment samples was smaller upstream than downstream. This would suggest mobilisation of sediment normally expected to be immobile, due to the enhanced forces in the wake of the object, or higher mobilisation of the finer fraction, resulting to the higher amount of coarse sediment in the troughs.

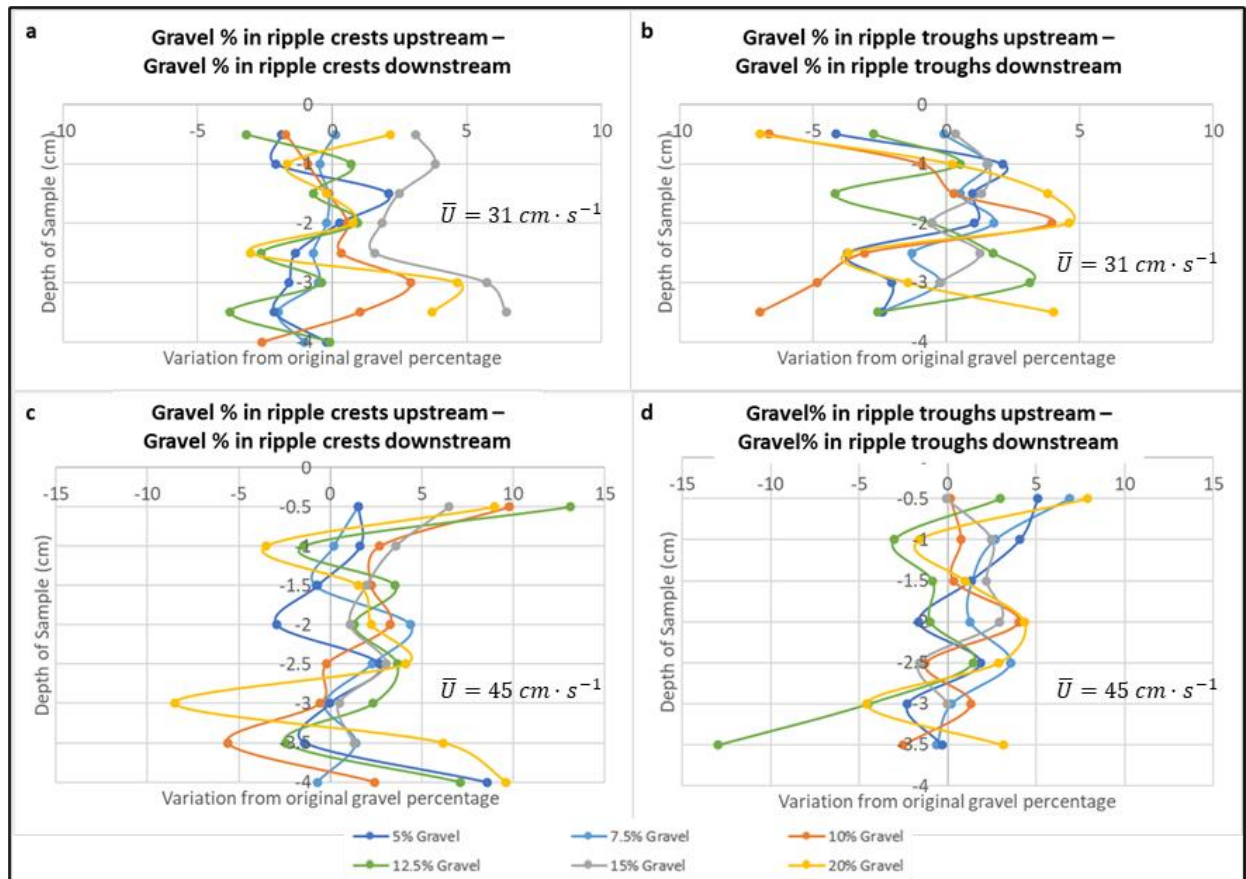


Figure 4.53: Difference in the gravel % observed in the ripple crests upstream and downstream (a, c) and ripple troughs upstream and downstream (b, d) for the experiments conducted at the flow speed mobilising only sand (a, b) and the experiments conducted at the flow speed mobilising both fractions (c, d).

For the experiments conducted at the flow speed mobilising both sand and gravel fractions ( $45 \text{ cm} \cdot \text{s}^{-1}$ ), gravel percentage is lower in the ripple crests and troughs downstream compared to the ripple crests and troughs upstream of the object. The results suggest that gravel potentially moved further than the “active layer” due to ripple formation processes. The deviation observed further down-core was expected as the ripples formed in the experiments conducted at the flow speed mobilising both fractions were higher. The explanation of bedform formation from [Allen \(1994\)](#) was explained in [Section 3.4.1](#). Although this process can explain the large variation at certain depths throughout the sedimentary column, it is unknown what has caused the variation further down-core, underneath what was assumed to be the “actively mobilised layer”. A potential cause for the higher gravel percentage observed down-core is that coarser material was pushed from the syringe when sampling and was therefore sampled at the end of each ‘core’, when the syringe was in contact with the base of the flume. However, this is not supported by the results of the preliminary analyses presented in [Figure 4.33](#), as the analyses of the samples collected from the ‘initial flat bed’ prior to the experiments suggest an undisturbed sampling process.

## 4.5 Conclusions

In this chapter, the aims were to assess and quantify:

- v. The impact of the enhanced flow around a cylinder on bed mobility in the wake of the object;
- vi. the impact of the enhanced flow around a cylinder on the sediment composition in the wake of the object;
- vii. the impact of the sediment composition on bed mobility, and
- viii. to update a 3-D numerical model that can accurately predict scour around a cylinder placed on different sand/gravel mixtures.

These aims were addressed through a series of 30 laboratory experiments in the Armfield recirculating flume. Six sediment mixtures were used in the experiments in addition to pure sand and pure gravel. Two initial flow velocities were used, calculated (and visually inspected) to mobilise either only the finer (sand) fraction, or both the fine and coarse (gravel) fractions of the sediment mixtures.

- i) The impact of the enhanced flow around a cylinder on bed mobility in the wake of the object.

Depth averaged flow velocities were measured upstream and downstream of the object, with measurements showing slight increase (maximum of 5% and 8% at flow speeds of  $31 \text{ cm}\cdot\text{s}^{-1}$  and  $45 \text{ cm}\cdot\text{s}^{-1}$  respectively) of the depth averaged flow velocities downstream. Ripple formation was monitored upstream and downstream of the object, with the results showing higher and shorter ripples downstream of the object than upstream, as a result of the disturbed flow (from the interaction with the object). These characteristics of the ripples downstream of the object, result from the interaction of the lee wake vortices with the downstream bed. Ripple migration rates upstream indicated higher migration rates in the sediment mixtures of 7.5%, 10% and 12.5% gravel for lower flow conditions. The ripple migration as recorded upstream of the object was observed to be 15% higher in the sediment mixture containing 10% gravel than for the 12.5% gravel mix (2<sup>nd</sup> faster). For the higher flow speed experiments, ripple migration rates upstream of the object reduced exponentially, with increasing gravel content in the sediment mixture. Ripples formed downstream of the object caused difficulties in scour edge delineation. According to [Whitehouse \(1998\)](#) and [Quinn \(2006\)](#), bedforms can also be part of the scour processes. Mean scour depth measured in the flume experiments was deepest in the 20% gravel mix, for both speeds. It was also observed that the scour mark was more pronounced in the experiments conducted using this sediment mixture, due to the absence of bedform development.

- ii) The impact of the enhanced flow around a cylinder on the sediment composition in the wake of the object.

In the higher flow speed experiments, gravel was observed in the upstream ripple crests and was absent in the downstream crests. In contrast, for the lower speed runs, no gravel was observed in the first 0.5 cm of the 'down-core' sediment samples. The general distribution of sand and gravel within the scour mark developed in the flume was similar to that observed around SS *Apapa* ([Section](#)



3.3.3), where the coarser fraction was found in the scour mark and the bedform troughs. Sediment samples from the flume showed an increase of the gravel percentage with depth. During ripple formation, coarse material is deposited at the lower part of the lee slopes (troughs) and the finer material rolls (or suspends) and deposits on the stoss side of the following bedform. As ripples migrate, former troughs become crests.

iii) The impact of the sediment composition on bed mobility

The impact of sediment composition on scour development was investigated. Results showed that at the lower flow speed, beds comprising 20% gravel developed longer, wider and deeper scour marks. At higher speeds, wider and deeper scour marks developed in 5% gravel beds and the longest scour signatures developed in 12.5% gravel beds. Scour edges were delineated to the first formed ripple downstream of the object, although, it is acknowledged that bedforms can be part of the scour process. In the cases of the experiments where the bed comprised of more than 15% gravel, ripples were observed to develop further downstream.

iv) To update a 3-D numerical model that can predict accurately scour around a cylinder placed on different sand/gravel mixtures.

In the flume experiments and in the coupled model, maximum bed disturbance was initiated at the edges (vertical sides) of the cylindrical object. Depth averaged flow velocities were derived from the TELEMAC 2D/3D hydrodynamic numerical model and compared to flow velocities measured using the UDVP instrument. Good correlation was noted between the numerical model outputs and the UDVP measurements, with discrepancies within the instrument's error margin. The coupled numerical model also shows good prediction of the scour marks formed downstream of the objects but did not identify scour formation upstream of the object. For the lower flow speeds, the modelled scour marks (using the numerical model) were within 5% of the observed scour marks in the flume experiments. At higher flow speeds, the numerical model overestimated the observed scour marks by about 27%. In the case of pure sand, the model overestimated the scour mark by almost 93%. Ripples play an important role here again, as they cause problems in scour delineation, and they could not be accounted for in the model.

## Chapter 5

### 5. Discussion

#### 5.1 Highlights of the observations and aims of this discussion chapter

Chapter 3 focused on the seabed evolution around the shipwreck of *SS Apapa* based on real-world data. The ADCP dataset collected over and around the wreck confirmed increased flow velocities downstream of the wreck with an amplification of background currents up to 2.3 times, with the highest values observed at the stern and bow during slack tides. The highest variation observed at slack tides, can be explained by the fact that the current velocity is low, and the slightest variation appears to be significant. Also, during slack waters, it is expected that lower values of turbulence will occur, making any amplification easier to spot using the ADCP. The numerical model predicted amplifications of the depth averaged flow speed of up to 0.8 times at the stern and bow of the wreck when compared to the background (potentially undisturbed) flow. These observations agree with computational fluid dynamic (CFD) simulations reported in the literature for the quantification of flow downstream of wrecks (Smyth & Quinn, 2014; Quinn & Smyth, 2018) that have identified flow amplification of up to 0.81 times at the site where the flow hit first. The seabed sampled around the wreck consists of a mixture of coarse sand and gravel/pebbles. Sediment within the influence of the wreck, predicted to be immobile using the Soulsby (1997) formulae was observed to be mobile to an even greater degree than sediment predicted to be mobile using the same method (and at similar flow speeds). It is interpreted that this results from the hiding-exposure effect, as coarser sediment, when present in a sediment mixture requires less forcing to be mobilised, due to a more pronounced exposure of the larger grains to the flow. Some uncertainty regarding the role of sediment composition remains as the spatial coverage in offshore sampling is limited.

These observations inspired physical modelling work in a controlled laboratory environment to better quantify this component, with the resulting study presented in Chapter 4. The laboratory experiments included quantification of the scour development around a cylinder sitting on different sand and gravel mixtures. An amplification of the depth averaged flow velocity was observed downstream of the object. This amplification was in the order of 1.1% (mean amplification downstream) for the flow velocity mobilising only sand (~5% at its maximum) and 1.9% (mean amplification downstream) for the experiments conducted at the flow speed mobilising both fractions (~8% at its maximum). It is reminded that no velocity measurements were taken downstream of the edges of the cylinder due to UDVP instrument's limitations, hence the difference in relative amplification when compared with the offshore observations around *SS Apapa*. Ripple migration rates upstream of the object showed a higher migration in the case of the 10% gravel bed for experiments conducted at the flow speed mobilising only the sand fraction. In contrast, at the experiments conducted using the flow speed mobilising both fractions, ripple migration rates reduced exponentially with increasing gravel content in the mixture. More specifically, the exponential trendline has an equation of  $y = 0.056e^{-0.028x}$  with

a  $R^2$  value of 0.92. At higher concentrations of the coarser fraction, the hiding-exposure effect but also the content of the coarse gravel needed higher shear stress to mobilise, something that the flow speeds used was not sufficient to provide. Although physical modelling through laboratory experiments can never fully replicate the complex offshore environment, it is very useful in providing a quantitative understanding about how enhanced forces downstream of the object mobilise a mixed bed of various composition, using various flow speeds and comparing results to what happens for beds made of pure sand or pure gravel. The experiments showed that there is a correlation between the geometry of the scour mark (depth and lateral extent) and the sediment composition and the flow speed: with increased gravel percentage and with a flow speed that mobilises both sand and gravel fractions, the scour mark was observed to be ~40% longer and ~50% deeper. For the experiments conducted at the lower flow speed, a longer, wider, and deeper scour mark was observed for the 20% gravel bed. For the experiments conducted at the higher current speed, a wider scour mark was observed at the experiments with the 5% gravel bed, the longest scour mark at the experiments with the 12.5% gravel bed and the deepest scour mark was observed at the experiments with the 20% gravel bed. Ripples downstream of the object were higher and longer, corroborating the general observation of increased mobility of mixed beds after flow alterations, because of turbulence generated by the interaction of the object with the flow and the lee-wake vortices that develop and travel downstream of the object.

The results of the two chapters also showed a dependance of the scour mark on the shape of the object, its orientation to the flow, and its exposure to the flow, in broad agreement with previous studies (i.e., Whitehouse, 1998; Saunders, 2005; Quinn, 2006; Smyth & Quinn, 2014, Quinn & Smyth, 2018). Importantly, the lateral and vertical extent of the scour mark was demonstrated to depend on the composition of the surrounding bed, with the scour formed at beds consisting of coarser material being longer and shallower than those formed on finer beds. To the author's knowledge, there are limited observation of this reported in the literature, with work conducted mostly on non-uniform sands (Porter, 2016). Numerical modelling work using a coupled hydrodynamic and sediment transport model (TELEMAC3D – GAIA) has produced outputs that matched the observations of analyses conducted in Chapters 3 and 4. On that basis, there is sufficient confidence to use the numerical model to test a few hypothetical scenarios to quantify the impact of changes to offshore and laboratory scenarios related to the bed, to the object and to the flow. This discussion chapter aims to compare the observations quantitatively with each other and with published data on scour in unimodal sediments. This discussion also serves to identify the implications of the effects of varying seabed infrastructure design on scour in different types of bed.

## **5.2 Impact of object's exposure, shape, and orientation on scour evolution**

The shape of the object, its exposure, and orientation to flow, are reported as controlling parameters in the formation and extent of lee wake vortices (Whitehouse, 1998; Hatipoglu & Avci 2003; Saunders 2005; Quinn, 2006). The object interacts with the flow producing horseshoe (upstream) and lee-wake

vortices (downstream). The disintegration of SS *Apapa* as described in Section 3.4.3 has proven that even a slight change of the object's shape can alter well-established hydrodynamic and sediment dynamic processes around the submerged object. For example, the established bedform migration pattern was reversed immediately for one of the bedforms downstream of the wreck after the trigger event. In addition, areas at the NW and SE parts of the scour mark, that were consistently eroding over the years, suddenly filled with sediment ( $\sim 300 \text{ m}^3$ ) immediately after the trigger event, likely due to a change in forces from the disintegration and shifting of the wreck. The impact on scour due to the varying shape of the object has been also discussed in the literature (Saunders, 2005; Quinn, 2006; Smyth & Quinn, 2014; Quinn et al., 2016; Quinn & Smyth, 2018) with studies referring to the sharp edges at the stern and bow of the wreck causing higher forces due to enhanced turbulence.

It has been observed and reported in the literature that other wrecks similar in age to SS *Apapa* (just over 100 years) have also started disintegrating (Firth, 2020) at this stage in their history. The physical, biological and mostly chemical (corrosion) processes (MacLeod, 1993; Quinn, 2006) at the open wreck environments have contributed to the disintegration of these metal wrecks, leading to calls for preservation in cases where needed (Quinn, 2006; Firth, 2020).

In summary, the analyses conducted for the current thesis has shown dependance of the formed scour mark on:

- The object's exposure to the flow;
- the incoming flow and its interaction with the object, and;
- the surrounding bed composition.

Numerical modelling work conducted in Chapters 3 and 4, has shown good correlation between the numerical model outputs and the observed scour mark, in the prediction of scour around SS *Apapa* and the cylinder in the laboratory experiments (physical modelling). The coupled numerical model, with the adaption of the immersed boundary method (Yin et al., 2016) and the inclusion of the hiding-exposure correction (McCarron et al., 2019), allows for all three parameters above to be included and monitored. This discussion chapter uses the modelling capacity built up throughout the project to test the sensitivity of scour formation related to these processes.

### **5.2.1 Impact of different exposure of the object to the evolution of scour**

Previous studies have discussed the extent of scour mark development dependance on the width to height (W:H) ratio of the object (Whitehouse, 1998; Saunders, 2005; Quinn, 2006; Lambkin et al., 2006). They established that objects that are more exposed to the flow are likely to cause more scour than objects that are less exposed to the flow, with scour formation leading to even more exposure of the object. This is due to the interaction of larger surface area of the object with the incoming flow creating enhanced forces downstream (i.e., turbulence and vortices) and the lee-wake vortices produced from the interaction of the incoming flow with the object, travelling far further downstream than when the object is less exposed.

To identify and quantify changes in scour mark geometry as a function of exposure to flow for objects on mixed coarse beds, the numerical model described in Sections 3.3.4 and 4.3.5 was used. The effect on the flow and on the bed from hypothetical changes in the object's vertical position was investigated. Numerical modelling of the SS *Apapa* site was conducted using the wreck in two different vertical positions:

1. at the position observed in 2012: ~31m; W:H~0.5, sitting partially submerged over an artificial flat bed (with a mean depth of ~42.5m) (Figure 3.29g; Figure 5.1a).
2. at the likely position when the wreck firstly sank: the wreck artificially 'lifted' and placed on top of the surrounding artificial flat bed, with the shallower point being at ~23m; W:H~1.0 (Figure 3.29f; Figure 5.1b).

Figure 5.1 shows the two vertical positions where the wreck of SS *Apapa* was placed to identify changes in the scour mark's formation due to the exposure of the object and its interaction with the incoming flow.

The numerical model outputs from the runs with the different vertical positioning of the wreck show differences not only in the modelled scour depth and lateral extent, but also in the modelled turbulent kinetic energy (TKE) generated downstream of SS *Apapa* potentially as a result of the wreck's exposure to the flow in the computation domain.

Figure 5.2 shows the numerical model outputs, with the model run using the wreck positioned vertically (at two different levels) as outlined in Figure 5.1. In the case where the wreck was placed partially submerged in the artificial flat bed (at the depth where the wreck was observed in 2012), the modelled scour mark after 16 full tidal cycles is shorter and less wide than the scour mark observed in the real-world data. In the case where the wreck was artificially lifted and forced to sit over the artificial flat bed (fully exposed to the flow), the modelled scour mark (for the same computational time) is longer, but almost as wide as the scour mark observed in the real world. It is noted that the real-world scour mark around the wreck is almost the average (in length) of the two modelled cases. If the assumption is correct that the surrounding bed was flat when the wreck sunk, then the lee wake vortices resulting from the interaction of the object with the flow initially propagated longer distances, causing longer initial scour marks. While the surrounding bed was lowered due to scour, the wreck potentially lowered as well to the point where scour processes reached a dynamic equilibrium. Lowering of the wreck may have resulted from the collapse of the sediment that the wreck sat on because of the high slopes formed by the scour formation.



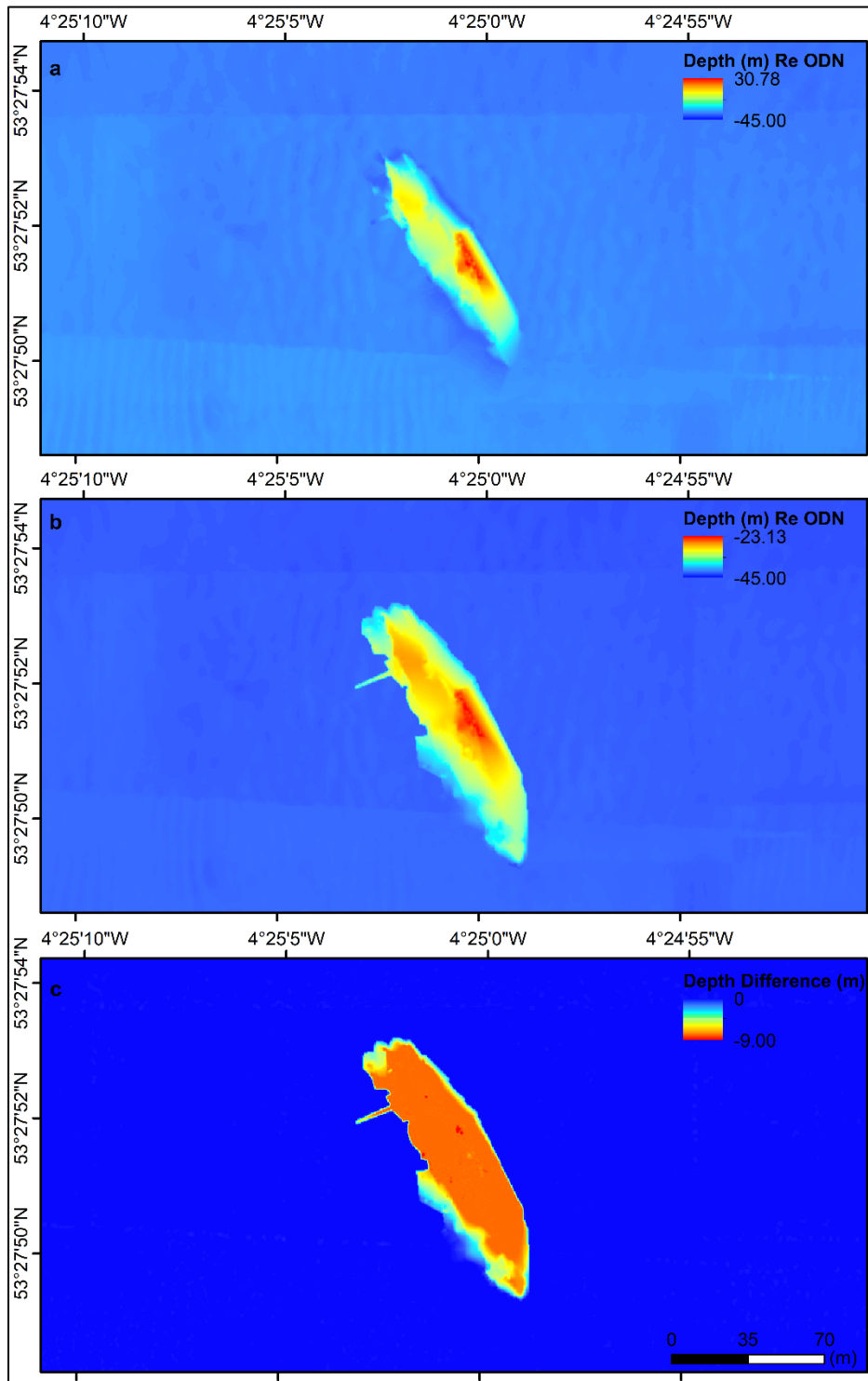


Figure 5.1: Numerical model input - vertical positioning of the wreck to test the scour formation at different exposure of the wreck. a) Wreck positioned at the depth observed in 2012 (partially submerged into the artificial flat bed), b) wreck artificially lifted over the artificial flat bed (fully exposed to the incoming flow) and c) the depth difference between a and b.

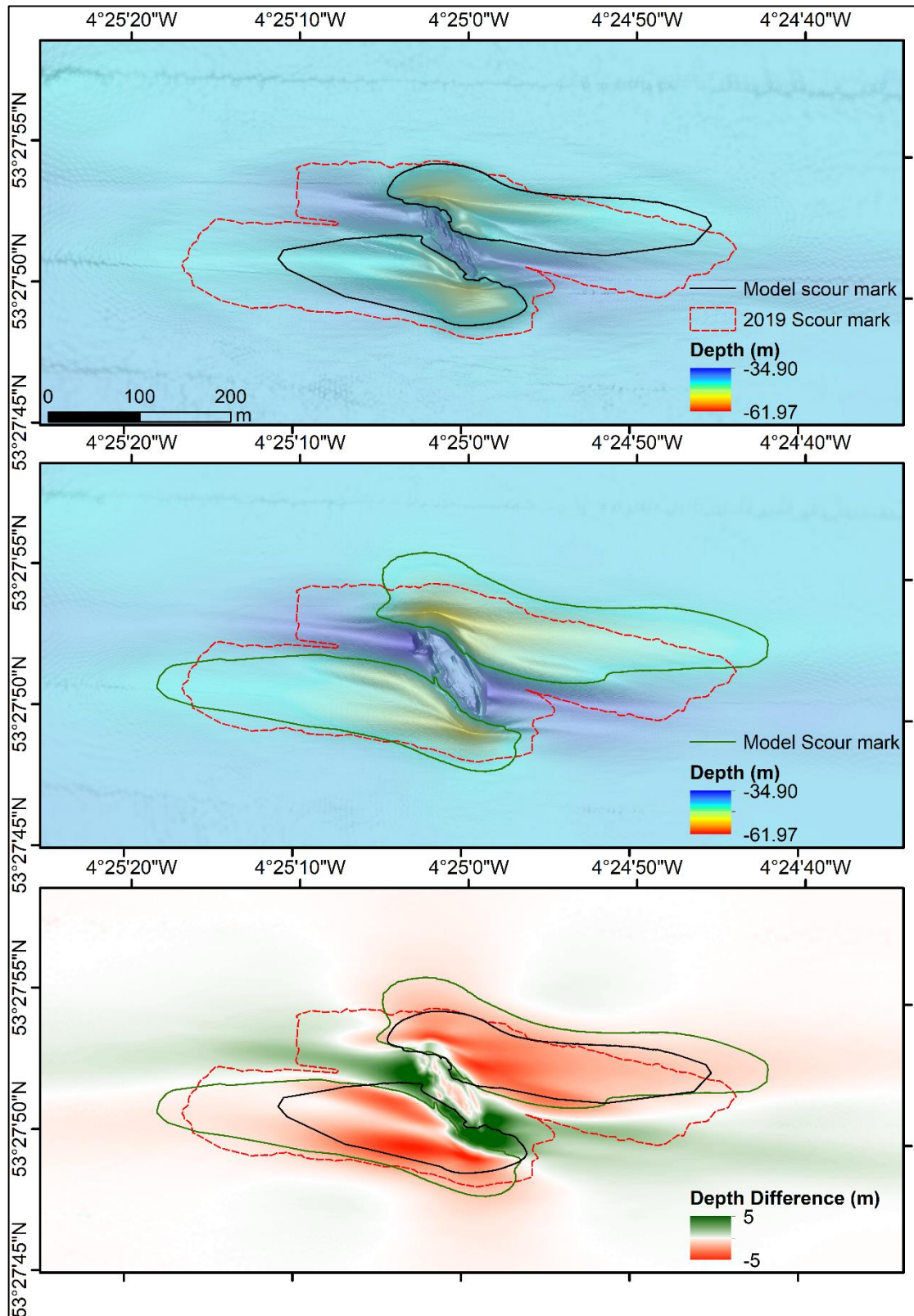


Figure 5.2: Prediction of scour formation from the coupled numerical model over the first 16 full tidal cycles (8 days) a) with the wreck sitting at the depth as observed in the 2012 survey (partially submerged), b) with the wreck 'lifted' 8m to sit on top of the artificial bed and c) depth difference between b and a.

The model produced high values of TKE around the wreck on the initial (artificial) flat bed that are in the areas where the scour is observed around the wreck today. Predicted TKE values show up to 0.02 J/kg (or ~33%) difference between the two cases (Figure 5.3). More specifically, in the case

where the wreck was artificially ‘lifted’ and sat over the flat bed (Figure 5.1a), the TKE propagates farther (almost as long as the observed offshore scour mark) and is of higher magnitude. In the numerical model case simulating the case when the wreck sank, turbulence seems to form only in areas where scour marks develop. In contrast, in the numerical model case where the wreck was placed partially submerged in the bed, turbulence seems to also form directly over the wreck. In both cases, the high values of TKE seem to be initiated from the stern and bow of the wreck. A similar study (Quinn & Smyth, 2018) has identified values of TKE as high as  $0.06 \text{ J}\cdot\text{kg}^{-1}$  for a computational fluid dynamic model, running at a unidirectional flow of  $1.3 \text{ m}\cdot\text{s}^{-1}$  over a wreck placed at  $60^\circ$  to the flow and exposed by 5 m over the bed (Figure 5.3d). In the present study’s numerical model case where the wreck was partially submerged in the initial flat bed (at the depth observed today), the observed TKE is as high as  $0.05 \text{ J}\cdot\text{kg}^{-1}$ , for incoming depth averaged bi-directional flow speeds of up to  $1.4 \text{ m}\cdot\text{s}^{-1}$  over a wreck placed at  $60^\circ$  to the flow and exposed by  $\sim 8.5 \text{ m}$  over the bed (Figure 5.3a). Finally, in the case where the wreck was artificially placed over the flat bed, with the wreck fully exposed to the flow (Figure 5.3b), the observed TKE is as high as  $0.07 \text{ J}\cdot\text{kg}^{-1}$ , for incoming depth averaged bi-directional flow speeds of up to  $1.4 \text{ m}\cdot\text{s}^{-1}$  over a wreck placed at  $60^\circ$  to the flow and exposed by  $\sim 16.5 \text{ m}$  over the bed.

Figure 5.3c shows the TKE difference as modelled (using the coupled numerical model) for the two aforementioned cases for the present thesis. TKE values seems to be higher over the wreck in the case of the wreck being submerged into the seabed (at the depth observed today). In contrast, the modelled case where the wreck is more exposed to the flow, seems to have higher values of TKE at the stern and bow of the wreck, due to the more exposed sharp edges of the wreck. Also, the TKE in the case where the wreck is more exposed to the flow has higher lateral extent, potentially due to the lee-wake vortices being stronger and able to migrate longer distances. The TKE extent compares well with the aforementioned explanation for the scour mark’s extent in the two modelled cases (Figure 5.2).

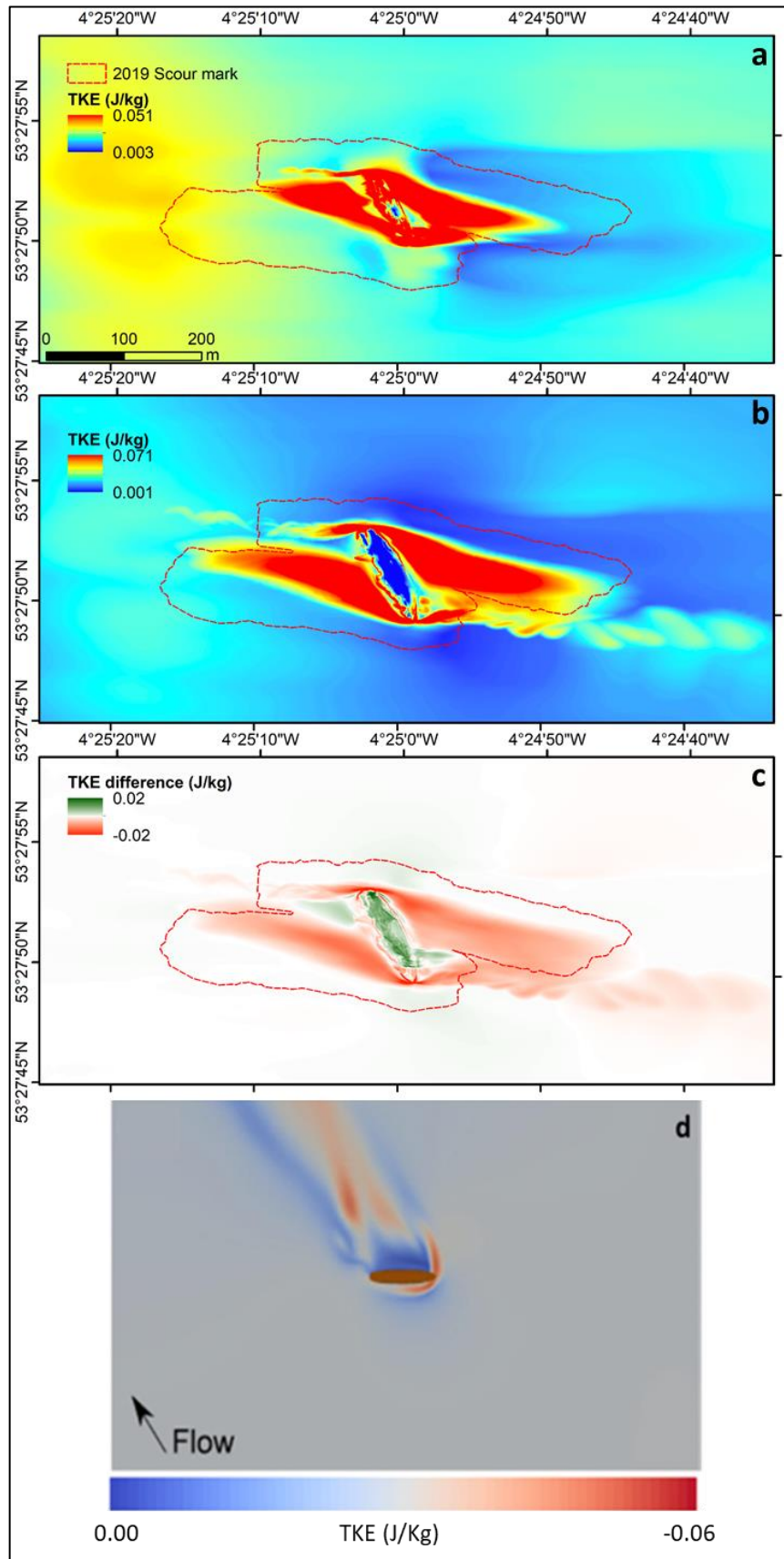


Figure 5.3: Prediction of turbulent kinetic energy (TKE) formation from the coupled model over the first 16 full tidal cycles (8 days) a) with the wreck sitting at the depth as observed in the 2012 survey, b) with the wreck 'lifted' 8m to sit on top of the artificial bed, c) TKE difference between a and b d) TKE as calculated by a CFD model with the wreck at 60° to the flow and exposed 5m over the bed (Quinn & Smyth, 2018).



According to CFD simulations by Quinn & Smyth (2018) for a wreck sitting at 60° to the flow an upstream vortex developed at the bow of the wreck (side first hit by flow) lead to the development of vortices in the lee (downstream) of the wreck. Although a vortex is developed in the lee of the stern, it is smaller in terms of magnitude and spatial extent (Figure 5.4).

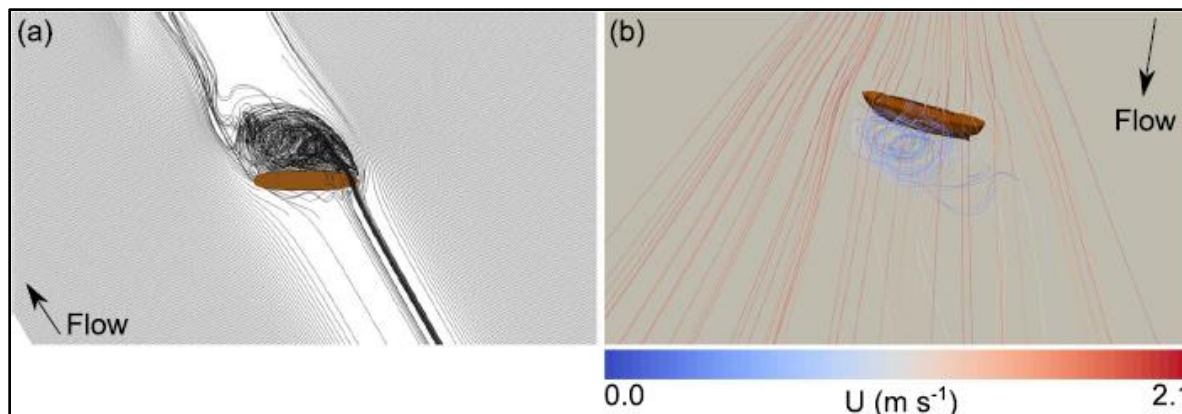


Figure 5.4: 2-dimensional flowlines (a) and 3-dimensional flow lines (b) as derived from a CFD model (Quinn & Smyth, 2018).

The numerical model outputs from the site around SS *Apapa* have been tested to identify areas with enhanced hydrodynamics and diverted flow downstream of the wreck, as a result of the incoming flow interaction with the object, and the formation of horseshoe and lee wake vortices. The observations include flow contraction upstream of the structure at plane 2 (1<sup>st</sup> plane above the bed), and flow contraction at the stern and bow of the wreck, with higher contraction at the area of the stern. The outputs of the Quinn & Smyth (2018) CFD model suggested that the higher disruption was observed at the bow of the wreck. In their model case, the bow was the part of the wreck that was firstly exposed to the flow. In the case of SS *Apapa*, presented in Figure 5.5a, the stern is the one first exposed. From the observed geometry of the developed scour mark at the SS *Apapa* site, and as suggested from the numerical modelling work, the higher (and longer) flow amplification of the bi-directional flow happens in the wake of the part of the wreck that experiences the flow first. The numerical model also suggests flow deviation at the wake of the wreck, possibly due to the formation of lee wake vortices in the vicinity of SS *Apapa*'s hull. The numerical modelling work (Figure 5.5a) also shows that lee wake vortices developed downstream of the wreck, with flow contraction towards areas with lower flow velocities, i.e., the depositional feature. These processes can therefore explain the deposition of finer sediment (curried in suspension) at these areas. The depth averaged flow velocity (Figure 5.5b) shows increased flow velocities at the stern and bow of the wreck, having a longer spatial extent. The average direction of the flow also shows a variation at the stern, bow and hull of the wreck. Although the predicted flow using the coupled numerical model conducted for this study showed similarities with the modelling work conducted by Quinn & Smyth (2018), there are differences in the observed (from *in-situ* depth measurements at the SS *Apapa* site) and modelled (from the coupled TELEMAC3D – GAIA) erosional and depositional features. More specifically, the flow amplification from the numerical model compared well with the model



outputs of Quinn & Smyth (2018). The Quinn & Smyth (2018) study has used a computational fluid dynamic model, that details in 3-D the hydrodynamics around the objects. The CFD model allows for holes to be placed in the hull of the wreck, that can potentially alter the hydrodynamics downstream, as there are more areas for the enhanced (from the object) flow to escape (or generate more complex flows). In contrast, in the coupled numerical model used for the present study, the object was treated as a solid, without holes that may exist on the hull. Also, in the case of *SS Apapa*, the wreck does not sit vertically on the bed, but it lies on the side. In the *SS Apapa* site when the flow approaches from the east, it hits the smooth bottom part of the wrecks hull and amplifies at the stern of the wreck. When the flow approaches from the west, it hits the hull of the wreck (similar to a vertical wall) and gets amplified at the bow (side that the flow hits first). In the modelling work of Quinn & Smyth (2018), not only does the hull of the wreck contain holes allowing the flow to escape, but the wreck sits over the bed, with the bow and stern elevated. This potentially reduces the hydrodynamic forcing acting on the bed because of the existence of the sharp edges of the wreck.

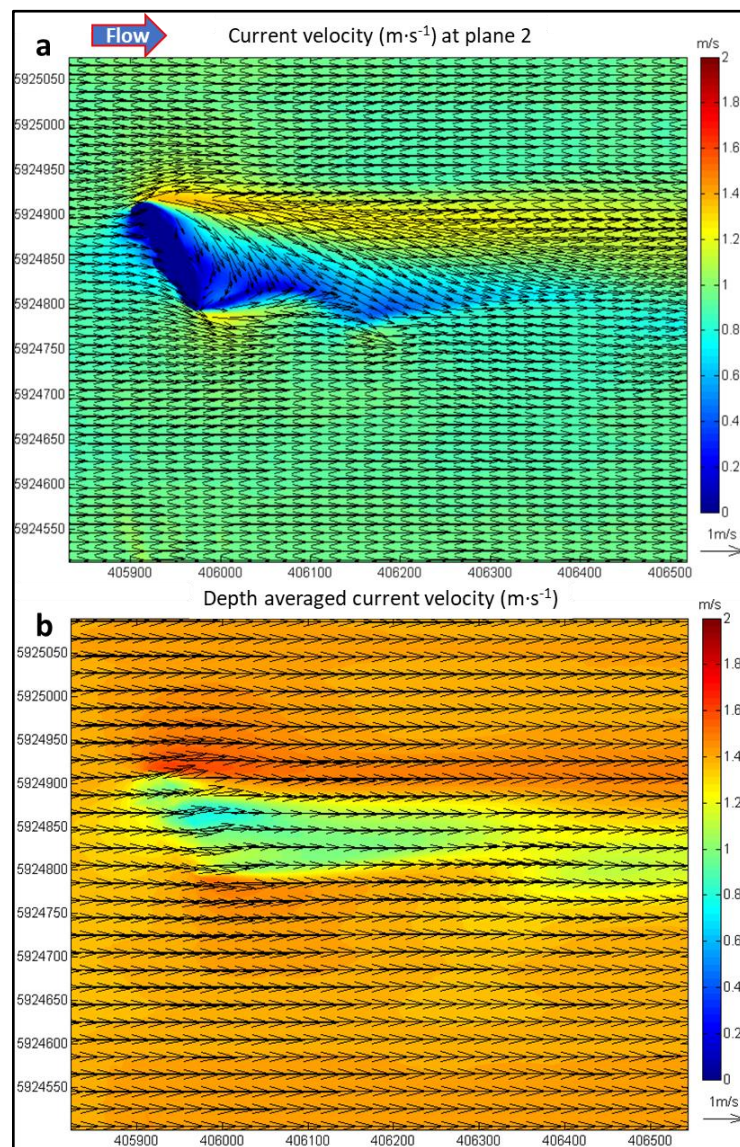


Figure 5.5: Numerical model outputs for depth averaged flow speeds with *SS Apapa* orientated at 58° to the flow. a) Observed flow velocity and direction at the first plane above the bed (plane 2) and b) observed depth averaged velocity.

Figure 5.5 presents the numerical model outputs for the depth averaged flow velocity and the average observed flow velocity at the first plane above the bed (plane 2). For the modelling work conducted around the SS *Apapa* site, the vertical component of the model was split into 20 planes, with the 1<sup>st</sup> plane being the sedimentary bed (or the wreck itself). The first plane above the bed therefore relates to the first ~2 m above the bed. The presentation of the flow velocities at that plane was chosen, as it is probably more representative of the flow velocity applied on the bed downstream of the object, causing the sediment mobilisation and the subsequent scour formation.

### 5.2.2 Impact of gradual changes in exposure of object to the evolution of scour

The gradual exposure of an object causes positive feedback that can result in even more scour. This is widely applicable in seabed infrastructure studies, as structures and cables might require less (or no) protection, if their exposure to the flow does not allow initiation of scour. If the object's exposure is monitored correctly prior to installation, costs can be reduced significantly. The exposure of SS *Apapa* has been previously discussed in this chapter using the numerical modelling work. The differences in the observed scour formation and stresses acting on the bed, caused by the exposure of the object to the flow, were also present in the numerical modelling work conducted for the controlled laboratory experiments. Although there was no change in the object's shape during the laboratory experiment, the scour developed upstream of the object caused changes in both the object's position and orientation to the flow, and also 'protected' the object from the incoming flow. As explained in Section 4.2.6, the immersed boundary method (IBM; Yin et al., 2016) enabled the object to be placed at any depth while treating the embedded part of the cylinder as solid. Therefore, as a test, different vertical positioning of the cylinder was applied in the model, keeping all the other parameters constant. This test case aims to answer if the gradual exposure of an object due to scour provides positive feedback resulting in even more scour. These tests can be widely applicable in seabed infrastructure studies to identify scour formation and resultant structural instability and are also needed for scour protection. The test cases presented in Figure 5.6 were run with the constant parameters (i.e., time, sediment mixture, flow velocity etc.) with exposure of the object to the flow being the sole variable. Figure 5.6 shows the results for the object sitting at the sediment mixture formed by 90% sand and 10% gravel, with the object embedded by 15, 20, and 25% and the object's exposed W:H ratio at 2.85, 2.69, and 2.54 respectively.

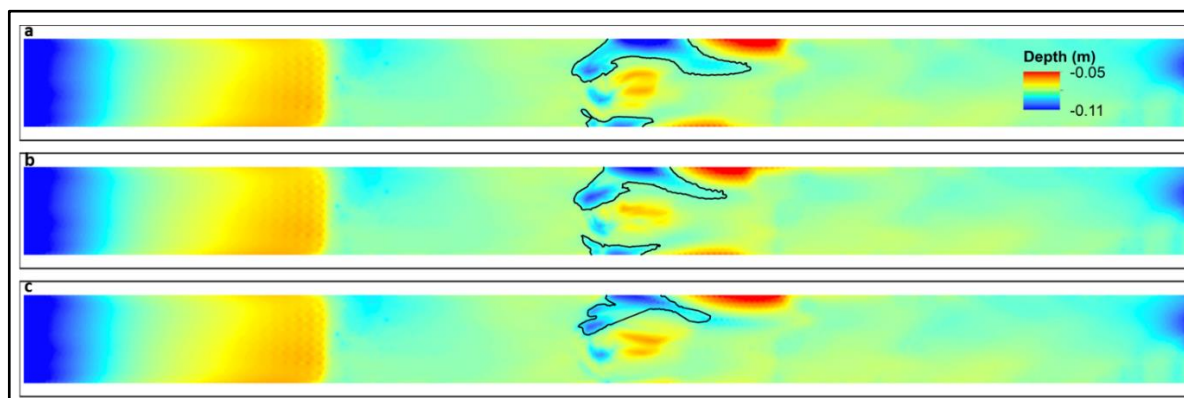


Figure 5.6: Numerical model prediction of the sedimentary bed after computation of 140 minutes for the laboratory experiment run with the sedimentary mixture consisting of 10% gravel and 90% sand. The object is exposed by: a) 85%, b) 80% and c) 75%.

The numerical model outputs for the runs presented in [Figure 5.6](#), show that the more exposed the object to the flow, the longer the scour mark. Also, for the case where the object was placed with 75% exposure, only one scour mark is predicted, at the ‘north’ site of the object.

Previous CFD simulations for a cylinder placed at 90° to the incoming flow with 100% exposure, 80% exposure and 50% exposure ([Hatipoglu & Avci, 2003](#)) show that with less exposure, disturbance of the flow downstream decreases. The numerical model outputs agree with the outcome of this study, as the higher the exposure to the flow of the object, the longer (and deeper) the scour mark that develops. The numerical modelling work around the object in the flume has also identified the problem caused by the walls of the flume (wall effect) and their interactions with the processes (hydrodynamic and sediment transport) happening in the flume.

The numerical model shows erosion of sediment that starts because of the enhancement of the incoming flow due to interaction with the object. The erosion of sediment increases once that disturbed (from the object) flow interacts with the flume’s wall (wall effect). The laboratory experiments were designed with that flow interaction in mind (hence the size and placement of the cylinder). The eroded sediment is transported and deposited further downstream. This comes due to the increased flow velocities and flow deviation around the object, and also due to the formation of lee wake vortices downstream of the object. A study ([Hatipoglu & Avci, 2003](#)) suggests for an object exposed to 80% of the flow, the resulting vortices alter the flow to a distance of ~3 times the object’s diameter ([Figure 5.7a](#)). This agrees with the results of the present study that identified variation of flow velocities (and direction) at a distance of ~3 times the diameter of the object at plane 2 (1<sup>st</sup> plane above the bed), when the object was modelled to be at the orientation of the [Hatipoglu & Avci \(2003\)](#) study (90° to the flow). The aforementioned study, does not, however refer to the flow deviation happening at the ends of the cylinder, as a result of the flow interaction with the ‘sharp’ vertical edges of the object, something that is obvious in the results of the current study ([Figure 5.7b](#)). Additionally, in the numerical model outputs of this study, there appears to be a secondary deviation of flow, at ~5 times the diameter of the object, caused by the edges of the object. The object used in the [Hatipoglu & Avci \(2003\)](#) study had a diameter (8.9 cm) of almost double the



diameter of the object used in the laboratory experiments (4.4 cm). However, since the exposure of the object to the flow is identical (20%), the results can be compared quantitatively.

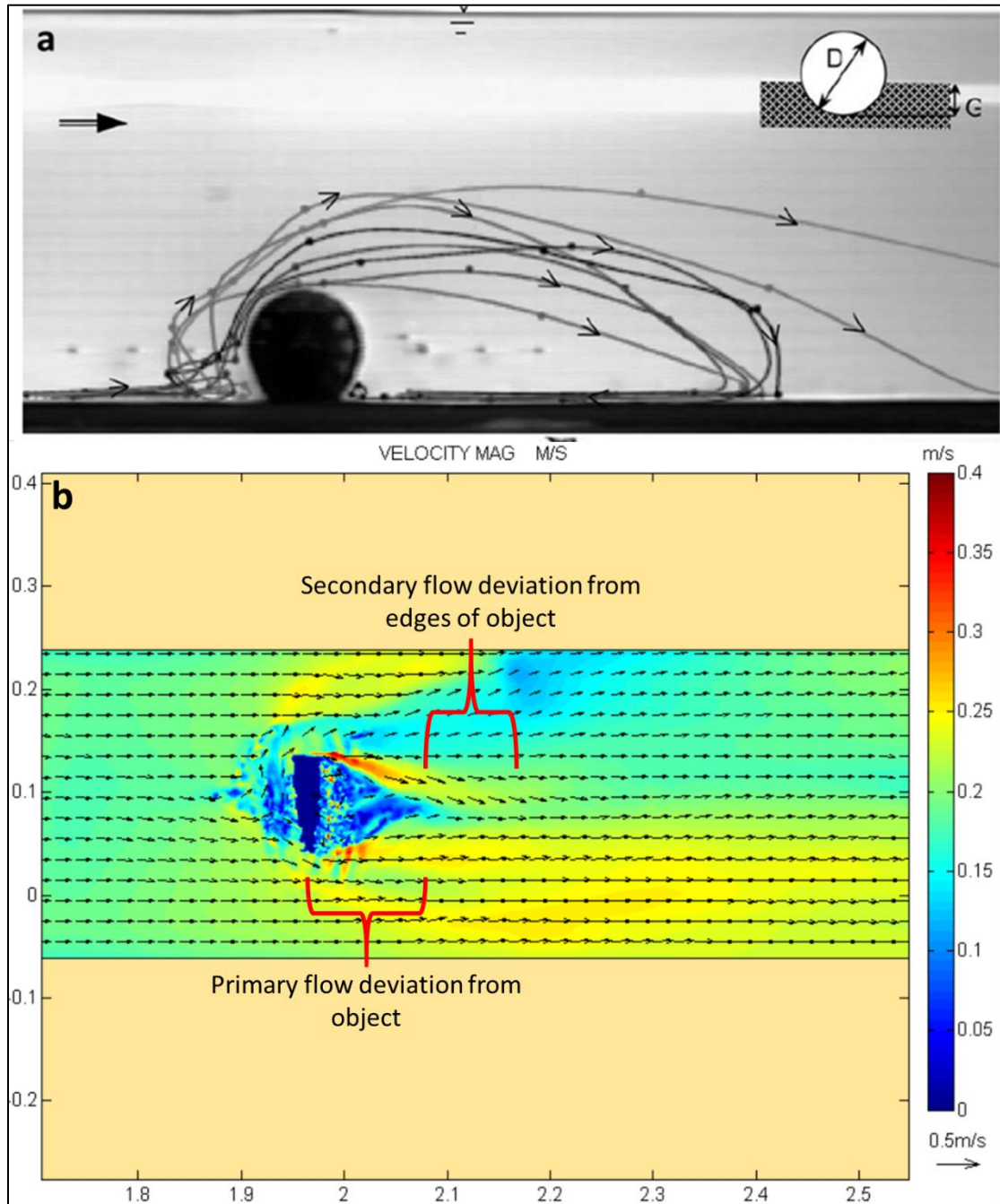


Figure 5.7: a) Output from CFD model with the object embedded by 20% at a 90° angle to the flow (Hatipoglu & Avci, 2003) and b) output of the coupled TELEMAC3D – GAIA numerical model developed for the present study with the object embedded by 20% at a 90° angle to the flow.

### 5.2.3 Impact of different orientation and shape of the object to the evolution of scour

The observations for the expected erosion and deposition patterns around objects sitting at 60° to the flow from Quinn & Smyth (2018) do not match the real-world and laboratory observations of the present study. The modelling work by Quinn & Smyth (2018) was conducted using a CFD model, and although CFD models can accurately compute flow dynamics, they cannot provide direct information on erosional and depositional processes. The coupled numerical model used in the

current study, calculates the hydrodynamic forces, and uses the calculated shear stress at the wake of the object to estimate the bed mobility for every time step. The sediment transport component of the model then uses the calculated (from the hydrodynamic model) bed shear stress to estimate the sediment movement and then updates the bathymetric grid used in the hydrodynamic model for the next step of the computation. The Quinn & Smyth (2018) study predicted erosion starting from the stern and bow ends of the 'wreck' (sitting at 60° to the flow), joined further downstream to form a long and wide scour mark (Figure 5.8a). In contrast, in the case of the scour formed around SS *Apapa* (sitting at 58° to the flow) and the laboratory experiments (object at 60° to the flow) there is an obvious deviation of the scour marks caused by the two ends of the wreck/object. The flow deviation that happens due to the interaction of flow/object at the first part of the wreck that the flow hits, dominates the flow development caused by the other parts of the wreck. The reduced flow development and formation of less strong lee wake vortices at the part of the wreck that the flow hits last, results in a much shorter and less pronounced scour mark at that site. Also, in the case of SS *Apapa* and the laboratory experiments the depositional feature is more pronounced in the middle of the two scour marks formed by the stern and bow (or either ends of the cylinder), with no sediment deposition at the ends of the scour mark at the north and south sites (Figure 5.8 b, c). This difference from the predicted scour mark and depositional feature modelled by the Quinn & Smyth (2018) study, can possibly be explained by the fact that in both the lab and real-world SS *Apapa* cases, the object is at the same level as the sedimentary bed. In the aforementioned study the sharpest edges of the wreck (stern and bow) were elevated, potentially causing less disturbance to flow influencing the surrounding sedimentary bed. Finally, the Quinn & Smyth (2018) study used only a uni-directional flow, where for the present study, a bi-directional flow was used for the numerical modelling simulations.

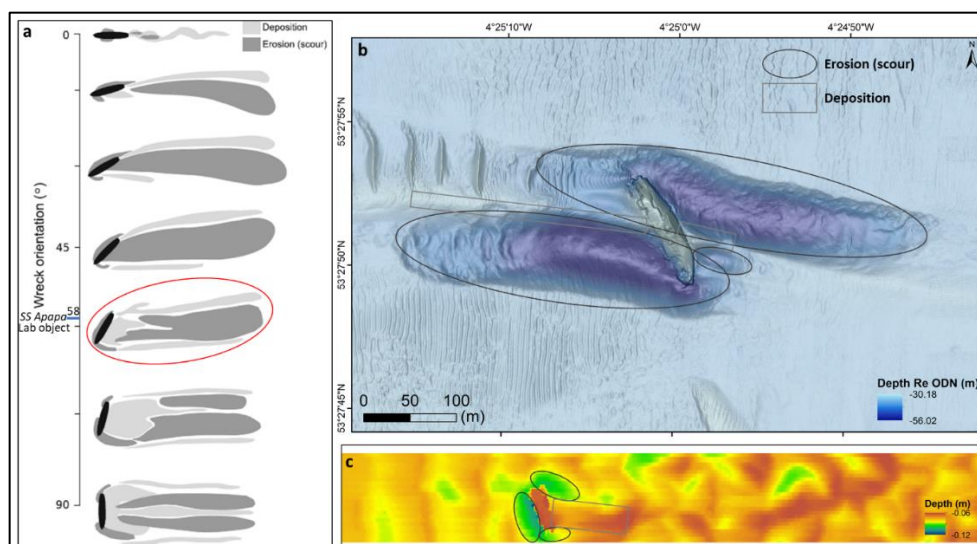


Figure 5.8: a) Erosion and deposition prediction around shipwreck sitting at different orientations to the flow as predicted from a CFD model (Quinn & Smyth, 2018). b) Scour as observed offshore around the wreck of SS *Apapa* and c) scour around a cylinder as observed the laboratory experiments with the sedimentary bed consisting of pure sand.



It is accepted that the shape of the object, its orientation to the flow and its exposure over the bed are controlling parameters of scour formation and development. Scour predictors developed in the literature (i.e., Melville, 2008; Pandey et al., 2020; Rady, 2020) to predict scour around simple structures (i.e., vertically placed cylinders, piers, bridges) cannot predict scour formation and development around objects with sharp edges. This is mainly due to limitations in understanding the flow interaction with sharp exposed edges of the object, causing additional turbulence (lee-wake vortices) downstream of the object. Also, gaps in the object itself, such as holes in a wreck's hull can produce even more complex flow patterns downstream (Astley et al., 2014).

### **5.3 Impact of mixed sediment composition on scour evolution around an object**

Another important limitation of the most existing scour predictors is that they are based on scour prediction around objects sitting on uniform beds and often use a single statistical value to define bed composition (i.e.,  $d_{50}$ ) where these single statistical values are not representative of bimodal (or multi-modal) sediments. As an example, for the laboratory experiments, the  $d_{50}$  of the mixtures used in the experiments suggested minor changes, from the pure sand (0.255 mm) to the mixture containing 20% gravel (0.284 mm). The reality is that the two modes of the mixture containing 20% sit between 0.18 mm for the finer fraction and 2.4 mm for the coarse fraction. Existing scour predictors therefore over- or under-estimate scour formation, increasing the cost needed for infrastructure installation and protection. There are currently limited studies in the literature focusing on the scour development around objects sitting on mixed beds and are mainly focused on finer sediment mixtures such as sand and mud, or mixed sands (Whitehouse et al., 2008; Porter, 2016; Rady, 2020).

#### **5.3.1 Sediment composition around SS Apapa**

Sediment sample analyses and co-registered BS intensity (see Section 3.3.3) suggests that sediments around SS Apapa are mixed and coarse, with the general trend of finer sediment concentrated at the bedform crests and the depositional features formed in the wake of the wreck. Coarser sediment is present within the scour marks and the bedform troughs. These observations agree with other observations (Quinn et al., 2016). From sediment sample analyses and flow measurements, the threshold of motion of those sediments can be calculated. Seabed mobility was quantified from repeat bathymetry data. This integration of data suggested that there is a difference in the sediment mobilisation at similar flow speeds. Coarse, bimodal sediment, expected to be immobile when using the Soulsby (1997) formulae for critical sediment transport, appeared to be part of the seabed that was more mobile than expected. The estimation of sediment movement was made by using the modes of sediment. In cases where both modes were predicted to be immobile, sediment movement occurred, supporting the fact that it is unknown how bimodal sediment will act

as a whole, due to other parameters, such as the hiding exposure effect. As shown in [Figure 3.28](#) the  $d_{50}$  (0.646 mm) of the presented sample was biased towards the finer sediment (a dominant mode 1 of 0.421 mm). However, there was also a significant amount (~35%) of coarse material (with a mode 2 of 26.95 mm), that was not represented by the  $d_{50}$  value. The sediment sample predictors normally use single-class models, as a single fraction value (i.e.,  $d_{50}$ ) and they are not representative of mixed bimodal sediment ([Wilson et al., 2018](#)). The hiding-exposure effect has been quantified for a grain size ratio (of sand and gravel fractions) of ten ([McCarron et al., 2019](#)) and it is yet uncertain how the coarse bimodal sediment in the example of the SS *Apapa* site (with a grain size ratio of 64) will mobilise ([McCarron et al., 2019](#)).

[McCarron et al. \(2019\)](#) monitored the critical shear stress needed to mobilise mixtures of sand and gravel, with gravel at 5% intervals within the mixture, up to a maximum of 50%. The study showed that increased critical shear stress (up to 75%) is needed to mobilise the sand fraction in the mixture, with a decrease (up to 64%) for the mobilisation of the gravel fraction, compared to that needed to mobilise the well-sorted unimodal sediment of similar size. The work in [Chapters 3 and 4](#) takes this knowledge of McCarron's study and applies it to the observed mobility and backscatter intensity of the bed made of coarse bimodal sediment. In this Section, the differences in the bedload transport up- and downstream of an object will be modelled using the numerical model, along with changes in scour development, around objects sitting on mixed coarse beds. In addition, the differences in suspended load transport will be modelled, as it is the dominant process of sediment transport within the scour mark ([Whitehouse, 1998](#); [Saunders, 2005](#)). The examples of the SS *Apapa* site and the laboratory experiments will be used.

### 5.3.1.1 Erosion and deposition around a wreck, guided by bed composition

During the collection of grab samples around the SS *Apapa* site, sediment samples could not be attained from the deepest points of the scour marks, coinciding with areas that no change in bathymetry was observed over the years. The deepest areas of the scour mark are immobile either due to the coarseness of the sediments, the glacial compaction of the till that is observed sub-cropping the seabed nearby ([Van Landeghem & Chiverrell, 2020](#)), due to exposed bedrock, or due to the scour being in a dynamic equilibrium state.

The offshore environment is uncontrollable and the only information about the sediment composition at the erosional and depositional features is provided from sediment sample analyses and some indication of sediment composition from the BS strength maps. The coupled numerical model used in the current study was run as explained in [Section 3.3.4](#) for the case of the SS *Apapa* site consisting of 78% gravel and 22% sand, information gained from the sediment sample analyses. To test the ability of the numerical model to identify differences in bed composition, model cases were run to identify differences in sediment transport, erosion, and deposition, in the case where the sand and gravel percentages in the mixture were *vice versa* (22% gravel and 78% sand) and for the case of

the sedimentary bed consisting of pure sand. The outcomes of the model run over 20 full tidal cycles (10 days) of computation is presented in [Figure 5.9](#).

In the model case where the sediment was composed of 78% gravel, the scour mark's length and width were up to 10% longer and narrower than the scour marks developed in the real world. These observations were made for both the 'northeast' and 'southeast' sides. In the model case where the sediment was composed of 22% gravel, the 'northeast' scour mark observed in the real-world data appears shorter and wider than the modelled scour mark. The 'southeast' scour mark observed in the multibeam data is longer and less wide than the modelled scour mark. In the case of the bed consisting of pure sand (0% gravel), both the 'northeast' and 'southwest' modelled scour marks were shorter (~25%) and narrower (~40%) than those in the real world. The model outcomes therefore suggest that mixed beds have higher mobility than the pure sand case.

As [Figure 5.9c](#) shows, the modelled scour mark was deeper in the case of the bed consisting of 78% sand and 22% gravel and the depositional feature was wider and higher, than the case of the modelled scour mark where the bed was consisting of 22% sand and 78% gravel and pure sand. The depositional feature was 3.1 m less high in the case of the modelled scour with the bed consisting of 78% sand and 22% gravel, within the first 10 days of computation. The scour mark was 4.87 m deeper at its maximum when compared with the modelled scour with the bed consisting of 22% sand and 78% gravel. In the case of pure sand, the depositional feature was less high, and the scour mark's maximum depth was lower (shallower) than both modelled cases with mixed sediments. The maximum point of the real-world scour mark is deeper than the modelled cases, and the depositional feature appears to be shallower. Although comparison with the real-world data can provide a first idea of similarities, numerical model comparison with the offshore environment cannot be accurately done at this stage, as the numerical model has only computed the initial scour formation within the first 10 days of when the wreck sank (with many assumptions made). The observed variations in the results of the modelling work conducted using the three cases, show the importance of sediment composition to resultant scour mark dimensions. The hiding exposure effect plays a major role in sediment mobilisation, with evidence ([McCarron et al., 2019](#); [McCarron, 2020](#)) showing the larger variations at cases where the gravel exists at lower than 50% within the mixtures. The longer, wider, and higher depositional feature in the cases of mixed sediment composition comes due to the larger amount of sediment mobilised at areas with higher stresses (areas within the scour mark) and the mobilisation in suspension and deposition of the larger amount of fine sediment ([Quinn et al., 2016](#)). Similarly, erosion of sediment in the case of the mixed beds is enhanced by the hiding-exposure effect, causing deeper scour marks than the modelled case of the bed consisting of pure sand.

For the numerical model presented in [Section 3.3.4](#), the sediment composition of the SS *Apapa* site was assumed to be 78% gravel and 22% sand, due to the evidence of the sediment sample analyses conducted for the site. It can be argued that sediment composition from the undisturbed bed should have been taken as input for the model and not the information from the analyses of sediment

samples collected within the scour mark. However, it is believed that the underlying coarser sediments exposed very quickly (within the first few tidal cycles) and that these coarser sediments are more representative of most of the scouring processes that happened over the years.

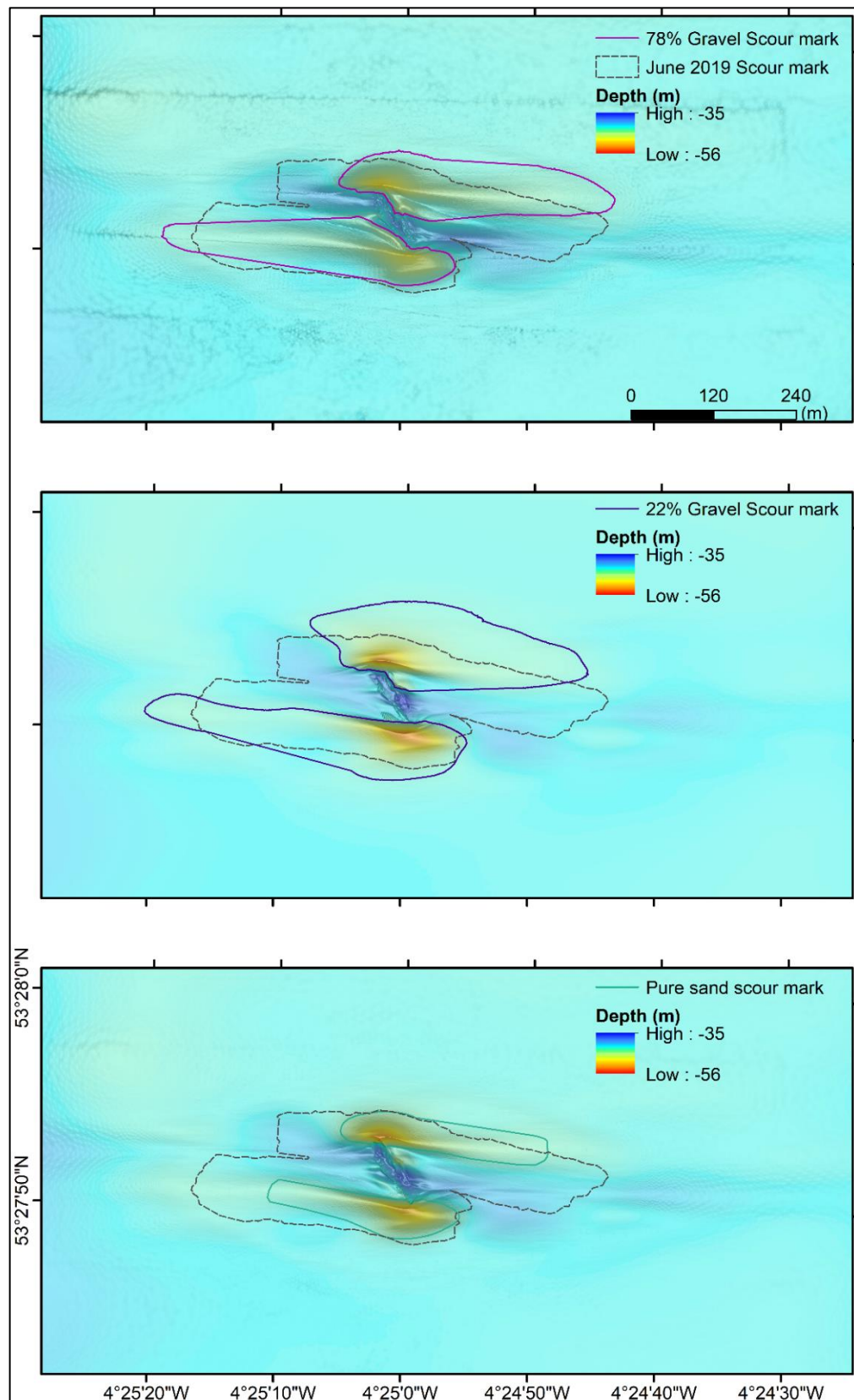


Figure 5.9: Numerical model runs over the first 20 full tidal cycles (10 days) with the sediment composition around the SS *Apapa* site consisting of a) 78% gravel and 22% sand, b) 22% gravel and 22% sand and c) 100% sand.

The coupled numerical model used, cannot only provide significant information about the importance of sediment composition and its effect on scour development and composition, but it can also provide information about the sediment transported either by bedload (Figure 5.10), or suspended load (Figure 5.11). The bedload transport downstream of the wreck is enhanced by the enhanced flow downstream (due to the interaction of the incoming flow with the object) especially at the stern and bow of the wreck during ebbing and flooding of the tidal current. The horseshoe vortices cause suspension of material upstream of the wreck, and the already disturbed fine fraction of the bed mobilises in suspension downstream of the object because of the lee-wake vortices, transporting material far downstream from the wreck.

The maximum predicted bedload around *SS Apapa* in the case of 78% sand and 22% gravel beds is ~4 times (at its maximum) higher than when the bed consists of 78% gravel and 22% sand (Figure 5.10). In the case of the bed consisting of pure sand, the maximum predicted bedload is 0.2 times higher than when the bed consists of 78% sand and 22% gravel. This can explain to an extent the wider northeast and longer southwest scour mark. The highest values of bedload are present in the areas of the stern and bow of the wreck, where as explained the hydrodynamic forces were also predicted to be amplified the most.

Figure 5.11 shows that the maximum suspended load was higher in the case where the bed consisted of 78% sand and 22% gravel. This figure also shows that the scour mark's extent is almost identical to the extent of the areas with higher modelled suspended load. In all the model cases, the higher suspended load concentrations are observed at the stern and bow of the wreck, at the areas where, as previously mentioned there was an increased flow velocity. For the numerical model case with the bed consisting of 78% gravel and 22% sand there is an area with increased suspended load at the hull area of the wreck on the eastern side. Around *SS Apapa*, as observed offshore, that area has a depositional feature. In the modelled cases of the bed consisting of 78% sand and 22% gravel and pure sand, the scour extent also seems to be controlled by the extent of higher suspended load. The suspended load is higher overall in the model cases of the bed consisting of pure sand and 22% gravel than when the bed consisted of 78% gravel. This is especially noticeable at the depositional feature (~3 times higher) and at the stern and bow of the wreck (~4 times higher). An important outcome from the coupled numerical model, is that in the case of pure sand, the lateral extent of the bedload transport is smaller, than the other two cases and its concentration is smaller than the case where the bed consisted of 22% gravel. This can possibly be explained by mobilisation of the finer fraction due to the hiding-exposure effect that then enters suspension due to the lee-wake vortices downstream of the wreck. Therefore, the model predicts that when the bed consists of pure sand, the deposition and erosion of sediment are driven mostly by the bedload transport, where in the case of the bed consisting of mixtures of sand and gravel, by both the bedload and the suspended load.



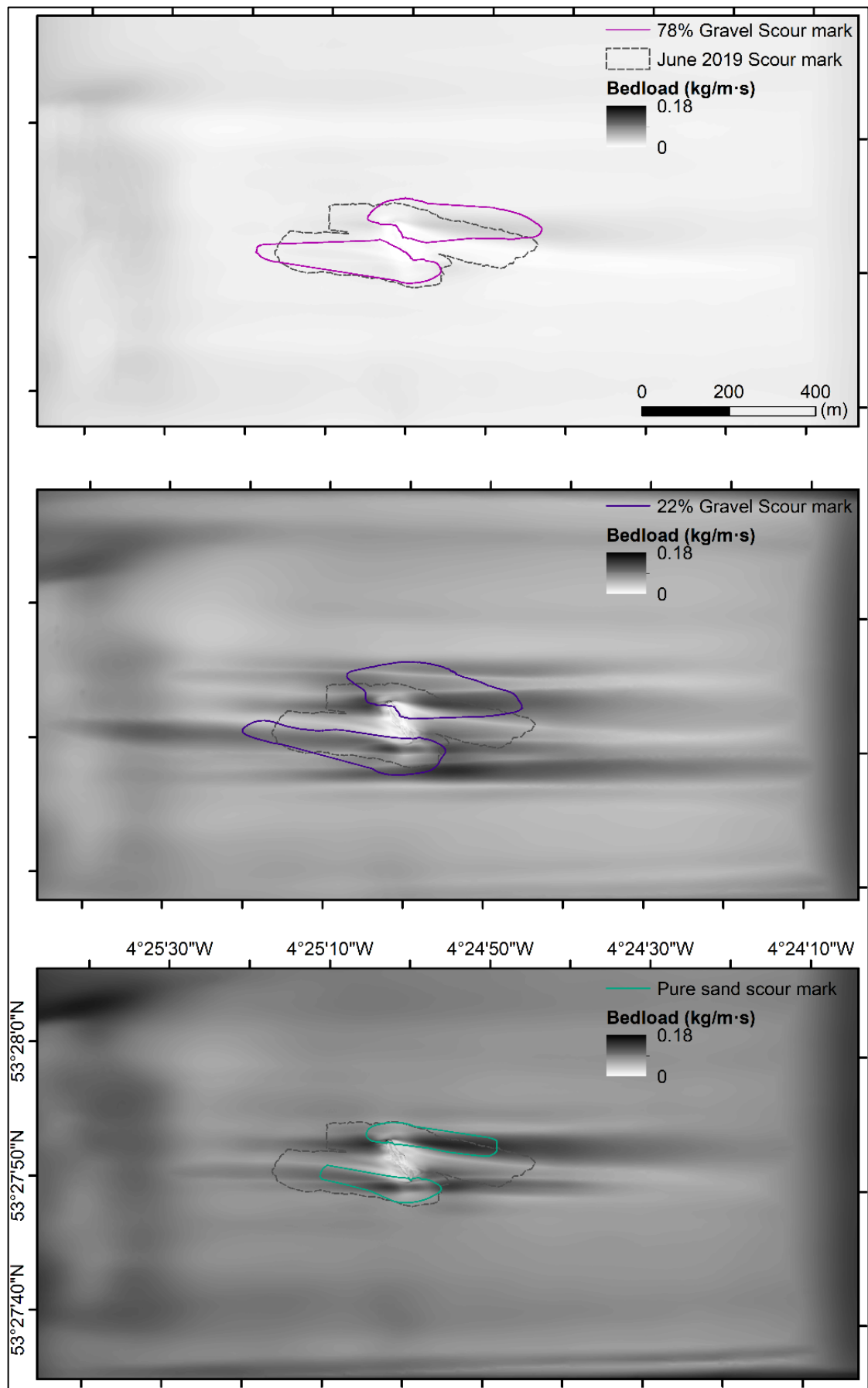


Figure 5.10: Predicted (from the coupled numerical model) maximum bedload for the case of the bed around SS *Apapa* consisting of 78% gravel and 22% sand (offshore observations; top), the bed consisting of 78% sand and 22% gravel (test case; middle) and the bed consisting of 100% sand (HE sensitivity test; bottom).

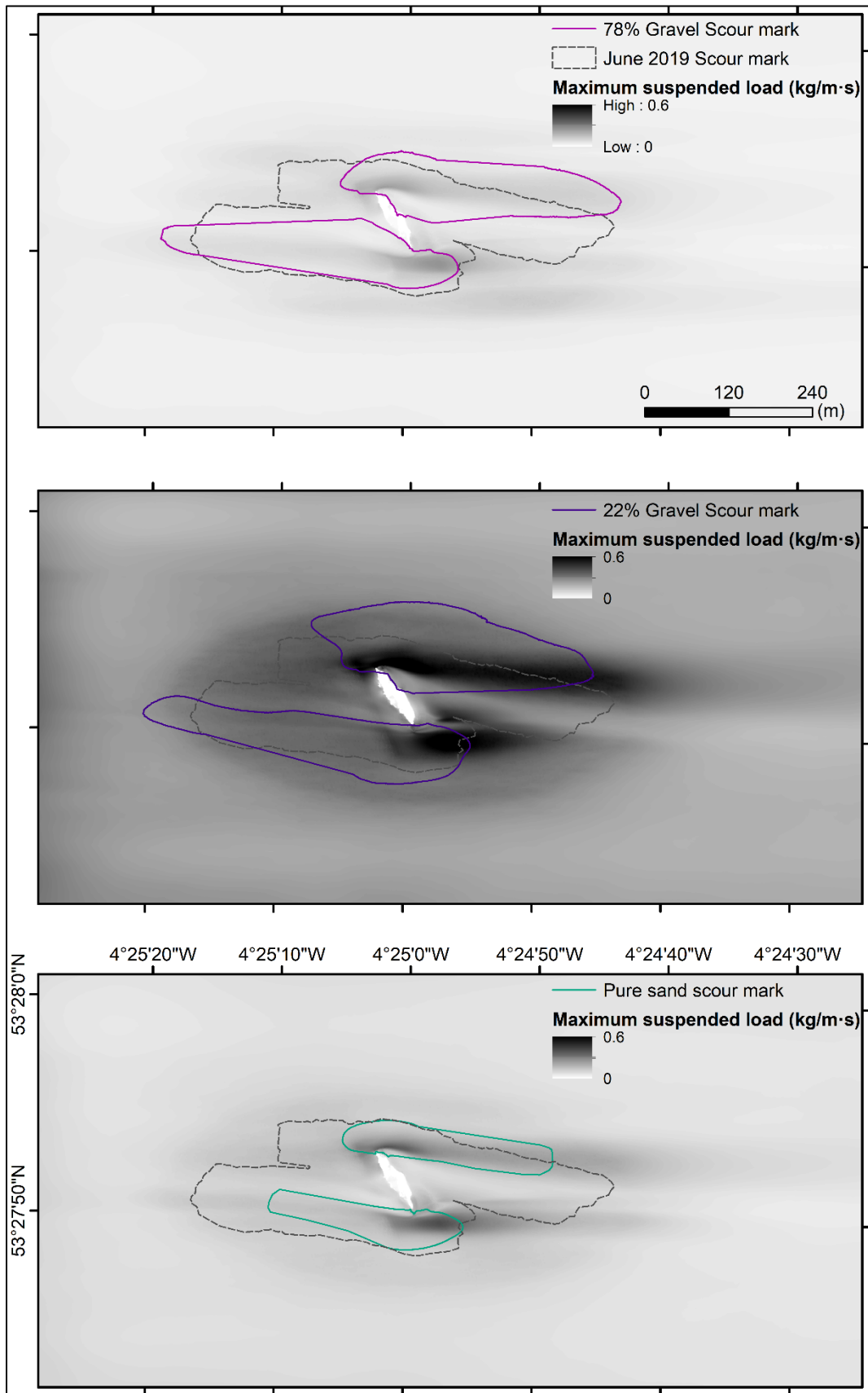


Figure 5.11: Predicted (from the coupled numerical model) maximum suspended load transport for the case of the bed around SS *Apapa* consisting of 78% gravel and 22% sand (offshore observations; top) and the bed consisting of 78% sand and 22% gravel (test case; middle) and the bed consisting of 100% sand (HE sensitivity test; bottom).

### 5.3.2 Quantifying bed mobility of bimodal sediment fractions around the object

The SS *Apapa* site provided significant information about the mobilisation of coarse bimodal sediment. The initial bed conditions when SS *Apapa* sank, are not known, nor is the exact composition of the entire bed now. Numerical model results can therefore only be compared with the offshore observations with limited confidence. However, a full quantification of bed mobility in the wake of an object was done via controlled laboratory experiments, based on the observations of McCarron et al. (2019).

The investigations around SS *Apapa* identified sediment mobility where it was predicted to be immobile (using the Soulsby 1997 formulae). The laboratory experiments showed that at the experiments where the incoming flow speed was predicted to mobilise only the finer (sand) fraction of the sediment mixtures, the upstream mobilisation of sediment appeared to depend on the gravel percentage in the mixture. More specifically, as shown in Figure 4.18a faster ripple migration rates are recorded upstream of the object, for beds containing 7.5%, 10% and 15% gravel in the case of the flow being able to mobilise only the finer fraction. Ripple migration rates relate mostly to bedload sediment transport (Allen, 1984), so it can be inferred that bed mobility from bed load is controlled by the gravel percentage in the sediment mixture.

Suspended load influences bed mobility within the scour mark, and partially controls the scour mark's dimensions (depth, width and length). For gravel percentage between 5-15%, the scour length increases when the gravel percentage in the mixture increases at both flow velocities. The expression of scour includes the alteration of bedforms downstream of the object (cf. Whitehouse, 1998; Quinn, 2006; Astley, 2016), but it makes exact scour delineation difficult, so scour edge delineation didn't include bedforms for the offshore or the laboratory studies. For gravel between 15-20% the scour mark was tracked to be longer because the ripples downstream were less pronounced. As explained in Sections 3.2.2 and 4.2.3, the scour mark was tracked to the first bedform downstream of the wreck/object.

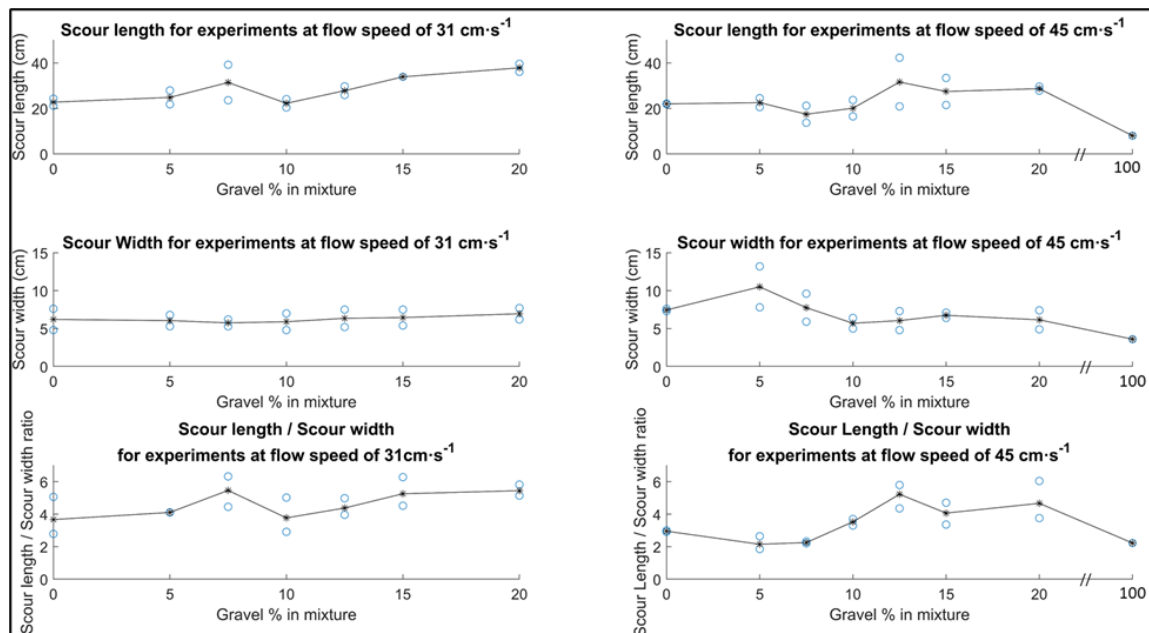


Figure 5.12: Observed scour length, width and depth as observed from the laboratory experiments using the incoming flow speed mobilising only sand (31 cm·s<sup>-1</sup>) and both sand and gravel (45 cm·s<sup>-1</sup>).

In the flume experiments where the flow speed was able to mobilise both sediment fractions, increasing the gravel percentage in the mixtures decreases the bed mobility, upstream of the object. An increased variation of the scour mark's depth and lateral extent was observed between the mixtures consisting of between 5% and 12.5% gravel. In the experimental run with the bed consisting of 12.5% gravel and the experiment conducted at high current speed, there was a large variation of the scour mark's length. This can partially be explained by the change in the object's orientation and exposure to the flow. In the flume experiments where the sediment mixture consisted of 20% gravel, the scour mark was narrower but deeper. The more pronounced scour marks were identified at the experiments conducted with the bed consisting of 7.5% gravel.

The larger grains were observed within the scour mark (just as they were in the scour of *SS Apapa*). There was also an observed separation of sand and gravel, with gravel existing at the side immediately after the depositional feature (Figure 4.52). As a reminder, at the *SS Apapa* site, large pebbles were observed at the deeper points of the scour mark where samples were obtained. In contrast, at the depositional feature and the surrounding environment, the sediment samples and the MBES backscatter strength data showed the presence of finer material along with the presence of unimodal fine sediment.

The results from the flume laboratory experiments and the influence that the bed composition had in the scour development (Figure 5.12), inspired numerical modelling tests to identify the ability of the model to predict changes in bed mobility of sediment mixtures consisting of different fractions of sand and gravel. The model was therefore run by only varying the sand and gravel percentage in the mixtures, keeping all other parameters constant, where in the modelling work presented in Section 4.3.5 the angle and exposure of the object were also changed to reflect the actual object's location in the flume at the end of the laboratory experiments, as explained in Section 4.2.6.

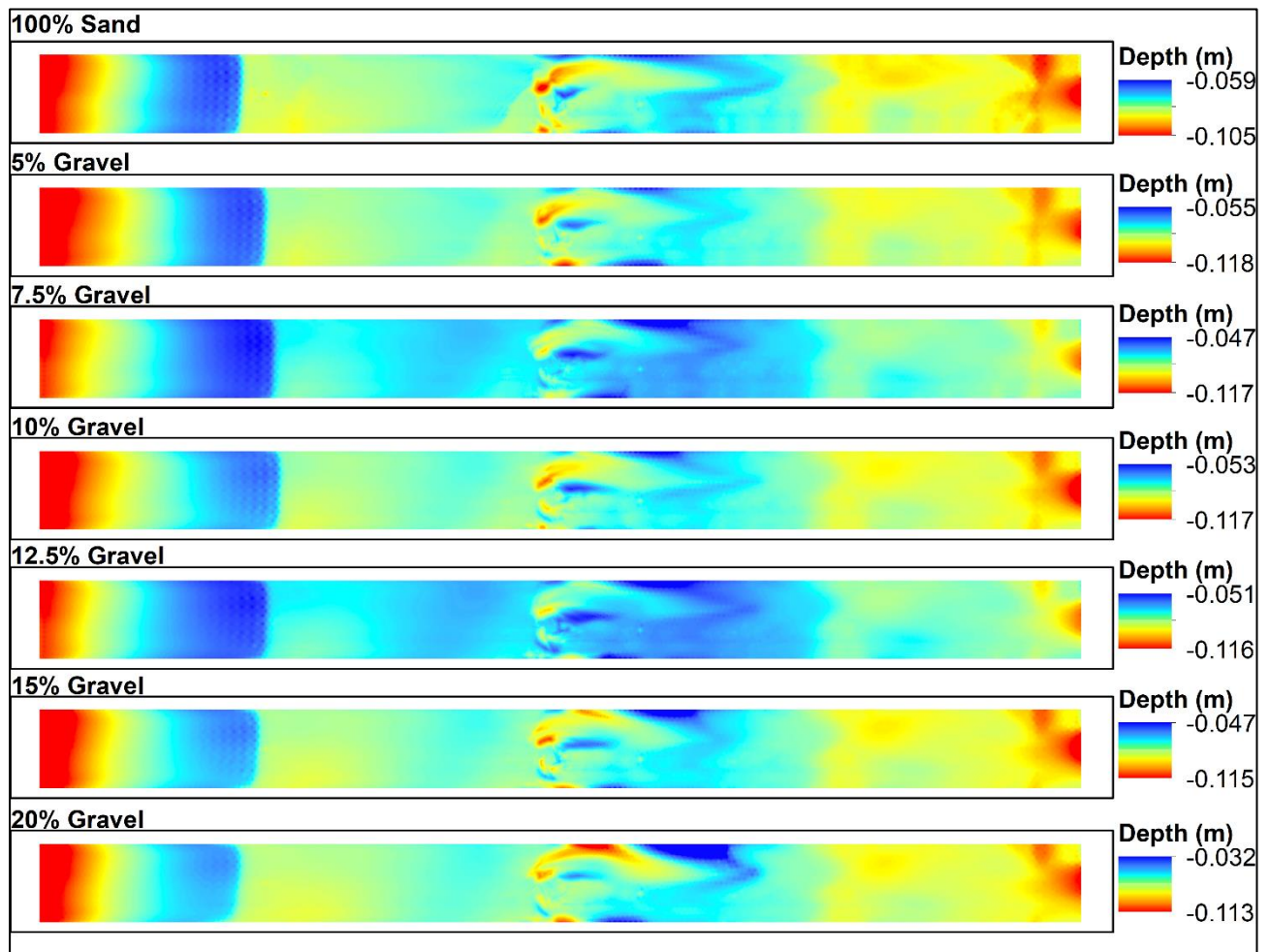


Figure 5.13: Numerical model estimations of scour development around the object with only variable the bed composition (sand and gravel % in the mixtures).

The numerical model predicts that for the flow mobilising only the fine fraction ( $31 \text{ cm}\cdot\text{s}^{-1}$ ), the shallowest and shortest scour marks were observed in the cases where the sedimentary bed consisted of 7.5% and 12.5% gravel (Figure 5.13). These numerical model outputs represent the two cases where the numerical model outputs do not agree with the results of the laboratory work. In the model cases where the bed consisted of 15% and 20% gravel in the mixture, there was a modelled influence of the scour mark's formation from the 'north' wall of the flume (wall effect). In the laboratory experiments, at the areas where the numerical model predicts scour formation due to 'wall effect', ripples were formed. As mentioned in Section 3.4.3 and 4.3.5, the coupled numerical model was not able to predict bedform formation, when tested for the real-world or the laboratory experiments cases. However, the quadratic friction coefficient relating to the skin roughness,  $C_f'$ , is calculated using the grain, or skin related roughness,  $k_s'$ , instead of  $k_s$  in Equation 2.8 that relates to the median grain diameter,  $d_{50}$ , using the Nikuradse law with  $k_s' = 3d_{50}$ . The model has predicted well the 'zone of influence' of the 1<sup>st</sup> ramp (used to hold sediment together in the laboratory experiments) to the upstream of the object bed. The model run using the coupled TELEMAC3D – GAIA numerical model, with the sedimentary bed consisting of 5% gravel and 95% sand, shows a great example of that ability of the numerical model. As Figure 5.14 shows, there is a drop in the



ripple heights (Figure 5.14c) at the point where the model predicts reduction in bedload transport (from red to green in Figure 5.14a).

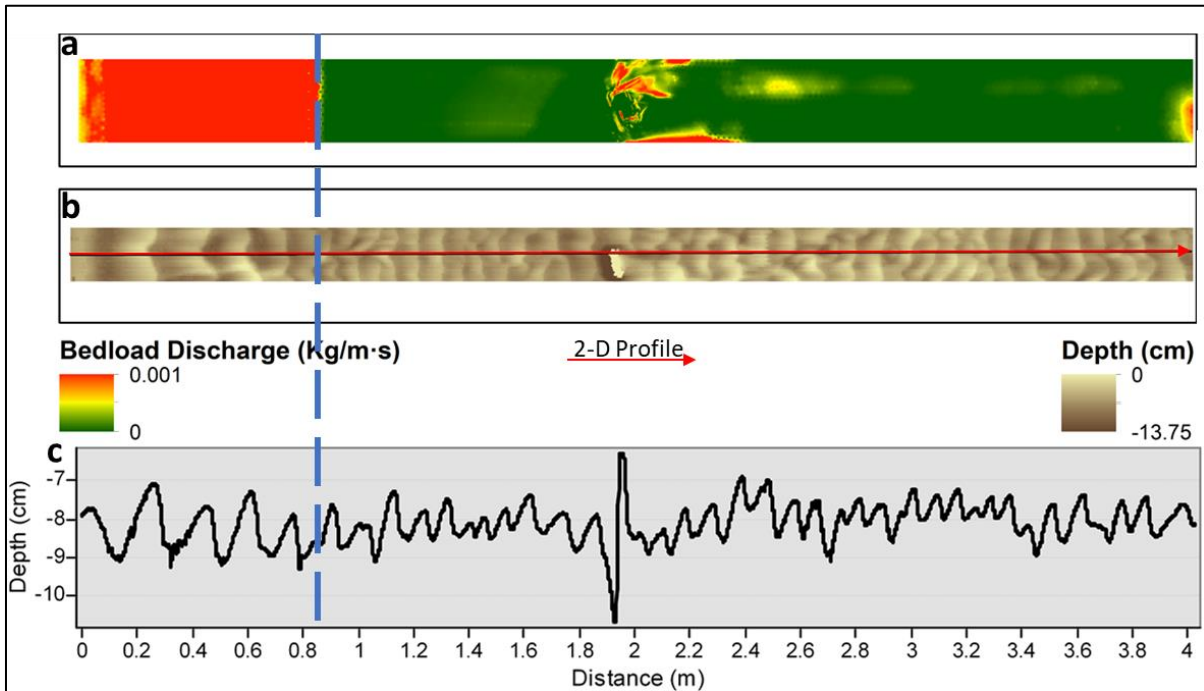


Figure 5.14: a) Maximum bedload transport as predicted using the coupled model for a run at with the sedimentary bed consisting of 95% sand and 5% gravel, b) DEM produced from the final scan using the SeaTek transducers and c) 2-D profile showing the bed levels upstream and downstream of the object (red on c).

As a reminder, the model was set to run for the exact same time as the laboratory experiments. Therefore, although bedform formation is not predicted by the model, the model identified the existence of higher forces in that area (in the cases of the bed consisting of 15% and 20% gravel), resulting to a wider and longer scour mark. Also, both the model outputs and the laboratory experiment results showed that the longer scour marks were observed in the cases of the bed consisting of 20% gravel. It is however worth mentioning, that the coupled model lacks in prediction of the upstream for the object scour formation.

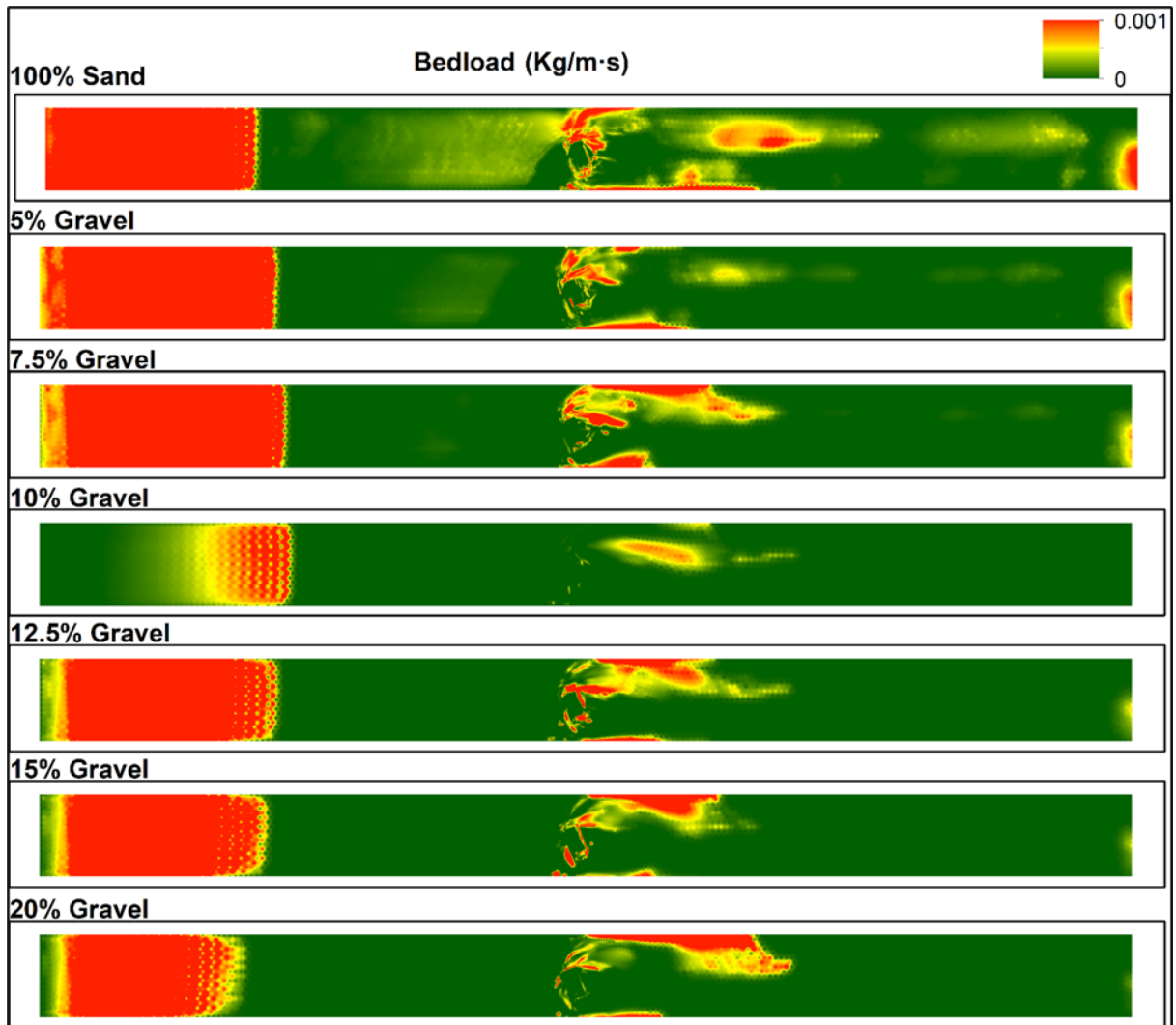


Figure 5.15: Maximum bedload as predicted from the coupled numerical model for test runs with only variable the bed composition (sand and gravel percentages in the mixtures).

Figure 5.15 shows the maximum bedload transport as predicted from the coupled numerical model, for the bed consisting as of the laboratory experiments (same sediment mixtures). The numerical model runs were set so the orientation of the object to the flow and its exposure were constant, and the only variable was the sediment composition. The numerical model outputs suggest that there is bedload transport at the 'north' and 'south' areas downstream of the object and high values of bedload transport at the edges of the object, that do not follow in full length the scour marks as shown in Figure 5.13.

The modelled maximum suspended load at plane 2 (1<sup>st</sup> plane above the bed) for all the runs is presented in Figure 5.16. The modelled suspended load shows once again increased values at the edges of the object, with slight increase in the suspended load at the areas of the scour marks. Shorter extents of suspended load are estimated at the runs where the bed comprised of pure sand and 5% gravel. The longest extents of high suspended load are observed in the numerical model cases of the bed comprising of 7.5%, 10%, and 12.5% gravel. In the numerical model cases where the bed comprised of 15% and 20% gravel, the areas where high suspended load was estimated

from the model are wider (compared to the runs with less gravel content) close to the object's edges. The modelled suspended load show an increase at the walls of the flume (wall effect), with increased gravel percentage in the sediment mixtures.

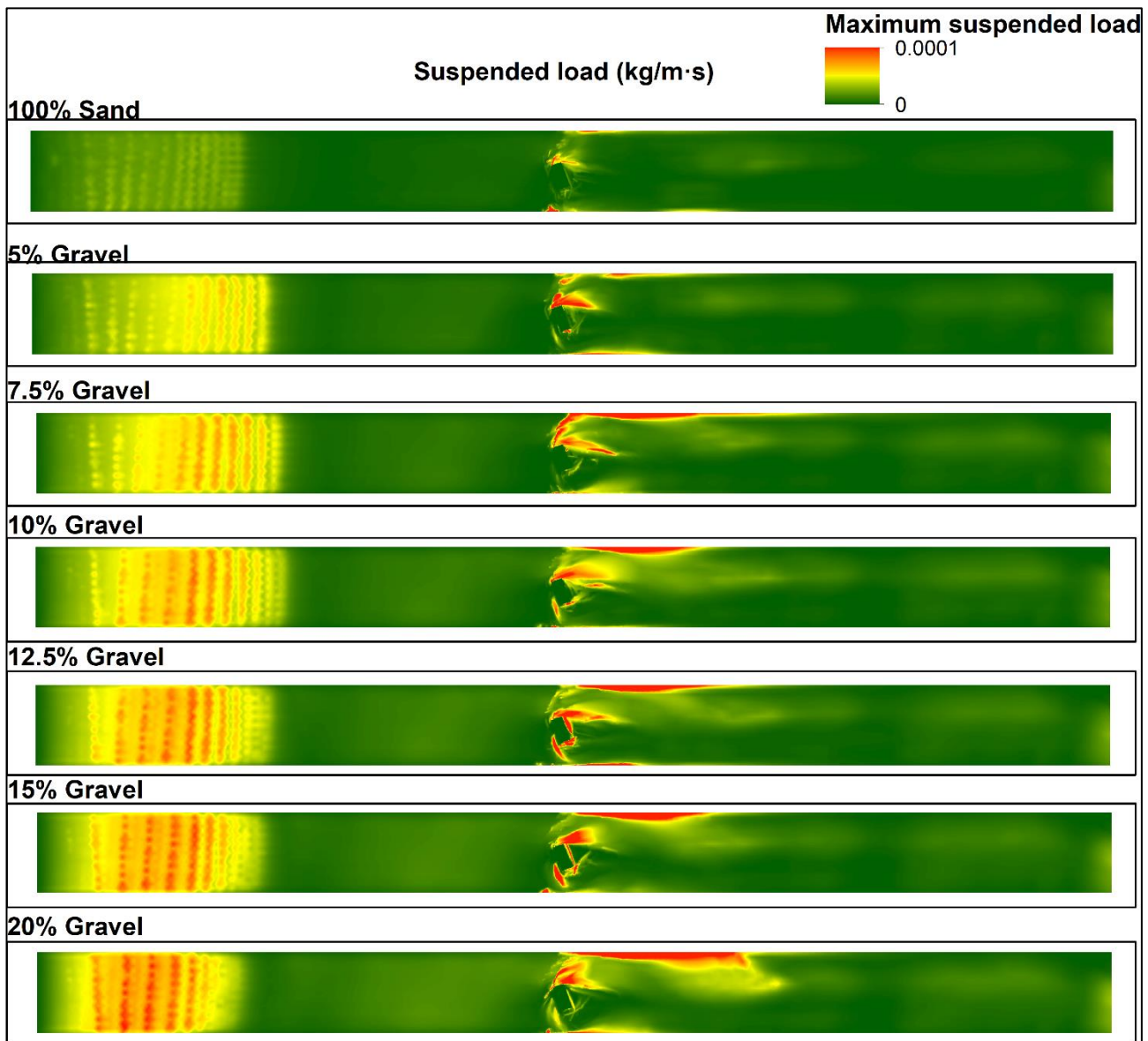


Figure 5.16: Suspended load transport as predicted from the coupled numerical model for test runs with only variable the bed composition (sand and gravel content in the mixtures).

The numerical modelling work presented in this section has shown that the numerical model predicts well the scour formation around the cylinder and can distinguish the difference between the difference sediment mixtures. It is also observed, that even not directly related with the laboratory experiments (as in this case only the sediment mixture was altered), the numerical model outputs agree with the trends described previously of larger variations in sediment transport and subsequent bed changes observed at the sediment mixtures containing 7.5-12.5% gravel. In the physical experiments conducted using these sediment mixtures, faster ripple migration rates were observed upstream of the object, the scour mark's length increased when the gravel % in the mixture increased and the deepest scour was observed.

## 5.4 Implications for better predicting scour around complex objects in mixed beds

### 5.4.1 Anthropogenic infrastructure and scour

There is currently an ever-increasing need for seabed infrastructure enabling offshore centralised storage (BBC News, 2018) and renewable energy extraction, with the United Nation goal for net-zero emission energy production by 2050 (European Commission, 2020). There is therefore an increased need for complex shaped objects to be placed on the seabed for energy extraction, conversion, and transport (Velenturf et al., 2021). Currently, monopile foundations are used in 75% - 80% of offshore wind turbines installations (Zhixin et al., 2009), as they are simple and relatively cheap to install (Lacal-Aránegui et al., 2018). However, the offshore industry is currently attempting to optimise the foundation design as scour processes can lead to the complete failure and collapse of seafloor infrastructures (Kallehave et al., 2015; Oh et al., 2018). Scour formation can also become catastrophic for the flora and fauna of an area as it can destroy seabed habitats (McArthur, 2010). The environmental impact of offshore anthropogenic infrastructure is currently being considered, with governments announcing projects (e.g., ECOWind; NERC, 2021) to investigate the nature and scale of environmental impact of engineering structures. Infrastructure for marine renewables has traditionally been installed directly on the seabed to support wind or wave turbines, or wave buoys (European Commission, 2020). Pile diameters of 5 – 10 m can be used (Zdravković et al., 2015) and piles can be buried up to 50 m below the seabed (Augustesen et al., 2009; Empire Engineering, 2019). Site-specific designs are based on detailed seabed and sub-surface conditions (Kallehave et al., 2015).

The installation cost involved and the risk to the environment and the infrastructure itself, has forced scientists and engineers to investigate more sustainable solutions. Floating structures are now being designed to produce energy while reducing space requirements, cost, and the disturbance of the structure to the seabed. However, any possible design, floating or not, requires connection to the seabed, either directly via anchoring or via cables that will transfer the produced electricity onshore (Bentley & Smith; 2008). Different shapes of anthropogenic infrastructure will require different scour mitigation, inevitably increasing the installation and manufacturing costs, making the marine renewables sector less cost effective. Traditional scour predictors rely on empirical equations and often use one statistical value (i.e.,  $d_{50}$ ) to predict the scour formation around infrastructures. This study has provided significant information about the mobilisation of coarse bimodal sediment, existing at different depths in the North and Irish Sea, due to deposition of glacial tills and has quantified what sediment mixtures appear to be creating the longer, wider and deeper scour marks. The information provided in the current thesis, can potentially be used for anthropogenic infrastructure development in more complex environments.

### 5.4.2 Object's shape and exposure to the flow influencing the scour mark formation

Installation of infrastructure for marine renewable energy extraction is nowadays focusing on waters with depths up to 300 m, with preference to floating infrastructure to reduce the impact to the seabed while reducing the cost significantly (European Commission, 2020). Wrecks have existed for decades at these depths and can therefore provide vital information as live examples of scour formation and subsequent seabed disturbance. Wrecks can also provide information about scour development at sites with different sediment composition as their site formation can be back engineered to an extent (Astley, 2016). Wreck sites are open systems allowing the exchange of material such sediment, organic and inorganic objects, and energy, like wave, tidal and storm across the system boundaries (Quinn, 2006). Wrecks present an extended record of engineered objects that are in dynamic equilibrium with respect to the natural environment and can provide significant insights into the expected longevity and operation of offshore renewables.

Engineering studies to date have focused mostly on scour around infrastructures with shapes commonly used in the marine environment for energy extraction, conversion, and storage (i.e., monopiles, bridges, piers, cables, pipelines) (i.e., Whitehouse, 1998; Hatipoglu & Avci, 2003; Melville, 2008; Zhixin et al., 2009). Numerical modelling work performed and presented this thesis shows the importance of the object's exposure to the flow in scour formation. More specifically, it is estimated that change of 5% in the exposure of the object can reduce by ~20% the scour mark's length around a vertically placed cylinder with sharp vertical edges. Also, the less exposed the object is, the less disturbance is caused to the surrounding bed, and largely qualitative observations (i.e., Whitehouse, 1998; Hatipoglu & Avci, 2003; Saunders, 2005) are now underpinned by quantitative estimates where with a reduction of 5% in the exposure, there is a ~12% reduction in bedload and ~21% reduction in suspended load (maximum values) downstream of the object. The offshore study around SS *Apapa* highlighted the importance of the object's shape and how a small change in that shape (trigger event) can cause a sudden shift in the otherwise stable depositional and erosional regimes. Scour formation due to interaction of the incoming flow with an object, appears to be controlled by a combination of the object's shape, orientation to the flow, exposure to the flow, and critically, the surrounding sediment type.

Scour protection around seabed infrastructures, might not have to completely rely on burial of cables and converters. Coupled numerical models, like the TELEMAC3D – GAIA one used in this study, can provide significant information about the expected scour development and the possibility of the scour reduction by burial of some parts of the structure to minimise or prevent scour development. This can result in installation, manufacturing, and protection cost reduction of offshore infrastructures.

The resultant numerical model can aid scour prediction of offshore infrastructure sitting on mixed coarse beds (sand and gravel) as it allows the inclusion of both mixed sediment beds and correction for the hiding-exposure effect (McCarron et al., 2019) on the bedload transport calculations. The McCarron et al. (2019) quantification of the HE is for grain ratios of 10:1 but has however identified



differences in seabed sediment composition for grain ratios of 64:1 for the *SS Apapa* case. The resultant numerical model can be used for the prediction of irregularly shaped objects, where uncertainties exist in both the hydrodynamics and forces acting on the bed due to the presence of the object, and the knowledge gained from this thesis can also be used for the parametrisation of larger scaled models for the prediction of sediment mobilisation around offshore asset arrays. The coupled numerical model can also be used for wreck stability and preservation studies, in cases where sudden changes (i.e., disintegration) are observed on wrecks sitting on complex mixed seabeds).

#### 5.4.3 Implications for seabed stability and preservation

Shipwreck sites exist in a state of dynamic (not steady state) equilibrium with the natural environment (Quinn, 2006), as most of them can be characterised as already being part of the system (Whitehouse, 1998) due to the time that they are present in their environment. Wreck sites can be also characterised by negative disequilibrium, leading to wreck disintegration (Quinn, 2006), due to the time and the physical, chemical, and biological processes, acting on both the exposed (to the flow) and buried (in the sediment) parts of the wreck. This wreck disintegration, can be a localised event, characterised as a trigger, causing rapid changes to both the hydrodynamics and sediment dynamics of the surrounding environment. In the case of the laboratory experiments presented in this thesis, the trigger happened at the point of the object's unintended movement, changing both the exposure, and the orientation of the object to the incoming flow. A new system state is reached once the changes in both the hydrodynamics and sediment dynamics settle and the wreck becomes part of the system again, resulting in a new dynamic equilibrium (Whitehouse, 1998; Quinn & Boland, 2010). *SS Apapa's* disintegration happened at the duration of this PhD project and can further support evidence from the literature (i.e., Whitehouse, 1998; Quinn & Boland, 2010; Firth, 2020). Putting *SS Apapa* case into the plot shown in Figure 5.17, can aid identification of the rapid changes happening around the wreck after the disintegration. Changes in the system's state can result in both nearfield and far field changes around the wreck. For example, a localised event causing a slight change in the wreck's shape has caused changes in the hydrodynamics and subsequent sediment dynamics of the surrounding area. It was observed that a slight shifting and a variation of about 0.5 m at the wreck's hull caused features that were observed to be consistently erosional between 2012 and 2018 to suddenly fill with ~300 m<sup>3</sup> of sediment in 2019, potentially due to a linked shift in hydrodynamics. Difference-modelling between the 2018 and 2019 surveys showed that the site went from one of net erosion to net deposition of sediment. However, it is known that scour processes (erosional and depositional) happen within the first few tidal cycles (Harris et al., 2010) so it is likely that the oscillation shown in Figure 5.17 (Quinn & Boland, 2010) was not captured by a single survey.

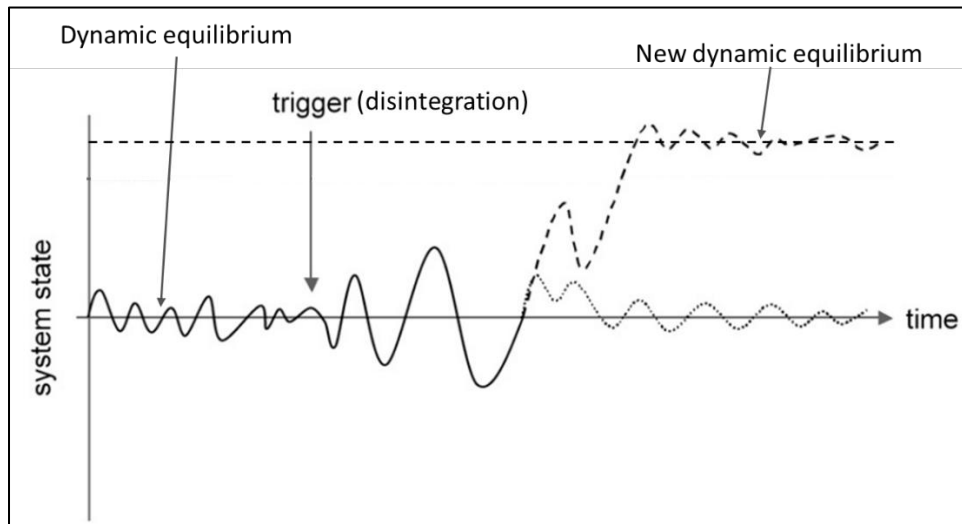


Figure 5.17: Explanation of a dynamic equilibrium of a wreck site over time. The site is initially at a dynamic equilibrium with the surrounding environment. After a localised event (disintegration), rapid changes are observed until the site reaches a new dynamic equilibrium. Adapted from Quinn & Boland (2010).

This shifting / disintegration event showed the importance of the wreck's stability and preservation and its effects to the surrounding environment. Understanding scouring around shipwreck sites is also important from archaeological perspectives (Quinn, 2006; Astley, 2016). For example, sediment transport around shipwrecks can alternatively bury and expose parts of the wreck, enhancing artefact deterioration, resulting in the loss of significant archaeological information (Heldberg et al., 2004). Some wrecks and their containers are of great archaeological value and if not managed correctly, may deteriorate, and be destroyed. This study has also attempted to reconstruct to an extent the original seabed on which the wreck sank for the *SS Apapa* site. The numerical modelling work's outputs suggested that initial scour formation happened in the first 20 tidal cycles, proving that site reconstruction can be done in the cases of other wrecks, supporting evidence from the literature (i.e., Tomalin et al., 2000; O'Shea, 2004; Church, 2014). The information gained from this study can be used to prevent the loss of invaluable archaeological resources.

Metal shipwrecks of the age of *SS Apapa* seem to have nowadays reached a critical point in terms of their structural integrity and they have started disintegrating (Firth, 2020). These rapid changes in wreck stability are important at sites of archaeological or scientific interest, and at sites considered as hazardous (i.e., *SS Richard Montgomery*; Astley, 2016). Wrecks such as *SS Richard Montgomery* (World War II), carrying a dangerous cargo of unexploded ordnance (1,400 tons), are of similar age to *SS Apapa*, meaning that they might soon disintegrate and potentially cause environmental and navigational disasters if not treated correctly.

## Chapter 6

### 6 Summary and Synthesis

#### 6.1 Brief summary of the rationale behind this research

The purpose of the work presented in this thesis was to investigate, understand and quantify the hydrodynamic disturbance and subsequent scour formation around objects sitting on mixed coarse beds. There is currently an ever-increasing need for seabed infrastructure, enabling offshore renewable energy production (commercially) to achieve the United Nation goal for net-zero CO<sub>2</sub> emissions by 2050 (IEA-OES, 2021). Introduction of an object to the seabed, will modify the flow regimes around the object and its immediate environments, causing flow contraction, enhanced stress on the bed and scour formation due to sediment mobilisation (Whitehouse, 1998; Quinn, 2006; Smyth & Quinn, 2014; Quinn & Smyth, 2018). Scour formation can cause infrastructure failure (Quinn, 2006) and can impact seabed habitats (McArthur et al., 2010). Scour predictors have been developed over the years mainly for the prediction of the equilibrium scour depth around vertically placed structures (i.e., Melville, 2008; Pandey et al., 2020; Rady, 2020), with knowledge gap for scour dynamics in the wake of non-uniformly shaped objects (i.e., shipwrecks) or objects sitting on mixed beds (Rady, 2020). While the shape of the object has been incorporated in scour prediction using CFD models (i.e., Smyth & Quinn, 2014; Quinn & Smyth, 2018; Majcher et al., 2022), to the author's knowledge the case of scour formation on mixed beds has not yet been fully quantified/understood in the literature. In mixed beds, the degree of a sediment grain's exposure to the flow compared to the surrounding grains can affect the forces needed for the initiation of motion, an effect known as hiding-exposure effect (Egiazarof, 1965; Soulsby, 1997; Janssen, 2010; McCarron et al., 2019). Over 25% of the seabed surface around the UK consists of mixed sediments and understanding of scour formation around seabed infrastructures placed in these environments can increase the potential areas for seabed development.

#### 6.2 Answer to the questions asked

The overall aim of this work was to predict seabed scour and mobility (seabed integrity) around objects placed on mixed beds. This section aims to provide quantitative answers to the questions asked at the introduction chapter (Chapter 1) to achieve the objectives of the current study as detailed below:

##### **Where is flow modification around the object strongest?**

Amplification of 2.3 times higher than the maximum background current was observed at the stern and bow of the wreck. The highest amplification was observed at the site of the wreck where the flow hits first and was observed during slack tides. Due to the low current speeds at slack tides, even

the smallest variation appears to be large when comparing the two flow speeds (undisturbed and amplified due to the interaction with the object). Identification of higher flow amplification during ebbing and flooding is possibly not feasible to be recorded by the ADCP instrument, due to the high values of turbulence generated at the wake of the wreck due to lee-wake vortices formation downstream, mixing the water and the particles that the ADCP instrument uses to measure the flow velocity. ADCP measurements subject to many sources of uncertainties, depending mainly on the beams spreading and the assumptions made on flow homogeneity. Although 4-beam ADCP instruments can be used for the turbulence characterisation, instruments with higher number of beams are normally preferred for these types of measurements (Mercier et al., 2021). Data from a 4-beam instrument can be used with the so-called variance method that uses the along-beam velocity measurements, using differences between the velocity variance along the opposing beams to solve two out of six components of the Reynolds stress tensor. In contrast, 5-beam ADCP instruments can estimate five components of the Reynolds stress tensor (Guerra et al., 2017), and recent 7-beam instruments can solve all components of the Reynolds stress tensor. For the present study, the ADCP instrument measurements were not used for turbulence estimations. The coupled numerical model used to model the SS *Apapa* site (hydrodynamic component), has identified an 80% increase of the depth averaged flow velocity downstream of the wreck when compared to the background (undisturbed) depth averaged velocity. The flow amplification at the part of the wreck where the flow hits first, can also be identified in the scour formation. In the case of SS *Apapa*, the scour formation was initiated at this point for both ebbing and flooding. This information was provided by both the deepest points of scour, but also from the numerical modelling work conducted around the site, that identified a 0.5 m deep scour mark within the first hour of computation, initiated from the site of the wreck where the flow hit first (See Figure 3.69). It is important to mention that amplification of flow was not only recorded downstream of the wreck but also directly over, with flows up to 2 times higher when compared to the background flow, at depths as shallow as ~6 m, where the wreck of SS *Apapa* sits at a maximum depth of 35 m. Considering that the wreck sits on the site, and the width of SS *Apapa* is 17.5 m, this means that there is a flow obstruction up to 1.66 the “height” of the wreck (as it sits on the bed). In the case of offshore infrastructures, this flow amplification can have significant consequences at the population of the animal species living in the area, and it is something that must be considered when addressing the environmental impact assessment for a site development.

In the case of the laboratory experiments, measuring of the flow amplification at the edges of the cylinder was not possible using the UDVP instrument. However, it was observed (visually and from the coupled numerical model) that scour was initiated from the part of the cylinder where the flow hit first. Also, estimations of the depth averaged flow velocities using the hydrodynamic component of the coupled numerical model used, shows a 10% increase in the depth averaged flow velocity downstream of the part of the cylinder that the flow hit first, for the numerical modelling work conducted using the flow speed of 31 cm·s<sup>-1</sup>. For the numerical modelling work conducted at the

flow speed of  $45 \text{ cm}\cdot\text{s}^{-1}$ , the model predicts an increase of the depth averaged flow speed of up to 7% at the same location.

### **What is the lateral extent of flow amplification in relation to object size and background hydrodynamics?**

Analysis of the ADCP dataset collected over two full tidal cycles around the *SS Apapa* site has shown amplified hydrodynamic values between 102 m and 311 m away from the wreck. This means that the extent of the amplified flow reaches the extent of 0.76 to 2.3 times the length of the *SS Apapa* wreck, depending on the state of the tide. More specifically, the longest extent of flow amplification is observed during ebbing and flooding. During slack tides, where the flow was observed to have the highest amplification at the stern and bow of the wreck, the survey lines did not record the lateral extent of flow amplification. In the case of the laboratory experiments, amplification of the depth averaged flow speeds measured in the middle of the flume's width, and not at the edges of the cylinder showed amplified flows of up to 1.5 m downstream of the object. This means a lateral extent of flow amplification of up to ~16 times the length of the cylindrical object used (9.4 cm). This can be a result of the ripples generated in the flume and the fact that due to bed level change during the measurements, the UDVP instrument might have not been accurately measuring the depth averaged flow speed. As a reminder, the depth that the UDVP instrument was placed was chosen such, that the measured flow velocity was the equivalent to the elevation over the bed where the depth-averaged velocity ( $\bar{U}$ ) would be observed assuming a logarithmic velocity profile. Bed elevations change due to bedform migration would have changed the distance between the bed and the UDVP transducer. Also, at this length, was the maximum observed disturbance on the bed, as observed from the ripple formation downstream of the object (Figure 4.8).

Identification of the flow's lateral extent in relation to the object, subjects to the survey methods. In the case of the *SS Apapa* environment, the flow was not constantly measured using the same survey lines, for ease of navigation. In the case of the laboratory experiments, the UDVP instrument has only provided a first indication of the flow amplification downstream of the object with measurements taken in the middle of the flume's width. However, indirect measurements of flow amplification were also made by identifying the 'zones of bed mobility' or 'zones of influence' in both the offshore and the laboratory experiments. In Section 3.3.2.1, two 'zones of maximum bed mobility' were identified around *SS Apapa*. These zones were observed at 0.32 and 0.84 times the length of the wreck at the west and 0.27 and 1 times the length of the wreck at the east. It is worth mentioning that at these zones, a drop in the bed mobility was accompanied by a 30 % drop in depth averaged flow speed, when compared with the background (undisturbed) flow. For the east side, this flow reduction reached 35 %. The two consistent 'zones of bed mobility' were also observed in the case of the laboratory experiments (Section 4.3.1.2) using the different sediment mixtures, at different distances away from the object. For the experiments conducted at the low flow speed, the average distances for the two zones were at 2.6 and 9 times the length of the object. The maximum extents were



observed at the experiments with beds consisting of 15% gravel (~4 times the object's length) and 12.5% gravel (10.7 times the object's length) for the first and second zones respectively. For the experiments conducted using the high current speed, the average distances for the two zones were at 2.2 and 8.6 times the length of the object. The maximum extents were observed at the experiments with beds consisting of 20% gravel (2.5 times the object's length) and 12.5% gravel (10.8 times the object's length) for the first and second zones respectively.

### **How does a change in the object's shape impact flow modification (strength and extent) and how does that change impacts the evolution of scour?**

The object's shape was investigated in this present study due to the disintegration of the *SS Apapa* between the March 2018 and June 2019 surveys. This disintegration/shifting of the wreck altered the existing hydrodynamic conditions at the area and the subsequent forces acting on the bed. This change in hydrodynamics, was observed by the changes in the erosional and depositional rates and areas at the site. Between the two surveys, the wreck has shifted and appeared 7.8 m deeper at the west side and 7.4 m shallower at the east side (Figure 3.80), with an overall change of ~0.5 m over the wreck's hull. This change of the wreck's shape and its impact on the hydrodynamics allowed for a deposition of ~300 m<sup>3</sup> of sediment at the NW part of the scour mark, at an area that was up to 2019 constantly eroding. Also, this change of the wreck's positioning has caused the migration of the first large bedform at the NW to the east (at a migration rate of ~9.7 m·y<sup>-1</sup>), where these bedforms were constantly observed to be migrating to the west (at a mean migration rate of ~3.4 m·y<sup>-1</sup>), at the direction of the dominant current.

Investigation of the shape's impact to the hydrodynamics, investigated using the coupled numerical model, showed the importance of the W:H ratio of the object. Change in the W:H ratio from 0.5 to 1 (i.e., more exposed object to the flow) in the case of *SS Apapa*, produced a ~55% longer scour mark (maximum difference) and caused the formation of ~33% more turbulent kinetic energy downstream of the wreck. The extent of the disturbed flow in the two cases varied from 1.2 to 2.1 times the length of the wreck. In the case of the numerical modelling work conducted for the laboratory experiments, the numerical model outputs showed that a change of 0.3 in the W:H ratio (10% change in the object's exposure to the flow) caused a 66% longer scour mark, due to the enhanced flow dynamics downstream of the object.

### **How does the amplified flow downstream of the object impact the sediment movement of mixed coarse (sand and gravel) beds?**

The existence of the object and the interaction with the incoming flow, causing enhanced hydrodynamics downstream has been reported to be increasing the bed shear stress downstream of objects by up to a factor of four (Whitehouse, 1998; Quinn, 2006). This flow enhancement downstream of the object was identified to cause enhanced sediment movement of mixed sediment downstream of the object/wreck. Modelling work (using the coupled numerical model) conducted

around the SS *Apapa* site showed that the enhanced hydrodynamics downstream of the wreck produced a 44% wider and up to 11% shorter scour mark (within 20 full tidal cycles) in the case of the bed consisting of 22% gravel and 78% sand when compared with the observed offshore scour mark. In contrast, in the case of the bed consisting of 78% gravel and 22% sand, the scour mark produced (within 20 full tidal cycles) was 10% longer but 23% less wide when compared with the observed offshore scour mark. In the case of the bed consisting of pure sand, the bed was both less wide (69%) and shorter (38%) when compared to the observed offshore scour mark. In the case of the laboratory experiments, the scour mark's lateral extent and depth provided information about the impact of the enhanced flow dynamics downstream of the object to the sediment movement of mixed beds. In the laboratory experiments, the impact of the amplified flow was also investigated through the ripple characteristics downstream of the object. In the experiments conducted at low flow speed, the ripples formed downstream were 27.1% higher at the mixture containing 15% gravel but 23.1% less long at the mixture containing 12.5% gravel when compared to the ripples formed upstream of the object. Higher variations of ripple characteristics were observed at the mixtures containing 7.5% to 15% gravel. For the experiments conducted at high current speed, the ripples downstream were between 15% and 20.8% higher for the experiments conducted with gravel percentage between 7.5% and 12.5% when compared to the ripples formed upstream of the object.

### **How does the mixed sediment composition impact scour evolution at different levels of grain entrainment?**

In mixed sediments, each fraction of the sediment mixture acts uniquely to sediment movement, because of the hiding-exposure effect. Larger grains are more exposed to the flow and therefore require less shear stress to mobilise (up to 75%), where smaller grains, are hidden, and therefore more protected, requiring higher (up to 64%) values of shear stress to mobilise (McCarron et al., 2019). In the case of SS *Apapa*, sediment expected to be immobile when using the Soulsby (1997) formulae appeared to be more mobile than finer sediment, expected to be mobile. Areas with sediment expected to be immobile appeared to be having variations in the standard deviations of bathymetry over the years. The mean depth difference at the sampled locations over the years, showed that areas with sediment expected to be immobile (both fractions) had variations only 10% less than areas where the finer fraction of the mixed sediment was expected to be mobile. These results show the significance of the HE and the fact that a single statistical value of grain distribution (i.e.,  $d_{50}$ ) cannot be representative of the whole mixture.

### **For which bimodal non-cohesive sediment mixture will the scour be the greatest (in terms of depth and extent)?**

Physical modelling through laboratory experiments showed that at flow speed mobilising only the sand (finer) fraction of the mixes (sand and gravel), the longest, widest, and deepest scour mark was observed when the bed consisted of 20% gravel. When compared to the experiments conducted

with the bed consisting of pure sand, the mean scour was 66.4% longer, 12.05% wider and 4.8% deeper. The results of the laboratory experiments at this mixture, have however also shown absence of bedforms in the immediate downstream environment of the object, with a more pronounced scour mark. In the case of experiments conducted at flow speeds mobilising both fractions, the longest scour mark was observed at the mixture consisting of 12.5% gravel, with a difference of 43.6% when compared to pure sand. The widest scour was observed at the experiments with the sediment mixture containing 5% gravel and was 40.9% wider than pure sand. Finally, the deepest scour mark was observed at the experiments conducted using the sediment mixture of 20% gravel, with the mean scour being 13% deeper than the pure sand case.

### **Using more appropriate statistics of particle size distribution of mixed beds, which of those parameters will allow for the spatial extent of scour formation to be best predicted?**

The present study has shown that using a single statistical value for grain size distribution (i.e.,  $d_{50}$ ) is not ideal in the case of mixed sediment, as a single value cannot be representative of the whole mixture. For the present study, each fraction's  $d_{50}$  was used instead, and the numerical modelling work allowed the thorough mixing of the two fractions at certain percentages within the 'sedimentary bed'. The coupled numerical model predicted well the scour development around objects for 93% of the work. The numerical model appears to lack in the accurate prediction of the scour mark for the case of the laboratory experiments at high current speed, with the bed consisting of less than 10% gravel. It is however important to mention that in these cases, 3-D bedforms were developed during the laboratory experiments. Also, implementation of the HE correction (McCarron et al., 2019) has increased the ability of the model to predict sediment mobilisation of coarse bimodal sediment. Due to higher volumes of coarser sediment transported with bedload transport, finer sediment is potentially exposed at the bed surface and can easily be mobilised by suspended load, especially at higher flow speeds (during ebbing and flooding). A mixed bed does not remain mixed at the same proportion after the scour formation processes (or during bedform development). Subsequently, there is an interactive change of the bed composition, and the scour formation processes that makes the relation between the two difficult to investigate fully.

### **6.3 Summary of implications of this work**

The present study has identified variations of the seabed dynamics (scour, depositional feature and bedform migration) downstream of differently shaped submerged objects. These variations are results of the incoming flow interaction with the object and enhanced forces (flow speed ~2.3 times higher) and generated turbulence downstream of the object. The study has also quantified the scour extent expected at several sediment mixtures and also identified the sediment mixtures that maximum sediment mobilisation is expected. Understanding these parameters can increase the

potential of differently shaped objects to be placed on the seabed. This understanding can also aid in increasing the density of assets on the seabed, without increasing the costs for scour mitigation. Implementation of the knowledge gained from the present study can also aid increasing the areas where seabed development can be achieved, due to the enhanced knowledge of the mixed sediment response to the enhanced flow downstream of the objects. Knowledge gained by the work conducted on the exposure of the object to the flow, showed that objects sitting on the beds do not necessarily be fully submerged or protected using other methods. Identification of the ideal burial of a structure and implementation of a numerical model like the one used for the present study can reduce the costs involved for scour protection and subsequently the installation costs significantly. Finally, the analyses from different modelling around the *SS Apapa* site, along with the information provided after the wreck's disintegration, can aid preservation of wrecks of similar age.

#### **6.4 Recommendations for future research into flow and bed dynamics in complex seabeds**

The increased need for seabed infrastructure to achieve the UN goal for net-zero emissions by 2050 increases the need for more research to be conducted in the presented field. Further investigation of scour development around seabed infrastructure can significantly contribute to cost reduction in offshore energy production. Scour impacts on many aspects of infrastructure such as installability, maintainability, manufacturability, and survivability (IEA – OES, 2021). The real-world and lab-based studies in this thesis demonstrated the significance of bed composition and the object's shape to the scour formation. The disintegration of the wreck and enhanced exposure of the object in the laboratory experiments proved that even a slight change to the object's shape can cause significant changes in the downstream bed dynamics. However, there is a need for more surveys around wrecks sitting in different environments to further enhance the outcomes of this current thesis, and to ensure that *SS Apapa* and its environment is not an isolated case. Shipwrecks around the Isle of Anglesey and the Irish Sea in general have been studied in detail through the U-Boat project (<https://uboatproject.wales/>) and information is available for several of them. One example is the wreck of *SS Cambank*, that sits NW of the Isle of Anglesey (Figure 6.1).

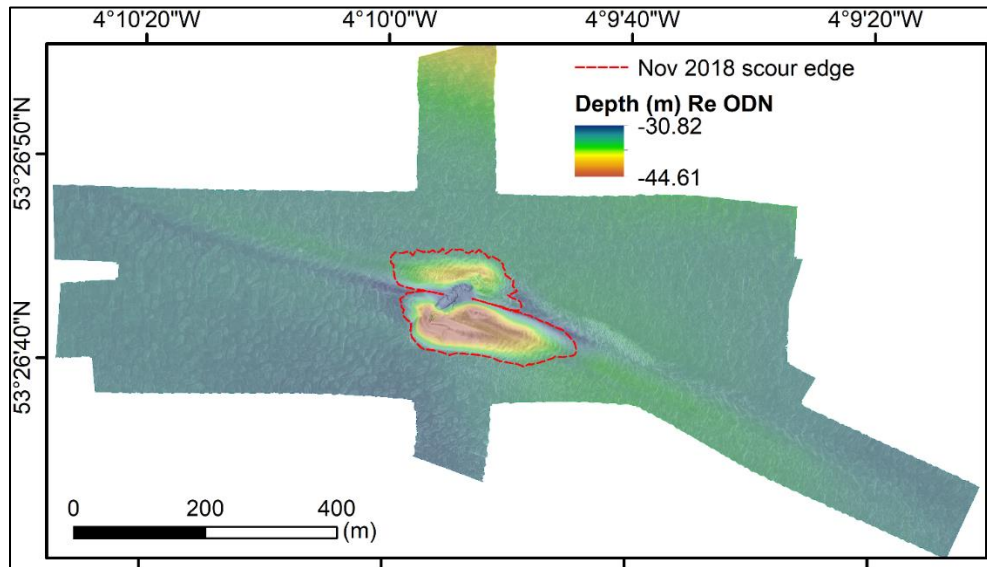


Figure 6.1: Digital elevation model (DEM) of the site around the wreck of *SS Cambank* with the depths (re ODN) as observed on November 11th, 2018.

Data about bathymetric and bed composition changes around *SS Cambank* using MBES have been collected for several years and is another site that could be monitored. *SS Cambank* sits at an angle to the flow similar to *SS Apapa* but the site has lower flow velocities of tidal currents, where the sediment composition at the area consists of finer mixed sediment (sand and gravel). Wrecks at similar angles and flow speeds, but with different sediment composition to the two wrecks can be found and be investigated in detail to enhance the knowledge of the parameters involved in both the sediment transport and the hydrodynamics, along with the actual detailed dependance of the scour formation and the object's shape. The laboratory experiments presented in the current study were focused on only one size of sand and gravel, with a 1:10 ratio, requiring further experiments at differently sized fractions (and ratios), to ensure that the observations are not isolated cases.

The numerical modelling work conducted using the coupled TELEMAC3D – GAIA model has provided a significant tool that can be used for the prediction of scour formation and development around objects sitting on mixed coarse beds. Further research can be conducted by placing a cylinder (of similar size to the wreck) instead of *SS Apapa* in the computation domain of the offshore case and/or a scaled down version of *SS Apapa* (of similar size to the cylinder) in the computation domain of the laboratory case. This could aid understanding and quantification of the object's shape influence to the flow, the subsequent forces acting on the bed and the erosion and deposition rates. The coupled model used in the present study can be further developed to include bedform formation. This would aid understanding of the object's interaction with bedforms (and their migration rates) and detail the actual object's influence on the flow and the downstream sedimentary bed. Bedforms can be considered as part of the scour process (Whitehouse, 1998; Quinn, 2006) and information about their formation due to the enhanced forces can assist seabed management at offshore development sites. Running the model with and without the bedform formation component, can aid understanding of bedform development due to the background flow and due to the disturbed (and



enhanced from the object) flows. A study by Goll (2016) used a similar coupled numerical model (TELEMAC3D – SISYPHE) and has included corrections for bedform formation and migration. Inclusion of the corrections suggested in the aforementioned study were not able to be included in this study, due to time restrictions. Although scour is mostly influenced by the suspended load, inclusion of the bedform migration along with the enhanced bedload transport caused by the bedform migration can amend the flow regimes and provide better understanding of the interaction between bedload transport and suspended load transport. As explained, the HE effect influences the sediment movement of coarse bimodal sediment, and therefore sediment mobilisation (via bedload transport) of sediment expected to be immobile. This mobilisation of coarser sediment can possibly alter the forces and cause increased sediment transport of the finer fraction of the sediment mixture via suspended load. Also, the inclusion of the HE effect can be further analysed using the same methodology at similar sand-gravel mixtures but extending as far as practically possible in terms of grain sizes, to ensure the wider applicability of the HE inclusion in the calculation of the bed shear stress as used in the present work. Test cases of wrecks sitting at different sand-gravel mixtures can be taken from areas in the North Sea, where glacial tills existed.

The present study has shown that a sediment mixture does not always remain mixed with the same fractions of sediments. Therefore, the HE effect for the fractions of sediments should be possibly updated with new fractions for different areas of the computation domain after each time step of computation.

Finally, the analyses and results of the present study along with the numerical model can be used to parametrise larger scaled models that can predict sediment transport and hydrodynamic processes around large sites with arrays of assets placed on the seabed (i.e., offshore windfarm foundations).

## 7 References

- Abd El-Hady Rady, R. (2020). Prediction of local scour around bridge piers: artificial-intelligence-based modelling versus conventional regression methods. *Applied Water Science*, 10 (2). <https://doi.org/10.1007/s13201-020-1140-4>.
- Ahmad, N., Bihs, H., Myrhaug, D., Kamath, A., & Arntsen, Ø. A. (2018). Three-dimensional numerical modelling of wave-induced scour around piles in a side-by-side arrangement. *Coastal Engineering* 138, 132–151. <https://doi.org/10.1016/j.coastaleng.2018.04.016>.
- Allen, J. (1984). *Sedimentary Structures; Their Character and Physical Basis*. Elsevier
- Amoudry, L. O., & Souza, A. J. (2011). Deterministic coastal morphological and sediment transport modelling: A review and discussion. *Reviews of Geophysics*, 49 (2). <https://doi.org/10.1029/2010RG000341>.
- Amoudry, L., Bell, P. S., Black, K. S., Gatliff, R. W., Helsby, R., Souza, A. J., ... Wolf, J. (2009). A Scoping Study on Research into Changes in Sediment Dynamics Linked to Marine Renewable Energy Installations. Building.
- Ashida, K. and Michiue, M. (1972). Study on hydraulic resistance and bed-load transport rate in alluvial streams. *Proceedings of the Japan Society of Civil Engineers*, 59–69.
- Astley A. J., Dix, J. K., Thompson, C., Sturt, F. (2014). A seventeen year, nearannual, bathymetric time-series of a marine structure (SS Richard Montgomery). In: Cheng, L., Draper, S. and An, H. (Eds.), *Scour and Erosion: Proceedings of the 7th International Conference on Scour and Erosion*. Taylor & Francis, pp. 715–724.
- Astley, A.J. (2016). *The Taphonomy of Historic Shipwreck Sites*. PhD Thesis, University of Southampton.
- Audouin, Y., Benson, T., Delinares, M., Fontaine, J., Glander, B., Huybrechts, N., Kopmann, R., Leroy, A., Pavan, S., Pham, C.T., Taccone, F., Tassi, P., Walther, R. (2019). Introducing GAIA, the brand-new sediment transport module of the TELEMAC-MASCARET System. TELEMAC User Club: Toulouse.
- Augustesen, A. H., Brødbæk, K. T., Møller, M., Sørensen, S. P. H., Ibsen, L. B., Pedersen, T. S., & Andersen, L. (2009). Numerical Modelling of Large-Diameter Steel Piles at Horns Rev. In B. H. V. Topping, L. F. C. Neves, & R. C. Barros (Eds.), *Proceedings of the Twelfth International Conference on Civil, Structural and Environmental Engineering Computing Civil-Comp Press*. Civil-Comp Proceedings No. 91.
- Baas, J. H. (1993). *Dimensional Analysis of Current Ripples in Recent and Ancient Depositional Environments*. PhD thesis. University of Utrecht, The Netherlands.
- Baas, J. H. (1994). A flume study on the development and equilibrium morphology of current ripples in very fine sand. *Sedimentology*, 41 (2), 185–209. <https://doi.org/10.1111/j.1365-3091.1994.tb01400.x>.

- Baas, J. H. (Feb. 1999). An empirical model for the development and equilibrium morphology of current ripples in fine sand. *Sedimentology* 46, 123–138.
- Baas, J. H., Best, J. L. and Peakall, J. (2011). Depositional processes, bedform development and hybrid bed formation in rapidly decelerated cohesive (mud-sand) sediment flows. *Sedimentology* 58, 1953–1987.
- Baas, J. H., Van Dam, R. L. and Storms, J. E. (2000). Duration of deposition from decelerating high-density turbidity currents. *Sedimentary Geology* 136, 71–88.
- Bahaj, A. S. (2011). Generating electricity from the oceans. *Renewable and Sustainable Energy Reviews*. Elsevier Ltd. <https://doi.org/10.1016/j.rser.2011.04.032>.
- Baker, C. J. (1979). Vortex flow around the bases of obstacles (Doctoral thesis). <https://doi.org/10.17863/CAM.14045>.
- Ball, D.J., Stansby, P.K., and Alliston, N. (1996). Modelling shallow water flow around pile groups, *Proc., Instn. Civ. Engrs. Wat., Marit & Energy* 118, 226-236.
- BBC News. (2015). The bombs that lurk off the UK coast. URL <http://www.bbc.com/future/story/20151027-the-ticking-time-bomb-of-the-thames>. [Online] (Accessed 25 Nov 2020).
- BBC News. (2018). Microsoft sinks data centre off Orkney. [online] URL: <https://www.bbc.co.uk/news/technology-44368813> [Online] (Accessed 15 Dec. 2018).
- Benson, T., Villaret, C., Kelly, D. M. and Baugh J. (2014). Improvements in 3D sediment transport modelling with application to water quality issues. In: Betrand, O. and Coulet, C. (Eds.), *Proceedings of the 21<sup>st</sup> TELEMAC – MASCARET User Conference*. Artelia Eau & Environment, pp. 235-242.
- Bentley M., and Smith S. (2008). Scenario-based Reservoir Modelling: The Need for More Determinism and Less Anchoring. In: *The Future of Geological Modelling in Hydrocarbon Development*. Robinson, A., Griffiths, P., Price, S., Hegre, J., and Muggeridge, A. (Eds.), Geological Society, London, Special Publications 309, pp. 145–159. doi:10.1144/sp309.11.
- Berlamont, J., Ockenden, M., Toorman, E., & Winterwerp, J. (1993). The characterisation of cohesive sediment properties. *Coastal Engineering*, 21 (1–3), 105–128. [https://doi.org/10.1016/0378-3839\(93\)90047-C](https://doi.org/10.1016/0378-3839(93)90047-C).
- Blott, S. J. and Pye, K. (Oct. 2001). GRADISTAT: a grain size distribution and statistics package for the analysis of unconsolidated sediments. *Earth Surface Processes and Landforms* 26, 1237–1248.
- Bourillet, J-F., Edy, C., Rambert, F., Satra, C., Loubrieu, B. (1996) Swath mapping system processing: bathymetry and cartography. *Mar Geophys Res* 18, 487–506.
- Brown, C. J., & Blondel, P. (2009). The application of underwater acoustics to seabed habitat mapping (Guest editorial). *Applied Acoustics*, 70 (10), 1241-1241. <https://doi.org/10.1016/j.apacoust.2008.09.006>.

- Brown, C. J., Samento, J. A., Smith, S. J. (2012). Multiple methods, maps, and management applications: purpose made seafloor maps in support of ocean management. *Journal of Sea Research* 72, 1–13. doi:10.1016/j.seares.2012.04.009.
- Brown, C.J., Beaudoin, J., Brissette, M., Gazzola, V. (2017). Setting the Stage for Multispectral Acoustic Backscatter Research. In *Proceedings of the United States Hydrographic Conference*, Galveston, TX, USA.
- Brown, C.J., Smith, S.J., Lawton, P., Anderson, J.T. (2011). Benthic habitat mapping: a review of progress towards improved understanding of the spatial ecology of the seafloor using acoustic techniques. *Estuarine, Coastal and Shelf Science* 92, 502–520.
- Callaway, A., Smyth, J., Brown, C. J., Quinn, R., Service, M., & Long, D. (2009). The impact of scour processes on a smothered reef system in the Irish Sea. *Estuarine, Coastal and Shelf Science*, 84 (3), 409–418. <https://doi.org/10.1016/j.ecss.2009.07.011>.
- Cant, S. (2013). *England's Shipwreck Heritage: From Logboats to U-boats*. Swindon: English Heritage.
- Carling, P. A. (1999). Subaqueous gravel dunes. *Journal of Sedimentary Research*, 69 (3), 534–545. <https://doi.org/10.2110/jsr.69.534>.
- Caston, G. F. (1979). Wreck marks: indicators of net sand transport, *Marine Geology* 33, 193–204.
- CEFAS. (2006). *Scroby Sands Offshore Wind Farm – Coastal Processes Monitoring. Final Report AEO262 prepared for Marine Environment Division, Defra and Department of Trade and Industry*, p. 51.
- Chang, H. H. (1988). *Fluvial Processes in River Engineering*. John Wiley & Sons.
- Chen, L., & Lam, W. H. (2014). Methods for predicting seabed scour around marine current turbine. *Renewable and Sustainable Energy Reviews*. <https://doi.org/10.1016/j.rser.2013.08.105>.
- Chiew, Y. M. & Melville, B. W. (1987). Local scour around bridge piers, *Journal of Hydraulic Research* 25 (1), 15–26, DOI: 10.1080/00221688709499285.
- Chiew, Y. M. (1991). Prediction of maximum scour depth at submarine pipelines. *Journal of Hydraulic Engineering*, 117(4), 452–466.
- Chiew, Y.M. (1984). Local scour at bridge piers, Report No. 355, School of Engineering, The University of Auckland, Auckland, New Zealand, pp.200.
- Chollet, J. P. and Cunge, J. A. (Jan. 1979). New interpretation of some head loss-flow velocity relationships for deformable movable beds. *Journal of Hydraulic Research* 17, 1–13.
- Chotiros, N. P. (2006). Seafloor acoustic backscattering strength and properties from published data, *OCEANS – Asia Pacific*, pp. 1–6, doi: 10.1109/OCEANSAP.2006.4393905.
- Church, R. A. (2014). Deep-Water Shipwreck Initial Site Formation: The Equation of Site Distribution. *Journal of Maritime Archaeology*, 9 (1), pp. 27–40.
- Clarke G. K. C. (2005). Subglacial processes. *Annual Review Earth Planet Science letters* 33, 247– 276.

- Couldrey, A. J., Benson, T., Knaapen, M. A. F., Marten, K. V., Whitehouse, R. J. S. (2020). Morphological evolution of a barchan dune migrating past an offshore wind farm foundation. *Earth Surf. Processes Landforms*, 45(12), 2884-96.
- Crown Estate. (2019). Welsh National Marine Plan. [https://gov.wales/sites/default/files/publications/2019-11/welsh-national-marine-plan\\_5.pdf](https://gov.wales/sites/default/files/publications/2019-11/welsh-national-marine-plan_5.pdf). p. 16
- Dargahi, B. (1982): Local scour at bridge piers - A review of theory and practice, Bulletin No. TRITA-VBI-114, Hydraulics Laboratory, Royal Institute of Technology, Stockholm, Sweden
- de Moustier, C. (1986). Beyond bathymetry: mapping acoustic backscattering from the deep seafloor with Sea Beam. *Journal of the Acoustical Society of America* 79 (2), 316–331.
- Dietrich, W. E., Kirchner, J. W., Ikeda, H., & Iseya, F. (1989). Sediment supply and the development of the coarse surface layer in gravel-bedded rivers. *Nature*, 340 (6230), 215–217. <https://doi.org/10.1038/340215a0>.
- Edina Digimap. (2011). DiGSBS250K [SHAPE geospatial data], Scale 1:250000, Tiles: GB, Updated: 6 September 2011, BGS, Using: EDINA Geology Digimap Service, <<http://digimap.edina.ac.uk>>, Downloaded: 2018-07-18 12:20:43.613
- Egiazaroff, I. V. (1965). Calculations of Non-uniform Sediment Concentrations. *Journal of the Hydraulics Division, ASCE* 91, 225-247.
- Engelund, F. and Hansen, E. (1967). A monograph on sediment transport in alluvial streams. Technical report. Copenhagen. Teknisk Forlag, 65.
- Ettema, R. (1980). Scour at bridge piers. Report No. 216, School of Engineering, The University of Auckland, Auckland, New Zealand, pp. 527.
- European Commission (2020). Communication from the commission to the European parliament, the council, the European economic and social committee of the regions. An EU Strategy to harness the potential of offshore renewable energy for a climate neutral future, {SWD (2020) 273 final}.
- Fernández-Montblanc, T., Quinn, R., Izquierdo, A., Bethencourt, M. (2016). Evolution of a shallow water wave-dominated shipwreck site: Fougueux (1805), Gulf of Cadiz. *Geoarchaeology* 31 (6), 487–505. <https://doi.org/10.1002/gea.21565>.
- Fernández-Montblanc, T., Izquierdo, A., Quinn, R., & Bethencourt, M. (2018). Waves and wrecks: A computational fluid dynamic study in an underwater archaeological site. *Ocean Engineering*, 163, 232-250.
- Ferrini, V. L., & Flood, R. D. (2006). The effects of fine-scale surface roughness and grain size on 300 kHz multibeam backscatter intensity in sandy marine sedimentary environments. *Marine Geology*, 228(1–4), 153–172. <https://doi.org/10.1016/j.margeo.2005.11.010>.
- Firth, A. (2020). HMS Falmouth: addressing the significance of a light cruiser lost in the First World War off the coast of Yorkshire. *International Journal of Nautical Archaeology*, 49(1), 142–154. <https://doi.org/10.1111/1095-9270.12392>.



- Folk, R. and Ward, W. (1957). Brazos River bar: a study in the significance of grain size parameters. *Journal of Sedimentary Petrology* 1,3-26.
- Gaida, T. C., Ali, T. A. T., Snellen, M., Amiri-Simkooei, A., van Dijk, T. A. G. P., & Simons, D. G. (2018). A multispectral Bayesian classification method for increased acoustic discrimination of seabed sediments using multi-frequency multibeam backscatter data. *Geosciences* (Switzerland), 8(12). <https://doi.org/10.3390/geosciences8120455>.
- Garlan, T., Marches, E. and Brenon, E. (2015). A classification of scouring marks in macrotidal environments from analysis of long-term wreck marks. doi: 10.1142/9789814689977\_0202.
- Goff, J.A., Kraft, B.J., Mayer, L.A., Schock, S.G., Sommerfield, C.K., Olson, H.C., Gulick, S.P.S., Nordfjord, S. (2004). Seabed characterization on the New Jersey middle and outer shelf: correlatability and spatial variability of seafloor sediment properties. *Marine Geology* 209, 147–172.
- Goll, A. (2016). 3D Numerical modelling of dune formation and dynamics in inland waterways. *Mechanics of the fluids* [physics.class-ph]. Université Paris-Est. English <NNT:2016PESC1119>.
- Gribble, J. (2019). Seabed mobility around a submerged horizontal cylinder in mixtures of sand and gravel, MSc Thesis.
- Griffiths, C., Davies, I.L. and Reynolds, K. (2017). MEng Team Project: Automated Carriage System, MEng Thesis, page 157.
- Guerra, M., Cienfuegos, R., Thomson, J. and Suarez, L. (2017). Tidal energy resource characterization in Chacao channel, Chile. *International Journal of Marine Energy*, 20, 1-16. URL <https://doi.org/10.1016/j.ijome.2017.11.002>.
- Harris, J. M. and Whitehouse, R. J. S. (2014). Marine scour: Lessons from Nature's laboratory. *Scour and Erosion - Proceedings of the 7th International Conference on Scour and Erosion, ICSE 2014*. 10.1201/b17703-4.
- Harris, J. M., Whitehouse, R. and Benson, T. (2010). The time evolution of scour around offshore structures: The scour time evolution predictor (STEP) model. *Proceedings of ICE-Maritime Engineering* 163, 3-17.
- Harris, J. M., Whitehouse, R. J. S. (2014). Advanced numerical modelling of scour and erosion. In *Scour and Erosion*, pp. 315–462. CRC Press. <https://doi.org/10.1201/b17703-4>.
- Hatipoglu, F., & Avci, I. (2002). Flow around a partly buried cylinder in a steady current. *Ocean Engineering*, 30 (2), 239–249. [https://doi.org/10.1016/S0029-8018\(02\)00018-5](https://doi.org/10.1016/S0029-8018(02)00018-5).
- Hay, A. E., Speller, R. (2005). Naturally occurring scour pits in nearshore sands. *Journal of Geophysical Research. Earth Surf.* 110, 1–15. <https://doi.org/10.1029/2004JF000199>.
- Hebsgaard, M., Ennemark, F., Spangenberg, S., Fredsøe, J. and Gravesen H. (1994). Scour Model tests with bridge piers. *PIANC bulletin*, 82, 84-92.
- Hefner, B. T.; Jackson, D. R.; Ivakin, A. M., Tang, D. (2010). High frequency measurements of backscattering from heterogeneities and discrete scatters in sand sediments. In *Proceedings of*

the Tenth European Conference on Underwater Acoustics (ECUA2010), Istanbul, Turkey, 5–9 July 2010; Volume 3, pp. 1386–1390.

Heldtberg, M., Macleod, I. D., & Richards, V. L. (2004). Corrosion and cathodic protection of iron in seawater: a case study of the James Matthews (1841). *Metal* 2004, (October), 75–87.

Hocking, C. (2019). Sediment transport in sand and gravel mixtures: the seabed dynamic layer. MSc Thesis, page 21.

Holmes, M. H., & Garcia, M. H. (2008). Flow over bedforms in a large sand-bed river: A field investigation. *Journal of Hydraulic Research*, 46(3), 322–333. <https://doi.org/10.3826/jhr.2008.3040>.

Hughes-Clarke, J.E., Danforth, B.W., Valentine, P. (1997). Areal seabed classification using backscatter angular response at 95 kHz. In: *High Frequency Acoustics in Shallow Water*. NATO SACLANT Undersea Research Centre, Lerici, Italy.

IEA - OES (2021), Annual Report, An Overview of Ocean Energy Activities in 2020.

Image Analyst (2021). Thresholding an image (<https://www.mathworks.com/matlabcentral/fileexchange/29372-thresholding-an-image>), MATLAB Central File Exchange. Retrieved January 28, 2021.

Inman, D. L., Jenkins, S. A. (2005). Scour and burial objects in shallow water. In: Schwartz, M. (Ed.). *Encyclopaedia of coastal science*. Dordrecht: Springer Verlag, pp. 825-830.

Innangi, S., Barra, M., Di Martino, G., Parnum, I. M., Tonielli, R. and Mazzola, S. (2015). Reson SeaBat 8125 backscatter data as a tool for seabed characterization (Central Mediterranean, Southern Italy): Results from different processing approaches. *Applied Acoustics*, 87, 109–122. <https://doi.org/10.1016/j.apacoust.2014.06.014>.

Jackson D. R., Richardson, M. (2007). *High frequency seafloor acoustic*. Springer, New York.

Jannsen, S. R. (2010). A part of transport – Testing sediment transport models under partial transport conditions. MA Thesis, University of Twente.

Kallehave, D., Byrne B. W., LeBlanc-Thilsted, C., Mikkelsen, K. K. (2015). Optimization of monopiles for offshore wind turbines. *Phil. Trans. R. Soc. A373*: 20140100. <http://dx.doi.org/10.1098/rsta.2014.0100>.

Kleinhans, M., Wilbers, A. W. E., De Swaaf, A. and Van Den Berg, J. H. (2002). Sediment Supply-Limited Bedforms in Sand-Gravel Bed Rivers. *Journal of Sedimentary Research* 72, 629-640.

Kuhnle, R. A., Horton, J. K., Bennetts, S. J., & Best, J. L. (2006). Bed forms in bimodal sand-gravel sediments: Laboratory and field analysis. *Sedimentology*, 53 (3), 631–654. <https://doi.org/10.1111/j.1365-3091.2005.00765.x>.

Lacal-Arántegui, R., Yusta, J. M., & Domínguez-Navarro, J. A. (2018). Offshore wind installation: Analysing the evidence behind improvements in installation time. *Renewable and Sustainable Energy Reviews*. Elsevier Ltd. <https://doi.org/10.1016/j.rser.2018.04.044>.

- Lamarche, G., & Lurton, X. (2018). Recommendations for improved and coherent acquisition and processing of backscatter data from seafloor-mapping sonars. *Marine Geophysical Research*, 39 (1–2), 5–22. <https://doi.org/10.1007/s11001-017-9315-6>.
- Lamarche, G., Lurton, X., Verdier, A. L., & Augustin, J. M. (2011). Quantitative characterisation of seafloor substrate and bedforms using advanced processing of multibeam backscatter-Application to Cook Strait, New Zealand. *Continental Shelf Research*, 31 (2 SUPPL.). <https://doi.org/10.1016/j.csr.2010.06.001>.
- Lambkin, D., Dix, J. and Turnock, S. (2006). Flow patterning associated with three- dimensional obstacles: a proxy for scour. In: *Proceedings of the Third International Conference on Scour and Erosion*. Gouda, The Netherlands: CURNET, pp. 162–170.
- Le Roux, J. (2004). An integrated law of the wall for hydrodynamically transitional flow over plane beds. *Sedimentary Geology* 163, 311-321.
- Leroy, A. (2019). TELEMAC-3D Theory guide.
- Lichtman, I. D., Baas, J. H., Amoudry, L. O., Thorne, P. D., Malarkey, J., Hope, J. A., Ye, L. (2018). Bedform migration in a mixed sand and cohesive clay intertidal environment and implications for bed material transport predictions. *Geomorphology* 315, 17–32. <https://doi.org/10.1016/j.geomorph.2018.04.016>.
- López, A., Stickland, M. T. and Dempster, W. (2018). CFD study of fluid flow changes with erosion. *Computer Physics Communications*, 227. pp. 27-41. ISSN 0010-4655.
- Lurton, X. (2010) *An introduction to underwater acoustics—principles and applications*, 2nd edn. Springer-Verlag, Berlin. p 680.
- Lurton, X., Lamarche, G. (2015). Backscatter measurements by seafloor mapping sonars: guidelines and recommendations. <http://geohab.org/wp-content/uploads/2013/02/BWSG-REPORT-MAY2015.pdf>.
- Ma, Z., Wu, Z., Li, T., Han, Y., Chen, J. and Zhang, L. (Aug. 2009). A Simplified Computational Model for the Location of Depth Averaged Velocity in a Rectangular Irrigation Channel. *Applied Sciences* 9, 3222.
- MacLeod, I. D. (1993). Metal corrosion on shipwrecks – Australian case studies. *Trends in Corrosion Research* 1, pp. 221-245.
- Macleod, I. D. (2006). Corrosion and conservation management of iron shipwrecks in Chuuk Lagoon, Federated States of Micronesia. *Conservation and Management of Archaeological Sites*, 7 (4), 203–223. <https://doi.org/10.1179/135050306793137359>.
- MacLeod, I. D. (2016). In-situ corrosion measurements of WWII shipwrecks in Chuuk Lagoon, quantification of decay mechanisms and rates of deterioration. *Frontiers in Marine Science*, 3(MAR). <https://doi.org/10.3389/fmars.2016.00038>.
- Majcher, J., Plets, R., Quinn, R. (2020). Residual relief modelling: digital elevation enhancement for shipwreck site characterisation. *Archaeol. Anthropol. Sci.* 12 <https://doi.org/10.1007/s12520-020-01082-6>.

- Majcher, J., Quinn, R., Plets, R., Coughlan, M., McGonigle, C., Sacchetti, F., Westley, K. (2021). Spatial and temporal variability in geomorphic change at tidally influenced shipwreck sites: the use of time-lapse multibeam data for the assessment of site formation processes. *Geoarchaeology* 36, 429–454. <https://doi.org/10.1002/gea.21840>.
- Majcher, J., Quinn, R., Smyth, T., Plets, R., McGonigle, C., Westley, K., Sacchetti, F., Coughlan, M. (2022). Using difference modelling and computational fluid dynamics to investigate the evolution of complex, tidally influenced shipwreck sites. *Ocean Engineering* 246. <https://doi.org/10.1016/j.oceaneng.2022.110625>.
- Mantovanelli, A., Ridd, P. V. (2006). Devices to measure settling velocities of cohesive sediment aggregates. A review of the in-situ technology. *Journal of Sea research* 56, pp. 199-226.
- McArthur, M.A., Brooke, B.P., Przeslawski, R., Ryan, D. A., Lucieer, V. L., Nichols, S., McCallum, A. W., Mellin, C., Cresswell, I.D. and Radke, L. C. (2010). On the use of abiotic surrogates to describe marine benthic biodiversity. *Estuarine, Coastal and Shelf Science*, 88, 21-32.
- McCarron, C. J. (2020). Bedload Transport of Sand-Gravel Mixtures in Coastal and Shelf-Sea Environments. PhD Thesis, Bangor University.
- McCarron, C. J., Van Landeghem, K. J. J., Baas, J. H., Amoudry, L. O., Malarkey, J. (2019). The hiding-exposure effect revisited: a method to calculate the mobility of bimodal sediment mixtures. *Mar. Geol.* 410, 22–31. <https://doi.org/10.1016/j.margeo.2018.12.001>.
- Melling, G.J. (2014). Hydrodynamic and Geotechnical Controls of Scour Around Offshore Monopiles. PhD Thesis, University of Southampton.
- Melville, B. (2008). The physics of local scour at bridge piers. *Proceedings of the 4th International Conference on Scour and Erosion*, (1), 28–40.
- Melville, B., Chiew, Y., M. (1999). Time scale for local scour at bridge piers. *Journal of Hydraulic Engineering* 125, 59-65. [10.1061/\(ASCE\)0733-9429\(1999\)125:1\(59\)](https://doi.org/10.1061/(ASCE)0733-9429(1999)125:1(59)).
- Mercier, P., Thiébaud, M., Guillou, S., Maisondieu, C., Poizot, E., Pieterse, A., ... Grondeau, M. (2021). Turbulence measurements: An assessment of Acoustic Doppler Current Profiler accuracy in rough environment. *Ocean Engineering*, 226. <https://doi.org/10.1016/j.oceaneng.2021.108819>
- Meyer-Peter, E. and Müller, R. (1948). Formulas for Bed-Load Transport. *Proceedings of the 2<sup>nd</sup> Meeting of the International Association of Hydraulic Structures Research*, 39-64.
- Min, B., Kim, H., & Ryoo, H. (2018). Scour depth around multiple piles for current and wave. *Vibroengineering Procedia*.
- Monteys, X., Scott, G., Hardy, D. (2013). Case Study 3: Seabed characterisation in shallow waters using multibeam backscatter data, in: Glaves, H., Miles, P. (eds.), *Standardisation and harmonisation in seabed habitat mapping: role and added value of geological data and information. Part A: Sediment characterisation*.
- Muckelroy, K. (1978). *Maritime archaeology*. Cambridge University Press, Cambridge.

- Natural Environment Research Council – NERC (2021). Ecological Consequences of Offshore Wind (ECOWind).
- Nelson, J. M., McLean, S. R., & Wolfe, S. R. (1993). Mean flow and turbulence fields over two-dimensional bed forms. *Water Resources Research*, 29 (12), 3935–3953. <https://doi.org/10.1029/93WR01932>.
- Nielsen, A. W., Hansen, E. A. (2007). Time-varying wave and current-induced scour around offshore wind turbines. In: ASME 2007 26th international conference on offshore mechanics arctic engineering, (OMAE 2007). San Diego, California, USA.
- National Oceanic and Atmospheric Administration (2021). URL <https://oceanservice.noaa.gov/facts/exploration.html> [Online] (Accessed 20 Dec 2021).
- O'Neil, S. (2002). Three-dimensional mobile bed dynamics for sediment transport modelling. *Civil Engineering*, Ph.D, 266.
- O'Shea, J. M. (2004). The identification of shipwreck site: a Bayesian approach. *Journal of Archaeological Science*, 31 (11), 1533-1552.
- Oh, K. Y., Nam, W., Ryu, M. S., Kim, J. Y., & Epureanu, B. I. (2018). A review of foundations of offshore wind energy convertors: Current status and future perspectives. *Renewable and Sustainable Energy Reviews*. Elsevier Ltd. <https://doi.org/10.1016/j.rser.2018.02.005>.
- Pandey, M., Zakwan, M., Khan, M. & Bhawe, S. (2020). Development of scour around a circular pier and its modelling using genetic algorithm. *Water Science & Technology Water Supply*. 20. 10.2166/ws.2020.244.
- Pope, N. D., Widdows, J., & Winsley, M. D. (2006) Estimation of bed shear stress using the turbulent kinetic energy approach - A comparison of annular flume and field data. *Continental Shelf Research*, 26, pp. 959– 970.
- Porter, K. E., (2016). Seabed scour around marine structures in mixed and layered sediments. EngD Thesis, UCL.
- Preston, J.M. (2009). Automated acoustic seabed classification of multi-beam images of Stanton Banks, *Applied Acoustics* 70, 1277-1287.
- Quinn, R. (2006). The role of scour in shipwreck site formation processes and the preservation of wreck-associated scour signatures in the sedimentary record - evidence from seabed and sub-surface data. *Journal of Archaeological Science*, 33 (10), 1419–1432. <https://doi.org/10.1016/j.jas.2006.01.011>.
- Quinn, R., & Boland, D. (2010). The role of time-lapse bathymetric surveys in assessing morphological change at shipwreck sites. *Journal of Archaeological Science*, 37 (11), 2938–2946. <https://doi.org/10.1016/j.jas.2010.07.005>.
- Quinn, R., & Smyth, T. A. G. (2018). Processes and patterns of flow, erosion, and deposition at shipwreck sites: a computational fluid dynamic simulation. *Archaeological and Anthropological Sciences*, 10 (6), 1429–1442. <https://doi.org/10.1007/s12520-017-0468-7>.



- Quinn, R., Saunders, R., Plets, R., Westley, K., Dix, J. (2016). Marine scour of cohesionless sediments. In Keith, M.E. (Ed.), *Site Formation Processes of Submerged Shipwrecks*. University Press of Florida, Gainesville, pp. 70-89.
- Rauen, W. B., Lin, B. and Falconer, R. A. (2009). Modelling ripple development under non-uniform flow and sediment supply-limited conditions in a laboratory flume. *Estuarine Coastal and Shelf Science* 82, 452-460.
- Roulund, A., Sumer, B. M., Fredsøe, J. and Michelsen, J. (2005). Numerical and experimental investigation of flow and scour around a circular pile. *Journal of Fluid Mechanics* 534, 351-401.
- Saunders, R. (2005). *Seabed Scour Emanating from Submerged Three-Dimensional Objects: Archaeological Case Studies*. PhD Thesis, University of Southampton.
- Schmitt, T., Mitchell, N. C. and Ramsay, A. T. S. (2008). Characterizing uncertainties for quantifying bathymetry change between time-separated multibeam echo-sounder surveys. *Continental Shelf Research*, 28 (9), pp. 1166-1176.
- Serhadlioglu S., Adcock, T. A. A., Houlsby, G. T., Draper, S. and Borthwick, A. G. L. (2013). Tidal Stream Energy resource assessment of the Anglesey Skerries. *International Journal of Marine Energy* 3-4, pp. 98-111.
- Shields, A. (1936). *Application of Similarity Principles and Turbulence Research to Bed-Load Movement*. PhD Thesis, Technical University of Berlin, page 47.
- Simpson, J. H., Wiles, P. J., & Lincoln, B. J. (2011). Internal seiche modes and bottom boundary-layer dissipation in a temperate lake from acoustic measurements. *Limnology and Oceanography*, 56 (5), 1893-1906. <https://doi.org/10.4319/lo.2011.56.5.1893>.
- Smith, H. D., Foster, D. L., Voropayev, S. I., Fernando, H. J. S. (2004). Modelling the turbulent processes around a 3-D cylinder, *Eos Trans. AGU* 85 (47) Fall Meeting Suppl. Abstract OS21B-1217.
- Smyth, T. A. G., Quinn, R. (2014). The role of computational fluid dynamics in understanding shipwreck site formation processes. *J. Archaeol. Sci.* 45, 220–225. <https://doi.org/10.1016/j.jas.2014.02.025>.
- Soulsby R. L., Whitehouse, R. J. S. and Marten, K. V. (2012). Prediction of time-evolving sand ripples in shelf seas. *Continental Shelf Research* 38, 47-62.
- Soulsby, R. L. (1997). *Dynamics of marine sands. A manual for practical applications*. Thomas Telford Ltd, London.
- Soulsby, R.L., Dyer, K.R. (1981). The form of the near-bed velocity profile in a tidally accelerating flow. *Journal of Geophysical Research—Oceans and Atmospheres* 86 (NC9), 8067–8074.
- Soulsby, R. L., and Whitehouse, R. J. S. (2005). *Prediction of Ripple Properties in Shelf Seas. Mark 2 Predictor for Time Evolution*. Technical report, Report TR 154. HR Wallingford.
- Stapleton, K.R., Huntley, D.A. (1995). Seabed stress determinations using the inertial dissipation method and the turbulent kinetic energy method. *Earth Surface Processes and Landforms* 20 (9), 807–815.

- Stephens, D., Diesing, M. (2015). Towards Quantitative Spatial Models of Seabed Sediment Composition, PLoS ONE 10 (11): e0142502. <https://doi.org/10.1371/journal.pone.0142502>.
- Sumer, B. M. (2007). Mathematical modelling of scour: A review. *Journal of Hydraulic Research* 45 (6), 723–735. <https://doi.org/10.1080/00221686.2007.9521811>.
- Sumer, B. M. (2007). Mathematical modelling of scour: A review. *J. Hydraulic Research* 45 (6), pp. 723-735.
- Sumer, B. M. and Fredsøe, J. (1991). Onset of scour below a pipeline exposed to waves. *International Journal of Offshore and Polar Engineering* 1, pp. 189-194.
- Sumer, B. M. and Fredsøe, J. (2002). The mechanics of Scour in the Marine Environment. *Advanced Series on Ocean Engineering* 17, World Scientific. <https://doi.org/10.1142/4942>.
- Sumer, B. M., Christiansen, N., Fredsøe, J. (1997) The horseshoe vortex and vortex shedding around a vertical wall-mounted cylinder exposed to waves. *J. Fluid Mech* 332, pp. 41–70.
- Sumer, B. M., Fredsøe, J. and Klavs B. (2005). Global And Local Scour At Pile Groups. Paper presented at the Fifteenth International Offshore and Polar Engineering Conference, Seoul, Korea.
- Sumer, B. M., Hatipoglu, F. and Fredsøe, J. (2007). Wave scour around a pile in sand, medium dense and dense silt. *Journal of Waterway, Port, Coastal and Ocean Engineering*, ASCE 133 (1), pp. 14-27.
- Sutherland, J., & Soulsby, R. L. (2011). Sediment dynamics. In Frostick, L.E., McLelland, S. J. and Mercer, T.G. (Eds.), *A User's Guide to Physical Modelling and Experimentation*, Chapter 4.
- Tassi, P., and Villaret, C. (2019). TELEMAC-3D User Manual.
- Teisson, C. (1991). Cohesive suspended sediment transport: feasibility and limitations of numerical modelling. *Journal of Hydraulic Research* 29 (6), pp. 755-769.
- Testik, F. Y., Voropayev, S.I. and Fernando, H. J. S. (2005). Flow around a short horizontal Bottom Cylinder Under Steady and Oscillatory Flows. *Physics of Fluids* 17, pp. 47-103.
- Thompson, C.E.L., Amos, C.L., et al., 2003. The manifestation of fluid-transmitted bed shear stress in a smooth annular flume—a comparison of methods. *Journal of Coastal Research* 19 (4), 1094–1103.
- Tomalin D. J., Simpson, P. and Bingeman, J. M. (2000). Excavation versus sustainability in-situ: a conclusion on 25 years of archaeological investigations at Goose Rock, a designated historic wreck-site at the Needles, Isle of Wight, England, *International Journal of Nautical Archaeology*, 29 (1), 3-42, DOI: 10.1111/j.1095-9270.2000.tb01380.x.
- Trembanis, A., Nebel, S., Skarke, A., Coleman, D. F., Ballard, R. D., Yankovsky, A., ... Voronov, S. (2011). Bedforms, coastal-trapped waves, and scour process observations from the continental shelf of the northern Black Sea. *Special Paper of the Geological Society of America*, 473, 165–178. [https://doi.org/10.1130/2011.2473\(10\)](https://doi.org/10.1130/2011.2473(10)).

- UNESCO (2014). Heritage for Peace – Centenary of World War I. URL <http://www.unesco.org/new/en/culture/themes/underwater-cultural-heritage/underwater-cultural-heritage/heritage-for-peace-wwi/>. [Online] (Accessed 2018-08-30).
- Van Landeghem, K. J. J., & Chiverrell, R. C. (2020). Bed erosion during fast ice streaming regulated the retreat dynamics of the Irish Sea Ice Stream. *Quaternary Science Reviews*, 245. <https://doi.org/10.1016/j.quascirev.2020.106526>.
- Van Landeghem, K. J. J., Baas, J. H., Mitchell, N. C., Wilcockson, D. and Wheeler, A. J. (Feb. 2012). Reversed sediment wave migration in the Irish Sea, NW Europe: A reappraisal of the validity of geometry-based predictive modelling and assumptions. *Marine Geology* 295-298, 95-112.
- Van Landeghem, K. J. J., Wheeler, A. J., Mitchell, N. C., & Sutton, G. (2009). Variations in sediment wave dimensions across the tidally dominated Irish Sea, NW Europe. *Marine Geology*, 263(1–4), 108–119. <https://doi.org/10.1016/j.margeo.2009.04.003>.
- Van Rijn, L. C. (1984). Sediment transport - Part II: suspended load. *Journal of Hydraulic Division*, HY11, 1631–1641.
- Van Rijn, L. C. (1993a). Principles of sediment transport in rivers, estuaries, seas and oceans. Amsterdam: Aqua publications III, page 700.
- Van Rijn, L. C. (1993b). Simple general formulae for sand transport in rivers, estuaries and coastal waters, 1-16.
- Van Rijn, L. C. (2007a). Unified View of Sediment Transport by Currents and Waves. I: Initiation of Motion, Bed Roughness, and Bed-Load Transport. *Journal of Hydraulic Engineering* 133, 649-667.
- Van Rijn, L. C. (2007b). Unified View of Sediment Transport by Currents and Waves. II: Suspended Transport. *Journal of Hydraulic Engineering* 133, 668-689.
- Velenturf, A. P. M., Emery, A. R., Hodgson, D. M., Barlow, N. L. M., Mohtaj Khorasani, A. M., Van Alstine, J., Peterson, E. L., Piazzolo, S. and Thorp, M. (2021). Geoscience Solutions for Sustainable Offshore Wind Development. *Earth Science, Systems and Society*, 1. <https://doi.org/10.3389/esss.2021.10042>.
- Wakelin, S. L., Holt, J., T. and Proctor, R. (2009). The influence of initial conditions and open boundary conditions on shelf circulation in a 3D ocean-shelf model of the North East Atlantic. *Ocean Dynamics* 59, 67-81.
- Wang, M., Wu, Z., Best, J., Yang, F., Li, X., Zhao, D., Zhou, J. (2021). Using multibeam backscatter strength to analyse the distribution of manganese nodules: A case study of seamounts in the Western Pacific Ocean. *Applied Acoustics* 173 (107729), 1-13.
- Ward, A. K. I., Larcombe, P., & Veth, P. (1998). Towards new process-oriented models for describing wreck disintegration - an example using the Pandora wreck. *Bulletin of the Australian Institute for Maritime Archaeology*, 22 (January), 109–114.

- Ward, S. L., Neill, S. P., Van Landeghem, K. J. J., Scourse, J. D. (2015). Classifying seabed sediment type using simulated tidal-induced bed shear stress. *Marine Geology* 367, 94-104. <https://doi.org/10.1016/j.margeo.2015.05.010>.
- Wardhana, K. and Hadipriono, F.C. (2003). Analysis of Recent Bridge Failures in the United States. *Journal of Performance of Constructed Facilities*, 17, 144-150. [https://doi.org/10.1061/\(ASCE\)0887-3828\(2003\)17:3\(144\)](https://doi.org/10.1061/(ASCE)0887-3828(2003)17:3(144)).
- Wheeler, A. J. (2002). Environmental Controls on Shipwreck Preservation: The Irish Context. *Journal of Archaeological Science* 29, 1149-1159.
- Whitehouse, R. J., Harris J., Sutherland, J., Rees, J. (2008). An Assessment on field data for scour at offshore wind turbine foundations. *Fourth International Conference on Scour and Erosion*, pp. 329-335.
- Whitehouse, R. J., Harris, J. M., Sutherland, J., Rees, J. (2011). The nature of scour development and scour protection at offshore windfarm foundations. *Mar Pollut Bull* 62 (1), 73-88. doi: 10.1016/j.marpolbul.2010.09.007. PMID: 21040932.
- Whitehouse, R. J. (1998). *Scour at Marine Structures: A Manual for Practical Applications*. United Kingdom: Thomas Telford, London.
- Wilcock, P. R. (1989). Southard, J. B. (1989). Bed load transport of mixed size sediment: Fractional transport rates, bed forms, and the development of a coarse bed surface layer, *AGU* 25 (7), pp. 1629-1641.
- Wilcock, P. R. (1993). Critical Shear Stress of Natural Sediments.
- Wilcock, P. R. (1998). Two-Fraction Model of Initial Sediment Motion in Gravel-Bed Rivers. *Science* 280, pp. 410-412.
- Wilson R. J., Speirs, D. C., Sabatino, A., & Heath, M. R. (2018). A synthetic map of the north-west European Shelf sedimentary environment for applications in marine science. *Earth System Science Data*, 10(1), 109–130. <https://doi.org/10.5194/essd-10-109-2018>.
- Wu, W., Wang, S. S. Y., & Jia, Y. (2000). Nonuniform sediment transport in alluvial rivers. *Journal of Hydraulic Research*, 38 (6), 427–434. <https://doi.org/10.1080/002216800009498296>.
- Ya-ping, W., Shu, G. and Kun-ye, L. A. (2000). A preliminary study on suspended sediment concentration measurements using an ADCP mounted on a moving vessel. *Chin. J. Ocean. Limnol.* 18, 183–189. <https://doi.org/10.1007/BF02842579>
- Yiannoukos, I., Benson, T., Van Landeghem, K. J. J., Couldrey, A., Whitehouse, R. J., McCarron, C. J., Quinn, R., Morgan, J., Roberts, M., Clayton-Smith, B. (2020). Modelling scour around submerged objects with TELEMAC3D - GAIA. In: Breugem, W.A., Frederickx, L., Koutrouveli, T., Kulkarni, R., Chu, K., Decrop, B. (Eds.), *Online Proceedings of the Papers Submitted to the 2020 TELEMAC- MASCARET User Conference*. International Marine & Dredging Consultants, pp. 68–73.

- Yin, Y., Li, M., Moulinec, C., Emerson, D. R. (2016). Simulation of the flow around a submerged structure using the Immersed Boundary Method. In Bourban Sébastien (Hg.), *Proceedings of the XXIIIrd TELEMAC-MMASCARET User Conference*, Paris, France, pp. 245-252.
- Yuan, C., Melville, B. W., Adams, K. N. (2017). Scour at wind turbine tripod foundation under steady flow. *Ocean Engineering* 141, pp. 277-282.
- Zdravković, L., Taborda, D. M. G., Potts, D. M., Jardine, R. J., Sideri, M., Schroeder, F. C., Byrne, B. W., McAdam, R., Burd, H.J, Houlsby, G. T., Martin, C. M., Gavin, K., Doherty, P., Igoe, D., Muir Wood A., Kallehave, D., Skov Gretlund, J. (2015). Numerical modelling of large diameter piles under lateral loading for offshore wind applications. In *Frontiers in Offshore Geotechnics III - Proceedings of the 3rd International Symposium on Frontiers in Offshore Geotechnics*, ISFOG 2015 (pp. 759–764). CRC Press/Balkema. <https://doi.org/10.1201/b18442-105>.
- Zhang, Q., Zhou, X. L., & Wang, J. H. (2017). Numerical investigation of local scour around three adjacent piles with different arrangements under current. *Ocean Engineering*, 142, 625–638. <https://doi.org/10.1016/j.oceaneng.2017.07.045>.
- Zhixin, W., Chuanwen, J., Qian, A., & Chengmin, W. (2009). The key technology of offshore wind farm and its new development in China. *Renewable and Sustainable Energy Reviews*, 13 (1), 216-222.

## 8 Appendices

### A. Multi-beam Echosounder (MBES) Specifications

SeaBat® 7125

Teledyne RESON

PLD13777-13

# SeaBat® 7125

## UltrahighResolutionMultibeam Echosounder





The new generation SeaBat 7125 builds on the field experience and feedback from many users around the world and brings unparalleled resolution and installation flexibility. The system is available in three separate configurations; one designed specifically for installation on survey vessels and 6000m depth rated systems for either ROV or AUV.

Each of these configurations provides superlative data quality and ease of use over depths from 0.5m to 500m. Enhanced features such as X-Range and Full Rate Dual Head bring unsurpassed performance levels to the SeaBat 7125.

Special emphasis has been put on maximizing operational efficiency and features such as variable swath width and roll stabilisation combined with a high ping rate and excellent data quality.

**Surface Vessel Installation – SV2**  
The new SeaBat 7125-SV2 is a highly integrated single or dual frequency system designed with ease of installation and operation as a high priority. The system consists of a surface

transceiver with integrated multiport card and a standard 25m cable run to the transducers. The transceiver hardware is suitable for running data acquisition software and is available with Teledyne RESON PDS2000 software pre-installed and configured.

**ROV2**  
For deep-water use, the ROV version of the SeaBat 7125 is depth rated to 6000m and includes a titanium interface bottle. System performance is identical to other members of the SeaBat 7125 family and with optional features such as FlexMode and Full Rate Dual Head, the system provides state-of-the-art pipeline and umbilical profiling capability.

**AUV**  
The AUV version of the 7125 provides on-board data processing and logging as well as interface to third party sensors. The electronics are supplied mounted on an aluminium frame for ease of integration and an optional 6000m depth-rated titanium electronics housing is available. The 7125-AUV provides high quality data and performance commensurate with the other versions of the 7125.

### FEATURES

<b>BEAM DENSITY</b> Up to 512 beams in selectable modes optimises operations for any survey type	<b>DEPTH</b> Dual frequency provides seamless coverage from 0.5 to 500m depth	<b>HIGH SPEED</b> High ping rate allows highspeed operations without compromising data density
<b>ROLL STABILIZATION</b> Real-time roll stabilization maximizing usable swath	<b>IHO</b> Compliance with IHO SP44Ed5 over entire depth range	<b>WATER COLUMN DATA</b> Allows collection of high density water column data for advanced processing
	<b>DIAGNOSTICS</b> Advanced diagnostics	

**TELEDYNE RESON**  
Everywhereyoulook®



# SeaBat® 7125

## SEABAT 7125 SYSTEM SPECIFICATIONS

	7125 SV2	7125 ROV2	7125 AUV
Power requirement	Typical: 110-220VAC, 50/60 Hz, 250 W.  Max: 110-220VAC, 50/60Hz, 700 W.	Processor Typical: 110-220 VAC, 50/60 Hz, 110 W.  Processor Max: 110-220VAC, 50/60 Hz, 400 W.  Wet end Typical: 48 VDC (+/- 10%), 115 W.  Wet end Max: 48 VDC (+/- 10%) 250 W.  Power requirements when Wet-ends are powered from sonar processor: 110-220VAC, 50/60 Hz, 700 W.	48V DC (± 10%)
Transducer cable length	25m standard	3m standard 10m optional	3m standard 10m optional
LCU to processor cable length	N/A	25m (st), 3 m	N/A
System depth rating	25m	6000m	6000m optional
Frequency	200kHz or 400kHz (dual frequency available)		
Along-track transmit beamwidth	2° at 200kHz & 1° at 400kHz		
Across-track receive beamwidth	1° at 200kHz & 0.5° at 400kHz		
Max ping rate	50Hz (± 1Hz)		
Pulse length	30µs – 300µs Continuous Wave; 300µs – 20ms Frequency Modulated (X-Range)		
Number of beams	512EA/ED at 400kHz, 256EA/ED at 200kHz		
Max swath angle	140° in Equi-Distant Mode; 165° in Equi-Angle Mode		
Typical depth <sup>2)</sup>	0.5m to 150m at 400kHz, 0.5m to 400m at 200kHz		
Max depth <sup>3)</sup>	>175m at 400kHz; 450m at 200kHz		
Depth resolution	6mm		
Data output	Bathymetry, sidescan and snippets 7K data format		
Temperature:	-2° to +35°C		
Flexmode:	Optional		
Full Rate Dual Head	400 KHz for ROV/ AUV		

For relevant tolerances for dimensions above and detailed outlined drawings: see Product Description

<sup>1)</sup> All beam widths measured at -3dB, unsteered with a sound velocity of 1480m/s.

<sup>2)</sup> This is a depth range within which the system is normally operated, from the minimum depth to a depth value corresponding to the max. swath -50%.

<sup>3)</sup> This is the single value corresponding to the depth at which the swath is reduced to 10% of its max. value. For actual swath performance refer to Product Description.

# SeaBat® 7125

## SEABAT 7125 SYSTEM SPECIFICATIONS

Component	7125 SV2	7125 ROV2	7125 AUV
EM 7216 receiver	✓	✓	✓
TC 2181 dual frequency 200/ 400 khz projector	✓		
TC 2160 400khz projector		✓	✓
TC 2163 200khz projector (optional)		✓	✓
7-link control unit		✓	
Sonar processor unit with monitor, keyboard and pointer device		✓	
SV transceiver with monitor, keyboard and pointer device	✓		
7-i integrated control and processor unit			✓

Measurements	Height [mm]	Width [mm]	Depth [mm]	Weight [kg/air]	Weight [kg/water]
TC 2181 df 200/ 400 khz projector	87	93	280	4.5	3.4
TC 2160 400 khz projector	77	62	285	2.7	1.7
TC 2163 200khz projector	115	100	280	7.5	5
EM 7216 200/400 khz receiver	137	496	102	10.7	5.7
Surface transceiver	5U	19"	557	20	N/A
LCU bottle	530	Ø174	N/A	23.5	12.0
ICPU frame	172	166	497	10	N/A
Sonar processor	5U	19"	630	30	N/A

### OPTIONS:

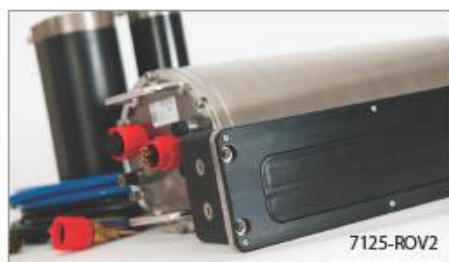
- Mounting Bracket with Fairing
- SVP-70 sound velocity probe with 25m cable
- Extended warranty/ support & maintenance contracts
- Fiber-optic conversion for ROV installations

# SeaBat® 7125

## Ultrahigh Resolution Multibeam Echosounder



7125-SV2



7125-ROV2

### WHY CHOOSE A SEABAT 7125 SYSTEM?

- Maximum productivity during data collection
  - Up to 165° swath
  - Roll Stabilization
  - Up to 512 beams in operator selectable modes
- Uncompromised clean data sets
  - Quality Filters/flags
  - Interactive, Comprehensive GUI
  - Industry leading bottom detect methods
- Ease of Installation and Use
  - Fully automatic operation
  - Single highly integrated topside transceiver
  - Integrated Multibeam acquisition and processing software
  - Extremely portable wet-end
- Maximum Operational Flexibility
  - 400 and 200kHz operation for seamless data collection from 0.5m to 500m
  - Advanced beam-forming with variable and steerable swath
  - Simultaneous output of bathymetry, Sidescan, Snippets backscatter, and raw water column data
  - Optional X-Range for increased range performance, ultra-high resolution and resistance to external noise

For more details visit [www.teledyne-reson.com](http://www.teledyne-reson.com) or contact your local Teledyne RESON Office. Teledyne RESON reserves the right to change specifications without notice. 2013©Teledyne

**Teledyne RESON A/S**  
Denmark  
Tel: +45 4738 0022  
[info@teledyne-reson.com](mailto:info@teledyne-reson.com)

**Teledyne RESON Inc.**  
U.S.A.  
Tel: +1 805 964-6260  
[sales@teledyne-reson.com](mailto:sales@teledyne-reson.com)

**Teledyne RESON Ltd.**  
Scotland U.K.  
Tel: +44 1224 709 900  
[sales@reson.co.uk](mailto:sales@reson.co.uk)

**Teledyne RESON B.V.**  
The Netherlands  
Tel: +31 (0) 10 245 1500  
[info@reson.nl](mailto:info@reson.nl)

**Teledyne RESON Pte. Ltd.**  
Singapore  
Tel: +65 6725 9851  
[singapore@teledyne-reson.com](mailto:singapore@teledyne-reson.com)

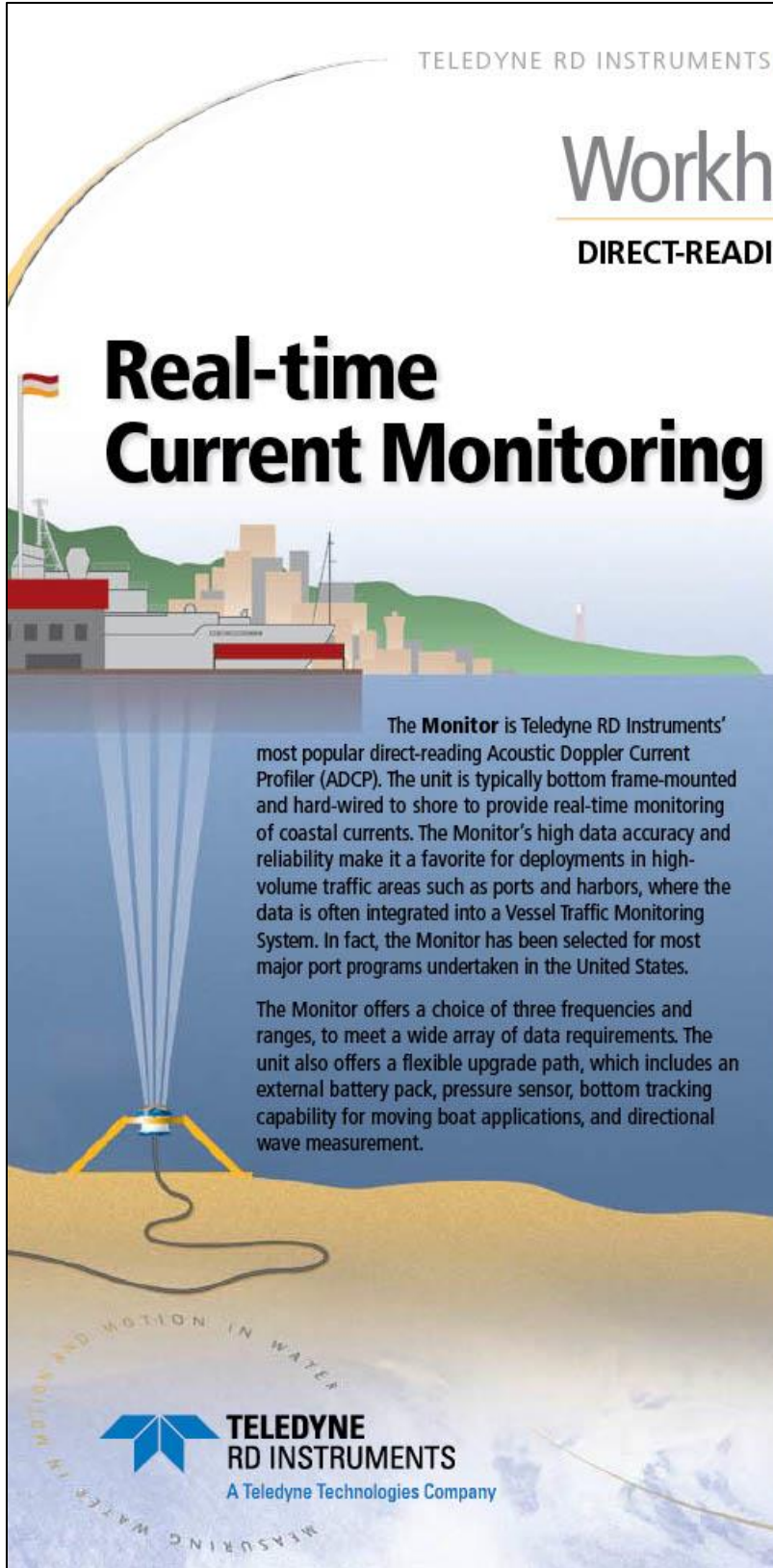
**Teledyne RESON Shanghai Office**  
Shanghai  
Tel: +86 21 64186205  
[shanghai@teledyne-reson.com](mailto:shanghai@teledyne-reson.com)

Copyright Teledyne RESON, all specification subject to change without notice  
[www.teledyne-reson.com](http://www.teledyne-reson.com)





## B. Acoustic Doppler Current Profiler (ADCP) Specifications



TELEDYNE RD INSTRUMENTS MARINE MEASUREMENTS

# Workhorse Monitor


DIRECT-READING 1200, 600, 300 kHz ADCP


## Real-time Current Monitoring

The **Monitor** is Teledyne RD Instruments' most popular direct-reading Acoustic Doppler Current Profiler (ADCP). The unit is typically bottom frame-mounted and hard-wired to shore to provide real-time monitoring of coastal currents. The Monitor's high data accuracy and reliability make it a favorite for deployments in high-volume traffic areas such as ports and harbors, where the data is often integrated into a Vessel Traffic Monitoring System. In fact, the Monitor has been selected for most major port programs undertaken in the United States.

The Monitor offers a choice of three frequencies and ranges, to meet a wide array of data requirements. The unit also offers a flexible upgrade path, which includes an external battery pack, pressure sensor, bottom tracking capability for moving boat applications, and directional wave measurement.

MEASURING WATER IN MOTION AND MOTION IN WATER

 **TELEDYNE RD INSTRUMENTS**  
A Teledyne Technologies Company



**The Workhorse Monitor offers:**

- **Extreme accuracy and reliability:** *The Monitor is ideally suited for the most demanding environments, including high traffic areas such as ports and harbors.*
- **Versatility:** *This direct reading unit can easily be upgraded to tackle a wide variety of coastal applications. Typical upgrades include pressure sensor, external battery pack, bottom tracking, and directional wave measurement—a single instrument can do it all!*
- **Precision data:** *Teledyne RDI's patented Broadband signal processing delivers very low-noise data, resulting in unparalleled data resolution and minimal power consumption.*
- **A four-beam solution:** *Teledyne RDI's patented 4-beam design improves data reliability by providing a redundant data source in the case of a blocked or damaged beam; improves data quality by delivering an independent measure known as error velocity; and improves data accuracy by reducing variance in your data.*

# Workhorse Monitor

DIRECT-READING 1200, 600, 300 kHz ADCP



## Technical Specifications

Water Profiling						
Depth	Typical Range <sup>2</sup> 12m		Typical Range <sup>2</sup> 50m		Typical Range <sup>2</sup> 110m	
Cell Size <sup>1</sup>	1200kHz		600kHz		300kHz	
Vertical Resolution (m)	Range <sup>3</sup>	Std. Dev. <sup>4</sup> (cm/s)	Range <sup>3</sup>	Std. Dev. <sup>4</sup> (cm/s)	Range <sup>3</sup>	Std. Dev. <sup>4</sup> (cm/s)
0.25	11-14	12.9				
0.5	13-16	6.1	39	12.9	see note <sup>1</sup>	
1	14-18	3.0	43	6.1	92-71	12.8
2	15-20 <sup>2</sup>	2.0	47	3.0	102-78	6.1
4	see note <sup>1</sup>		52 <sup>2</sup>	2.0	113-86	3.0
8					126-95 <sup>2</sup>	2.0

<sup>1</sup>User's choice of depth cell size is not limited to the typical values specified.

<sup>2</sup>Longer ranges available.

<sup>3</sup>Profiling range based on temperature values at 5°C and 20°C, salinity = 35ppt.

<sup>4</sup>Broadband mode single-ping standard deviation (Std. Dev.).

## Long Range Mode

	Range (m)	Depth Cell Size (m)	Std. Dev. (cm/s)
1200kHz	24	2	3.8
600kHz	70	4	4.2
300kHz	165	8	4.2

## Profile Parameters

Velocity accuracy:

- 1200, 600: 0.3% of the water velocity relative to the ADCP  $\pm 0.3$  cm/s
- 300: 0.5% of the water velocity relative to the ADCP  $\pm 0.5$  cm/s

Velocity resolution: 0.1 cm/s

Velocity range:  $\pm 5$  m/s (default)  
 $\pm 20$  m/s (maximum)

Number of depth cells: 1-128

Ping rate: 2Hz (typical)

## Echo Intensity Profile

Vertical resolution: Depth cell size

Dynamic range: 80dB

Precision:  $\pm 1.5$  dB

## Transducer and Hardware

Beam angle: 20°

Configuration: 4-beam, convex

Internal memory: Two PCMCIA card slots; no memory card included

Communications: Serial port selectable by switch for RS-232 or RS-422. ASCII or binary output at 1200-115,400 baud.

## Standard Sensors

Temperature (mounted on transducer):

Range: -5° to 45°C

Precision:  $\pm 0.4$  °C

Resolution: 0.01°

Tilt: Range:  $\pm 15$ °

Accuracy:  $\pm 0.5$ °

Precision:  $\pm 0.5$ °

Resolution: 0.01°

Compass (fluxgate type, includes built-in field calibration feature):

Accuracy:  $\pm 2$ °<sup>5</sup>

Precision:  $\pm 0.5$ °<sup>5</sup>

Resolution: 0.01°

Maximum tilt:  $\pm 15$ °

<sup>5</sup> $\leq 1.0$ ° is commonly achieved after calibration

## Power

Input power: 20-50VDC

## Environmental

Standard depth rating:

200m; optional to 6000m

Operating temperature\*: -5° to 45°C

Storage temperature

without batteries: -30° to 60°C

Weight in air: 7.6kg

Weight in water: 3.0kg

\* Without batteries

## Software

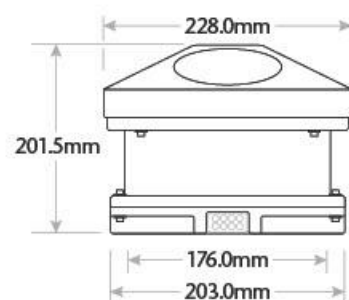
Teledyne RDI's Windows™-based software included:

- WinSC—Data Acquisition System
- WinADCP—Data Display and Export

## Available Options

- Memory: 2 PCMCIA slots; total 4GB
- Pressure sensor
- External battery case
- High-resolution water-profiling modes
- Bottom tracking
- AC/DC power converter, 48VDC output
- Conversion kit for internal power supply and memory
- Directional Waves Array

## Dimensions



**TELEDYNE RD INSTRUMENTS**  
A Teledyne Technologies Company  
[www.rdinstruments.com](http://www.rdinstruments.com)



Free online product training



Free 24/7 emergency support

Teledyne RD Instruments

14020 Stowe Drive, Poway, CA 92064 USA

Tel. +1-858-842-2600 • Fax +1-858-842-2822 • E-mail: [rdisales@teledyne.com](mailto:rdisales@teledyne.com)

Les Nertieres 5 Avenue Hector Pintus 06610 La Gaude France

Tel. +33-49-211-0930 • Fax +33-49-211-0931 • E-mail: [rdie@teledyne.com](mailto:rdie@teledyne.com)



Specifications subject to change without notice.

© 2008 Teledyne RD Instruments, Inc. All rights reserved. MIM-1017, Rev. 01/08

## C. Ultra-Short BaseLine (USBL) instrument specifications



Applied Acoustic Engineering Ltd  
Marine House, Marine Park,  
Gipton Hall Road, Great Yarmouth  
NR31 0NB, United Kingdom

T +44 (0)1493 440395  
E [general@appliedacoustics.com](mailto:general@appliedacoustics.com)  
W [appliedacoustics.com](http://appliedacoustics.com)

# Easytrak Nexus Lite, Model 2695



### Key features

- Bi-directional Sigma Spread Spectrum acoustics
- Full hemispherical tracking
- 8 target tracking
- Internal data logging
- USB connected console
- Optional graphical overlay
- Optional calibration software

### Easytrak Nexus Lite Overview

Easytrak Nexus Lite is an advanced USBL positioning and tracking system that determines the position of dynamic subsea targets through the transmission and reception of acoustic signals between the submerged transceiver and a target beacon. It incorporates Sigma 1 Spread Spectrum technology to provide a secure acoustic link. By incorporating Sigma 1 technology the wide bandwidth transmissions reduce the system's susceptibility to interference.

Designed for ease of installation in a vessel's operations room, the surface console has been mounted within a rugged 1U enclosure for connection to a laptop or tablet PC.

Easytrak Nexus Lite retains legacy compatibility with tone beacons.



## Nexus Lite Technical Specification

### EASYTRAK NEXUS LITE CONSOLE, MODEL EZT-2695

Provides DC power, high speed digital communications to the transceiver with a USB interface to user PC running Easytrak Nexus Lite software.

Dimensions	1U, 254 x 54 x 260mm
Weight	1.0kg
Power requirements	48Vdc / Vac Adapter Input: 90Vac – 230Vac 47–63Hz typically 3A
Connection to transceiver	Rear panel connector for 2683 Transceiver
Temperature	Operating: -10° to +40°C Storage: -20° to +50°C
Front panel indicators	LED indicators for power and serial status.
Serial communications	4 x Console RS-232 Data Ports. System utilises PC ports if available
Data Output	AAE format V1 and V2, TP-II2EC, TP-EC W/PR, Simrad 300P, Simrad 309, Simrad \$PSIMSSB, Pseudo \$GPRMC, NMEA \$GPGGA, NMEA \$GPVTG, NMEA \$GPTLL, Pseudo \$GPGGA, KLEIN 3000 (Quick set) Multiple outputs available
Compass Input	SGB-HTDS, SGB-HTDt, NMEA HDT, HDM, HDG
VRU Input	TCM-2X, \$HCXDR, TSS1
Calibration	Optional EasyCal 2 USB L Calibration tool.
GPS / D GPS Input	NMEA; GLL, GGA, RMC Optional Geo Referenced Graphical Overlay. GeoTiff, DXF
Target Heading Input	NMEA HDM, HDT, HDG, PNI TCM2
Target Depth Input	NMEA DBT, DBK, DBS, DPT, AAE
Time in	GPS Time synch
Responder Output	Positive 12V pulse 5ms long
Audio	Audible activity indicator

### EASYTRAK TRANSCIVER, TYPE EZT-2683

Factory calibrated multi-element transceiver head complete with integral AHRS and temperature sensor.

Material	316 Stainless Steel
Weight in air/water	11kg/8.5kg
Dimensions	100mm x 500mm (Ø x L)
Temperature	Operating: -10° to +40°C Storage: -20° to +50°C
Depth rating	30m
Electrical supply	48Vdc
Temperature sensor	1° resolution between -10° and +40° C
Cable	30m standard (20-100m options) with connectors. 12.8mm Ø



Due to continual product improvement specification information may be subject to change without notice.  
Easytrak Nexus Lite Model 2695/Dec 2018  
Caae technologies Ltd.



## Accuracy/Performance

Accuracy is based on the correct speed of sound being entered,  
no ray bending and an acceptable S/N ratio

Position accuracy	1.0% of slant range, with external sensors Acoustic accuracy excluding heading correction errors
Range resolution	Calculated to 0.1m resolution
Frequency band (MF)	18 - 30 kHz
Tracking beam pattern	Hemispherical, 180°
Transmitter	190dB re 1µPa at 1m
Integrated AHRs:	Bearing resolution: 0.1° displayed. Internally calculated to 0.01° Heading sensor accuracy: 0.8° rms standard; +/- 0.1° resolution/repeatability Pitch/Roll sensor accuracy: +/- 0.20° rms +/- 0.1° resolution/repeatability
Beacon types	AAE Sigma 1 Digital Spread Spectrum and AAE Tone channels. AAE V-NAV channels. HPR 400 channels 110Q, 1000, 1200A, 1300A Series Beacons, Digital Depth Transponders, AAE Release and Telemetry Beacons.
Interrogation rate	Internally set or external key
System	Externally assessed for immunity and emissions; conforms to 89/336/EEC. RoHS compliant

## D. Boud Minerals Technical Specification



### Technical Data Sheet

#### DKI Quartz 0.1-3.0mm mix

DKI Quartz is a light coloured, naturally rounded, pre-blended quartz sand.

It is washed, dried and graded.

#### Chemical Analysis

	%
SiO <sub>2</sub>	96.9
Fe <sub>2</sub> O <sub>3</sub>	0.1
Al <sub>2</sub> O <sub>3</sub>	1.4
CaO	0.04
MgO	0.02
Na <sub>2</sub> O	0.04
K <sub>2</sub> O	0.04

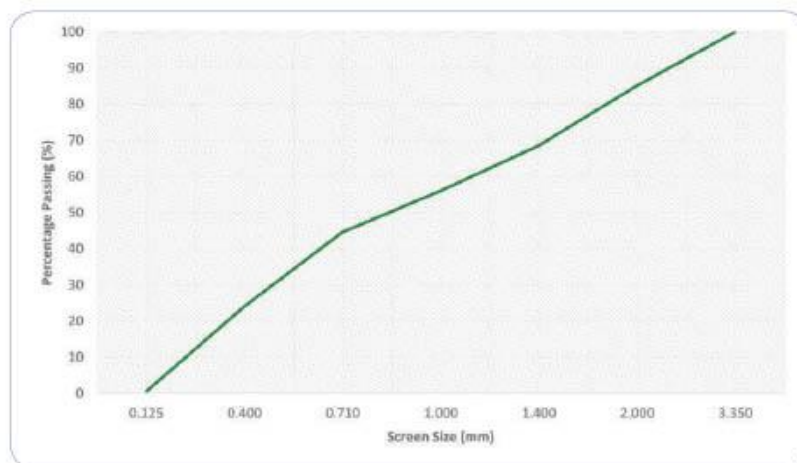
#### Physical Data

Particle Shape	Rounded
Colour	Grey
Specific Gravity g/cm <sup>3</sup>	2.65
Hardness (Mohs)	7.0
Polished Stone Value	55
Loss on Ignition	0.1%

#### Commodity Code

2505 100000

#### Particle Size Distribution



#### Packing

25 kilo bags on pallets of 1000 kilos, bulk bags and bulk

Issue 1 February 2016

All information is given in good faith but is indicative only and does not constitute a specification.

#### Boud Minerals Limited

West Bank, Sutton Bridge  
Lincolnshire PE12 9UR, UK  
Tel: +44 (0)1406 351988  
Fax: +44 (0)1406 350897  
Email: [sales@boud.com](mailto:sales@boud.com)  
Web: [www.boud.com](http://www.boud.com)

#### Boud Minerals AB

Håkantorpsvägen 109  
SE-26391 Höganäs, Sweden  
Tel: +46 42 333741  
Fax: +46 42 333829  
Email: [sweden@boud.com](mailto:sweden@boud.com)  
Web: [www.boud.com](http://www.boud.com)

## DKI Quartz 2.5-3.0mm

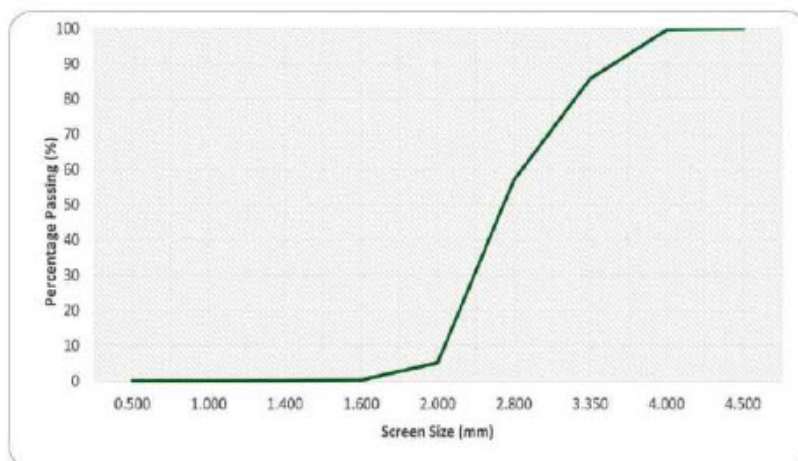
DKI Quartz is a light coloured, naturally rounded quartz gravel. It is washed, dried and graded.

Chemical Analysis	%	Physical Data	
SiO <sub>2</sub>	96.9	Particle Shape	Rounded
Fe <sub>2</sub> O <sub>3</sub>	0.1	Colour	Grey
Al <sub>2</sub> O <sub>3</sub>	1.4	Specific Gravity g/cm <sup>3</sup>	2.65
CaO	0.04	Hardness (Mohs)	7.0
MgO	0.02	Polished Stone Value	55
Na <sub>2</sub> O	0.04	Loss on Ignition	0.1%
K <sub>2</sub> O	0.04		

### Commodity Code

2505 100000

### Particle Size Distribution



### Packing

25 kilo bags on pallets of 1000 kilos, bulk bags and bulk

### Issue 1 February 2016

All information is given in good faith but is indicative only and does not constitute a specification.

### Boud Minerals Limited

West Bank, Sutton Bridge  
Lincolnshire PE12 9UR, UK  
Tel: +44 (0)1406 351988  
Fax: +44 (0)1406 350897  
Email: [sales@boud.com](mailto:sales@boud.com)  
Web: [www.boud.com](http://www.boud.com)

### Boud Minerals AB

Häikantorsvägen 109  
SE-26391 Höganäs, Sweden  
Tel: +46 42 333741  
Fax: +46 42 333829  
Email: [sweden@boud.com](mailto:sweden@boud.com)  
Web: [www.boud.com](http://www.boud.com)

## E. Dean Tranter Technical Specification



### WET GROUND MICA POWDERS - STANDARD RANGE

Wet ground mica powders have a high aspect ratio, refractive index, thermal resistance. They also combine a good lustre and thermal resistance and are therefore widely used as fillers and extenders in the building, paint, plastic, rubber industries.

#### CHEMICAL PROPERTIES

SiO <sub>2</sub>	Al <sub>2</sub> O <sub>3</sub>	K <sub>2</sub> O	Na <sub>2</sub> O	MgO	CaO	TiO <sub>2</sub>	Fe <sub>2</sub> O <sub>3</sub>	PH
47 – 50%	28 – 33%	8 – 11%	0.6 – 0.9%	0.5 – 0.8%	0.3 – 0.6%	0.6 – 0.9%	2.1 – 4.2%	7.8

#### PHYSICAL PROPERTIES

Heat resistance	Colour	Mohs hardness	Elastic coefficient	Transparency	Melting point	Purity
650° C	silver	2.5	(1475.9 – 2092.7) x 10 <sup>6</sup> Pa	71.7 – 87.5%	1250° C	> 99.5 %

#### PRODUCT SPECIFICATIONS

PRODUCT	Bulk density (g/cm <sup>3</sup> )	Whiteness (L.a.b)	Particle size (µ m)	Aspect ratio	Moisture (%)	Oil absorption (ml/100g)	LOI 1000°C
MicaSilk M60	0.26	78	106	75	< 0.4	61	4.0
MicaSilk M100	0.25	81	73	76	< 0.4	62	4.0
MicaSilk M200	0.25	82	52	79	< 0.5	65	4.1
MicaSilk M325	0.22	82	45	79	< 0.5	65	4.1
MicaSilk M400	0.22	86	32	80	< 0.5	65	4.3
MicaSilk M600	0.20	86	23	80	< 0.5	68	4.3
MicaSilk M800	0.20	87	15	80	< 0.5	68	4.3
MicaSilk M1250	0.18	88	10	78	< 0.5	70	4.5
MicaSilk M2000	0.15	88	8	75	< 0.5	70	4.5

Dean + Tranter Ltd  
Fordingbridge  
United Kingdom, SP6 1RA

Tel: +44 (0)1425 654012  
office@deantranter.co.uk  
www.deantranter.co.uk

## F. IBM Implementation in TELEMAC

```
! *****
! SUBROUTINE TELEMAC3D
! *****
!
! &(PASS, NIT_ORI)
!
! *****
! TELEMAC3D V8P0
! *****
!
!brief
!
!history JACEK A. JANKOWSKI PINXIT
!+ 01/03/1999
!+
!+ FORTRAN95 VERSION
!
!history J-M HERVOUET (LNHE)
!+ 05/05/2010
!+ V6P0
!+ K-OMEGA MODEL BY HOLGER WEILBEER (ISEB/UHA)
!
!history N.DURAND (HRW), S.E.BOURBAN (HRW)
!+ 13/07/2010
!+ V6P0
!+ Translation of French comments within the FORTRAN sources into
!+ English comments
!
!history N.DURAND (HRW), S.E.BOURBAN (HRW)
!+ 21/08/2010
!+ V6P0
!+ Creation of DOXYGEN tags for automated documentation and
!+ cross-referencing of the FORTRAN sources
!
!history J-M HERVOUET (LNHE)
!+ 02/08/2011
!+ V6P1
!+ CALL MITTIT(18,AT,LT) changed into CALL MITTIT(19,AT,LT)
!+ CALL MITTIT(19,AT,LT) changed into CALL MITTIT(20,AT,LT)
!+ 2 fractional steps were not correctly labelled in the listing
!
!history J-M HERVOUET (LNHE)
!+ 12/08/2011
!+ V6P2
!+ Calls to CHECK and BIL3D changed
!
!history J-M HERVOUET (LNHE)
!+ 02/04/2012
!+ V6P2
!+ Clean restart implemented.
!
!history J-M HERVOUET (LNHE)
!+ 01/06/2012
!+ V6P2
!+ Call to vector before call to Tel4del corrected (GRAZCO)
!+ Initialisation of TAN after call to condim.
!
!history J-M HERVOUET (LNHE)
!+ 18/12/2012
!+ V6P3
!+ Call to IFAB3DT added, arguments of cstkep removed.
```



```

!
!history J-M HERVOUET (LNHE)
!+ 25/01/2013
!+ V6P3
!+ TAN renamed TRN, copy of TRN on TA moved from after CONDIM to
!+ after BIEF_SUITE, FLULIM set to 1 before first call to PREADV
!
!history J-M HERVOUET (LNHE)
!+ 11/03/2013
!+ V6P3
!+ Call to METEO modified. Stop if variables not found for a 2D
!+ continuation.
!
!history R. KOPMANN (EDF R&D, LNHE)
!+ 16/04/2013
!+ V6P3
!+ Adding the file format in calls to FIND_IN_SEL.
!
!history J-M HERVOUET (LNHE)
!+ 18/03/2013
!+ V6P3
!+ Dealing with the newly created FILE FOR 2D CONTINUATION.
!
!history J-M HERVOUET (LNHE)
!+ 25/04/2013
!+ V6P3
!+ AKN and EPN initialised in case of computation continued, for the
!+ first call to PREADV.
!+ Mesh better updated in case of coupling with Sisyphe.
!
!history J-M HERVOUET (LNHE)
!+ 20/09/2013
!+ V6P3
!+ CALL PLANE_BOTTOM added at the beginning of time loop (otherwise
!+ when calling kepcl3 IPBOT is done with ZPROP at the first iteration
!+ and with Z for the others, while ZPROP is always sent as argument.
!+ This could trigger unexpected divisions by 0.
!
!history J-M HERVOUET (LNHE)
!+ 15/11/2013
!+ V6P3
!+ After second call to bief_suite, checking that Z has been found,
!+ otherwise stop
!
!history C. VILLARET & T. BENSON & D. KELLY (HR-WALLINGFORD)
!+ 27/02/2014
!+ V7P0
!+ New developments in sediment merged on 25/02/2014.
!
!history J-M HERVOUET (LNHE)
!+ 14/03/2014
!+ V7P0
!+ CALL BIL3D put out of the IF(S3D_SEDI) test. Address of depth-averaged
!+ tracers from 38 to 37+NTRAC in ALIRE2D.
!
!history J-M HERVOUET (EDF LAB, LNHE)
!+ 19/03/2014
!+ V7P0
!+ Boundary segments have now their own numbering, independent of
!+ boundary points numbering. Differents calls changed accordingly.
!
!history J-M HERVOUET (EDF LAB, LNHE)
!+ 02/05/2014

```

```

!+    V7P0
!+    Argument ZR added to FONVAS. S3D_HDEPupdated differently after calling
!+    Sisyphe, to avoid truncation errors that would give S3D_HDEP<0.
!
!history J-M HERVOUET (EDF LAB, LNHE)
!+    31/07/2014
!+    V7P0
!+    Call to METEO moved just before the first call to FSGRAD, not just
!+    after (atmospheric pressure gradients now systematically added
!+    to free surface gradients).
!
!history C VILLARET (HRW+EDF) & J-M HERVOUET (EDF - LNHE)
!+    18/09/2014
!+    V7P0
!+    Calls to sisyphe and wac changed.
!
!history G. ANTOINE & M. JODEAU & J.M. HERVOUET (EDF - LNHE)
!+    13/10/2014
!+    V7P0
!+    New developments in sediment for mixed sediment transport
!
!history R. ATA (EDF LAB, LNHE)
!+    05/11/2014
!+    V7P0
!+    add optional variables to meteo in a sake of harmonization
!+    with telemac-2d
!
!history J-M HERVOUET (EDF LAB, LNHE)
!+    31/03/2015
!+    V7P1
!+    Just a few extra debugger prints, up to CALL KEPINI, where was the
!+    last user bug I looked for.
!
!history Y AUDOUIN (LNHE)
!+    25/05/2015
!+    V7P0
!+    Modification to comply with the hermes module
!
!history J-M HERVOUET (EDF LAB, LNHE)
!+    26/06/2015
!+    V7P1
!+    2D and 3D RESULT FILE can be optional. Tests for writing them added.
!
!history A. JOLY (EDF LAB, LNHE)
!+    27/08/2015
!+    V7P1
!+    Imposed flowrates on the bed.
!
!history J-M HERVOUET (EDF LAB, LNHE)
!+    21/01/2016
!+    V7P1
!+    Initial conditions of results file in restart mode were forgotten
!+    they are useless but now requested by the Hermes module...
!
!history J-M HERVOUET (EDF LAB, LNHE)
!+    08/02/2016
!+    V7P2
!+    Adding the argument HPROP in the call to Sisyphe.
!
!history J-M HERVOUET (EDF LAB, LNHE)
!+    24/03/2016
!+    V7P2
!+    Adapting to new CVDF3D, saving Z at time T(n) in ZN.

```

```

!
!history J-M HERVOUET (EDF LAB, LNHE)
!+ 27/05/2016
!+ V7P2
!+ Allowing k-epsilon model on a direction and not on the other.
!
!history J-M HERVOUET (EDF LAB, LNHE)
!+ 30/05/2016
!+ V7P2
!+ In a continued computation, K, Epsilon and the dynamic pressure
!+ must not be read if they are not necessary because their arrays
!+ are not allocated.
!
!history J-M HERVOUET (EDF LAB, LNHE)
!+ 22/08/2016
!+ V7P2
!+ Adding TB2 in the call to CVDF3D.
!
!history M.JODEAU (EDF LAB, LNHE)
!+ 08/2016
!+ V7P3
!+ Water quality: AED2 coupling
!
!history R. ATA (EDF LAB, LNHE)
!+ 12/01/2017
!+ V7P3
!+ Bug fix in the call of DERIVE: now zchar, nplan, transf are well
!+ introduced
!
!history J,RIEHME (ADJOINTWARE)
!+ November 2016
!+ V7P2
!+ Replaced EXTERNAL statements to parallel functions / subroutines
!+ by the INTERFACE_PARALLEL
!
!history J-M HERVOUET (EDF LAB, LNHE)
!+ 11/09/2017
!+ V7P3
!+ Adding NELMAX2 in list of arguments of ifab3d, ifab3dt, TBORD,
!+ flux_ef_vf_3d and make_zconv.
!
!~~~~~
!~~~~~
!
USE BIEF
USE DECLARATIONS_TELEMAC
USE DECLARATIONS_TELEMAC3D
USE OILSPILL
USE INTERFACE_TELEMAC3D, EX_TELEMAC3D => TELEMAC3D
USE INTERFACE_TELEMAC2D
USE INTERFACE_SISYPHE, ONLY: SISYPHE
USE INTERFACE_GAIA, ONLY: GAIA_STEP
USE INTERFACE_TOMAWAC, ONLY: WAC
USE TEL4DEL, ONLY: TEL4DELWAQ
USE DECLARATIONS_GAIA, ONLY: NSICLA,FLUDP,FLUDPT,FLUER,NSUSP_TEL,
& XMVS0,NUM_ISUSP_ICLA,SETDEP,SLVSED
USE DECLARATIONS_WAQTEL,ONLY: TAIR,WAQPROCESS
USE GOTM_COUPLING
!
USE DECLARATIONS_SPECIAL
IMPLICIT NONE
!
!-----

```

```

! DECLARES LOCAL VARIABLES FOR TELEMACH3D
!-----
!
  INTEGER,      INTENT(IN) :: PASS
  INTEGER,      INTENT(IN) :: NIT_ORI
!
!-----
!
  INTEGER ITRAC,ISOUSI,IPOIN,ISUSP
  INTEGER SCHDVI_HOR,SCHDVI_VER,SCHCVI_HOR,SCHCVI_VER
  INTEGER IBID,I,K,I3D,IP
!
!
  DOUBLE PRECISION TETADIVER
  DOUBLE PRECISION UMIN, UMAX, SIGMAU, VMIN, VMAX, SIGMAV
  DOUBLE PRECISION WMIN, WMAX, SIGMAW
  DOUBLE PRECISION TAMIN, TAMAX, SIGMTA,TETATRA
!
  LOGICAL CLUMIN, CLUMAX, CLVMIN, CLVMAX, CLWMIN, CLWMAX
  LOGICAL CTAMIN, CTAMAX, YASEM3D,YAS0U,YAS1U
  LOGICAL CLKMIN, CLKMAX, CLEMIN, CLEMAX, CLNUMIN,CLNUMAX
  LOGICAL YAWCHU,NEWDIF,LBID,LBID2,BC
!
  CHARACTER(LEN=24), PARAMETER :: CODE1='TELEMACH3D
  CHARACTER(LEN=16) FORMUL
!
  INTRINSIC MOD
!
  TYPE(SLVCFG) :: SLVD
!
  DOUBLE PRECISION, POINTER, DIMENSION(:) :: SAVEZ

  TYPE(BIEF_OBJ), POINTER :: MULTI1, MULTI2, MULTI3, MULTI4
!
!
!!! Immersed boundary method
! commented - we will use PRIVE arrays instead
ccc  INTEGER IMMERSED_BOUNDARY(99999), INSIDE_IB(99999)
      INTEGER N_IB, N_INSIDE_IB
!!! Immersed boundary method
!=====
!
!
! TODO: temporary !!! Remove also in deall_telemach3d
  IF(.NOT.INCLUS(COUPLING,'GAIA ').AND.PASS.LE.0) THEN
    ISUSP=1
    SETDEP=-1
    NSUSP_TEL=0
!
    CALL ALLBLO(FLUDP, 'FLUDP ')
    CALL ALLBLO(FLUDPT,'FLUDPT')
    CALL ALLBLO(FLUER, 'FLUER ')
!
    CALL BIEF_ALLVEC_IN_BLOCK(FLUDP,1,1,'FLUDP ',IELM2H,1,2,MESH2D)
    CALL BIEF_ALLVEC_IN_BLOCK(FLUDPT,1,1,'FLUDPT',IELM2H,1,2,MESH2D)
    CALL BIEF_ALLVEC_IN_BLOCK(FLUER,1,1,'FLUER ',IELM2H,1,2,MESH2D)
!
    ALLOCATE(NUM_ISUSP_ICLA(1))
    NUM_ISUSP_ICLA(1)=1
!
  ENDIF
! temporary !!!
#if defined COMPAD

```

```

CALL AD_TELEMAC3D_BEGIN
#endif
!
! READS TRACERS IN PREVIOUS FILES
!
IF(NTRAC.GT.0) THEN
DO I=ADR_TRAC,ADR_TRAC+NTRAC-1
ALIRE3D(I)=1
ENDDO
DO I=39,38+NTRAC
ALIRE2D(I)=1
ENDDO
!
! THIS IS S3D_ESOMT...
! IF(S3D_SEDI) ALIRE2D(37)=1
!
ENDIF
!
! DO NOT READ K AND EPSILON IF NOT NECESSARY
!
IF(ITURBH.NE.3.AND.ITURBV.NE.3.AND.ITURBV.NE.6.AND.
& ITURBH.NE.7.AND.ITURBV.NE.7) THEN
ALIRE3D(8)=0
ALIRE3D(9)=0
ENDIF
!
! DO NOT READ DYNAMIC PRESSURE IF NOT NECESSARY
!
IF(.NOT.NONHYD) ALIRE3D(12)=0
!
=====
! FOR DROQUES (CALLS TO FLOT3D WILL INCREASE OR DECREASE NFLOT)
=====
!
NFLOT=0
!
=====
! FOR COMPUTING FLUXES OF ADVECTED VARIABLES
=====
!
! NO FLUX COMPUTED FOR U,V,W,K,EPSILON
DO I=1,5
CALCFLU(I)=.FALSE.
ENDDO
! DEPENDING ON BILMAS FOR TRACERS
IF(NTRAC.GT.0) THEN
DO I=6,5+NTRAC
CALCFLU(I)=BILMAS
ENDDO
ENDIF
!
=====
! FOR TAKING INTO ACCOUNT RAIN IN ADVECTION OF VARIOUS VARIABLES
=====
!
! NO RAIN FOR U,V,W,K,EPSILON
DO I=1,5
CALCRain(I)=.FALSE.
ENDDO
! DEPENDING OF RAIN FOR TRACERS
IF(NTRAC.GT.0) THEN
DO I=6,5+NTRAC
CALCRain(I)=RAIN

```



```

        ENDDO
    ENDIF
!
!=====
! INITIALISATION: READS, PREPARES AND CHECKS
!=====
!
    IF(PASS.EQ.0) THEN
        WRITE(LU,*) 'INITIALISING TELEM3D FOR ',CODE1
        WRITE(LU,*) 'INITIALISING TELEM3D'
    ELSEIF(PASS.EQ.1) THEN
        GO TO 700
    ELSEIF(PASS.NE.-1) THEN
        WRITE(LU,*) 'WRONG ARGUMENT PASS: ',PASS
        CALL PLANTE(1)
        STOP
    ENDIF

    CALL TELEM3D_INIT
!
!=====
! THE TIME LOOP BEGINS HERE
!=====
!
    IF(PASS.EQ.0) THEN
        WRITE(LU,*) 'TELEM3D INITIALIZED'
        RETURN
    ENDIF
!
700 CONTINUE
!
    LT = LT+1

    AT = AT + DT
!
    #if defined COMPAD
        CALL AD_TELEM3D_TIMESTEP_BEGIN
    #endif
!
    SAVING ORIGINAL ELEVATIONS (FOR DISTRIBUTIVE SCHEMES)
!
    CALL OS('X=Y ',X=ZN,Y=Z3)
!
    IF(DEBUG.GT.0) WRITE(LU,*) 'BOUCLE EN TEMPS LT=',LT
    INFOGR = .FALSE.
    IF (MOD(LT,LISPRD) == 0) INFOGR = .TRUE.
    INFOGR = LISTIN .AND. INFOGR
    IF (INFOGR) CALL MITTIT(1,AT,LT)
!
!=====
!
! IPBOT HAS BEEN MODIFIED FOR CVDF3D IN THE PREVIOUS TIME STEP,
! IT IS RESTORED HERE WITH ZPROP
! NOTE: DIFFERENT IPBOT_Z AND IPBOT_ZPROP WOULD BE CLEARER....
    IF(LT.GT.1) THEN
        CALL PLANE_BOTTOM(IPBOT%I,ZPROP%R,NPOIN2,NPLAN,SIGMAG,OPTBAN)
    ENDIF
!
!=====
! SOURCES : COMPUTES INPUTS WHEN VARYING IN TIME
! IF NO VARIATION IN TIME QSCE2=QSCE AND TASCE2=TASCE
!=====
!

```

```

IF(NPTSCE.GT.0) THEN
  DO I=1,NPTSCE
    QSCE2(I)=T3D_DEBSCE(AT,I,QSCE)
  ENDDO
  IF(NTRAC.GT.0) THEN
    DO I=1,NPTSCE
      DO ITRAC=1,NTRAC
        TA_SCE%ADR(ITRAC)%P%R(I)=T3D_TRSCE(AT,I,ITRAC)
      ENDDO
    ENDDO
  ENDIF
ENDIF
IF(NBUSE.GT.0) THEN
  IF(DEBUG.GT.0) WRITE(LU,*) 'CALLING BUSE'
  CALL BUSE(RELAXB,NBUSE,ENTBUS,SORBUS,GRAV,
&      H%R,ZF%R,DBUS%R,LRGBUS%R,HAUBUS%R,CLPBUS%I,
&      ALTBUS%R,CSBUS%R,CEBUS%R,ANGBUS%R,LBUS%R,
&      NTRAC,TA,TBUS,UBUS,VBUS,U%R,V%R,INFOGR,
&      CV%R,C56%R,CV5%R,C5%R,CTRASH%R,FRICBUS%R,
&      LONGBUS%R,CIRC%I,DELBUS%R,OPTBUSE,V2DPAR,DT,
&      SECBUS%R,MAXSCE,NPTSCE,NPOIN2,KSCE)
  IF(DEBUG.GT.0) WRITE(LU,*) 'BACK FROM BUSE'
  DO I=1,NBUSE
    QSCE2(NPTSCE+I) =-DBUS%R(I)
    QSCE2(NPTSCE+NBUSE+I)= DBUS%R(I)
  ENDDO
  IF(NTRAC.GT.0) THEN
    DO I=1,NBUSE
      DO ITRAC=1,NTRAC
        TA_SCE%ADR(ITRAC)%P%R(NPTSCE+I) = TBUS%ADR(ITRAC)%P%R(I)
        TA_SCE%ADR(ITRAC)%P%R(NPTSCE+NBUSE+I)=
&          TBUS%ADR(ITRAC)%P%R(NBUSE+I)
      ENDDO
    ENDDO
  ENDIF
ENDIF
!
!=====
! END OF CAMILLE LEQUETTE'S MODIFICATIONS
!=====
!
! COUPLING WITH TOMAWAC
!
  IF(INCLUS(COUPPING,'TOMAWAC').AND.
& PERCOU_WAC*((LT-1)/PERCOU_WAC).EQ.LT-1) THEN
!
  CALL CONFIG_CODE(3)
  IF(DEBUG.GT.0) WRITE(LU,*) 'APPEL DE TOMAWAC'
  CALL T3D_WAC_CPL_UPDATE(NIT_ORI)
  CALL WAC(PART=1)
  IF(DEBUG.GT.0) WRITE(LU,*) 'RETOUR DE TOMAWAC'
  CALL CONFIG_CODE(1)
!
  ENDIF
!
!=====
!
! SAVES H, TA, TP, AK, EP
! IN  HN,TRN,TPN,AKN,EPN
!
  CALL OS ('X=Y ',X=HN, Y=H )
  CALL OS ('X=Y ',X=VOLUN,Y=VOLU )
  IF(NCSIZE.GT.1) CALL OS('X=Y ',X=VOLUNPAR,Y=VOLUPAR)

```

```

CALL OS ( 'X=Y   ', X=UN,  Y=U   )
CALL OS ( 'X=Y   ', X=VN,  Y=V   )
IF(NONHYD) CALL OS ( 'X=Y   ', X=WN, Y=W)
CALL OS ( 'X=Y   ', X=GRADZN,Y=GRADZS)
! TRACERS (IF LT=1 DONE AFTER CALL CONDIM AND READ_DATASET)
IF(NTRAC.GT.0.AND.LT.1) CALL OS ('X=Y   ', X=TRN, Y=TA)
!
IF(ITURBV.EQ.3.OR.ITURBH.EQ.3.OR.ITURBV.EQ.7.OR.ITURBH.EQ.7) THEN
  CALL OS ( 'X=Y   ', X=AKN, Y=AK )
  CALL OS ( 'X=Y   ', X=EPN, Y=EP )
ENDIF
IF(ITURBV.EQ.5.OR.ITURBV.EQ.9) THEN
  CALL OS( 'X=Y   ', X=NUN, Y=NU )
ENDIF
!
IF(BILMAS) THEN
  MASSEN_WATER = MASSE_WATER
  CALL OS ( 'X=Y   ', X=MASSEN, Y=MASSE )
ENDIF
!
! COMPUTES MEAN UN AND VN IN THE VERTICAL
!
  IF(DEBUG.GT.0) WRITE(LU,*) 'APPEL DE VERMOY'
  CALL VERMOY(UN2D%R,VN2D%R,UN%R,VN%R,2,Z,
&      T3_01%R,T3_02%R,T3_03%R,1,NPLAN,NPOIN2,NPLAN,OPTBAN)
  IF(DEBUG.GT.0) WRITE(LU,*) 'RETOUR DE VERMOY'
!
! INTEGRATES USTOKES AND VSTOKES OVER DEPTH
!
  IF(INCLUS(COUPLING,'TOMAWACT3D')) THEN
    IF(DEBUG.GT.0) WRITE(LU,*) 'APPEL DE VERMOY POUR VIT STOKES'
    CALL VERMOY(US2D%R,VS2D%R,USTOKES%R,VSTOKES%R,2,Z,
&      T3_01%R,T3_02%R,T3_03%R,1,NPLAN,NPOIN2,NPLAN,
&      OPTBAN)
    IF(DEBUG.GT.0) WRITE(LU,*) 'RETOUR DE VERMOY POUR VIT STOKES'
  ENDIF
!
!-----
!
! COMPUTES FRICTION COEFFICIENT
!
! TIME VARIATIONS OF RUGOF (CORSTR IS IN TELEMAT-2D LIBRARY)
! MUST BE USER-IMPLEMENTED - NOTHING DONE IN STANDARD
CALL CORSTR
!
IF(.NOT.INCLUS(COUPLING,'TOMAWACT3D')) THEN
  IF(DEBUG.GT.0) WRITE(LU,*) 'APPEL DE COEFRO'
  CALL COEFRO(CF,H,UN2D,VN2D,KARMAN,KFROT,RUGOF,GRAV,MESH2D,T2_01,
&      .FALSE.)
  IF(DEBUG.GT.0) WRITE(LU,*) 'RETOUR DE COEFRO'
ELSE
! FRICTION COEFFICIENT MODIFIED TO TAKE INTO ACCOUNT WAVES+CURRENTS
DO IP=1,NPOIN2
  CF%R(IP) = CFWC%R(IP)
ENDDO
ENDIF
!
!-----
!
! CHECKS AND HARMONISES THE BOUNDARY CONDITION TYPES
!
  IF(DEBUG.GT.0) WRITE(LU,*) 'APPEL DE LICHEK'
  CALL LICHEK(LIMPRO%I,NPTFR2,

```

```

&      MESH2D%IKLBOR%,MESH2D%NELEB,MESH2D%NELEBX)
IF(DEBUG.GT.0) WRITE(LU,*) 'RETOUR DE LICHEK'
!
! BOUNDARY CONDITIONS FOR THE K-EPSILON MODEL
!
IF(ITURBV.EQ.3.OR.ITURBH.EQ.3.OR.ITURBV.EQ.7.OR.ITURBH.EQ.7) THEN
  CALL KEPICL(LIKBOF%,LIEBOF%,LIUBOF%,
&      LIKBOL%,LIEBOL%,LIUBOL%,
&      LIKBOS%,LIEBOS%,
&      NPTFR2,NPLAN,NPOIN2,KENT,KSORT,KENTU)
ENDIF
!
! BOUNDARY CONDITIONS FOR THE S-A MODEL
!
IF(ITURBV.EQ.5.OR.ITURBV.EQ.9) THEN
IF(DEBUG.GT.0) WRITE(LU,*) 'APPEL DE SAPICL'
  CALL SAPICL(LINUBOF%, LIUBOF%,
&      LINUBOL%, LIUBOL%,
&      LINUBOS%,
&      NPTFR2, NPLAN, NPOIN2, KENT, KSORT)
IF(DEBUG.GT.0) WRITE(LU,*) 'RETOUR DE SAPICL'
ENDIF
!-----
! FORCING AT THE BOUNDARIES
!
! METEOROLOGICAL CONDITIONS
!
IF (VENT.OR.ATMOS.OR.INCLUS(COUPLING,'WAQTEL')) THEN
  IF(DEBUG.GT.0) WRITE(LU,*) 'APPEL DE METEO'
  CALL METEO(PATMOS%R,WIND%ADR(1)%P%R,WIND%ADR(2)%P%R,FUAIR,FVAIR,
&      AT,LT,NPOIN2,VENT,ATMOS,
&      T3ATMA,T3ATMB,T3D_FILES,
&      LISTIN,PATMOS_VALUE,INCLUS(COUPLING,'WAQTEL'),PLUIE,
&      OPTWIND)
  IF(DEBUG.GT.0) WRITE(LU,*) 'RETOUR DE METEO'
! RAIN TEMPERATURE EQUAL TO THE AIR TEMPERATURE OR 1.D0
! IS BETTER THAN 0.D0
  IF(IND_T.NE.0.AND.INCLUS(COUPLING,'WAQTEL')) THEN
    TRAIN(IND_T) = MAX(TAIR%R(1),1.D0)
  ENDIF
  IF( (INCLUS(COUPLING,'WAQTEL') ).AND.
&      (13*INT(WAQPROCESS/13).EQ.WAQPROCESS) ) THEN
    DO I=1,NPOIN2
      WINDSPD%R(I) = SQRT(WIND%ADR(1)%P%R(I)**2
&      +WIND%ADR(2)%P%R(I)**2)
    ENDDO
  ENDIF
ENDIF
!
!-----
!
! SEDIMENT
!
IF(S3D_SEDI) THEN
!
! COMPUTES THE SEDIMENT SETTLING VELOCITY
!
  CALL VITCHU(S3D_WCHU,S3D_WCHU0,U,V,
& S3D_TURBA,S3D_TURBB,T3_01,T3_02,T3_03,SVIDE,MESH3D,IELM3,
& NPOIN2,NPOIN3,
& NPLAN,NTRAC,MSK,MASKEL,UETCAR,TA,HN,S3D_FLOC,
& S3D_FLOC_TYPE,
& S3D_HINDER,S3D_HIND_TYPE,S3D_CGEL,S3D_CINI)

```

```

!
!   BOUNDARY CONDITIONS FOR THE SEDIMENTOLOGY
!
IF(DEBUG.GT.0) WRITE(LU,*) 'APPEL DE CLSEDI'
!GA: CLSEDI HAS BEEN MODIFIED TO ALLOW TWO SEDIMENT CLASSES
IF(S3D_MIXTE) THEN

    DO ITRAC = NTRAC-1,NTRAC

        CALL CLSEDI
&      (ATABOF%ADR(ITRAC)%P%R,BTABOF%ADR(ITRAC)%P%R,
&      S3D_WCHU%R,
&      Z, H, DELTAR%R, T3_01, T3_02%R,
&      S3D_EPAI, S3D_CFDEP,S3D_CONC, S3D_HDEP%R, S3D_FLUER%R,
&      S3D_FLUDPT%R, LITABF%ADR(ITRAC)%P%I,
&      KLOG, NPOIN3, NPOIN2, NPLAN, S3D_NCOUCH,
&      DT, RHO0, S3D_RHOS,
&      S3D_TOCD,S3D_MPART,S3D_TOCE,UETCAR%R,
&      GRAV,S3D_SEDCO,S3D_DMOY,S3D_CREF,ZREF,CF,S3D_AC,
&      S3D_KSPRATIO,S3D_ICR,S3D_ICQ,
&      RUGOF,S3D_SETDEP,S3D_HSED,
&      S3D_WCS%R, S3D_EPAICO%R, S3D_EPAINCO%R, S3D_MIXTE,
&      S3D_SEDNCO, S3D_FLUDPTC%R, S3D_FLUDPTNC%R, S3D_FLUERC%R,
&      S3D_FLUERNC%R, NTRAC, ITRAC)
!   ATABOF AND BTABOF ARE NO LONGER 0 FOLLOWING CLSEDI
    ATABOF%ADR(ITRAC)%P%TYPR='Q'
    BTABOF%ADR(ITRAC)%P%TYPR='Q'

    ENDDO

ELSEIF (S3D_SEDCO.OR.S3D_SEDNCO) THEN

    CALL CLSEDI
&      (ATABOF%ADR(NTRAC)%P%R,BTABOF%ADR(NTRAC)%P%R,
&      S3D_WCHU%R,
&      Z, H, DELTAR%R, T3_01, T3_02%R,
&      S3D_EPAI, S3D_CFDEP,S3D_CONC, S3D_HDEP%R, S3D_FLUER%R,
&      S3D_FLUDPT%R, LITABF%ADR(NTRAC)%P%I,
&      KLOG, NPOIN3, NPOIN2, NPLAN, S3D_NCOUCH,
&      DT, RHO0, S3D_RHOS,
&      S3D_TOCD,S3D_MPART,S3D_TOCE,UETCAR%R,
&      GRAV,S3D_SEDCO,S3D_DMOY,S3D_CREF,ZREF,CF,S3D_AC,S3D_KSPRATIO,
&      S3D_ICR,S3D_ICQ,RUGOF,S3D_SETDEP,S3D_HSED,
&      S3D_WCS%R, S3D_EPAICO%R, S3D_EPAINCO%R, S3D_MIXTE, S3D_SEDNCO,
&      S3D_FLUDPTC%R, S3D_FLUDPTNC%R, S3D_FLUERC%R, S3D_FLUERNC%R,
&      NTRAC, ITRAC)
!
!   ATABOF AND BTABOF ARE NO LONGER 0 FOLLOWING CLSEDI
    ATABOF%ADR(NTRAC)%P%TYPR='Q'
    BTABOF%ADR(NTRAC)%P%TYPR='Q'
!
ELSE
!
    WRITE(LU,*) ' '
    WRITE(LU,*) 'SEDI3D : ERROR ON SEDIMENT KEY WORD'
    CALL PLANTE(1)
    STOP
!
ENDIF

IF(DEBUG.GT.0) WRITE(LU,*) 'RETOUR DE CLSEDI'
ENDIF
!

```

```

! PREPARING BOUNDARY CONDITIONS FOR THOMPSON METHOD
!
IF (THOMFR.AND.NFRLIQ.GT.0) THEN
!
CALL CPSTVC(H,T2_01)
CALL PREBOR(HBOR%R,UBOR2D%R,VBOR2D%R,TABORL,U2D%R,V2D%R,H%R,
& T2_01%R,TA,MESH2D%NBOR%I,
& MESH2D%NPOIN,MESH2D%NPTFR,
! & NTRAC SET TO ZERO PROVISIONALLY
& 0,NFRLIQ,FRTYPE,NUMLIQ%I)
! RESTORING USER BOUNDARY CONDITIONS BEFORE CALLING BORD3D
! TO AVOID UNDUE CALLS TO SL3, ETC.
CALL THOMPS_BC(3)
!
ENDIF
!
! UPDATES BOUNDARY CONDITION VALUES
!
IF (DEBUG.GT.0) WRITE(LU,*) 'APPEL DE BORD3D'
CALL BORD3D(NFRLIQ)
IF (DEBUG.GT.0) WRITE(LU,*) 'RETOUR DE BORD3D'
!
IF (THOMFR.AND.NFRLIQ.GT.0) THEN
!
NOW THAT BORD3D HAS BEEN CALLED
CHANGING AGAIN BOUNDARY CONDITIONS FOR THOMPSON
CALL THOMPS_BC(2)
!
ENDIF
!
!!! First step of immersed boundary method: mask boundary node
!
! modified to use PRIVE arrays (3,4=IBM nodes,2=zf_orig)
if (LT.eq.1) then
CALL MASK_IB(PRIVE%ADR(3)%P,N_IB,
& PRIVE%ADR(4)%P,N_INSIDE_IB,
& PRIVE%ADR(2)%P)
endif
!
!!! First step of immersed boundary method: mask boundary node
!
! BOUNDARY CONDITIONS FOR THE VELOCITY ON LATERAL BOUNDARIES
!
IF (DEBUG.GT.0) WRITE(LU,*) 'APPEL DE TBORD'
CALL TBORD(AUBORL%R,
& RUGOL%R,
& MESH2D%DISBOR%R,MESH2D%NELBOR%I,MESH2D%NULONE%I,
& MESH2D%IKLE%I,NELMAX2,
& U%R,V%R,W%R,
& NBOR2%I,NPOIN2,NPLAN,NPTFR2,DNUVIH,DNUVIV,
& KARMAN,LISRUL,KFROTL,
& UETCAL%R,NONHYD,
& T2_02%R,MESH2D)
IF (KFROTL.EQ.0) THEN
AUBORL%TYPR='O'
ELSE
AUBORL%TYPR='Q'
ENDIF
IF (DEBUG.GT.0) WRITE(LU,*) 'RETOUR DE TBORD, APPEL DE TFOND'
!
! BOUNDARY CONDITIONS FOR THE VELOCITY ON THE BOTTOM
!
CALL TFOND(AUBORF%R,

```



```

&      CF%R,UN2D%R,VN2D%R,U%R,V%R,W%R,KARMAN,
&      LISRU,F,DNUVIV,Z,NPOIN2,KFROT,RUGOF%R,UETCAR%R,
&      NONHYD,OPTBAN,HN%R,GRAV,IPBOT%I,NPLAN)
AUBORF%TYPR='Q'
IF(DEBUG.GT.0) WRITE(LU,*) 'RETOUR DE TFOND'
!
! BOUNDARY CONDITIONS FOR K-EPSILON MODEL + COMPUTES CONSTRAINTS
! AT THE BOTTOM AND LATERAL BOUNDARIES IF K-EPSILON IS REQUIRED
!
IF(ITURBV.EQ.3.OR.ITURBH.EQ.3) THEN
  IF(DEBUG.GT.0) WRITE(LU,*) 'APPEL DE KEPCL3'
  CALL KEPCL3(KBORF%R,EBORF%R,LIKBOF%I,LIEBOF%I,
&      KBORL%R,EBORL%R,LIKBOL%I,LIEBOL%I,LIUBOL%I,
&      KBORS%R,EBORS%R,
&      LIKBOS%I,LIEBOS%I,
&      MESH2D%DISBOR%R,AK%R,H%R,ZPROP%R,
&      NBOR2%I,NPOIN2,NPLAN,NPTFR2,
&      KARMAN,CMU,
&      KMIN,EMIN,
&      KENT,KENTU,KSORT,KADH,KLOG,
&      UETCAR%R,FICT)
  IF(DEBUG.GT.0) WRITE(LU,*) 'RETOUR DE KEPCL3'
!
ELSEIF(ITURBV.EQ.7.OR.ITURBH.EQ.7) THEN
!
  IF(DEBUG.GT.0) WRITE(LU,*) 'APPEL DE KOMCL3'
  CALL KOMCL3(KBORF%R,EBORF%R,LIKBOF%I,LIEBOF%I,LIUBOF%I,
&      KBORL%R,EBORL%R,LIKBOL%I,LIEBOL%I,LIUBOL%I,
&      EBORS%R,LIEBOS%I,
&      MESH2D%DISBOR%R,AK%R,
&      U%R,V%R,H%R,ZPROP%R,
&      NBOR2%I,NPOIN2,NPLAN,NPTFR2,
&      KARMAN,BETAS,OMSTAR,
&      KMIN,EMIN,
&      KENTU,KENT,KADH,KLOG,UETCAR%R,UETCAL%R)
  IF(DEBUG.GT.0) WRITE(LU,*) 'RETOUR DE KOMCL3'
!
ELSEIF(ITURBV.EQ.5.OR.ITURBV.EQ.9) THEN
!
  IF(DEBUG.GT.0) WRITE(LU,*) 'APPEL DE SACL3'
  CALL SACL3(NUBORF%R,LINUBOF%I,
&      NUBORL%R,LINUBOL%I,LIUBOL%I,
&      H%R,ZPROP%R,
&      NBOR2%I,NPOIN2,NPLAN,NPTFR2,
&      KARMAN,UETCAR%R,NUMIN,
&      KENT,KENTU,KSORT,KADH,KLOG,FICT)
!
  IF(DEBUG.GT.0) WRITE(LU,*) 'RETOUR DE SACL3'
ENDIF
!
! CLIPS HBOR
!
IF(OPTBAN.EQ.2) THEN
  CALL CLIP(HBOR,HMIN,.TRUE.,1.D6,.FALSE.,0)
ENDIF
!
!-----
!
! THOMPSON BOUNDARY CONDITIONS
!
IF(THOMFR) THEN
!
  IF(DEBUG.GT.0) WRITE(LU,*) 'APPEL DE THOMPS'

```

```

! T2_01 IS HERE A VALUE OF H SAVED BEFORE CALLING BORD3D
CALL THOMPS(HBOR%R,UBOR2D%R,VBOR2D%R,TABORL,U2D,V2D,T2_01,
& TA,ZF,MESH2D%X%R,MESH2D%Y%R,MESH2D%NBOR%I,
& FRTYPE,T2_02,T2_03,T2_04,T2_06,T2_07,
& LIHBOR%I,LIUBOL%I,LIVBOL%I,IT1%I,
& T2_08%R,T2_09%R,W1%R,T2_21,T2_22,T2_23,
& TAC,T2_10,MESH2D%SURDET%R,MESH2D%IKLE%I,
& MESH2D%IFABOR%I,MESH2D%NELEM,MESH2D,
& MESH2D%XNEBOR%R,MESH2D%YNEBOR%R,
! NTRAC SET TO ZERO
& MESH2D%NPOIN,MESH2D%NPTFR,DT,GRAV,0 ,
& NFRLIQ,KENT,KENTU,MSK,MASKEL,
& MESH2D%NELMAX,1,T2_11%R,NUMLIQ%I,MAT2D%ADR(1)%P%X%R,
& T2_12%R,T2_13%R,T2_14%R,IT3,IT4,
& T2_15,T2_16,T2_17,T2_18,T2_19,T2_20,T3_01)
IF(DEBUG.GT.0) WRITE(LU,*) 'RETOUR DE THOMPS'
!
! DUPLICATING ON THE VERTICAL
!
IF(DEBUG.GT.0) WRITE(LU,*) 'APPEL DE THOMPS_2DTO3D'
CALL THOMPS_2DTO3D
IF(DEBUG.GT.0) WRITE(LU,*) 'RETOUR DE THOMPS_2DTO3D'
!
ENDIF
!
!-----
! SOURCE TERMS
!
IF(NPTSCE.GT.0) THEN
CALL FINDKSCE(NPOIN2,NPLAN,Z3%R,NPTSCE,ISCE,ZSCE,KSCE,INFOGR)
ENDIF
IF(NBUSE.GT.0) THEN
CALL FINDKSCE(NPOIN2,NPLAN,Z3%R,NBUSE,ENTBUS,ALTBUS%R,
& KENTBUS,INFOGR)
CALL FINDKSCE(NPOIN2,NPLAN,Z3%R,NBUSE,SORBUS,ALTBUS%R,
& KSORBUS,INFOGR)
ENDIF
!
IF(DEBUG.GT.0) WRITE(LU,*) 'APPEL DE TRISOU'
CALL TRISOU
& (S0U%R,S0V%R, S0U,S0V,UN%R,VN%R,X,Y,Z,
& T3_01%R, DELTAR, MESH3D, FCOR, CORIOL, NTRAC,
& AT, SURFA2%R, T3_02%R, T3_02, W1%R,
& MESH3D%M%X%R(1:6*NELEM3),MESH3D%M%X%R(6*NELEM3+1:12*NELEM3),
& GRAV, NPOIN3, NELEM3, NPOIN2, NELEM2, NPLAN, NETAGE,
& IKLE3%I, LV, MSK, MASKEL%R, INCHYD,
& VOLU,SVIDE,IELM3,MASKEL,NREJEU,ISCE,KSCE,QSCE2,
& U_SCE%R,V_SCE%R,
& GRADZS%ADR(1)%P,GRADZS%ADR(2)%P,MESH2D,
& T3_03, T3_03%R, T3_04, T3_04%R, LONGIT,
& YASEM3D,SCHCVI,DENLAW,FXH,FYH,COUROU,NPTH,T3D_FILES,T3DBI1)
IF(DEBUG.GT.0) WRITE(LU,*) 'RETOUR DE TRISOU, APPEL DE SOURCE'
!
!!! Second step of immersed boundary method: compute source term
CALL SOURCE_IB(S0U,S0V,S0W,S1U,S1V,S1W,
& U,V,WS,W,
& VOLU,VOLUN,T3_01,T3_02,
& NPOIN3,NTRAC,LT,AT,DT,PRIVE,NONHYD,
ccc & IMMERSED_BOUNDARY,N_IB,
& N_IB,
& SVIDE,MESH3D,IELM3,MSK,MASKEL,PH)
!

```

```

      IF(DEBUG.GT.0) WRITE(LU,*) 'RETOUR DE SOURCE'
!!! Second step of immersed boundary method: compute source term
!
!   SAVES BOUNDARY VALUES FOR TIME TN
!
      IF(NSOUSI.GT.1) THEN
        DO IP=1,NPTFR3
          UBORSAVE%R(IP)=UN%R(NBOR3%I(IP))
          VBORSAVE%R(IP)=VN%R(NBOR3%I(IP))
        ENDDO
        IF(NONHYD) THEN
          DO IP=1,NPTFR3
            WBORSAVE%R(IP)=WN%R(NBOR3%I(IP))
          ENDDO
        ENDIF
        IF(ITURBV.EQ.3.OR.ITURBH.EQ.3.OR.
& ITURBV.EQ.7.OR.ITURBH.EQ.7) THEN
          DO IP=1,NPTFR3
            KBORSAVE%R(IP)=AKN%R(NBOR3%I(IP))
            EBORSAVE%R(IP)=EPN%R(NBOR3%I(IP))
          ENDDO
        ELSEIF(ITURBV.EQ.5.OR.ITURBV.EQ.9) THEN
          DO IP=1,NPTFR3
            NUBORSAVE%R(IP)=NUN%R(NBOR3%I(IP))
          ENDDO
        ENDIF
        IF(NTRAC.GT.0) THEN
          DO ITRAC=1,NTRAC
            DO IP=1,NPTFR3
              TRBORSAVE%ADR(ITRAC)%P%R(IP)=
& TRN%ADR(ITRAC)%P%R(NBOR3%I(IP))
            ENDDO
          ENDDO
        ENDIF
      ENDIF
!
!=====
! THE SUB-ITERATIONS LOOP BEGINS HERE
!=====
!
      SUBITER: DO ISOUSI = 1,NSOUSI
!
!if defined COMPAD
      CALL AD_TELEMAC3D_SUBITERATION_BEGIN
!endif
!
!   RESTORES BOUNDARY VALUES FOR TIME TN
!
      IF(ISOUSI.GT.1) THEN
        DO IP=1,NPTFR3
          UN%R(NBOR3%I(IP))=UBORSAVE%R(IP)
          VN%R(NBOR3%I(IP))=VBORSAVE%R(IP)
        ENDDO
        IF(NONHYD) THEN
          DO IP=1,NPTFR3
            WN%R(NBOR3%I(IP))=WBORSAVE%R(IP)
          ENDDO
        ENDIF
        IF(ITURBV.EQ.3.OR.ITURBH.EQ.3.OR.
& ITURBV.EQ.7.OR.ITURBH.EQ.7) THEN
          DO IP=1,NPTFR3
            AKN%R(NBOR3%I(IP))=KBORSAVE%R(IP)
            EPN%R(NBOR3%I(IP))=EBORSAVE%R(IP)

```

```

        ENDDO
    ELSEIF(ITURBV.EQ.5.OR.ITURBV.EQ.9) THEN
        DO IP=1,NPTFR3
            NUN%R(NBOR3%I(IP))=NUBORSAVE%R(IP)
        ENDDO
    ENDIF
    IF(NTRAC.GT.0) THEN
        DO ITRAC=1,NTRAC
            DO IP=1,NPTFR3
                TRN%ADR(ITRAC)%P%R(NBOR3%I(IP))=
&         TRBORSAVE%ADR(ITRAC)%P%R(IP)
            ENDDO
        ENDDO
    ENDIF
ENDIF
ENDIF

!
!   BUILDS THE MESH FOR PROPAGATION STEP
!
    IF(DEBUG.GT.0) WRITE(LU,*) 'APPEL DE MESH_PROP'
    CALL MESH_PROP(HPROP,HN,H,PROLIN,HAULIN,TETAH,NSOUSI,ZPROP,
&         IPBOT,NPOIN2,NPLAN,OPTBAN,SIGMAG,OPT_HNEG,
&         MESH3D,VOLU3D,VOLU3DPAR,
&         UNSV3D,MASKEL,IELM3)
    IF(DEBUG.GT.0) WRITE(LU,*) 'RETOUR DE MESH_PROP'

!
    IF(ISOUSI.GT.1) THEN
!   REBUILDS THE INITIAL MESH
!   NOTE: EVOLUTION OF ZF IS NOT TAKEN INTO ACCOUNT HERE - INVESTIGATE
        CALL CALCOT(Z,HN%R)
        CALL OS('X=Y',X=VOLU,Y=VOLUN)
        IF(NCSIZE.GT.1) CALL OS('X=Y',X=VOLUPAR,Y=VOLUNPAR)
        CALL GRAD2D(GRADZF%ADR(1)%P,GRADZF%ADR(2)%P,ZPROP,NPLAN,SVIDE,
&         UNSV2D,T2_02,T2_03,T2_04,
&         IELM2H,MESH2D,MSK,MASKEL)
        CALL FSGRAD(GRADZS,ZFLATS,Z(NPOIN3-NPOIN2+1:NPOIN3),
&         ZF,IELM2H,MESH2D,MSK,MASKEL,
&         UNSV2D,T2_01,NPOIN2,OPTBAN,SVIDE)
    ENDIF

!
!   SOURCES AND SINKS OF WATER
!
!   TEMPORARILY PUTS ZPROP IN MESH3D%Z
    SAVEZ =>MESH3D%Z%R
    MESH3D%Z%R=>ZPROP%R
    IF(DEBUG.GT.0) WRITE(LU,*) 'APPEL DE SOURCES_SINKS'
    CALL SOURCES_SINKS
    IF(DEBUG.GT.0) WRITE(LU,*) 'RETOUR DE SOURCES_SINKS'

!
    IF(INCLUS(COUPPING,'TOMAWACT3D')) THEN
!   ADD THE NEW TERMS ASSOCIATED WITH THE USTOKES AND VSTOKES
!   INTEGRATED OVER DEPTH
        CALL OS('X=YZ',X=DUS2D,Y=US2D,Z=H)
        CALL VECTOR(DUS2DX,'','GRADF',X',IELMH,1.D0,DUS2D,
&         SVIDE,SVIDE,SVIDE,SVIDE,SVIDE,MESH2D,.FALSE.,MASKEL,
&         ASSPAR=.TRUE.)

!
        CALL OS('X=YZ',X=DVS2D,Y=VS2D,Z=H)
        CALL VECTOR(DVS2DY,'','GRADF',Y',IELMH,1.D0,DVS2D,
&         SVIDE,SVIDE,SVIDE,SVIDE,SVIDE,MESH2D,.FALSE.,MASKEL,
&         ASSPAR=.TRUE.)

!
        CALL OS('X=X-Y',X=SMH,Y=DUS2DX)
        CALL OS('X=X-Y',X=SMH,Y=DVS2DY)

```

```

ENDIF
! RESTORES Z
MESH3D%Z%R=>SAVEZ

IF(BEDBOU)THEN
  IF(DEBUG.GT.0) WRITE(LU,*) 'DEUXIEME APPEL DE BED_FLUXES'
  CALL BED_FLUXES
  IF(DEBUG.GT.0) WRITE(LU,*) 'RETOUR DE BED_FLUXES'
ENDIF
!
! SETS ADVECTION AND DIFFUSION PARAMETERS TO MONITOR CVDF3D
! DIFFUSION AND SOURCE TERMS ARE DONE IN WAVE_EQUATION
! IN CVDF3D (THIS IS DONE IN WAVE_EQUATION)
!
! DIFFUSION OF U AND V IS DONE IN WAVE_EQUATION
SCHDVI_HOR = 0
SCHDVI_VER = SCHDVI
!
SCHCVI_HOR = SCHCVI
SCHCVI_VER = SCHCVI
! ADVECTION IS NOT DONE AT THE FIRST TIME-STEP (THIS WAS VERSION 6.1)
! IF(LT.EQ.1.AND.ISOUSH.EQ.1) THEN
!   SCHCVI_HOR = 0
!   SCHCVI_VER = 0
! ENDIF
!
! WHEN SCHCVI=ADV_SUP DIFF3D IS CALLED AND
! SOURCE TERMS WOULD BE TREATED TWICE
YAS0U=.FALSE.
YAS1U=.FALSE.
!
!-----
! ADVECTION-DIFFUSION STEP FOR VELOCITY COMPONENTS
!-----
!
! HERE DIFFUSION IS DONE IN MESH3D%Z, IT IS DIFFERENT FROM ZPROP IF
! FROM THE SECOND SUB-ITERATION ON. SO IPBOT IS REDONE HERE
!
IF(ISOUSH.GT.1) THEN
  CALL PLANE_BOTTOM(IPBOT%I,Z,NPOIN2,NPLAN,SIGMAG,OPTBAN)
ENDIF
!
IF(INFOGR) THEN
  IF (NONHYD) THEN
    CALL MITTIT(17,AT,LT)
  ELSE
    CALL MITTIT(4,AT,LT)
  ENDIF
ENDIF
!
SIGMAU = 1.D0
UMIN   = 0.D0
UMAX   = 1.D0
CLUMIN = .FALSE.
CLUMAX = .FALSE.
YAWCHU = .FALSE.
! YASEM3D = DONE IN TRISOU
NEWDIF=.TRUE.
!
IF(DEBUG.GT.0) WRITE(LU,*) 'APPEL DE CVDF3D POUR U'
CALL CVDF3D
& (UD,UC,UN,VISCVI,SIGMAU,S0U,YAS0U,S1U,YAS1U,
& UBORL,UBORF,UBORS,AUBORL,AUBORF,AUBORS,

```

```

& BUBORL, BUBORF, BUBORS, LIUBOL, LIUBOF, LIUBOS,
& FLUX%R(1), FLUEXT, FLUEXTPAR, UMIN, CLUMIN, UMAX, CLUMAX,
& SCHCVI_HOR, SCHDVI_HOR, SLVDVI, TRBAVI, INFOGR, NEWDIF,
& CALCFLU(1), T2_01, T2_03,
& T3_01, T3_02, T3_03, T3_04, MESH3D, IKLE3, MASKEL, MTRA1,
& NPTFR3, MMURD, MURD_TF, VOLU3D, VOLU3DPAR, VOLU3D, VOLU3DPAR,
& NBOR3, NPOIN3, NPOIN2, DT, MSK, NELEM3,
& NPLAN, IELM3, MSUPG, IELM2H, IELM2V, MDIFF, MTRA2,
& INCHYD, MASKBR, MASKPT, SMU, YASEM3D, SVIDE, IT1,
& TRAV3, MESH2D, OPTBAN, TETADI, YAWCHU, WCHU, S3D_WCHU,
& AGGLOD, NSCE, SOURCES, U_SCE%R, NUMLIQ%I, DIRFLU, NFRLIQ,
& VOLUT, ZT, ZPROP, CALCRAIN(1), PLUIE, PARAPLUIE, 0.D0, FLODEL, FLOPAR,
& SIGMAG, IPBOT%I, MAXADV, FLUDPT, FLUDP, FLUER, VOLU2D, V2DPAR, SETDEP,
& S3D_FLUDPT, S3D_FLUDP, S3D_FLUER, S3D_SETDEP, OPTSOU, ZN%R,
& OPTADV_VI, NCO_DIST, NSP_DIST, TB2)
IF(DEBUG.GT.0) WRITE(LU,*) 'RETOUR DE CVDF3D POUR U'
!
SIGMAV = 1.D0
VMIN = 0.D0
VMAX = 1.D0
CLVMIN = .FALSE.
CLVMAX = .FALSE.
YAWCHU = .FALSE.
! YASEM3D = DONE IN TRISOU
! MDIFF ALREADY COMPUTED FOR U
NEWDIF=.FALSE.
!
IF(DEBUG.GT.0) WRITE(LU,*) 'APPEL DE CVDF3D POUR V'
! USE OF AUBORL,AUBORF,AUBORS IS NOT A MISTAKE
CALL CVDF3D
& (VD, VC, VN, VISCVI, SIGMAV, S0V, YAS0U, S1V, YAS1U,
& VBORL, VBORF, VBORS, AUBORL, AUBORF, AUBORS,
& BVBORL, BVBORF, BVBORS, LIVBOL, LIVBOF, LIVBOS,
& FLUX%R(2), FLUEXT, FLUEXTPAR, VMIN, CLVMIN, VMAX, CLVMAX,
& SCHCVI_HOR, SCHDVI_HOR, SLVDVI, TRBAVI, INFOGR, NEWDIF,
& CALCFLU(2), T2_01, T2_03,
& T3_01, T3_02, T3_03, T3_04, MESH3D, IKLE3, MASKEL, MTRA1,
& NPTFR3, MMURD, MURD_TF, VOLU3D, VOLU3DPAR, VOLU3D, VOLU3DPAR,
& NBOR3, NPOIN3, NPOIN2, DT, MSK, NELEM3,
& NPLAN, IELM3, MSUPG, IELM2H, IELM2V, MDIFF, MTRA2,
& INCHYD, MASKBR, MASKPT, SMV, YASEM3D, SVIDE, IT1,
& TRAV3, MESH2D, OPTBAN, TETADI, YAWCHU, WCHU, S3D_WCHU,
& AGGLOD, NSCE, SOURCES, V_SCE%R, NUMLIQ%I, DIRFLU, NFRLIQ,
& VOLUT, ZT, ZPROP, CALCRAIN(2), PLUIE, PARAPLUIE, 0.D0, FLODEL, FLOPAR,
& SIGMAG, IPBOT%I, MAXADV, FLUDPT, FLUDP, FLUER, VOLU2D,
& V2DPAR, SETDEP, S3D_FLUDPT, S3D_FLUDP, S3D_FLUER, S3D_SETDEP, OPTSOU,
& ZN%R, OPTADV_VI, NCO_DIST, NSP_DIST, TB2)
IF(DEBUG.GT.0) WRITE(LU,*) 'RETOUR DE CVDF3D POUR V'
!
IF(NONHYD) THEN
!
SIGMAW = 1.D0
WMIN = 0.D0
WMAX = 1.D0
CLWMIN = .FALSE.
CLWMAX = .FALSE.
YASEM3D=.FALSE.
YAWCHU = .FALSE.
NEWDIF=.TRUE.
! TETADI MAY BE EQUAL TO 2 FOR U AND V, WHEN THE WAVE EQUATION
! IS USED - NOT DONE ON W SO FAR
TETADIVER = MIN(TETADI, 1.D0)
!

```



```

    IF(DEBUG.GT.0) WRITE(LU,*) 'APPEL DE CVDF3D POUR W'
!   USE OF AUBORL,AUBORF,AUBORS IS NOT A MISTAKE
    CALL CVDF3D
& (WD,WC,WN,VISCVI,SIGMAW,S0W,.TRUE.,S1W,.TRUE.,
& WBORL, WBORF, WBORS, AUBORL, AUBORF, AUBORS,
& BWBORL, BWBORF, BWBORS, LIWBOL, LIWBOF, LIWBOS,
& FLUX%R(3), FLUEXT,FLUEXTPAR,WMIN,CLWMIN,WMAX,CLWMAX,
& SCHCVI_VER,SCHDVI_VER,SLVDVI,TRBAVI,INFOGR,NEWDIR,
& CALCFLU(3),T2_01,T2_03,
& T3_01,T3_02,T3_03,T3_04, MESH3D , IKLE3 , MASKEL , MTRA1,
& NPTFR3,MMURD,MURD_TF,VOLU3D,VOLU3DPAR,VOLU3D,VOLU3DPAR,
& NBOR3,NPOIN3,NPOIN2,DT,MSK,NELEM3,
& NPLAN,IELM3,MSUPG,IELM2H,IELM2V,MDIFF,MTRA2,
& INCHYD,MASKBR,MASKPT,SEM3D,YASEM3D,SVIDE,IT1,
& TRAV3,MESH2D,OPTBAN,
& TETADIVER,YAWCHU,WCHU,S3D_WCHU,AGGLOD,NSCE,SOURCES,W_SCE%R,
& NUMLIQ%,DIRFLU,NFRLIQ,VOLUT,ZT,ZPROP,CALCRAIN(3),PLUIE,
& PARAPLUIE,0.D0, FLODEL,FLOPAR,
& SIGMAG,IPBOT%i,MAXADV,FLUDPT,FLUDP,FLUER,VOLU2D,
& V2DPAR,SETDEP,S3D_FLUDPT,S3D_FLUDP,S3D_FLUER,S3D_SETDEP,OPTSOU,
& ZN%R,OPTADV_VI,NCO_DIST,NSP_DIST,TB2)
!
    IF(DEBUG.GT.0) WRITE(LU,*) 'RETOUR DE CVDF3D POUR W'
    ENDIF
!
!-----
! DIFFUSION AND PROPAGATION STEP BY WAVE EQUATION
!-----
!
    IF(INFOGR) THEN
        CALL MITTIT(6,AT,LT)
    ENDIF
!   TEMPORARILY PUTS ZPROP IN MESH3D%Z
    SAVEZ =>MESH3D%Z%R
!   ALL PROPAGATION WILL BE DONE WITH ZPROP INSTEAD OF Z
    MESH3D%Z%R=>ZPROP%R
!   IPBOT HAS BEEN MODIFIED FOR CVDF3D, IT IS RESTORED HERE WITH ZPROP
    IF(ISOUSI.GT.1) THEN
        CALL PLANE_BOTTOM(IPBOT%i,ZPROP%R,NPOIN2,NPLAN,SIGMAG,OPTBAN)
    ENDIF
    IF(DEBUG.GT.0) WRITE(LU,*) 'APPEL DE WAVE_EQUATION'
!
    CALL WAVE_EQUATION(ISOUSI)
!
    IF(DEBUG.GT.0) WRITE(LU,*) 'RETOUR DE WAVE_EQUATION'
!
    RESTORES Z
    MESH3D%Z%R=>SAVEZ
!
!-----
! CLIPS NEGATIVE DEPTHS
!-----
!
    IF(DEBUG.GT.0) WRITE(LU,*) 'APPEL DE CORRECTION_DEPTH_3D'
    CALL CORRECTION_DEPTH_3D(MESH2D%GLOSEG%i,MESH2D%GLOSEG%DIM1)
    IF(DEBUG.GT.0) WRITE(LU,*) 'RETOUR DE CORRECTION_DEPTH_3D'
!
!-----
! BUILDS NEW MESH WITH THE NEW FREE SURFACE
!-----
!
    IF(DEBUG.GT.0) WRITE(LU,*) 'APPEL DE CALCOT'
    CALL CALCOT(Z,H%R)

```

```

! IPBOT UPDATED ACCORDINGLY, E.G. FOR CALLS TO PREDIV AND CVDF3D
CALL PLANE_BOTTOM(IPBOT%I,Z,NPOIN2,NPLAN,SIGMAG,OPTBAN)
IF(DEBUG.GT.0) WRITE(LU,*) 'RETOUR DE CALCOT'
!
!-----
!
! GENERATES DATA FOR DELWAQ
!
! IF(INCLUS(COUPPING,'DELWAQ')) THEN
!
! COMPUTING FLODEL (POINT TO POINT FLUXES)
!
! FORMUL = 'VGRADP    HOR'
! FORMUL(8:8) = '2'
! ADVECTION FLUXES PER NODE (STORED IN MESH3D%W%R)
! THE ASSEMBLED RESULT IN T3_04 IS NOT USED HERE
! SAVEZ    =>MESH3D%Z%R
! MESH3D%Z%R=>ZPROP%R
! IF(DEBUG.GT.0) WRITE(LU,*) 'APPEL DE VECTOR'
! CALL VECTOR(T3_04,'=',FORMUL,IELM3,-1.D0,DM1,SVIDE,GRAZCO,
! &          UCONV,VCONV,SVIDE,MESH3D,MSK,MASKEL)
! IF(DEBUG.GT.0) WRITE(LU,*) 'RETOUR DE VECTOR'
! CALL FLUX_EF_VF_3D(FLODEL%R,MESH2D%W%R,MESH3D%W%R,
! &          MESH2D%NSEG,NELEM2,NELMAX2,
! &          MESH2D,TRUE.,
! &          2,2,MESH3D%TYPELM+1,NPLAN,
! !          2: HORIZONTAL FLUXES FROM TOP TO BOTTOM
! &          MESH3D%IKLE%I,MESH3D%NELMAX,MESH2D%KNOLG%I)
! ! FLUX LIMITATION (FLULIM IS 2D, SO NUMBERING FROM TOP TO BOTTOM
! !          MAKES NO PROBLEM)
! IF(OPT_HNEG.EQ.2) THEN
!   CALL FLUX3DLIM(FLODEL%R,FLULIM%R,NPLAN,MESH2D%NSEG,NPOIN2,1)
! ENDIF
! MESH3D%Z%R=>SAVEZ
!
! NOW CALLING TEL4DELWAQ WITH FLODEL COMPLETED
!
! SENDS UCONV AND VCONV AS ADVECTING FIELD (SEE WAVE_EQUATION)
! IF(DEBUG.GT.0) WRITE(LU,*) 'APPEL DE TEL4DELWAQ'
! CALL TEL4DELWAQ(NPOIN3,NPOIN2,MESH2D%NSEG,
! & MESH2D%IKLE%I,MESH2D%ELTSEG%I,MESH2D%GLOSEG%I,
! & MESH2D%GLOSEG%DIM1,X,Y,MESH3D%NPTFR,LIHBOR%I,MESH3D%NBOR%I,
! & NPLAN,AT,DT,LT,NIT_ORI,H%R,HPROP%R,MESH3D%Z%R,UCONV%R,
! & VCONV%R,TA%ADR(MAX(IND_S,1))%P%R,TA%ADR(MAX(IND_T,1))%P%R,
! & VISCVI%ADR(3)%P%R,TITCAS,
! & T3D_FILES(T3DGEO)%NAME,T3D_FILES(T3DCLI)%NAME,WAQPRD,
! & T3DDL1,T3DDL2,T3DDL3,T3DDL5,T3DDL6,T3DDL7,T3DL11,T3DDL4,
! & T3DDL8,T3DDL9,T3DL10,INFOGR,NELEM2,SALI_DEL,TEMP_DEL,VELO_DEL,
! & DIFF_DEL,MARDAT,MARTIM,FLODEL%R,V2DPAR%R,MESH2D%KNOLG%I,
! & T3D_FILES)
! IF(DEBUG.GT.0) WRITE(LU,*) 'RETOUR DE TEL4DELWAQ'
!
! ENDIF
!
!-----
!
! MASKING
!
! IF(ISOUSI.EQ.NSOUSI) THEN
!   IF(MSK) THEN
!     IF(DEBUG.GT.0) WRITE(LU,*) 'APPEL DE MASK3D'
!     IF(MSK) CALL MASK3D(MESH3D%IFABOR%I,MASKEL%R,MASKPT,MASKBR%R,
! &          X2%R,Y2%R,ZF%R,ZFE%R,H%R,HMIN,AT,LT,IT1%I,

```

```

&      MESH3D%NELBOR%,NELMAX2,NELEM2,NPOIN2,MESH2D%NELEB,
&      NPLAN,NETAGE,IELM3,MESH2D)
  IF(DEBUG.GT.0) WRITE(LU,*) 'RETOUR DE MASK3D'
  ENDIF
ENDIF
!
! COMPUTES SURFACE GRADIENTS AT TIME LEVEL N+1 AND DSSUDT
!
  IF(DEBUG.GT.0) WRITE(LU,*) 'APPEL DE FSGRAD'
  CALL FSGRAD(GRADZS,ZFLATS,Z(NPOIN3-NPOIN2+1:NPOIN3),
&      ZF,IELM2H,MESH2D,MSK,MASKEL,
&      UNSV2D,T2_01,NPOIN2,OPTBAN,SVIDE)
  IF(DEBUG.GT.0) WRITE(LU,*) 'RETOUR DE FSGRAD'
!
  CALL OS( 'X=Y-Z ', X=DSSUDT, Y=H, Z=HN )
  CALL OS( 'X=CX ', X=DSSUDT, C=1.D0/DT )
!
! COMPUTES THE VOLUMES ASSOCIATED WITH NODES
!
  CALL VECTOR(VOLU, '=', 'MASBAS ', IELM3, 1.D0-AGGLOH,
&      SVIDE,SVIDE,SVIDE,SVIDE,SVIDE,SVIDE,MESH3D,.FALSE.,MASKEL)
  IF(AGGLOH.GT.1.D-6) THEN
    CALL VECTOR(VOLU, '+', 'MASBAS2 ', IELM3, AGGLOH,
&      SVIDE,SVIDE,SVIDE,SVIDE,SVIDE,SVIDE,MESH3D,.FALSE.,MASKEL)
  ENDIF
  IF(NCSIZE.GT.1) THEN
    CALL OS('X=Y ', X=VOLUPAR, Y=VOLU)
    CALL PARCOM(VOLUPAR, 2, MESH3D)
  ENDIF
!
! IN 2D, ONLY IF MASKING (OTHERWISE NOTHING CHANGED)
!
  IF(MSK) CALL MASBAS2D(VOLU2D,V2DPAR,UNSV2D,
&      IELM2H,MESH2D,MSK,MASKEL,T2_01,SVIDE)
!
!-----
! CONTINUITY STEP (NON-HYDROSTATIC OPTION) IN NEW MESH
!-----
!
  IF(NONHYD.AND..NOT.DPWAVEQ) THEN
!
    IF(DEBUG.GT.0) WRITE(LU,*) 'DANS NONHYDRO1'
    IF(INFOGR) CALL MITTIT(19,AT,LT)
!
    CALL OS( 'X=Y ', X=W, Y=WD )
!
!-----
!
! COMPUTES THE DYNAMIC PRESSURE
!
!   WITH WAVE EQUATION, DYNAMIC PRESSURE HERE IS INCREMENTAL
!   THUS WITHOUT BOUNDARY CONDITIONS
  BC=.NOT.DPWAVEQ
  IF(DEBUG.GT.0) WRITE(LU,*) 'APPEL DE PREDIV'
  CALL PREDIV(DP,U,V,W,INFOGR,BC,1,.TRUE.,.TRUE.,.TRUE.)
  IF(DEBUG.GT.0) WRITE(LU,*) 'RETOUR DE PREDIV'
!
!-----
! VELOCITY PROJECTION STEP
!-----
!
  IF(INFOGR) CALL MITTIT(20,AT,LT)
!

```

```

CALL VELRES(U,V,W,DP,
&      T3_01,T3_02,T3_03,MSK,MASKEL,MESH3D,
&      SVIDE,IELM3,OPTBAN,T3_04,.TRUE.,NPOIN3,NPOIN2,
&      SIGMAG,IPBOT%I,AGGLOH,KSORT,NPTFR3,LIUBOL,CONCOR)
!
!   BOUNDARY CONDITIONS ON W AT THE BOTTOM AND FREE SURFACE
!
!   FREE SURFACE (NOT ALWAYS TO BE DONE, DSSUDT IS SOMETIMES TOO BIG)
!
IF(CLDYN) THEN
!
CALL OV('X=Y ',X=W%R(NPOIN3-NPOIN2+1:NPOIN3), Y=DSSUDT%R,
&      DIM1=NPOIN2)
CALL OV('X=X+YZ ',X=W%R(NPOIN3-NPOIN2+1:NPOIN3),
&      Y=GRADZS%ADR(1)%P%R,
&      Z=U%R(NPOIN3-NPOIN2+1:NPOIN3), DIM1=NPOIN2)
CALL OV('X=X+YZ ',X=W%R(NPOIN3-NPOIN2+1:NPOIN3),
&      Y=GRADZS%ADR(2)%P%R,
&      Z=V%R(NPOIN3-NPOIN2+1:NPOIN3), DIM1=NPOIN2)
!
ENDIF
!
!   BOTTOM
!
IF(VELPROBOT) THEN
IF(SIGMAG.OR.OPTBAN.EQ.1) THEN
DO I=1,NPOIN2
DO IP=0,IPBOT%I(I)
I3D=IP*NPOIN2+I
W%R(I3D)=GRADZF%ADR(1)%P%R(I)*U%R(I3D)
&      +GRADZF%ADR(2)%P%R(I)*V%R(I3D)
ENDDO
ENDDO
ELSE
DO I=1,NPOIN2
W%R(I)=GRADZF%ADR(1)%P%R(I)*U%R(I)
&      +GRADZF%ADR(2)%P%R(I)*V%R(I)
ENDDO
ENDIF
ENDIF
!
!   RE-ENSURES THE DIRICHLET BOUNDARY CONDITIONS AND U.N = 0
!
CALL AIRWIK2(LIHBOR%I, UBORF%R, VBORF%R, WBORF%R,
&      LIUBOF%I, LIVBOF%I, LIWBOF%I,
&      UBORL%R, VBORL%R, WBORL%R,
&      LIUBOL%I, LIVBOL%I, LIWBOL%I,
&      UBORS%R, VBORS%R, WBORS%R,
&      LIUBOS%I, LIVBOS%I, LIWBOS%I,
&      U%R,V%R,W%R,MESH2D%XNEBOR%R,MESH2D%YNEBOR%R,
&      NBOR2%I,NPTFR2,NPLAN,NPOIN2,KENT,KADH,KLOG,KENTU,
&      VELPROLAT)
!
ENDIF ! IF NONHYD
!
=====
! INTERNAL COUPLING WITH GAIA
=====
!
IF( INCLUS(COUPPING,'GAIA ')) THEN
!
!   U AND V WITH 2D STRUCTURE : BOTTOM VELOCITY AS A
!   2D VARIABLE

```

```

CALL CPSTVC(U2D,U)
CALL CPSTVC(V2D,V)
!   TFOND IS CALLED FOR AN UPDATE OF
!   UETCAR at TIME N+1
CALL TFOND(AUBORF%R,
&         CF%R,U2D%R,V2D%R,U%R,V%R,W%R,KARMAN,
&         LISRUF,DNUVIV,Z,NPOIN2,KFROT,RUGOF%R,UETCAR%R,
&         NONHYD,OPTBAN,HN%R,GRAV,IPBOT%I,NPLAN)
!
!   NOW RUNS ONE TURN OF GAIA'S TIME LOOP AND RETURNS CALL
CALL CONFIG_CODE(5)
IF(DEBUG.GT.0) WRITE(LU,*) 'CALL GAIA_STEP'
!
CALL GAIA_STEP(
&   LT,GRAPRD,LISPRD,NIT_ORI,U2D,V2D,H,ZF,
&   UETCAR,DELTAR,CF,RUGOF,CODE1,
&   U,V,AT,VISCVI,DT,CHARR_TEL,SUSP_TEL,
&   RHO0,GRAV,
!   VARIABLES TRANSMITTED FROM TOMAWAC
&   DIRMOY,HM0,TPR5,ORBVEL,.TRUE.)
IF(DEBUG.GT.0) WRITE(LU,*) 'BACK GAIA_STEP'
CALL CONFIG_CODE(1)
!
!   RETRIEVES ORIGINAL U AND V STRUCTURE
CALL CPSTVC(UN,U)
CALL CPSTVC(VN,V)
!
ENDIF
!
=====
! INTERNAL COUPLING WITH SISYPHE
=====
!
IF( INCLUS(COUPPING,'SISYPHE') .AND.
& (PERCOU_SIS*(LT/PERCOU_SIS).EQ.LT.OR.LT.EQ.1) ) THEN
!
!   U AND V WITH 2D STRUCTURE : BOTTOM VELOCITY AS A 2D VARIABLE
CALL CPSTVC(U2D,U)
CALL CPSTVC(V2D,V)
!
!   NOW RUNS ONE TURN OF SISYPHE'S TIME LOOP AND RETURNS
CALL CONFIG_CODE(2)
IBID=1
LBID=.FALSE.
LBID2=.FALSE.
IF(DEBUG.GT.0) WRITE(LU,*) 'APPEL DE SISYPHE'
CALL SISYPHE(1,LT,GRAPRD,LISPRD,NIT_ORI,U2D,V2D,H,HN,ZF,
&   UETCAR,CF,RUGOF,LBID,IBID,LBID2,CODE1,PERCOU_SIS,
&   U,V,AT,VISCVI,DT*PERCOU_SIS,S3D_CHARR,S3D_SUSP,
!   1 PRECLUDES THE USE OF THE 4 FOLLOWING ARGUMENTS
&   FLBOR,1,DM1,UCONV,VCONV,ZCONV,
!   VARIABLES TRANSMITTED FROM TOMAWAC
&   DIRMOY,HM0,TPR5,ORBVEL,.TRUE.)
IF(DEBUG.GT.0) WRITE(LU,*) 'RETOUR DE SISYPHE'
CALL CONFIG_CODE(1)
!
!   S3D_HDEPMUST BE UPDATED BECAUSE SISYPHE CHANGED ZF
IF(S3D_SEDI) CALL OS('X=Y-Z ',X=S3D_HDEP,Y=ZF,Z=ZR)
!
!   RETRIEVES ORIGINAL U AND V STRUCTURE
CALL CPSTVC(UN,U)
CALL CPSTVC(VN,V)
!

```

```

ENDIF
!
!-----
!
! SEDIMENT
!
! IF(NSUSP_TEL.GT.0) THEN
!
!   COMPUTES THE SEDIMENT SETTLING VELOCITY
!
!   CALL COMPUTE_SETTLING_VEL(WCHU,U,V,
! &   T3_01,T3_02,T3_03,SVIDE,MESH3D,IELM3,NPOIN2,NPOIN3,
! &   NPLAN,MSK,MASKEL,UETCAR,TA,HN)
!
!   BOUNDARY CONDITIONS FOR THE
!   SEDIMENTOLOGY
!
!   CALL COMPUTE_BC_SEDI
!
! ENDIF
!
!-----
!
! PREPARING SOURCE TERMS FOR ADVECTION-DIFFUSION STEP
!-----
!
! PREPARING SOURCE TERMS FOR K-EPSILON AND K-OMEGA MODELS
!
! IF(ITURBV.EQ.3.OR.ITURBH.EQ.3.OR.ITURBV.EQ.7.OR.ITURBH.EQ.7) THEN
!
!   IF (INFOGR) CALL MITTIT(7,AT,LT)
!
!   S0AK%TYPR='Q'
!   S0EP%TYPR='Q'
!   S1AK%TYPR='Q'
!   S1EP%TYPR='Q'
!
!   IF(ITURBV.EQ.3.OR.ITURBH.EQ.3) THEN
!
!     IF(DEBUG.GT.0) WRITE(LU,*) 'APPEL DE SOUKEP'
!     CALL SOUKEP(S0AK%R,S0EP%R,S1AK%R,S1EP%R,
! &       U,V,W,DELTAR,RI%R,T3_01,T3_02,T3_03,T3_04,
! &       T3_05,T3_06,T3_07,T3_08,T3_09,
! &       T3_10,AK%R,EP%R,C1,C2,CMU,GRAV,
! &       NPOIN3,MSK,MASKEL,MESH3D,IELM3,SVIDE,
! &       VENT,WIND,NPOIN2,KMIN,PRANDTL)
!     IF(DEBUG.GT.0) WRITE(LU,*) 'RETOUR DE SOUKEP'
!
!   ENDIF
!
!   IF(ITURBV.EQ.7.OR.ITURBH.EQ.7) THEN
!
!     IF(DEBUG.GT.0) WRITE(LU,*) 'APPEL DE SOUKOM'
!     CALL SOUKOM(S0AK,S0EP,S1AK,S1EP,U,V,W,
! &       DELTAR,T3_01,T3_02,T3_03,
! &       T3_04,T3_05,T3_06,T3_07,T3_08,
! &       T3_09,T3_10,T3_12,T3_13,
! &       T3_14,T3_15,T3_16,T3_17,
! &       ROTAT,AK,EP,ALPHA,BETA,BETAS,GRAV,
! &       T3_11,NPOIN3,MSK,MASKEL,MESH3D,IELM3,SVIDE)
!     IF(DEBUG.GT.0) WRITE(LU,*) 'RETOUR DE SOUKOM'
!
!   ENDIF

```



```

!
ELSEIF(ITURBV.EQ.5.OR.ITURBV.EQ.9) THEN
!
  IF (INFOGR) CALL MITTIT(33,AT,LT)
  S0NU%TYPR='Q'
  S1NU%TYPR='Q'
  IF(DEBUG.GT.0) WRITE(LU,*) 'APPEL DE SOUSA'

  CALL SOUSA(S0NU%R,S1NU%R,U,V,W,ROTAN,STRAIN,T3_01,
&          NU,NPOIN3,MSK,MASKEL,MESH3D,
&          IELM3,SVIDE,WDIST,NPOIN2, ITURBV)
!
  IF(DEBUG.GT.0) WRITE(LU,*) 'RETOUR DE SOUSA'
ENDIF
!
! PREPARING SOURCE TERMS FOR TRACERS
!
  IF( (INCLUS(COUPPING,'WAQTEL') ).AND.
&    (13*INT(WAQPROCESS/13).EQ.WAQPROCESS) ) THEN
!    ORDER: NUMBER OF THE PLANES FROM TOP TO BOTTOM
!    THEN NUMBER OF THE 2D NODES
    DO I=1,NPOIN2
      K=1
      THICK4AED2%R(1+(I-1)*NPLAN) = (Z(I+(NPLAN-1)*NPOIN2)
&    - Z(I+(NPLAN-2)*NPOIN2))*0.5D0
      THICK4AED2%R(1+(I-1)*NPLAN) = (Z(I+NPOIN3-NPOIN2)
&    - Z(I+NPOIN3-2*NPOIN2))*0.5D0
      DO K=2,NPLAN-1
        THICK4AED2%R(K+(I-1)*NPLAN) = (Z(I+(NPLAN-K+1)*NPOIN2)
&    - Z(I+(NPLAN-K-1)*NPOIN2))/2.D0
      ENDDO
      K=NPLAN
      THICK4AED2%R(I*NPLAN) = (Z(I+NPOIN2)-Z(I))*0.5D0
    ENDDO
!
    DO I=1,NPOIN2
      BENTH4AED2%I(I) = NPLAN
      DO K=NPLAN,2,-1
        IF(THICK4AED2%R(K+(I-1)*NPLAN).LT.EPS_AED2) THEN
          BENTH4AED2%I(I) = K-1
        ENDIF
      ENDDO
    ENDDO
!
!    ORDER: NUMBER OF THE PLANES FROM TOP TO BOTTOM
!    THEN NUMBER OF THE 2D NODES
    DO I=1,NPOIN2
      DO K=1,NPLAN
        TEMP4AED2%R(K+(I-1)*NPLAN) =
&    TA%ADR(IND_T)%P%R(I+(NPLAN-K)*NPOIN2)
        SALI4AED2%R(K+(I-1)*NPLAN) =
&    TA%ADR(IND_S)%P%R(I+(NPLAN-K)*NPOIN2)
      ENDDO
    ENDDO
!
  ENDIF
!
  IF(DEBUG.GT.0) WRITE(LU,*) 'APPEL DE SOURCE_TRAC'
  IF(NTRAC.GT.0) CALL SOURCE_TRAC
  IF(DEBUG.GT.0) WRITE(LU,*) 'APPEL DE SOURCE_TRAC'
!
!-----
! ADVECTION-DIFFUSION STEP FOR ALL ADVECTED VARIABLES

```

```

!-----
!
! ALL ADVECTION SCHEMES EXCEPT SUPG
!
IF (INFOGR .AND. (.NOT.NONHYD)) CALL MITTIT(9,AT,LT)
IF(DEBUG.GT.0) WRITE(LU,*) 'APPEL DE PREADV'
CALL PREADV(W,WS,ZPROP,ISOUSI,LT,VOLU,VOLUN)
IF(DEBUG.GT.0) WRITE(LU,*) 'RETOUR DE PREADV'
!
!-----
! NOW CVDF3D WILL DO SUPG AND DIFFUSION
!-----
!
IF(ITURBV.EQ.3.OR.ITURBH.EQ.3.OR.ITURBV.EQ.7.OR.ITURBH.EQ.7) THEN
!
CLKMIN = .TRUE.
CLKMAX = .TRUE.
YASEM3D = .FALSE.
YAWCHU = .FALSE.
NEWDIF = .TRUE.
TETATRA=MIN(TETADI,1.D0)
!
IF(DEBUG.GT.0) WRITE(LU,*) 'APPEL DE CVDF3D POUR AK'
CALL CVDF3D
& (AK,AKC,AKN,VISCVI,SIGMAK,S0AK,.TRUE.,S1AK,.TRUE.,
& KBORL,KBORF,KBORS,AKBORL,AKBORF,AKBORS,
& BKBORL,BKBORF,BKBORS,LIKBOL,LIKBOF,LIKBOS,
& FLUX%R(1),FLUEXT,FLUEXTPAR,KMIN,CLKMIN,KMAX,CLKMAX,
& SCHCKE,SCHDKE,SLVDKE,TRBAKE,INFOGR,NEWDIF,CALCFLU(4),
& T2_01,T2_03,
& T3_01,T3_02,T3_03,T3_04,MESH3D,IKLE3,MASKEL,MTRA1,
& NPTFR3,MMURD,MURD_TF,VOLU,VOLUPAR,VOLUN,VOLUNPAR,
& NBOR3,NPOIN3,NPOIN2,DT,MSK,NELEM3,
& NPLAN,IELM3,MSUPG,IELM2H,IELM2V,MDIFF,MTRA2,
& INCHYD,MASKBR,MASKPT,SEM3D,YASEM3D,SVIDE,IT1,
& TRAV3,MESH2D,OPTBAN,TETATRA,
& YAWCHU,WCHU,S3D_WCHU,AGGLOD,NSCE,SOURCES,AK_SCE%R,
& NUMLIQ%I,DIRFLU,NFRLIQ,VOLUT,ZT,ZPROP,CALCRAIN(4),
& PLUIE,PARAPLUIE,0.D0,FLODEL,FLOPAR,SIGMAG,IPBOT%I,MAXADV,
& FLUDPT,FLUDP,FLUER,VOLU2D,V2DPAR,SETDEP,
& S3D_FLUDPT,S3D_FLUDP,S3D_FLUER,S3D_SETDEP,OPTSOU,
& ZN%R,OPTADV_KE,NCO_DIST,NSP_DIST,TB2)
!
IF(DEBUG.GT.0) WRITE(LU,*) 'RETOUR DE CVDF3D POUR AK'
!
CLEMIN = .TRUE.
CLEMAX = .TRUE.
YASEM3D = .FALSE.
YAWCHU = .FALSE.
!
! NEGLECTS MOLECULAR DIFFUSIVITY...
! DIFFUSION MATRIX NOT RECOMPUTED
NEWDIF = .FALSE.
CALL OM('M=CM ',M=MDIFF,C=SIGMAE/SIGMAK,MESH=MESH3D)
!
IF(DEBUG.GT.0) WRITE(LU,*) 'APPEL DE CVDF3D POUR EP'
CALL CVDF3D
& (EP,EPC,EPN,VISCVI,SIGMAE,S0EP,.TRUE.,S1EP,.TRUE.,
& EBORL,EBORF,EBORS,AEBORL,AEBORF,AEBORS,
& BEBORL,BEBORF,BEBORS,LIEBOL,LIEBOF,LIEBOS,
& FLUX%R(1),FLUEXT,FLUEXTPAR,EMIN,CLEMIN,EMAX,CLEMAX,
& SCHCKE,SCHDKE,SLVDKE,TRBAKE,INFOGR,NEWDIF,CALCFLU(5),

```

```

& T2_01,T2_03,
& T3_01,T3_02,T3_03,T3_04, MESH3D , IKLE3 , MASKEL , MTRA1,
& NPTFR3,MMURD,MURD_TF,VOLU,VOLUPAR,VOLUN,VOLUNPAR,
& NBOR3,NPOIN3,NPOIN2,DT,MSK,NELEM3,
& NPLAN,IELM3,MSUPG,IELM2H,IELM2V,MDIFF,MTRA2,
& INCHYD,MASKBR,MASKPT,SEM3D,YASEM3D,SVIDE,IT1,
& TRAV3,MESH2D,OPTBAN,TETATRA,
& YAWCHU,WCHU,S3D_WCHU,AGGLOD,NSCE,SOURCES,EP_SCE%R,
& NUMLIQ%I,DIRFLU,NFRLIQ,VOLUT,ZT,ZPROP,CALCRAIN(5),
& PLUIE,PARAPLUIE,0.D0,FLODEL,FLOPAR,SIGMAG,IPBOT%I,
& MAXADV,FLUDPT,FLUDP,FLUER,VOLU2D,V2DPAR,
& SETDEP,S3D_FLUDPT,S3D_FLUDP,S3D_FLUER,S3D_SETDEP,
& OPTSOU,ZN%R,OPTADV_KE,NCO_DIST,NSP_DIST,TB2)
!
!
    IF(DEBUG.GT.0) WRITE(LU,*) 'RETOUR DE CVDF3D POUR EP'
!
ELSEIF(ITURBV.EQ.5.OR.ITURBV.EQ.9) THEN
!
    CLNUMIN = .TRUE.
    CLNUMAX = .FALSE.
    YASEM3D = .FALSE.
    YAWCHU = .FALSE.
    NEWDIF = .TRUE.
    TETATRA=MIN(TETADI,1.D0)
!
    IF(DEBUG.GT.0) WRITE(LU,*) 'APPEL DE CVDF3D POUR NU'
    CALL CVDF3D
& (NU,NUC,NUN,VISCNU,SIGMANU,S0NU,.TRUE.,S1NU,.TRUE.,
& NUBORL, NUBORF, NUBORS, ANUBORL, ANUBORF, ANUBORS,
& BNUBORL, BNUBORF, BNUBORS, LINUBOL, LINUBOF, LINUBOS,
& FLUX%R(1), FLUEXT,FLUEXTPAR,NUMIN, CLNUMIN, NUMAX, CLNUMAX,
& SCHCKE,SCHDKE,SLVDKE,TRBASA,INFOGR,NEWDIF,CALCFLU(4),
& T2_01,T2_03,
& T3_01,T3_02,T3_03,T3_04, MESH3D , IKLE3 , MASKEL , MTRA1,
& NPTFR3,MMURD,MURD_TF,VOLU,VOLUPAR,VOLUN ,VOLUNPAR,
& NBOR3,NPOIN3,NPOIN2,DT,MSK,NELEM3,
& NPLAN,IELM3,MSUPG,IELM2H,IELM2V,MDIFF,MTRA2,
& INCHYD,MASKBR,MASKPT,SEM3D,YASEM3D,SVIDE,IT1,
& TRAV3,MESH2D,OPTBAN,TETATRA,
& YAWCHU,WCHU,S3D_WCHU,AGGLOD,NSCE,SOURCES,NU_SCE%R,
& NUMLIQ%I,DIRFLU,NFRLIQ,VOLUT,ZT,ZPROP,CALCRAIN(4),
& PLUIE,PARAPLUIE,0.D0,
& FLODEL,FLOPAR,SIGMAG,IPBOT%I,MAXADV,FLUDPT,FLUDP,
& FLUER,VOLU2D,V2DPAR,SETDEP,S3D_FLUDPT,S3D_FLUDP,S3D_FLUER,
& S3D_SETDEP,OPTSOU,ZN%R,OPTADV_KE,NCO_DIST,
& NSP_DIST,TB2)
    IF(DEBUG.GT.0) WRITE(LU,*) 'RETOUR DE CVDF3D POUR NU'
    ENDIF
!
!-----
!
! COMPUTES THE VISCOSITIES VISCVI, VISCTA AND VISCTP
!
    IF(ITURBH.EQ.1.OR.ITURBV.EQ.1) THEN
!
        IF(DEBUG.GT.0) WRITE(LU,*) 'APPEL DE VISCOS'
        CALL VISCOS(VISCVI,VISCTA,DNUTAV,DNUTAH,
& DNUVIV,DNUVIH,NTRAC,ITURBH,ITURBV)
        IF(DEBUG.GT.0) WRITE(LU,*) 'RETOUR DE VISCOS'
!
    ENDIF
!

```

```

!
IF(ITURBV.EQ.2) THEN
!
  IF(DEBUG.GT.0) WRITE(LU,*) 'APPEL DE VISCLM'
  CALL VISCLM(VISCVI,VISCTA,RI,U,V,DELTAR,Z3,H,
&      T3_01, T3_02, T3_03, T3_04, T3_05, T3_07,
&      MESH3D, IELM3, GRAV, NPLAN,
&      NPOIN3, NPOIN2, NTRAC, MSK, MASKEL,
&      MIXING,DAMPING,DNUVIV,DNUTAV,KARMAN,
&      PRANDTL,KFROT,RUGOF,ZF,LINLOG,IPBOT%)
  IF(DEBUG.GT.0) WRITE(LU,*) 'RETOUR DE VISCLM'
!
ENDIF
!
IF(ITURBV.EQ.3.OR.ITURBH.EQ.3) THEN
!
  IF(DEBUG.GT.0) WRITE(LU,*) 'APPEL DE VISCKE'
  CALL VISCKE(VISCVI,VISCTA,AK,EP,NTRAC,CMU,
&      DNUVIH,DNUVIV,DNUTAH,DNUTAV,EMIN,
&      ITURBH,ITURBV,PRANDTL)
  IF(DEBUG.GT.0) WRITE(LU,*) 'RETOUR DE VISCKE'
!
ENDIF
!
IF(ITURBH.EQ.4) THEN
!
  IF(DEBUG.GT.0) WRITE(LU,*) 'APPEL DE VISSMA'
  CALL VISSMA(VISCVI,VISCTA,
&      DNUTAH,DNUVIH,DNUVIV,DNUTAV,
&      U,V,W,T3_01,T3_02,T3_03,T3_04,T3_05,T3_06,
&      SVIDE,MESH3D,
&      IELM3,NTRAC,MSK,MASKEL,ITURBV)
  IF(DEBUG.GT.0) WRITE(LU,*) 'RETOUR DE VISSMA'
!
ENDIF
!
IF(ITURBV.EQ.7.OR.ITURBH.EQ.7) THEN
!
  IF(DEBUG.GT.0) WRITE(LU,*) 'APPEL DE VISCKO'
  CALL VISCKO(VISCVI,VISCTA,ROTAT,AK,EP,NTRAC,
&      DNUVIH,DNUVIV,DNUTAH,DNUTAV,ITURBH,ITURBV,
&      T3_01,T3_02)
  IF(DEBUG.GT.0) WRITE(LU,*) 'RETOUR DE VISCKO'
!
ENDIF
!
IF(ITURBV.EQ.5.OR.ITURBV.EQ.9) THEN
  IF(DEBUG.GT.0) WRITE(LU,*) 'APPEL DE VISCSA'
  CALL VISCSA(VISCVI,VISCNU,NU,
&      DNUVIH,DNUVIV,AK,EP,STRAIN)
  IF(DEBUG.GT.0) WRITE(LU,*) 'RETOUR DE VISCSA'
ENDIF
!
IF(ITURBV.EQ.6) THEN
  IF(DEBUG.GT.0) WRITE(LU,*) 'APPEL DE GOTM_COUPLING_STEP'
  CALL GOTM_COUPLING_STEP
  IF(DEBUG.GT.0) WRITE(LU,*) 'RETOUR DE GOTM_COUPLING_STEP'
ENDIF
!
IF(INCLUS(COUPLING,'TOMAWACT3D')) THEN
!
  ADDING VERTICAL MIXING DUE TO WAVES
  CALL OS('X=X+Y ',X=VISCVI%ADR(3)%P,Y=FDK)
ENDIF
!

```

```

IF(OPTBAN.EQ.1) THEN
!
  CALL VISCLIP(VISCVI,VISCTA,H,NPLAN,NPOIN2,NTRAC,HLIM)
!
ENDIF
!
=====
! OIL SPILL MODEL (UNDER DEVELOPMENT IN MYGRHYCAR PROJECT)
=====
!
IF(SPILL_MODEL) THEN
!
  IF(DEBUG.GT.0) WRITE(LU,*) 'APPEL DE OIL_SPILL_3D'
  CALL OIL_SPILL_3D(LT,IELM2H,MESH2D,NFLOT_MAX,T3D_FILES,
&      MAXLU_T3D,NPOIN2,T3DMIG,UCONV,VCONV,WCONV,
&      NFLOT,NPLAN,MESH3D,AT,DT,GRAV,CF,X,Y,Z,H,HN,
&      IELM3,NPOIN3,NELEM2,XFLOT,YFLOT,ZFLOT,SHPFLO,
&      SHZFLO,TAGFLO,ELTFLO,ETAFLO,FLOPRD,T3DFLO,
&      IT1,IT2,T3_01,T3_02,T3_03,MTRA1,MTRA2,VISCVI,
&      WIND,UNSV3D,NTRAC,TRN,TRAV3,ATABOS,T2_17,
&      VENT)
  IF(DEBUG.GT.0) WRITE(LU,*) 'RETOUR DE OIL_SPILL_3D'
!
ENDIF
!
-----
! ADVECTION-DIFFUSION OF TRACERS
!
!GA: POINTERS ARE USED TO ALLOW TWO SEDIMENT CLASSES (MULTI1,2,3,4)
IF(NTRAC.GT.0) THEN
!
  IF (INFOGR) CALL MITTIT(5,AT,LT)
!
  SIGMTA = 1.D0
  TAMIN = 0.D0
  TAMAX = 1.D0
  CTAMIN = .FALSE.
  CTAMAX = .FALSE.
  YASEM3D = .FALSE.
  NEWDIF = .TRUE.
  TETATRA=MIN(TETADI,1.D0)
!
DO ITRAC = 1,NTRAC
!
  MULTI1 => S3D_FLUDPT
  MULTI2 => S3D_FLUDP
  MULTI3 => S3D_FLUER
  MULTI4 => S3D_WCHU
!
  IF(ITRAC.GE.IND_SED.AND.ITRAC.LE.IND_SED+NSUSP_TEL-1) THEN
    ISUSP=ITRAC-IND_SED+1
    YAWCHU=.TRUE.
!    SOLVER STRUCTURE
    SLVD=SLVSED
  ELSEIF(S3D_SEDI.AND.ITRAC.EQ.NTRAC) THEN
    YAWCHU=.TRUE.
!    SOLVER STRUCTURE
    SLVD=S3D_SLVDSE
  ELSE
    YAWCHU=.FALSE.
!    SOLVER STRUCTURE
    SLVD=SLVDTA(ITRAC)
  ENDIF

```

```

!
IF(S3D_SEDI.AND.S3D_MIXTE.AND.ITRAC.EQ.(NTRAC-1)) THEN
  YAWCHU=.TRUE.
  SLVD=S3D_SLVDSE
  MULTI1 => S3D_FLUDPTNC
  MULTI2 => S3D_FLUDPNC
  MULTI3 => S3D_FLUERNC
  MULTI4 => S3D_WCS
ELSEIF(S3D_SEDI.AND.S3D_MIXTE.AND.ITRAC.EQ.NTRAC) THEN
  MULTI1 => S3D_FLUDPTC
  MULTI2 => S3D_FLUDPC
  MULTI3 => S3D_FLUERC
ENDIF
!
IF(DEBUG.GT.0) THEN
  WRITE(LU,*) 'APPEL DE CVDF3D POUR TRACEUR ',ITRAC
ENDIF
!
CALL CVDF3D
& (TA%ADR(ITRAC)%P,TAC%ADR(ITRAC)%P,TRN%ADR(ITRAC)%P,
& VISCTA%ADR(ITRAC)%P,SIGMTA,
& S0TA%ADR(ITRAC)%P,TRUE.,S1TA%ADR(ITRAC)%P,TRUE.,
& TABORL%ADR(ITRAC)%P,TABORF%ADR(ITRAC)%P,TABORS%ADR(ITRAC)%P,
& ATABOL%ADR(ITRAC)%P,ATABOF%ADR(ITRAC)%P,ATABOS%ADR(ITRAC)%P,
& BTABOL%ADR(ITRAC)%P,BTABOF%ADR(ITRAC)%P,BTABOS%ADR(ITRAC)%P,
& LITABL%ADR(ITRAC)%P,LITABF%ADR(ITRAC)%P,LITABS%ADR(ITRAC)%P,
& FLUX%R(5+ITRAC),FLUEXT,FLUEXTPAR,
& TAMIN,CTAMIN,TAMAX,CTAMAX,SCHCTA(ITRAC),
& SCHDTA,SLVD,TRBATA,INFOGR,NEWDIR,CALCFLU(5+ITRAC),
& T2_01,T2_03,T3_01,T3_02,T3_03,T3_04,MESH3D,IKLE3,MASKEL,
& MTRA1,NPTFR3,MMURD,MURD_TF,VOLU,VOLUPAR,VOLUN,VOLUNPAR,
& NBOR3,NPOIN3,NPOIN2,DT,MSK,NELEM3,NPLAN,IELM3,MSUPG,
& IELM2H,IELM2V,MDIFF,MTRA2,INCHYD,MASKBR,MASKPT,SEM3D,YASEM3D,
& SVIDE,IT1,TRAV3,MESH2D,OPTBAN,TETATRA,
& YAWCHU,WCHU%ADR(ITRAC)%P,MULTI4,AGGLOD,NSCE,SOURCES,
& TA_SCE%ADR(ITRAC)%P%R,
& NUMLIQ%I,DIRFLU,NFRLIQ,VOLUT,ZT,ZPROP,CALCRAIN(5+ITRAC),
& PLUIE,PARAPLUIE,TRAIN(ITRAC),FLODEL,FLOPAR,SIGMAG,IPBOT%I,
& MAXADV,FLUDPT%ADR(NUM_ISUSP_ICLA(ISUSP))%P,
& FLUDP%ADR(NUM_ISUSP_ICLA(ISUSP))%P,
& FLUER%ADR(NUM_ISUSP_ICLA(ISUSP))%P,VOLU2D,V2DPAR,SETDEP,
& MULTI1,MULTI2,MULTI3,S3D_SETDEP,OPTSOU,
& ZN%R,OPTADV_TR(ITRAC),NCO_DIST,NSP_DIST,TB2)
!
NEWDIR=.FALSE. (POSSIBLE IF SIGMTA UNCHANGED)
!
IF(DEBUG.GT.0) THEN
  WRITE(LU,*) 'RETOUR DE CVDF3D POUR TRACEUR ',ITRAC
ENDIF
!
ENDDO
!
-----
! COMPUTES DELRA RHO / RHO FOR THE BUOYANCY TERMS
!
IF(DEBUG.GT.0) WRITE(LU,*) 'APPEL DE DRSURR'
CALL DRSURR(DELTA,TA,BETAC,T0AC,RHO,RHO0,XMVS0,S3D_RHOS,
& DENLAW,S3D_SEDI,NTRAC,IND_T,IND_S,IND_SED,NSUSP_TEL,
& S3D_MIXTE,NUM_ISUSP_ICLA,NSICLA)
IF(DEBUG.GT.0) WRITE(LU,*) 'RETOUR DE DRSURR'
!
IF( (INCLUS(COUPPING,'WAQTEL') ).AND.
& (13*INT(WAQPROCESS/13).EQ.WAQPROCESS) ) THEN

```



```

! ORDER: NUMBER OF THE PLANES FROM TOP TO BOTTOM
! THEN NUMBER OF THE 2D NODES
  DO I=1,NPOIN2
    DO K=1,NPLAN
      RHO4AED2%R(K+(I-1)*NPLAN) = RHO%R(I+(NPLAN-K)*NPOIN2)
    ENDDO
  ENDDO
ENDIF
!
!
!!! Third step of immersed boundary method:
!!! apply zero velocity condition
!
ccc  CALL ZERO_IB(INSIDE_IB,N_INSIDE_IB)
      CALL ZERO_IB(PRIVE%ADR(4)%P,N_INSIDE_IB)
!
!!! Third step of immersed boundary method:
!!! apply zero velocity condition
!
#if defined COMPAD
  CALL AD_TELEMAC3D_SUBITERATION_END
#endif
!
  END DO SUBITER
!
!-----
!
! SEDIMENTOLOGY : FLUDP SENT TO GAIA
!
  IF(NSUSP_TEL.GT.0) THEN
    DO ITRAC=IND_SED, IND_SED+NSUSP_TEL-1
      ISUSP=ITRAC-IND_SED+1
!
      IF(SETDEP.NE.1) THEN
        IF(OPTBAN.EQ.1) THEN
          DO IPOIN=1,NPOIN2
! correction for tidal flats: take the first point above crushed planes
! IPBOT=0: no tidal flats
! IPBOT=NPLAN-1: dry element
          IF(IPBOT%I(IPOIN).NE.NPLAN-1) THEN
            FLUDP%ADR(NUM_ISUSP_ICLA(ISUSP))%P%R(IPOIN)=
&          FLUDPT%ADR(NUM_ISUSP_ICLA(ISUSP))%P%R(IPOIN)*
&          TA%ADR(ITRAC)%P%R(IPBOT%I(IPOIN)*NPOIN2+IPOIN)
            FLUDP%ADR(NUM_ISUSP_ICLA(ISUSP))%P%R(IPOIN)=
&          MAX(FLUDP%ADR(NUM_ISUSP_ICLA(ISUSP))%P%R(IPOIN),
&          0.D0)
          ELSE
            FLUDP%ADR(NUM_ISUSP_ICLA(ISUSP))%P%R(IPOIN)=0.D0
          ENDIF
        ENDDO
      ELSE
        DO IPOIN=1,NPOIN2
          FLUDP%ADR(NUM_ISUSP_ICLA(ISUSP))%P%R(IPOIN)=
&          FLUDPT%ADR(NUM_ISUSP_ICLA(ISUSP))%P%R(IPOIN)*
&          TA%ADR(ITRAC)%P%R(IPOIN)
! FLUDP MUST BE POSITIVE, EVEN IF TA<0 DUE TO TRUNCATION ERRORS PROBLEM
! SEEN WITH TA=-1.D-87 !!!!!
          FLUDP%ADR(NUM_ISUSP_ICLA(ISUSP))%P%R(IPOIN)=
&          MAX(FLUDP%ADR(NUM_ISUSP_ICLA(ISUSP))%P%R(IPOIN),
&          0.D0)
        ENDDO
      ENDIF
    END DO
  ENDIF

```

```

        ENDIF
!
        ENDDO
    ENDIF
!
! SEDIMENTOLOGY SEDI3D: BOTTOM TREATMENT
!
    IF(S3D_SEDI) THEN
!
!         FONVAS DOES ZF=ZR+S3D_HDEP, THUS S3D_HDEPMUST INCLUDE BEDLOAD
!         EROSION, HAS BEEN TAKEN INTO ACCOUNT INTO CLSEDI ABOVE
! GA: FONVAS HAS BEEN MODIFIED TO ALLOW TWO SEDIMENT CLASSES
        IF (S3D_MIXTE) THEN
            IF(DEBUG.GT.0) WRITE(LU,*) 'APPEL DE FONVAS S3D_MIXTE'
            CALL FONVAS
&      (S3D_EPAI,S3D_CONC,
&      S3D_HDEP%R,S3D_FLUDP%R,S3D_FLUDPT%R,S3D_FLUER%R,ZF%R,
&      TA%ADR(NTRAC)%P%R,
&      NPOIN2,NPOIN3,S3D_NCOUCH,DT,
&      S3D_ZF_S%R,S3D_ESOMT%R,VOLU2D,S3D_MASDEP,S3D_SETDEP,ZR%R,
&      TA%ADR(NTRAC-1)%P%R,S3D_FLUDPTC%R,S3D_FLUDPTNC%R,
&      S3D_FLUERC%R,S3D_FLUERNC%R,S3D_MIXTE,S3D_FLUDPC%R,
&      S3D_FLUDPNC%R,S3D_PVSCO%R,S3D_PVSNCO%R,S3D_CFDEP,
&      S3D_EPAICO%R,S3D_EPAINCO%R)

            IF(DEBUG.GT.0) WRITE(LU,*) 'RETOUR DE FONVAS S3D_MIXTE'
!
        ELSEIF (S3D_SEDCO.OR.S3D_SEDNCO) THEN

            IF(DEBUG.GT.0) WRITE(LU,*) 'APPEL DE FONVAS '
            CALL FONVAS
&      (S3D_EPAI,S3D_CONC,
&      S3D_HDEP%R,S3D_FLUDP%R,S3D_FLUDPT%R,S3D_FLUER%R,ZF%R,
&      TA%ADR(NTRAC)%P%R,
&      NPOIN2,NPOIN3,S3D_NCOUCH,DT,
&      S3D_ZF_S%R,S3D_ESOMT%R,VOLU2D,S3D_MASDEP,S3D_SETDEP,ZR%R,
&      TA%ADR(NTRAC)%P%R,S3D_FLUDPTC%R,S3D_FLUDPTNC%R,
&      S3D_FLUERC%R,S3D_FLUERNC%R,S3D_MIXTE,S3D_FLUDPC%R,
&      S3D_FLUDPNC%R,S3D_PVSCO%R,S3D_PVSNCO%R,S3D_CFDEP,
&      S3D_EPAICO%R,S3D_EPAINCO%R)

            IF(DEBUG.GT.0) WRITE(LU,*) 'RETOUR DE FONVAS '
        ELSE
!
            WRITE(LU,*) ''
            WRITE(LU,*) 'SEDI3D : ERROR ON SEDIMENT KEY WORD'
            CALL PLANTE(1)
            STOP
        ENDIF
    ENDIF
!
!
! IF(INCLUS(COUPLING,'GAIA ').AND.NSUSP_TEL.GT.0) THEN
!
!     U AND V WITH 2D STRUCTURE : BOTTOM VELOCITY AS A 2D
!     VARIABLE
!     CALL CPSTVC(U2D,U)
!     CALL CPSTVC(V2D,V)
!
!     NOW RUNS ONE TURN OF GAIA'S TIME LOOP
!     AND RETURNS
!     CALL CONFIG_CODE(5)
!     IF(DEBUG.GT.0) WRITE(LU,*) 'CALLING GAIA_STEP 2'

```

```

CALL GAIA_STEP(
&   LT,GRAPRD,LISPRD,NIT_ORI,U2D,V2D,H,ZF,
&   UETCAR,DELTAR,CF,RUGOF,CODE1,
&   U,V,AT,VISCVI,DT,CHARR_TEL,SUSP_TEL,
&   RHO0,GRAV,
!   VARIABLES TRANSMITTED FROM TOMAWAC
&   DIRMOY,HM0,TPR5,ORBVEL,.TRUE.)
IF(DEBUG.GT.0) WRITE(LU,*) 'BACK GAIA_STEP 2'
CALL CONFIG_CODE(1)
!
!   check if this is necessary
!   RETRIEVES ORIGINAL U AND V STRUCTURE
CALL CPSTVC(UN,U)
CALL CPSTVC(VN,V)
!   end check
ENDIF
!
! UPDATES GEOMETRY IF THE BOTTOM HAS EVOLVED
!
IF(INCLUS(COUPPLING,'SISYPHE').OR.INCLUS(COUPPLING,'GAIA '))
& .OR.S3D_SEDI) THEN
!
!   COPIES MODIFIED BOTTOM TOPOGRAPHY INTO Z AND ZPROP
CALL OV('X=Y ',X=Z(1:NPOIN2),Y=ZF%R,DIM1=NPOIN2)
CALL OV('X=Y ',X=ZPROP%R(1:NPOIN2),Y=ZF%R,DIM1=NPOIN2)
!   COMPUTES NEW BOTTOM GRADIENTS AFTER SEDIMENTATION
CALL GRAD2D(GRADZF%ADR(1)%P,GRADZF%ADR(2)%P,ZPROP,NPLAN,SVIDE,
&   UNSV2D,T2_02,T2_03,T2_04,
&   IELM2H,MESH2D,MSK,MASKEL)
!   COMPUTES NEW Z COORDINATES
CALL CALCOT(Z,H%R)
!   USEFUL ? NOT SURE, IS DONE AT EACH TIMESTEP ELSEWHERE, SO..
!   CALL CALCOT(ZPROP%R,HPROP%R)
CALL FSGRAD(GRADZS,ZFLATS,Z(NPOIN3-NPOIN2+1:NPOIN3),
&   ZF,IELM2H,MESH2D,MSK,MASKEL,
&   UNSV2D,T2_01,NPOIN2,OPTBAN,SVIDE)
CALL VECTOR(VOLU,'=', 'MASBAS ',IELM3,1.D0-AGGLOH,
&   SVIDE,SVIDE,SVIDE,SVIDE,SVIDE,SVIDE,MESH3D,.FALSE.,MASKEL)
IF(AGGLOH.GT.1.D-6) THEN
CALL VECTOR(VOLU,'+', 'MASBAS2 ',IELM3,AGGLOH,
&   SVIDE,SVIDE,SVIDE,SVIDE,SVIDE,SVIDE,MESH3D,.FALSE.,MASKEL)
ENDIF
IF(NCSIZE.GT.1) THEN
CALL OS('X=Y ',X=VOLUPAR,Y=VOLU)
CALL PARCOM(VOLUPAR,2,MESH3D)
ENDIF
!
ENDIF
!
!-----
!
! PREPARES 2D AND 3D OUTPUT
!
!   ALWAYS CALLED (SEE E.G. OUTPUT MAXZ)
!
CALL PRERES_TELEMAC3D
!
!   CALLED IF OUTPUTS REQUESTED
!
IF(MOD(LT,GRAPRD).EQ.0.AND.LT.GE.GRADEB) THEN
!
!   3D OUTPUT
!

```

```

        IF(T3D_FILES(T3DRES)%NAME(1:1).NE.' ') THEN
            CALL BIEF_DESIMP(T3D_FILES(T3DRES)%FMT,VARSO3,
&                NPOIN3,T3D_FILES(T3DRES)%LU,AT,LT,
&                LISPRD,GRAPRD,
&                SORG3D,SORIM3,MAXVA3,TEXT3,GRADEB,LISDEB)
        ENDIF
!
! 3D OUTPUT FOR RESTART
!
        IF(LT.EQ.NIT_ORI.AND.RESTART_MODE
&        .AND.T3D_FILES(T3DRST)%NAME(1:1).NE.' ') THEN
            CALL BIEF_DESIMP(T3D_FILES(T3DRST)%FMT,VARSO3,NPOIN3,
&                T3D_FILES(T3DRST)%LU,AT,LT,
&                1,NIT_ORI,SOREST,SORIS3,MAXVA3,TEXT3,0,0)
        ENDIF
!
! 2D OUTPUT
!
        IF(T3D_FILES(T3DHYD)%NAME(1:1).NE.' ') THEN
            CALL BIEF_DESIMP(T3D_FILES(T3DHYD)%FMT,VARSOR,
&                NPOIN2,T3D_FILES(T3DHYD)%LU,AT,LT,
&                LISPRD,GRAPRD,
&                SORG2D,SORIMP,MAXVAR,TEXTE,GRADEB,LISDEB)
        ENDIF
!
        ENDIF
!
! SEDIMENTOLOGY OUTPUT FOR SEDI
!
        IF(S3D_SEDI.AND.T3D_FILES(S3D_T3DSED)%NAME(1:1).NE.' ') THEN
            IF(DEBUG.GT.0) WRITE(LU,*) 'APPEL DE DESSED'
            CALL DESSED(NPF%I,S3D_IVIDE%R,S3D_EPAI,S3D_HDEP%R,
&                S3D_TEMP%R,ZR%R,NPOIN2,S3D_NPFMAX,
&                S3D_NCOUCH,GRAPRD,LT,S3D_DTC,S3D_TASSE,
&                S3D_GIBSON,T3D_FILES(S3D_T3DSED)%LU,TITCAS,
&                S3D_BIRSED,0)
            IF(DEBUG.GT.0) WRITE(LU,*) 'RETOUR DE DESSED'
        ENDIF
!
! OPTIONAL USER OUTPUT
!
        CALL UTIMP(GRADEB,GRAPRD,LISDEB,LISPRD)
!
! SEDIMENT OUTPUT FOR SEDI
!
        IF(S3D_SEDI) THEN
            IF(DEBUG.GT.0) WRITE(LU,*) 'APPEL DE IMPSED'
            CALL IMPSED(S3D_IVIDE%R,S3D_EPAI,S3D_CONC,S3D_TEMP%R,S3D_HDEP%R,
&                S3D_PDEPO%R,S3D_FLUER%R,
&                ZR%R,ZF%R,TA%ADR(NTRAC)%P%R,S3D_WCHU%R,X,Y,
&                NPOIN2,NPOIN3,S3D_NPFMAX,S3D_NCOUCH,NPF%I,LT,
&                S3D_RHOS,S3D_CFMAX,
&                S3D_CFDEP,S3D_EPAI0,S3D_TASSE,S3D_GIBSON,
&                PRIVE,LISPRD)
            IF(DEBUG.GT.0) WRITE(LU,*) 'RETOUR DE IMPSED'
        ENDIF
!
!=====
! DROQUES/FLOATS/BUOYS
!=====
!
        IF(NFLOT_MAX.GT.0.AND..NOT.SPILL_MODEL) THEN

```

```

IF(SPHERI) THEN
  CALL OS('X=Y/Z ',X=UCONV,Y=UCONV,Z=MESH3D%COSLAT)
  CALL OS('X=Y/Z ',X=VCONV,Y=VCONV,Z=MESH3D%COSLAT)
ENDIF
!
!   ADDING AND REMOVING DROGUES
!
IF(DEBUG.GT.0) WRITE(LU,*) 'CALLING FLO3D'
CALL FLOT3D(XFLOT%R,YFLOT%R,ZFLOT%R,NFLOT,NFLOT_MAX,X,Y,Z,
&    MESH3D%IKLE%I,
&    MESH3D%NELEM,MESH3D%NELMAX,NPOIN3,NPLAN,
&    TAGFLO%I,SHPFLO%R,SHZFLO%R,ELTFLO%I,ETAFLO%I,
&    MESH3D,LT,NIT_ORI,AT)
IF(DEBUG.GT.0) WRITE(LU,*) 'BACK FROM FLO3D'
!
IF(INFOGR) CALL MITTIT(12,AT,LT)
!
!   MOVING THEM
!
IF(DEBUG.GT.0) WRITE(LU,*) 'CALLING DERIVE'
CALL DERIVE(UCONV%R,VCONV%R,WCONV%R,DT,AT,
&    X,Y,Z,
&    MESH2D%IKLE%I,MESH3D%IFABOR%I,LT,IELM3,UCONV%ELM,
&    3,3,
&    NPOIN3,NPOIN2,NELEM2,MESH2D%NELMAX,
&    MESH2D%SURDET%R,XFLOT%R,YFLOT%R,ZFLOT%R,
&    SHPFLO%R,SHZFLO%R,TAGFLO%I,ELTFLO%I,ETAFLO%I,
&    NFLOT,NFLOT_MAX,FLOPRD,MESH3D,T3D_FILES(T3DFLO)%LU,
&    IT1%I,T3_01%R,T3_02%R,T3_03%R,IT2%I,
!           NO STOCHASTIC DIFFUSION
&    MTRA1%X%R,MTRA2%X%R,NPOIN3,0,SVIDE,
&    NPLAN,ZCHAR%R,TRANSF)
IF(DEBUG.GT.0) WRITE(LU,*) 'BACK FROM DERIVE'
!
IF(SPHERI) THEN
  CALL OS('X=XY ',X=UCONV,Y=MESH3D%COSLAT)
  CALL OS('X=XY ',X=VCONV,Y=MESH3D%COSLAT)
ENDIF
!
ENDIF
!
!-----
!
! MASS BALANCE FOR THE CURRENT TIMESTEP
!
IF (BILMAS) THEN
!
  IF (.NOT.INFMAS) INFOGR = .FALSE.
  INFOGR = INFOGR .AND. LISTIN
  IF (INFOGR) CALL MITTIT(10,AT,LT)
!
  IF(DEBUG.GT.0) WRITE(LU,*) 'APPEL DE MASS3D'
  CALL MASS3D(INFOGR)
  IF(DEBUG.GT.0) WRITE(LU,*) 'RETOUR DE MASS3D'
!
!
  IF(S3D_SEDI) THEN
!
    DETERMINE S3D_MASSUSP: MASS IN SUSPENSION
    S3D_MASBED: MASS OF SEDIMENT BED
    S3D_MASDEP: DEPOSITED MASS
    S3D_MASSUSP= MASSE%R(5+NTRAC)
!
    INITIALISATION

```

```

        IF(LT.EQ.1) S3D_MASSUSP0= S3D_MASSUSP
!
!GA: SED3D HAS BEEN MODIFIED TO ALLOW TWO SEDIMENT CLASSES
        IF(INFOGR) THEN
            IF(DEBUG.GT.0) WRITE(LU,*) 'APPEL DE SED3D'
            CALL SED3D(S3D_MASBED,S3D_MASBED0, S3D_MASDEP,
&                S3D_EPAI,S3D_CONC,
&                T2_01%R,
&                NPOIN2,S3D_NCOUCH,
&                AT,VOLU2D%R,
&                S3D_CFDEP,S3D_EPAICO%R,S3D_EPAINCO%R,S3D_MIXTE)
!
            IF(DEBUG.GT.0) WRITE(LU,*) 'RETOUR DE SED3D'
            ENDIF
!
        ENDIF
!
        IF(DEBUG.GT.0) WRITE(LU,*) 'APPEL DE BIL3D'
        CALL BIL3D(LT,NIT_ORI,MESH3D%IKLBOR%I,NPTFR2,NETAGE)
        IF(DEBUG.GT.0) WRITE(LU,*) 'RETOUR DE BIL3D'
!
    ENDIF
!
! COMPARES WITH REFERENCE FILE
!
    IF(VALID.AND.T3D_FILES(T3DRES)%NAME(1:1).NE.' ') THEN
        IF(DEBUG.GT.0) WRITE(LU,*) 'APPEL DE BIEF_VALIDA'
        CALL BIEF_VALIDA(TRAV3,TEXT3,
&                T3D_FILES(T3DREF)%LU,T3D_FILES(T3DREF)%FMT,
&                VARSO3,TEXT3,
&                T3D_FILES(T3DRES)%LU,T3D_FILES(T3DRES)%FMT,
&                MAXVA3,NPOIN3,LT,NIT_ORI,ALIRE3D)
        IF(DEBUG.GT.0) WRITE(LU,*) 'RETOUR DE BIEF_VALIDA'
        ELSEIF(VALID.AND.T3D_FILES(T3DRES)%NAME(1:1).EQ.' '.AND.
&            LT.EQ.NIT_ORI) THEN
            WRITE(LU,*) ''
            WRITE(LU,*) ''
            WRITE(LU,*) 'NO VALIDATION IF NO'
            WRITE(LU,*) '3D RESULT FILE!!!'
        ENDIF
!
!
! CHECKS VALUES SHARED BETWEEN SUBDOMAINS
!
! CALL CHECK_DIGITS(H ,T2_01,MESH2D)
! CALL CHECK_DIGITS(U ,T3_01,MESH3D)
! CALL CHECK_DIGITS(V ,T3_01,MESH3D)
! CALL CHECK_DIGITS(W ,T3_01,MESH3D)
! IF(NTRAC.GT.0) THEN
!     DO ITRAC=1,NTRAC
!         CALL CHECK_DIGITS(TA%ADR(ITRAC)%P,T3_01,MESH3D)
!     ENDDO
! ENDIF
!
!#if defined COMPAD
!    CALL AD_TELEMAC3D_TIMESTEP_END
!#endif
!
! IF(LT.LT.NIT) GO TO 700
! END OF TIME LOOP
!
!=====
! THE TIME LOOP ENDS HERE

```



```

=====
!
  IF(PASS.NE.1) THEN
    IF(LISTIN) WRITE(LU,19)
19  FORMAT(/,1X,'END OF TIME LOOP',///)
  ENDIF
!
!-----
!
!if defined COMPAD
  CALL AD_TELEMAC3D_END
!endif
!
  RETURN
  END
!
!          *****
!          SUBROUTINE SOURCE_IB
!          *****
!
!      & (S0U,S0V,S0W,S1U,S1V,S1W,
!      & UN3,VN3,WSN3,WN3,
!      & VOLU,VOLUN,TRAV1,TRAV2,
!      & NPOIN3,NTRAC,LT,AT,DT,PRIVE,NONHYD,
ccc  & IMMERSED_BOUNDARY,N_IB,
!      & N_IB,
!      & SVIDE,MESH3,IELM3,MSK,MASKEL,PRESSURE)
!
!*****
! TELEMAC3D  V6P1                      21/08/2010
!*****
!
!brief  PREPARES SOURCE TERMS FOR DIFFUSION OF TRACERS.
!
!history CDG/SOGREAH
!+      **/06/2001
!+
!+  TRACER SOURCES
!
!history J-M HERVOUET (LNHE)
!+      29/08/2008
!+      V5P6
!+
!
!history N.DURAND (HRW), S.E.BOURBAN (HRW)
!+      13/07/2010
!+      V6P0
!+  Translation of French comments within the FORTRAN sources into
!+  English comments
!
!history N.DURAND (HRW), S.E.BOURBAN (HRW)
!+      21/08/2010
!+      V6P0
!+  Creation of DOXYGEN tags for automated documentation and
!+  cross-referencing of the FORTRAN sources
!
!-----
!| AT      |-->| TIME
!| DT      |-->| TIME STEP
!| ISCE     |-->| NODE ADRESSES IN 2D MESH FOR SOURCES
!| KSCE     |<->| NUMBER OF PLANE FOR SOURCES
!| LT       |-->| ITERATION NUMBER
!| MAXSCE   |-->| MAXIMUM NUMBER OF SOURCES
!| NONHYD   |-->| LOGICAL FOR NON-HYDROSTATIC OPTION
!| NPOIN2   |-->| NUMBER OF POINTS IN 2D

```

```

!| NPOIN3      |-->| NUMBER OF POINTS IN THE MESH
!| NSCE       |-->| NUMBER OF GIVEN POINTS FOR SOURCES
!| NTRAC      |-->| NUMBER OF TRACERS
!| PRIVE      |-->| BLOCK OF ARRAYS FOR USER
!| QSCE       |-->| WATER DISCHARGE OF SOURCES
!| S0U        |-->| EXPLICIT SOURCE TERMS ON VELOCITIES U
!| S0V        |-->| EXPLICIT SOURCE TERMS ON VELOCITIES V
!| S0W        |-->| EXPLICIT SOURCE TERMS ON VELOCITIES W
!| S1U        |-->| IMPLICIT SOURCE TERMS ON VELOCITIES U
!| S1V        |-->| IMPLICIT SOURCE TERMS ON VELOCITIES V
!| S1W        |-->| IMPLICIT SOURCE TERMS ON VELOCITIES W
!| T3         |-->| WORK ARRAY: NOT USED
!| UN3        |-->| COMPONENTS OF VELOCITY AT PREVIOUS TIME STEP
!| USCE       |-->| VELOCITY FOR SOURCE
!| VN3        |-->| COMPONENTS OF VELOCITY AT PREVIOUS TIME STEP
!| VOLU       |-->| VOLUME AROUND POINTS AT TIME N+1
!| VOLUN      |-->| VOLUME AROUND POINTS AT TIME N
!| VSCE       |-->| VELOCITY FOR SOURCE
!| WN3        |-->| COMPONENTS OF VELOCITY AT PREVIOUS TIME STEP
!| WSN3       |-->| SIGMA-TRANSFORMED VERTICAL VELOCITY COMPONENT

```

```

!
USE BIEF

```

```

!   USE DECLARATIONS_TELEMAC
!   USE DECLARATIONS_TELEMAC3D
!   USE DECLARATIONS_SPECIAL
!

```

```

IMPLICIT NONE

```

```

!
!+++++

```

```

!   INTEGER, INTENT(IN)      :: NPOIN3,NTRAC,LT
!

```

```

!   TYPE(BIEF_OBJ), INTENT(IN)  :: UN3,VN3,WSN3,WN3
!   TYPE(BIEF_OBJ), INTENT(INOUT) :: S0U,S0V,S1U,S1V,S0W,S1W
!   TYPE(BIEF_OBJ), INTENT(INOUT) :: TRAV1,TRAV2

```

```

!   TYPE(BIEF_OBJ), INTENT(IN)  :: VOLU,VOLUN,PRIVE
!

```

```

!   DOUBLE PRECISION, INTENT(IN) :: AT,DT
!   LOGICAL, INTENT(IN)          :: NONHYD
!

```

```

ccc   INTEGER :: IMMERSED_BOUNDARY(99999)

```

```

!   INTEGER :: N_IB,II,I_IBM
!   TYPE (BIEF_OBJ), INTENT(IN)  :: MASKEL
!   TYPE (BIEF_OBJ), INTENT(INOUT) :: SVIDE
!   TYPE (BIEF_MESH)             :: MESH3
!   LOGICAL, INTENT(IN)          :: MSK
!   INTEGER, INTENT(IN)          :: IELM3
!

```

```

!   TYPE (BIEF_OBJ), INTENT(IN)  :: PRESSURE
!

```

```

!   integer :: iii
!

```

```

!   DOUBLE PRECISION :: x_test, y_test, z_test
!
!+++++

```

```

!
!-----
!

```

```

!   BEWARE : BE SURE TO DO S0U = S0U + YOUR SOURCE TERMS
!           BECAUSE S0U HAS ALREADY BEEN INITIALISED IN TRISOU
!

```

```

!
! INITIALISES OTHER SOURCE TERMS
!
S0U%TYPR='Q'
S0V%TYPR='Q'
!
S1U%TYPR='0'
S1V%TYPR='0'
IF(NONHYD) THEN
  S0W%TYPR='0'
  S1W%TYPR='0'
ENDIF
!
DO II = 1, N_IB
ccc  I_IBM = IMMERSED_BOUNDARY(II)
     I_IBM = int(PRIVE%ADR(3)%P%R(II))
!
     S0U%R(I_IBM)=S0U%R(I_IBM)+
& (0.D0-UN3%R(I_IBM))/DT
!
     S0V%R(I_IBM)=S0V%R(I_IBM)+
& (0.D0-VN3%R(I_IBM))/DT
!
ENDDO
!
!-----
!
RETURN
END
!
*****
SUBROUTINE MASK_IB
*****
!
&(IMMERSED_BOUNDARY,N_IB,INSIDE_IB,N_INSIDE_IB,ZF_ORIG)
!
*****
! TELEMAC3D V7P1 20/03/2017
*****
!
USE BIEF
ccc  USE DECLARATIONS_TELEMAC
     USE DECLARATIONS_TELEMAC3D, only: ZF,NPOIN2,NPLAN,X,Y,Z,
& S0U,S0V,S1U,S1V,NPOIN3
!
IMPLICIT NONE
!
! we will use prive 3 and 4 instead (there are 4 prive arrays by default)
ccc  INTEGER :: IMMERSED_BOUNDARY(99999),INSIDE_IB(99999)
     TYPE (BIEF_OBJ) :: IMMERSED_BOUNDARY,INSIDE_IB,ZF_ORIG
     DOUBLE PRECISION :: WreckLevel
     DOUBLE PRECISION :: NODE_DISTANCE
     INTEGER :: N_IB, I_IBM, N_INSIDE_IB, I_INSIDE_IBM
     INTEGER :: NP, I, IJK, K
!
WreckLevel = -0.074
!
DO NP = 1,NPLAN
  DO I=1,NPOIN2
!
    IJK = (NP-1)*NPOIN2+I
!
    S0U%R(IJK)=0.D0
    S0V%R(IJK)=0.D0

```

```

        S1U%R(IJK)=0.D0
        S1V%R(IJK)=0.D0
        IMMERSED_BOUNDARY%R(IJK)=0.D0
        INSIDE_IB%R(IJK)=0.D0
!
        ENDDO
    ENDDO
!
!!! mask the nodes on the immersed boundary
!
        call incylinder(IMMERSED_BOUNDARY%R,N_IB,
&            npoin3,npoin2,nplan,x,y,z)
!
!!! mask the nodes inside of cylinder
        call incylinder(INSIDE_IB%R,N_INSIDE_IB,
&            npoin3,npoin2,nplan,x,y,z)
!
        RETURN
    END SUBROUTINE MASK_IB
!
!
!           *****
!           SUBROUTINE ZERO_IB
!           *****
!
&(INSIDE_IB,N_INSIDE_IB)
!
!*****
! TELEM3D   V7P1                      20/03/2017
!*****
!
    USE BIEF
ccc    USE DECLARATIONS_TELEMAC
    USE DECLARATIONS_TELEM3D, only : U,UC,V,VC
!
ccc    INTEGER :: INSIDE_IB(99999)
    TYPE (BIEF_OBJ) :: INSIDE_IB
    INTEGER :: N_INSIDE_IB, I_INSIDE_IBM
    INTEGER :: I
!
    DO I = 1, N_INSIDE_IB
!
        I_INSIDE_IBM = int(INSIDE_IB%R(I))
!
        U%R(I_INSIDE_IBM)=0.D0
        UC%R(I_INSIDE_IBM)=0.D0
        V%R(I_INSIDE_IBM)=0.D0
        VC%R(I_INSIDE_IBM)=0.D0
!
    ENDDO
!
    RETURN
END SUBROUTINE ZERO_IB

!*****
! SUBROUTINE INCYLINDER
!*****
        subroutine incylinder(incyl,ninside,npoin3,npoin2,nplan,x,y,z)

        USE BIEF
        USE DECLARATIONS_SPECIAL
        IMPLICIT NONE
!
        double precision incyl(npoin3),x(npoin3),y(npoin3),z(npoin3)

```

```

double precision cyl_x0,cyl_y0,cyl_z0
double precision cyl_diam,cyl_len,cyl_theta
double precision cot,sit,pi,AL,BL,CL,XL(2),YL(2),DET,D
double precision tx(4),ty(4),dz,r
integer      npoin3,npoin2,iplan,nplan,ipoin2,ipoin3,ninside
!
! INTRINSIC SQRT,ATAN,COS,SIN
!
! define a cylinder centre point, dimensions and rotation angle
cyl_x0 = 1.94025 ! centre x coordinate (m)
cyl_y0 = 0.070775 ! centre y coordinate (m)
cyl_z0 = -0.072 ! centre z coordinate (m)
cyl_diam = 0.044 ! diameter (m)
cyl_len = 0.094 ! length (m)
cyl_theta = -14.0362 ! angle in degrees from north
!
! =====
!
! define pi (as done in fortran since there is no intrinsic pi variable)
pi = 4.D0 * atan( 1.D0 )
!
! make plan view reactangle coordinates
cot = cos(-cyl_theta*pi/180.0)
sit = sin(-cyl_theta*pi/180.0)
!
! coordinates of rectangle
tx(1) = cyl_x0 - cyl_diam/2*cot + cyl_len/2.0*sit
ty(1) = cyl_y0 - cyl_diam/2*sit - cyl_len/2.0*cot
tx(2) = cyl_x0 + cyl_diam/2*cot + cyl_len/2.0*sit
ty(2) = cyl_y0 + cyl_diam/2*sit - cyl_len/2.0*cot
tx(3) = cyl_x0 + cyl_diam/2*cot - cyl_len/2.0*sit
ty(3) = cyl_y0 + cyl_diam/2*sit + cyl_len/2.0*cot
tx(4) = cyl_x0 - cyl_diam/2*cot - cyl_len/2.0*sit
ty(4) = cyl_y0 - cyl_diam/2*sit + cyl_len/2.0*cot
!
! make a centreline through cylinder
cot = cos(cyl_theta*pi/180.0)
sit = sin(cyl_theta*pi/180.0)
XL(1) = cyl_x0 - cyl_len/2.0*sit
YL(1) = cyl_y0 - cyl_len/2.0*cot
XL(2) = cyl_x0 + cyl_len/2.0*sit
YL(2) = cyl_y0 + cyl_len/2.0*cot
!
! calculate distance to line parameters (outside loop)
AL=YL(1)-YL(2)
BL=-XL(1)+XL(2)
CL=XL(1)*YL(2)-XL(2)*YL(1)
DET=sqrt(AL**2+BL**2)
!
! zero ninside
ninside = 0
!
! find coordinates in rectangle
do ipoin2=1,npoin2
!
! check z if in 2d rectangle
IF( INPOLY(X(ipoin2),Y(ipoin2),tx,ty,4) ) then
!
! loop through z planes
do iplan=1,nplan
!
! 3d index
ipoin3=ipoin2+npoin2*(iplan-1)

```

```

!
! initialise to zero
ccc      incyl(ipoin3)=0.D0
!
! get the horizontal distance to the cylinder centreline
D=((AL*x(ipoin3))+(BL*y(ipoin3))+CL)/DET
!
! calculate the radius of the 3D point from the centreline
dz=(z(ipoin3)-cyl_z0)
r=sqrt(D**2+dz**2)
!
! check that the fish are within radius
if (r.LE.cyl_diam/2.0) then
    ninside=ninside+1
    incyl(ninside)=dble(ipoin3)
endif
!
    enddo
!
endif
!
enddo
!
RETURN
END

```



## G. HE Implementation in TELEMAC

```

!
! *****
! SUBROUTINE BEDLOAD_HIDING_FACTOR_GAIA
! *****
!
! &(ACLADM, HIDFAC, NPOIN, HIDI, DCLA, K_H_Y, HIDING)
!
! *****
! GAIA
! *****
!
!>@brief Hiding factor for each node, sediment class and time step.
!
! ~~~~~
!>@param[in] ACLADM Mean diameter of active layer
!>@param[in] DCLA Sediment grain diameter
!>@param[in] HIDFAC Hiding factor formulas
!>@param[in] HIDI Hiding factor for particular size class (hidfac =0)
!>@param[in,out] HIDING Hiding factor correction
!>@param[in] K_H_Y Karim, holly & yang constant
!>@param[in] NPOIN Number of points
! ~~~~~
!
! USE INTERFACE_GAIA,
! & EX_BEDLOAD_HIDING_FACTOR => BEDLOAD_HIDING_FACTOR_GAIA
! USE BIEF
! USE DECLARATIONS_SPECIAL
!>>>TBE - need the ratio of gravel, so get RATIO_SAND variable
! USE DECLARATIONS_GAIA, ONLY : RATIO_SAND
!<<<TBE
! IMPLICIT NONE
!
! TYPE(BIEF_OBJ), INTENT(IN) :: ACLADM
! INTEGER, INTENT(IN) :: HIDFAC, NPOIN
! DOUBLE PRECISION, INTENT(IN) :: HIDI, DCLA, K_H_Y
! TYPE(BIEF_OBJ), INTENT(INOUT) :: HIDING
!
!
! INTEGER :: IPOIN, J
! DOUBLE PRECISION :: C1, C2
!
! =====
! =====
! PROGRAM !
! =====
! =====
!
! *****
! IA - CONSTANT HIDING FACTOR
! *****
!
! IF (HIDFAC == 0) THEN
!
! CALL OS('X=C ', X=HIDING, C=HIDI)
!
! *****
! IB - EGIAZAROFF FORMULATION
! *****
!
! ELSEIF (HIDFAC == 1) THEN
!
! C1 = LOG10(19.D0)

```

```

C2 = 19.D0*DCLA
DO J = 1, NPOIN
  HIDING%R(J) = (C1/LOG10(C2/ACLADM%R(J)))**2
ENDDO

!
! *****
! IC - ASHIDA AND MICHIE FORMULATION
! *****
!
ELSEIF (HIDFAC == 2) THEN
!
  C1 = LOG10(19.D0)
  C2 = 19.D0*DCLA
  DO J = 1, NPOIN
!
    IF(DCLA/ACLADM%R(J) >= 0.4D0) THEN
      HIDING%R(J) = (C1 / LOG10(C2/ACLADM%R(J)) )**2
    ELSE
      HIDING%R(J) = 0.85D0*(ACLADM%R(J)/DCLA)
    ENDIF
!
  ENDDO
!
!>>>TBE - added Connor's formulation as option 3
! *****
! ID - C. MCCARRON & A.G. DAVIES FORMULATION
! *****
!
ELSEIF (HIDFAC == 3) THEN
!
  DO J = 1, NPOIN
    C1 = RATIO_SAND(2,1,IPOIN)
    ! hard coded for size class 2 (gravel), layer 1 (active layer)
    C2 = 0.68+(0.86-0.68)*C1**1.73D0
    HIDING%R(J) = (DCLA/ACLADM%R(J))**(-1.D0*C2)
  ENDDO
!<<<TBE
!
! *****
! IE - KARIM, HOLLY AND YANG FORMULATION
! *****
!
ELSEIF (HIDFAC == 4) THEN
!
  CALL OS('X=1/Y ', X=HIDING, Y=ACLADM)
  CALL OS('X=CX ', X=HIDING, C=DCLA)
  CALL OS('X=Y**C ', X=HIDING, Y=HIDING, C=K_H_Y)
!
ELSE
!
  WRITE(LU,*) 'UNKNOWN HIDING FACTOR FORMULA: ',HIDFAC
  CALL PLANTE(1)
  STOP
!
ENDIF
!
=====
=====
!
RETURN
END SUBROUTINE BEDLOAD_HIDING_FACTOR_GAIA

! *****

```

```

SUBROUTINE BEDLOAD_MEYER_GAIA
*****
!
!
&(TETAP,HIDING,HIDFAC,DENS,GRAV,DCLA,AC,ACP,QSC,SLOPEFF,COEFPN,
& XMVS)
!
!*****
! GAIA
!*****
!
!>@brief Meyer-Peter bedload transport formulation.
!
!~~~~~
!>@param[in]  AC    Critical shields parameter
!>@param[in,out] ACP  Modified shields parameter
!>@param[in,out] COEFPN Correction of transport for sloping bed effect
!>@param[in]  DENS  Relative density of sediment
!>@param[in]  DCLA  Sediment grain diameter
!>@param[in]  GRAV  Acceleration of gravity
!>@param[in]  HIDFAC Hiding factor formulas
!>@param[in]  HIDING Hiding factor correction
!>@param[in,out] QSC  Bed load transport rate
!>@param[in]  SLOPEFF Formula for slope effect
!>@param[in]  TETAP  Adimensional skin friction
!>@param[in]  XMVS  Sediment density
!~~~~~
!
USE BIEF
USE INTERFACE_GAIA, EX_BEDLOAD_MEYER => BEDLOAD_MEYER_GAIA
USE DECLARATIONS_GAIA, ONLY : MPM_ARRAY
USE DECLARATIONS_SPECIAL
IMPLICIT NONE
!
!!+--+--+--+--+--+--+--+--+--+--+--+--+--+--+--+--+--+--+--+--+--+
!
TYPE(BIEF_OBJ), INTENT(IN)  :: TETAP, HIDING
INTEGER,          INTENT(IN)  :: HIDFAC, SLOPEFF
DOUBLE PRECISION, INTENT(IN)  :: DENS, GRAV, DCLA, AC, XMVS
TYPE(BIEF_OBJ), INTENT(INOUT) :: ACP ! WORK ARRAY T1
TYPE(BIEF_OBJ), INTENT(INOUT) :: QSC, COEFPN
!
!!+--+--+--+--+--+--+--+--+--+--+--+--+--+--+--+--+--+--+--+--+--+
!
INTEGER I
DOUBLE PRECISION :: C2
!
=====
!
PROGRAM                                !
=====
!
CALL CPSTVC(QSC,ACP)
CALL OS('X=C ', X=ACP, C=AC)
!
! SLOPE EFFECT: SOULBY FORMULATION
!
IF(SLOPEFF.EQ.2) THEN
CALL OS('X=XY ', X=ACP, Y=COEFPN )
ENDIF
!
! BEDLOAD TRANSPORT CORRECTED FOR EXTENDED GRAIN SIZE
! WITH VARIABLE MPM_COEFFICIENT
!
C2 = SQRT(GRAV*DENS*DCLA**3)

```

```

!
!>>>TBE - included HIDFAC option 3 (was unused) for Connor's hiding function
ccc  IF(HIDFAC.EQ.1.OR.HIDFAC.EQ.2) THEN
      IF(HIDFAC.EQ.1.OR.HIDFAC.EQ.2.OR.HIDFAC.EQ.3) THEN
!<<<TBE
!  CALL OS('X=XY  ', X=ACP, Y=HIDING)
!  CALL OS('X=Y-Z  ', X=QSC, Y=TETAP, Z=ACP)
!  CALL OS('X=+(Y,C)', X=QSC, Y=QSC, C=0.D0)
!  CALL OS('X=Y**C  ', X=QSC, Y=QSC, C=1.5D0)
!  CALL OS('X=CX   ', X=QSC, C=C2)
!  CALL OS('X=XY   ', X=QSC, Y=MPM_ARRAY)
      DO I=1,QSC%DIM1
        QSC%R(I)=C2*MPM_ARRAY%R(I)
      &      *SQRT(MAX(TETAP%R(I)-ACP%R(I)*HIDING%R(I),0.D0))**3
      ENDDO
    ELSE
!  CALL OS('X=Y-Z  ', X=QSC, Y=TETAP, Z=ACP)
!  CALL OS('X=+(Y,C)', X=QSC, Y=QSC, C=0.D0)
!  CALL OS('X=Y**C  ', X=QSC, Y=QSC, C=1.5D0)
!  CALL OS('X=CX   ', X=QSC, C=C2)
!  CALL OS('X=XY   ', X=QSC, Y=HIDING)
!  CALL OS('X=XY   ', X=QSC, Y=MPM_ARRAY)
      DO I=1,QSC%DIM1
        QSC%R(I)=C2*MPM_ARRAY%R(I)*HIDING%R(I)*SQRT(
      &      MAX(TETAP%R(I)-ACP%R(I),0.D0))**3
      ENDDO
    ENDIF
!
!  SOLID DISCHARGE IS TRANSFORMED IN [kg/(m*s)]
!
      CALL OS('X=CX   ', X=QSC, C=XMVS)
=====
!
      RETURN
      END

```